University of California
Santa Barbara

Tailored composite microstructures via direct ink writing with acoustophoresis

A dissertation submitted in partial satisfaction
of the requirements for the degree

Doctor of Philosophy
in
Materials

by

Leanne Friedrich

Committee in charge:

Professor Matthew Begley, Chair
Professor Daniel Gianola
Professor Robert McMeeking
Professor Carl Meinhart

March 2020

The Dissertation of Leanne Friedrich is approved.

Professor Daniel Gianola

Professor Robert McMeeking

Professor Carl Meinhart

Professor Matthew Begley, Committee Chair

January 2020

Tailored composite microstructures via direct ink writing with acoustophoresis

Leanne Friedrich

Dedicated to Grandma Lily and Uncle Doug

Acknowledgements

My advisor Matthew Begley has been instrumental in making this research happen, and I am incredibly grateful for his professional and intellectual guidance. I would also like to acknowledge the rest of my committee, Daniel Gianola, Robert McMeeking, and Carl Meinhart, for their input and support. The Begley group has been a crucial resource, and I particularly want to thank Rachel Collino, Tyler Ray, James Cornell, and Rachel Fleming for pioneering DIW with acoustophoresis and for sharing their expertise with me. Additionally, I'd like to acknowledge my group mate Drew Melchert and interns T.J. Polk and Simon Blome, who have contributed considerable work to the development of DIW with acoustophoresis. Finally, many patient and insightful lab staff members have helped me with this research, including David Bothman, Deryck Stave, Rachel Behrens, Joshua Johnson, Aidan Hopkins, and Don Freeborn.

This work was supported by the Institute for Collaborative Biotechnologies through contract no. W911NF-09-D-0001 from the U.S. Army Research Office and a UCSB Chancellor's Fellowship. The work used the Microfluidics Laboratory and the NanoStructures Cleanroom Facility at the California Nanosystems Institute, the Nanofabrication Facility (a part of the NSF-funded National Nanotechnology Infrastructure Network), and the Polymer Characterization Facility supported by the MRSEC Program of the National Science Foundation under award NSF DMR 1121053 (a member of the NSF-funded Material Research Facilities Network) at UCSB.

Curriculum Vitæ

Leanne Friedrich

Education

2020	Doctor of Philosophy (Ph.D.) in Materials (Expected) University of California, Santa Barbara.
2015	Bachelor of Science (B.S.) in Materials Science and Engineering Northwestern University.

Research

2015–2020	**Graduate student researcher**, Prof. Matthew Begley Materials, UC Santa Barbara
2015	**Research intern**, Prof. Dirk Gillespie Physiology & Biophysics, Rush University
2013–2015	**Undergraduate student researcher**, Prof. Derk Joester Materials Science and Engineering, Northwestern University
2014	**Research intern**, Dr. Brett Helms Molecular Foundry, Lawrence Berkeley National Laboratory
2013	**Research intern**, Prof. Kerry Hipps Materials Science & Engineering, Washington State University
2012–2013	**Undergraduate student researcher**, Dr. William Russin Biology, Northwestern University

Teaching

Fall 2018	**Teaching Assistant**, MATRL 100A: Structure and Properties I

Publications

1. **L. Friedrich**, M. R. Begley, "Printing direction dependent microstructures in direct ink writing," Submitted for Publication, 2020.

2. **L. Friedrich**, M. R. Begley, "Changes in filament microstructures during direct ink writing with yield stress fluid support," Submitted for Publication, 2020.

3. **L. Friedrich**, M. R. Begley, "Corner accuracy in direct ink writing with support material," Submitted for Publication, 2020.

4. **L. Friedrich**, W. S. Lam, L. Gordon, L. Brooker, R. Chipman, and D. Joester, "Kaleidoscope Eyes: Microstructure and Optical Performance of Chiton Ocelli," In Preparation, 2019.

5. D.S. Melchert, R. R. Collino, T. R. Ray, N. Dolinski, **L. Friedrich**, M. R. Begley, and D. S. Gianola, "Flexible Conductive Composites with Programmed Electrical Anisotropy Using Acoustophoresis," Advanced Materials Technologies, vol. 4, no. 12, pp. 1900586, 2019.

6. **L. Friedrich** and M. Begley, In Situ Digital Image Analysis in Direct Ink Writing, Polymer Additive Manufacturing: Recent Developments, pp. 131–149, 2019.

7. **L. Friedrich** and M. Begley, "In situ characterization of low-viscosity direct ink writing: stability, wetting, and rotational flows," Journal of Colloid and Interface Science, vol. 529, pp. 599–609, 2018.

8. R. R. Collino, T. R. Ray, **L. M. Friedrich**, J. D. Cornell, C. D. Meinhart, and M. R. Begley, "Scaling relationships for acoustic control of two-phase microstructures during direct-write printing," Materials Research Letters, vol. 6, no. 3, pp. 191–198, 2018.

9. **L. Friedrich**, R. Collino, T. Ray, and M. Begley, "Acoustic control of microstructures during direct ink writing of two-phase materials," Sensors and Actuators A Physical, vol. 268, pp. 213–221, 2017.

10. **L. Friedrich**, R. Collino, T. Ray, and M. Begley, "Scaling relationships for direct ink writing with acoustic focusing," in TMS 2017 146th Annual Meeting & Exhibition Supplemental Proceedings, 2017, pp. 137–145.

11. **L. Friedrich** and D. Gillespie, "Improving charge-sensitive biomolecule sensors with the right choice of electrolyte," Sensors and Actuators B Chemical, vol. 230, pp. 281–288, 2016.

Presentations

1. **L. Friedrich** and M. R. Begley, "Embedded 3D Printing with Acoustic Focusing," APS March Meeting, Boston, MA, 2019.

2. **L. Friedrich** and M. Begley, "Composite Ink Extrusion Behaviors in Direct Ink Writing with Acoustic Focusing," APS March Meeting, Los Angeles, CA, 2018.

3. **L. Friedrich** and M. Begley, "Extrusion of Direct-write Inks with Particle Gradients," TMS Annual Meeting & Exhibition, Phoenix, AZ, 2018.

4. **L. Friedrich**, R. Collino, T. Ray, and M. Begley, "Scaling relationships for direct ink writing with acoustic focusing," TMS Annual Meeting & Exhibition, San Diego, CA, 2017.

Abstract

Tailored composite microstructures via direct ink writing with acoustophoresis

by

Leanne Friedrich

Additive manufacturing techniques which enable control over the placement and orientation of particles within composite inks can produce structures with tailored gradients in structural and functional properties. One such technique is direct ink writing with acoustophoresis (DIWA), wherein a composite ink is extruded through a direct-write nozzle containing a standing bulk acoustic wave which aligns and positions particles. Driving force-based scaling relationships contextualize processing-structure relationships in DIWA. In a series of experiments which progress in geometric complexity from basic primitives to complete structures, a physical framework is constructed for controlling filament microstructures and external geometries in DIWA. In isolated filaments, there are trade-offs between focusing and form holding. Increasing the ink viscosity, increasing the print speed, and decreasing the acoustic wave amplitude widen the spatial distribution of particles in agreement with scaling relationships for acoustophoresis, but more viscous inks improve form holding. In the print bead between the nozzle and substrate, digital image analysis is used to measure filament stability, nozzle wetting, and rotational flows in the low-viscosity inks required for acoustophoresis. Viscocapillary lubrication theory accurately predicts the bounds of stability, and the contact line position and angle can be used to detect the beginnings of filament rupture, allowing for algorithms which prevent rupture *in-situ*. In polygonal prisms, the internal structure of filaments changes during deposition into layer-by-layer and bath support gels. Filament microstructures change during deposition, during relaxation, and when the nozzle returns to write neighboring lines. Experimental flow fields and particle distributions suggest that inertia and viscoplasticity influence the

filament microstructure just after deposition and the microstructure of neighboring filaments, and interfacial energy and gravity cause filaments to spread after deposition. An analytical model is proposed to diagnose sources of direction dependent microstructures as a function of acoustics, inertia, viscous dissipation, and stage calibration. The support geometry can be used to accentuate or suppress aspects of this direction dependence. Finally, inertia swells written corners, and capillarity smooths written corners, leading to distortions in filament microstructures at corners. Bath support suppresses these corner defects.

Contents

List of Figures

List of Tables

Chapter 1

Introduction

1.1 Motivation

Additive manufacturing enables the fabrication of structures with high geometric and functional complexity. Notably, additive manufacturing of composite materials has enabled functional structures including living tissues,[1, 2, 3, 4] orthopedic scaffolds,[5, 6, 7] lightweight load-bearing structures,[2, 6] heat sinks,[6] and electrical circuits.[6] On-the-fly manipulation of encapsulated phases within composite filaments enables an additional layer of design complexity through spatial variation in the structural and functional properties of the deposited material. This work establishes instrumentation, materials, and printing parameters for one such method: direct ink writing with integrated acoustophoresis (DIWA).

In DIWA, a composite ink is extruded through a nozzle onto a substrate and cured after deposition. A piezoelectric actuator attached to the nozzle establishes a standing bulk acoustic wave in the nozzle, which aligns and assembles particles at the wave nodes or antinodes. DIWA has been used to print composites with variations in stiffness,[8] electrical conductivity,[9] and cell orientation.[10] This work maps the printing space for DIWA in terms of material properties and printing parameters and establishes a fundamental framework to

describe behavior of composite filaments during the course of the printing process.

There has been considerable work in the literature describing methods to manipulate polymer matrix composite microstructures during 3D printing (Fig. 1.1). Polymer matrix composite 3D printing techniques have included fused deposition modeling (FDM), stereolithography additive manufacturing (SLA), inkjet printing, and direct ink writing (DIW). Composite manipulation methods which have been incorporated into those techniques include acoustic fields, magnetic fields, electric fields, shear migration and alignment, and active mixing. Other promising techniques include optical fields, which have been used to manipulate fixed volumes of cells in biomaterials.[11] Many of these papers provide only a single-layer demonstration of the printing technique, while others print in three dimensions.

Acoustic fields have been incorporated into DIW to produce colloidal solids,[12], structural composites,[13] flexible electrically conductive composites,[9] and biomaterials[10, 14] (Fig. 1.1A). Piezos can be attached directly and indirectly to a variety of nozzles including glass-on-silicon microfluidic chips,[13, 15, 16] square glass capillaries,[12, 17, 18, 19, 20, 21] rectangular glass capillaries,[9] and cylindrical glass pipets.[10, 14] While a range of materials has been manipulated in direct-write nozzles including polymer microparticles in water and corn syrup, ceramic microparticles in polymer nanocomposites, and cells in biopolymers, only the paper presented in Chapter 6 has demonstrated three-dimensional writing capabilities.[19]

Acoustic fields have been incorporated into SLA to produce biomaterials,[22, 23, 24, 25] structural composites,[26] electrically conductive composites,[27, 28] and thermal transport devices[29] (Fig. 1.1B). Piezos can be attached to the edges of the print bath and used two at a time to produce a finite set of particle orientations within the bath[27, 29] or used in combinations to produce more complex patterns like crossed lines[23, 24, 30] and periodic clusters of particles.[22, 25, 31, 32] A quasi-3D implementation of SLA with acoustophoresis has also fabricated more complex, non-periodic structures using physical hologram plates which template the acoustic field.[33] Three-dimensional implementations have only been executed with

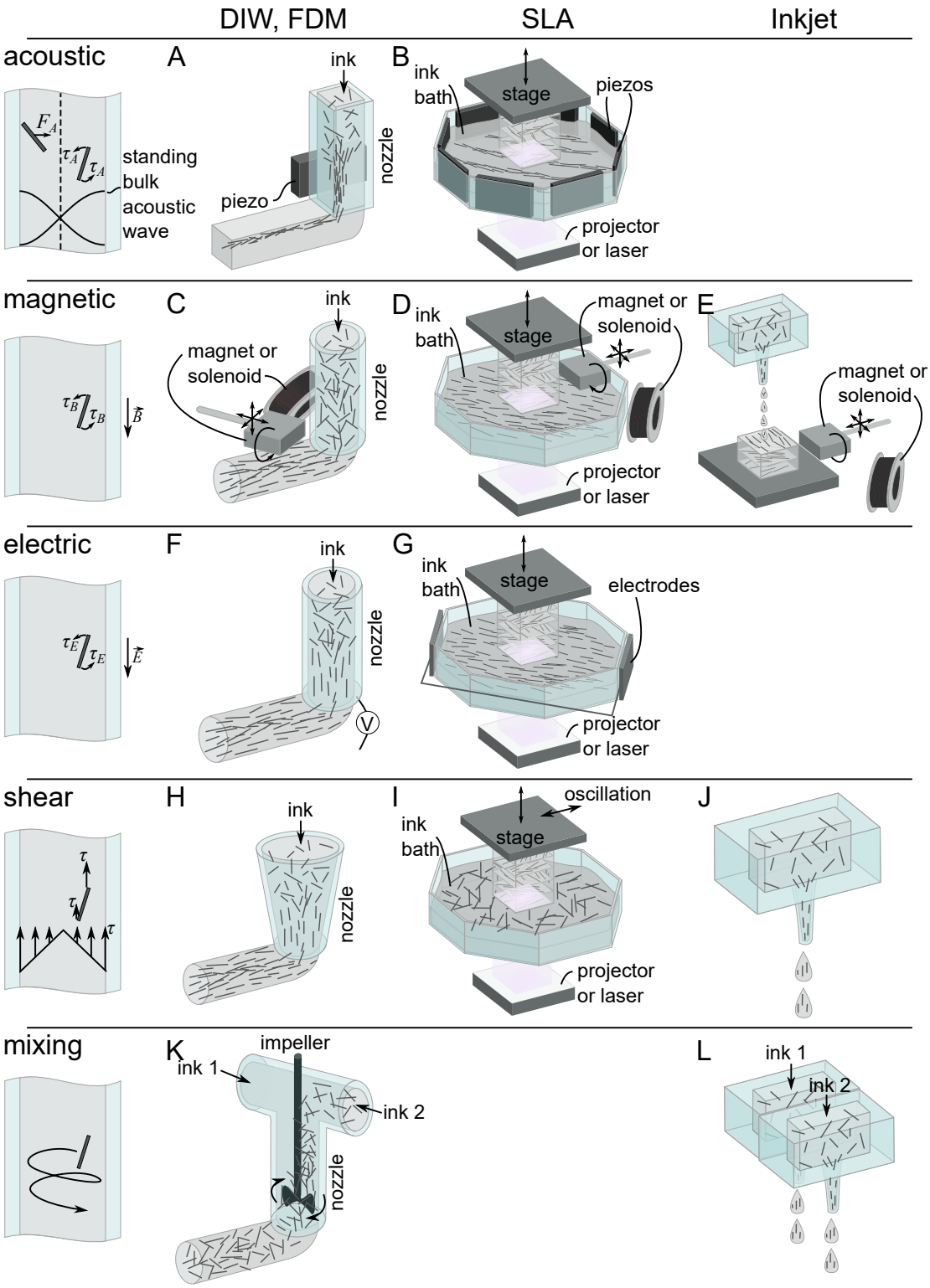

Figure 1.1: Schematics of printing modalities for manipulating microstructures of polymer matrix composites using external fields.

carbon, metallic, and PDMS microparticles in low-viscosity photopolymers.[27, 28, 29, 30, 33]

Acoustic fields have also been used to manipulate metallic microstructures in laser beam melting[34] and laser engineered net shaping[35, 36]. Of course, acoustic fields are often a major component of inkjet printing, but they have only been used to eject droplets from the print head, not to manipulate the internal structure of the droplets.[37]

Magnetic fields have been incorporated into DIW by introducing solenoids at the nozzle exit, manipulating the particle orientation after deposition (Fig. 1.1C).[38, 39] Magnetic fields have also been incorporated by introducing a permanent magnet that can rotate and translate near the written structure.[40] The three-dimensional implementations published so far used ceramic particles in epoxies.[38, 40]

Magnetic fields have been incorporated into SLA for bioprinting,[41] structural composites, [42, 43] and electrically conductive structures[44] (Fig. 1.1D). Magnetic fields are introduced by rotating and translating a permanent magnet underneath the resin vat[45, 46, 47, 48] or positioning orthogonal solenoids around the print bath.[49, 50] The three-dimensional implementations published so far used ferromagnetic microparticles in low-viscosity resins.[45, 47, 48, 49, 50]

Magnetic fields are the only actuated fields that have been used to manipulate particles in inkjet printing (Fig. 1.1E). An electromagnet[51] or permanent magnet[52, 53] is introduced at the substrate, which makes this technique similar to the DIW techniques which implement an on-substrate magnetic field.[40] In one case, the print nozzle is shielded from the magnetic field.[52]

Electric fields have been introduced into FDM to fabricate piezoelectrics (Fig. 1.1F).[54, 55, 56] A voltage is established between the nozzle and the substrate which aligns the piezoelectric particle dipoles within the matrix.[54, 55, 56] During DIW, electric fields have been used to align silver nanowires, which are too small to focus with acoustophoresis.[57]

Electric fields have been incorporated into SLA for structural applications (Fig. 1.1G).[58]

By attaching electrodes to the curing source[59] or inserting electrodes into the resin bath,[58] electrically conductive particles can be aligned in low-viscosity resins. Like acoustic fields, electric fields have also been implemented in inkjet printing, but only to aid expulsion of droplets, not to manipulate the microstructure of the droplets.

Shear-induced alignment of elongated particles has been long and oft-described as a way to manipulate the properties of printed composite filaments in DIW[60, 61, 62, 63, 64, 65, 66, 67, 68] and FDM[69, 70, 71, 72, 73, 74, 75]. Due to differences in shear stress between the surface and center of the nozzle, particles rotate to align with the printing direction (Fig. 1.1H).[76] However, shear-induced alignment or hydrodynamic alignment in the nozzle cannot be actuated like acoustic, magnetic, and electric fields, so gradients cannot be created with shear alignment in DIW and FDM. The one way to produce shear-induced gradients in DIW is rotational 3D printing, wherein rotation of the nozzle induces a shear stress between the nozzle and substrate which aligns particles in prescribed orientations.[77] Similarly, in SLA, oscillatory motion of the stage relative to the resin bath can align particles within layers (Fig. 1.1I).[78] In inkjet printing, like DIW and FDM, particles align at the exit of the nozzle (Fig. 1.1J).[79]

Finally, particle concentrations can be modulated throughout the print through multimaterial mixing, which has been demonstrated several times in DIW (Fig. 1.1K).[40, 80, 81, 82, 83, 84, 85, 86] By introducing multiple sources of ink into the print nozzle and mixing them using an active mixer[83] or by leveraging the design of the nozzle to introduce instabilities that drive mixing,[40, 80, 82] a smoothly varying particle concentration can be introduced into the printed part. Mixing can also be combined with other techniques like magnetic fields for further control over part properties.[40] Mixing is also commercially implemented in multimaterial inkjet printing, although multimaterial inkjet printing usually puts different inks in different cartridges, so any mixing that occurs must occur on the substrate.[87] Because inkjet printing uses very low viscosity fluids, it is possible for inks to mix on the substrate via diffu-

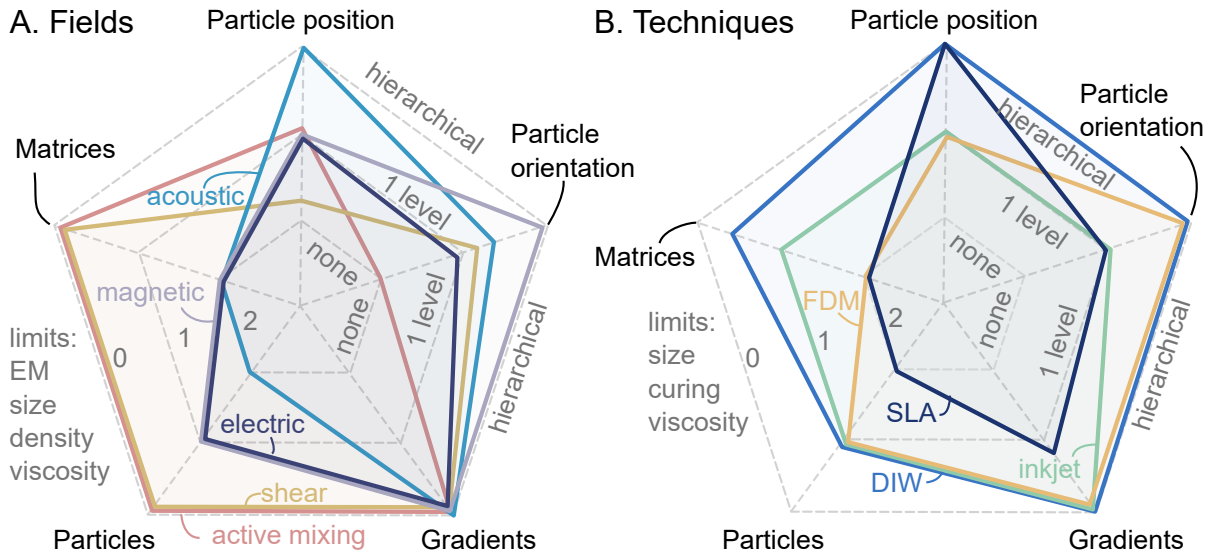

Figure 1.2: Best demonstrated manipulation of particle position, particle orientation, and property gradients in terms of no control, printing-level control, and hierarchical control; matrix and particle limitations in terms of electromagnetic, particle size, matrix and particle density, matrix viscosity, and matrix curing limits for A) fields and B) printing methods.

sion, unlike DIW inks, which are higher-viscosity and require active mixing.

There are trade-offs associated with each printing method (Fig. 1.2). Methods can offer no control, one level of control, or hierarchical control over particle positions, particle orientations, and smooth gradients. The single level of control is usually imposed via the print path, while hierarchical control is achieved in both the print path and within the printed filament.

In all techniques, particle positioning can be achieved in some capacity (Fig. 1.2A). Shear can only control the placement of particles through the creation of positive and negative space in the part, but it cannot control the placement of particles within the matrix. A single level of control over particle positioning implies that particles can be placed within the matrix. In active mixing, particles can be placed within the part by changing the ratio of particle-filled to particle-poor feedstocks along the print path. Magnetic and electric fields can be imposed within a printed layer to induce particle migration.[40] Acoustic fields offer more complex hierarchical control over particle positioning because they can position particles within sub-

units of the printed structure. For example, multiple nodes or complexly shaped pressure fields can be established within a layer in SLA or within the nozzle in DIW.[9, 33]

The various fields exhibit a large range of capabilities for controlling particle orientation. A single level of control implies that a single particle orientation across the part is achievable, while hierarchical control enables control over orientation within a printing subunit like a layer or filament. Active mixing cannot control particle orientation within the matrix or the overall part. Although it is conceptually possible to implement hierarchical control using electric fields, electric fields have only been demonstrated to align particles with the printing direction.[54, 55, 56, 57] Shear via nozzle rotation can produce a continuum between alignment with the print direction and transverse to the printing direction, putting it a slight step above single-level orientation control.[77] Acoustic fields can produce particle orientations which are either random, aligned with the print direction, or somewhere in between, landing acoustic fields in between single-level and hierarchical control over orientation.[13, 15] Only magnetic fields have been demonstrated to enable hierarchical control over particle orientation, since changing the orientation of the magnetic field can change the orientation of particles within a printed filament across a multidimensional continuum.[38]

All five fields can produce hierarchical gradients in material properties through modulation of properties within and between printed layers and filaments, but this is not necessarily true for every implementation (Fig. 1.2A). While magnetic, electric, and acoustic fields can be smoothly varied through modulation of the field amplitude, and active mixing can be smoothly varied by changing the flow rates of the supplied inks, shear alignment can only be smoothly varied in the case of a rotating nozzle.[77] In typical shear alignment applications, the particle orientation can only be aligned with the printing direction, dropping shear down to one level of gradient control.

Printability can be measured in terms of the number of restrictions that are imposed on the ink materials (Fig. 1.2A). Notably, this is not the same as the percentage of all materials

that are eliminated. For example, acoustics limit the printable particles in size and acoustic contrast factor with the matrix (a combination of densities and compressibilities), since the primary acoustic radiation force scales with particle size and acoustic contrast factor.[15, 16] Electric and magnetic fields are restricted to only particles with electromagnetic permittivity contrast with the matrix, but can manipulate smaller particles than can be manipulated with acoustic fields.[88] Note that non-magnetic materials like cells can be functionalized with magnetic particles and molecules to enable magnetic focusing.[11] Thus, even though acoustics still can manipulate a larger range of particles than magnetic fields because there are far more non-magnetic particles than magnetic particles (where magnetic refers to permittivity contrast with polymeric matrices), more factors must be considered when selecting particles for acoustophoresis. Of course, particles still experience size-dependent Stokes' drag under magnetic fields, but acoustic fields feature additional size scaling.[15, 16] Shear and active mixing place no restrictions on the types of particles which can be used.

Similarly, shear and active mixing place no restrictions on matrices, although mixing is faster in low-viscosity matrices, and shear-induced changes in particle orientation are likely best preserved in high-viscosity matrices. Acoustic, magnetic, and electric fields all place two limits on matrices, one of which is viscosity. High viscosity matrices pose larger Stokes' drag forces, limiting the speed at which particles can rotate and migrate during acoustic, magnetic, and electric focusing. As mentioned earlier, matrices for acoustic fields must have a high acoustic contrast with the particles, and matrices for magnetic and electric fields must have a high electromagnetic contrast with the particles.

The techniques with which the fields are paired also place restrictions on the controllability of the process and the eligible material systems (Fig. 1.2B). Direct ink writing and SLA enable hierarchical particle positioning, since particles can be placed in complex patterns within a filament or SLA layer using acoustic fields, and filaments can be placed within the printed part.[15, 18, 19, 20, 33] While FDM hypothetically could enable particle positioning

within the filament via acoustic fields and placement of filaments, this has not yet been demonstrated. Hypothetically, placement of particles within inkjet droplets should also be possible using acoustophoresis, but this has not been demonstrated.

As with particle positions, only DIW and FDM enable hierarchical control of particle orientation, since the orientation of the particles within the filament can be controlled using acoustic, magnetic, or electric fields, and the orientation of the filament provides a second level of orientation control.[15, 39, 56] In SLA and inkjet printing, orientations are uniform throughout the print bath or printed structure, enabling only a single level of orientation control using magnetic, electric, acoustic, or shear fields.

Hierarchical gradients can be achieved in DIW, FDM, and inkjet printing by smoothly varying properties within the filament or droplet and between filaments or droplets.[13, 51, 56] While SLA could loosely be considered to have gradients within layers through particle placement with acoustic fields and gradients between layers by varying that particle placement, the variations do not fall as smoothly on a continuum as the variations achievable with DIW and FDM.[27]

The techniques also place restrictions on material properties. In FDM, inkjet, and DIW, particles are limited in size because particles that are too large will cause clogging. In SLA, particularly for through-volume approaches, particles must be transparent in order to allow curing. This is also an issue for many DIW and inkjet approaches which use photopolymers, although DIW and inkjet printing can be executed through solvent evaporation[89] or thermal curing.[15]

DIW and inkjet place viscosity limits on matrices, where inkjet inks must be very low viscosities,[90] and DIW inks generally need to be viscous, although support material expands the range of possible inks for DIW. In addition to having a high enough viscosity to hold form after deposition, FDM inks must be thermoplastics. In addition to having a low enough viscosity to flow into the curing gap, SLA inks must be photopolymers.

1.2 Requirements and constraints for DIW

Considerable theoretical, numerical, and experimental work has been performed to predict the printability of materials and printing conditions in DIW. Printability can be characterized in terms of flow rates, rheology of the ink and support, the shape of the printed filament, spanning lengths, deformation of existing layers, and printer configurations.

1.2.1 Flow rates

Models may be used to predict flow rates within the nozzle as a function of geometry and extrusion pressures [91, 92, 93, 94, 95, 96, 97]. Chapters 5–8 do not use these formulations because they tend to be written for nozzles with circular cross-sections and inks which perfectly fit rheological models. In contrast, inks used in this dissertation exhibit slight deviations from the common rheological models, requiring adjustment factors as shown in Chapter 4. Additionally, nozzles used in this work have rectangular cross-sections. As such, Chapters 5–8 calibrate extrusion speeds by measuring extruded masses, ensuring more accurate flow rates than the predictions.

1.2.2 Rheology

The behavior of DIW inks depends on the storage modulus (G') and loss modulus (G''), determined using a stress sweep on a rheometer. These moduli vary throughout the printing process as varying shear stresses are imposed on the inks. If $G' > G''$, the material behaves as a solid. If $G'' > G'$, the material behaves as a liquid. Duty, et. al. subdivide these behaviors into four viscoelastic categories.[91] Elastic solids such as cured thermosets have $G' >> G''$. Viscoelastic solids such as hydrogel support baths for DIW have $G' > G''$ under static conditions. Viscoelastic liquids such as most DIW inks have $G'' > G'$ under printing conditions. Viscous liquids such as many embedded DIW inks have $G'' >> G'$.[91] In addition to the storage and

d	Diameter of written filament
d_{in}	Inner diameter of circular nozzle
d_{out}	Outer diameter of circular nozzle
d_x, d_y	Line spacing in x and y
E	Young's modulus
g	Acceleration due to gravity
G'	Storage modulus
G'_0	Zero shear storage modulus
G''	Loss modulus
h	Stand-off distance
h_b	Height of the bead
h_{fs}	Maximum height of unsupported filament
h_m	Height of the model
H^*	Dimensionless standoff distance $h/(\alpha d_{in})$
K	Consistency index
l_c	Critical feature length
L_{span}	Span length
n	Dimensionless flow index
t_{layer}	Characteristic layer time
t_p	Characteristic processing time
t^*	Characteristic time scale for viscous flow
V^*	Dimensionless velocity v_s/v_f
v_s	Translation speed
v_f	Flow speed
y	Position along filament
α	Die swell factor
γ	Surface tension
$\dot{\gamma}$	Shear strain rate
δ, δ_{limit}	Beam deflection distance, maximum acceptable beam deflection distance
ϵ_{limit}	Acceptable deformation strain
η	Viscosity
η_0	Zero shear viscosity
η_∞	Infinite shear viscosity
λ	Relaxation time
ρ	Density
σ_{HP}	Hydrostatic pressure
τ	Shear stress
τ_y	Shear yield stress

Table 1.1: Variables involved in material property requirements for DIW.

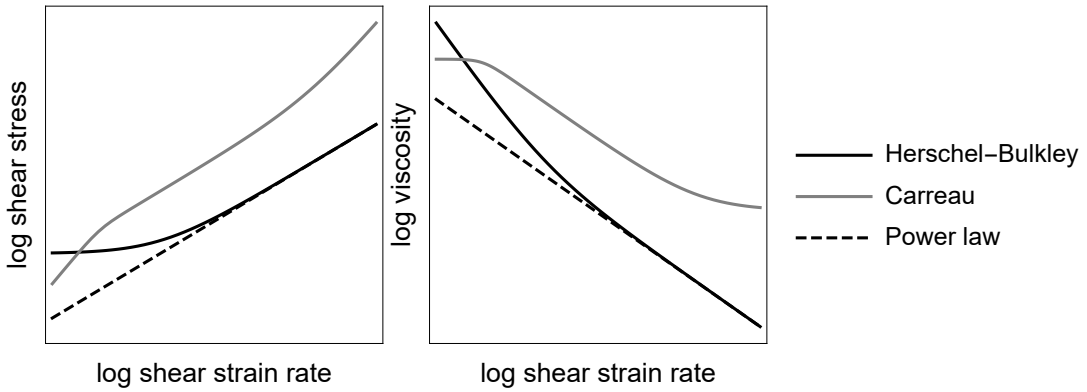

Figure 1.3: Examples of rheology curves for the Herschel Bulkley, Carreau, and power law models.

loss moduli, the viscosity η of the ink can be used to characterize its behavior during printing. High viscosity inks under no shear hold their form after extrusion, while low viscosity inks under high shear strain rates $\dot{\gamma}$ can be extruded through direct-write nozzles. Shear stresses τ relate to viscosities via the shear strain rate.

$$\tau = \eta\dot{\gamma} \tag{1.1}$$

Conventionally, unsupported DIW inks are viscoelastic solids at low shear stresses and viscoelastic liquids at printing stresses and have a non-zero yield stress τ_y.[92, 98] The same rheological framework can also be applied to viscoelastic support materials.[99] Many viscoelastic materials can be fitted to the Herschel-Bulkley model where K is the consistency index and n is the dimensionless flow index (Fig. 1.3).[80, 95, 100]

$$\eta = K\dot{\gamma}^{n-1} + \tau_y\dot{\gamma}^{-1} \tag{1.2}$$

Other viscoelastic liquids can be fitted to the Carreau model, where η_∞ is the viscosity at very high shear, η_0 is the viscosity at zero shear, and λ is the relaxation time (Fig. 1.3).[101,

102]

$$\frac{\eta - \eta_\infty}{\eta_0 - \eta_\infty} = (1 + (\lambda\dot{\gamma})^2)^{-n/2} \tag{1.3}$$

Some shear thinning fluids, including many viscoelastic materials at high shear stresses, follow power law viscosity behaviors (Fig. 1.3).[66, 103]

$$\eta = K\dot{\gamma}^{n-1} \tag{1.4}$$

1.2.3 Printed filament shape

Models may be used to predict the behavior of a printed filament after extrusion as a function of material properties and printing parameters. First, several models pose a fundamental limit where the printed bead's own hydrostatic stress causes it to spread. Jiang, et. al. use the Von Mises yield criterion to predict that a viscoelastic filament will start to spread on the substrate according to Equation 1.5, where ρ is the ink density, g is the acceleration due to gravity, h_m is the height of the model, and τ_y is the yield stress of the ink.[92]

$$\frac{\rho g h_m}{\sqrt{3}} \geq \tau_y \tag{1.5}$$

Duty, et. al. split this relationship out into different categories depending on the material type, incorporating viscous components into the model. These critical time parameters depend on the layer time t_{layer}, the characteristic processing time t_p, the acceptable deformation strain ϵ_{limit}, the low shear stress storage modulus G_0', and the hydrostatic pressure $\sigma_{HP} = \rho g h_m$.[91]

For viscous liquids, the critical viscosity η_0 is:[91]

$$\eta_0 > \frac{\sigma_{HP} t_p}{\epsilon_{limit}} \tag{1.6}$$

For viscoelastic liquids, the critical viscosity is:[91]

$$\eta_0 = \frac{\sigma_{HP} t_p}{\epsilon_{limit} - \sigma_{HP} G_0'} \tag{1.7}$$

For viscoelastic solids, the critical time constant $\tau_0 = \eta_0 / G_0'$ is:[91]

$$\tau_0 > \frac{-t_{layer}}{\ln(1 - \frac{\epsilon_{limit} G_0'}{\sigma_{HP}})} \tag{1.8}$$

Additionally, Duty, et. al. propose a spreading criterion which predicts the maximum height of an unsupported filament h_{fs} as a function of the surface tension γ.[91]

$$h_{fs} = 2\sqrt{\frac{\gamma}{g\rho}} \tag{1.9}$$

Similarly, Rao, et. al. propose a characteristic time scale t^* for capillary-driven viscous flow of a deposited filament depending on the inner nozzle diameter d_{in}.[104]

$$t^* = \frac{\eta d_{in}}{\gamma} \tag{1.10}$$

Finite element models have been constructed to model the three-dimensional shape of viscoelastic filaments based on fluid dynamics and surface tension,[102, 105, 106, 107] and based on elasticity.[108, 109] These numerical models could be more accurate than the simpler analytical models. As such, FEA could guide material selection and part design, given sufficient computational speed and model accessibility.

Some works have leveraged the deformation imposed during deposition to manipulate the structure of the deposited filament. The works manipulate filament shape as a function of the dimensionless nozzle speed $V^* = v_s / v_f$, where v_s is the translation speed and v_f is the extrusion speed.[110] Particularly for polymeric inks, the filament swells after it leaves the

nozzle because of entropic effects; this is called die swell. Filament shape is a function of the dimensionless standoff distance $H^* = h/(\alpha d_{in})$, where h is the stand-off distance, α is the die-swelling factor, and d_{in} is the inner diameter of the nozzle.[110] Diagnosing these printing modes requires studies at multiple resolutions. Two studies used the same silicone elastomer SE1700, but Athanasiadis, et. al. found instabilities where $V^* \geq 1.5$ and $H^* \leq 0.1$,[111] and Yuk et. al. found instabilities where $V^* \geq 3.5$ and $1 \leq H^* \leq 10$.[110] These instability boundaries depend on parameters including surface tension and viscosity.[112]

At combinations of very low H^* and high V^*, at all very high V^*, and at all very high H^* filaments rupture.[110, 111, 113] At lower V^*, written filaments are continuous but thinner than the original filament.[110] Only at a critical $V^* = \alpha^2$ is the written filament the exact size of the initial filament.[110] Below this critical value, die swelling dominates, and written filaments are larger than the initial filament.[110, 113] Within the regime which ranges from thinning to swelling, the diameter of the printed fiber is $d = \alpha d_{in}/\sqrt{V^*}$.[110] Below a critical value of $V^* = 1$, deviations in the print path are introduced.[110] Waves, random coils, periodic coils, ribbons, and grooved filaments may be written by varying V^* and H^*.[110, 111]

1.2.4 Spanning

One criterion for shape stability is the ability of the material to span unsupported gaps. For elastic solids, beam theory can be used to determine the deflection of an elastic circular cylinder supported at its two ends as a function of distance from the supports y, the elastic modulus E, and the span length L_{span}.[96]

$$\delta(y) = \frac{\rho g y}{6E}(2L_{span}y^2 - y^3 - L_{span}^3) \tag{1.11}$$

Building on the elastic beam model, Rao, et. al. propose a critical storage modulus G_0' to

limit deflection of a circular filament based on a critical $\delta_{limit} = 0.05 d_{in}$.[104]

$$G_0' \geq 1.4 \rho g L_{span}^4 / d_{in}^3 \tag{1.12}$$

Duty, et. al. incorporate viscous sagging into beam theory to propose bridging criteria based on the acceptable deflection distance δ_{limit}. The gap length L_{span} is assumed to be ten times the bead height h_b, the bead width is w, and the filament is assumed to be rectangular.[91] For viscous and viscoelastic liquids, the critical time to print a layer to prevent sagging is:[91]

$$t_{layer} > \frac{4 \delta_{limit}^2 \eta}{\rho g h_b L_{span}^2} \tag{1.13}$$

For viscoelastic solids, the critical deflection is:[91]

$$\delta_{limit} > \frac{60}{384} \frac{\rho g L_{span}^4}{G_0' h_b^2} \tag{1.14}$$

1.2.5 Deformation of existing layers

There is a gap in the literature concerning deformation of DIW inks after deposition due to the stress imposed by deposition of successive layers. Existing layers must impose a stress on the new filament in order to impose a 90° turn on the extruded filament and, for circular nozzles, an additional stress to deform a circular filament into a pseudo-rectangular one.[91] Those stresses are in turn imposed on the existing layers. Although these stresses likely change the internal microstructure of both the new and existing layers, the complex models necessary to predict the influence of thermal transport and fluid dynamics on deformation of yielded existing filaments have not yet been developed.

1.2.6 Support baths

An extension of DIW is embedded direct ink writing,[86] also known as freeform reversible embedding,[114] freeform reconfigurable embedding,[115] suspended layer additive manufacturing,[116] and other aliases. During embedded direct ink writing, a nozzle travels through a viscoelastic support material, producing a crevasse into which a line of ink is deposited. The crevasse then closes above the printed line, holding it in place.[99, 117] When the nozzle returns to write a neighboring line, the support must locally yield without displacing the existing line. Fundamentally, printing into a support bath requires displacing support to make space for ink. Ideally, the displaced support is exactly the volume and shape of the ink line to be deposited, and it displaces out of the plane. If it displaces in the plane or if a smaller volume yields, support will remain between ink filaments. If a larger volume yields, the bath will not support the shape of the ink and existing lines will be displaced. Thus, even though support material provides a critical function in maintaining the shape of the printed structure, it introduces new challenges for fusion between neighboring lines.[99, 117, 118] Translation speed (the rate of nozzle movement), flow speed (the rate of ink flowing through the nozzle), viscosities of ink and support, interfacial energies, and yield stress of the support all influence the volume of the yielded support and its direction of movement.[117, 119] As such, the ink and support compositions and printing speeds are tools for controlling fusion between neighboring deposited filaments.

Scaling relationships centered on inertia, viscoplasticity, and interfacial energy have been used to predict the quality of individual filaments.[97] Those scaling relationships could help to predict fusion quality and provide initial bounds for the materials and processing parameter space. Through inertia, fluid flows are influenced by how the fluid is already flowing. Inertia can produce surface roughness and disrupt the internal structure of new and existing lines.[19, 97, 117] Through viscoplasticity, viscous fluids resist flow, and solid-like support becomes

fluid-like above a yield stress.[97] For support to fill in crevasses after the nozzle passes through the support, gravity must overcome the yield stress of the support.[99]

Through interfacial energy, reducing the contact area of dissimilar fluids is energetically favorable. At small length scales, interfacial energy can cause filaments to break into beads, so features must be above a critical size.[97] The effect of interfacial energy on fusion has been debated,[97, 118] possibly because of the intersection between miscibility and interfacial energy. Miscibility governs how the fluids interact in the bulk, i.e., the ability of a filament to mix with and travel through the support. Interfacial energy governs how the fluids interact at surfaces, i.e., the tendency of a filament to change its shape to increase or decrease contact with support. High interfacial energies could drive ink filaments to fuse to reduce their surface area, while high miscibilities could enable ink to mix with support to contact neighboring filaments. A controlled experiment could disentangle the effects of miscibility and interfacial energy.

The print path, i.e., the order and spacing at which lines are deposited, is likely critical for fusion. Jin, et. al. proposed line spacing requirements based on geometry.[120]

$$d_{in}/2 < d_x, d_z < \sqrt{2}d_{in}/2 \tag{1.15}$$

The within-layer spacing d_x influences the height of the printed layer, since excess volume from overlap between filaments is diverted upwards in z. The layer height is linearly proportional to the spacing d_x/d.[121] The between-layer spacing d_z should be chosen with this written layer height in mind. Inertia, interfacial energy, and viscoplasticity likely place additional constraints on line spacing.[19] Poor fusion in tubes printed along the tube length,[122] poor fusion on the last layer of prints,[118] and flows within neighboring lines during printing[19] indicate that the pressure from the nozzle during deposition of neighboring lines may be critical for fusion.

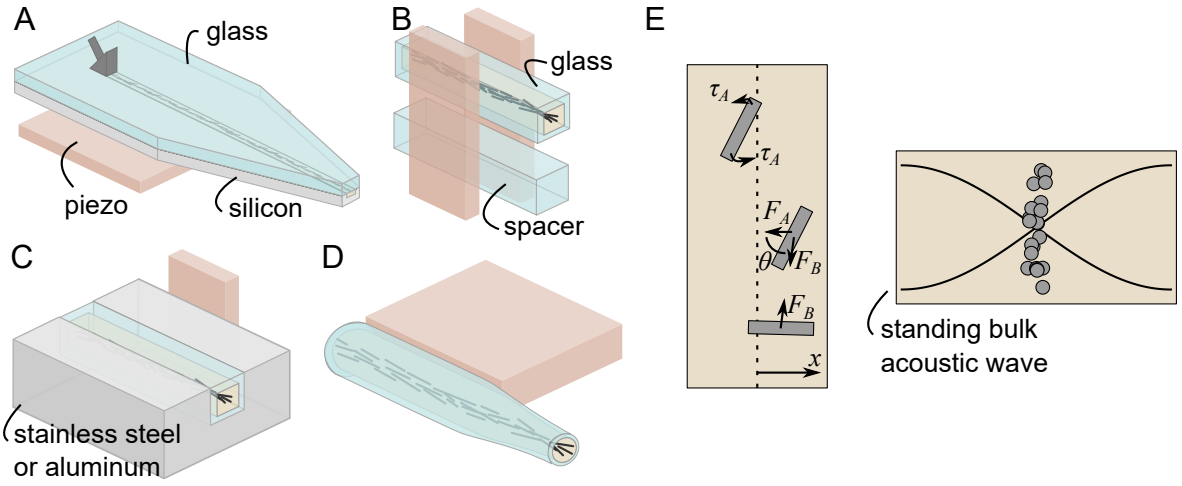

Figure 1.4: Nozzle and piezo geometries for DIWA printing. A) In a Lund resonator, the piezo is coupled to a glass-on-silicon microfluidic chip containing an etched rectangular channel. B) Coupled piezos are directly attached to a square glass capillary with a spacer for alignment. C) Rectangular glass capillary rests inside of stainless steel or aluminum resonator which is glued to a piezo. D) Circular glass pipette is glued directly to a single piezo. E) Cross-sections of focusing channels. A bulk acoustic wave applies a primary acoustic radiation force F_A and a torque τ_A on particles.

1.2.7 Printer configuration

In addition to material properties, DIW of composites places restrictions on the nozzle geometry. DIW bioprinting is limited in both the extrusion pressure and nozzle diameter, since high pressures damage cell membranes, and narrow nozzles impose high shear stresses which can damage cells.[92] In inorganic inks, nozzle diameters clog at a critical size, and certain combinations of print speed and nozzle diameter cause the printed structures to dry out.[123]

1.3 Requirements and constraints for acoustophoresis

Acoustophoresis was primarily developed as a microfluidics method for separating particles by size, concentrating particles, medium switching, filtration, and valving.[124, 125] It has been used widely in biological applications to manipulate blood, urine, fermentation broths, milk, and cell cultures.[126] Many chip and piezo configurations have been devel-

oped for microfluidic applications.[125, 126] For DIWA, a few configurations have been published in recent years. First, the Lund resonator configuration was adapted from microfluidics, wherein a rectangular channel is etched into a silicon wafer and capped with a borofloat layer. A piezoelectric transducer is attached to the silicon wafer using ultrasonic gel (Fig. 1.4A).[8, 13, 15, 16, 125] The piezo converts a sinusoidal electrical signal into acoustic waves which resonate the fluid in the channel. While the Lund resonator limits acoustic losses, it has limitations. The Lund chips are more likely to clog at the inlet than devices which do not contain a turn at the inlet. The rectangular channel is better suited to unidirectional coatings than 3D printing. Chip fabrication is relatively expensive and time-consuming. Thus, more recent DIW implementations have used glass capillaries, which have also been used in microfluidic contexts.[126] One DIW implementation directly attaches coupled piezos to opposite sides of a square capillary, with a spacer in between for alignment (Fig. 1.4B).[17, 21] Another implementation attaches the piezo to a stainless steel or aluminum channel holder which holds a square or rectangular capillary (Fig. 1.4C).[9, 18, 19, 20] A third implementation directly glues the narrow face of a piezo to a circular glass pipette (Fig. 1.4D).[10, 14] No studies have directly compared the acoustic focusing quality of these three geometries. It is likely that in addition to the device geometry, factors such as the type of adhesive used, channel holder dimensions, clamping pressure, and heat transport influence focusing quality.[126] In this work, Chapter 4 and 5 use the Lund configuration in Figure 1.4A, and Chapters 6–8 use the configuration in Figure 1.4C because the two nozzle configurations have large flat faces which are easy to align on a printer and allow clogged or dirty nozzles to be replaced quickly without using a new piezo.

In all of the acoustophoresis assemblies used in DIWA, a piezo establishes a standing bulk acoustic wave inside of a channel, through which a particle-laden fluid travels. While many implementations use a single node acoustic wave, some use multiple nodes.[9] Depending on the acoustic contrast factor ϕ, particles rotate and move toward the nodes or antinodes of the

a	Radius of spherical particle
d	Distance between particles
F_A	Primary acoustic radiation force
F_B	Secondary acoustic radiation force
k	Wave number $2\pi/\lambda$
p_0	Acoustic pressure amplitude
v_A	Velocity of single sphere from primary acoustic radiation force and Stokes' drag
V_p	Volume of particle
x	Distance between particle and node
β_p, β_f	Compressibility of particle and fluid
η	Viscosity of fluid
λ	Wavelength
ρ_p, ρ_f	Density of particle and fluid
ϕ	Acoustic contrast factor
ω	Frequency

Table 1.2: Variables used in acoustophoresis physics.

standing wave.[125]

$$\phi(\beta,\rho) = \frac{5\rho_p - 2\rho_f}{2\rho_p + \rho_f} - \frac{\beta_p}{\beta_f} \tag{1.16}$$

ρ_p is the density of the particles, ρ_f is the density of the fluid, β_p is the compressibility of the particles, and β_f is the compressibility of the fluid. If the acoustic contrast factor is positive, particles move toward the nodes of the acoustic wave, and if the factor is negative, particles move toward the antinodes. Generally, this means that dense particles move toward nodes, and bubbles move toward antinodes, but compressibility contrast can also facilitate acoustic focusing.

A single particle is pushed toward the nodes with primary acoustic radiation force F_A (Fig. 1.4E).[125]

$$F_A = -\Big(\frac{\pi k p_0^2 V_p \beta_f}{4}\phi(\beta,\rho)\Big)\sin(2kx) \tag{1.17}$$

In Equation 1.17, p_0 is the acoustic pressure amplitude which is proportional to electrical

voltage amplitude, V_p is the volume of a single particle, k is the wave number defined by $2\pi/\lambda$ where λ is the wavelength, and x is the distance from the node. The position-dependent velocity v_A of a particle moving toward a node can be determined by balancing the primary acoustic radiation force against Stokes drag. Equation 1.18 shows the velocity for a single sphere.[127]

$$v_A(x) = \frac{\phi(\beta,\rho)\beta_f k a^2 p_o^2}{6\eta}\sin(2kx) \tag{1.18}$$

In Equation 1.18, η is the viscosity of the fluid. The derivative of Equation 1.18 can be used to determine the position x of the particle as a function of time t.[127]

$$x(t) = \frac{1}{k}\arctan\Big(\tan(kx(0))\exp\big(\frac{\phi\beta_f(kap_o)^2}{3\eta}t\big)\Big) \tag{1.19}$$

Particles scatter acoustic waves, leading to secondary forces between particles known as Bjerknes forces.[125] The secondary acoustic radiation force F_B has been calculated for two spheres:[125]

$$F_B(x) = 4\pi a^6\Big(\frac{(\rho_p-\rho_f)^2(3\cos^2\theta-1)}{6\rho_f d^4}v^2(x) - \frac{\omega^2\rho_f(\rho_p-\rho_f)^2}{9d^2}p^2(x)\Big) \tag{1.20}$$

In Equation 1.20, a is the particle radius, d is the interparticle spacing, θ is the angle between the secondary force direction and the primary force direction, v is the local wave velocity, p is the local wave pressure, and ω is the frequency of the pressure and velocity waves (Fig. 1.4E).[16] Generally, particles repel each other when they are aligned transverse to the printing direction, and they attract when they are aligned parallel to the printing direction. Secondary scattering can be leveraged to manipulate the sizes and shapes of assemblies of focused particles during flow.[16]

1.4 Scope and key issues addressed in this work

- Instrumentation and software for printing composite inks with DIWA are described. Digital image analysis algorithms for quantifying fluid behaviors were developed.

- There is a critical trade-off between acoustic focusing and form holding. High viscosity inks hold form well, but they limit the achievable contrast in structural and functional properties between focused and unfocused composite filaments.

- Viscocapillary lubrication theory can be used to predict print bead stability. Via lubrication theory, the ink-substrate contact line position and angle can be used to monitor the stability of the print bead *in-situ*. To avoid nozzle wetting, flow and translation speeds and stand-off distances near the boundary between stable and unstable filaments should be chosen.

- Deposited filaments interact with fluids on the substrate such as viscoelastic support materials and existing ink filaments. Particle distributions in the filaments shift and widen relative to the print path at three points in the printing process: during deposition, after deposition during relaxation, and during shear when the nozzle returns to write neighboring filaments. Two different support material geometries, layer-by-layer and bath support, improve different aspects of the printed structure.

- The microstructure of deposited filaments changes depending on the printing direction due to machine calibration, fluid flows around a square nozzle, deformation of a square filament as it is deposited onto the substrate, and formation of rotationally asymmetric particle distributions inside the nozzle. A model is proposed to diagnose sources of direction dependence in DIW.

- Written corners in DIW can swell outward due to double deposition, smooth inward due

to capillarity, and widen due to swift changes in direction. Bath support suppresses these geometric inaccuracies at written corners.

1.5 Outline of the dissertation

Chapter 2 describes the custom instrumentation and graphical interfaces developed to 3D print composite structures via DIWA. Chapter 3 describes digital image analysis algorithms used to extract performance metrics from videos and images of the printing process and printed structures. Chapters 4 to 8 provide a detailed investigation into the processing-structure relationships that govern DIWA (Fig. 1.5). These processing-structure relationships are considered in the context of a suite of driving forces: acoustics, gravity, inertia, interfacial energy, viscoplasticity, and viscous dissipation. Studies progress from primitive to complex geometries, building a framework of particle and matrix behavior while considering a few driving forces at a time. Chapter 4 probes a primitive geometry, a single line on a substrate, which allows us to fit particle distributions and the surface profile of the filament to a few scaling relationships. Chapter 5 examines how the filament interacts with the nozzle and substrate and uses visco-capillary lubrication theory to predict the stability of the DIW print bead. Chapter 6 probes the influence of support material and neighboring lines on particle distributions. The increased complexity of the boundary conditions means that several interacting driving forces influence the particle distribution over the course of the print. Chapter 7 builds on the geometry from Chapter 6 to consider printing direction, which can be modeled using a linear combination of several scaling expressions based on driving forces and machine calibration parameters. Chapter 8 builds on Chapter 6 and 7 to consider corners in written structures, which are influenced by a limited set of forces. Together, these five chapters provide a framework for selection of processing variables and features to monitor during the printing process. These fundamental relationships can be used to print parts with precisely controlled geometries and microstruc-

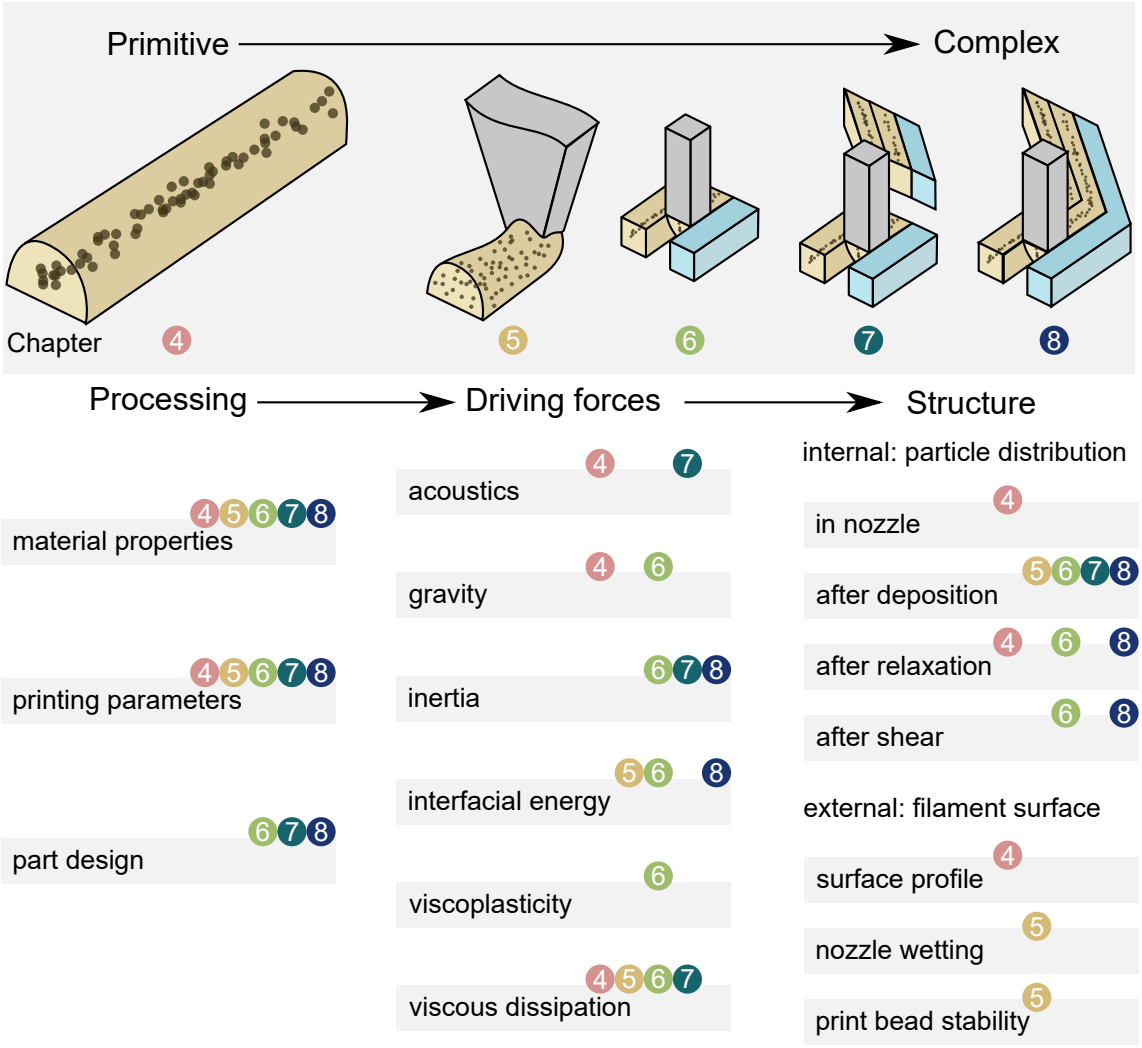

Figure 1.5: Summary of described experiments. Examined geometries increase in complexity from chapter 4 to 8. Select processing parameters, driving forces, and structure metrics are considered for each geometry.

tures. While these studies were conducted on DIWA, many of their conclusions apply to other field-assisted DIW strategies because they largely focus on what happens after the ink leaves the nozzle.

Chapter 2

Hardware and software for a custom direct-write printer

Direct ink writing (DIW) is an additive manufacturing technique that is amenable to a chemically and rheologically diverse set of materials such as colloidal gels,[95] heat-curing thermosets, [15, 61] light-curing thermosets,[128] ionic-crosslinking hydrogels,[99] and slow-crosslinking thermosets.[118] To adapt to a variety of inks, DIW printers should be as modular and customizable as possible, allowing for incorporation of curing and support material stations suited to the ink of choice. The experiments described in this dissertation rely heavily on *in-situ* digital image analysis, which is useful for basic science studies, calibration, and quality control. As such, space must be made for cameras and lighting. To conduct the experiments described in this dissertation, a custom 3D printer was constructed from a Shopbot Desktop D2418 CNC mill. James Cornell, Rachel Collino, and Tyler Ray made initial modifications. This chapter describes the final structure used in Chapter 6–8.

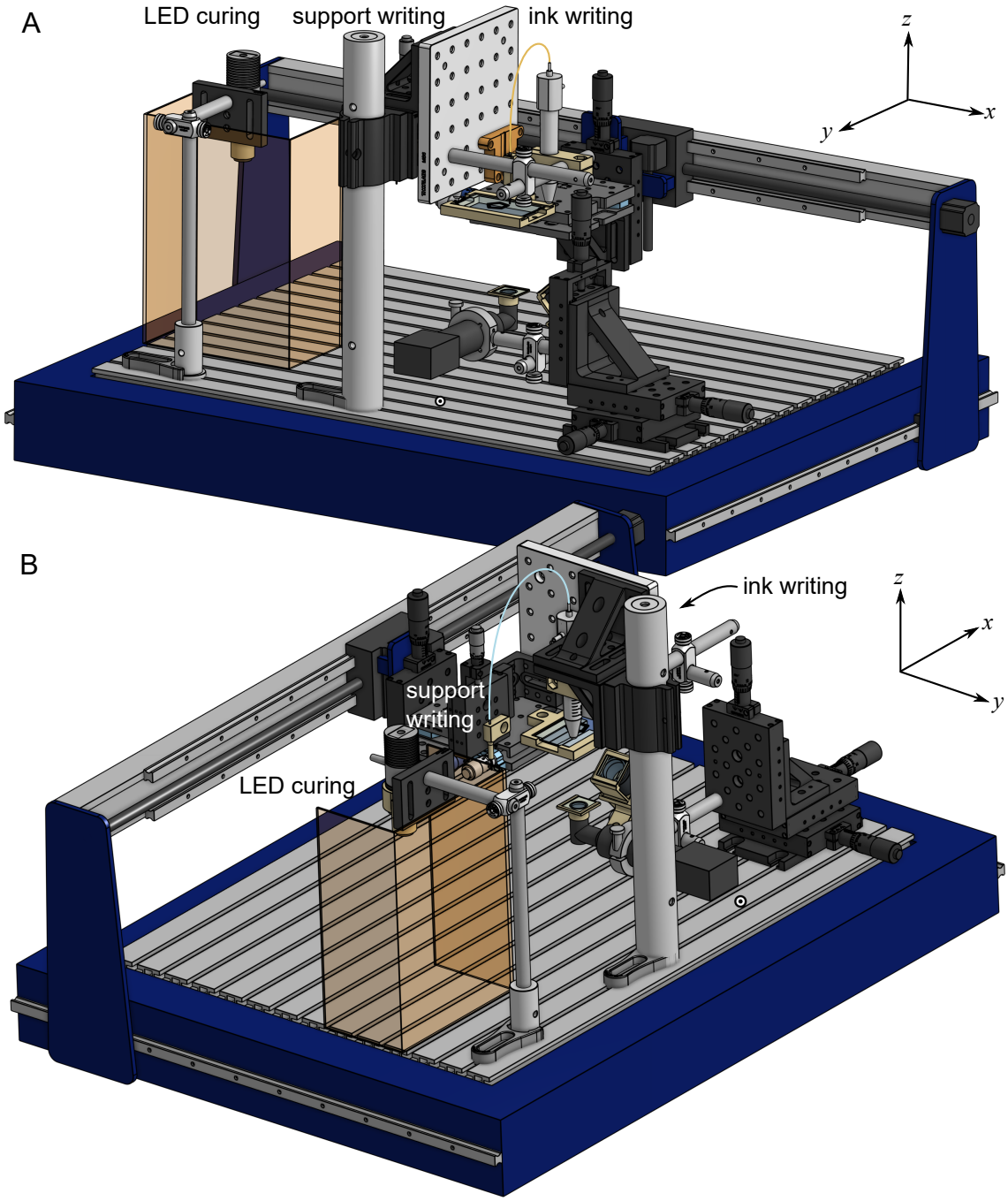

Figure 2.1: Full model of all printer components, in two perspectives. A printed polygon is shown on the stage.

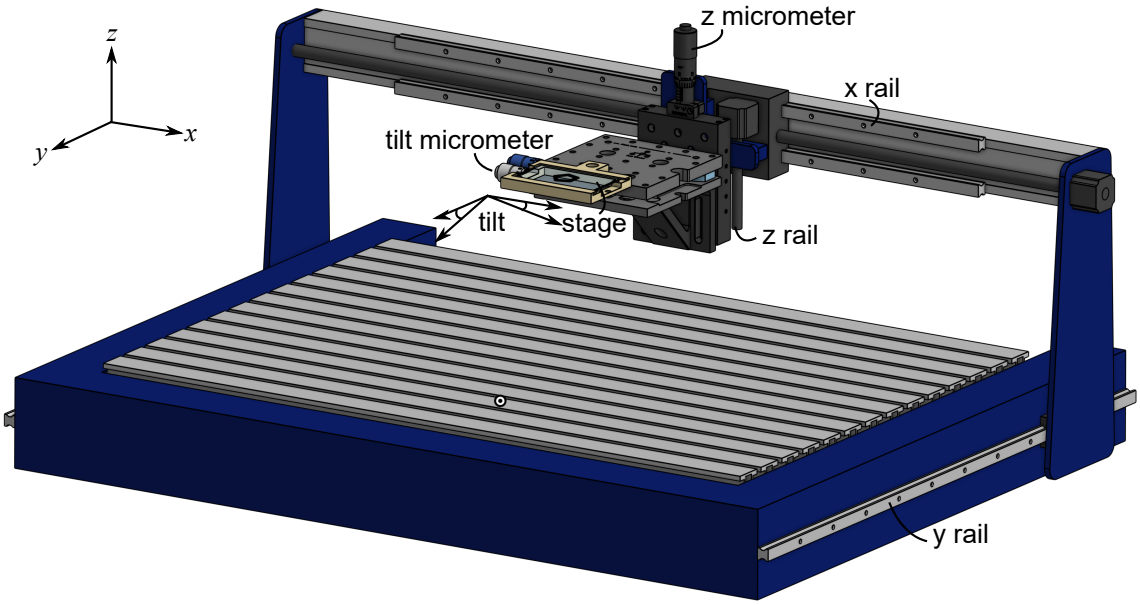

Figure 2.2: Figure 2.1A, but with only the gantry and stage. The stage can mechanically move in x, y, and z. Manual micrometers allow for manual calibration of z position and the three-dimensional tilt of the stage relative to the x, y, and z gantry orientations.

2.1 Hardware

A full model of the 3D printer is shown in Figure 2.1. A moving stage travels between three stations: a LED curing station, a support writing station, and an ink writing station. The stage is attached to the 3-axis gantry of the CNC mill, where ordinarily a drill would be attached to the CNC mill. The support writing and ink writing components are fixed to the base of the gantry via a shared post. The LED curing components are fixed to the base of the gantry via a separate post. The support capillary is attached to a z micrometer which allows for precise calibration of the support stand-off distance to match the ink stand-off distance. The imaging components are fixed to the base of the gantry via a separate xyz micrometer which allows for precise positioning and focusing of the camera.

To construct the printer, one must first remove the drill from the CNC mill, then attach the stage. The moving stage is shown in Figure 2.2. The stage, which is composed of a glass slide inside of a slide holder, moves in x, y, and z. A micrometer allows for manual adjustment of

the stage z height. The z micrometer is primarily used to zero the stage height so that the gantry can accurately control the stand-off distance. A tilt micrometer allows for manual adjustment of the stage tilt in order to ensure a level stage. The tilt micrometer is crucial for ensuring a consistent stand-off distance across the entire print, since small rotations about screws in the assembly of the stage can build up to tilt the stage out of the x-y plane. A digital image analysis-enabled method for calibrating stage tilt is described in Chapter 3.

Two 3D printed stage adapters adapt to the type of support used. Adapters are built for 3 inch by 2 inch by 1 mm glass slides. When using layer-by-layer or no support, the slide holder in Figure 2.3A can be used. The slide slides snugly into the holder, preventing the slide from lifting out of the holder during printing. The bottom of the adapter is open, allowing the camera to capture videos from below the nozzle. When using a deep bath of support, the adapter in Figure 2.3B can be used. The slide sits on top of a rubber gasket that runs around the border of an open-bottomed basin which allows imaging from below the nozzle. Another basin with a rubber gasket running around the perimeter on the bottom sits on top of the slide and fits snugly into the bottom basin, preventing the slide from moving during printing. The top basin can be filled with support gel. To prevent entrapment of air bubbles in the support bath, it is best to mix the support gel in a planetary mixer to remove bubbles, then transfer a single dollop into the basin and scrape off the excess using a glass slide or spatula.

After attaching the stage to the moving portion of the gantry, the static components of the gantry should be attached to the static base of the gantry. Key static components of the printer are shown in Figure 2.4. These components are divided into four groups: light curing (Fig. 2.4A), support writing (Fig. 2.4B), ink writing (Fig. 2.4C), and imaging (Fig. 2.4D). The stage travels between the support writing, ink writing, and light curing stations during printing. The imaging station captures videos of the ink nozzle during printing from below, such that images of the nozzle and extruded ink are collected through the glass slide.

At the light curing station, a mounted 470 nm LED (Thorlabs M470L3) produces blue light

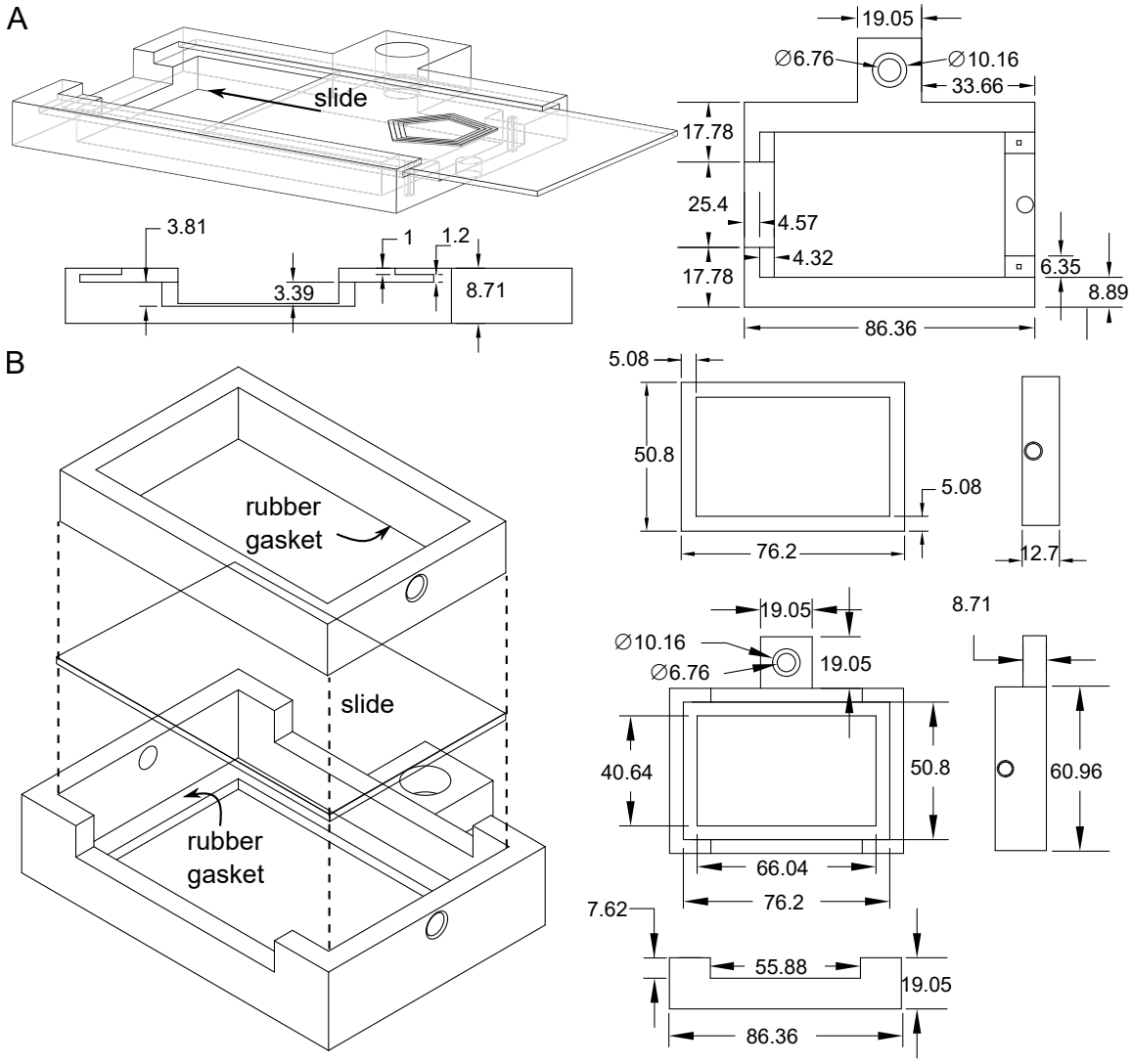

Figure 2.3: Stage assembly. Dimensions of adapters are shown in mm. A printed polygon is shown on the stage.

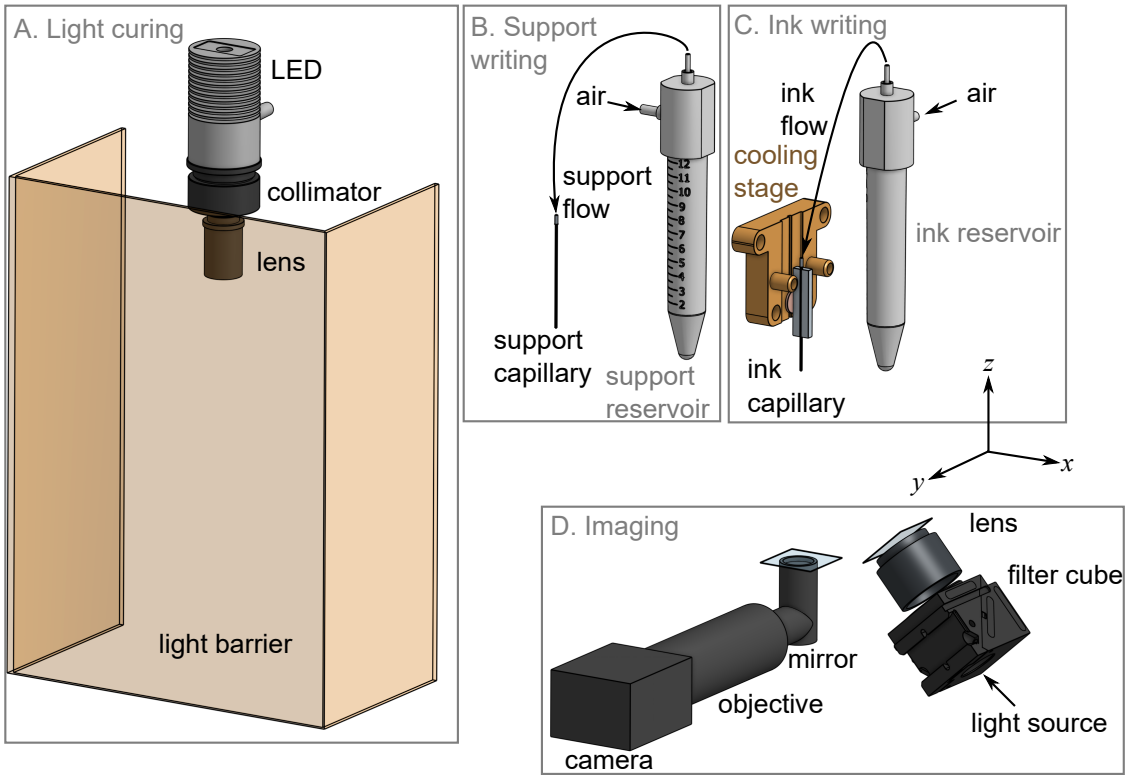

Figure 2.4: Figure 2.1A, but with only the key static components. A) At the light curing station, light passes from an LED through a collimator and lens into a spot. An opaque light barrier, shown here as translucent for illustrative purposes, blocks light from reaching the ink writing station. B) At the support writing station, air pressure controls extrusion of support fluid through a capillary nozzle. C) At the ink writing station, air pressure controls extrusion of ink through a capillary nozzle which is fed through a stainless steel channel holder. The holder is attached to a piezo which is mounted on a cooling stage. D) At the imaging station, light passes through a filter cube and lens to produce a spot on the underside of the stage. A camera, objective, and mirror collect images from underneath the stage.

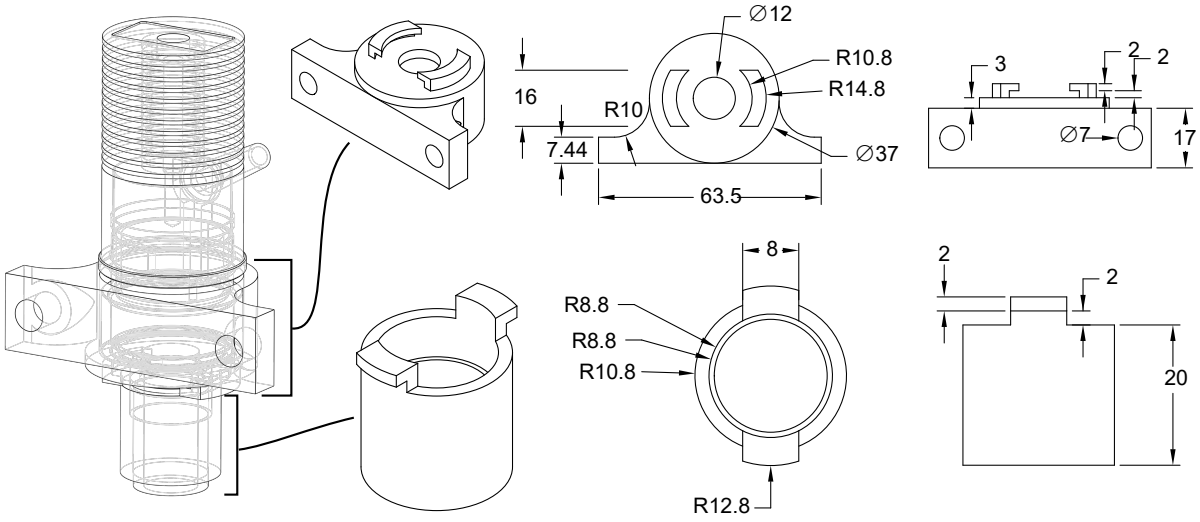

Figure 2.5: LED curing assembly. Dimensions of 3D printed adapters are shown in mm.

which passes through a collimator (Thorlabs SM1V05) and is focused with a lens (Infinity 18 mm/2x) to a 0.64 cm^2 spot size on the stage (Fig. 2.5). The height of the LED is calibrated using a light meter (Thorlabs S130C) to produce a total power of 17.42 mW, or 27.4 mW/cm^2. The LED is driven with a variable current driver (Thorlabs LEDD1B). An opaque PMMA light barrier (shown as translucent in Figure 2.4) provides user eye safety and blocks stray light from reaching the ink capillary. The collimator fits into a 3D printed adapter, and the lens fits into a separate 3D printed adapter (Fig. 2.5). The two adapters twist together and allow for quick lens changes.

At the support and ink writing stations, flow rates are controlled using a Fluigent MFCS-EZ mass flow controller. The mass flow controller imposes an air pressure within the ink or support Falcon tube, inducing flow of fluid through 0.04"ID x 0.07"OD microbore tubing (Cole-Parmer) (Fig. 2.6). This tubing fits over a steel wire ferrule attached to a capillary using epoxy (Devcon HP250). Both the ink and support nozzles are composed of square glass capillaries. The glass capillaries have a 300 μm square inner width and a 600 μm square outer width (Fig. 2.7). To use different sized capillaries, the adapters in Figure 2.7 and 2.8C would

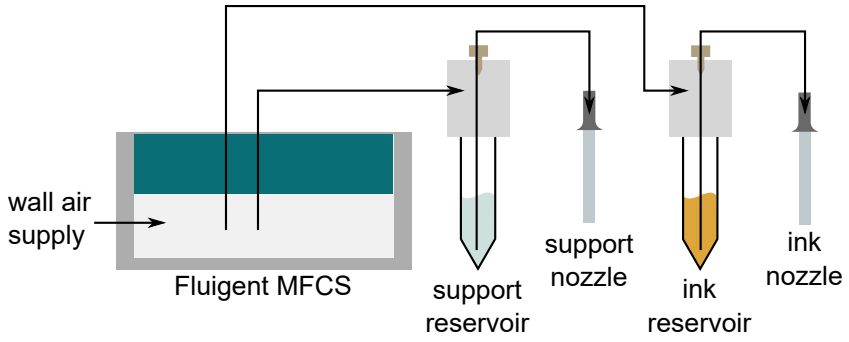

Figure 2.6: Diagram of pressure control tubing, with fluid flow directions noted.

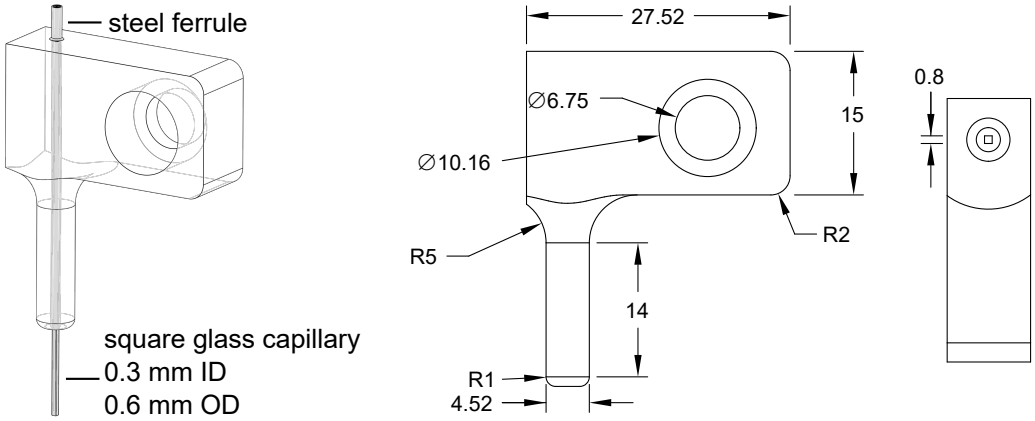

Figure 2.7: Support writing assembly. Dimensions of 3D printed adapter are shown in mm.

need to be redesigned.

At the support writing station, the support capillary fits into a 3D printed adapter, which fixes the nozzle to a manual micrometer for height calibration, allowing the support nozzle height to match the ink nozzle height (Fig. 2.7).

At the ink writing station, the ink capillary slides vertically into a stainless steel adapter that contains a 700 μm square groove lined with ultrasonic coupling gel (Fig. 2.8C). The steel adapter sits in a 3D printed adapter that is screwed into the cooling stage (Fig. 2.8E). A 3D printed cover slides into the 3D printed adapter to block light from reaching the capillary during focusing (Fig. 2.8D). A piezoelectric chip (1 mm thick Navy I material, American Piezo) is bonded to the steel adapter with epoxy (Devcon HP250) (Fig. 2.8B). The piezo is thermally

coupled to a cooling stage using thermal joint compound (Wakefield Type 120) (Fig. 2.8A). Ethylene glycol runs through the copper cooling stage at temperatures between 10°C and 40°C. Temperatures are monitored with a Fluke 289 multimeter.

The piezo is driven using a signal generator (HP 33120A) and amplifier (Mini-Circuits LZY-22+) attached to a power supply (Tenma 72-7245), and signals are measured using an oscilloscope (Agilent DSO-X 2024A) (Fig. 2.9).

At the imaging station, the camera and illumination apparatus are fixed in position relative to each other and are attached to a three-axis micrometer (Fig. 2.10). A camera (Point Grey GS3-U3-2356C-C) with an Infinitube FM-200 objective and $\times 0.66$ lens (Infinity) are attached to a 90° mirror which enables the camera to collect videos from below the stage, through the bottom of the glass slide. The lens is covered with a cover slip and 3D printed adapter (Fig. 2.10B) to protect the lens from spills.

A 3D printed adapter assembles all of the lighting components (Fig. 2.10C). A fiber-optic light cable attached to a light source (Edmund MI-150) is inserted into the base and fixed in place with a set screw. The light then passes through a red filter cube (Nikon 96306 G-2A) so that illumination does not cure the blue-curing ink and is then focused to a wide ($>$2 inch) spot using an objective (Edmund Optics near UV achromatic 25mm $\times$ 50mm). A cover slip protects the objective from spills.

Extra cameras can be attached to the printer. In particular, a small-footprint pen webcam pointed at the LED spot is useful for calibration and monitoring of the curing process. Additional webcams can be located at the ink and support nozzles to streamline monitoring of the printing process and to aid in calibration.

Variations on this printer configuration are described in Chapter 4–5. For Chapter 4, a linear stage was used for imaging studies, and the Shopbot was configured with a moving nozzle instead of a moving stage for printing lattices. For Chapter 5, no support was used, the tilt micrometer was absent, and cameras were rearranged.

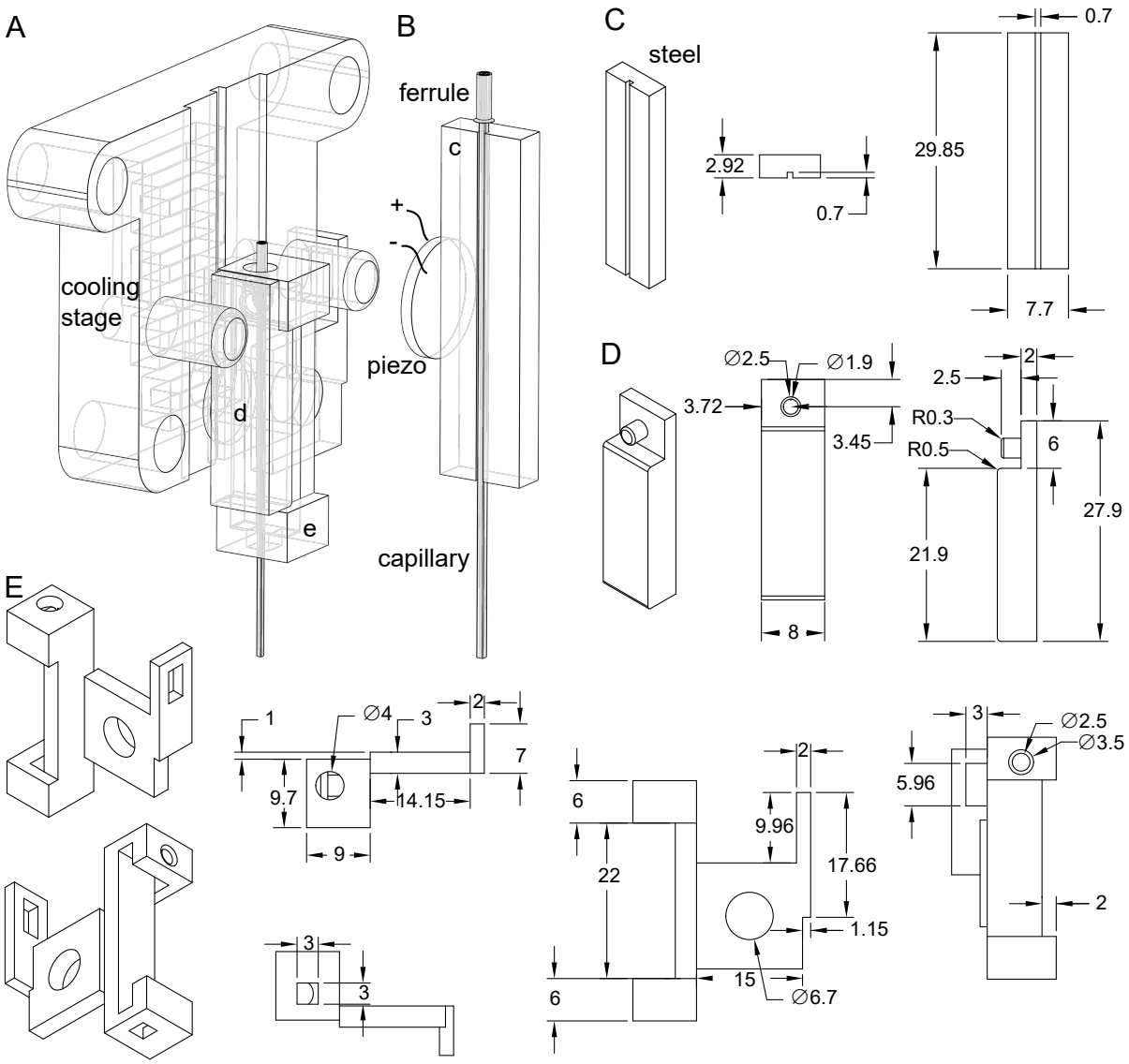

Figure 2.8: Ink writing assembly. Dimensions of adapters are shown in mm.

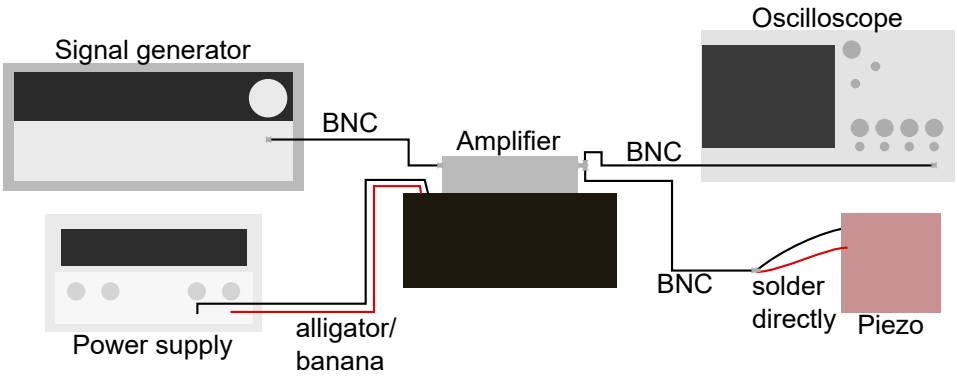

Figure 2.9: Piezo wiring diagram. Plug types are noted. The signal generator outputs a sinusoidal electrical signal that is amplified by the amplifier. The amplifier is powered by a power supply. The signal out of the amplifier is split and sent to the oscilloscope, which displays the amplified signal, and the piezo. The signal generator, power supply, and oscilloscope are plugged into a standard surge protector.

2.2 Software

The printer was controlled using a custom Matlab GUI built in App Designer. A screenshot of the GUI is shown in Figure 2.11.[129] On startup, the program creates a connection to the Fluigent mass flow controller and to any cameras attached to the printer. The SB3 Shopbot control software should be opened separately.

In the "Fluigent" section of the GUI, a running timer updates a graph that shows the pressure inputs to the Fluigent channels. Input boxes in the GUI can be used to set the pressures.

In the "Ink", "Support", and "LED" sections of the GUI, buttons provide printing and imaging options. "Preview" buttons launch external windows that show a feed from the relevant cameras. "Record" buttons start and stop recording. Videos are automatically saved in a fixed folder using timestamps as a naming convention. Checkboxes and input boxes indicate printing settings. "Record" checkboxes indicate that the program should record a video while printing a file. "Write" checkboxes indicate that the process should be included in the composition of the file. Checking "Write ink" means that ink will be written. Checking "Write support" means that support will be written, and "1st layer support" means that an extra layer of support that

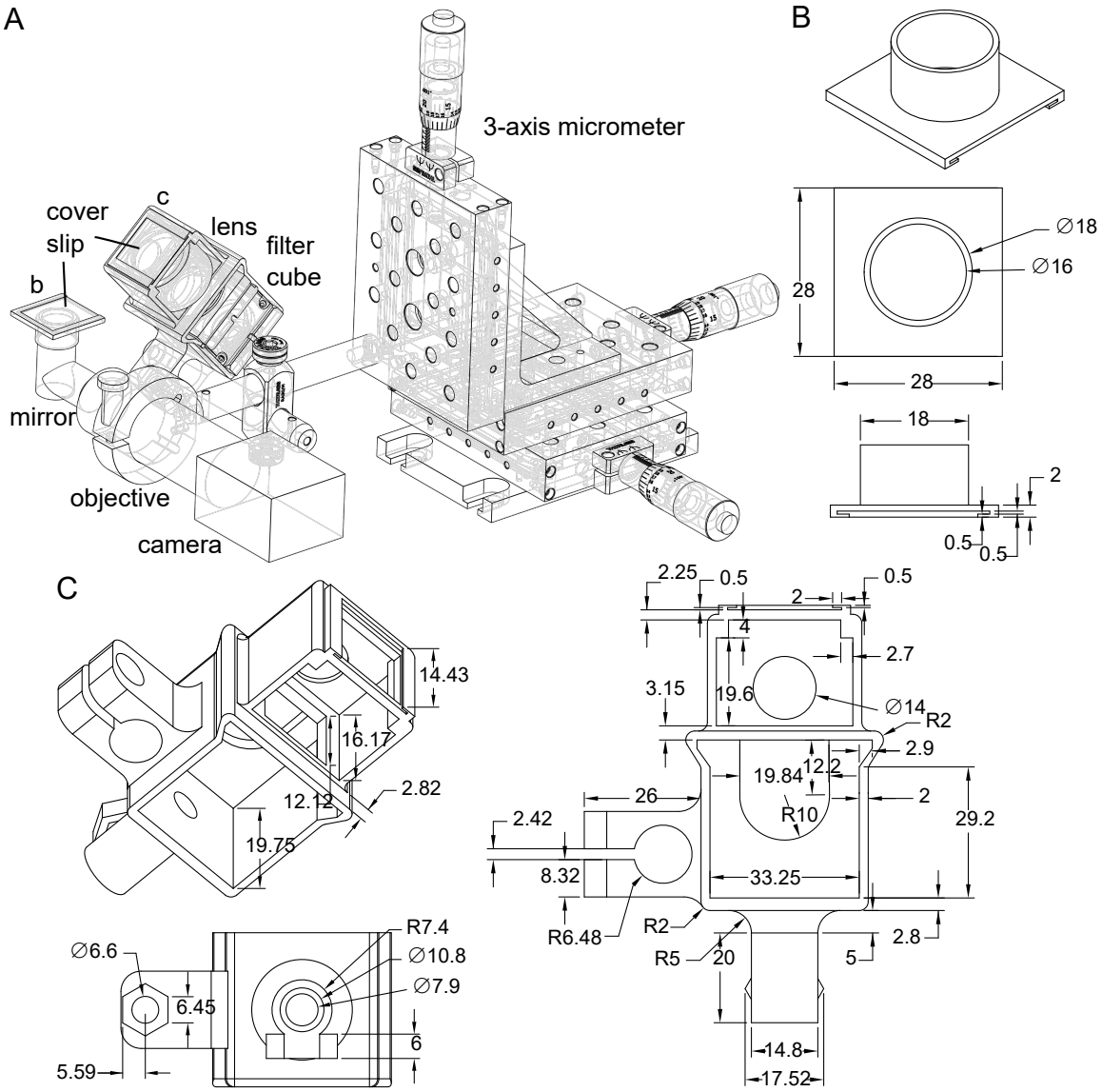

Figure 2.10: Imaging assembly. Dimensions of adapters are shown in mm.

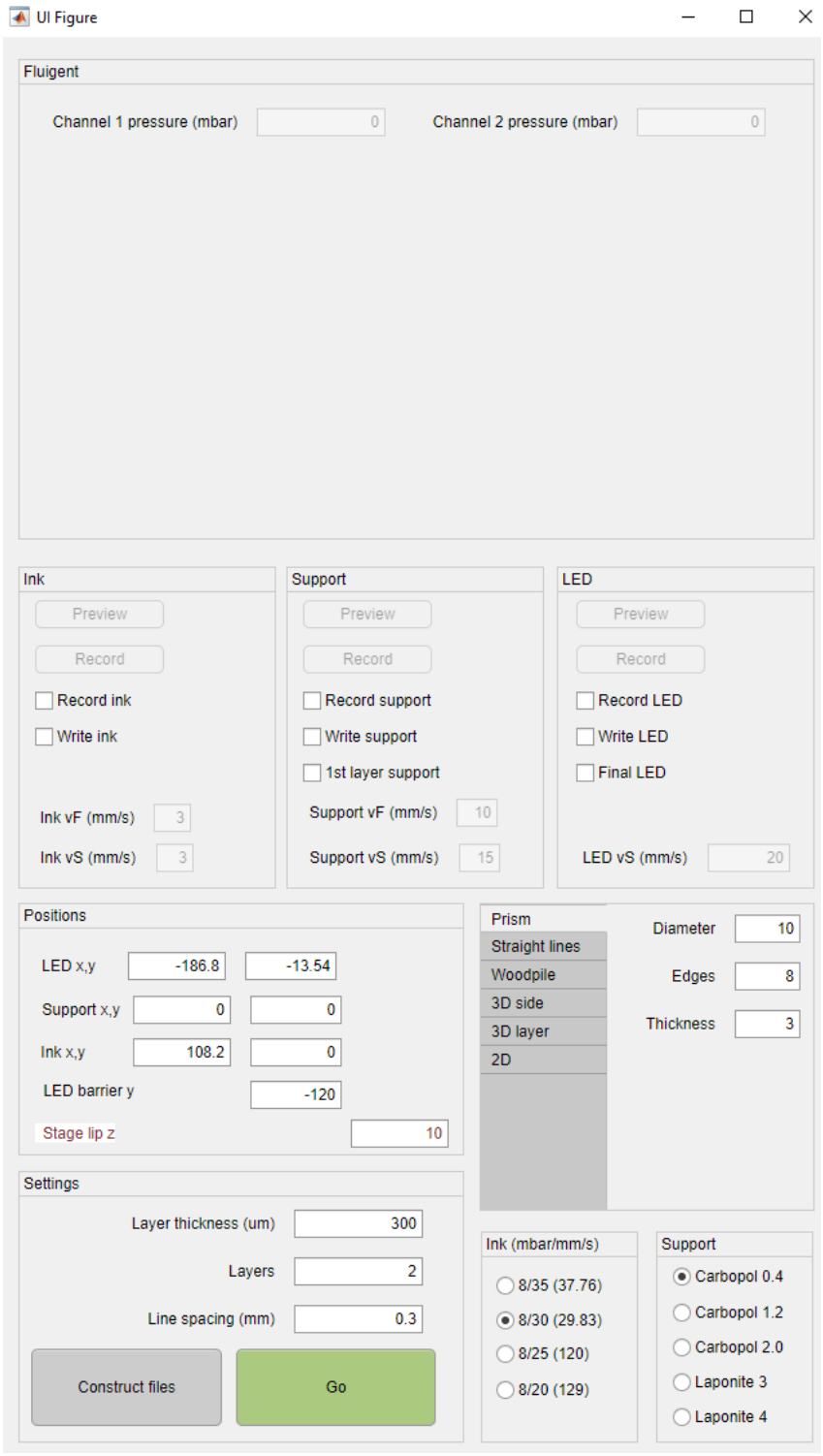

Figure 2.11: Printer control GUI. Top panel contains a constantly updating time graph of the two channel pressures. Preview buttons can be used to open camera feeds in separate windows.

also provides a base for the first ink layer will be written on the first layer. Checking "Write LED" means that the stage will go to the LED curing station on each layer, and "Final LED" means that the stage will go to the curing station on the last layer. Input boxes can be used to set flow (vF) and stage (vS) speeds.

The "Positions" section is used to calibrate the positions of the LED, support nozzle, ink nozzle, light barrier, and top of the slide holder, which is particularly important when using bath support. A suggested calibration procedure when using layer-by-layer support and light curing is shown below.

1. Extrude support until a small droplet of support sits at the tip of the nozzle. Touch to stage. Zero x and y in SB3 software.
2. Move stage to ink nozzle with SB3 software.
3. Touch stage to ink nozzle using manual stage micrometer. Zero z in SB3 software.
4. Move ink nozzle to deposited support droplet using SB3 software. Input x and y positions into GUI under "Ink x,y".
5. Input height of stage lip into GUI under "Stage lip z".
6. Move stage to support nozzle with SB3 software and go to $z = 0$.
7. Touch the stage to the nozzle using the manual support micrometer.
8. Move stage to the back of the ink barrier. Input y position into GUI under "LED barrier y".
9. Use LED camera to align support droplet with LED spot. Input x and y positions in GUI under "LED x,y".
10. Move stage to support nozzle to prepare for beginning of print.

The “Settings” section is used to set the layer thickness, number of layers including the first support layer, and the spacing between lines.

The “Ink (mbar/mm/s)” section is used to set the ink pressure. Preset options are used for common inks. The custom scale box can be used to set a pressure scale in mbar/mm/s, relative to the ink vF.

The “Support” box is used to mark the type of support used, which is for file handling purposes only.

The tabs on the right side are used to select the type of print. The “Prism” tab can be used to print empty polygonal prisms with a given diameter, number of edges, and thickness in number of lines. The “Woodpile” tab can be used to print woodpiles with a given number of struts and strut thickness given in number of lines. The “2D” tab is used in Chapter 6 to print a series of slides with preset prisms across a given range of speeds.

Once all settings are complete, the “Construct files” button constructs and saves .sbp files for the given application. .sbp files are instruction files used by the SB3 software and are comparable to G-code but use a different syntax. For the 2D routines, variables are used to speed up compiling. For example, assume the ink nozzle is at (3,4). To move 2 left of and 4 behind the nozzle, instead of writing

Listing 2.1: SBP: move to x=1, y=0

```
M2, 1, 0
```

it is more efficient to write

Listing 2.2: SBP: move to x=1, y=0 with variables

```
M2, &inkx - 2, &inky - 4
```

and add lines at the beginning of the file:

Listing 2.3: SBP: initialize variables

```
&inkx = 3
&inky = 4
```

As such, it is not necessary to recompile the entire .sbp file after calibration, but instead it is only necessary to adjust the preamble.

Pressing "Go" calculates the ink and support pressures and saves them as global variables, creates a new .sbp file with the current positions, and begins any requested camera recordings. Matlab sends the .sbp file to the SB3 software for execution using the command

Listing 2.4: MATLAB: send command to printer

```
command = strcat('"C:\Program Files (x86)\ShopBot\ShopBot
    3\Sb3.exe" " ', app.matlabdir, '\temp.sbp "," ",4,"
    ",0," "2," "," "&');
```

This command concatenates three strings: the program name, the directory to save the .sbp file in, and the file name followed by some command inputs. "`app.matlabdir`" can be replaced with the folder name, and "`'\temp.sbp`" can be replaced with the name of the sbp file. Matlab watches the windows registry keys to determine when the print has ended, then stops and saves the video recordings.

Windows registry keys can be used to coordinate the Shopbot and Fluigent. The Shopbot has eight output bits that can be used to signal to external programs that the Shopbot has reached a certain point in the .sbp file. The second output bit can be set to true using the line

Listing 2.5: SBP: set Shopbot output flag 2 to true

```
SO, 2, 1
```

and false using the line

Listing 2.6: SBP: set Shopbot output flag 2 to 0

```
SO, 2, 0
```

Matlab can read these output bits because they are stored as Windows registry keys.

Listing 2.7: MATLAB: read Shopbot output flags

```
output = str2double(winqueryreg('HKEY_CURRENT_ USER', '
    Software\VB and VBA Program Settings\Shopbot\UserData',
    'OutPutSwitches'));
```

This line of Matlab code reads the keys as a single number `output`, where the four bits represent one number expressed in binary, where bit 1 represents the ones place, bit 2 represents twos, bit 3 represents fours, and bit 4 represents eights. For example, if bit 1 and 2 are true, and 3 and 4 are false, the output is 0011 in binary, or three in base ten. If bit 2 and 4 are true, and bit 1 and 3 are false, the output is 1010 in binary, or ten in base ten.

The Matlab GUI contains a timer function that continually loops to update the pressure-time graph. Within that timer function, Matlab reads the Windows registry keys. If `output`=0, the timer function turns both pressures to 0. If bit 1 is on, it sets the ink pressure to the globally defined ink pressure. If bit 2 is on, it sets the support pressure to the globally defined support pressure. It is possible to have both pressures on at the same time.

Chapter 3

Digital image analysis techniques for surface energies and direct ink writing

3.1 Introduction

Extrusion-based coating processes are ubiquitous in manufacturing of polymers, polymer matrix composites, and slurries.[130] In metered coating processes such as direct ink writing, slot die coating, and curtain coating, the morphological characteristics of the extruded bead can inform *in-situ* adjustment of printing parameters such as extrusion pressure and raster speed.[128, 130, 131] Digital image analysis enables rapid and reliable measurement of these morphological characteristics for deployment from small scale laboratories to large scale industrial processes.

Monitoring the print bead *in-situ* can provide information that can be used to improve the quality and reliability of DIW. One way to do so is by utilizing digital image analysis. Because the only additional hardware required is a camera, digital image analysis can be a rapid, small-footprint, low-cost way to monitor print quality. Common digital image analysis techniques are readily available in free packages such as OpenCV and ImageJ as well as high-level languages

like Matlab and Mathematica.[129, 132, 133, 134, 135, 136] As such, digital image analysis is an accessible and powerful tool for monitoring print quality *in-situ*. While these methods were developed for direct ink writing, they can also be applied to other coating processes like slot die coating and curtain coating. These algorithms have enabled comprehensive video-based studies which inform selection of printing parameters and ink compositions for DIW with acoustic focusing.[15, 128]

Digital image analysis techniques for *in-situ* analysis of extrusion processes can ensure quality control in large and small scale manufacturing processes. Monitoring the contact line and contact angle and adjusting printing parameters on the fly can prevent the breakup of deposited films in slot die coating and filaments in direct ink writing. Similarly, monitoring the movement of the contact line in direct deposition of droplets can ensure uniformity of deposited droplets. Algorithms that can quickly measure these morphological characteristics could enable manufacturing processes to automatically adapt processing parameters to changes in environmental conditions, remove flawed parts, or flag damaged equipment such as ineffective nozzle coatings. *In-situ* methods for analysis of print bead morphology are also useful for research applications. Correlating fluid behaviors with theory through Laplace pressures and contact line positions can guide device design and printing parameter selection.

Image analysis can be used to complement computational studies or provide a foundation for experimental studies. Previous studies have employed finite element modeling and manual image analysis to predict and characterize stability.[105, 106, 107] Experimental studies enabled by digital image analysis complement and verify those finite element studies. Lubrication theory informs the interpretation of metrics extracted by digital image analysis.[128] Similarly, dense optical flow and PIV complement finite element models and serve as powerful analytical tools for experimental studies on the effects of printing parameters and ink composition on the internal structure of a filament.[99, 106, 120, 128, 137, 138, 139]

Automating image measurements does not just save time; it also improves the precision of

measurements by removing the unreliability of human perception. However, because of the persistence of human bias, automation does not necessarily improve or worsen the accuracy of the measurements. Designing algorithms to take into account non-ideal images is crucial for extracting accurate and artifact-free data sets. This work used a combination of trends within videos and periodic visual verification to identify inaccuracies in image detection. Sudden temporal changes in print bead contact line position, for example, may indicate that the algorithm is detecting features inside the print bead rather than the surface of the print bead. When rarely occurring, such outliers can be discarded. Alternatively, those sudden changes may be the product of ambiguities in the source image, so if the change happens often, visual verification is necessary. Examples of applications applying digital image analysis to printing include monitoring of print bead stability in direct ink writing,[128] monitoring of filament microstructures in the nozzle during direct ink writing with acoustophoresis,[15] and monitoring of the geometric accuracy of printed structures.[140]

This chapter describes methods to measure surface tensions, contact points, contact angles, and Laplace pressures for moderate viscosity fluids in extrusion. This chapter also describes methods to monitor fluid flows using tracer particles. There are still other ways to make these measurements, but the methods described in this chapter provide adaptable approaches.

Future digital image analysis frameworks could utilize convolutional neural networks.[141] However, neural networks are even more sensitive to the training set than conventional digital image analysis.[142] For example, increasing the stage speed increases the likelihood that a filament will break into droplets. If the illumination in the training set is brighter than average at high stage speeds, a hastily implemented neural network could label all bright images as droplets. Thus, implementation of neural networks for digital image analysis of DIW should entail careful construction of training sets and thoughtful consideration of the physical significance of the network's weights and biases.

3.1.1 Glossary of Digital Image Analysis Terms

- **Connected component labeling:** Given a binary image, the process of labeling clusters of connected pixels. This technique is useful for isolating features from an image.[133]

- **Dense optical flow:** Given two grayscale or color images, determination of the flow field from the intensity gradient between the two images. Variations are described in [134] and [135].

- **Edge detection:** Given a grayscale image, calculation of a binary image consisting of local maxima in gradient intensity (e.g., Figure 3.9C). Only points with a gradient intensity above a certain threshold are included. Common techniques include Canny, Sobel, and Shen Castan edge detection.[136]

- **Hough transform:** Given a binary image, a matrix of slopes and intersections representing all lines that could be present in the image is constructed. For each pixel, one is added to each line in the matrix to which the pixel could belong. Dominant lines are selected.[136] Variations including the probabilistic Hough transform and randomized Hough transform are described in [143].

- **Gaussian smoothing/blurring:** Given an array of values such as a grayscale image or a list of points, calculation of a blurred array. For each value, the value and its nearest neighbors up to a certain distance are weighted by a Gaussian distribution and summed.[133]

- **Image product:** Given two images of the same size, the product of the intensities at each pixel. The calibration section of this chapter uses the intensity of the product of two binary images, which is equal to the number of pixels the two images have in common, because each pixel intensity is 0 or 1.

- **Kernel:** The grid of pixels used when calculating a gradient or a Gaussian. For example, a 5 by 3 kernel would use the pixel, its nearest neighbors along the length and width, and its second nearest neighbors along the width of the image.

- **Particle image velocimetry (PIV):** Given two binary, grayscale, or color images, the process of breaking the images into regions and using cross-correlation functions to determine how the regions move between images. Particle tracking velocimetry uses a similar technique to track single particles rather than regions. Variations are described in Refs. [144] and [145].

3.2 Sessile droplet contact angles

The algorithm described in this section was used in Chapter 5.[128]

The measurement of contact angles is critical for predicting behaviors of fluids derived from interfacial energies. Most famously, the contact angle is an indicator of relative interfacial energies at liquid-solid-gas three phase contact lines, via Young's equation (Equation 3.1).[146]

$$\gamma_{SG} = \gamma_{SL} + \gamma_{LG} \cos\theta \tag{3.1}$$

Knowing the contact angle of a sessile droplet, the surface tension of the liquid and the surface energy of the substrate, one can calculate the interfacial energy between the solid and the liquid. The surface tension of the liquid can be determined using pendant droplet tensiometry, which is described in the following section. The surface energy of the substrate can be determined using the Owens Wendt method.[146, 147] Assume that the surface energy of a liquid or solid can be split into polar and dispersive components γ^p and γ^d, where $\gamma = \gamma^p + \gamma^d$.

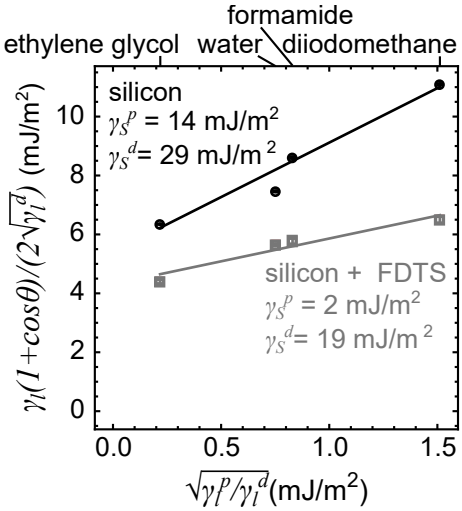

Figure 3.1: Example of Owens Wendt procedure for determining surface energy of silicon and silicon coated with perfluorodecyltricholorosilane (FDTS).

The reversible work of adhesion predicts the contact angle of a liquid droplet via Equation 3.2.

$$\frac{\gamma_L(1+\cos\theta)}{2\sqrt{\gamma_L^d}} = \sqrt{\gamma_S^p}\sqrt{\gamma_L^p/\gamma_L^d} + \sqrt{\gamma_S^d} \tag{3.2}$$

By measuring contact angles of sessile drops of several liquids with known polar and dispersive components, one can produce a scatter plot of $\sqrt{\gamma_L^p/\gamma_L^d}$ vs. $\gamma_L(1+\cos\theta)/(2\sqrt{\gamma_L^d})$ (Fig. 3.1). A linear regression of the scatter plot produces $\sqrt{\gamma_S^p}$ and $\sqrt{\gamma_S^d}$, allowing one to estimate the solid surface energy γ_S.

Determination of contact angles is thus useful for measuring solid surface energies and solid-liquid interfacial energies. In addition, the contact angle may be used directly to measure wetting of a liquid on a surface.

The apparatus used to collect contact angles was a PMMA box, where one wall contained an off-white panel which was used as a light diffuser and a backdrop for the drop (Fig. 3.2). On the other side of the box, a camera viewed the drop through a hole covered with a glass slide. The remainder of the box was opaque to eliminate reflections on the surface of the drop. A hole in the top of the box allowed a syringe to dispense drops onto a substrate. The front of

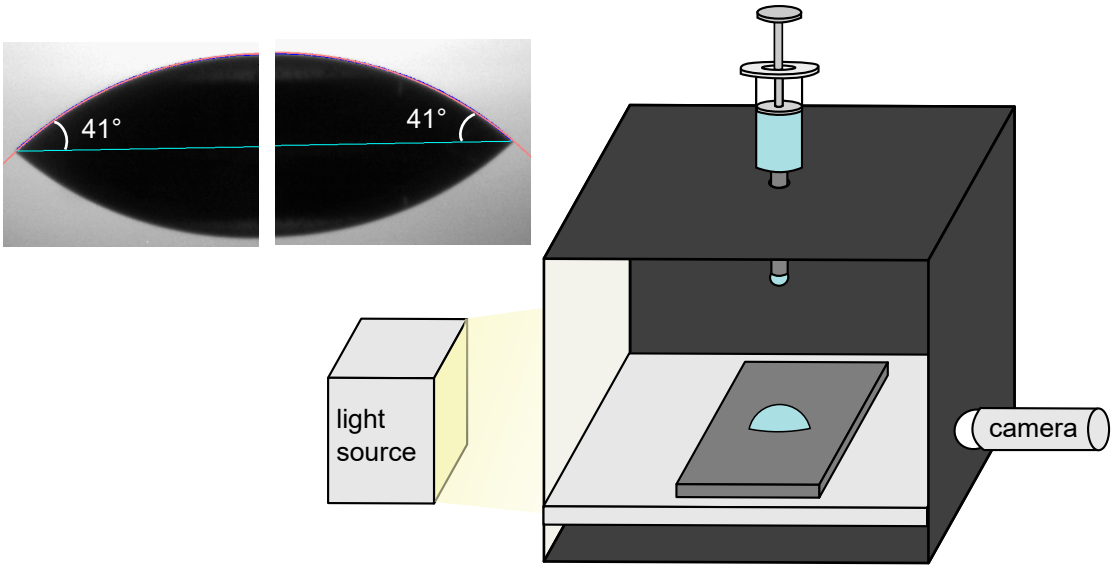

Figure 3.2: Schematic of contact angle image collection and example of fitted image.

the box was open to allow for rapid access to the substrate.

Roughly, contact angle measurement uses edge detection to identify the surface of the droplet and its reflection, then uses circle fitting to measure the angle between the liquid surface and the substrate. The general strategy of this contact angle fitting algorithm is to split the image into quadrants: the left and right halves of the drop and the left and right halves of the reflection. A circle is fit to each quadrant and determine the intersections of those circles to find the actual contact lines. The line between those two intersections is the substrate, which may be tilted relative to the camera. The contact angle is the angle between the tangent to the fit circles and the substrate.

Several complicating factors can interfere with splitting the image into quadrants. As such, the majority of the code developed for this work is devoted to error checking and categorization of the droplet shape. Dust on the substrate, the edge of the substrate, or gradients in the backlighting could appear in the edge image and must be filtered out. The droplet reflection or the droplet surface could be blurry, creating discontinuities in the edge image. The contact angle could be greater than or less than 90°, complicating segmentation of the edge image

into the drop and its reflection. The surface of the droplet is usually not circular. Others have developed polynomial-based[148] and Young-Laplace equation-based[149] strategies for fitting such surfaces. The present technique instead fits the portion near the substrate to a circle.

3.3 Pendant droplet tensiometry

This algorithm described in this section was used to measure surface tensions for Chapter 5.[128]

This section describes a new pendant droplet tensiometry routine for moderate viscosity ($\sim$10–1000 Pa·s) fluids. Conventionally, pendant droplet tensiometry is restricted to low viscosity fluids because the equations governing the method assume no viscous dissipation. Surface tensions of higher viscosity fluids tend to be measured using the de Nouy ring or Wilhelmy plate methods, which require more specialized instrumentation than pendant droplet tensiometry.[150] This section describes a method to measure surface tensions of moderate viscosity fluids using a syringe, a linear stage, and a camera. This section addresses nuances of the Levenberg Marquardt Fletcher algorithm used to fit the droplets, then describes an the experimental and analytical process for measuring surface tensions from pendant droplets.

The apparatus used in this work consists of the same PMMA box used for contact angles (Fig. 3.3). A syringe passes through a hole in the top of the box, and a linear stage controls depression of the plunger to express and withdraw droplets. Light is blocked on four sides, a camera views the droplet through a hole in the PMMA box covered with a glass slide, and an off-white light diffusing panel backlights the pendant droplet. In this case, a door on the front of the box is closed to prevent airflow.

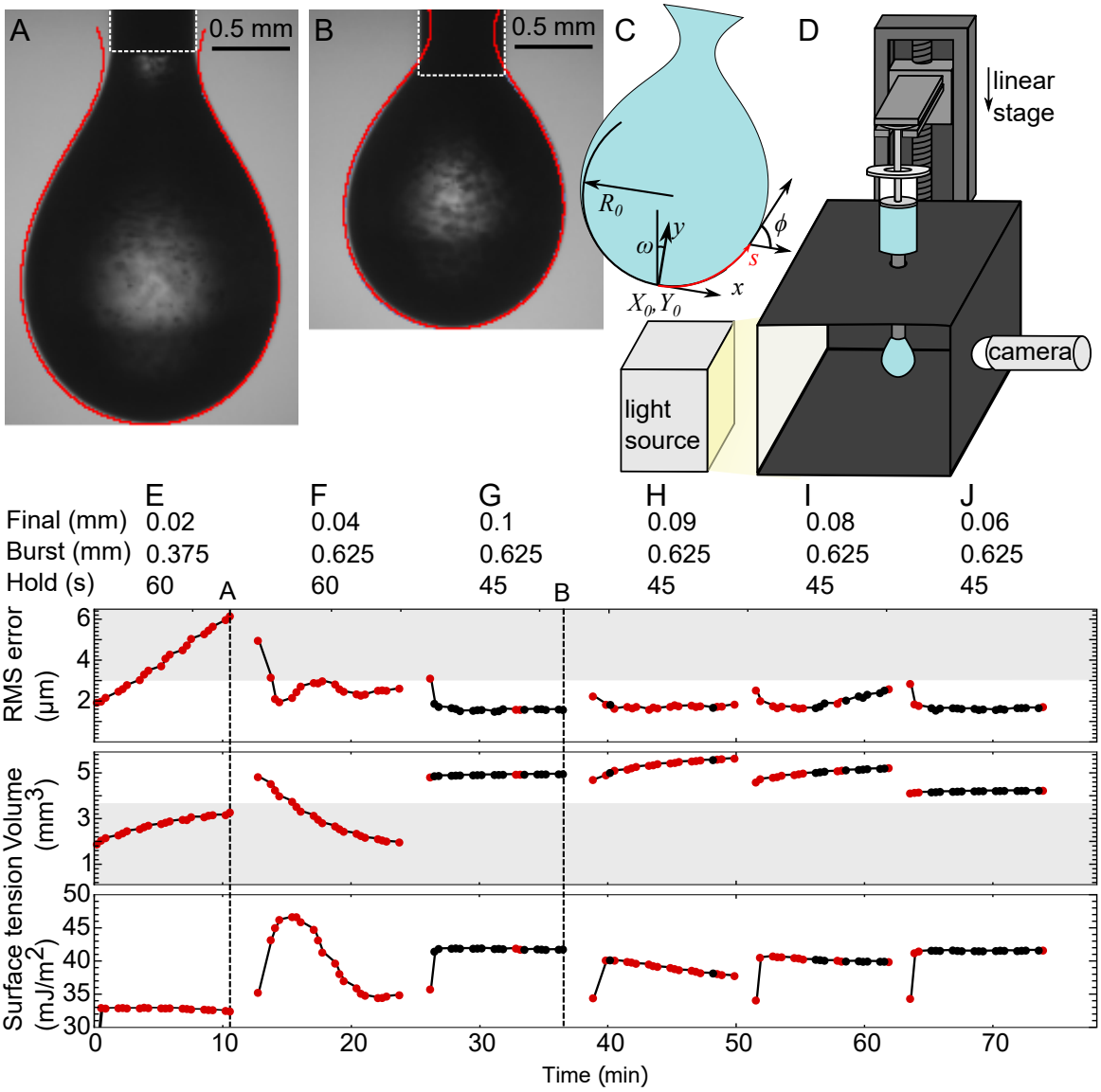

Figure 3.3: A,B) Examples of droplet fits in red. Syringe tips are outlined in white. C) Variables used in pendant drop fitting. D) Schematic of pendant droplet image collection. E-J) Droplet evolution over time, for six example droplets composed of diurethane dimethacrylate, fumed silica, and triethylene glycol dimethacrylate. "Final" is the plunger depression length after growth, "burst" is the depression length during growth, and "hold" is the growth time. First frame is collected immediately after withdrawal. Red points do not meet criteria for inclusion in averages. E) Droplet that continues to grow after withdrawal. F) Droplet that shrinks after withdrawal. G-J) Droplets at quasi-static equilibrium after withdrawal.

3.3.1 The Levenberg Marquardt Fletcher algorithm

The pendant droplet tensiometry algorithm used in this routine is structured as a Levenberg Marquardt Fletcher algorithm. Though the Levenberg Marquardt algorithm is popular, implementation via pendant drop tensiometry reveals some of the structural issues and often-ignored inefficiencies and inaccuracies inherent to the algorithm. The Levenberg Marquardt algorithm is a common numerical search technique particularly suited for least squares problems. Both Mathematica and MATLAB implement the Levenberg Marquardt algorithm for nonlinear model fitting.[129, 151] Applications include models of medical imaging,[152] polymer mechanics,[153] pendant droplets,[154] neural networks,[155] and circuits.[156]

The aim of the Levenberg Marquardt algorithm is to identify a parameter vector β of length m that minimizes an objective function. For example, Benjeddou, et. al. start with a list of stress-strain data points and fit a four-parameter Ogden's law.[153] Alternatively, Berry, et. al. start with a list of x-y data points and fit a five-parameter pendant droplet tensiometry differential equation.[154] This section uses pendant droplet tensiometry to illustrate the implications of choices made in the implementation of the Levenberg Marquardt algorithm. The fitted vector β is composed of $m = 5$ parameters: the x-position, y-position, radius of curvature of the droplet apex R_0, the Bond number Bo (a dimensionless metric of gravity against capillarity), and the image rotation ω (Fig. 3.3).

The Levenberg Marquardt algorithm iteratively chooses β values that describe a curve fit, then recommends a parameter step δ based on the gradient of the objective surface (Fig. 3.4). On each step, when fitting m parameters to n p-dimensional points in x and y, the $m \times 1$

parameter step vector δ is described by Equation 3.3.

$$\delta = (A + \lambda \mathbf{D})^{-1} v \tag{3.3a}$$

$$\mathbf{A} = \mathbf{J}^T \mathbf{J} \tag{3.3b}$$

$$v = \mathbf{J}^T e \tag{3.3c}$$

$$\mathbf{J}_{ij} = \sum_{k=1}^{p} \frac{e_i^k}{e_i} \frac{de_i^k}{d\beta_j} \tag{3.3d}$$

In Equation 3.3, the $n \times 1$ vector e is the error for each point, the $n \times m$ matrix $\mathbf{J}$ is the Jacobian, the $m \times m$ matrix $\mathbf{D}$ is a diagonal matrix, and scalar λ is the Levenberg-Marquardt parameter or damping parameter. The damping term $\lambda\mathbf{D}$ determines the speed and volatility of the algorithm. When $\lambda = 0$, the algorithm progresses as Gauss Newton. When $\lambda > 0$, the chance of overshooting the target is smaller, and issues with rank deficiency are addressed. λ updates on each step to adjust for progression speed.

The objective function S is a least squares fit between the experimental data and the fitted equation. For both experimental and theoretical drop profiles, the objective surface follows an elliptical trough as described by Marquardt.[158]

$$S = \sum_{i=1}^{n} e_i^2 \tag{3.4}$$

Equation 3.3 presents three major questions for the implementation of the Levenberg-Marquardt algorithm.

1. What parameters should be included in β?

2. What should the initial value of λ be?

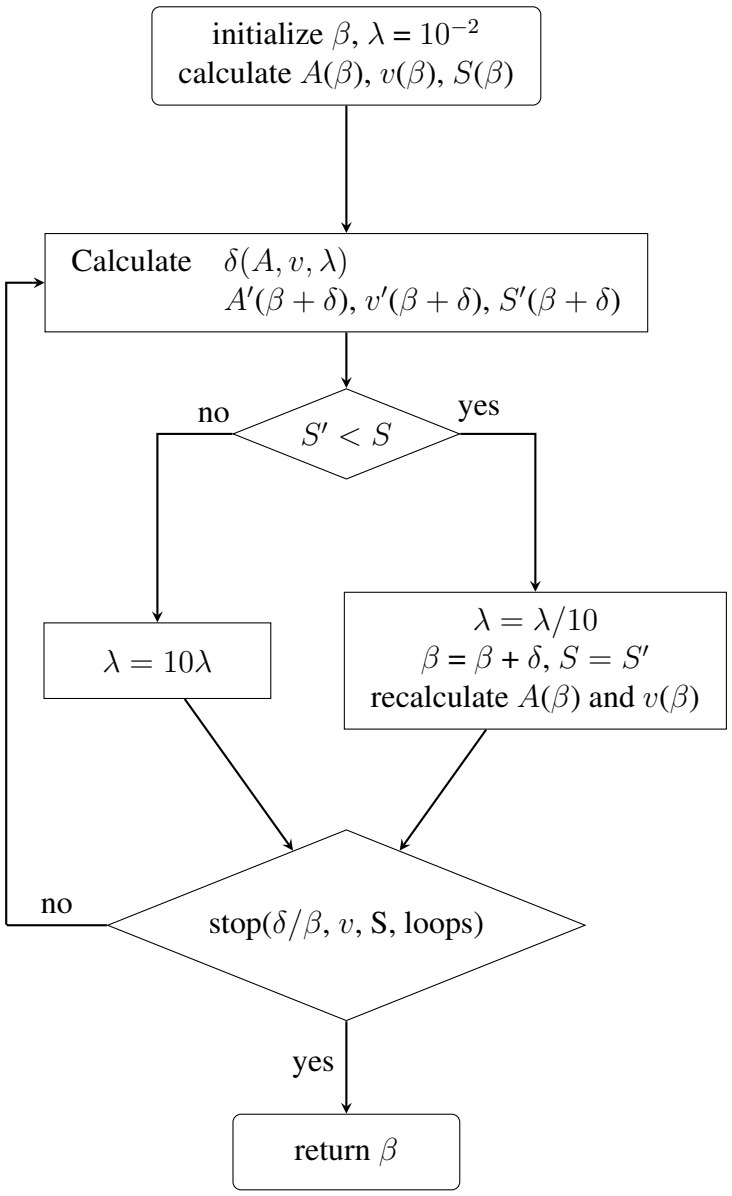

Figure 3.4: The Levenberg-Marquardt algorithm.[157]

3. What should **D** be?

Parameters for β

To understand how parameter selection influences algorithm performance, consider pendant drop tensiometry. The x-y profile of a pendant droplet surface can be described by a system of differential equations that describes an energetic balance between gravity and surface tension. This system describes the x-y profile and surface tangent ϕ as a function of arc length s from the droplet apex, where R_0 is the radius of curvature at the apex.

$$\frac{d\bar{y}}{d\bar{s}} = sin\phi \qquad \bar{y}(\bar{s}=0) = 0 \tag{3.5a}$$

$$\frac{d\bar{x}}{d\bar{s}} = cos\phi \qquad \bar{x}(\bar{s}=0) = 0 \tag{3.5b}$$

$$\frac{d\phi}{d\bar{s}} = 2 - Bo\bar{y} - \frac{sin\phi}{\bar{x}} \qquad \phi(\bar{s}=0) = 0 \tag{3.5c}$$

$$\bar{\xi} = \frac{\xi}{R_0} \tag{3.5d}$$

Note the Bond number Bo, a non-dimensional constant that describes the balance of gravity against surface tension. The Bond number can be described in terms of the density difference between the droplet and atmosphere $\Delta\rho$, the acceleration due to gravity g, and the surface tension γ.

$$Bo = \frac{\Delta\rho g R_0^2}{\gamma} \tag{3.6}$$

In an experimental context, $\Delta\rho$ and g are known. Thus, there are two eligible sets of parameters that can be used to solve this system. Berry uses X_0, Y_0, ω, Bo, and R_0, which are the apex x and y-position, the image rotation, the Bond number, and the apex radius of

curvature.[154] However, an equally valid alternative for β is the parameter set X_0, Y_0, ω, γ, and R_0. Equation 3.5c then becomes

$$\frac{d\phi}{d\bar{s}} = 2 - \frac{\Delta\rho g R_0^2}{\gamma}\bar{y} - \frac{sin\phi}{\bar{x}}, \qquad \phi(\bar{s}=0) = 0 \tag{3.7}$$

Given a set of parameters, Equation 3.5 can be solved numerically (optionally replacing Equation 3.5d with Equation 3.7) to determine an x-y profile. Then the sum of square residuals e between the experimental points and the solved profile can be measured to calculate the objective function S using Equation 3.4. However, calculation of the Jacobian **J** changes depending on whether one is solving for the Bond number Bo or the surface tension γ. As such, the speed of the algorithm changes depending on the variables chosen.

To solve for **J**, $\partial e_i^k/\partial\beta_j$ must be calculated. For a two-dimensional system of points (x_i, y_i), these partial derivatives can be calculated from the parameters ω, R_0, X_0, Bo, and Y_0.[154]

$$\frac{\partial e_i^x}{\partial X_0} = \mp\cos\omega \qquad \frac{\partial e_i^y}{\partial X_0} = -\sin\omega \tag{3.8a}$$

$$\frac{\partial e_i^x}{\partial Y_0} = \pm\sin\omega \qquad \frac{\partial e_i^y}{\partial Y_0} = -\cos\omega \tag{3.8b}$$

$$\frac{\partial e_i^x}{\partial R_0} = -\bar{x}_i = \frac{x_i}{R_0} \qquad \frac{\partial e_i^y}{\partial R_0} = -\bar{y}_i = \frac{y_i}{R_0} \tag{3.8c}$$

$$\frac{\partial e_i^x}{\partial Bo} = -R_0\frac{\partial\bar{x}}{\partial Bo} \qquad \frac{\partial e_i^y}{\partial Bo} = -R_0\frac{\partial\bar{y}}{\partial Bo} \tag{3.8d}$$

$$\frac{\partial e_i^x}{\partial\omega} = \mp(x_i - X_0)\sin\omega + (y_i - Y_0)\cos\omega \qquad \frac{\partial e_i^y}{\partial\omega} = (x_i - X_0)\cos\omega - (y_i - Y_0)\sin\omega \tag{3.8e}$$

However, note that the derivatives in the Bond number rely on another partial derivative $\frac{\partial\bar{k}}{\partial Bo}$. This describes how the droplet surface changes with the Bond number. From Equation 3.5, since $\frac{\partial}{\partial\bar{s}}\left(\frac{\partial X}{\partial Bo}\right) = \frac{\partial}{\partial Bo}\left(\frac{\partial X}{\partial\bar{s}}\right)$, a system of differential equations can be constructed in arc

length s that describes $\frac{\partial \bar{y}}{\partial Bo}$. Note that the only β parameter that appears in this equation outside of a partial derivative is in the second term of Equation 3.9c, $Bo\frac{\partial \bar{y}}{\partial Bo}$.

$$\frac{\partial}{\partial \bar{s}}\left(\frac{\partial \bar{y}}{\partial Bo}\right) = \cos\phi \frac{\partial \phi}{\partial Bo} \qquad \frac{\partial}{\partial \bar{s}}\left(\frac{\partial \bar{y}}{\partial Bo}\right)(\bar{s}=0) = 0 \quad (3.9a)$$

$$\frac{\partial}{\partial \bar{s}}\left(\frac{\partial \bar{x}}{\partial Bo}\right) = -\sin\phi \frac{\partial \phi}{\partial Bo} \qquad \frac{\partial}{\partial \bar{s}}\left(\frac{\partial \bar{x}}{\partial Bo}\right)(\bar{s}=0) = 0 \quad (3.9b)$$

$$\frac{\partial}{\partial \bar{s}}\left(\frac{\partial \phi}{\partial Bo}\right) = -\bar{y} - Bo\frac{\partial \bar{y}}{\partial Bo} - \frac{\cos\phi}{\bar{x}}\frac{\partial \phi}{\partial Bo} + \frac{\sin\phi}{\bar{x}^2}\frac{\partial \bar{x}}{\partial Bo} \qquad \frac{\partial}{\partial \bar{s}}\left(\frac{\partial \phi}{\partial Bo}\right)(\bar{s}=0) = 0 \quad (3.9c)$$

To recalculate Equation 3.8 for the γ formulation, only Equation 3.8d needs to be changed.

$$\frac{\partial e_i^x}{\partial \gamma} = -R_0\frac{\partial \bar{x}}{\partial \gamma}, \qquad \frac{\partial e_i^y}{\partial \gamma} = -R_0\frac{\partial \bar{y}}{\partial \gamma} \quad (3.10)$$

Here, instead of a partial derivative in Bo, Equation 3.10 leaves a partial derivative in γ. Accordingly, Equation 3.9 must be reformulated around γ.

$$\frac{\partial}{\partial \bar{s}}\left(\frac{\partial \bar{y}}{\partial \gamma}\right) = \cos\phi \frac{\partial \phi}{\partial \gamma} \qquad \frac{\partial}{\partial \bar{s}}\left(\frac{\partial \bar{y}}{\partial \gamma}\right)(s=0) = 0 \quad (3.11a)$$

$$\frac{\partial}{\partial \bar{s}}\left(\frac{\partial \bar{x}}{\partial \gamma}\right) = -\sin\phi \frac{\partial \phi}{\partial \gamma} \qquad \frac{\partial}{\partial \bar{s}}\left(\frac{\partial \bar{x}}{\partial \gamma}\right)(s=0) = 0 \quad (3.11b)$$

$$\frac{\partial}{\partial \bar{s}}\left(\frac{\partial \phi}{\partial \gamma}\right) = \frac{\bar{y}\Delta\rho g R_0^2}{\gamma^2} - \frac{\Delta\rho g R_0^2}{\gamma}\frac{\partial \bar{y}}{\partial \gamma} - \frac{\cos\phi}{\bar{x}}\frac{\partial \phi}{\partial \gamma} + \frac{\sin\phi}{\bar{x}^2}\frac{\partial \bar{x}}{\partial \gamma} \qquad \frac{\partial}{\partial \bar{s}}\left(\frac{\partial \phi}{\partial \gamma}\right)(s=0) = 0 \quad (3.11c)$$

Note that here two β parameters appear outside of partial derivatives: γ and R_0. These appear in the first two terms of Equation 3.11c, $\frac{\bar{y}\Delta\rho g R_0^2}{\gamma^2} - \frac{\Delta\rho g R_0^2}{\gamma}\frac{\partial \bar{y}}{\partial \gamma}$. The extra prominence of these two parameters influences $\mathbf{J}$ and thus δ in a way that merely rescaling R_0 between millimeters and pixels cannot. Fundamentally, this means that the two formulations of the

problem change how the parameter step δ responds to changes in the damping term $\lambda\mathbf{D}$. As such, the speed of the algorithm varies depending on whether one is solving for the surface tension or the Bond number (Fig. 3.5A–C).

Damping matrix D

The Levenberg-Marquardt algorithm is often referred to as a trust region algorithm. In trust region algorithms, the algorithm probes a region on the objective surface S, which is a function of the parameters in the vector β (Fig. 3.5D,E). The algorithm predicts a change in objective between the center and the edge of the trust region, then grows or shrinks the region based on the accuracy of the prediction.[159] For example, in Figure 3.5D, from point B the algorithm could have a large trust region which allows an 0.01 step in Bond number from point B to point C, or it could have a small trust region which only allows the Bond number to change by 0.005. The damping term $\lambda\mathbf{D}$ changes the size of the region. A larger λ shrinks the region, while a smaller λ grows it. A larger trust region means that the algorithm takes larger steps toward its destination, which can be faster if the objective surface is predictable but slower if the large step size leads the algorithm to overshoot its target. **D** changes the shape of the region. For example, in Figure 3.5D, from point B, a spherical trust region might have dimensions of 0.005 in Bond number and 0.005 mm in radius of curvature, and an elliptical trust region might have dimensions of 0.005 in Bond number and 0.02 mm in radius of curvature. The only requirement for **D** is that it must be a diagonal positive definite matrix with the same dimensions as **A**.[93] Recall that **A** can be roughly interpreted as a matrix that represents that gradient of the objective surface. Typically **D** is restricted to one of two choices: the identity matrix or a matrix containing the same diagonal as **A**.[93, 157, 158, 160] Using the identity matrix makes the trust region spherical, in that the same amount of territory in all parameters is probed at once, while the diagonal of **A** makes the trust region elliptical.[160] Essentially, using the diagonal fixes scaling issues, where β values can vary by several orders of magnitude

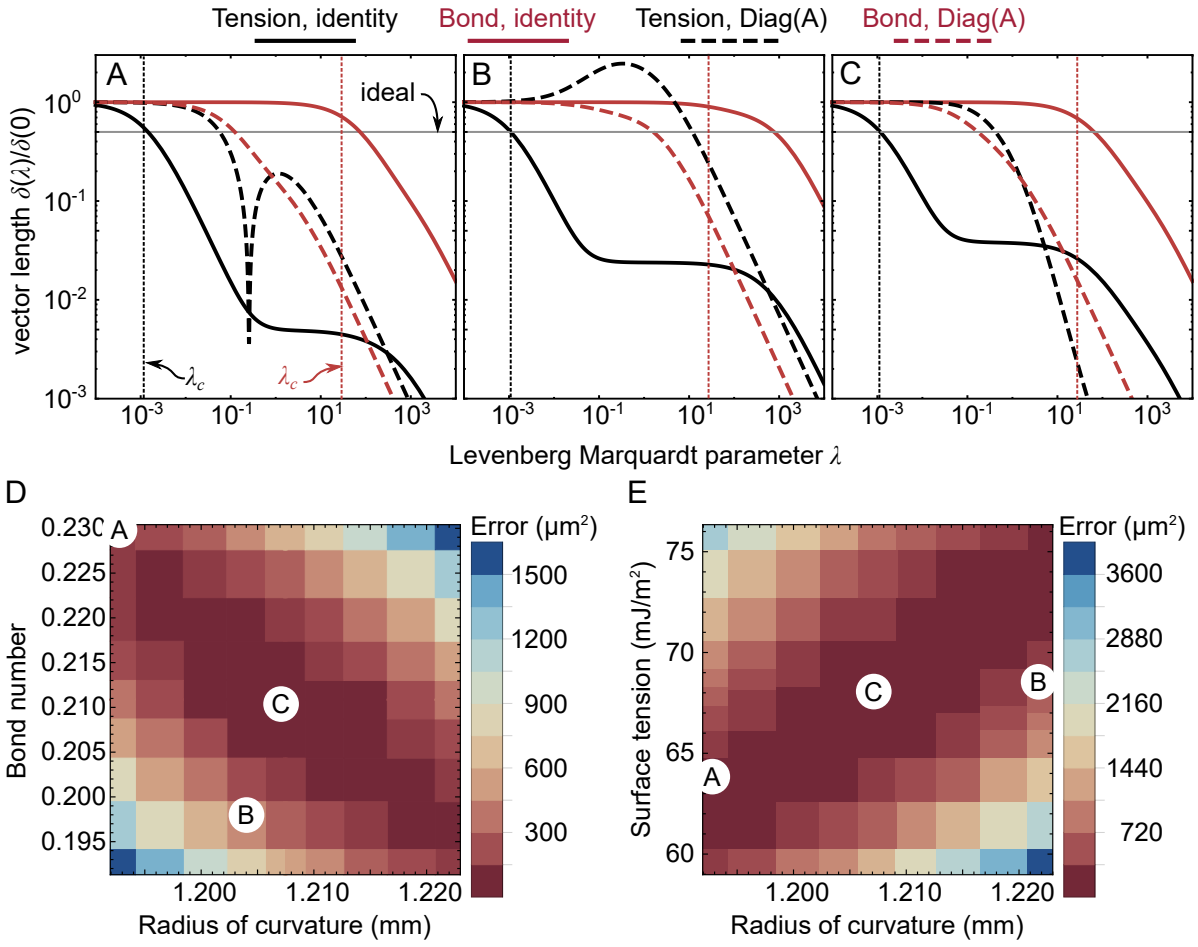

Figure 3.5: Varying β and **D** change dependencies of normalized step size on Levenberg–Marquardt parameter for an experimental water droplet. These dependencies vary at different points on the objective surface. A-C) Dependence of normalized step size on Levenberg–Marquardt parameter for point of similar objective. λ_c is calculated using eigenvalues. D-E) Objective surfaces for Bond number and surface tension formulations.

(e.g. surface tensions on the order of 10 mJ/m^2 and X_0 shifts on the order of 10^{-2} mm), and their gradients can also cover a wide range. The elliptical trust region allows for more predictable dependence of step size on λ. When using the identity, step sizes under the γ formulation decrease sharply at λ values on the order of 10^{-3}, while step sizes under the Bond formulation decrease at much higher λ values on the order of 10^2 (Fig. 3.5A–C). When using the diagonal of **A**, the gap between the two formulations decreases to 1-2 orders of magnitude in λ. As such, if using a fixed initial λ, it is best to use the elliptical trust region.

Levenberg-Marquardt damping parameter λ

The Levenberg-Marquardt damping parameter, in most implementations, is almost entirely arbitrary. Within Marquardt's algorithm, an arbitrary initial value is chosen. On each step, the rate of convergence R is calculated. If the algorithm is converging quickly, λ is reduced by a factor of 2, and the step size is increased. If the algorithm is converging slower than expected, λ is increased by a factor of 2 to 10 to avoid overshooting the target.[158]

As Fletcher notes, "an arbitrary initial choice of λ, if poor, can cause the wastage of a number of evaluations of S before a realistic value is obtained."[157] If λ is too small and the objective surface is unpredictable, the algorithm will waste steps increasing λ by a factor of 2 to 10 to reduce the size of the trust region. If λ is too large, the algorithm will waste many more steps decreasing λ by a factor of 2 to increase the size of the trust region while δ is too small to make any progress. While some prefer a too-large λ avoid Gauss Newton progression[161], others choose a conservatively small initial λ, beginning the algorithm as Gauss Newton and only investing steps to change to Levenberg Marquardt if necessary.[153, 162, 163] However, what value is sufficiently small? In this problem, λ=10^{-4} is small when solving for surface tension using the identity matrix, but when solving for the Bond number using the identity matrix, λ=1 may be sufficient (Fig. 3.5). As such, some researchers have attempted to make the initial λ value adaptive to the problem.

There are two commonly cited fixes in the literature: Fletcher's critical parameter[157] and Yamashita and Fukushima's residual scaling.[164] Both make some headway at addressing the issue with the arbitrary initial choice. However, careless implementation of the solutions can exacerbate the initial problem, such that there is still need for a universal implementation that can be handily wrapped into a black box function without sacrificing efficiency, as discussed in the following sections.

Fletcher's critical parameter

Fletcher reformulated the algorithm to adjust λ to 0 under certain circumstances (Fig. 3.6).[157]

Initially, λ is set to 0, allowing the algorithm to proceed as Gauss Newton. If the algorithm proceeds more slowly than anticipated, λ is set to some critical parameter λ_c. However, in the derivation of λ_c below, Fletcher makes multiple ill-advised assumptions.

On each loop, δ is determined using the matrix $\mathbf{A}$ and vector v.[157]

$$\delta = -(\mathbf{A} + \lambda \mathbf{I})^{-1} v \tag{3.12}$$

By eigendecomposition,

$$\mathbf{A} = \sum_i \mu_i E_i E_i^T \tag{3.13}$$

where μ_i and E_i are the eigenvalues and eigenvectors of the matrix A. Combining Equations 3.12 and 3.13,

$$\delta(\lambda) = \sum_i \frac{E_i E_i^T v}{\mu_i + \lambda} \tag{3.14}$$

Here, Fletcher arbitrarily chooses λ_c such that $\delta(\lambda)$ is at least half of the length of $\delta(\lambda = 0)$

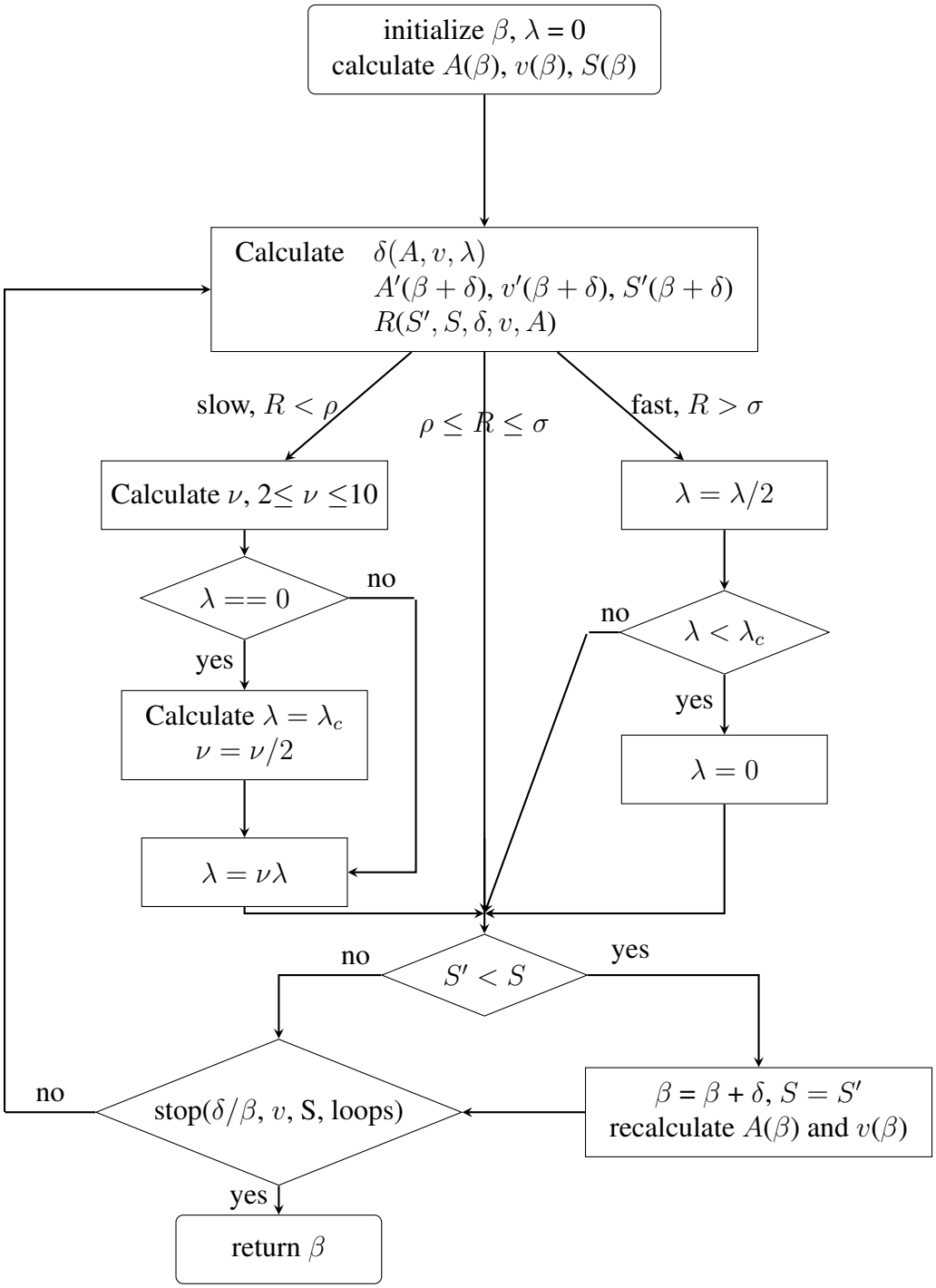

Figure 3.6: The Levenberg-Marquardt-Fletcher algorithm. Fletcher suggests $\rho = 0.25$ and $\sigma = 0.75$.[157]

given by the Gauss-Newton fastest convergence method.[157]

$$\frac{1}{4}\delta(0)^T\delta(0) = \sum_i \left(\frac{E_i^T v}{2\mu_i}\right)^2 \leq \sum_i \left(\frac{E_i^T v}{\mu_i + \lambda}\right)^2 = \delta(\lambda)^T\delta(\lambda) \tag{3.15}$$

Thus, if λ_c is less than the smallest eigenvalue of **A**, then $\delta(\lambda_c) \geq 1/2\delta(0)$. Fletcher and Berry list methods to approximate λ_c as it is defined by the eigenvalues of **A**.[154, 157] Fletcher proposes that a suitable estimate for λ_c is $1/max(tr(A^{-1}))$.[157] Alternatively, Berry uses $\lambda_c = 1/||A^{-1}||_\infty$, which is the inverse of the maximum row sum of $\mathbf{A}^{-1}$.[154] Usually, these approximations are similar, but they can vary by an order of magnitude in problems with imbalanced parameters, e.g. where one variable is on the order of 10^{-2} and another is on the order of 10.

Recall from Equation 3.3 that the step $\delta = (A + \lambda\mathbf{D})^{-1}v$. Fletcher's derivation of λ_c assumes that **D** is the identity matrix. When calculating δ with the identity, λ_c reliably cuts off δ at a value that is greater than or equal to 1/2$\delta(0)$ (Figure 3.5A-C). When solving for γ, $\delta(\lambda_c)$ is very close to $\delta(0)$ (Fig 3.5A-C). However, when solving for Bo, $\delta(\lambda_c)$ can be greater than 1/2$\delta(0)$ (Fig 3.5A-B). As such, when setting **D** equal to the identity matrix, Fletcher's algorithm has an advantage over Levenberg-Marquardt in that it wastes fewer steps reducing the size of the trust region, but it still wastes steps in some cases.

The larger problem with Fletcher's implementation comes from the use of the diagonal of **A**. Fletcher writes that it is acceptable to set **D** equal to either the identity matrix or the diagonal of **A**. When using the diagonal and solving for γ, λ_c is far too low and does not change δ relative to $\lambda = 0$, which is wasteful but not catastrophic. When using the trace and solving for Bo, λ_c is far too high, resulting in very small steps δ, dramatically stalling the algorithm (Fig 3.5A-C).

Residual scaling

A more recent trend in reformulation of the Levenberg-Marquardt parameter is to scale λ by the objective function $S = ||e||^2$. Yamashita and Fukushima suggested that $\lambda = S$,[164] while Fan and others have introduced additional scaling factors. Setting the Levenberg-Marquardt parameter equal to the objective function presents a clear problem derived from units. Consider Figure 3.5B. When solving for γ, an appropriate λ would be 10^{-3}. The error at B is roughly 1000 μm^2. The error could instead be expressed in terms of mm^2, leaving an objective on the order of 10^{-3}. However, when solving for Bo, an appropriate λ would be 10^3, so μm^2 would be better. Moreover, in Figure 3.5B, all four curves have the same error but require vastly different λ values, so Yamashita's method does not help to adjust for different formulations. When solving for Bo, Figure 3.5B, which has an error on the order of 1000 μm^2, requires a Levenberg Marquardt parameter that is one order of magnitude larger than Figure 3.5C, which has an error on the order of 1 μm^2. Thus, even though Yamashita's method scales λ by too much, it does scale λ in the right direction. A later adaptation used $S = ||e||^d, 0 < d < 2$ instead of $S = ||e||^2$ to reduce this scaling problem, but it introduces an extra arbitrary variable d which must be adjusted on each implementation.[165, 166] Later implementations speed up convergence by setting λ to a linear combination of $||e||^d$ and $||v||^d$, arguably improving performance only for experts, but most likely not for those who are only using the black box algorithms implemented in common commercial code packages.[167, 168]

Fan et. al. rescaled the Levenberg Marquardt parameter such that $\lambda = \mu S$, where μ is an arbitrary constant that rescales as in Figure 3.4 and Figure 3.6.[169] This modification adjusts for the unit issue but increases the number of arbitrary choices to two: what value to use for the initial μ and what units to use for S. Because they have not demonstrated consistent improvements in efficiency or accuracy, the works in this dissertation have not employed Yamashita's modifications to the Levenberg Marquardt Fletcher algorithm.

3.3.2 Droplet fitting routine

Pendant droplet tensiometry is a well-established digital image analysis technique used to measure fluid-fluid interfacial energies.[150, 154] By balancing gravity against capillarity, Equation 3.5 describes the surface of a droplet hanging from a narrow probe such as a blunt-tipped syringe. Here, experimental droplet profiles are fit to Equation 3.5 using the Levenberg Marquardt Fletcher algorithm, adapted from [154]. However, Equation 3.5 neglects viscous dissipation. Inks used in direct ink writing tend to have viscosities on the order of 100 Pa·s, so viscous dissipation is non-negligible. At these relatively high viscosities, it is necessary to collect several images of the same droplet over time to track residual stresses. Those images can then be filtered using fit error, droplet volume, and surface tensions to accurately measure surface tension.

A linear stage (Zaber T-LSR150B) controlled by MATLAB moves the plunger on a static syringe. For each droplet, depress the plunger by a **burst** distance, **hold** at that distance for some time, and then retract the plunger to a **final** distance. After retraction, images should be collected of the static pendant droplet over time. Burst, hold, and final values should be calibrated for each ink. The droplet should be large enough that it begins to neck at the end of the hold sequence and should stop changing size after retraction. This work used a 3 mL syringe with a 58.9 mm^2 inner diameter and a 12.7 mm tip with a 0.33 mm inner diameter. The ink used in Figure 3.3 has a zero shear viscosity of 87 Pa·s and a high shear viscosity of 1 Pa·s. Appropriate burst distances are 0.6–0.7 mm/s, hold times are 40–50 s, and final distances are 0.06–0.1 mm. Images of each droplet were collected over 10 minutes.

First, images were filtered using time. Because Equation 3.5 assumes that the droplet is at steady state, it is necessary to monitor the volume over time. If the droplet volume increases or decreases after retraction (Fig. 3.3A,B), measurements will be inaccurate because droplet growth is indicative of an internal fluid pressure not included in Equation 3.5. Thus, any image

that changes significantly from the previous image in the sequence should be discarded. This work uses a critical change in surface tension of 0.2 mJ/m^2 per minute.

Second, images were filtered by fit. If the droplet retains residual stresses, the droplet profile cannot be fit with Equation 3.5. As such, if the root mean square error between the theoretical profile and the experimental profile is too large, the image should be discarded. This work uses a 3 μm critical error for droplet volumes on the order of 5 mm^2.

Third, images were filtered by volume. In Equation 3.5, a change in γ will have the largest effect on x and y at long arc lengths (s). When the droplet is small, the maximum arc length is also small, so droplets of different surface tensions have very similar droplet profile. As a result, if a droplet is too small, the image should be discarded because of a large margin of error.[154] This work uses a critical droplet volume of 65% of the maximum detected volume for the entire data set.

These three filters produce a surface tension for a 63:12:25 UDMA:silica:TEGDMA ink of 40.23 $\pm$ 0.15 mJ/m^2. This is within one mJ/m^2 of a previously reported value for a 75:25 UDMA:TEGDMA mixture that had a surface energy of 39.3 mJ/m^2.[170] Thus, this routine is a reasonable and inexpensive way to measure surface tensions of fluids with viscosities on the order of 100 Pa·s.

3.4 Three-dimensional surface profiles of deposited lines

The algorithm described in this section was used in Chapter 4.[15] Three-dimensional surface profiles provide insight into the spreading behavior of printed lines. Surface profiles were collected using a Keyence VHX-5000 microscope (Fig. 3.7). Because the epoxy surface, glass substrate, and silver-coated glass particles in the line are reflective, glare can interfere with surface profile selection. As such, lines were coated with Helling 3D laser scanning anti-glare spray which obscured the internal structure of the line and prevented reflections.

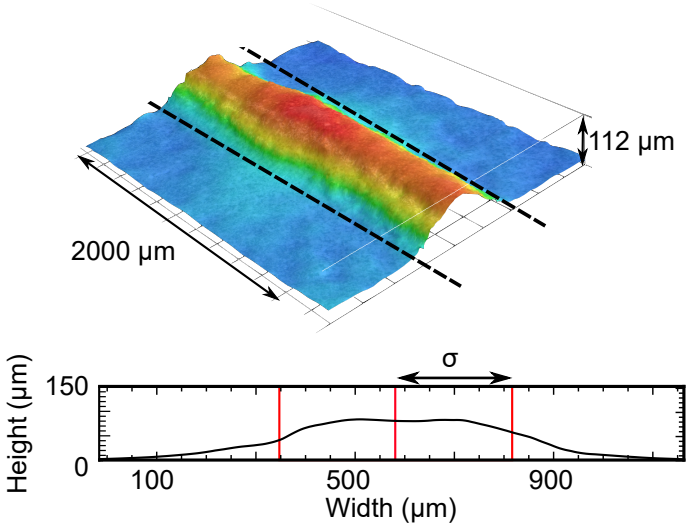

Figure 3.7: Example surface profile collected using Keyence microscope.

Three-dimensional surface profiles were collected at two places on the printed line. 3D tilt correction was executed using the VHX software using points on the glass substrate, and profiles were converted into .csv files using VHX3DExporter, which is a separate program from the software included with the microscope. .csv files consisted of a two-dimensional table of height values. Profiles were analyzed using Mathematica 10.1. The table was averaged along the length of the line to produce an average line profile (Fig. 3.7). To describe the line width, this work uses standard deviation rather than the full width at half maximum because it more accurately takes into account the spreading and shape of the line. A rectangle could have the same FWHM as a rounded profile with the same area and equal or lesser height, but it cannot have the same standard deviation. The height of the line is taken to be the maximum height of the averaged surface profile. Standard deviations and heights for a line are averaged between the two captured regions. The printed width is characterized by measuring the standard deviation of the particle distribution across the width of the line. To normalize distribution widths, the line profile standard deviation describes the volumetric ink distribution across the width of the line.

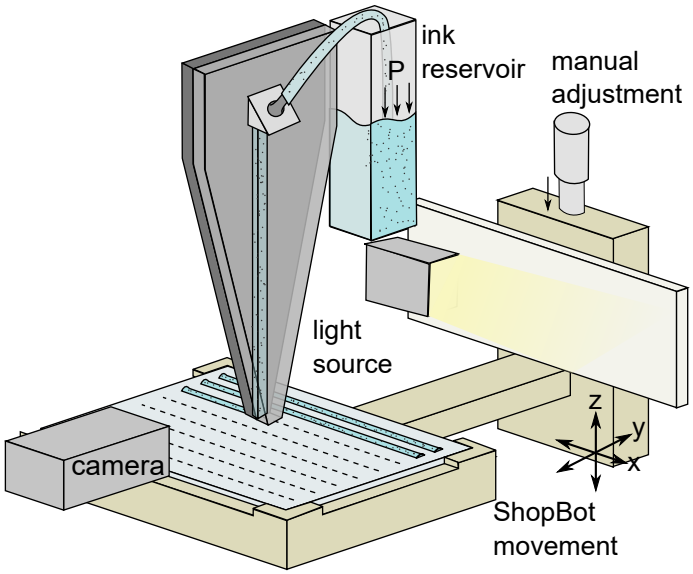

Figure 3.8: Schematic of video collection for meniscus fitting. Stage is simplified in the illustration.

3.5 *In-situ* monitoring of print bead deposition: nozzle to substrate meniscus

The algorithm described in this section was used in Chapter 5.[128, 171]

This section demonstrates how digital image analysis can be used to calibrate equipment geometry and monitor filament stability while printing relatively low-viscosity polymer matrix composite inks.[128, 171] Calibrating the machine geometry at the beginning of the print can allow printing software to automatically correct stage tilt and stand-off distances, but nozzle detection must adapt to variations in fluid lighting. Using a lubrication theory framework, monitoring filament stability can enable printing software to anticipate and prevent filament rupture and empower high-throughput experimental studies of the printing space (defined through parameters such as nozzle speed, flow rate, etc.). Extraction of fluid stability metrics must account for the diversity of fluid morphologies and the inherent quantization of pixels.

3.5.1 Printer configuration and typical printing parameters

Straight lines were extruded from a static nozzle onto a moving substrate (Fig. 3.8). Substrates were 3 inches by 2 inches and were composed of either glass slides or cured ink-coated glass slides which rested on a custom slide holder fabricated using an inkjet 3D printer (Objet 30 Pro). Stage speeds and flow speeds ranged from 1.5 to 9.5 mm/s. A custom MATLAB GUI coordinated the pressure controller, cameras, gantry, and file handling. Inks were extruded at calculated pressures using a high pressure mass flow controller (Fluigent MFCS-EZ). The nozzle was thermally coupled to a water-chilled copper cooling stage using thermal joint compound (Wakefield Type 120) and maintained at 22 °C. The nozzle was attached to the cooling stage using a rubber-padded screw-fasted clamp. Stage movement was controlled by a ShopBot D2418 gantry, which was controlled by custom .sbp code run through Shopbot 3 software. One camera (Point Grey Grasshopper GS3-U3-2356C-C with an Infinity Infinitube FM-200 objective and $\times 0.66$ lens) viewed the extrusion process from the y-direction (orthogonal to the printing direction and the stand-off distance), and a light source illuminated an opaque taupe panel behind the nozzle such that the background of the video was bright, and the filament was dark.

Work flow for each video was as follows. First, Shopbot 3 software was used to move the stage to align the back left corner of the slide with the nozzle and move the stage upwards to be close to the nozzle. Next, the stage height was manually adjusted using the micrometer on the substrate so that the nozzle touched but did not push on the slide. Then, using pre-written .sbp code (gcode for the Shopbot 3 software), the stage lowered to the prescribed stand-off distance, jumped 3 mm inward on the slide, and moved 70 mm at a prescribed stage speed. A prescribed amount of time after MATLAB sent the run command to the Shopbot 3 software, MATLAB sent a command to the Fluigent software to apply a prescribed pressure to the reservoir, which began flow. At the end of the line, the stage jumped to a lower height, jumped to the beginning

x and y position of the new line, jumped to the prescribed stand-off distance, and proceeded to write another 70 mm line. This process was repeated for nine lines, increasing the stage movement speed between the third and fourth lines and between the sixth and seventh lines. After the ninth line finished printing, the stage lowered and moved out of the way, and the applied ink pressure was reduced to 0.

This work utilizes rectangular nozzles with 5° flared edges (Figure 3.8). Nozzles were fabricated in a clean room by etching 350 by 150 μm channels into a 525-μm-thick silicon wafer and then capping the channel with a 500-μm-thick glass wafer. For digital image analysis, nozzles could be larger, smaller, pyramidal, cylindrical, or conical, as long as the cameras are suited to the printing geometry.

The depth of field and resolution of the camera must be large enough to clearly discern the edges of the filament and nozzle, and the approximate geometry should be known. The frame rate of the camera must be high enough to capture oscillations in contact line position. The filament should be backlit to avoid glare on the fluid surface.

Because the cameras are mounted with the print head, calibration, stability monitoring, and rotational flow monitoring techniques can be applied throughout the entire build. However, the geometry calibration routine described here relies on a flat, reflective substrate, and the stability monitoring routine relies on a predictable substrate position. The algorithms described in this chapter assume that the substrate is horizontal in the frame, but tilted substrates could be accommodated given a strong visual indicator of orientation.

3.5.2 Geometry calibration

The stand-off distance, or the distance between the nozzle and the substrate, influences stability and rotational flows in a liquid filament.[128] Poor initial calibration of nozzle position relative to the substrate, vibration-induced movement of the nozzle or substrate, and substrate

tilt induce inaccuracies in the prescribed stand-off distance. On-the-fly calibration and adjustment of the stand-off distance and stage tilt can save time and material by anticipating and correcting problems with a build before it begins. The stand-off distance can be measured on the first layer while writing a skirt or support layer. Subsequently, instrument control software could adjust the stage using digitally-controlled stage adjustment screws or adjust the toolpath to match the stage. Though more challenging on rough and nonreflective substrates, calibration can be repeated throughout the print.

This section outlines a method for detecting nozzle and substrate positions within a frame. The nozzle should contrast with the background and constitute the longest vertical edges in the image. Filaments (as opposed to droplets) are convenient, but the technique only requires an image that has a reflection (Figure 3.9A). Including several nozzle widths worth of filament can improve the speed of substrate detection by introducing an initial estimate of the substrate position, but it is not strictly necessary.

Calibration of the system geometry used the following steps.

1. The nozzle left and right edges were detected for several frames and the median was selected.

2. The image resolution was calibrated by comparing the nozzle width in pixels to its known width.

3. An estimate of the substrate location was detected for several frames, and the median was selected.

4. The bottom edge of the nozzle was detected for several frames and filtered to select the best fit.

5. The channel exit location was estimated from the nozzle geometry.

6. The substrate location was measured across the video to calibrate the stage tilt.

This calibration process illustrates the benefits and costs of the two most common line fitting techniques: Hough transforms and least squares linear regressions. While Hough transforms are good at discarding small groups of extraneous points, they are vulnerable to noise.[136] Least squares regressions must take into account every point and handle vertical lines poorly, but they are better at handling small datasets (relative to the image size) because they are amenable to built-in assumptions.[136] The nozzle edges dominate the edge image in Figure 3.9C, but there are some outliers at the right and bottom edges of the nozzle, so Hough transforms are well suited to detect the left and right edges. There are many ways to draw a nearly horizontal line through Figure 3.9E and pick up an equivalent number of points. Knowing where the bottom edge should be relative to the noise in the filament and nozzle, filtering and linear regressions are well suited to detect the bottom edge.

Nozzle left and right edges

The nozzle width, which is consistent across videos, can be used to calibrate the image scale. The nozzle can be detected by performing a Hough transform on the edge image and filtering the list of lines to include only lines that are close to the prescribed nozzle orientation (here, within 3° of vertical) and then narrowing that selection to include only pairs of lines within an expected range of distances apart (here, 220–230 pixels, where the frame size is 960 by 280 pixels). The pair with the most similar slopes are the left and right edges of the nozzle. If fitting failed, the edge detection radius was increased. At a radius of 6 pixels, another frame was selected. For greater accuracy, one could average this process over several frames. The line-to-line distance and the known nozzle size can be used to determine the image scale in pixels per millimeter.

Substrate

Substrate detection utilizes the reflection of the nozzle off of the substrate. Recall that the camera is fixed to the nozzle, so when the substrate withdraws between lines, there is no substrate in the frame. Thus, to detect the substrate location, it is necessary to detect withdrawal events by identifying frames with no nozzle reflection. Specifically, frames with no points within a certain number of pixels from an extension of the nozzle edges into the bottom half of the frame were considered to have no reflection. To increase the speed of the algorithm, initial guesses for times of withdrawal events were used, and the algorithm searches near those guesses until it identifies the first and last frame of each withdrawal event.

Once the frames with substrates have been detected, the substrate is detected within those frames. Here, a long continuous filament (at least half of the width of the frame) is useful because it appears in a Hough transform. If the substrate is not level in the frame, a Hough transform can be performed on the filament, and the substrate angle can be calculated by averaging the angles of the topmost and bottommost lines, which are likely the top surface of the filament and its reflection. Using that angle, the frame should be rotated before reflections are collected. Once the substrate is level in the frame, the substrate can be detected. An initial guess is used to increase the algorithm speed. When extruding a filament, an initial estimate can be obtained using the average of the topmost and bottommost horizontal Hough transform lines. When extruding droplets, an effective initial guess is the center of mass of all points in the edge detection. Only one estimate of this type is necessary per video, as previously detected substrate positions can be used as estimates during tilt correction. The substrate will be at the line at which the upper segment and the reflection of the lower segment have the most points in common, which can be measured by taking the product of the upper and reflected lower segment (Figure 3.9B). Because the product intensity can be nonmonotonic with dividing line position, it is best to probe every pixel within a reasonable range rather than using a

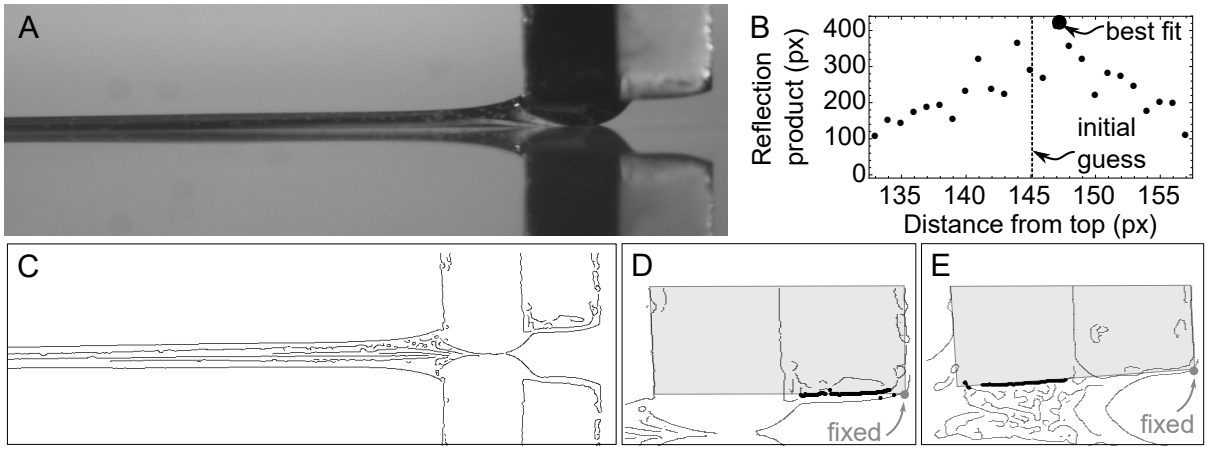

Figure 3.9: Nozzle and substrate detection. (A) Initial frame. (B) Number of pixels in product of image and reflection for a range of probed reflection planes. (C) Edge detection. (D, E) Linear regression of bottom edge for two frames. Gray points are the front nozzle corner, black points are bottom edge points, and the gray area is the extracted nozzle.

slope-based search algorithm (Figure 3.9B).

Bottom edge

The bottom edge of the nozzle can be detected using a linear regression. The regression should use the side with the most contrast with the fluid, which is the glass side in Figure 3.9D and the silicon side in Figure 3.9E. If the glass side has the highest contrast, the second lowest points on the right half of the nozzle should be used. If the silicon side has the highest contrast, the highest points on the left half of the nozzle should be used. In both cases, it is useful to define the bottom edge as a line that intersects the lowest point on the nozzles right-most vertical edge (Figure 3.9D and E). Fixing the corner mitigates inaccuracies due to local surface roughness and chips on the glass on silicon nozzle.

Tilt

In all systems, the stage has some tilt. Because the stand-off distance impacts filament stability and deposited filament geometry, calibrating the tilt can inform printing parameter

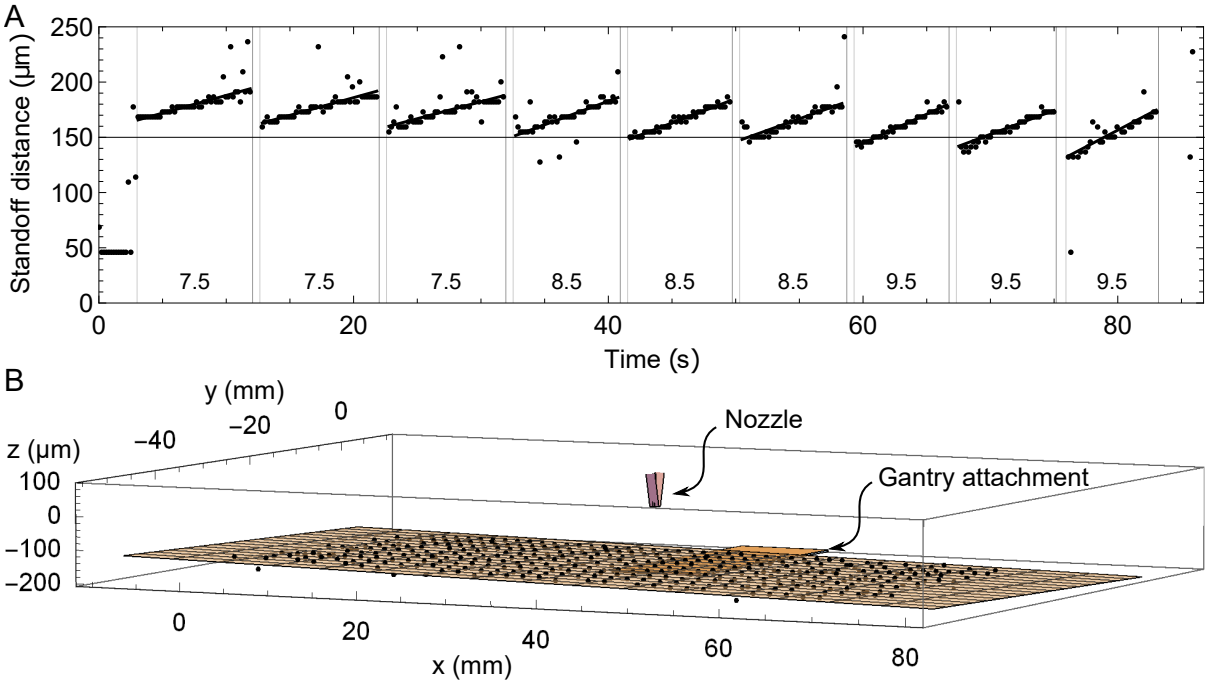

Figure 3.10: Calibration of a stage with severe tilt, for an intended stand-off distance of 150 μm. A) Stand-off distance as a function of video time. Grid lines indicate beginnings and ends of written lines, and numbers indicate stage speed. B) Measured stand-off distance and linear interpolation with exaggerated height scale.

selection and post-print diagnostics. Further, knowing the exact position of the substrate at each frame is necessary for contact line measurement. Rather than re-measuring the substrate position on each frame (which for this system was up to 20,000 frames for 630 mm of printing length), it is faster and more accurate to first gather a rough estimate for the whole video using 3-5 frames, then finely calibrate the tilt on the entire stage using 20-100 frames. By correlating frames with no reflection with programmed line transitions, video times can be translated to stage locations, allowing for a linear interpolation of the substrate plane (Fig. 3.10). From this linear interpolation, the stand-off distance can be predicted at any time in the video, and the stage leveling screws or print path can be adjusted between calibration and the start of the build.

3.5.3 Monitoring filament stability

In DIW, filaments are prone to rupture at a given combination of flow speed, raster speed, and stand-off distance.[106, 110, 128] Digital image analysis, in conjunction with lubrication theory, can predict and prevent the conditions under which the filament will rupture.[128] Finite element analysis has been used elsewhere to predict filament morphology and rupture,[105, 106, 107] and manual image analysis has been used to reveal discrepancies between experimental filament morphology, models, and finite element simulations.[105, 107] Digital image analysis provides more rigorous insight than manual image analysis into the effects of printing parameters on filament stability and perturbation recovery by processing large quantities of experimental data describing the dynamic morphology of stable and unstable filaments. Furthermore, digital image analysis can inform surface modification in detailed numerical models of stability. Though some finite element models fix the liquid-substrate contact angle and the wetting length,[105, 107] experiments show that the contact angle and wetting length are useful dynamic indicators of filament stability.[128] The following sections describe an approach for extracting these and other indicators from extrusion videos.

Algorithms do not eradicate biases; they calcify them. Consequently, computer vision remains one of the most difficult challenges available to artificial intelligence. To extract features from an image, programmers must carefully establish a set of assumptions about what they expect to see. Famously, programmer biases inhibit the accuracy of facial recognition and image labeling software.[172, 173] Similarly, a poor assumption set used to analyze a systematic study could erroneously present statistically significant effects in the output data set that actually come from biases baked into the algorithm, not physical reality. For example, assuming that the extruded fluid is visually uniform will lead to misidentification of particles and reflections within the print bead as part of the fluid surface (Figure 3.11A and 3.11D). Assuming that the upstream fluid meniscus is an arc, as is used in the viscocapillary theory derived by Hig-

gins and Scriven,[131] will lead to mischaracterization of necking filaments (Figure 3.11C). Assuming that the substrate is clean will lead to misidentification of dust as part of the meniscus (Figure 3.11D). Anticipating how a set of images will deviate from their ideal behavior is critical for extracting accurate data.

Using hundreds of videos consisting of 5,000 to 20,000 frames each, the following protocol was developed to extract and fit fluid surfaces when extruded from a rectangular nozzle onto a flat substrate. Unlike nozzle detection, which only needs to be performed once per video, surface detection and fitting must be performed on each frame in the video. Because manual analysis is not scalable, the following automated procedures make feature detection possible. These frames exhibit a variety of lighting conditions, fluid surface morphologies, and surface irregularities. Of course, there is more than one way to extract contact points and points of maximum curvature. Further refinement may be necessary when transitioning to the second layer of a print, when printing geometry and lighting conditions are drastically different, when ink viscosities are low enough to produce satellite droplets, or when ink viscosities are high enough to produce unruly ruptured filaments.

As with substrate detection, surface detection begins with an edge image of a blurred grayscale image. The edge image is converted into a list of eligible points that is then separately filtered into upstream points and downstream points. Linear regressions can extract contact points and angles from the lists of points. Fitting the points with interpolations and nonlinear regressions can identify points of maximum curvature. If surface detection fails, the Gaussian blur and edge detection kernel sizes should be modified.

3.5.4 Meniscus point collection

Meniscus profile points were collected by blurring the frame at a given radius to remove noise, running a Canny edge detection on the blurred frame to collect surface points, and

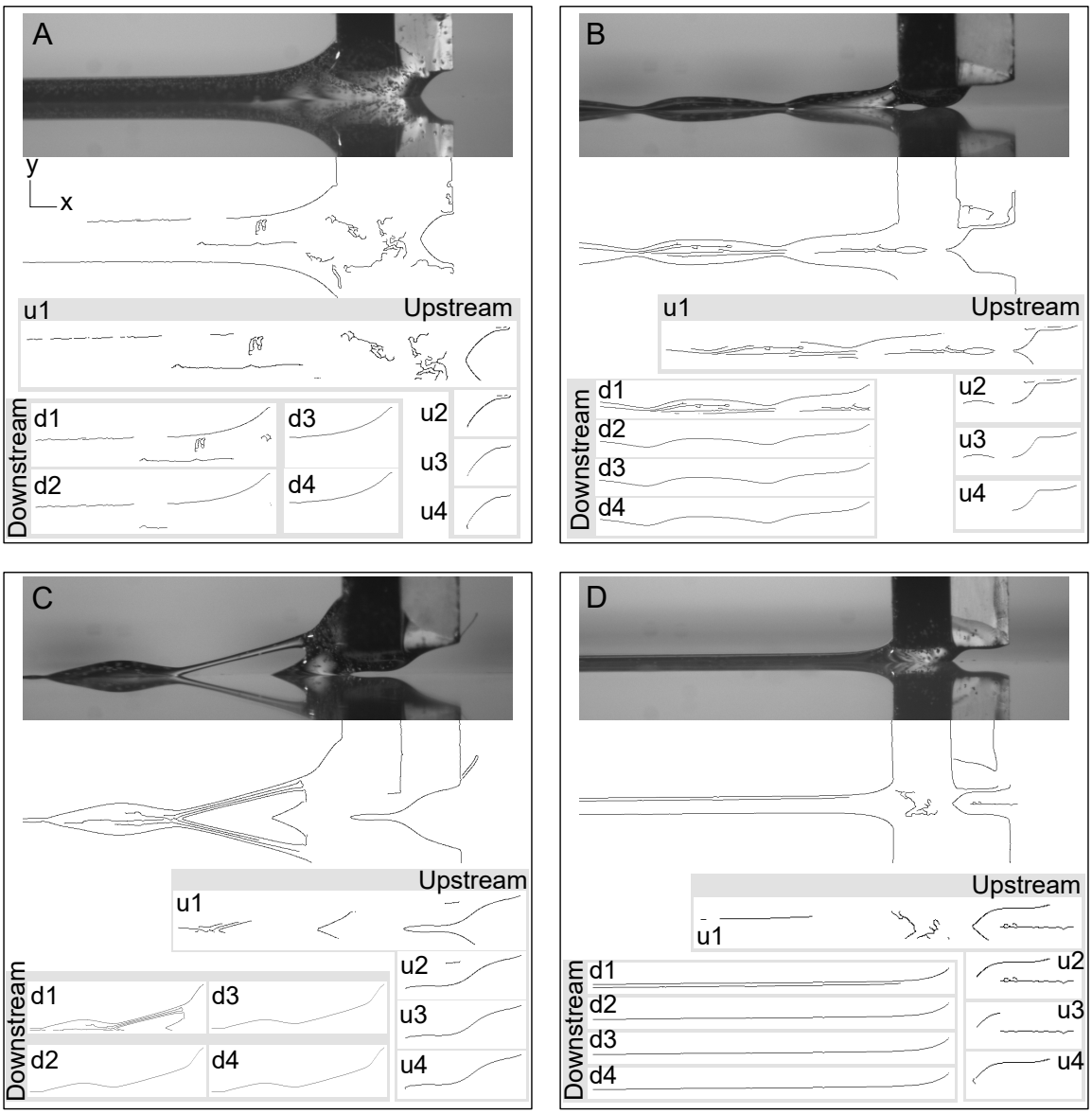

Figure 3.11: Upstream and downstream meniscus points selection for four non-ideal frames. (A) Unfocused image produces broken downstream surface edge. (B) Contact point forms. (C) Filament with multiple contact points, about to rupture. (D) Debris on substrate.

filtering the points into upstream and downstream surfaces. If surface detection failed, the blur radius was increased and the segmentation process was repeated for the set that failed.

Upstream meniscus points must span the substrate to the bottom of the nozzle, with no gaps. Upstream point selection uses the following protocol to filter lists of points.

u1. Select points between nozzle and substrate. Automatically pad this selection by the margin of uncertainty of substrate detection (here, half of the distance between the nozzle and substrate). Because the contact line sometimes reaches behind or ahead of the nozzle, the left and right nozzle edges cannot be used for filtering.

u2. To remove points inside the fluid and on the downstream meniscus, select the right-most points at each y-position. This may pick up erroneous points if there is debris on the substrate, as in Figure 3.11D, or a reflection on the substrate, as in Figure 3.11AD. Unfortunately, this loses points in surfaces containing horizontal spans, including necking filaments, as in Figure 3.11C, and wetting on the underside of the nozzle, as in Figure 3.11B and 3.11D. Furthermore, poor focus and glare can produce gaps in edge images (Figure 3.11A, downstream). If there are gaps in the upstream surface, this step picks up points in the downstream surface or in the print bead. To remove points inside the fluid far from the meniscus, iteratively remove the leftmost point if it is well above the substrate (here, 10 pixels above the substrate). To correct for reflections, select from the edge image all points above and to the right of the leftmost point.

u3. To remove points inside the fluid near the meniscus, select the lowest point at each x-position (Figure 3.11AC).

u4. To remove erroneous points from debris on the substrate as in Figure 3.11D and necks between contact points as in Figure 3.11B, select the longest continuous span in x that nearly reaches both the nozzle and the substrate (here, within 10 pixels). To ensure that

the contact point is included, expand the span using neighboring points to reach both the substrate and nozzle (Figure 3.11D).

Downstream meniscus points must reach the back of the nozzle. Downstream point selection uses the following protocol to filter lists of points:

d1. Select points to the left of the nozzle and above the substrate. Again, to adjust for substrate location uncertainty, pad the selection. To remove deposited droplets that are not connected to the print bead, select the rightmost span that is continuous in x (here, a gap distance below 10 pixels).

d2. To remove points inside the filament, select the top-most point at each x-position (Figure 3.11AD).

d3. To adjust for imaging conditions that produce a gap in the downstream edge surface, select the rightmost span that is continuous in y (here, a gap distance below 10 pixels) (Figure 3.11C).

d4. To ensure that the contact point is included, expand the selection as necessary to reach the nozzle.

There are several plausible ways to modify this algorithm, but all come with trade-offs. Connected component labeling and gradient operators could enhance point selection, though care should be taken to ensure that the former accounts for gaps in the meniscus and the latter accounts for necking.[133] Some issues with erroneous points could be resolved by changing the parameters of the edge detection, but not without causing new problems. This work uses a 5 by 5 edge detection kernel and automatic thresholding by Wolfram Mathematica.[132] Increasing the edge detection kernel size can remove erroneous points, but it turns sharp fluid-substrate contact lines into smooth curves. Similarly, increasing the gradient threshold for edge detection can filter out smooth shadows inside the print bead, but under some focusing

and lighting conditions, a higher threshold filters out fluid surface points but not sharp shadows inside the print bead. Using the fit of the previous frame as an initial guess could improve the speed and accuracy of the algorithm, but may cause the program to miss formation of new contact lines. Incorporating horizontally biased kernels into the edge detection process could eliminate dust on the substrate but would also eliminate valid portions of the upstream and downstream menisci (Figure 3.11D).[136]

3.5.5 Point fitting

The extrusion stability of low-to-moderate viscosity fluids depends strongly on surface tensions. Specifically, in slot die coating, the stability of a print bead depends on an energetic balance between viscous dissipation and capillarity.[130] A similar effect is demonstrated in direct ink writing. As such, knowing the curvature of the fluid surface, which determines the Laplace pressure differential between the upstream and downstream meniscus, is critical for measuring stability. To obtain curvatures to estimate the Laplace pressure, equations are needed that describe the full fluid surface. One can either use interpolations or nonlinear regressions to describe these surfaces. Where y describes an upstream or downstream surface, the curvature κ_1 is described by Equation 3.16.

$$\kappa_1 = \frac{y\prime}{(1 + y\prime\prime^2)^{3/2}} \tag{3.16}$$

Assuming that the orthogonal surface is an arc intersecting the nozzle width w and spanning the stand-off distance h, the curvature κ_2 in the other dimension can be approximated using Equation 3.17.

$$\kappa_2 = \left(\frac{h}{2} + \frac{w^2}{8h} \right)^{-1} \tag{3.17}$$

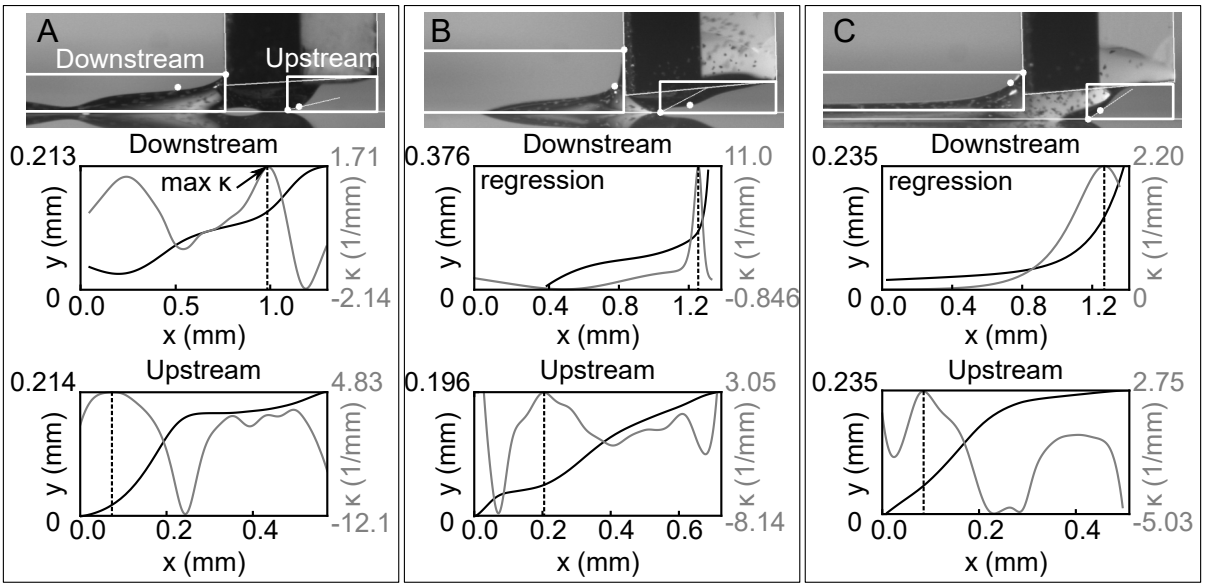

Figure 3.12: Meniscus point fitting examples. Nozzle, substrate, and plotted regions are annotated. (A), (B) Droplets. (C) Balanced filament.

From these two curvatures, the Laplace pressure differential ΔP_L is described by Equation 3.18, where γ is the fluid surface tension.

$$\Delta P_L = \gamma(\kappa_1 + \kappa_2) \tag{3.18}$$

The central challenge of fitting pixels is that their positions are restricted to integers. Where the surface is nearly horizontal or vertical, small steps from one pixel to the next appear jagged, resulting in errant spikes in first and second derivatives. Regressions avoid these pixel effects and are often appropriate for downstream surfaces. The downstream meniscus usually follows a nonlinear regression on fitting parameters a, b, c, d, f, and g (Figure 3.12B and 3.12C).

$$y = a + bx + ce^{d(x-xmax)} + fsin(gx), 0 \leq\ c, 0 \leq g \leq \frac{3\pi}{xrange} \tag{3.19}$$

These regressions contain three terms: a linear component to describe tilt, an exponential to describe nozzle wetting, and a sinusoid to describe necking and dropletting. This fit accurately

describes continuous filaments, as in Figure 3.12C, and some droplets, as in Figure 3.12B, even though the viscocapillary model assumes that the downstream meniscus is an arc.[130, 131]

Upstream surfaces and some dropletting downstream surfaces exhibit diverse morphologies for which there are no obviously appropriate regressions. As such, interpolations are appropriate for the more irregular surfaces. After smoothing, points are filtered to remove duplicate points in x and then interpolated. A list is calculated from the derivative of the interpolation and then smoothed with a Gaussian filter and interpolated. The process is repeated for the second derivative and curvature of the surface as a function of x-position. To avoid noise from the inherent quantization of pixel locations, the interpolation method must include smoothing.[174] However, smoothing can report erroneously high radii of curvature. Furthermore, Gaussian smoothing can introduce periodic noise known as ringing, which could be amplified over successive derivatives.[136] Smoothing must be adaptive to the slope of the pixels. The horizontal and vertical stretches require long range blurs to remove quantization effects (e.g., Figure 3.12A and 3.12B downstream), whereas sharply changing surfaces require short range blurs to avoid reducing the apparent curvature of the surface (e.g., Figure 3.12C upstream). This work uses moving average background estimation.[175] Another option is a moving Gaussian filter that adapts its kernel size to the gradient direction or to the distance in the list to the next step in y-position.[175] Additional methods for finding points of maximum curvature from a list of pixels have been developed by Bennamoun and Boashash.[174, 176]

3.6 Particle distributions

The single-peak methods described in this section were used in Chapter 4.[15] The multi-peak methods were used in Chapter 6–8.

Measurement of particle distributions is central to evaluation of acoustophoresis performance. Narrow distributions of particles in the focused state and wide distributions in the unfo-

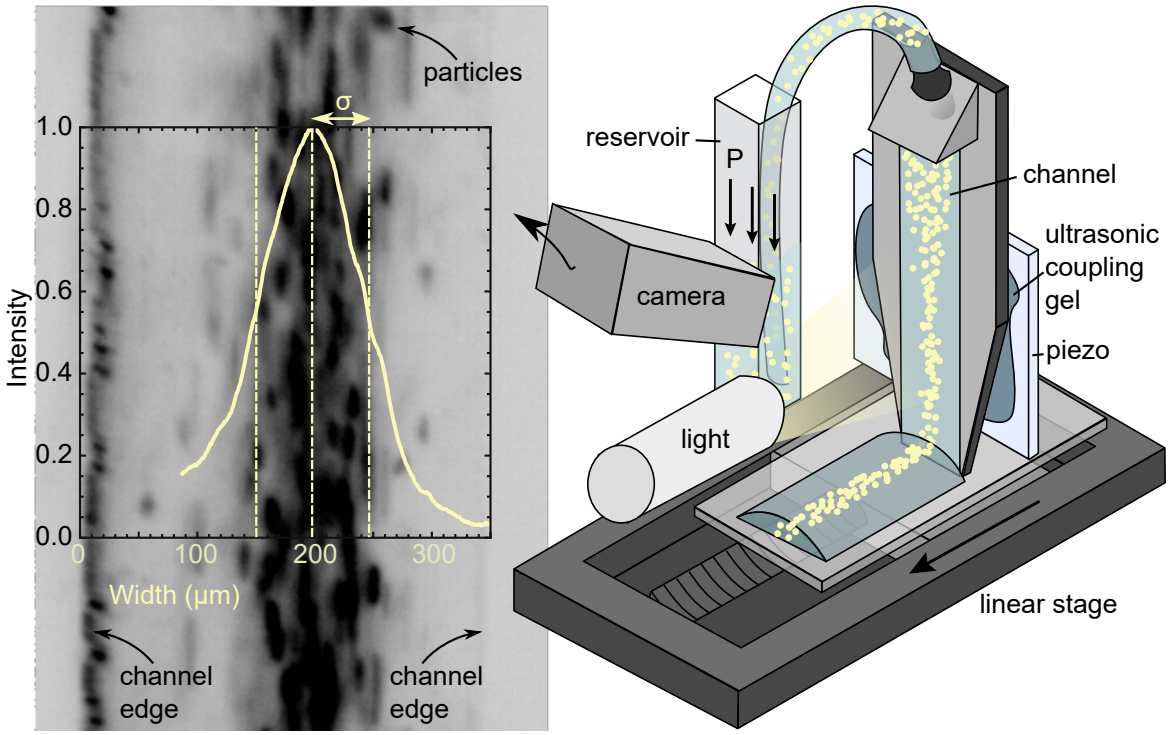

Figure 3.13: Schematic of video collection in nozzle and example of distribution collected from single frame. Frame is inverted.

cused state indicate that acoustic focusing is an effective way to manipulate the microstructure of the line. This section describes three settings in which the particle distribution can be measured: within the channel, within a cured line, and within the printed line during the printing process.

3.6.1 Within the channel

Measurement of particle distributions within the channel requires a camera directed at the channel and a light that illuminates the particles and edges of the channel (Fig. 3.13). This work uses an Infinitube FM-200 objective with a Guppy Pro F-503B camera. The field of view and depth of field of the camera should be sufficient to capture the entire width and depth of the channel, and the exposure time should be short enough that the distance that particles move during the exposure is much shorter than the particle length.

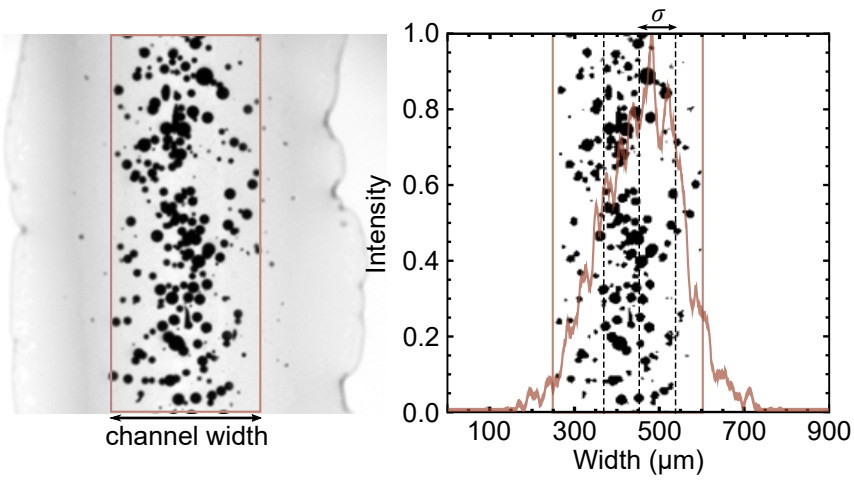

Figure 3.14: Collection of particle distributions from the printed line.

Wolfram Mathematica 10.1 was used to process the videos.[132] First, the left edge of the channel was detected as follows. The first frame of the video was transformed into an intensity-weighted edge image using a Shen Castan edge detection algorithm (EdgeDetect). Then, a Hough transform (ImageLines, threshold = 0.25) was used to detect the left edge of the channel. Edge detection parameters (pixel range, straight edge parameter, and image compression) were iteratively tested until a line was detected within an appropriate location and slope margin. Next, 35 intensity profiles were taken across the channel, for each of 8 frames. Because the captured area of each frame encompasses 0.67 mm, and the ink flows 5 mm per frame used, the only double-counting involved in this intensity profile happens because particles travel some distance during camera exposure. The left quarter of the channel was discarded because a bright reflection off of the left channel edge obscured data (Fig. 3.13). The average of all profiles was calculated to create a composite profile. For each profile and for the composite profile, the intensity was normalized onto a 0–1 range. The focusing width was measured as the standard deviation of the composite intensity profile, divided by the standard deviation of a uniform distribution (76 μm).

3.6.2 Within cured lines

Particle distributions in printed lines were measured after curing (Fig. 3.14). Images were captured of 10.9 mm of each printed line using an inverted light microscope (Nikon TI-U Eclipse). Images were analyzed using Wolfram Mathematica 10.1.[132] Images were thresholded to detect only particles (MorphologicalBinarize, threshold = 0.3–0.85), and the resultant binary images were summed along the length of the printed line and normalized to create a composite intensity profile (Fig. 3.14). The particle distribution can be described by the standard deviation of the composite profile.

3.6.3 Within the printed line during printing

To track changes in the particle distribution within the printed line over the course of the print, videos were collected from below the nozzle (Fig. 3.15). These videos were also used for particle image velocimetry, discussed in the following section. The nozzle and substrate were illuminated using light transmitted through a red filter cube, to prevent curing. Videos were collected from underneath the nozzle through the glass substrate using a Point Grey Grasshopper GS3-U3-2356C-C camera with an Infinity Infinitube FM-200 objective and $\times$0.66 lens, at 86 fps. The camera depth of field must be large enough to capture all particles, the lighting conditions should illuminate just the particles, and the frame rate must be high enough that the interrogated regions do not travel more than the distance between interrogation regions between frames.[144] Videos were analyzed using Matlab R2018b.[129]

Metadata (also used in PIV)

Videos consisted of printing of several polygons, each of which consisted of three passes. In order to label frame data with the polygon type, pass number, edge number, and time from the corner, timestamps of corners were determined manually.

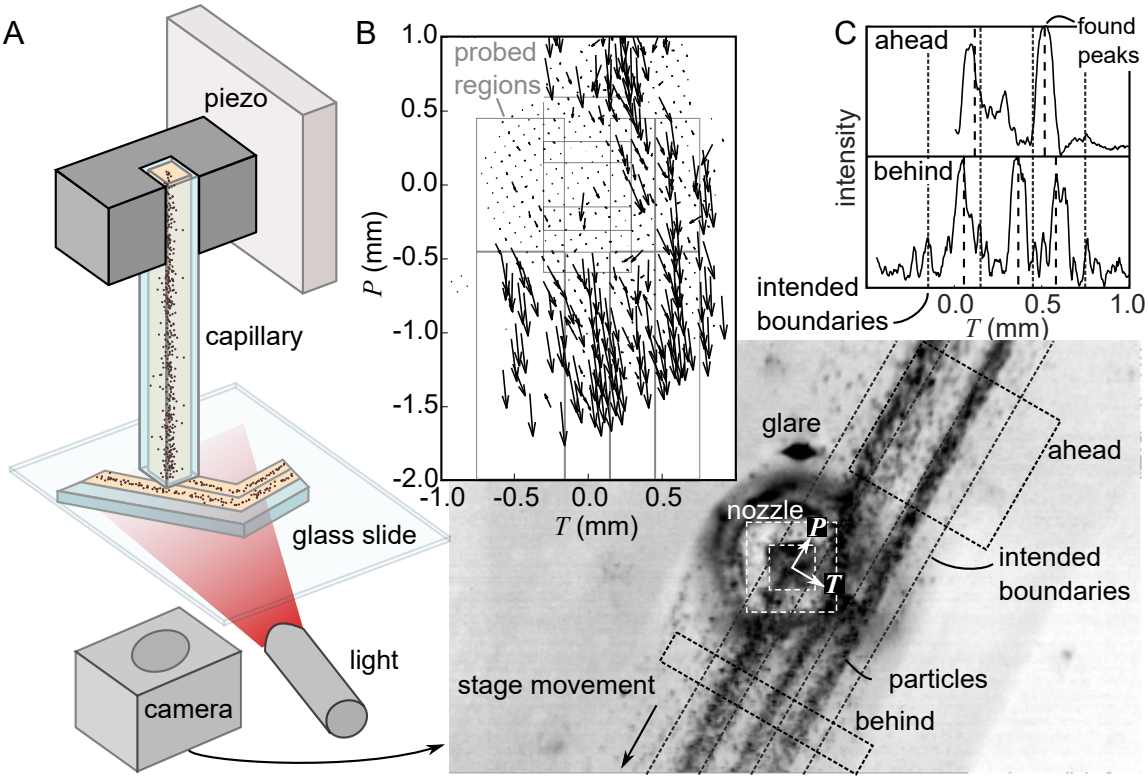

Figure 3.15: A) Schematic of video collection setup and example of analyzed frame. Image is inverted. B) Fluid displacement field is measured using PIV and rotated into the Parallel-Transverse coordinate system. Probed regions are outlined in white. C) Intensities are summed along the parallel direction ahead of and behind the nozzle. Distribution positions and widths are found as a function of transverse position.

The nozzle was detected in the frame using rotation. This strategy leverages the fact that, from below, the nozzle looks the same when the image is rotated by 90°, while the rest of the frame changes because it is full of particles. The image was cropped to roughly the center of the frame. A second copy of the image was rotated by 90° and displaced by some displacement, and subtracted from the initial frame. The displacement that produced the smallest difference from the initial frame was used to determine the center of the nozzle. Cropping for comparison of images in Matlab is described by Equation 3.20.

$$\begin{aligned} im_1(c_x, c_y) &= im[c_x - w : c_x + w, c_y - w : c_y + w] \\ im_2(c_x, c_y) &= im_{rotated}[H - c_y - w : H - c_y + w, c_x - w : c_x + w] \\ S(c_x, c_y) &= \sum (im_2 - im_1) / \sum im_1 \end{aligned} \tag{3.20}$$

In Equation 3.20, w is half of the inner width of the nozzle, and H is the height of the image. The combination of c_x and c_y that minimizes S is the center of the nozzle. After adjusting for the initial crop size, c_y must be subtracted from the image height.

Because the camera is fixed in place as the nozzle draws a polygon, the image must be rotated to measure flows and distributions within the $T - P$ coordinate system. The rotation angle can be determined from the programmed writing direction (v_x, v_y).

$$\theta = sign(v_x) cos^{-1}\left(v_y / \sqrt{v_x^2 + v_y^2}\right) \tag{3.21}$$

The rotation angle θ can be used to determine a rotation matrix R that will convert vectors from the $x - y$ coordinate system to the $T - P$ coordinate system.

$$R = \begin{pmatrix} \cos(\theta) & \sin(\theta) & 0 \\ sin(\theta) & \cos(\theta) & 0 \\ 0 & 0 & 1 \end{pmatrix} \tag{3.22}$$

Images can be rotated using the Matlab function *imrotate*. After rotation, the center of the nozzle moves relative to the image frame, so the center (c_x', c_y') must be calculated. Regions for PIV and distribution collection are adjusted to the new center. Where the original image has width D and height H,

$$A = \begin{cases} \begin{pmatrix} -c_y & D - c_x \\ c_x - D & H - c_y \end{pmatrix} & (v_x < 0, v_y < 0) \\ \begin{pmatrix} -c_y & c_x \\ c_x - D & c_y \end{pmatrix} & (v_x < 0, v_y > 0) \\ \begin{pmatrix} c_y & 0 \\ D - c_x & 0 \end{pmatrix} & (v_x < 0, v_y = 0) \\ \begin{pmatrix} H - c_y & D - c_x \\ c_x & H - c_y \end{pmatrix} & (v_x > 0, v_y < 0) \\ \begin{pmatrix} H - c_y & c_x \\ c_x & c_y \end{pmatrix} & (v_x > 0, v_y > 0) \\ \begin{pmatrix} c_y - H & 0 \\ -c_x & 0 \end{pmatrix} & (v_x > 0, v_y = 0) \\ \begin{pmatrix} 0 & c_x - D \\ 0 & c_y - H \end{pmatrix} & (v_x = 0, v_y < 0) \\ \begin{pmatrix} 0 & c_x \\ 0 & c_y \end{pmatrix} & (v_x < 0, v_y > 0) \end{cases} \tag{3.23}$$

$$\theta_c = \begin{cases} sign(\theta)\pi - \theta & |\theta| > \pi/2 \\ \theta & |\theta| \leq \pi/2 \end{cases}$$

$$\begin{pmatrix} c_x' \\ c_y' \end{pmatrix} = A \begin{pmatrix} \sin\theta_c \\ \cos\theta_c \end{pmatrix}$$

Because the written lines intersect the edge of the frame at an angle, using the entire region would cause distributions to skew towards positive or negative T. As such, it is necessary to calculate a new cut-off point for the bottom of the regions behind the nozzle and the top of

regions ahead of the nozzle. The size of the rotated image is

$$\begin{pmatrix} H' \\ D' \end{pmatrix} = \begin{pmatrix} |D\sin\theta_c| + |H\cos\theta_c| \\ |D\cos\theta_c| + |H\sin\theta_c| \end{pmatrix} \tag{3.24}$$

The position of the corner of the original image on the rotated image x_c and the sign of the direction of the end of the lines s is

$$\begin{cases} x_c = D\cos\theta_c & (0 < \theta < \pi/2), (-\pi < \theta < -\pi/2) \\ s = 1 & \\ x_c = D' - D\cos\theta_c & (\pi/2 \geq \theta \leq \pi), (-\pi/2 \leq \theta \leq 0) \\ s = -1 & \end{cases} \tag{3.25}$$

Given a list of two positions X, the new bottom of the interrogated region behind the nozzle y_{max} can be determined using the following algorithm:

$$\begin{cases} P_i = |x_c - X_i| \tan|\pi/2 - \theta_c| & s \times (X_i - x_c) > 0 \\ P_i = |x_c - X_i| \tan|\theta_c| & s \times (X_i - x_c) \leq 0 \end{cases} \tag{3.26}$$
$$y_{min} = max(P_i)$$

If determining the top of the region ahead of the nozzle, y_{max} can be determined by modifying equation 3.26, where $x_c = D' - x_c$, $s = -s$, and $y_{min} = H' - y_{min}$.

Distributions

To measure distributions, backgrounds were removed using a 15 px disk structuring element. This ensures that only particles are measured, not the gray background. Where the origin is at the nozzle center and the inner diameter half-width is w, the largest fully imaged region

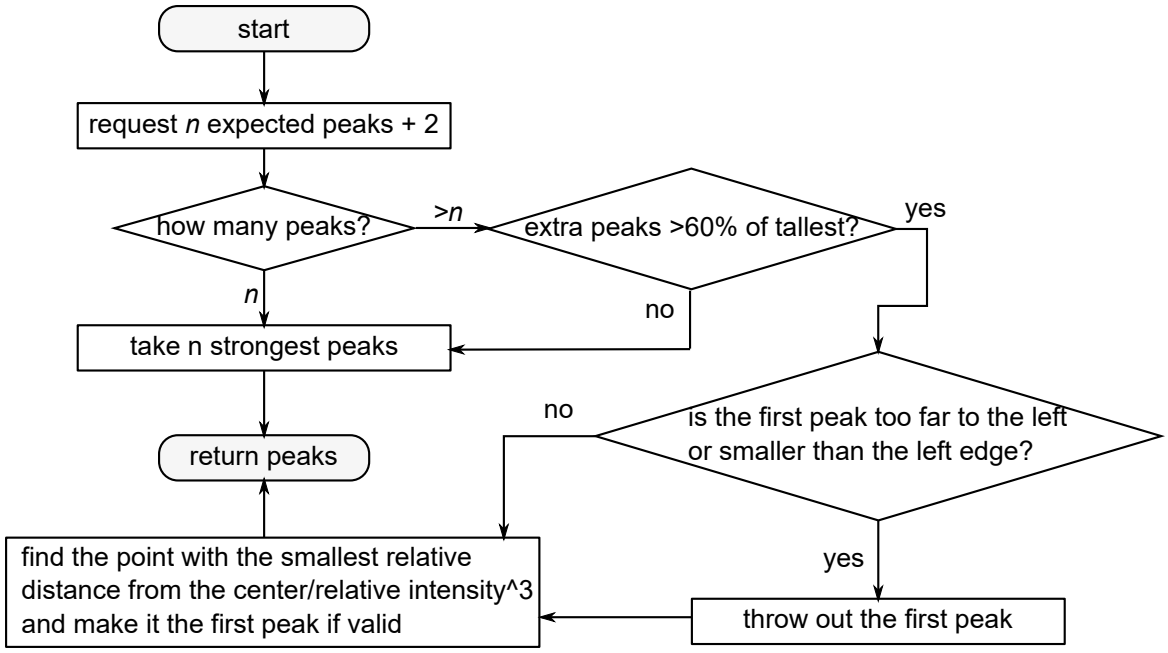

Figure 3.16: Peak finding algorithm.

upstream of the nozzle from $T = 0$ to $T = 7w$ and downstream of the nozzle from $T = -3w$ to $T = 7w$ were each summed along the print direction.

Peaks were identified using the Matlab function `findpeaks` with a minimum peak-to-peak distance of w. Because the distribution sometimes includes glare at the interface between the ink and the support, extra peaks were requested and then filtered based on intensity and distance from the center (Fig. 3.16).

Frames in which the corner of the polygon is visible were removed. The width is the standard deviation of the distribution within w of the peak, divided by the width of a uniform distribution of the same size.

3.7 Particle flows with Particle Image Velocimetry

The algorithm described in this section was used in Chapter 6–8.

Particle image velocimetry (PIV), which uses cross-correlation functions to track the move-

ment of particles embedded in a fluid, has been previously used to track fluid flows in direct ink writing.[144] PIV has been used to study the length and time scales of support material disruption and the direction of flows near the nozzle in embedded DIW.[99, 100, 120] Additionally, PIV and its single-particle offshoot particle tracking velocimetry have been used to characterize spatial variations in fluid velocity within the nozzle.[137, 138, 139] Still, PIV has its limitations. As with image displacements, the accuracy of PIV decreases at faster flow speeds and is vulnerable to background noise.[100] Furthermore, PIV at the micron scale is usually performed with fluorescent particles and narrow chromatic bandwidth illumination with a short depth of field to limit inaccuracies due to light scattering, so deployment of the technique during printing is challenging.[145] To date, characterization of fluid flows in DIW has been limited to two dimensions, imaging near the surface of the filament or one focal field of the support.

Fluid flows were measured in Matlab R2018b using a modified version of OpenPIV using the inputs in Table 3.1.[177] Given a pair of images, OpenPIV identifies flow fields using Fast Fourier transform-based cross-correlation. Before rotation, the images are broken into interrogation regions of 32 by 32 pixels, with no overlap between regions. The full frame was normalized from 0 to 1. To probe only the regions with particles, only interrogation regions with an average intensity above 0.1 and a maximum intensity above 0.5 were inspected. Corresponding interrogation regions from the two regions were transformed using a 2-D fast Fourier transform (Matlab function `fft2`)[129]. The product of the two transforms was collected and filtered to include only positive, real values. The largest peak was located, and the displacement between the peak and the center of the interrogation region was determined. The displacement is the flow vector for that region.

Once the full flow field was determined, it was filtered to remove outliers. Vectors that are more than 100 times the average non-zero flow velocity were removed. Deviating from OpenPIV, holes were not filled.[177] Outliers were further removed using adaptive local median

OpenPIV variable	value	significance
`ittWidth`, `ittHeight`	32	32×32 px interrogation region
`ovlapHor`, `ovlapVer`	16	16×16 px spacing between interrogation regions
`s2ntype`	2	Compare peak to mean intensity
`s2n1`	1	Virtually no signal to noise filtering
`outl`	100	Remove velocities more than 100 times the average

Table 3.1: Settings used for OpenPIV.

Table 3.2: PIV regions in multiples of the nozzle inner half-width w, where the origin is in the center of the nozzle.

region	T_{min}	T_{max}	P_{min}	P_{max}
in nozzle	-1	1	-1	1
ahead	-2	2	1	4
just behind	-2	2	-4	-1
behind left	-5	-1	y_{min}	-3
far behind	-1	1	y_{min}	-3
behind NN1	1	3	y_{min}	-3
behind NN2	3	5	y_{min}	-3
left	-5	-1	-3	3
NN1	1	3	-3	3
NN2	3	5	-3	3

filtering.

After the full flow field was collected, it was rotated into the $T - P$ reference frame using the rotations collected in the previous section. Flow fields were separated into regions in order to facilitate comparisons. In multiples of the nozzle inner half-width, the regions are shown in Table 3.2.

Future applications of PIV in direct ink writing could use stereo PIV, holography, 3D particle tracking velocimetry (PTV) , defocusing digital PIV, or tomographic PIV to visualize fluid movement inside the filament in three-dimensions.[145, 178] Such studies would be useful for separating the effects of viscous dissipation from capillarity on rotational flows, as well as comprehensively quantifying the effect of printing parameters and ink composition on the internal microstructure of composite filaments.

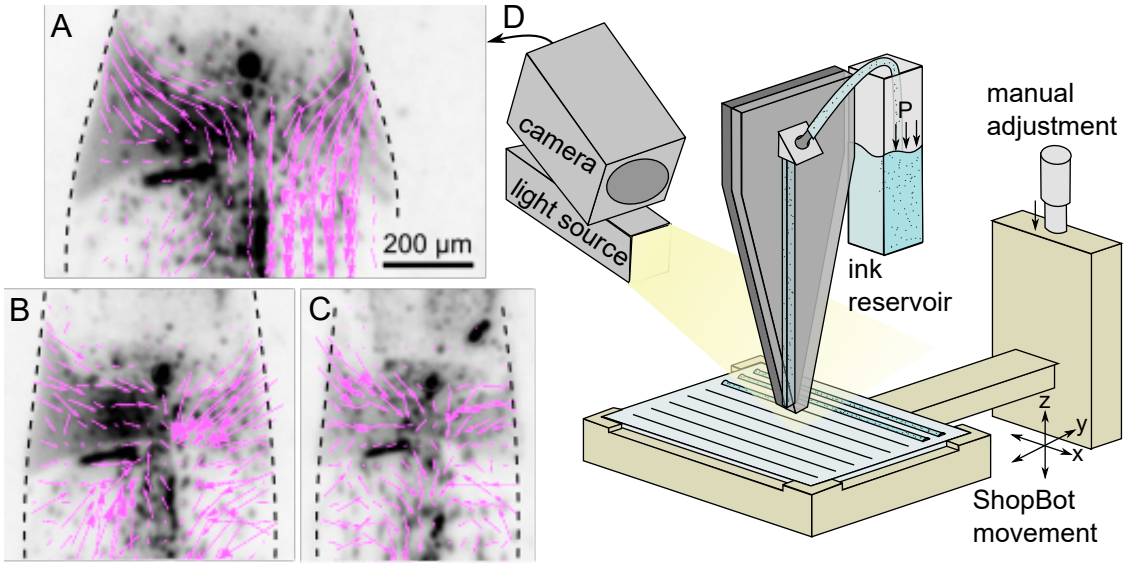

Figure 3.17: Schematic of video collection and examples of flows collected from frames. Frames are inverted. Dotted lines indicate the fluid surface.

3.8 Particle flows with Dense Optical Flow

The technique described in this section was used in Chapter 5.[128, 171]

Dense optical flow is a video processing technique developed mainly for tracking motion in applications like stereoscopy, object tracking, and feature extraction in complex images that contain many types of features like vehicles, landscapes, and background clutter.[134] This section uses dense optical flow to track the movement of particles in the print bead between the nozzle and substrate. Although grayscale images of particle movement are simpler than most videos analyzed using dense optical flow, the repetition of features and lack of visual contrast between glare and particles makes dense optical flow potentially less accurate than particle image velocimetry for tracking fluid flows. Dense optical flow has limited accuracy in poorly lit filaments, images with glare, and fast flows. This is apparent in the left half of the filament in Figure 3.17B, where fluid appears to move backward toward the nozzle due to glare.

Videos were collected at an angle relative to particle movement, which curves in and out of the plane of focus (Fig. 3.17D). The camera was a Point Grey FL3-U3-32S2M-CS with

an Infinity Infiniprobe objective. The field of view of camera must be large enough to see the entire filament, the resolution must be sufficient to image individual particles, and the frame rate should be high enough and the exposure short enough that the distance that particles move between frames is much smaller than the particle-to-particle distance.[134] A light source next to the camera illuminated the filament so the silver-coated nickel particles used for flow tracking appeared as light against a dark matrix (Fig. 3.17A–C, images are inverted). Particles must exhibit strong visual contrast with the matrix, and the matrix should be transparent enough to avoid scattering or absorbing light reflected off of the particles. Particle volume fractions must fall within an appropriate range to track fluid movement.[144]

Dense optical flow was performed using the Mathematica function `ImageDisplacements`,[132] which produces a vector field for each pair of subsequent frames that indicates the direction and velocity of flow. Averaging the vector field across several frames, the particles exhibit the strongest transverse rotational flows directly behind the nozzle (Figure 3.17A–C). The average transverse component of the particle velocity distills the vector field into a single number that can be used to compare prints.

Chapter 4

Channels and lines: filament microstructure and surface profile

4.1 Introduction

Additive manufacturing has expanded the manufacturing landscape to include structures with unprecedented three-dimensional complexity. Extrusion-based additive manufacturing techniques allow for additional complexity through variations in the three-dimensional print path. These techniques include fused deposition modeling (FDM), where solid thermoplastics are heated during extrusion and cooled after deposition, and direct ink writing (DIW), where fluid inks are extruded onto a substrate and subsequently solidified.[98] By modifying the microstructure of the extruded material along the print path, gradations in structural and functional properties may be introduced to additively manufactured components.[8, 40]

Multiphase materials present a pathway to microstructural gradients in 3D printed components. Several multiphase materials for additive manufacturing have been developed, both on the nanoscale[98] and on the microscale, for FDM[72, 179, 180] and DIW.[61, 181, 182] Despite the extensive research into 3D printed composites, there remains a need for tech-

niques that can create spatially graded components or structures with a high volume fraction of aligned microparticles. While particles in fluids may be manipulated through the use of magnetic fields or electrical fields, those methods require particles with specific electromagnetic properties.[40, 42, 183, 184, 185] A promising technique which only depends on physical properties is acoustic focusing, a method commonly used to manipulate particle motion in microfluidic channels. Acoustic focusing has been used to control the placement of ceramic particles in polymer matrices using DIW[8, 13] and stereolithography[186]. This work uses DIW because it allows for more complex spatial variations in particle packing and alignment by coordinating focusing with nozzle placement. However, the materials selection design space for acoustic focusing with DIW remains uncharted. In this work, this design space is experimentally defined in order to guide materials selection for 3D printing multiphase components with spatially graded properties.

In this printing method, a glass microparticle-laden epoxy resin flows through a direct ink writing nozzle composed of a rectangular glass-capped silicon microfluidic channel.[125] A piezoelectric actuator generates a standing half pressure wave in the channel, thereby establishing a bulk acoustic wave across the channel width. Particles flowing through the channel assemble at the node of this acoustic wave and subsequently extrude onto a glass substrate.[125] To build three-dimensional structures with this technique, it is necessary to use viscous inks. However, acoustic focusing properties depend on the viscosity of the fluid.

From [125], the amplitude of the primary acoustic radiation force F_0 on a single particle in a channel can be described as

$$F_0 = \frac{\pi^2 a^3 \beta_f p_o^2 \phi}{3W} \tag{4.1}$$

where a is the particle radius, β_f is the compressibility of the fluid, p_o is the acoustic pressure amplitude, W is the width of the channel, and ϕ is the acoustic contrast factor.

Assuming that the primary acoustic radiation force on the particle is balanced against drag

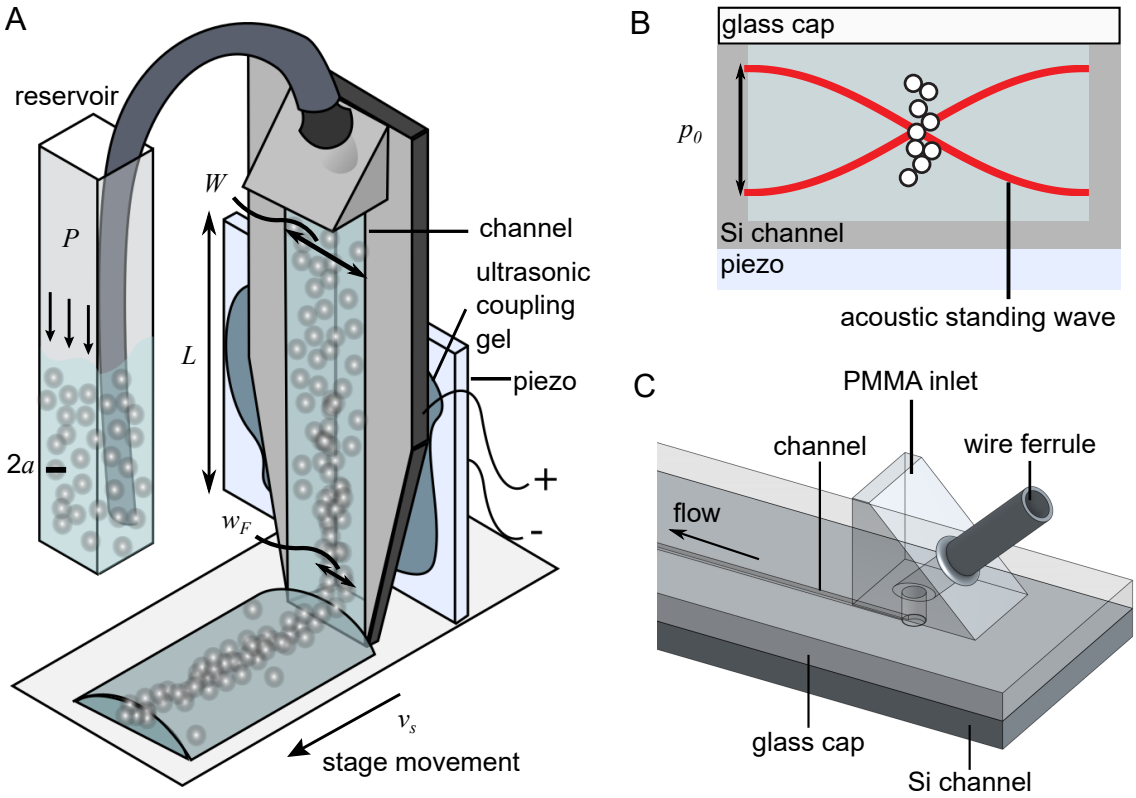

Figure 4.1: Schematic of printing setup. a) Fluid flows through nozzle and extrudes onto moving linear stage. b) Particles move to the node of an acoustic standing wave. c) To-scale schematic of nozzle inlet.

forces, the velocity of the particle can be determined.

$$v_F = \frac{\pi a^2 \beta_f p_o^2 \phi}{18 W \eta} \tag{4.2}$$

Placing the origin at the center of the channel, where $v_F t < W/2$, the final position w_P of a particle that starts at the edge of the channel after traveling through the focusing zone for a time t can be described by:

$$w_P = \frac{W}{2} - v_F t \tag{4.3}$$

Thus, a particle that travels through a focusing zone of length L at a speed v_s will have a final position w_P of

$$w_P = \frac{W}{2} - \frac{\pi a^2 \beta_f p_o^2 \phi L}{18 W \eta v_s} \tag{4.4}$$

Assuming no interactions between particles or acoustic scattering forces, the focusing width w_F of a distribution of particles is therefore the distance between two particles that start on opposite sides of the channel.

$$w_F = W - \frac{\pi a^2 \beta_f p_o^2 \phi L}{9 W \eta v_s} \tag{4.5}$$

Assuming that the particles are much smaller than the channel, there are no interactions between particles, and inertia is negligible, the focusing zone is related to channel parameters and acoustic pressures according to:

$$w_F = W - \frac{\pi a^2 \beta_f p_o^2 \phi L}{9 W \eta v_s}, \tag{4.6}$$

where w_F is the focusing width (the width of the particle distribution after focusing), W is

the channel width, a is the particle radius, β_f is the fluid compressibility, p_o is the acoustic pressure amplitude, ϕ is the acoustic contrast factor, L is the focusing zone length (which may be approximated as the length of the piezoelectric actuator), η is the fluid viscosity, and v_s is the average material extrusion speed (Fig. 4.1a,b).[16]

This equation forms the framework of this study and establishes several performance trade-offs. By Equation 4.6, the particle travel distance, $W - w_F$, scales inversely with viscosity. As such, viscous inks produce wide particle distributions, wherein small increments in viscosity will produce large increases in focusing width. However, experiments have shown that the speed at which the deposited ink spreads scales inversely with the root of viscosity.[187] As a result, viscous inks will spread on the substrate slowly, resulting in good form holding, which is the ability of the ink to maintain shapes. Together, these phenomena establish a trade-off: particle focusing worsens as form holding improves. To adjust to this trade-off, this work uses shear-thinning inks composed of epoxy, fumed silica, and acetone. The benefits of these inks are three-fold. First, after deposition the viscosity will be high because the strain rate is zero. Second, the high strain rate in the nozzle will reduce the viscosity of the flowing ink, thereby necessitating low extrusion pressures. Third, because the viscosity of the ink will be low during extrusion, Equation 4.6 dictates that the focusing width will be narrow.

Equation 4.6 establishes additional relationships between processing parameters and focusing performance. First, the particle travel distance scales with the square of the acoustic pressure amplitude, which scales with the peak-to-peak voltage (V_{pp}) of the electrical signal to the piezoelectric actuator. Thus, small increases in the piezoelectric actuator input voltage should result in large decreases in the focusing width. Second, the particle travel distance scales inversely with print speed, such that higher print speeds will result in less time in the focusing zone. To map these processing effects onto a real material system, this work uses acoustic focusing with direct ink writing to print epoxy, fumed silica, and acetone matrices laden with silver-coated glass microparticles.

Here, the relationships established by Equation 4.6 are verified through a combinatorial experiment that varies the ink viscosity (through varying loadings of silica filler and acetone), the peak-to-peak voltage, and the print speed. To evaluate these effects on the focusing width, particle distributions are measured in the channel and in the printed line using optical microscopy. The ability of the inks to hold shapes is quantified by measuring surface profiles of printed lines and printing woodpile structures. These experiments establish fundamental trade-offs associated with DIW with acoustic focusing. Further, this work establishes a printable range for filler and solvent loadings in epoxy-based matrices. Finally, optical methods to characterize particle focusing quality are established. Equation 4.6 adequately predicts the effect of silica loading and acoustic wave amplitude on focusing. This study informs the design of acoustically-actuated print nozzles through modeling and measurement of processing-structure relationships in direct ink writing.

4.2 Experimental approach and characterization

4.2.1 Ink preparation and printing approach

Base inks (those without particles or acetone) were prepared by mixing designated weight percentages of epoxy (Miller-Stephenson EPON 828) and fumed silica (Evonik Aerosil R106) (5, 6, 6.5, 7, 8, 9, and 10 w% silica), then adding a heat-curing agent (Basionics VS03 1-ethyl-3-methylimidazolium dicyanimide) in a 20:1 epoxy:curing agent weight ratio. After each addition, base inks were mixed for 3 minutes at 2000 rpm in a planetary mixer (Thinky ARE-310). Because mixing fumed silica into resin proved to be more achievable in large, wide-mouthed containers, base inks were prepared in 20–50 g batches and stored for the expected pot life of 30 days.[61]

Printed inks (those with particles and acetone) were prepared by combining 14–31 μm di-

ameter silver-coated glass spheres (Cospheric SLGMS-AG-2.74) with base ink in designated sphere:base weight ratios (1:25 and 7:30, roughly 1.7 and 9 v%) and adding acetone in designated weight percentages (8, 16, and 24 w%). For the high particle loading, only 2:25 acetone:base and 5, 7, and 9 w% silica were tested. The three components were hand-mixed, then mixed for 3 minutes at 2000 rpm in a planetary mixer. Weights were measured on a microbalance (Mettler AE163). To avoid particle waste and solvent evaporation, inks were mixed immediately before printing in 3–4 g batches.

The given silica loadings were chosen because 5 w% silica demonstrated good focusing qualities but poor form holding qualities,[13] and 10 w% silica is the highest silica loading that can be driven by this system at reasonable flow speeds, with a maximum pressure of 7 bar. The given acetone loadings were chosen because previously, 8 w% acetone demonstrated good focusing qualities for low silica loadings, but higher silica loadings require more diluent to extrude.

Dynamic frequency sweeps were conducted on a TA Instrument Company ARES-LS1 rheometer, using 25 mm diameter flat plates and a 2 mm gap. The material was held at a constant strain of 15%, and the shear strain rate was swept from 0.01 Hz to 10 Hz, with 6 points per decade. A 60 second steady preshear was maintained at 1 Hz, followed by a 10 minute pause. Tests were conducted at room temperature (17–19 °C for lower silica w% inks and 21–22 °C for the highest two silica w% inks).

Models of non-Newtonian fluids in rectangular channels indicate that the wall shear stress-shear strain rate curve of an ink can be fit to a power law (Fig. 4.S3).[188] Thus, to determine ink extrusion pressures, measured rheology curves were fit to power laws, where τ is the shear stress in Pa, $\dot{\gamma}$ is the shear strain rate in Hz, k is a constant in $Pa \cdot s^n$, and n is a dimensionless constant (Eq. 4.7).

$$\tau = k\dot{\gamma}^n \tag{4.7}$$

Pressures were calculated to match stage speeds using the power law fits from Equation 4.7 as described in Ref. [188] (Eq. 4.8), where L, H, and W are the length, depth, and width of the channel (35, 0.15, and 0.35 mm), v_s is the stage speed in mm s^{-1}, and a^*, b^*, and f^* are numerically-determined constants that depend on the channel geometry (a^* = 0.2538, b^* = 0.7414, f^* = 0.6634).

$$\Delta P = 3\,k\,L\,f^* e^{-n}\Big(4v_s\Big)^n\Big(\frac{H+W}{HW}\Big)^{n+1}\Big(b^* + \frac{a^*}{n}\Big)^{n-1} \tag{4.8}$$

Because some rheology curves deviate from the power law fit (Fig. 4.S3), the pressures required to achieve a sufficient flow rate to extrude a continuous line were lower than the calculated pressures. As a result, mass flow controller pressures were calibrated manually. Equation 4.9 describes the typical calibrated pressures.

$$P = \Delta P/A \begin{cases} v_s = 1 & A = 22 - 26 \\ v_s = 5 & A = 15 - 18 \\ v_s = 10 & A = 9 - 10 \\ v_s = 20 & A = 5 - 6 \end{cases} \tag{4.9}$$

Printing nozzles consisted of etched silicon channels anodically bonded to glass capping layers, as described in Ref. [8]. Channels were 150 μm deep, 350 μm wide, and 35 mm long. Fluidic vias were pre-drilled in the glass capping layer using a CNC diamond drill. Inlets were fabricated by cutting 4.37 mm-wide isosceles right triangles into 3.24 mm-thick poly(methyl methacrylate) sheets using a laser cutter (Trotec Speedy 100). 750 μm wide channels were drilled at a 45-degree angle to the base of the inlet using a Dremel drill. Wire ferrules were bonded to inlets, and inlets were bound to vias using epoxy (Devcon HP250) and small amounts of cyanoacrylate adhesive (Fig. 4.1c).

Print nozzles were attached to piezoelectric actuators (10 mm square x 1 mm thick Navy I material, American Piezo) using ultrasonic coupling gel. Actuators were driven with an amplifier (Mini-Circuits LZY-22+) linked to a sinusoidal function generator (Fluke 294). Signals were generated at 2.09 MHz, using peak-to-peak voltages of 0, 30, and 50 V_{pp} measured using an oscilloscope (Agilent DSO-X 2024A). The piezoelectric material generates heat during operation, especially at high peak-to-peak voltages. This heat caused three problems in preliminary tests. First, the heat changes the ink viscosity and can cure the ink in the channel. Second, enough heat can melt the solder on the piezo connecting wires. Third, the piezoelectric properties of the material can change at high temperatures. Thus, for all tests the piezoelectric actuators were thermally coupled to a copper cooling stage using thermal joint compound (Wakefield Type 120) and maintained at $20°$C using a home built liquid cooling unit.

Printed lines were deposited by extruding inks through a stationary print nozzle positioned normal to a level glass slide, which was mounted on a screw-driven linear stage (Zaber T-LSR150B) moving parallel to the depth of the silicon channel (Fig. 4.1a). Inks were extruded using a high-pressure mass flow controller (Fluigent MFCS-EZ). Extrusion pressures were matched to stage speeds as described in the previous section. Lines were cured on a hot plate at $180°$C for 90 minutes.

Three-dimensional structures were printed by attaching a print nozzle, piezoelectric chip, chip cooling stage, and Fluigent mass flow controller to a ShopBot D2418 gantry. Toolpaths were designed using Mathematica and executed using ShopBot software. The stage speed was 2 mm/s. Structures were printed on static glass substrates. Images of structures were collected using a Keyence VHX-5000 microscope.

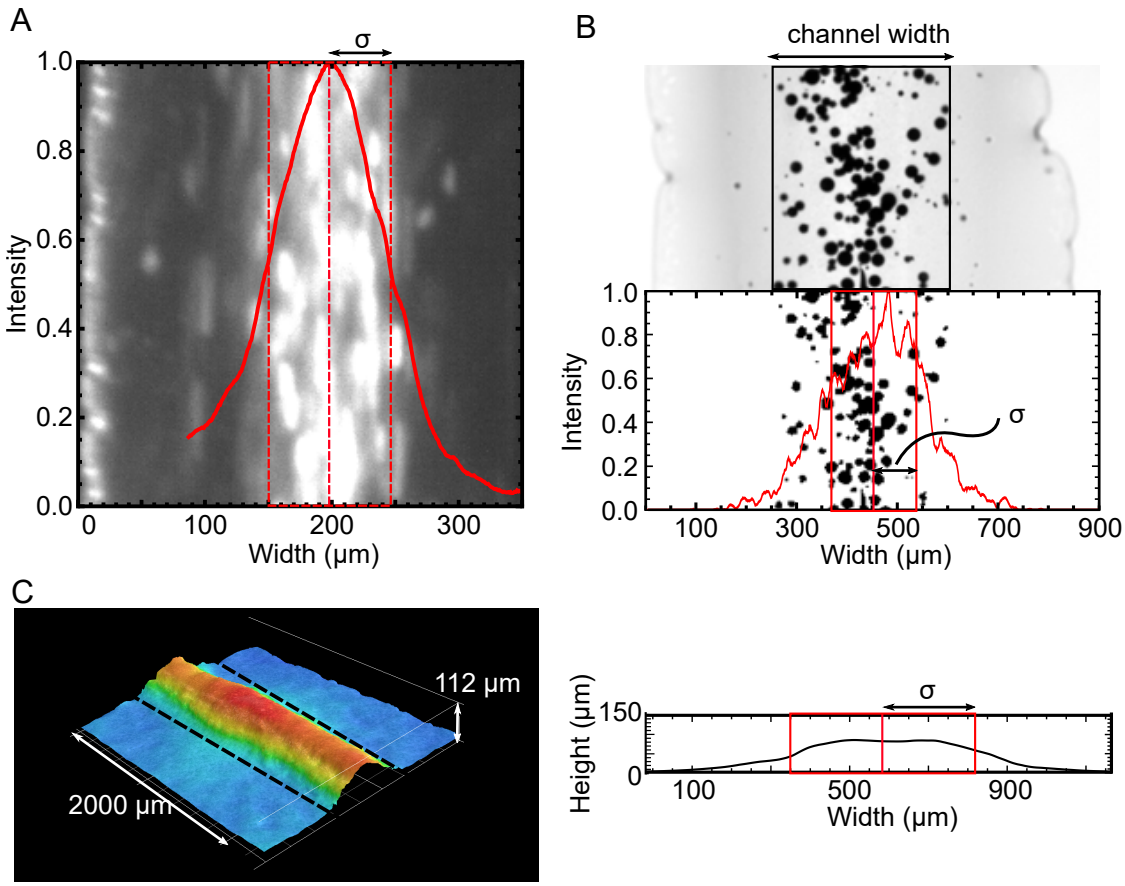

Figure 4.2: Examples of analysis procedures. a) Focusing width, defined as the normalized width of the particle distribution in the channel. Particles (light) flowing within the channel (dark). Overlay: intensity profile across channel width, for all rows and frames combined. b) Printed width, defined as the normalized width of the particle distribution in the printed line. Still image of particles (dark) in cured line (light); thresholded image of particles; intensity profile across line width for all lengths combined. c) Line profile. Three-dimensional height profile of cured line (dotted lines indicate line edges); cross-section of line height, for all cross-sections combined. The form holding metric is the height of the line profile divided by σ, the standard deviation of the line profile.

4.2.2 Characterization of printed lines

Videos of the channel, between the base of the piezoelectric element and the nozzle tip, were captured for each print using an Infinitube FM-200 objective with a Guppy Pro F-503B camera. Wolfram Mathematica 10.1 was used to process the videos. First, the left edge of the channel was detected as follows. The first frame of the video was transformed into an intensity-weighted edge image using a Shen Castan edge detection algorithm (EdgeDetect). Then, a Hough transform (ImageLines, threshold = 0.25) was used to detect the left edge of the channel. Edge detection parameters (pixel range, straight edge parameter, and image compression) were iteratively tested until a line was detected within an appropriate location and slope margin. Next, 35 intensity profiles were taken across the channel, for each of 8 frames. Because the captured area of each frame encompasses 0.67 mm, and the ink flows 5 mm per frame used, the only double-counting involved in this intensity profile happens because particles travel some distance during camera exposure. The left quarter of the channel was discarded because a bright reflection off of the left channel edge obscured data (see left of Fig. 4.2a). The average of all profiles was calculated to create a composite profile. For each profile and for the composite profile, the intensity was normalized onto a 0-to-1 range. The focusing width was measured as the standard deviation of the composite intensity profile, divided by the standard deviation of a uniform distribution (76 μm) (Fig. 4.2a). Assuming 31 μm-diameter spheres, the perfectly focused condition for a particle volume fraction below 9.2 v% would have a focusing width of 0.12, and the perfectly unfocused condition would have a focusing width of 1.

To measure printed line width and height, three-dimensional surface profiles were captured of cured lines using a Keyence VHX-5000 microscope. Cured lines were coated with a thin layer of Helling 3D laser scanning anti-glare spray. 3D tilt correction was executed, and profiles were converted into table files using VHX software. Profiles were analyzed using Wolfram

Mathematica 10.1. Surface profiles of two regions in each line were captured, and the average profile of all line cross-sections for each region was calculated. The width of the line is taken as the average of the profile standard deviations for the two regions. The height of the line is measured as the average of the maximum heights of the two regions (Fig. 4.2c). The height/width was defined as a metric of form holding. A line that perfectly matches the shape of the channel would have a height/width of 1.5. This work uses standard deviation rather than the full width at half maximum because it more accurately takes into account the spreading and shape of the line. A rectangle could have the same FWHM as a rounded profile with the same area and equal or lesser height, but it cannot have the same standard deviation. The printed width is defined as the standard deviation of the particle distribution across the width of the line. To normalize the printed width, the line profile standard deviation is used to describe the volumetric ink distribution across the width of the line.

For printed width and height/width measurements, samples with cross-sections comprising less than 80% or greater than 150% of the area of the channel cross-section were not included, where cross-sectional area was calculated as the sum of the line profile between the left and right minima of the line profile. Additionally, samples which produced beads instead of continuous lines were excluded. Discontinuous and thin lines are indicative of a flow rate that is too slow, which would produce an artificially small focusing width for a given stage speed. Similarly, lines that are thicker than the channel cross-section are symptoms of a flow rate that is too fast, resulting in an artificially large focusing width for a given stage speed. Thus, filtering the data by area includes only samples whose flow speeds were close to the stage speed.

After curing, images were captured of 10.9 mm of each printed line using an inverted light microscope (Nikon TI-U Eclipse). Using Wolfram Mathematica 10.1, images were thresholded to detect only particles (MorphologicalBinarize, threshold = 0.3 - 0.85), and the binary images were summed along the length of the printed line and normalized to create a composite intensity profile (Fig. 4.2b). The particle packing distribution can be described by the standard deviation

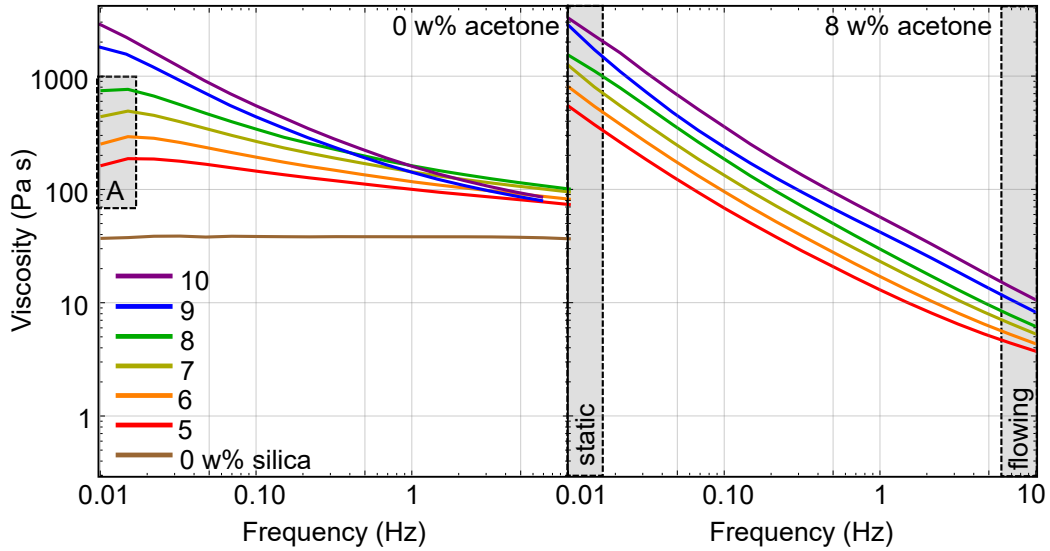

Figure 4.3: Log-log plots of viscosity as a function of shear strain rate, for varying silica filler and acetone loadings and no particles. The highest two silica loadings were tested at 3°C warmer than the lower silica inks. Region A indicates shear thickening for low-silica inks.

of the composite profile. Because extrusion speeds deviated slightly from print speeds, cross-sectional areas were not exactly equal to the cross-sectional area of the channel. Extrusion pressures that were too high resulted in cross-sectional areas that were larger than the channel and thus particle distributions that were artificially wide. The opposite is true for extrusion pressures that were too low. To compensate for the skewed particle distributions, the printed width was defined as the standard deviation of the intensity profile divided by the measured line width. ANOVA was used to concisely assess whether correlations between variables are statistically significant, and p-values are reported. For all metrics, p-values below .05 are considered significant.[189]

4.3 Results

4.3.1 Rheological properties of epoxy-silica-acetone inks

Epon 828 resin is Newtonian, as previously demonstrated (Fig. 4.3).[13] Adding fumed silica to Epon 828 increases the viscosity at all strain rates, with the largest increases at low strain rates (Fig. 4.3). As a result, while high-silica inks are much more viscous than low-silica inks after deposition, the viscosity difference between the inks is small during extrusion. Adding acetone to silica-laden inks further increases shear thinning behavior (Fig. 4.S2). Inks with small amounts of acetone have larger power law exponents and zero shear viscosities than base inks partly because base inks experience shear thickening at low strain rates (Fig. 4.3A). With a small amount of acetone, neither silica loading nor acetone loading have an appreciable effect on the shear thinning exponent (Fig. 4.3). Further acetone decreases the viscosity uniformly across shear strain rates, and adding silica to acetone-thinned inks uniformly increases the viscosity across shear strain rates (Fig. 4.S4).

4.3.2 Focusing quality

To evaluate the effect of ink formulation on particle focusing performance, this work probed the effect of silica and acetone on focusing width, or the standard deviation of the particle distribution in the channel normalized by the standard deviation of a theoretical uniform distribution. To determine the effect of printing parameters on particle focusing, this work varied the printing speed and the amplitude of the input voltage to the piezoelectric actuator, which is proportional to the acoustic wave amplitude.

The acoustic wave amplitude has the strongest influence on focusing width. Figure 4.4d shows that increasing the acoustic wave amplitude decreases the focusing width as predicted ($p < .001$). Further, Figure 4.5a indicates that the particle travel distance scales with the square

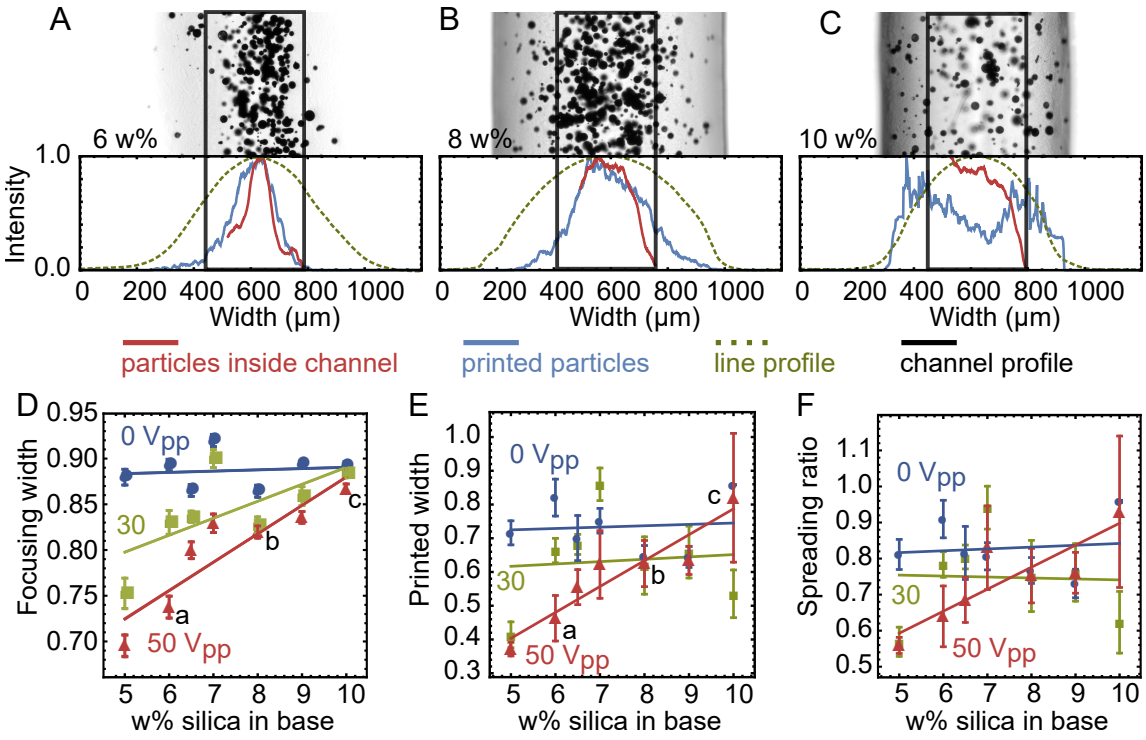

Figure 4.4: Focusing quality as a function of silica w% and acoustic wave amplitude for 1.7 v% particles in the printed line. (a-c) Image of ink in line, normalized intensities in channel and in line, and line surface profile normalized by line height. Values are given for varying silica loadings at 50 V_{pp}, 1 mm/s, and 8 w% acetone. Dark grey regions of the images correspond to large line profile slopes. (d) Focusing width of particle packing distribution. (e) Printed width of particle packing distribution. (f) The spreading ratio, defined as the printed width divided by focusing width.

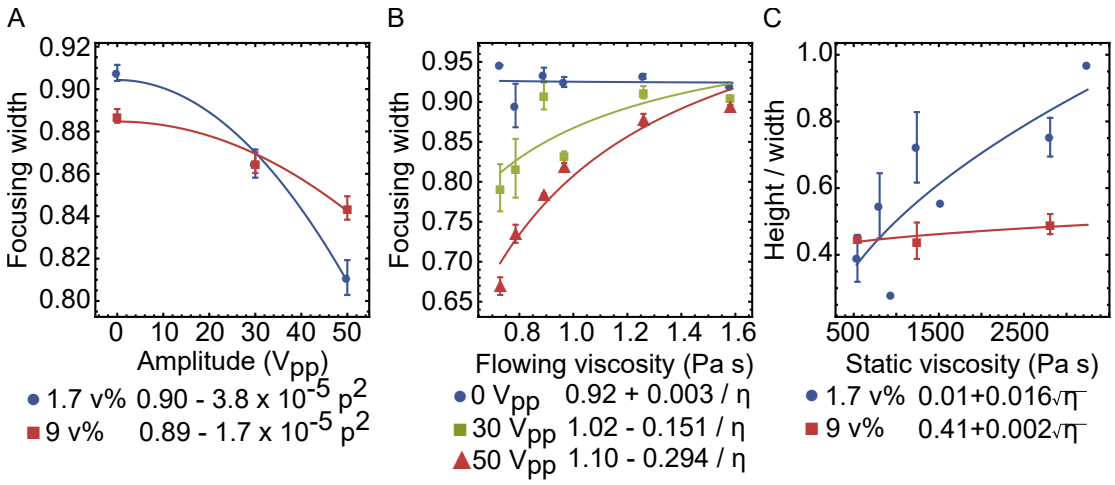

Figure 4.5: Experimental data fit to theoretical scaling relationships. a) Focusing width as a function of acoustic wave amplitude for varying particle volume fractions for 8 w% acetone. b) Focusing width as a function of calculated viscosity in the flowing state for 1.7 v% particles, 8 w% acetone, and a speed of 1 mm/s. c) Height/width as a function of measured viscosity at a strain rate of 0.01 Hz, for 8 w% acetone and 1 mm/s.

of the peak-to-peak amplitude of the input signal to the piezoelectric actuator.

Silica loading has a significant impact on focusing width. For low particle loadings, adding silica to the base significantly increases the focusing width ($p < .001$) (Fig. 4.4d). This effect is greatest at large acoustic wave amplitudes. At an input amplitude of 50 V_{pp}, the focusing width increases linearly with silica loading ($p = .005$) (Fig. 4.4d). When focusing is not employed, there is no significant correlation between focusing width and silica loading ($p = .100$). Moreover, there is an inverse relationship between focusing width and viscosity, in agreement with Equation 4.6. This is most apparent when only the lowest acetone loading and the slowest speed are considered (Fig 4.5b).

For each speed, there is a cutoff silica loading where there is nearly no difference in focusing width between the focused and unfocused conditions. For these channel dimensions, at stage speeds between 5 and 10 mm/s, the cutoff is 10 w% silica (Fig. 4.4d). At a stage speed of 1 mm/s, the cutoff is above 10 w% silica, and at a stage speed of 20 mm/s, the cutoff is closer to 8 w% (Fig. 4.S7).

To evaluate how well the inks maintained the shape of the focused particle distribution, this work uses the printed width, or the standard deviation of particle placement within printed lines, normalized by the standard deviation of the line profile. At the lower particle loading, silica has a significant effect on printed width ($p < .001$) (Fig. 4.4e). This effect varies with acoustic wave amplitude. At an acoustic wave amplitude of 50 V_{pp}, the printed width increases linearly with silica loading ($p = .002$). At an amplitude of 0 V_{pp}, there is no significant linear regression ($p = .853$). For each amplitude, the trend of the printed width follows the trend of the focusing width, indicating a correlation between particle distributions inside the channel and after deposition (Fig. 4.4d-e).

The change in particle distribution during deposition can be quantified by measuring the spreading ratio, or the ratio of the printed width to the focusing width. This measures how much of the line is occupied by particles relative to how much of the channel was occupied. The scaling ratio is governed by two phenomena: spreading of the particle-rich region in the line center and spreading of the particle-depleted regions on the line edges. If the edges spread more than the center, the spreading ratio is small. If the center spreads more than the edges, the spreading ratio is large. Applications which require a wide matrix layer around the particle-rich center, such as inkjet-like builds with thin layer heights but precise particle placement, are best served by matrices which produce small spreading ratios. In contrast, applications which require minimal spreading of both the center and edges, such as thick-layered builds and insulated electrical interconnects, are best served by larger spreading ratios.

When there is no focusing, there is no significant relationship between silica loading and spreading ratio ($p = .351$) (Fig. 4.4f). However, at the highest acoustic wave amplitude, the spreading ratio increases linearly with silica loading ($p = .011$) (Fig. 4.4f). Though particles spread out from their initial position in all inks (Fig. 4.4a-c), most post-deposition motion is edge motion, not center motion. Lower viscosity matrices spread from the initial channel shape more than particles spread from their initial positions in the channel (Fig. 4.4a-c).

Acetone does not impact focusing properties as significantly as silica, regardless of its effects on the viscosity of the ink. For the lower particle loading, acetone has an effect on focusing width ($p < .001$), but the linear relationship between acetone and focusing width is not significant ($p = .531$ for 50 V_{pp}, $p = .156$ for 0 V_{pp}). Increasing acetone decreases the focusing width for all acoustic wave amplitudes (Fig. 4.S8a). It may be tempting to explain the decrease in focusing width with acetone by the corresponding decrease in volume percent particles in the channel. However, in the printed line, where the volume percent of particles should remain constant across all acetone loadings, the printed width still decreases with acetone loading for all amplitudes (Fig. 4.S8b). This effect is considerably larger than the effect on focusing width, but the linear relationship between acetone loading and printed width is also not significant ($p = .224$ for 50 V_{pp}, $p = .542$ for 0 V_{pp}). Similarly, there is no significant linear relationship between acetone loading and spreading ratio ($p = .322$ for 50 V_{pp}, $p = .894$ for 0 V_{pp}).

Decreasing print speed improves focusing in the channel ($p < .001$) (Fig. 4.S9a). Speed only affects the particle distribution when focusing is employed. At 50 V_{pp}, focusing width linearly increases with speed ($p = .012$), but speed has no effect on printed width ($p = .110$). At 0 V_{pp}, speed has no effect on focusing width ($p = .706$) or printed width ($p = .548$). Similarly, while speed does not have a significant effect on the printed width ($p = .924$), for high amplitudes and low particle loadings increasing the speed causes a linear increase in printed width ($p = .050$) (Fig. 4.S9b).

4.3.3 Form holding

After deposition, an ideal ink would maintain the shape of the print nozzle. In contrast, a suboptimal ink would widen and flatten onto the substrate. The nature of this wetting is largely governed by two factors: interfacial energy and viscosity. While the effect of interfacial energy can be measured at the line edges, viscous flow governs the shape of the bulk of the line (Fig.

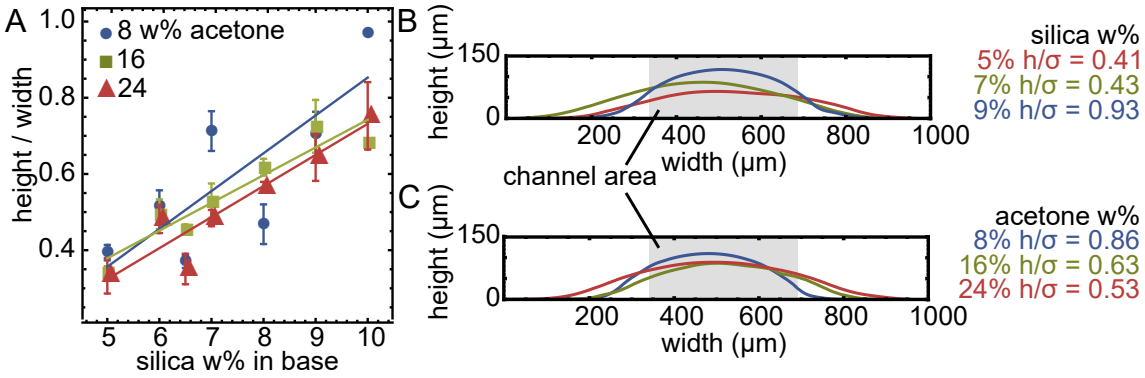

Figure 4.6: Form holding, measured as the height/width of the line for 1.7 v% particles in the printed line. A large height/width indicates good form holding. a) Height/width as a function of print speed and acoustic wave amplitude. b) Composite cross-sectional profiles of lines with 24 w% acetone printed at an amplitude of 0 V_{pp} and speed of 10 mm/s. c) Composite cross-sectional profiles of lines with 7 w% silica in the base ink printed at an amplitude of 30 V_{pp} and a speed of 10 mm/s.

4.6b-c). This chapter focuses on the viscous contributions to spreading, and thus the used metrics for form holding focus on the central portion of the line's cross-sectional profile. The inks studied here have rounded surface profiles as opposed to the rectangular shape of the print nozzle. Thus, this work uses the standard deviation of the line profile (the width) and the maximum height of the profile to evaluate deviation from the original nozzle shape. A large height/width ratio corresponds to good form holding.

Form holding quality is dominated by the silica content of the matrix ($p < .001$)(Fig. 4.6a). For the lowest acetone loading, height/width scales with the root of the low-strain-rate viscosity, although some scatter in the data is apparent (Fig. 4.5c).

Spreading has adverse effects on printed shapes, as demonstrated by two-layer woodpile structures (Fig. 4.7b-c). At low silica loadings, parallel ink lines merge after deposition (Fig. 4.7b). At high silica loadings, parallel ink lines do not spread far enough to merge, but successive layers flatten and merge (Fig. 4.7c). None of the tested silica loadings are capable of producing spanning segments

Acetone loading does not significantly impact form holding ($p = .152$). At some silica

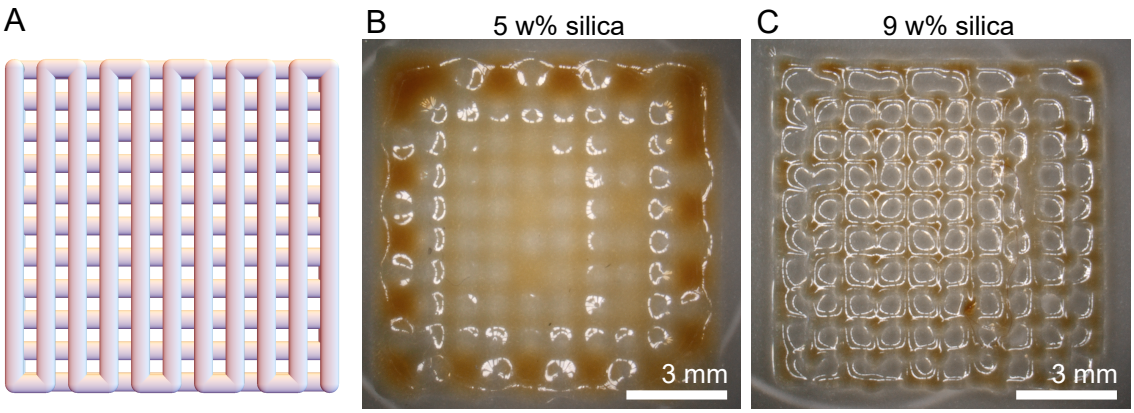

Figure 4.7: Woodpile structures with no particles. a) Simulated shape of woodpile structure. b-c) Structures printed with inks containing 8 w% acetone and b) 5 w% and c) 9 w% silica.

loadings, decreasing acetone increases the height/width (Fig. 4.6a). Additionally, contact angles between the printed line and the substrate increase with decreasing acetone loading (Fig. 4.6c). Because increasing acetone decreases the viscosity of the ink, higher acetone loadings are expected to cause poor form holding. However, just as with focusing width, large acetone weight fractions are not nearly as influential as small silica weight fractions on form holding.

These data indicate that there is a correlation between focusing and form holding, but they do not make a compelling case for causation. While ANOVA indicates that the acoustic wave amplitude has a significant effect on form holding ($p = 0.007$), the effect is confounded by the impact of cross-sectional line area, and the linear trend is not significant ($p = 0.264$). The height/width decreases slightly with increasing amplitude, such that poor form holding accompanies good focusing (Fig. 4.S10).

Increasing the particle loading decreases the line height/ width, but this too is confounded by differences in line area between particle loadings ($p < .001$) (Fig. 4.5c, Fig. 4.S10). Additionally, print speed does not significantly impact form holding ($p = .182$).

4.4 Discussion

4.4.1 Rheological properties of epoxy-silica-acetone inks

Because Epon 828 resin alone is Newtonian, it is not ideal for additive manufacturing because it is too viscous to extrude through small nozzles at a reasonable rate, yet too inviscid to hold form. To ameliorate this problem, fumed silica is introduced to Epon 828 to produce shear-thinning base inks. Still, the viscosities of these epoxy-silica base inks require high driving pressures and inhibit acoustic focusing. Thus, acetone is incorporated to decrease the viscosities of the inks. Because inks with acetone have a slight shear thickening effect at low shear strain rates, inks with acetone may actually have better form holding properties than the base inks after deposition. Inks with high acetone and low silica have promising viscosities for acoustic focusing, while inks with low acetone and high silica have promising viscosities for form holding.

4.4.2 Focusing quality

Equation 4.6 predicts how the focusing width should change with viscosity, flow speed, and acoustic wave amplitude. First, the particle travel distance is expected to scale with the square of the acoustic wave amplitude. A higher acoustic wave amplitude imposes a greater force on particles, reducing the focusing time and decreasing the focusing width. While focusing widths at 0 V_{pp} are narrower than focusing widths for a uniform distribution, these apparent particle concentration gradients may be a product of fluid shear.[190, 191] Experimental data support the relationship proposed by Equation 4.6. The same trend is apparent in the printed line. As the amplitude increases, the focusing width decreases, so the printed width should also decrease. Because the acoustic wave is only applied inside the channel, the decrease in printed width with amplitude indicates that the particle packing established inside of the channel is not

greatly disrupted during the deposition process.

Second, Equation 4.6 indicates that the focusing width should decrease with the inverse of the ink viscosity. These experiments support this theory. As silica loading increases, the matrix becomes more viscous, so particles experience more drag as they are driven towards the channel center by the acoustic force.[16] As a result, particles travel shorter lateral distances during the focusing process, resulting in a larger focusing width (Eq. 4.6). Silica should have no effect on the particle distribution when there is no focusing, as the particles should be randomly distributed throughout the channel regardless of viscosity. The lack of significance of the linear fit at 0 V_{pp} supports the idea that the effect of silica on focusing width comes from changes in acoustic focusing efficiency.

Equation 4.6 predicts that the focusing width should decrease with increasing acetone because increasing acetone decreases the viscosity. Instead, the focusing width decreases with increasing acetone for all acoustic wave amplitudes, indicating that the trend may be an artifact. It is apparent that between 8 and 24 w% acetone, the acetone loading does not have a large effect on focusing performance.

Third, the focusing width should decrease with the inverse of print speed, via Equation 4.6. These experiments confirm the direction but not the shape of the predicted trend. As the print speed increases, particles spend less time in the focusing region within the channel. Thus, the focusing force is applied for less time, and the particles do not have enough time to move towards the center of the channel. However, this effect alone does not govern the focusing width. Equation 4.6 indicates that the focusing width should vary inversely with print speed, but increasing the print speed decreases the viscosity, and the particle travel distance is also inversely proportional to the viscosity. As a result, the effect of reducing the time in the focusing zone counteracts the effect of reducing the viscosity, resulting in a net linear increase in focusing width with increasing speed (Fig. 4.S9a). Moreover, Equation 4.6 indicates that the focusing width is related to the inverse of the product of the speed and viscosity. To some

degree, experimental data follow the predicted trend, with larger deviations from the prediction at higher speeds (Fig. 4.S9c).

The spreading ratio lies at the nexus between focusing quality and form holding. One may expect the spreading ratio to decrease with silica because high viscosities would impede particle motion, but the opposite is true. This may be because the particle-depleted edges have a lower viscosity than the particle-rich center, such that the fluid at the edge of the line spreads farther than the fluid at the center of the line. Aggravating this spreading is the fact that lower viscosity matrices have narrower focusing widths, leaving larger swaths of the line depleted of particles and thus with a lower viscosity. As a result, low viscosity matrices spread out around the particles more than high viscosity matrices. Thus, if the absolute width of the particle region is more important than the proportion of the line that is occupied by particles, it may be sufficient to use a high silica matrix. However, if printed width relative to the width of the line is important, then low silica loadings should be used.

Higher particle loadings demonstrate similar but less compelling trends in focusing width, printed width, and spreading ratio. (Fig. 4.S5d). These deviations in effect strength are likely due to secondary scattering forces between particles as described in [125].

4.4.3 Focusing quality of high particle loadings

At the largest amplitude, increasing silica appears to increase the focusing width ($p = .319$). When focusing is not employed, the focusing width decreases, then increases with silica loading ($p = .394$). This may come from secondary scattering forces between particles. Particles which are aligned along the length of the channel exert attractive forces causing clustering, while particles aligned along the width exert repulsive forces, preventing focusing.[16] Equation 4.6 does not account for these secondary interactions. Higher concentrations of particles experience more repulsive secondary forces, so higher particle loadings are less capable of nar-

row channel focusing widths. As a result, the range of focusing widths for 9 v% particles is half of the range of focusing widths for 1.7 v% particles.

At high particle loadings, silica has a similar but insignificant effect on printed width to the low-particle effect. There is no linear relationship between silica loading and printed width ($p = .341$ for 50 V_{pp}, $p = .561$ for 0 V_{pp}) (Fig. 4.S5e). The trends in printed width do not follow the trends in focusing width, indicating that particle interactions may influence the way that particles spread out within the printed line. It is worth noting that high particle loadings experience smaller spreading ratios than low particle loadings. Particle-particle interactions may reduce how far particles spread relative to the matrix, which would reduce the spreading ratio for high particle loadings. Still, there is no significant linear correlation between silica loading and spreading ratio for the higher particle loading ($p = .401$ for 50 V_{pp}, $p = .493$ for 0 V_{pp}) (Fig. 4.S5f).

4.4.4 Form holding

Height/width values for these epoxy-based inks range from 0.2 to 1.0, but a line that maintains the same shape as the channel would have a height/width of 1.5. It is important to note that the line height/width is not bounded by this theoretical height/width because the line distorts during both extrusion and curing. Because shrinkage during acetone evaporation and curing is not necessarily uniform across the profile due to interface effects, even a profile with perfect form holding may not maintain the same aspect ratio as the channel and could have a higher or lower height/width.

Previous spreading experiments indicate that height/width, which scales inversely with spreading speed, scales with the root of the low strain rate viscosity.[187] Thus, as the silica loading increases, the low strain rate viscosity should increase, slowing the spreading rate of the deposited line and increasing the line height/width. This is borne out by these experi-

ments. However, none of the tested inks could produce spanning structures, so support material would be required to produce three-dimensional structures with acoustic focusing.

While acetone should impact form holding in the same way as silica, acetone does not have a significant effect on form holding. This may be because acetone evaporates quickly after exiting the nozzle, or the effect on viscosity is not large enough to make an appreciable difference. Thus, a low acetone loading should be employed to minimize part shrinkage.

Focusing could have an effect on form holding. Acoustic focusing splits the line into two regions: a viscous, particle-rich region in the center of the line and a low-viscosity, particle-depleted region at the edges of the line. Because the edges are less viscous than the center, they should flow faster than the center, causing the behavior discovered in the discussion of spreading ratio, where the edges of the line spread farther than the particles of the center of the line. This would suggest that focusing should cause the height/width to decrease, which is neither proven nor disproven by these data. While acoustic wave amplitude has an effect on height/width, the trend may occur merely because the area changes with acoustic wave amplitude due to an effect known as streaming. When the acoustic energy increases, the flow rate through the channel increases.[192] As a result, using the same pressure for all acoustic wave amplitudes for a given ink will produce different flow rates and thus different line areas. Adjustments were made to the pressures to account for this effect, but they undercompensated for streaming, resulting in larger, flatter focused lines and smaller, narrower unfocused lines.

It is apparent that local changes in particle concentration alone do not fully govern form holding behavior. If they did, then the 9 v% particle inks would have a larger height/width than the lower particle concentration, but the opposite is true (Fig. 4.5c). Inks with more particles are more viscous and require greater pressures to flow at the same rate as inks with few particles. Here, adjustments overcompensated for this fluidic resistance, resulting in larger, flatter lines for the higher particle loading.

Theoretically, speed could affect form holding, because the deposition speed changes the

strain rate on the ink and thus the viscosity during deposition. However, because deposition speed does not impact height/width, it is evident that speed-dependent shear thinning behavior does not impact form holding.

In sum, several processing parameters present trade-offs when direct ink writing is combined with acoustic focusing. While increasing the viscosity of the ink by adding silica improves form holding properties, it sacrifices the focusing quality. Similarly, while fast print speeds increase the output of a 3D printer, focusing quality improves with decreasing print speed.

Print nozzles can be designed to gain the benefits of fast print speeds and good form holding without sacrificing focusing quality. Namely, longer channels and piezoelectric actuators can be used, allowing particles to spend more time in the focusing zone. However, if the print line needs to switch between focused and unfocused states in a span shorter than the nozzle length, a long nozzle will not be useful. To counteract this, larger acoustic wave amplitudes can be used to ensure a short transition between focused and unfocused states. Still, longer nozzles require higher pressures, so the length of the nozzle is limited by the pressure that the mechanical system can deliver.

4.5 Concluding remarks

This work defines the trade-offs associated with matrix selection and printing parameters for direct ink writing with acoustic focusing and validates the model using silver-coated glass microspheres in epoxy-silica-acetone matrices. Because these relationships verify theoretical acoustic focusing models and droplet spreading experiments, they may be generalized to guide material selection for acoustic focusing with direct ink writing.

To improve focusing, it may be beneficial to use larger particles. The advantage is two-fold. First, larger particles experience a greater focusing force, so the particle focusing veloc-

ity scales with the square of the particle radius.[16] Second, larger particles activate a greater degree of shear thinning in the focusing direction. Together, these indicate that the focusing velocity should increase for larger particles, ignoring the effects of secondary scattering. However, larger particles are more likely to jam in the nozzle than smaller particles.

Finally, the curing method may change these focusing-form holding trade-offs. These experiments used a 90-minute heat-cure initiated within several minutes after deposition. However, rapid "on-the-fly" curing methods such as light curing may halt the spread of the matrix and particles. Further examination of the time scales within which the focusing zone distorts and the line profile spreads would aid in the design of such "on-the-fly" curing methods.

4.S1 Supplemental figures and tables

The focusing velocity v_F follows

$$v_F = \frac{\pi a^2 \beta_f p_o^2 \phi}{18 W \eta} \tag{4.S1}$$

where a is the particle radius, β_f is the fluid compressibility, p_o is the acoustic radiation force, ϕ is a constant depending on particle and fluid density and compressibility, W is the channel width, and η is the fluid viscosity.

The shear strain rate $\dot{\gamma}$ must scale with the velocity of the particle normalized by the radius of the particle.

$$\dot{\gamma} \propto \frac{v_F}{a} \tag{4.S2}$$

Inserting Equation 4.S1 into Equation 4.S2,

$$\dot{\gamma} \propto \frac{a}{\eta} \tag{4.S3}$$

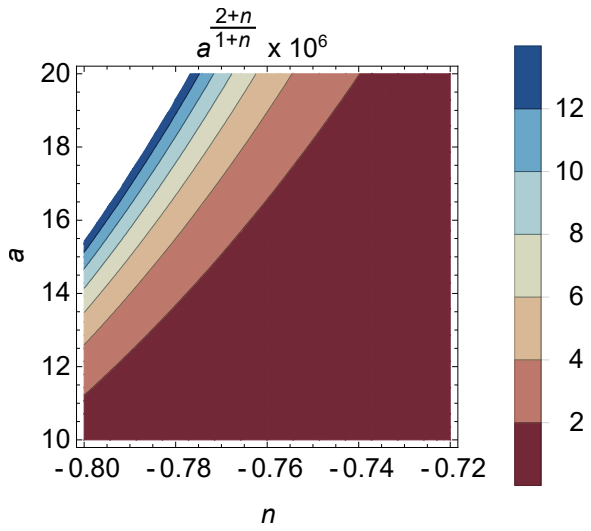

Figure 4.S1: Dimensionless particle velocity, as a function of particle radius A and viscosity power law exponent n. As the particle radius increases, focusing speed increases.

From rheology, the viscosity follows a power law relationship with the shear strain rate.

$$\eta \propto \dot{\gamma}^n \tag{4.S4}$$

Inserting Equation 4.S3 into Equation 4.S4,

$$\eta \propto a^{\frac{n}{n+1}} \tag{4.S5}$$

Substituting Equation 4.S5 into Equation 4.S1,

$$v_F \propto a^{\frac{2+n}{1+n}} \tag{4.S6}$$

Values of n range between -0.8 and -0.7 for these matrices.

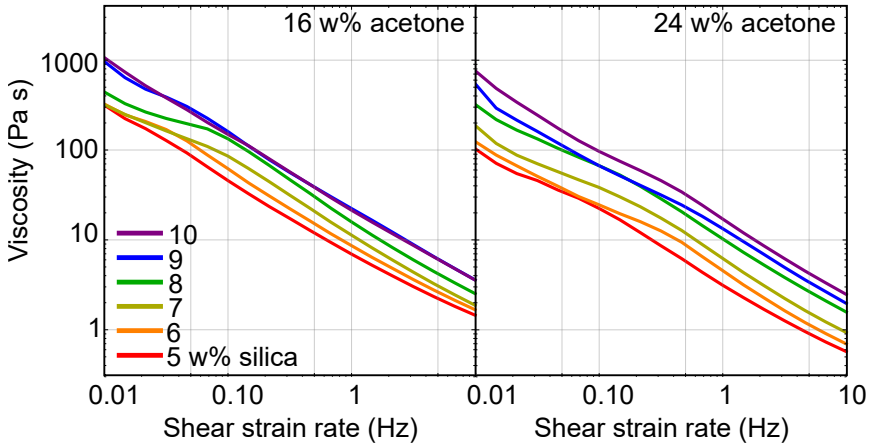

Figure 4.S2: Rheology curves for high acetone loadings. All silica loadings have the same shear thinning contrast when acetone is added. Adding acetone shifts viscosity curves downward.

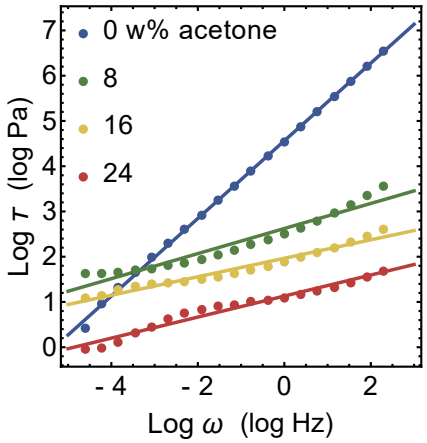

Figure 4.S3: Power law fits for rheology curves of 5 w% silica inks. While inks without acetone fit power laws well, inks with acetone exhibit some deviations at high and low frequencies.

	DF	SumOfSq	MeanSq	FRatio	PValue
silica w%	6	0.592	0.099	40.984	$0. \times 10^{-3}$
acetone w%	2	0.143	0.071	29.676	$0. \times 10^{-3}$
amplitude	2	0.764	0.382	158.761	$0. \times 10^{-3}$
speed	3	0.055	0.018	7.634	$0. \times 10^{-3}$
particle w%	1	$0. \times 10^{-3}$	$0. \times 10^{-3}$	0.413	0.521
Error	616	1.482	0.002		
Total	630	3.037			

Table 4.S1: ANOVA of focusing width. DF degrees of freedom, SumOfSq sum of squares.

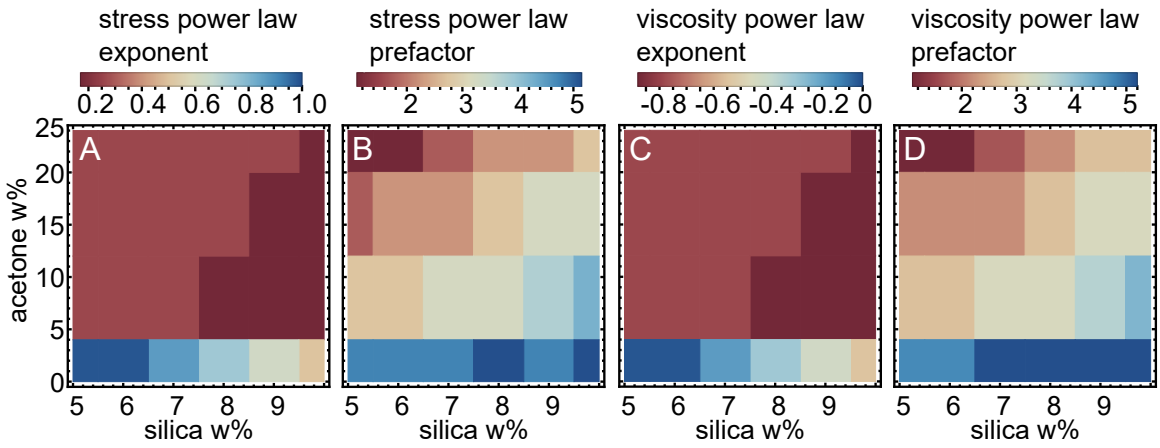

Figure 4.S4: Fitting parameters for shear frequency - stress and shear frequency - viscosity curves, following Eq. 4.7 and Eq. 4.S4. a,c) Shear thinning contrast increases with increasing silica when no acetone is included, but acetone increases shear thinning contrast beyond that of the highest silica loading. b,d) Adding silica and decreasing acetone increase the viscosity.

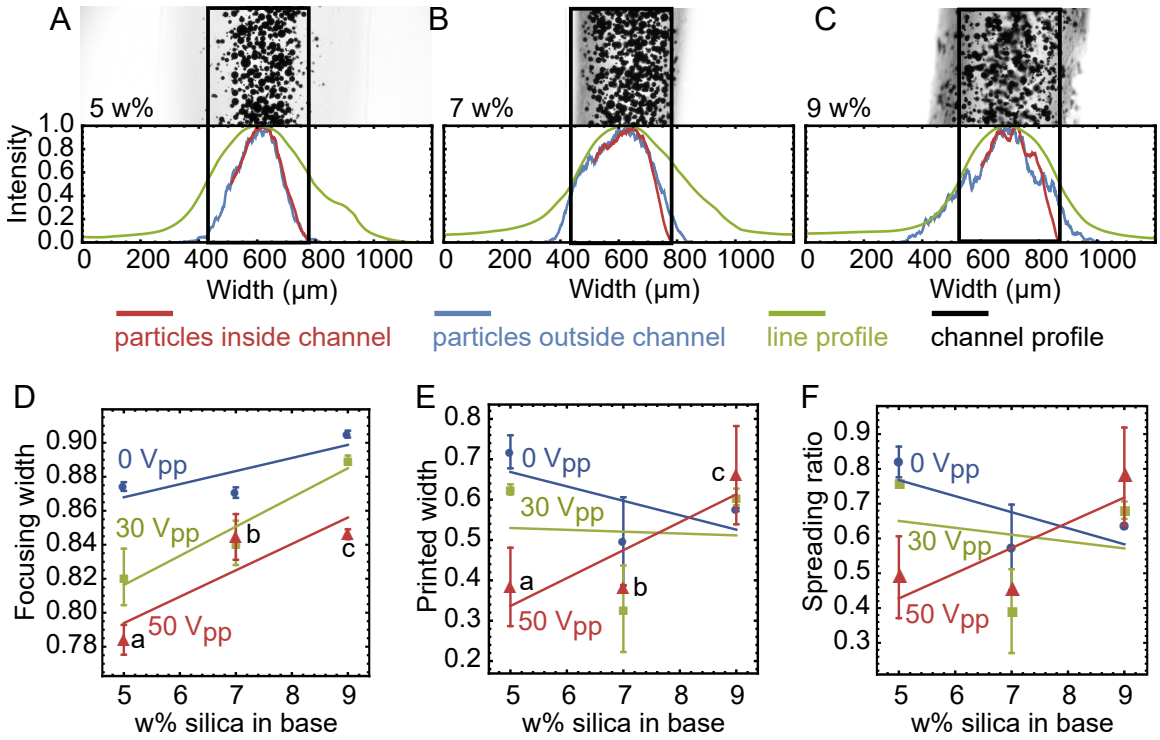

Figure 4.S5: Focusing quality as a function of silica w% and acoustic wave amplitude for 9 v% particles in the printed line, 8 w% acetone, and 1 mm/s. (a-c) Ink in line, normalized intensities in channel and line, and line surface profile normalized by line height. Values are given for 50 V_{pp}, 1 mm/s and 8 w% acetone for varying silica loadings. Dark grey regions correspond to high line profile slopes. (d) Channel focusing width. (e) Printed focusing width. (f) Spreading ratio, defined as the printed focusing width divided by channel focusing width.

	DF	SumOfSq	MeanSq	FRatio	PValue
silica w%	6	0.252	0.042	1.584	0.154
acetone w%	2	0.276	0.138	5.221	0.006
amplitude	2	0.821	0.410	15.502	$0. \times 10^{-3}$
speed	3	0.013	0.004	0.158	0.924
particle w%	1	0.458	0.458	17.303	$0. \times 10^{-3}$
Error	173	4.581	0.026		
Total	187	6.401			

Table 4.S2: ANOVA of printed width for continuous lines with cross-sections between 80% and 150% of the channel area.

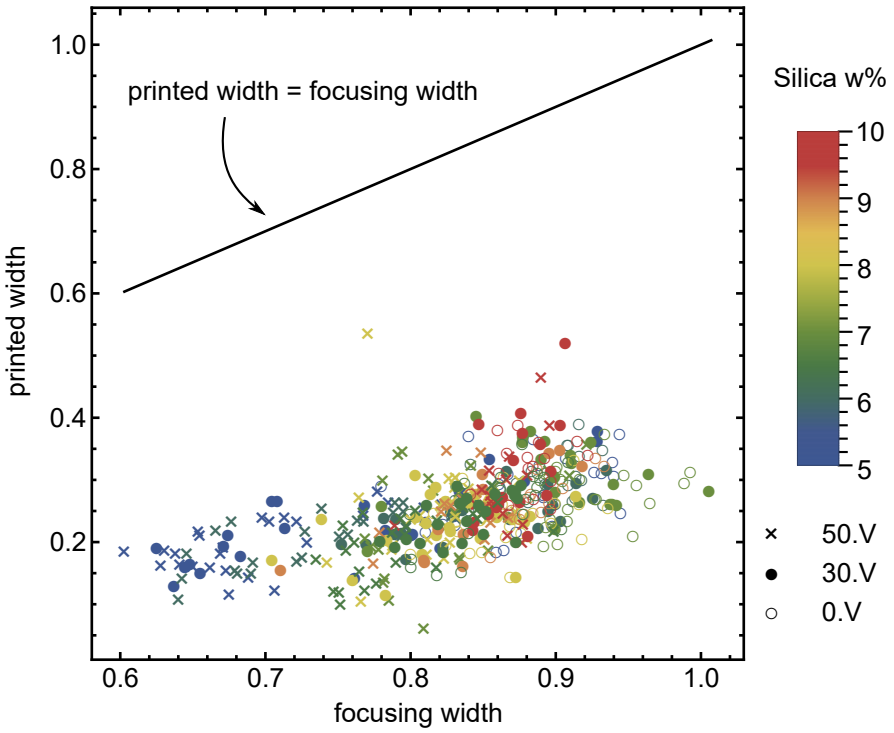

Figure 4.S6: Correlation between printed focusing width and channel focusing width as a function of silica loading and signal amplitude.

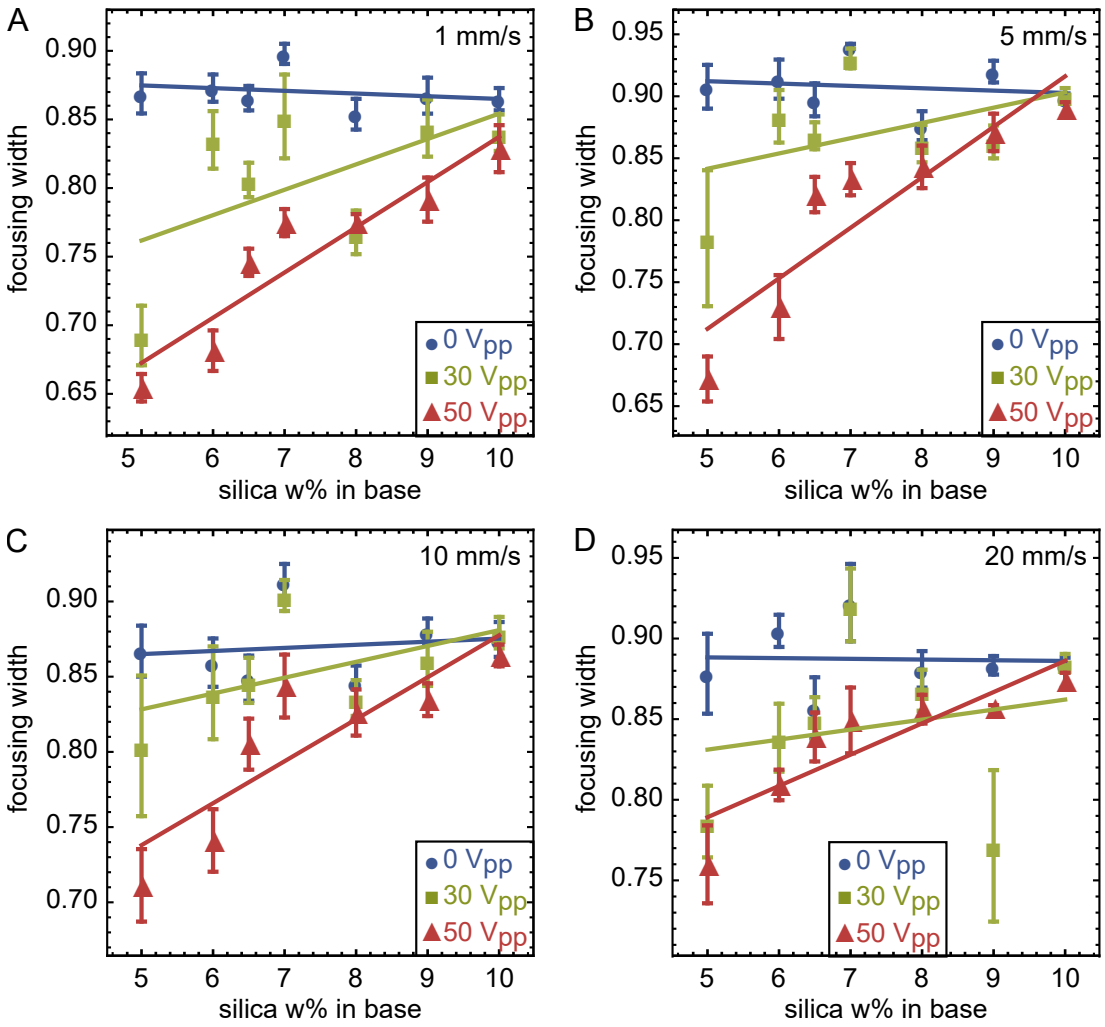

Figure 4.S7: Channel focusing width for 1.7 v% particles in the printed line as a function of silica loading in the base ink, for stage speeds of a) 1 mm/s, b) 5 mm/s, c) 10 mm/s, and d) 20 mm/s.

	DF	SumOfSq	MeanSq	FRatio	PValue
silica w%	6	0.163	0.027	0.894	0.501
acetone w%	2	0.239	0.120	3.945	0.021
amplitude	2	0.389	0.195	6.421	0.002
speed	3	0.005	0.002	0.051	0.985
particle w%	1	0.598	0.598	19.725	$0. \times 10^{-3}$
Error	172	5.212	0.054		
Total	186	6.605			

Table 4.S3: ANOVA of spreading ratio, defined as the printed width/focusing width, for continuous lines with cross-sections between 80% and 150% of the channel area. Video capture failed during printing of one sample, so this set includes one fewer sample than the sets for focused width and width/height.

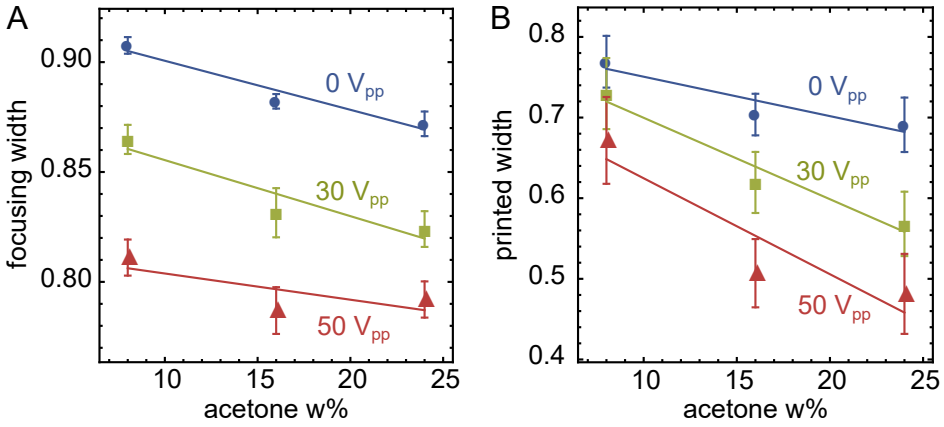

Figure 4.S8: Focusing quality as a function of acetone loading and amplitude for 1.7 v% particles in the printed line. a) Focusing width. b) Printed width. Acetone has no significant effect on focusing.

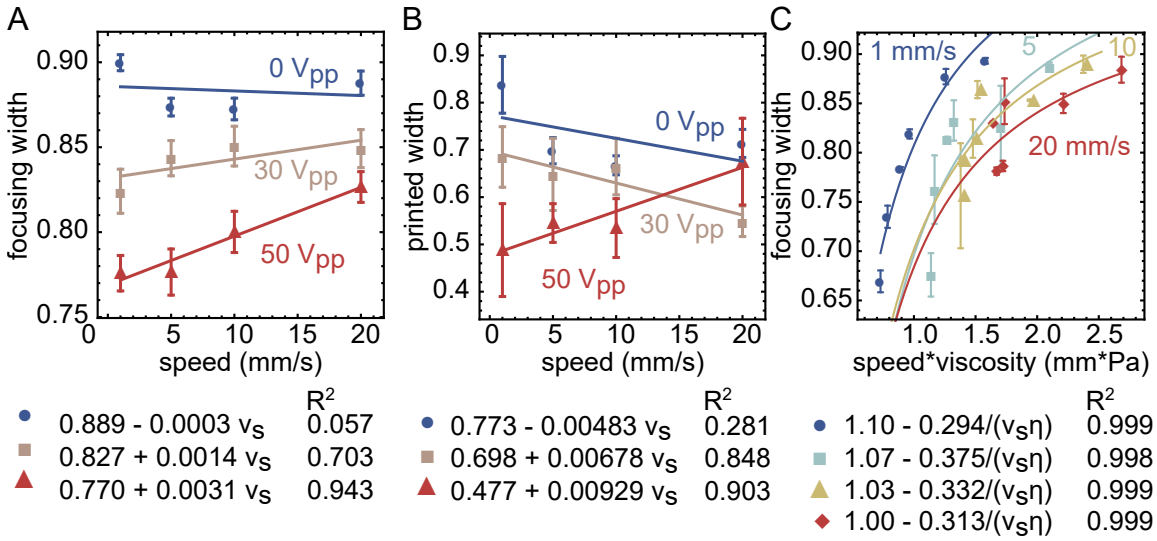

Figure 4.S9: Focusing quality as a function of printing parameters for inks with 1.7 v% particles. a) Focusing width as a function of print speed and acoustic wave amplitude. b) Printed width as a function of print speed and acoustic wave amplitude. c) Focusing width as a function of viscosity×print speed, for inks with 8 w% acetone printed at an acoustic wave amplitude of 50 V_{pp}.

	DF	SumOfSq	MeanSq	FRatio	PValue
silica w%	6	2.373	0.395	26.208	$0. \times 10^{-3}$
acetone w%	2	0.057	0.029	1.903	0.152
amplitude	2	0.153	0.077	5.076	0.007
speed	3	0.074	0.025	1.642	0.182
particle w%	1	0.451	0.451	29.882	$0. \times 10^{-3}$
Error	173	2.611	0.015		
Total	187	5.719			

Table 4.S4: ANOVA of height/width for continuous lines with cross-sections between 80% and 150% of the channel area.

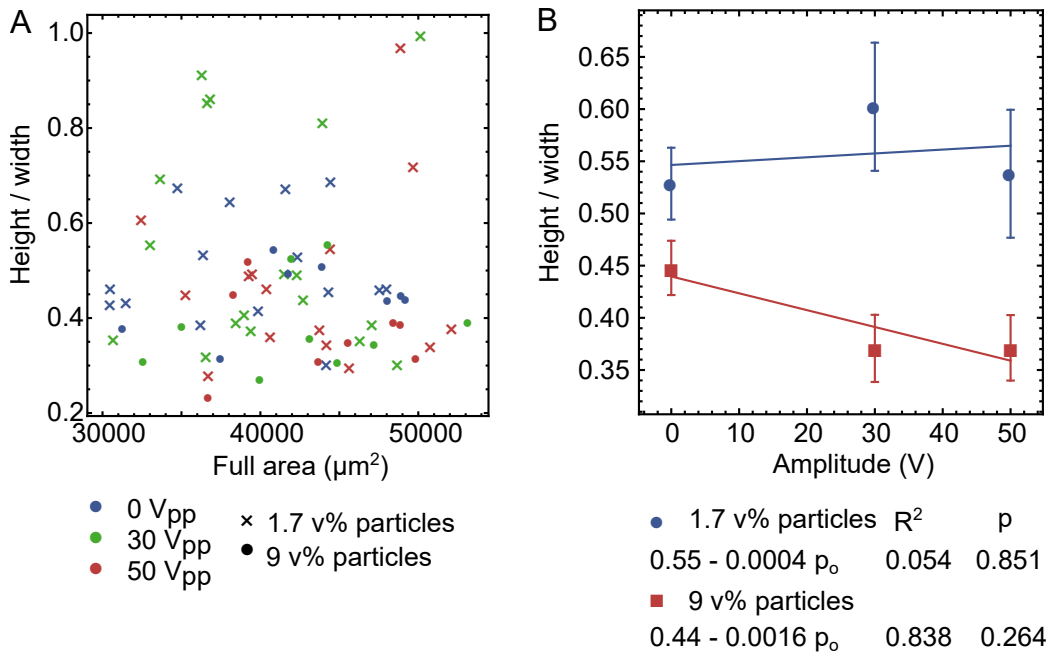

Figure 4.S10: a) Height/width compared to line cross-sectional area for 8 w% acetone. b) Height/width as a function of amplitude for 8 w% acetone.

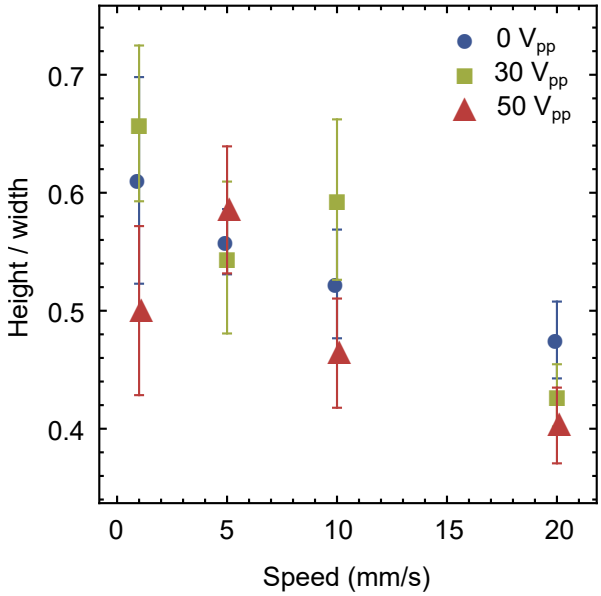

Figure 4.S11: Height/width as a function of print speed for inks with 1.7 v% particles in the printed line.

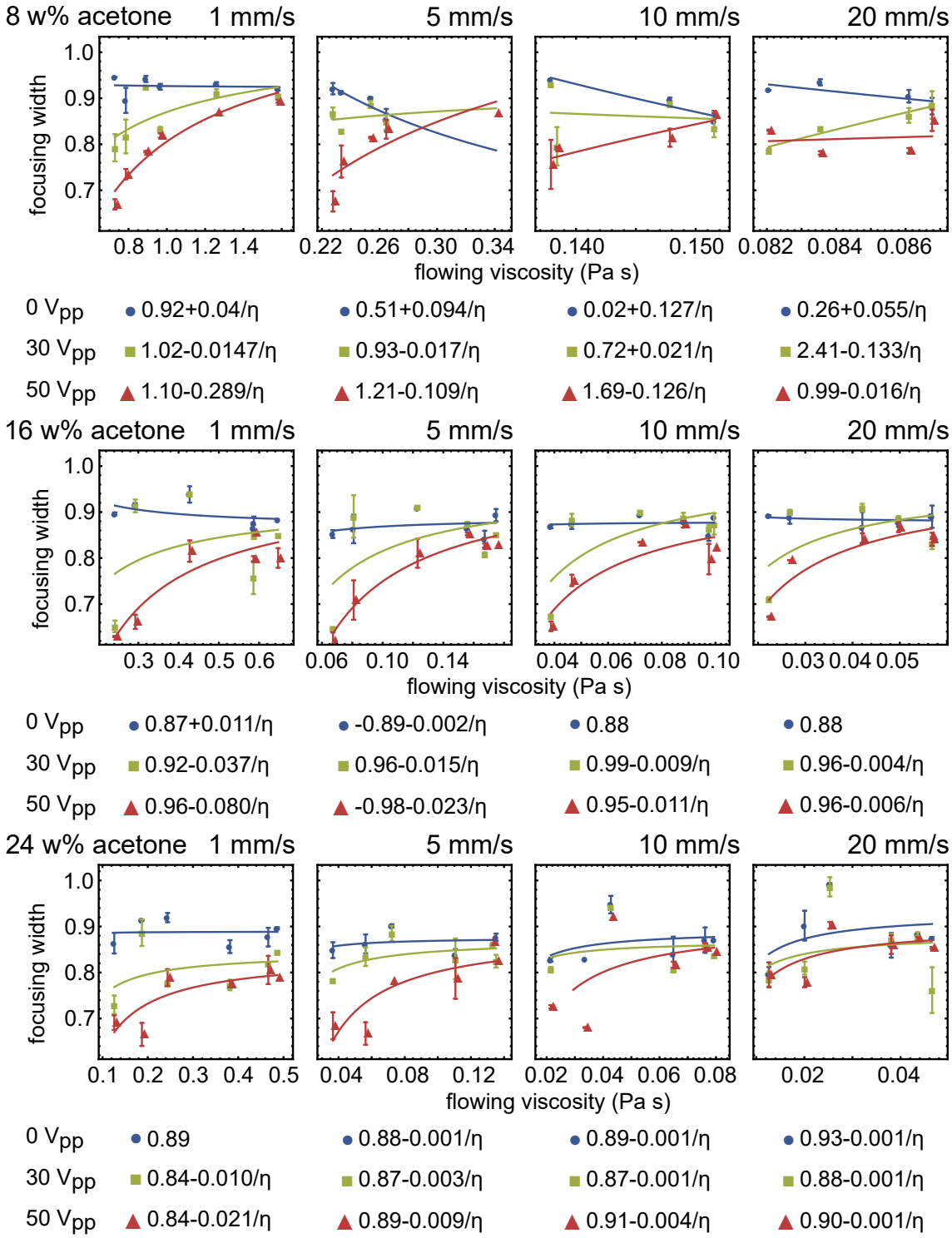

Figure 4.S12: Focusing width as a function of calculated flowing viscosity for inks with 1.7 v% particles in the printed line. Focusing width follows an inverse viscosity relationship, most clearly at low print speeds and acetone loadings.

Chapter 5

The print bead: wetting, stability and rotational flows

5.1 Introduction

Extrusion-based three-dimensional printing methods allow for gradients in structural and functional properties through *in-situ* modification of the filament microstructure along the print path.[13, 15, 40, 77] While fused deposition modeling is the most commercially prevalent extrusion method, direct ink writing (DIW) arguably enables a broader range of materials. In polymer DIW, shear thinning fluid thermoset resins are extruded through a nozzle and polymerized after deposition using light or heat.[86] DIW is particularly useful for imposing structural and functional gradients throughout 3D printed parts, as two-phase fluid inks can be integrated with acoustic, magnetic, and electric fields to control microstructure *in-situ*. Externally imposed fields can manipulate the positions and orientations of encapsulated ceramic, metallic, or polymeric microparticles, therein controlling the microstructure and consequent properties of the printed filament.

For example, consider integration of acoustic fields with DIW, wherein a piezoelectric ac-

tuator establishes a standing sound wave in a rectangular silicon channel. The associated pressure gradients move particles with a positive acoustic contrast toward the nodes of the standing wave and move particles with a negative acoustic contrast toward the antinodes of the standing wave. Effective use of acoustic fields requires a sufficient acoustic contrast factor, which depends on the densities and compressibilities of the particles and fluid.[8, 13, 15, 16] Acoustic fields have also been used in material processing techniques such as stereolithography (SLA) and bulk assembly.[26, 27, 32, 33, 186, 193, 194] Alternatively, imposing magnetic or electric fields across printed, uncured specimens can align and position particles that exhibit a sufficient contrast in conductivity or magnetic susceptibility with the matrix [40, 59]; electric fields can also form writable conductive filaments or orient particles in an SLA ink bath.[58, 195]

For all of these techniques that exploit an external field, viscous drag limits the time scale in which particles can reposition in the nozzle, which scales with the viscosity of the fluid. For a fixed nozzle length and flow speed, achievable particle packing contrast decreases with the inverse of the fluid viscosity.[15, 16] Thus, establishing a high contrast between unfocused and focused states is only feasible at low viscosities or low print speeds. Whereas conventional composite direct-write inks have zero shear viscosities on the order of 10^4 to 10^5 Pa·s,[61, 196, 197] acoustic and magnetic particle manipulation are only practical in fluids with zero shear viscosities less than $\sim 10^3$ Pa·s.[15, 40] At these lower viscosities, the energetic contribution of surface chemistry to filament stability is not negligible, such that mechanisms behind filament rupture are different from that of conventional DIW.

This work uses digital image analysis methods to characterize the quality of the printing process in this lower viscosity DIW regime and identify printing parameters associated with high quality prints. Namely, quantitative metrics are established for three printing criteria: filament stability, nozzle wetting, and rotational flows. Not only can these metrics verify theoretical relationships between processing parameters and print quality, they can also serve as *in-situ* monitoring metrics to allow for mid-print modifications to processing parameters, such

as extrusion pressure and stand-off distance.

First and foremost, filament stability dominates print quality. If the design calls for a continuous filament, the deposited filament should not break into droplets. Identifying the physical basis for filament instabilities can ensure the reliable deposition of filaments of controlled height and width. In alternative applications like droplet dispensing, locating the initiation of breakup can guide the deposition of droplets with controlled size and spatial periodicity. 2D lubrication theory is used to model print bead stability. This model tracks the contact line and the pressure differential between the upstream and downstream meniscus. Contact angle is a suitable proxy for pressure differential, and stability is evaluated on-the-fly using relative changes in contact line position and contact angle. Further, the meniscus position is mapped across flow speeds and stage speeds to identify three stability regimes: overflowing filaments, balanced filaments, and droplets. Similar qualitative maps across printing speeds have been constructed for DIW and slot die coating.[110, 130] This work expands on those maps by quantifying stability within regimes through the contact line position and using lubrication theory to predict qualitative boundaries in DIW. Finally, contact line oscillation sizes are measured within the droplet regime to evaluate recovery from perturbations.

Second, limiting wetting is essential to print quality. Ink that builds on the surfaces of the print nozzle can drag through or deposit onto the filament during printing. Vortices can form in fluid that collects on the nozzle, disturbing the internal structure established in the channel (either from laminar hydrodynamics or external fields).[130] Pulling the downstream meniscus upward on the nozzle (i.e. opposite nozzle flows) can destabilize filaments. Nozzle wetting decreases as the filament approaches an instability, necessitating low flow to stage speed ratios. Most numerical analyses of DIW neglect nozzle wetting[105, 107]; here, experimental measurements set the stage for future modeling efforts.

Third and finally, rotational flows established at the exit of the printing nozzle disturb any microstructures established in the nozzle. In conventional DIW, homogeneous internal struc-

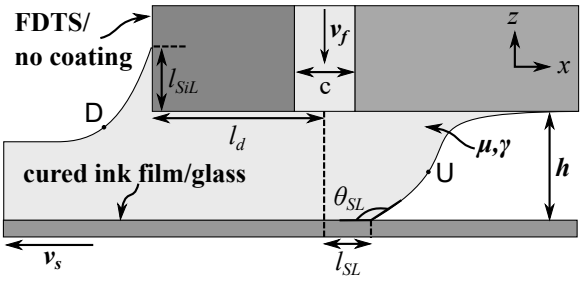

Figure 5.1: Variables used in viscocapillary model (Eqs. 5.1, 5.2). Independent variables controlled in the described experiments are in bold. U and D indicate the upstream and downstream points used for pressure estimates.

tures mean that mixing within the filament has no effect on print properties. In field-assisted DIW, lateral fluid movement changes material properties. Rotational flows are quantified by tracking particle movement. Similarly to nozzle wetting, printing at low flow to stage speed ratios limits rotational flows in the filament.

5.2 Theoretical background from slot die coatings

To predict the geometry of stable filaments and the conditions at which instabilities initiate, equations are borrowed from previous analyses of slot die coating processes. Because DIW uses no applied atmospheric pressure on either side of the nozzle, the pressure differential between the upstream and downstream meniscus surfaces due to viscous dissipation $\Delta P_{UD,V}$ should be equal to the pressure differential due to capillarity $\Delta P_{UD,L}$. In two dimensions, lubrication theory for slot die coating describes $\Delta P_{UD,V}$ as a function of the distance between the channel and upstream contact line l_{SL}; [130, 131, 198]

$$\Delta P_{UD,L} = \Delta P_{UD,V} = -\frac{6\mu v_s}{h^2} l_{SL} - \frac{6\mu l_d v_s}{h^2} + \frac{12\mu l_d v_f c}{h^3}, \tag{5.1}$$

where h is the stand-off distance, l_d is the distance between the channel and the downstream nozzle corner, μ is the ink viscosity, c is the channel depth, and the flow speed v_f and stage speed v_s are both positive (Fig. 5.1). Though this model is for Newtonian fluids, the shear strain rate v_s/h is used to approximate a constant viscosity in these non-Newtonian fluids throughout the coating gap. In this work, Equation 5.1 describe how changes in contact line position and angle can be used to evaluate the stability of the nozzle-to-substrate bridge *in-situ*.

To predict instability initiation, pinning of the downstream meniscus at the nozzle corner and other geometric assumptions are used to predict $\Delta P_{UD,L}$ as a function of surface tension γ, dynamic contact angle θ_{SL}, stand-off distance, flow speed, stage speed, viscosity, and channel depth.[131] Incorporating Higgins and Scriven's assumptions into Equation 5.1, an expression is evaluated relating l_{SL}, v_f, and v_s given a set of experimental conditions.[131] Using assumed l_{SL} values, rupture and dripping bounds for stability are determined in terms of flow speed and stage speed. At the rupture bound, where $l_{SL} = 0$, the filament breaks into droplets, analogous to air entrainment in slot die coating. At the dripping bound, where $l_{SL} = l_u$, the distance between the channel and the front of the nozzle, fluid leaks out of the upstream edge, analogous to dripping in slot die coating. From this viscocapillary model, the following stability criteria emerge:

$$\begin{aligned} 0 &= \frac{6\mu v_s l_d}{h^2}\left(1 - \frac{2v_f c}{h v_s}\right) + \frac{1.34\mu^{2/3} v_s^{5/3}\gamma^{5/3}}{v_f c} - \frac{\gamma(|\cos\theta_{SL}| + 1)}{h} \qquad \text{(rupture)} \\ 0 &= \frac{6\mu v_s l_d}{h^2}\left(1 + \frac{l_u}{l_d} - \frac{2v_f c}{h v_s}\right) + \frac{1.34\mu^{2/3} v_s^{5/3}\gamma^{5/3}}{v_f c} - \frac{\gamma(|\cos\theta_{SL}| + 1)}{h} \qquad \text{(dripping)} \end{aligned} \tag{5.2}$$

Equation 5.2 can be solved for v_f in terms of v_s to predict these two bounds.[130, 131] θ_{SL} is determined from Figure 5.7. At the rupture bound, θ_{SL} is the maximum contact angle achieved by filaments. At the dripping bound, θ_{SL} is the asymptote of θ_{SL} as a function of l_{SL}. These contact angles are listed in the supplemental information. The downstream edge

length l_d is 375 μm, the upstream edge length l_u is 500 μm, and the channel depth is 150 μm. Comparing the theoretical bounds described by Equation 5.2 to experimental bounds, trends in stability with printing parameters are rooted in viscous dissipation and capillarity.

5.3 Experimental approach

5.3.1 Material preparation

Inks were pre-mixed and refrigerated at 6 °C until use. Diurethane dimethacrylate (UDMA) composed the bulk of the ink (Sigma Aldrich, mixture of isomers with topanol inhibitor). Triethylene glycol dimethacrylate (TEGDMA) lowered the viscosity of the ink (Sigma Aldrich, with MEHQ inhibitor). Fumed silica imparted shear thinning behavior and raised the zero shear viscosity of the ink (Evonik Aerosil R106). Camphorquinone acted as a photosensitizer (Sigma Aldrich). 2-(Dimethylaminoethylmethacrylate) (DMAEM) acted as a photoinitiator (Sigma Aldrich, with monomethyl ether hydroquinone inhibitor). Silver-coated nickel microspheres allowed for flow tracking (Potters Beads Conduct-O-Fil, SN15P30, diameter 13 $\pm$ 5 μm). Inks were mixed in three steps, each for 3 minutes at 2000 rpm in a planetary mixer (Thinky ARE-310). Fumed silica was added to the UDMA in a 16:84 silica:UDMA weight ratio and mixed to produce the resin base. TEGDMA was added in 20:80, 25:75, 30:70, and 35:65 TEGDMA:base weight ratios, 0.2 w% camphorquinone and 0.8 w% DMAEM were added, and the ink was mixed.[170, 199] Finally, inks were divided into 4 g portions, 3 w% microspheres were added, and the ink was mixed again. Masses were measured using a microbalance (Mettler AE163). The resultant inks can be light-cured at a wavelength of 470 nm or heat-cured at 180 °C for 90 minutes.

Printing tests were conducted on two types of substrates: glass and cured ink. Cured ink substrates were prepared by sonicating 3 $\times$ 2 inch glass slides in a progression of acetone, iso-

propanol, and distilled water for 2 minutes on each step. Slides were air-dried with compressed nitrogen gas and then heat-dried on a 90 °C hot plate immediately before spinning. Glass slides were mounted in a spin coater (Laurell WS-400BZ-6NPP/LITE), and a large droplet of ink was deposited onto the slide and spun in a two step sequence: 2000 rpm for 20 seconds, then 5000 rpm for 40 seconds. Coated substrates were then cured in an oven at 180 °C for 90 minutes. Both the coated and uncoated slides were cleaned with a lint-free cloth before the printing process.

Nozzles were prepared as described in [15] and [8]. Briefly, channels measuring 150 μm deep, 350 μm wide, and 35 mm long were etched into silicon wafers and capped with borofloat glass. Nozzles were diced to produce 85° edges, where the nozzle width at the tip was equal to the channel width. Because this leaves very thin channel side walls, the walls near the tip are prone to chipping during dicing and surface functionalization. After applying coatings, nozzle tips were polished using a sequence of SiC papers up to 1200 grit until all gaps in channel walls were removed, maintaining a flat tip so the nozzle surface would be parallel with the substrate during printing. Wire ferrules were bonded to poly(methyl methacrylate) inlets fabricated using a laser cutter (Trotec Speedy 100), which were attached to fluidic vias in the glass capping layer using epoxy (Devcon HP250).

Some nozzles were coated with 2H,2H-perfluorodecyltrichlorosilane (FDTS) as described in [200]. Briefly, before the addition of inlets, bonded nozzles were etched in buffered hydrofluoric acid to remove the native oxide on the silicon side, oxidized with hydrogen peroxide to form a bonding layer, and then soaked in a 2 mM solution of FDTS and iso-octane in a PTFE beaker inside of an argon glove box for 30 minutes, with appropriate rinses. This leaves a monolayer of FDTS molecules bonded to the surface of both the silicon and glass components of the nozzle, which lowers its surface energy.

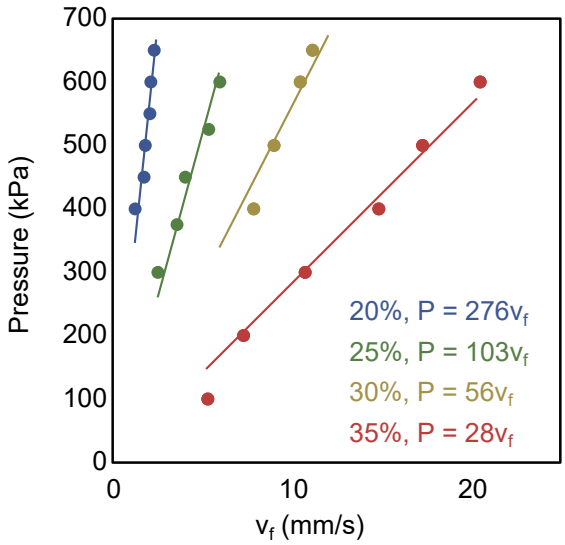

Figure 5.2: Applied pressure - flow velocity calibration curves for inks with varying TEGDMA w%.

5.3.2 Property measurements

Ink densities were measured by dispensing 0.4 mL of ink into a PMMA reservoir fabricated using a laser cutter and massing the ink using a microbalance (Mettler AE163). Extrusion speeds were calibrated by extruding inks for one minute at fixed pressures, measuring the mass of the extruded ink, calculating the volume of the extruded ink, and dividing the volume of ink per time by the cross-section of the channel (350 by 150 μm). Linear fits were applied to the pressure-speed curves (Fig. 5.2).

Viscosities were measured using a TA Instrument Company ARES-LS1 rheometer, with 25 mm diameter flat plates and a 2 mm gap at room temperature (21–22 °C). Tests maintained a constant strain of 15%, and the shear strain rate was swept from 0.01 Hz to 10 Hz, with 6 points per decade. A 60 second steady preshear was maintained at 1 Hz, followed by a 5 minute pause. To avoid curing during the test, inks used for rheology measurements did not contain photoinitiators. To avoid measurement errors due to particle settling, inks did not include metallic microspheres. At such a low loading (≈0.4 v%), particles can be expected to

have a negligible effect on viscosity.

Fluid surface tensions were measured using pendant droplet tensiometry. To avoid curing during measurement, inks contained neither DMAEM nor camphorquinone. Droplets were expressed from a blunt-tipped syringe, back-lit, and imaged in grayscale (Point Grey GS3-U3-2356C-C with an Infinitube FM-200 objective and $\times 0.66$ lens). Droplets were extruded from a 3 mL syringe with a 8.66 mm inner diameter, through a blunt-tipped PTFE-coated stainless steel syringe tip with a 0.33 mm inner diameter and 0.65 mm outer diameter. A custom droplet expression routine is used to adjust for residual stresses produced by viscous dissipation. Using a MATLAB-controlled linear stage (Zaber T-LSR150B), the plunger was advanced some distance (0.2 – 1.2 mm), held at that distance for some amount of time to allow the droplet to grow (5 – 60 s), and then retracted some distance to stop droplet growth (0.1 – 1 mm). These times and distances were calibrated for each ink such that the droplet sizes reached an asymptote over time. Images were collected every few seconds for 5 – 10 minutes to track droplet shape evolution over time. Images were then converted to surface profiles using a Canny edge detection, extracted from nozzle edges using a Hough transformation, and fit using code adapted from [154]. Fits were filtered to include only droplet volumes above a Worthington number (droplet volume/maximum possible volume) of 0.65 and root mean square errors below 3 μm, where the droplet volumes were on the order of 4-5 mm^3.

Contact angles used the same imaging apparatus as pendant drop tensiometry. Droplets of ink were dropped in-air onto substrates, and grayscale images were collected. Images were converted into surface profiles using a Canny edge detection. Droplet corners were fit to circles, and contact angles were calculated from arc lengths.

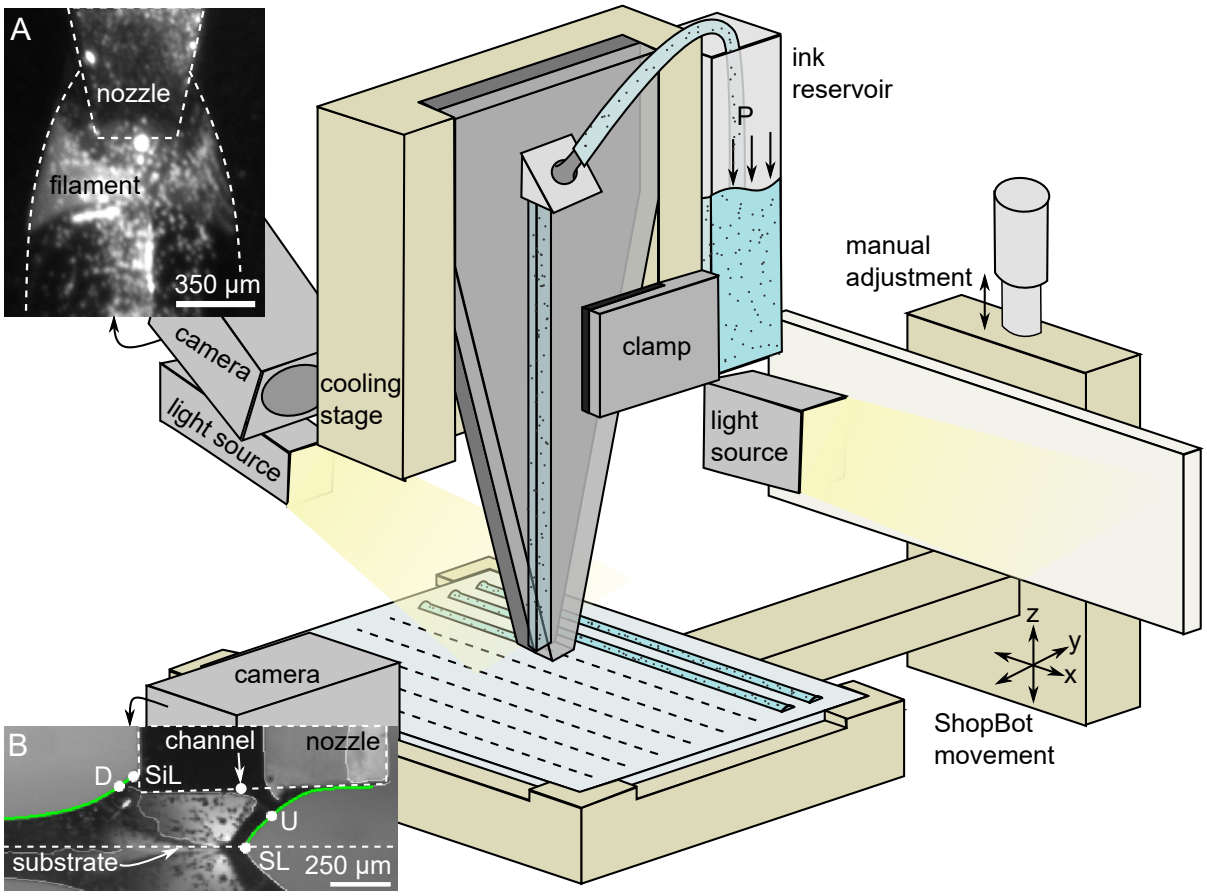

Figure 5.3: A stage moves under static nozzle, reservoir, and light sources to write lines, while cameras capture videos from two angles. Dimensions are not to scale. A) Example frame from the xz-direction. B) Example frame from the y-direction, where silicon-liquid (SiL) and substrate-liquid (SL) contact points and upstream (U) and downstream (D) points of maximum curvature are marked. Meniscus points are green, and initial edge detection points are white.

5.3.3 Video collection and image processing

Straight lines were extruded from a static nozzle onto a moving coated or uncoated glass slide (Fig. 5.3). Nine 70-mm lines were written on each slide, three at each stage speed. A custom MATLAB GUI coordinated the pressure controller, cameras, gantry, and file handling. Inks were extruded at calculated pressures using a high pressure mass flow controller (Fluigent MFCS-EZ). The nozzle was thermally coupled to a water-chilled copper cooling stage using thermal joint compound (Wakefield Type 120) and maintained at 22 °C. The nozzle was attached to the cooling stage using a rubber-padded screw-fasted clamp. Stage movement was controlled by a ShopBot D2418 gantry, which was controlled by custom .sbp code run through Shopbot 3 software. One camera (Point Grey Grasshopper GS3-U3-2356C-C with an Infinity Infinitube FM-200 objective and $\times 0.66$ lens) viewed the extrusion process from the y-direction, and a light source illuminated an opaque panel behind the nozzle such that the background of the video was bright, and the filament was dark (Fig. 5.3B). A second camera (Point Grey FL3-U3-32S2M-CS with an Infinity Infiniprobe objective) imaged the filament being extruded out of the nozzle from the xz plane (Fig. 5.3A). A light source next to the camera illuminated the filament so particles appeared as light against a dark matrix.

Video processing utilized *Wolfram Mathematica 11.1*.[132] For processing in the xy direction (Fig. 5.3B), the nozzle and substrate positions were detected across the video to calibrate the slight tilt inherent in the substrate. For each frame, meniscus points were extracted and fit, and appropriate measurements were collected. The left and right edges of the nozzle were extracted using a Hough transform, and the bottom edge of the nozzle was extracted using a linear regression. Candidate reflection planes were iteratively compared to identify the substrate location.

Meniscus profiles were collected by blurring and edge detecting the image, then filtering the points between menisci. The upstream meniscus was fit by smoothing and interpolating

the upstream points, the first derivative, the second derivative, and the curvature of the surface. The contact point was the lowest point, and the contact angle was found using the slope of the ten points nearest the contact point. The downstream meniscus was fit either using a nonlinear regression or interpolation. The wetting point was the intersection between the nozzle edge and a linear regression of the rightmost points.

For both the upstream and downstream meniscus, the Laplace pressure was calculated as $\Delta P_L = \gamma(\kappa_1 + \kappa_2)$, where κ_1 and κ_2 are curvatures in the xz plane and the orthogonal plane. κ_1 was calculated using the surface fit. κ_2 was approximated by assuming that the surface is an arc, where the width of the arc is equal to the channel width (350 μm), and the height of the arc is equal to the stand-off distance, adjusted for the tilt of the substrate. From geometry, $\kappa_2 = (h/2 + 0.35^2/(8h))^{-1}$, where h is the stand-off distance in mm and κ_2 is in mm^{-1}. The Laplace pressure difference $\Delta P_{UD,L}$ is the Laplace pressure of the upstream meniscus subtracted by the Laplace pressure of the downstream meniscus.

For processing in the $xz-$direction (Fig. 5.3A), videos were cropped to ten frames and segmented to the region directly behind the nozzle, inside the filament. Image displacements were calculated between each set of subsequent frames and averaged to produce a discrete vector field of particle movement. The y-velocity was the average absolute value of the y-component of all vectors in the region.

5.4 Results

5.4.1 Measured parameters

The UDMA-TEGDMA-fumed silica inks used in these experiments are shear thinning. Viscosity-frequency curves follow the Carreau Yasuda Cross model (Table 5.1), with near-zero shear viscosities between 20 and 120 Pa·s. Given that shear strain rates are equal to the stage

w% TEGDMA	Viscosity (Pa·s)
20	$1.8 + 125/((1 + 18\dot{\gamma}^{1.3})^{0.5})$
25	$0.8 + 86/((1 + 38\dot{\gamma}^{1.6})^{0.4})$
30	$0.5 + 55/((1 + 5e31\dot{\gamma}^{18})^{0.03})$
35	$0.4 + 4.4/((1 + 3e4\dot{\gamma}^{5})^{0.1})$

Table 5.1: Viscosities in Pa·s as a function of shear strain rate $\dot{\gamma}$.

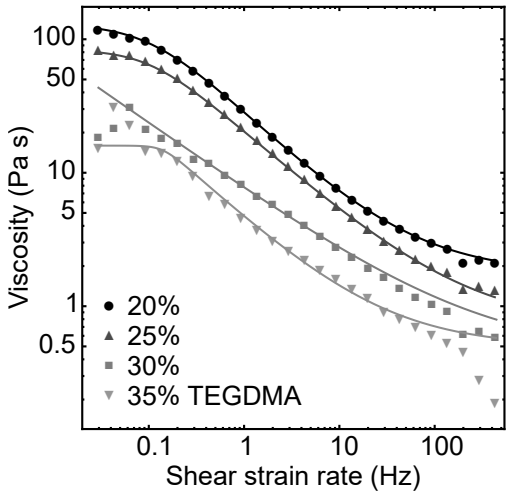

Figure 5.4: Apparent shear viscosity of UDMA/TEGDMA/silica inks, fit to Carreau Yasuda Cross model.

speed (1.5-9.5 mm/s) divided by the stand-off distance (100-250 μm), shear strain rates in this experiment are on the order of 10-100 Hz in the nozzle-substrate gap, where viscosities are on the order of 0.5 to 5 Pa·s. Increasing the TEGDMA loading decreases the viscosity of the ink, as expected. Measured viscosities are in the same range as those used in previous experiments involving direct ink writing with acoustic focusing.[13, 15]

Surface energies measured using pendant drop tensiometry agree with trends reported in the literature. From pendant drop tensiometry, the surface tension decreases with increasing TEGDMA concentration (Table 5.2), which is consistent with previous findings that adding TEGDMA to UDMA decreases the surface tension of the fluid.[201]. A 75:25 UDMA:TEGDMA mixture was reported to have a surface energy of 39.3 mJ/m^2, which is within 1 mJ/m^2 of these 63:12:25 UDMA:silica:TEGDMA ink.[201] The ink-cured ink static contact angle is lower

w% TEGDMA	20	25	30	35
Density (g/cm^3)	1.304 (0.005)	1.265 (0.015)	1.239 (0.005)	1.219 (0.006)
Surface tension (mJ/m^2)	41.24 (0.15)	40.23 (0.15)	37.89 (0.11)	34.48 (0.23)
θ_{static} (°) (cured ink)	48.24 (0.19)	34.57 (0.45)	32.73 (0.52)	32.95 (0.47)
θ_{static} (°) (glass)	55.57 (0.14)	42.90 (0.26)	43.13 (0.15)	41.15 (0.12)
θ_{static} (°) (Si)	42.47 (0.29)	32.16 (0.29)	41.14 (0.18)	43.69 (0.18)
θ_{static} (°) (FDTS)	79.10 (0.24)	71.15 (0.15)	69.12 (0.39)	68.07 (0.44)

Table 5.2: Ink properties. Standard errors are in parentheses. Interfaces not used in this paper are shown in gray.

than the ink-glass contact angle (Table 5.2). Coating the silicon nozzle with FDTS increases the static contact angle (Table 5.2), consistent with previous findings.[200]

5.4.2 Stability

Three issues are pertinent to stability: what is the morphology of stable filaments, when do instabilities initiate, and how can the system recover from temporary instabilities?

Filament stability can be monitored using changes in filament morphology (Fig. 5.6, 5.7, Equation 5.1). Measuring the Laplace pressure differential against the contact line position connects lubrication theory with experiments (Fig. 5.6A). Measuring the contact angle against the contact line position is faster and more reliable because it does not require taking second derivatives of interpolations (Fig. 5.6B). Both relationships exhibit three regimes. In the overflow regime, characterized by fluid pushing well ahead of the channel, the Laplace pressure and contact angle slightly increase as the contact line moves downstream (Fig. 5.6G,H). In the balanced regime, characterized by the fluid front remaining close to the channel, the Laplace pressure differential and contact angle greatly increase as the contact line moves downstream (Fig. 5.6E,F). In the droplet regime, the contact line position, Laplace pressure differential, and contact angle oscillate, and contact lines can advance upstream of the critical contact line position at which instabilities initiate (Fig. 5.6C,D). These regimes illustrate how filament stability and instability initiation vary with experimental parameters.

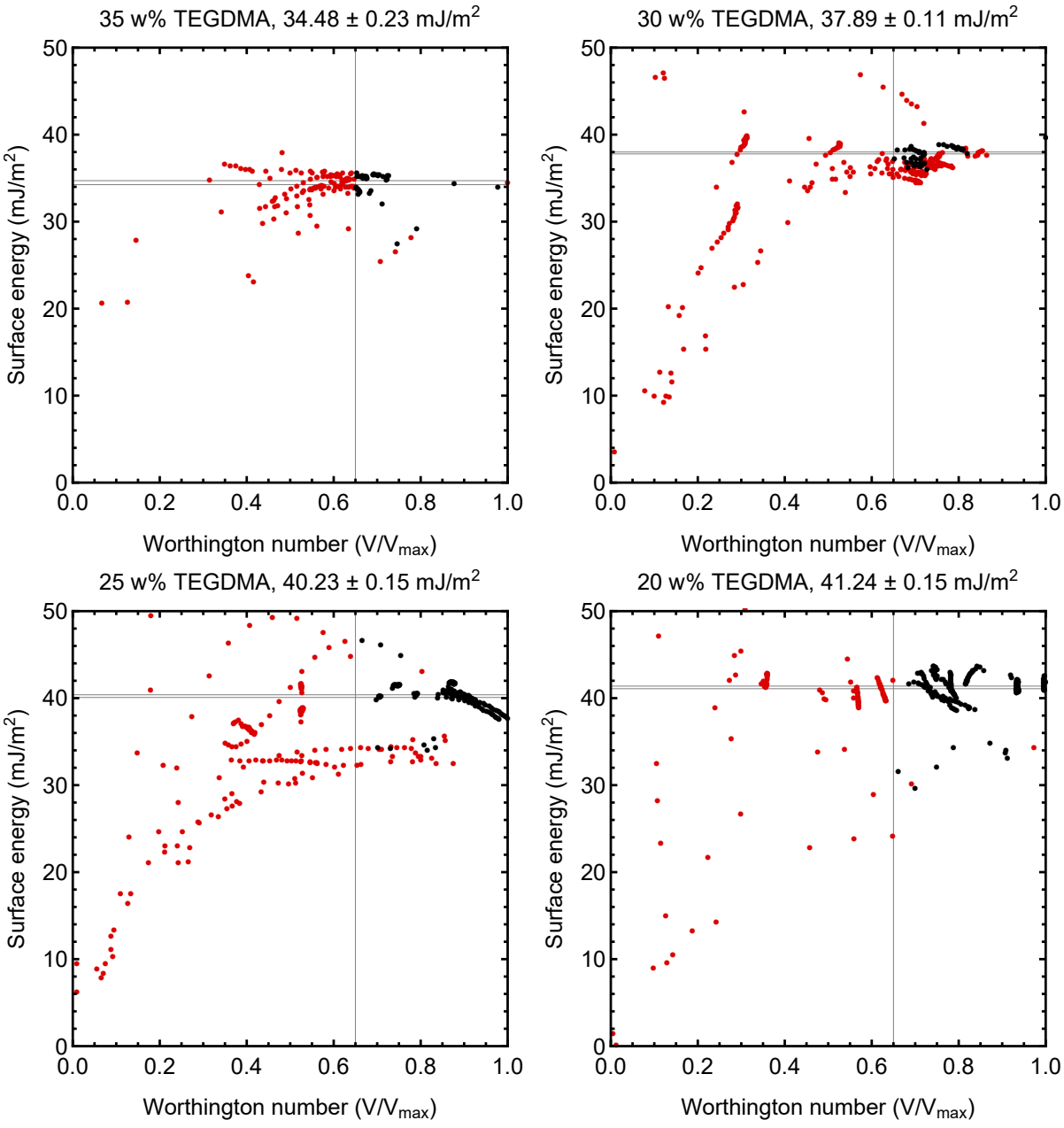

Figure 5.5: Surface energies of inks used, for many frames. Points in red are not included in averages due to low volume or poor fit. Surface energy grid lines indicate the mean ± one standard error.

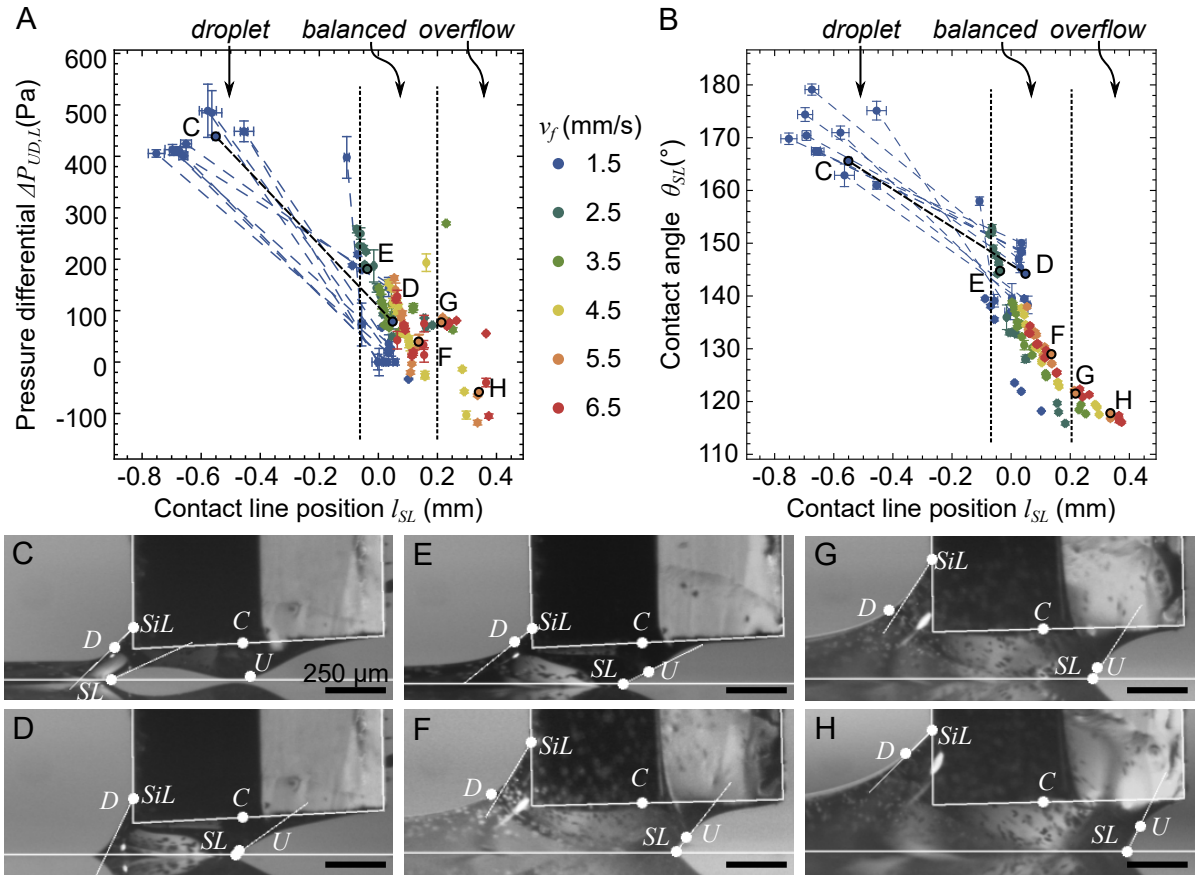

Figure 5.6: A) Laplace pressure differential and B) dynamic contact angle vs. contact line position for 25 w% TEGDMA ink, 150 μm stand-off distance, FDTS-coated nozzle, and film-coated substrate, for varying extrusion and stage speeds. For droplets, peak values of oscillations are represented by two points connected by dashed lines, while filaments are represented by single points. Each point corresponds to one written line. C-H) Example frames, where contact points (SL, SiL), points of maximum curvature (U, D), channel exit (C), and back left corner of nozzle are marked. Nozzles, substrates, and fluid surface tangents are outlined in white.

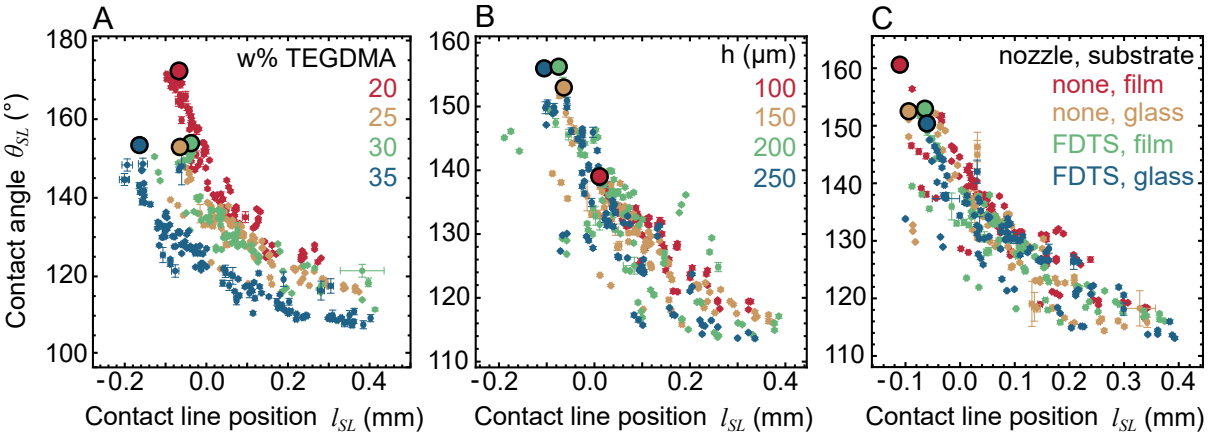

Figure 5.7: Contact angle vs. distance between contact line and channel for varying flow speeds and stage speeds, only for filaments. Points of maximum contact angle are highlighted. Unless otherwise noted, the ink is 25 w% TEGDMA, the stand-off distance is 150 μm, the nozzle is coated with FDTS, and the substrate is coated with a film of cured ink.

Initial printing parameter selection must be informed by the stage speed and flow speed at which instabilities initiate (Fig. 5.8, 5.9, Equation 5.2). For a given ink composition, stand-off distance, and surface conditions, there exists a boundary where ink leaks out of the upstream edge of the nozzle (analogous to dripping in slot die coating) and a boundary where the filament ruptures (analogous to air entrainment in slot die coating). The two-dimensional viscocapillary model predicts these boundaries (Equation 5.2). Comparing the boundaries determined using this two-dimensional model to the boundaries found in this three-dimensional experimental system, the 2D model, despite its approximate nature, informs selection of flow and stage speeds for printing stable filaments near instabilities. Further, oscillation sizes in the droplet regime indicate how experimental parameters influence perturbation recovery.

Filament morphology

Changes in filament morphology indicate filament stability. Both the overflowing and balanced filament regimes are governed by Equation 5.1, where the contact angle decreases with the product of the stage speed and the contact line position. The critical difference between the

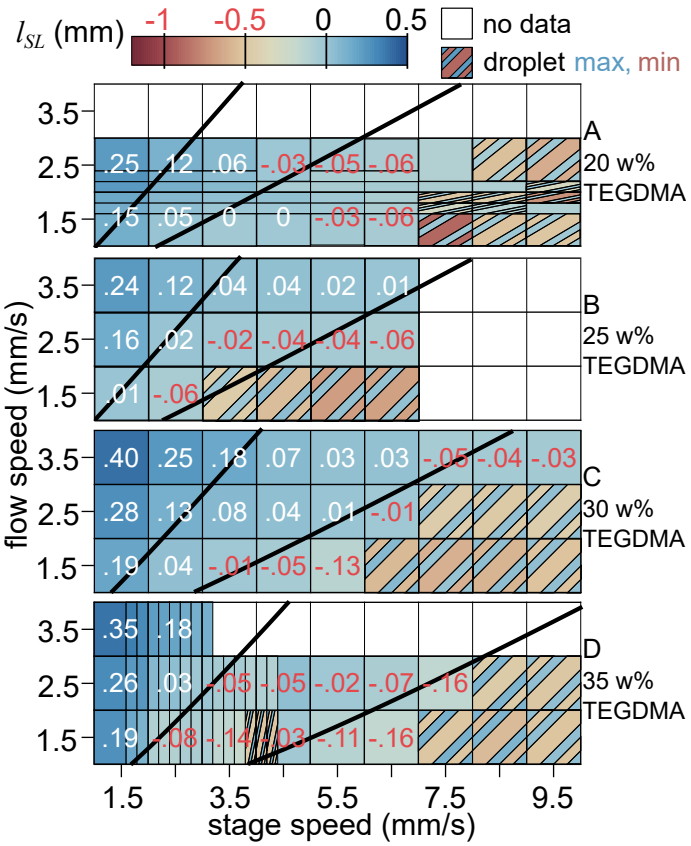

Figure 5.8: Contact line distance l_{SL} as a function of flow and stage speeds. The stand-off distance is 150 μm, the nozzle is coated with FDTS, and the substrate is coated with cured ink. Bold lines indicate predicted instability boundaries from Equation 5.2.

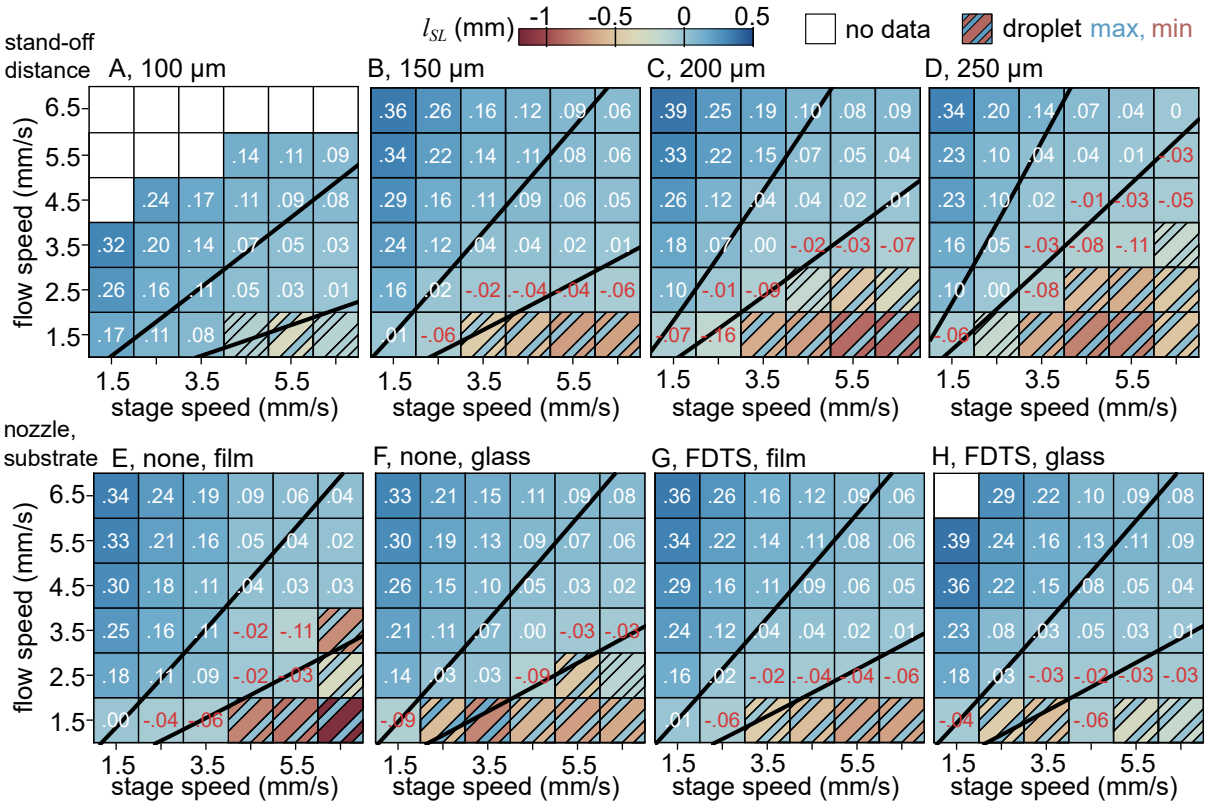

Figure 5.9: Contact line distance l_{SL} as a function of flow and stage speeds. The ink composition is 25 w% TEGDMA, and unless otherwise noted, the stand-off distance is 150 μm, the nozzle is coated with FDTS, and the substrate is coated with cured ink. Bold lines indicate predicted instability boundaries from Equation 5.2.

overflowing and balanced filament regimes is the slope of the θ_{SL} - l_{SL} line. In the overflowing filament regime, large changes in contact line position correlate with small changes in contact angle. In the balanced regime, the reverse is true.

Equation 5.1 predicts how the contact line position changes with printing conditions. Given a contact angle, the contact line moves downstream with an increase in flow speed (Fig. 5.6B), decrease in TEGDMA loading (Fig. 5.7A), or increase in stand-off distance (Fig. 5.7B). Nozzle and substrate coatings have no significant effect on dynamic contact angle (Fig. 5.7C).

Equation 5.2 similarly predicts trends in contact line position with printing conditions. Given a stage speed, the contact line moves downstream with a decrease in flow speed (Fig. 5.8, 5.9) or increase in stand-off distance (Fig. 5.9A-D). Though Equation 5.2 predicts that, at a given a flow speed and stage speed, the contact line should move downstream with decreasing TEGDMA loading, experiments show no significant difference between TEGDMA loadings (Fig. 5.8). Further, at slow stage speeds and fast flow speeds the predicted contact line-channel distances are much higher than observed distances. Specifically, at the upper stability bound where the model predicts that the contact line should be 500 μm ahead of the channel, the contact line is usually around 100 μm ahead of the channel (Fig. 5.8, 5.9). This numerical discrepancy likely derives from the two-dimensional nature of Equation 5.2 and might be corrected in a three-dimensional model.

Instability initiation

Neither the contact position or contact angle is the decisive factor in the formation of an instability. To illustrate this conflict, consider the ink composition. Between 20 and 30 w% TEGDMA, instabilities initiate when the contact line is 100 μm behind the channel, while at 35 w% TEGDMA, at a low viscosity, the contact line can reach 200 μm behind the channel (Fig. 5.7A). However, between 25 and 35 w% TEGDMA instabilities initiate at a contact angle of 155°, whereas at 20 w% TEGDMA, at a high viscosity, instabilities initiate at 175° (Fig. 5.7A,

TEGDMA w%	h (μm)	Nozzle	Substrate	Droplet angle (°)	Overflow angle (°)
20	150	FDTS	film	173	125
25	100	FDTS	film	140	120
25	150	FDTS	film	152	117
25	150	none	film	160	120
25	150	none	glass	155	115
25	150	FDTS	glass	150	115
25	200	FDTS	film	157	115
25	250	FDTS	film	157	115
30	150	FDTS	film	155	120
35	150	FDTS	film	155	110

Table 5.3: Dynamic contact angles used to calculate viscocapillary model boundaries. "h" is the standoff distance. "film" refers to a thin film of cured ink.

Table 5.3). Thus, one cannot conclusively define instability initiation criteria based on a critical pressure differential, a critical meniscus position, or some other metric.

When the stand-off distance is equal to the channel depth and the ink is 25 w% TEGDMA, instabilities initiate when the contact line is 100 μm behind the channel regardless of the nozzle and substrate coatings (Fig. 5.7B). The stand-off distance has little effect on the critical contact position or contact angle when the stand-off distance is equal to or greater than the channel depth (Fig. 5.7B). However, when the stand-off distance is less than the channel depth, instabilities initiate when the contact line is in line with the channel rather than 100 μm behind it, at a contact angle of 140° rather than 155° (Fig. 5.7B). This may be due to the experiment resolution (Fig. 5.9A).

As indicated in Figures 5.8 and 5.9, Equation 5.2 accurately predicts trends in the critical flow speed-stage speed line where instabilities initiate. Above 20 w% TEGDMA, instabilities initiate at a faster flow speed and slower stage speed with decreasing TEGDMA loading (Fig. 5.8B-D) and increasing stand-off distance (Fig. 5.9A-D). At 20 w% TEGDMA, the ink is much more stable than predicted. Equation 5.2 does not adequately take surface coatings into account. Whereas experiments show that coating the nozzle with FDTS improves stability, the model predicts no difference (Fig. 5.9E-H).

Perturbation recovery

The amplitude and direction of fluid movement in the droplet regime can inform perturbation recovery. It is best to print at low flow to stage speed ratios, near the instability point, to limit wetting and rotational flows. If a perturbation pushes the system into the droplet regime, ideally the system should be able to recover quickly and restore the steady-state contact line position. To assess the vulnerability of a system to perturbations, it is useful to consider the amplitude of the contact line position during droplet formation. If the amplitude is large, the oscillations will be more difficult to dampen. Decreasing the TEGDMA loading and increasing the stand-off distance slightly increase the oscillation amplitude at the stability-instability border (Fig. 5.8, 5.9A-D). Printing on glass and coating the nozzle with FDTS greatly decrease oscillation amplitude (Fig. 5.9E-H).

Perturbation recovery is related to the kinetics of droplet formation. The Laplace pressure differential, contact angle, and contact line are linked but not synchronized (Fig. 5.10). At the moment that a new contact line forms, the upstream Laplace pressure and contact angle sharply drop. In the time until the formation of a new contact line, the contact angle increases, peaks at the onset of local variations in curvature on the upstream meniscus, then decreases as the neck elongates. Meanwhile, the Laplace pressure differential decreases as the downstream Laplace pressure increases until the neck ruptures, then increases with the upstream Laplace pressure as the new neck elongates. Still, the three metrics are connected by fluid movement in the neck. Contact formation facilitates neck formation because it draws fluid upstream, and neck elongation facilitates contact formation because it siphons fluid upstream.

5.4.3 Wetting

The importance of printing at the precipice of instability is obvious when considering the influence of the flow and stage speeds on wetting of the nozzle. The upward climb of fluid

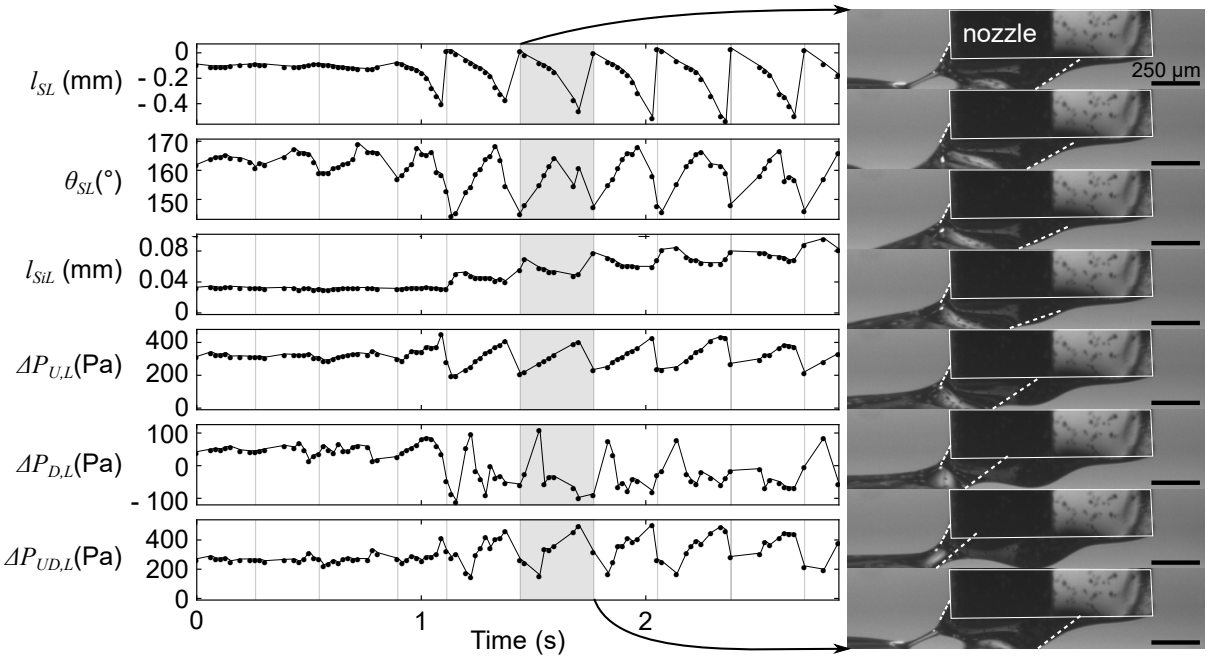

Figure 5.10: Contact line position, dynamic contact angle, wetting length, upstream Laplace pressure, downstream Laplace pressure, and Laplace pressure differential vs. time for 25 w% TEGDMA ink, 150 μm stand-off distance, FDTS-coated nozzle, and film-coated substrate, printing at a flow speed of 1.5 mm/s and a stage speed of 5.5 mm/s. Due to transients, initially a filament is extruded, but at 1.2s, the filament breaks into droplets. Grid lines indicate formation of new contact lines. Right: Frames over the formation of one droplet. Dashed white lines indicate position and angle of nozzle and substrate contact lines. Nozzle is outlined in white.

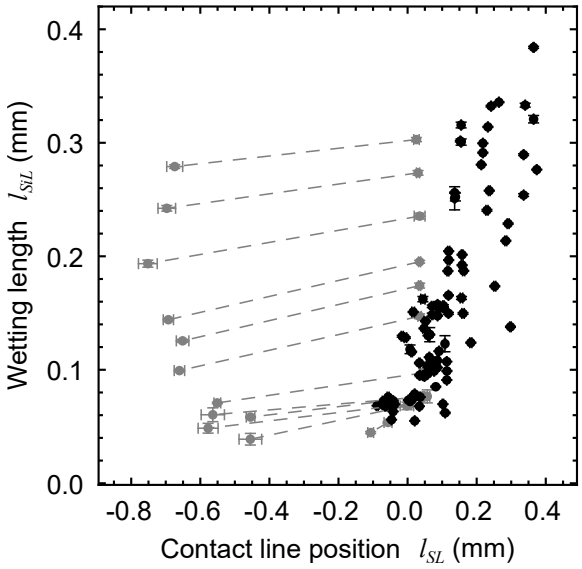

Figure 5.11: Nozzle wetting length vs. contact line position for varying flow speeds and stage speeds. The stand-off distance was 150 μm, the ink was 25 w% TEGDMA, the nozzle was coated with FDTS, and the substrate was coated with cured ink. Filaments are shown as single points, while maximum and minimum values for droplets are connected by a dashed line.

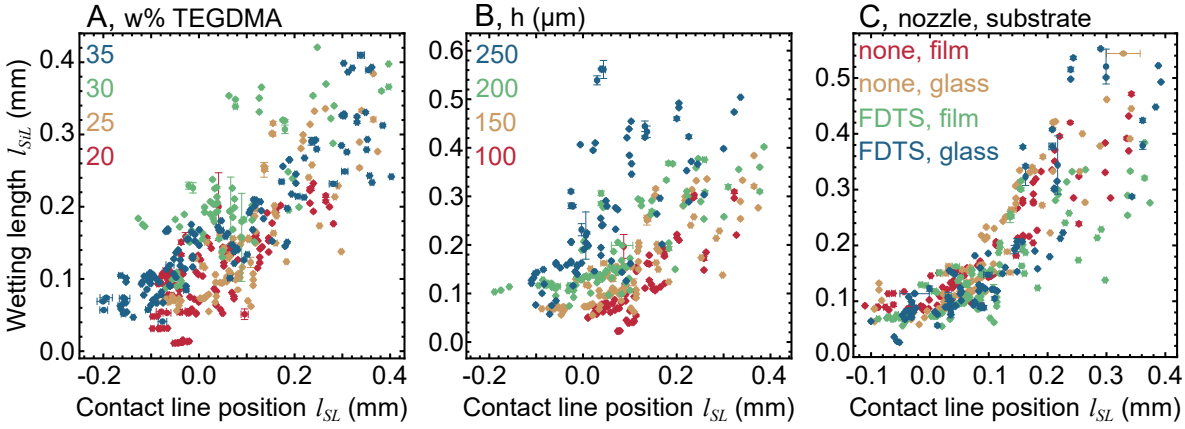

Figure 5.12: Nozzle wetting length vs. distance between contact line and channel for varying flow speeds and stage speeds, only for filaments. Unless otherwise noted, the stand-off distance was 150 μm, the ink was 25 w% TEGDMA, the nozzle was coated with FDTS, and the substrate was coated with cured ink.

onto the downstream end of the nozzle, or the wetting length l_{SiL} was measured using digital image analysis. The wetting length decreases as the upstream contact line moves downstream, but at the onset of instabilities, the wetting length dramatically increases (Fig. 5.11). This pattern is also present in the progression of wetting length over time. During the formation of each droplet, the wetting length decreases, but when the filament ruptures, the wetting length jumps higher than its initial position (Fig. 5.10). Increasing the TEGDMA w% in the fluid, i.e. decreasing the viscosity and surface tension, does not have a large effect on the wetting length (Fig. 5.12A). More significantly, increasing the stand-off distance dramatically increases the wetting length (Fig. 5.12B). Intuitively, coating the nozzle with FDTS slightly decreases the wetting length for a given contact line distance (Fig. 5.12C).

5.4.4 Rotational flows

Rotational flows disrupt microstructures established inside the nozzle, so the transverse (y) component of the fluid velocity should be minimized. Particles exhibit maximal transverse velocities directly downstream of the nozzle (Fig. 5.13A-C). Suitably adjusting printing parameters can reduce the size of rotational flows in this region. As the contact line moves upstream, the fluid transverse velocity increases (Fig. 5.13D,E). When the contact line is far ahead of the channel, the transverse velocity increases with decreasing TEGDMA loading, i.e. increasing viscosity (Fig. 5.13D). Near instabilities, there is no significant difference between TEGDMA loadings. Further, as the stand-off distance increases, the transverse velocity increases (Fig. 5.13E). Nozzle and substrate coatings show no significant effects on transverse displacement.

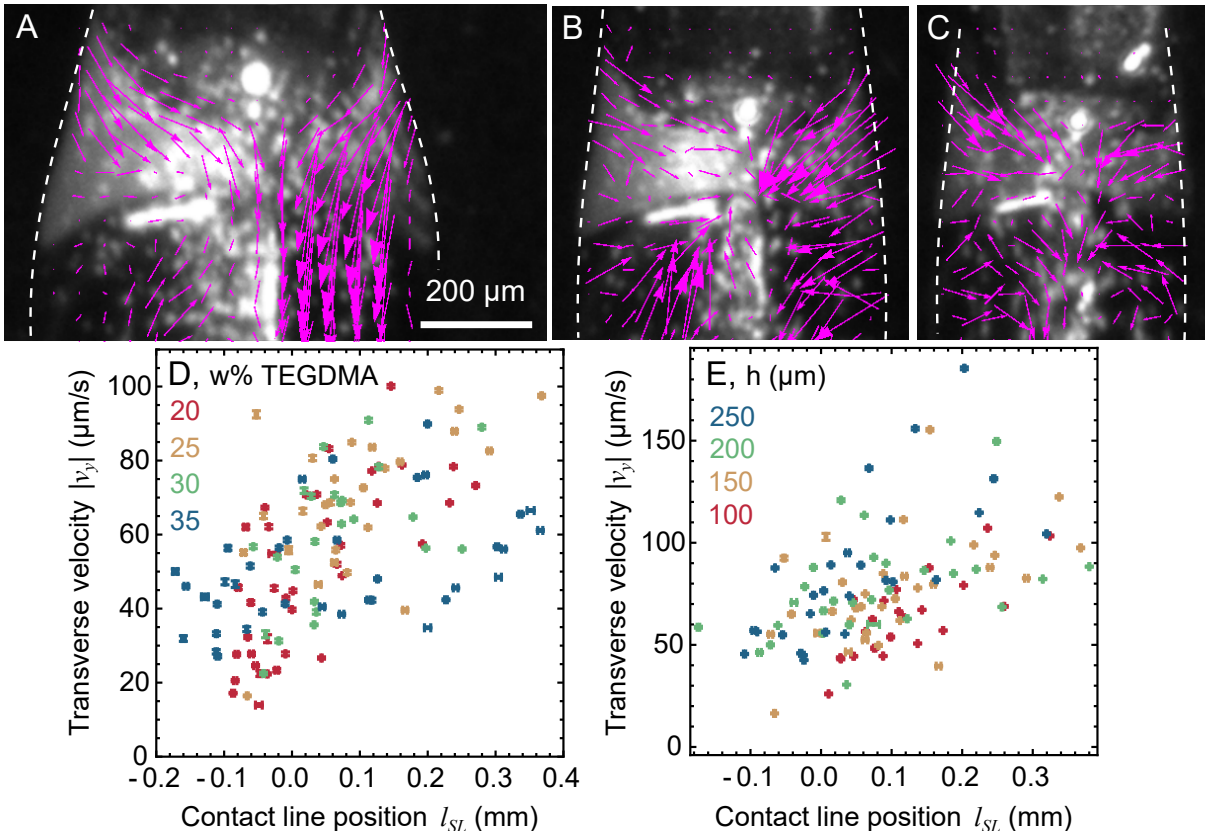

Figure 5.13: A-C) Particle displacements across 30-frame videos, plotted over the first frame of the set for 25 w% TEGDMA, h = 150μm, no nozzle coating, no substrate coating, and v_f = 4.5 mm/s. Scale bar corresponds to 200 μm. Backwards-oriented vectors in fast-moving fluid are likely a frame rate artifact. A) v_s = 1.5 mm/s, $|v_y|$ = 0.103 mm/s. B) v_s = 2.5 mm/s, $|v_y|$ = 0.092 mm/s. C) v_s = 3.5 mm/s, $|v_y|$ = 0.073 mm/s. White dashed lines indicate filament edges. D, E) Mean absolute displacements of particles in the y-direction across the filament, directly downstream of the nozzle. Unless otherwise noted, the TEGDMA loading is 25 w%, the stand-off distance is 150 μm, the nozzle is coated with FDTS, and the substrate is coated with cured ink.

5.5 Discussion

5.5.1 Stability

Designation of three printing regimes is useful for *in-situ* adjustment of printing parameters and could potentially also be used in slot die and curtain coating. Though the regimes have been morphologically described for slot die and curtain coating,[130] measuring changes in contact line position and angle may be a useful addition to process monitoring. Across DIW, slot die coating, and curtain coating, the contact line position changes less than the contact angle as the system approaches instabilities.[107, 202, 203] *In-situ* measurement systems could enable increases in the flow speed, decreases in the stage speed, or increases in the stand-off distance if oscillations in contact angle become much larger than oscillations in contact line position. Because the flow speed, stage speed, contact line position, and contact angle at which instabilities initiate varies between experimental conditions, relative changes remain the most reliable and universal metric for stability.

Though the 2D viscocapillary model can inform parameter selection, it should not be used as a predictor of contact line position because it is limited to two dimensions and assumes that ink is pinned at the nozzle corner, leading to overestimation of the contact line position. In 2D, excess fluid can only be diverted to the front lip of the nozzle. In 3D, that ink can instead travel outwards and up the sides of the nozzle. This means that in DIW, ink is less likely to collect on the front of the nozzle. However, it also means that the printed line width varies with flow speed and stage speed. Further, Equation 5.2 assumes that the downstream contact line is pinned at the bottom of the nozzle, so excess fluid can only be diverted upstream. Because the inks wet the nozzles used in this experiment, excess fluid can be diverted both upstream and up the back of the nozzle. Despite these gaps in the model, the agreement between lubrication theory and experiments on trends in printing parameter effects indicates that the model can be used to inform printing parameter selection. Numerical models of DIW with cylindrical

nozzles indicate that the critical flow speed for instability decreases as the stand-off distance increases, which is qualitatively consistent with these findings.[105, 107]

Perturbation recovery is governed by the kinetic and surface energy of fluid necks. One can conceptualize the transition between droplets and stable filaments as an energy barrier. Oscillation size in the droplet region is indicative of the energy barrier size in both regions because it is influenced by kinetics. Ruptured necks that recoil quickly or upwards cause ink to climb the back of the nozzle, drawing fluid away from the filament and increasing the energy barrier. Longer necks recoil faster, so larger oscillations are indicative of larger energy barriers. Low TEGDMA loadings have larger oscillations because more viscous dissipation produces longer necks.[204, 205, 206, 207] Larger stand-off distances increase the angle between the neck and the substrate, so ruptured filaments recoil upwards above the new filament. Allowing the ink to wet the nozzle and substrate draws fluid away from the neck, preventing perturbation recovery.

5.5.2 Wetting

To limit wetting, it is necessary to print near the precipice of instability. The wetting length decreases as the contact line moves backward because as the Laplace pressure differential increases, fluid is drawn away from the nozzle toward the point of minimum curvature on the downstream meniscus, which is at the lowest Laplace pressure. During filament formation, this point is between the nozzle and the point where the filament flattens out. At rupture, the loose end recoils toward the nozzle. As such, droplet formation is damaging not just to the morphology of the print at the onset of the instability; it is also damaging for the rest of the print, because it leaves excess fluid on the surface of the nozzle which may cure and scrape through deposited lines or build up and suddenly deposit during writing.

Coating the nozzle with FDTS decreases the wetting length because wetting becomes less

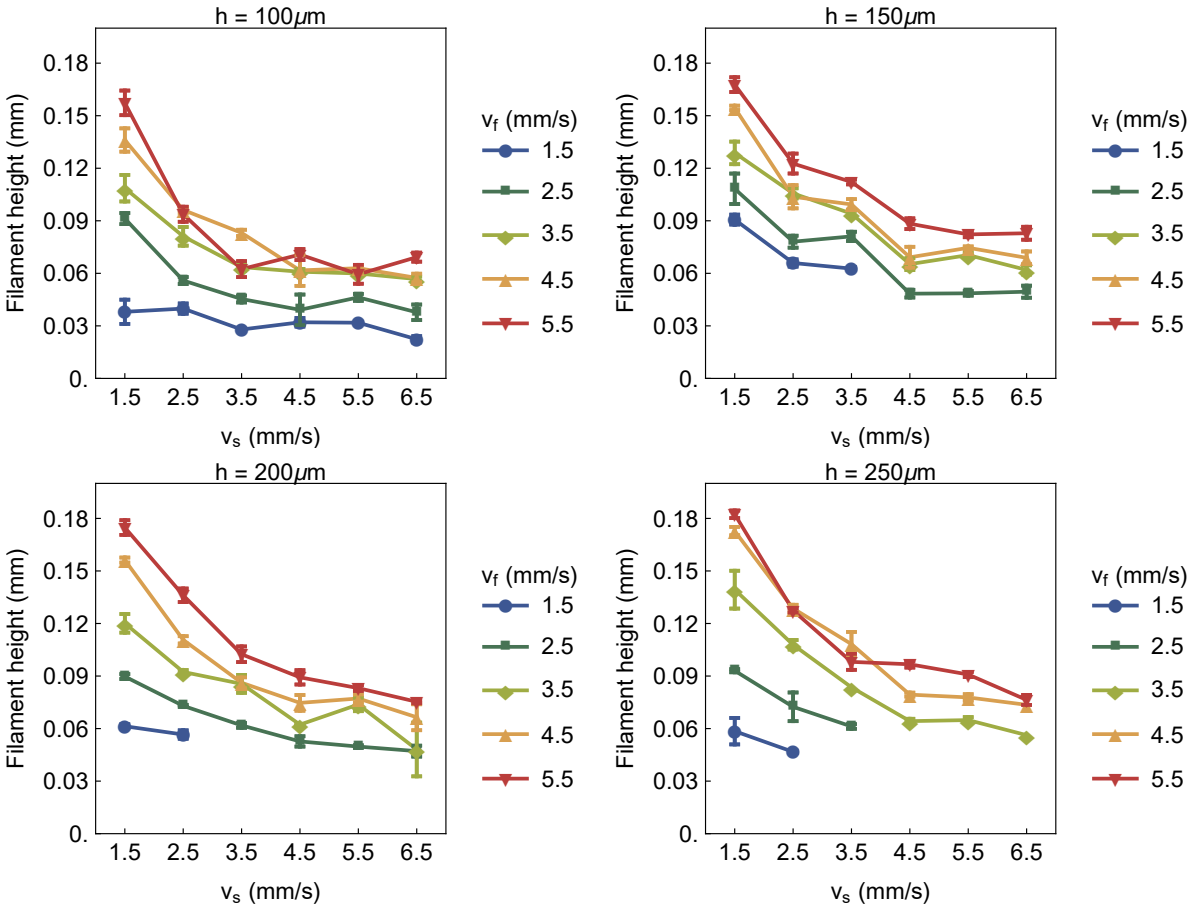

Figure 5.14: Filament heights as a function of stage speed v_s and flow speed v_f for varying stand-off distances.

energetically favorable when the surface energy of the nozzle is low. Likewise, the dependence of wetting length on ink composition may be explained by contact angles. The ink-FDTS static contact angle decreases with increasing TEGDMA loading, so wetting should be more energetically favorable at higher TEGDMA loadings.

The increase in wetting length with stand-off distance is counter-intuitive but may be correlated with the height of the filament in the z-dimension (Fig. 5.14). The height of the deposited filament increases with increasing stand-off distance, but causation is unclear. First, consider the possibility that the taller filament height causes more wetting. Envision the nozzle as a parallel plate that pushes downward on the filament, spreading it out in the y-direction. Larger

stand-off distances push on the filament less, bringing the contact lines inward in the y-direction and producing taller filaments. As a result, the taller height pushes the wetting line upward. In numerical models of DIW without nozzle wetting, the width of the deposited filament decreases with increasing stand-off distance, lending some credence to this mechanism.[107] Alternatively, consider the possibility that greater wetting increases the filament height. Envision the nozzle as an orthogonal plate that pulls upward on the filament. Larger stand-off distances produce longer wetting lengths, possibly because of transients. Namely, when the stand-off distance is taller, it takes longer for the initial droplet to hit the substrate, so fluid climbs higher on the nozzle before a filament is extruded. Even after the fluid establishes contact with the substrate and fluid is pulled away from the wetting line, a thin layer of ink remains, making wetting more energetically favorable. Those larger wetting lengths added to larger stand-off distances would produce taller filament heights. As a third alternative, there could be no causation at all between longer wetting lengths and taller filaments, as both could stem directly from stand-off distance.

5.5.3 Rotational flows

Assume, for a moment, that at a certain flow to stage speed ratio, a "perfect filament" in the gap between the nozzle and the substrate will fill an area exactly the width of the nozzle. No ink climbs onto the sides of the nozzle. Now, imagine a slight increase to the flow speed, which will produce excess ink. That excess ink will need to go somewhere: the fluid menisci on the sides of the filament will bulge outwards, and fluid will climb the sides of the nozzle and flow around the nozzle, disrupting flow within the "perfect filament." Though experiments demonstrated no instance of "perfect filament," this thought experiment mirrors these results. As the flow to stage speed ratio increases, and more excess fluid is produced, the transverse velocity of fluid increases, especially right behind the nozzle, since shear rates are greatest

near the deposition zone.[107] This technique measures the influence of this excess fluid on maintenance of microstructures established in the nozzle. Though insightful, this method is not an all-encompassing way to identify microstructure disruption. It does not identify what happens near the substrate, where excess ink that is pushed ahead of the nozzle may diverge outward. The increase in transverse velocity with viscosity may occur because the zone behind the nozzle where ink flows across the filament may become larger with less viscous dissipation.

5.6 Conclusions

The prediction that slot die coating models can be transferred to low-viscosity DIW for processing parameter selection has been borne out by *in-situ* characterization of the nozzle-substrate gap, and digital image analysis methods can be used to identify incipient changes in printing modality. Previous numerical and experimental analyses have described filament morphology given a set of processing conditions.[105, 107, 110] This study introduces an analytical model that describes both morphology of both filaments and droplets, allowing for quick selection of initial processing parameters and *in-situ* monitoring of stability. Further, previous DIW models assume no wetting.[105, 107, 110] This study provides new insight into the sources and consequences of wetting, as well as a computational framework to monitor it during printing. Additionally, though some experimental studies have used printed parts to investigate how intra-nozzle positioning methods and the nozzle-substrate gap influence filament microstructure,[61, 77, 196] this work presents a way to monitor rotational flows in the filament during printing. These experiments demonstrate the following principles for low viscosity direct ink writing:

- To limit nozzle wetting and rotational flows, use a low flow to stage speed ratio, even though this introduces a risk of instabilities.

- To rapidly and reliably monitor filament stability, measure the rate of change of the contact line position relative to the contact angle.

- To predict trends in contact angle and critical stage speed with viscosity, stand-off distance, and flow speed, use 2D lubrication theory with contact angle as a proxy for Laplace pressure differential, similar to slot die coating.[130, 131]

- To predict the onset of instabilities, one cannot assume a single contact line position, pressure differential, or contact angle for all experimental conditions, contrary to guidelines used in slot die coating.[130, 131]

- To transition from printing droplets to continuous filaments, leverage both energetics and kinetics. Long, upward-tilted, and surface-wetting necks inhibit perturbation recovery.

Adjusting printing parameters can achieve three objectives important to low viscosity direct ink writing: establishing and maintaining continuous filaments, limiting nozzle wetting, and limiting rotational flows. Low flow to stage speed ratios maintain microstructures established inside the nozzle and limit nozzle wetting, but they increase the risk of droplet formation. Inks with low viscosities and surface energies are beneficial for stability, perturbation recovery, and microstructure preservation. This is especially good news, since the contrast in material properties achievable using acoustic focusing increases as the ink viscosity decreases. Inks with high viscosities and surface energies are better for limiting wetting. Though this does present a trade-off, the importance of filament stability, microstructure preservation, and acoustic focusing contrast is greater than the importance of nozzle wetting. Small stand-off distances are beneficial for all objectives considered in this paper, although at very small stand-off distances, ink can be pushed upwards onto the nozzle and contact line positions can change quickly. It is best to print at a stand-off distance close to the channel depth. Lowering the nozzle surface energy improves stability and perturbation recovery and limits nozzle wetting, so it is useful

to coat silicon and glass nozzles with FDTS. Printing on a poorly wetting surface improves perturbation recovery. However, printing on cured ink is unavoidable, since all layers beyond the first layer are printed on cured ink.

Opportunities remain for a more generalized application of lubrication theory to DIW. For more numerical accuracy in prediction of the upstream meniscus position, future models could incorporate wetting on the downstream and side edges of the nozzle. Additional models and experimental studies could address pyramidal, cylindrical, conical, or rounded nozzles, as have been studied for slot die coating.[208, 209]

Chapter 6

Interactions with support and existing filaments: transverse flows

6.1 Introduction

Direct ink writing of polymer matrix composites allows for tailored structural and functional gradients in 3D printed parts through external fields that align and redistribute particles. Several techniques have been used to manipulate second phases within printed lines, including hydrodynamic alignment,[61, 64, 74, 196] nozzle rotation,[77] and magnetic fields.[40, 210] Acoustic fields have been used to manipulate ceramic, metallic, and polymer microparticles as well as living cells.[9, 13, 14, 15, 16, 21, 22] Direct ink writing with acoustophoresis (also known as acoustic focusing) works by establishing a bulk standing acoustic wave in a print nozzle using a piezoelectric actuator, as shown in Fig. 6.1. Particles align and move toward the nodes or antinodes of the wave, depending on the densities and compressibilities of the particles and the fluid.[13]

In low-viscosity inks, acoustophoresis can achieve sharp transitions between the unfocused and focused state leading to abrupt changes in microstructure.[15, 16] These changes in mi-

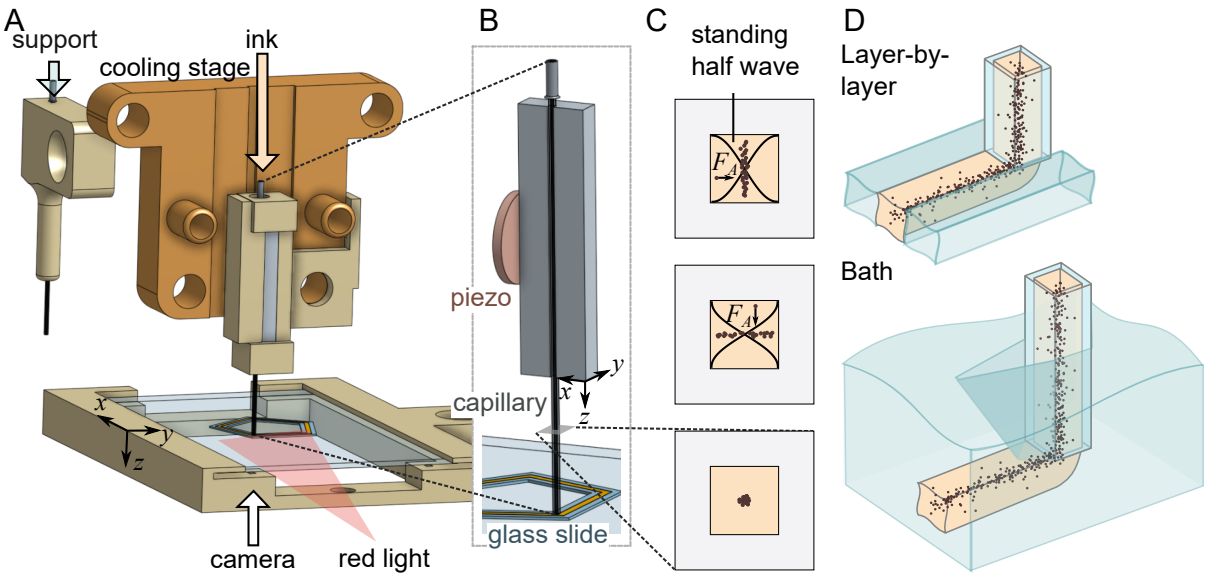

Figure 6.1: A) Using layer-by-layer support, the stage travels between support and ink nozzles while videos are collected from underneath the ink nozzle. x, y, and z refer to G-code coordinates. B) Ink is extruded onto a glass slide through a glass capillary seated in a stainless steel block attached to a piezo. C) Two standing half-waves in the x and y directions drive particles with acoustic force F_A toward the center of the channel. D) Layer-by-layer and bath support.

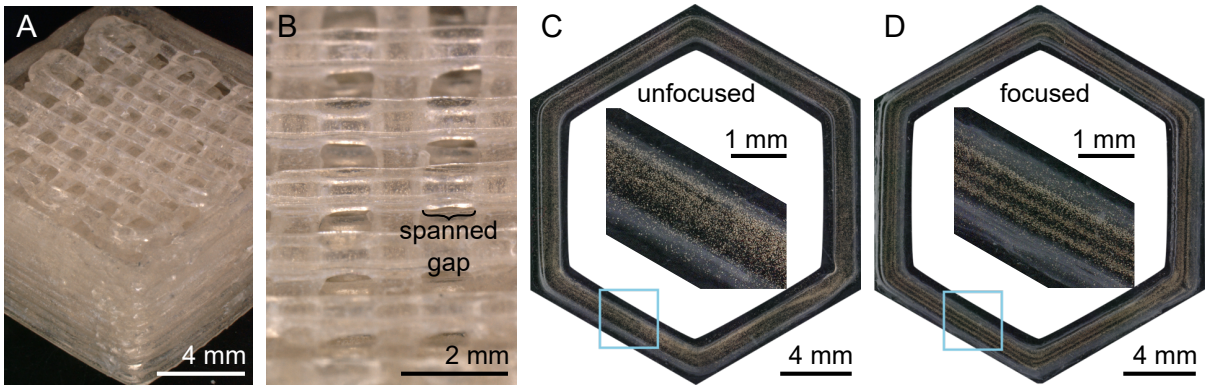

Figure 6.2: A,B) Lattice with spanning segments printed using layer-by-layer Carbopol support and layer-by-layer light curing. C,D) Single layer hexagons printed with and without acoustic focusing.

crostructure can influence properties like electrical conductivity and stiffness.[9, 13] Many biologically relevant inks have low viscosities and are well-suited to acoustic manipulation of suspended cells, which can aid cell viability and tissue formation.[22, 99, 211] To print three-dimensional structures with spanning segments like those in Fig. 6.2A and B, one can utilize a removable support material. The support material used in this study is Carbopol, which is a water-based yield stress fluid that can be removed from the printed part through dissolution in buffer or rinsing in water.[118] There are two common ways to utilize support material in an extrusion-based printing process (Fig. 6.1D). Layer-by-layer support, where support and ink layers are written alternately, is common in commercial inkjet printers. Bath support, where a submerged nozzle extrudes ink into a self-healing bath, is often used for biomaterials.[97, 99, 100, 118, 120, 212]

Because of decreased viscous dissipation, the structure of moderate viscosity filaments is impacted by competing driving forces and geometric constraints including support viscoplasticity (plastic flow), inertial flows (flow in disturbed zone), interfacial energy (capillary spreading), and gravity (gravity spreading). These effects act differently in regions ahead of, to the sides of, and behind the nozzle and manifest on different time scales. Toward that end, this chapter presents a comprehensive study of direct ink writing with acoustic focusing that addresses two questions. (1) Which features of the flow field and particle distributions are most strongly impacted by these driving forces? (2) How do these driving forces interact?

This work employs two types of video analysis to measure changes in the printed line microstructure during printing and identify sources of those changes. Particle image velocimetry (PIV) is used to track fluid flow fields within newly and previously deposited ink lines. Within ten interrogation regions, the average component of the flow velocity transverse to the printing direction is extracted. One can reasonably expect that changes in particle distributions are dominated by flows transverse to the printing direction. Digital image analysis is used to track the position and width of the particle distribution at three points in the printing process. The

particle distribution can change in the liquid bridge between the nozzle and substrate,[128] so it is useful to measure the distribution just after deposition. Distributions can change over time after deposition, so it is useful to measure the distribution after the printed line has time to relax. Finally, when the nozzle returns to write a neighboring line, the nozzle and extruded fluid can shear existing lines, so it is useful to measure the distribution after shear. By tracking the particle distribution over the course of the print, one can identify optimal places to implement in-situ curing, e.g. just after deposition, some time after deposition, or after the entire layer is printed.

In this study, single layer, three pass polygons are printed, where spherical particles are acoustically focused into the center of each filament (Fig. 6.2C,D). Lines are printed from inward to outward, relative to the center of the polygon. In this paper "inward" refers to both the inner edge of the polygon and existing printed lines, and "outward" refers to the outer edge. Each pass probes a different boundary condition, as shown in Fig. 6.4–6.6. In layer-by-layer support, the first pass is bordered by support and air, the second has ink and air, and the third has ink and support. In bath support, the first pass has support on both sides, and the second and third pass have support on one side and ink on the other. By examining differences in the particle distribution, flow field, and correlations therein between layer-by-layer and bath support, this work identifies the critical driving forces involved in each support geometry and highlight the advantages and disadvantages of each approach.

6.2 Hypotheses

This section describes four sources of transverse flows and changes in the particle distribution: viscoplasticity-derived plastic flow, inertial disturbed zone flows, capillary spreading, and gravity spreading. Additionally, after deposition, particles can settle within the filament due to gravity, changing the particle distribution width. Effects of settling are not apparent in

Table 6.1: Critical Oldroyd numbers Od (viscoplasticity), Reynolds numbers Re (inertia), and capillary lengths (capillarity, gravity) for fluids studied in this experiment. Minimum probed Od and Re numbers are provided in the supplemental information.

	Carbopol 1.2 w%	20 w% TEGDMA	25 w% TEGDMA	30 w% TEGDMA	35 w% TEGDMA
Max Od	2.0×10^{-1}	6.9×10^{-4}	9.6×10^{-4}	1.5×10^{-3}	2.0×10^{-3}
Max Re	3.1×10^{-3}	1.3×10^{-2}	1.8×10^{-2}	2.7×10^{-2}	3.7×10^{-2}
Capillary length (mm)	2.28	1.81	1.78	1.76	1.63

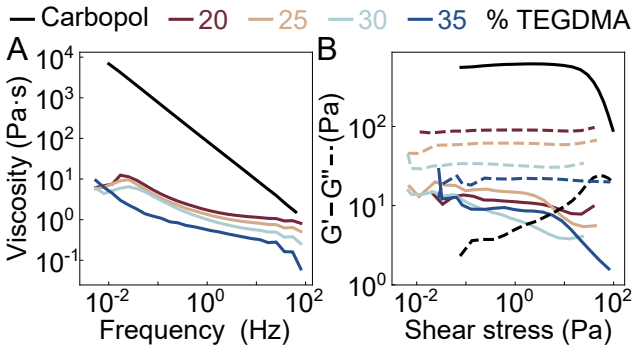

Figure 6.3: A) Viscosity as a function of frequency and B) Storage modulus (solid) and loss modulus (dashed) as a function of shear stress for Carbopol support and inks with varying w% TEGDMA. Carbopol stresses in (A) range from 40-60 Pa, indicating that the Carbopol has yielded during the test.

the experimental data. A more detailed treatment of settling that supports this conclusion is included in the supplemental information.

6.2.1 Plastic flow zone

Ink and support material in the neighborhood of the nozzle flow in response to the relative movement of the nozzle and stage. These materials can behave as fluids, where inertia is dominant, or they can behave as solids, where viscoplasticity is dominant. Oldroyd and Reynolds numbers are conventionally used to determine which flows are impacted by viscoplasticity and which are impacted by inertia.

First, rheology can be used to determine Oldroyd numbers, which indicate the importance

of viscoplasticity. Shear stress - modulus measurements (Figure 6.3B) can be used to determine the yield stresses (τ_y) of the fluids. There are multiple ways to define yield stress;[100] here, the yield stress is defined as the point where the storage modulus (G') transitions from a constant value to a decreasing value as a function of stress (τ). For the Carbopol support, the yield stress is 10 Pa. The inks have non-constant G' values beginning at a stress below 10^{-2} Pa, so the yield stress is defined here as 10^{-2} Pa to indicate that elastic behavior is negligible in the UDMA-based inks. The Herschel Bulkley model is used to fit shear strain rate ($\dot{\gamma}$) - shear stress (τ) curves:[100]

$$\tau = (K|\dot{\gamma}^{n-1}| + \tau_y/\dot{\gamma})\dot{\gamma} \tag{6.1}$$

where K is the consistency index and n is the dimensionless flow index. The Oldroyd number is

$$Od = \frac{\tau_y d^n}{KU^n} \tag{6.2}$$

where d is the outer diameter of the nozzle (0.6 mm) and U is the translation speed of the nozzle (3–12 mm/s). The Oldroyd numbers for the Carbopol support are on the order of 10^{-1}, so the support behaves as a viscoplastic liquid-like solid (Table 6.1). Oldroyd numbers for the inks are on the order of 10^{-3}, so they do not behave viscoplastically.

During bath printing, the nozzle creates a crevice in the support bath along the print path. This crevice closes when the hydrostatic stress at the bottom of the crevice exceeds the viscous stress induced by nozzle translation, $U\mu/(d\rho gh) < 1$, where μ is the support viscosity, ρ is the support density, g is acceleration due to gravity, and h is the crevice depth.[99] From printing parameters used in this study, crevice refilling occurs at a depth of 9.4 mm. Because hydrostatic pressure in deep baths can change ink flow rates, these experiments use a very shallow support bath (1 mm) to enable direct comparisons between bath and layer-by-layer

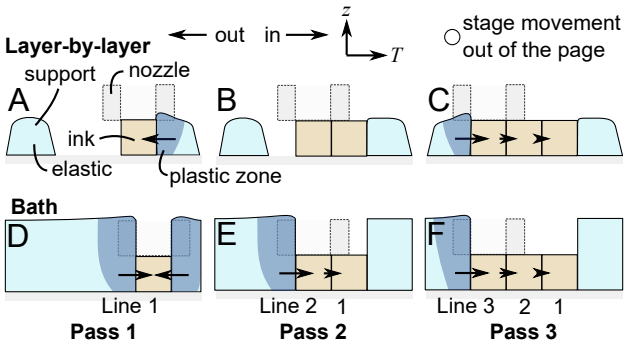

Figure 6.4: Proposed effect of plastic flow on printed lines, viewed from a cross-section of the printed lines. The plastic zone consists of viscoplastic liquid support and flows into the less viscous ink.

support. As such, there is no crevice refilling, so the ink is not constrained by the material above the tip of the nozzle during the printing process. Thus, because of the deformations inherent to bath printing[99] exacerbated by a lack of vertical constraint, the ink filaments can deform after printing.

In an ideal support bath, the plastic zone around the deposited filament, where the nozzle causes the support to yield, would re-solidify as a square crevice, matching the designed print path. However, it is reasonable to expect that just after deposition, the yielded support plastic zone spreads due to gravity (Fig. 6.4). The path of least resistance for this spreading is into the just-deposited ink filament. Flow of this viscous support fluid would cause the written ink lines to expand in z and compress in the transverse direction T, which has been reported in bath support before, even with crevice refilling.[99] Here, gravity is opposed by viscous dissipation, such that the more viscous material decreases in gravitational potential energy, and the less viscous material increases its gravitational potential energy. As a result, the particle distribution would narrow and shift during flow of the support plastic zone, depending on boundary conditions.

Because the flowing support interacts with flowing ink, support plastic flow should influence the ink flow field behind the nozzle, affecting the initial particle distribution in the deposited filament, and changing the particle distribution during subsequent relaxation. In

layer-by-layer support, plastic flow will cause outward flows in the deposited line in the first pass, no net flows in the second pass, and inward flows in all lines in the third pass. In bath support, plastic flow will cause no net flow in the first pass. Because only the outer support wall is compressed during printing of the second and third pass due to lack of reflow, unloading will produce inward flows in all lines in the second and third pass.

6.2.2 Flow in disturbed zone

Reynolds numbers can be used to determine if inertial flows are significant. For a Herschel-Bulkley fluid, the Reynolds number of fluid flows around a cylinder is defined in Equation 6.3.[100]

$$Re = \frac{\rho d^n U^{2-n}}{K} \tag{6.3}$$

Reynolds numbers for the Carbopol support are on the order of 10^{-4} to 10^{-3}, while Reynolds numbers for the inks are on the order of 10^{-3} to 10^{-2} (Table 6.1). These low Reynolds numbers indicate that turbulence is unlikely, but a small inertial influence near the nozzle is possible. Even in viscoplastic materials with Reynolds numbers on the order of 10^{-5} to 10^{-4}, disturbed zones with dimensions on the order of one nozzle radius have been detected, with implications for geometric printing fidelity.[100] Thus, there will likely be a disturbed zone within the deposited ink filament, any excess ink in front of and to the sides of the nozzle, and existing ink filaments. Because the support material has very low Reynolds numbers, there will also likely be a very small disturbed zone within the support material.

Movement of the stage relative to the nozzle produces a disturbed zone in the fluid surrounding the nozzle including within newly deposited ink, within existing deposited filaments, and within yielded support material (Fig. 6.5A). Within this disturbed zone, transverse flows will be present.[213, 214, 215, 216] Consider Figure 6.5G. Inertial transverse flows will be

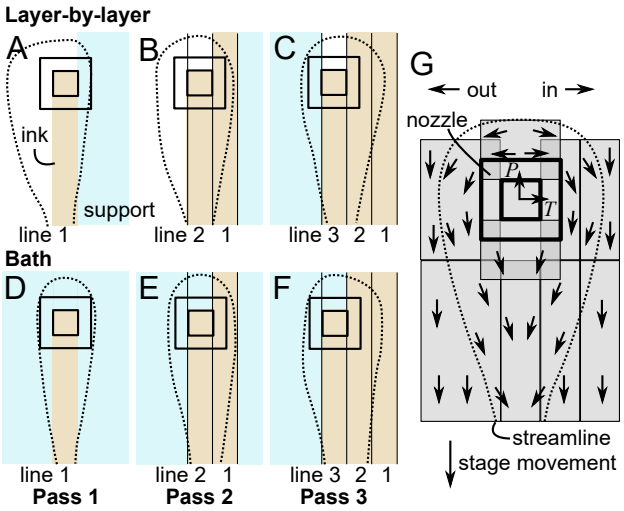

Figure 6.5: Schematic of disturbed zone streamlines, viewed from below the nozzle. A–F) Varying boundary conditions produce changes in the flow field. G) The disturbed zone produces average transverse flows across interrogation regions.

away from the print path ahead of the nozzle and toward the print path behind the nozzle.[216] The disturbed zone is elongated behind the nozzle, such that flows away from the print path are strong and compressed into a small region ahead of the nozzle, but flows toward the print path are weak and extend across a large region behind the nozzle. The asymmetry of the disturbed zone within the nearest neighbor and second nearest neighbor lines should cause the neighboring particle distributions to narrow and shift away from the nozzle.

The composition of the region near the nozzle should influence the disturbed zone shape (Fig. 6.5). Experimental studies of yield stress fluids show that increasing the Oldroyd number decreases the disturbed zone size,[99, 100] so one can expect a larger disturbed zone in ink than in support.

6.2.3 Spreading

The inks used in this study are less viscous than conventional unsupported direct write inks. As such, it is reasonable to expect them to spread onto the substrate after deposition. There are two possible sources of spreading: capillarity and gravity. These effects are shown schemati-

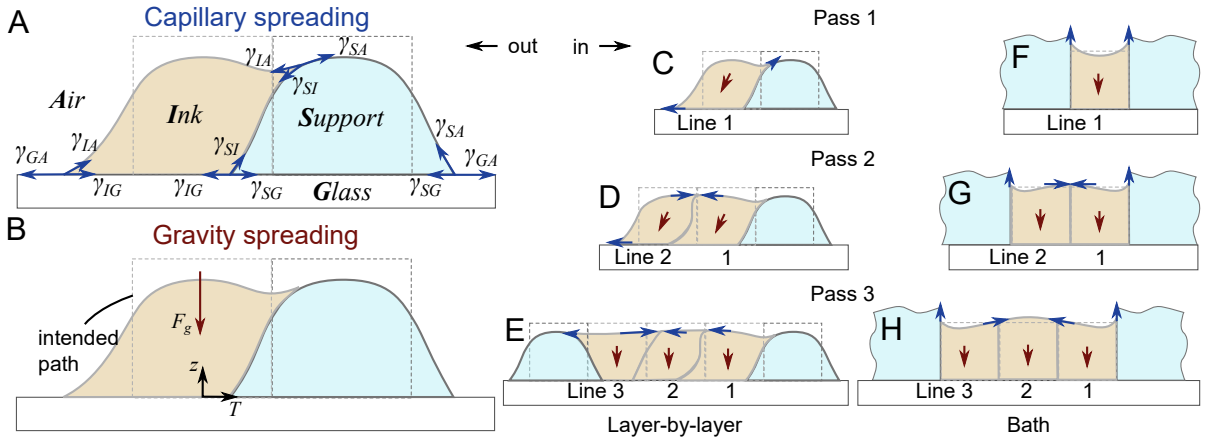

Figure 6.6: Proposed effects of capillary-driven and gravity-driven spreading on transverse flows and the particle distribution, viewed from a cross-section of the printed lines. C-H) Directions of capillary contact line movement (γ) and gravity-driven (F_g) bulk flow are shown.

cally in Figure 6.6. Below a critical size, spreading of droplets is governed by capillarity, and above the critical size, spreading is governed by gravity. This critical size, the capillary length λ, depends on the surface energy γ.[217]

$$\lambda = \left(\frac{\gamma}{\rho g}\right)^{1/2} \tag{6.4}$$

Inks have capillary lengths of 1.6–1.8 mm (Table 6.1). Individual lines have a width of 0.3 mm, and the entire three-line polygon has a thickness of 0.9 mm, so spreading should be governed by interfacial energy. The direction and velocity of spreading should depend on boundary conditions, i.e. different materials on the two sides of the line being printed. In layer-by-layer support, both capillarity and gravity should have an effect because of the asymmetry of the boundary conditions (Fig. 6.6C–E). Ink wets the support more favorably than glass (Fig. 6.S1), so contact lines should advance faster onto the support, but because the support interface is elevated in z, the center of mass of the printed line could move toward glass or toward support, depending on the shape of the support. In pass 1 and 2, gravity drives outward spreading away from existing lines, while capillarity pulls one contact line outward along the

substrate and another inward onto the support or existing ink (Fig. 6.6C–D). In pass 3, gravity does not cause spreading because the filament is bounded on both sides, but capillarity can still drive spreading onto the neighboring ink and support boundaries. Likewise, in all passes in bath support, capillarity can drive spreading onto existing ink and support boundaries, but gravity does not drive spreading because the ink is bounded on both sides (Fig. 6.6F–H). Capillarity can also drive movement of existing ink lines on pass 2 and 3 in both support geometries, as the existing ink lines are drawn toward the new ink line (Fig. 6.6D,E,G,H).

6.3 Experimental approach

This paper draws from the same data set that is used in Ref [18, 20], but this work only uses the center of each polygon edge and focuses on behaviors which are independent of printing direction. Data and code can be found at Ref. [218].

6.3.1 Materials

Inks consisted of diurethane dimethacrylate (UDMA) (Sigma Aldrich, mixture of isomers with topanol inhibitor), triethylene glycol dimethacrylate (TEGDMA) (Sigma Aldrich, with MEHQ inhibitor), fumed silica (Evonik Aerosil R106), camphorquinone (CQ) (Sigma Aldrich), and 2-(Dimethylaminoethylmethacrylate) (DMAEMA) (Sigma Aldrich, with monomethyl ether hydroquinone inhibitor). Bases were mixed in a 92:8 UDMA:fumed silica weight ratio and mixed in a planetary mixer (Thinky ARE-310) at 2000 rpm for 3 minutes. Inks were then mixed in 80:20, 75:25, 70:30, and 65:35 base:TEGDMA weight ratios with 0.2 w% CQ and 0.8 w% DMAEMA, plus 10 w% ($\approx$1.4 v%) silver-coated copper microspheres (Potters Beads Conduct-O-Fil, SC15S15, diameter 15 μm), which were acoustically focused and acted as PIV markers. Carbopol support gels were mixed by adding 1.2 w% Carbomer 940 to deionized water (pH 3-4) and mixing with an overhead stirrer for 5 minutes at 1500 rpm or until dissolved.

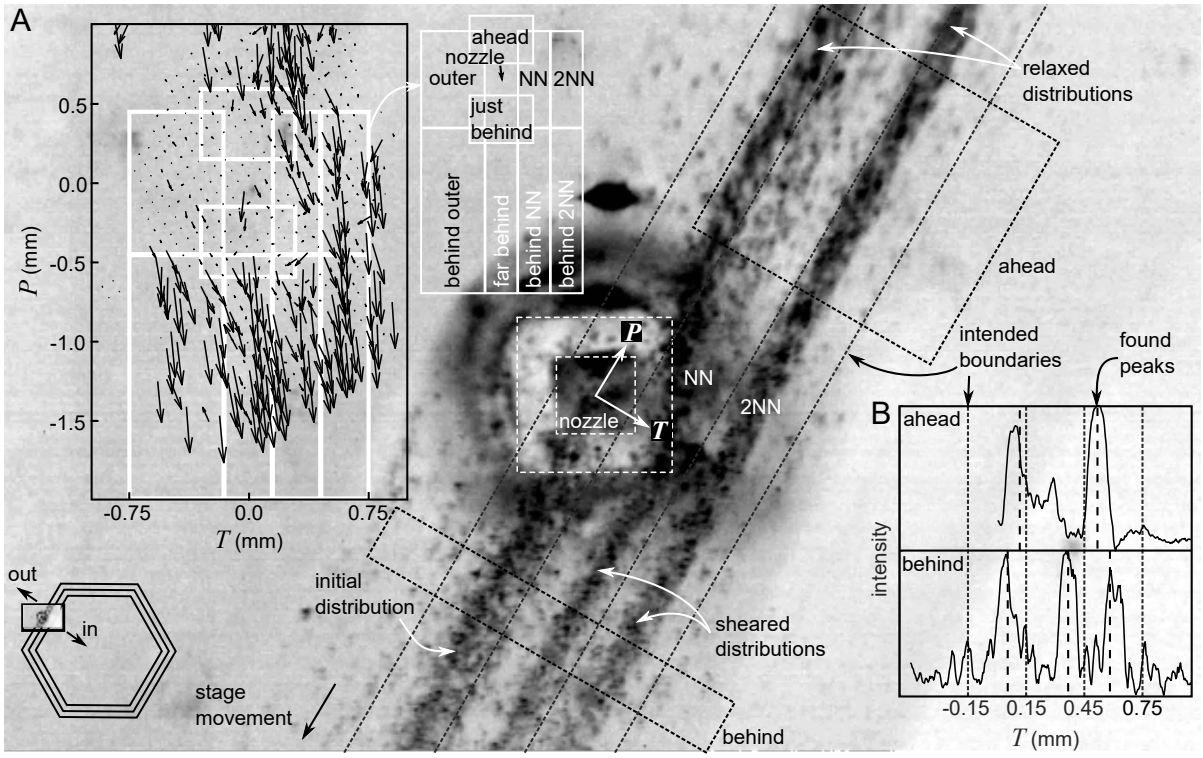

Figure 6.7: Example of analyzed frame, for layer-by-layer support. Image gray levels are inverted. A) Fluid displacement field is measured using PIV and rotated into the Parallel-Transverse coordinate system. Interrogation regions within which transverse flow velocities are averaged are outlined in white. "nozzle" indicates the inner area of the nozzle, assumed to be square with the reference frame. B) Intensities are summed along the parallel direction ahead of and behind the nozzle. Distribution positions and widths are found as a function of transverse position.

Gels were then neutralized using 50% NaOH (Sigma Aldrich) and mixed in a planetary mixer (Thinky ARE-310) at 2000 rpm for 3 minutes to remove bubbles.

6.3.2 Rheology

Viscosities were measured using a TA Instrument Company ARES-LS1 rheometer with 25 mm diameter flat plates and a 2 mm gap at room temperature. Dynamic frequency sweeps were conducted at 10% strain with increasing frequency. Dynamic strain sweeps were conducted at 10 Hz with increasing strain. To avoid curing and settling effects, inks did not contain photoinitiators or particles. Because the printed inks only contain $\approx$1.4 v% particles, the particles should not appreciably change the viscosities of the inks.

6.3.3 Video collection and processing

Inks and support gels were extruded through square borosilicate capillaries (Vitrocom, 0.3 mm ID, 0.6 mm OD, 50 mm length) onto glass slides. The ink capillary was seated in a stainless steel block containing a 0.7 mm square groove lined with ultrasonic coupling gel. A piezoelectric actuator (15 mm diameter x 1 mm thick Navy I material, American Piezo) was adhered to the steel block using epoxy (Devcon HP250). The piezo was driven using a signal generator (HP 33120A) and amplifier (Mini-Circuits LZY-22+), and signals were measured using an oscilloscope (Agilent DSO-X 2024A). Sinusoidal signals were generated at 2.249 MHz and a peak-to-peak voltage of 50 V_{pp}. The piezo was thermally coupled to a copper cooling stage using thermal couplant (Wakefield type 120). Steel inlets were bonded to capillaries using epoxy (Devcon HP250). Ink and support were extruded using a mass flow controller (Fluigent MFCS-EZ) at pressures calibrated by measuring masses extruded at fixed pressures and times. When printing ink, average extrusion speeds were set equal to translation speeds.

The ink nozzle and substrate were illuminated using light transmitted through a red filter

cube, to prevent curing. Videos were collected from underneath the nozzle through the glass substrate using a Point Grey Grasshopper GS3-U3-2356C-C camera with an Infinity Infinitube FM-200 objective and $\times$0.66 lens, at 86 fps.

For layer-by-layer support, the support gel was extruded through a square borosilicate capillary at a stage speed of 10 mm/s and an estimated peak flow speed of 15 mm/s. For bath support, a 1 mm-thick layer of support was spread onto the substrate. Parts were printed at a stand-off distance and line spacing of 0.3 mm, which is the inner width of the capillary. First, the three-line inner support polygon was printed from inside to outside, then the three-line outer support polygon from inside to outside, then the three-line ink polygon from inside to outside. Equilateral triangles, squares, pentagons, hexagons, and octagons were printed with 6, 8, 10, and 12 mm edge lengths. Flow velocities and particle distributions were measured from the middle 2 mm of each polygon edge to limit the influence of corners.

Fluid flows were measured in Matlab R2018b using a modified version of OpenPIV.[177] Only interrogation regions with an average intensity above 0.1 and a maximum intensity above 0.5 were inspected, where the full frame is normalized from 0 to 1. Collected vectors were filtered to remove outliers, but holes were not filled. Particle distributions were measured using Matlab R2018b. Backgrounds were removed using a 15 px disk structuring element. Where the origin is at the nozzle center and the inner diameter half-width is w, the largest fully imaged region upstream of the nozzle from $T = 0$ to $T = 7w$ and downstream of the nozzle from $T = -3w$ to $T = 7w$ were each summed along the print direction, as shown in Figure 6.7. Peaks were identified using the Matlab function *findpeaks* with a minimum peak-to-peak distance of w. The particle distribution width is the standard deviation of the distribution within w of the peak, normalized by the width of a uniform distribution of width $2w$.

Kendall τ tests were used to analyze data.[219] Kendall τ tests evaluate correlations between variables using a parameter $-1 \leq \tau \leq 1$. A τ value of 1 indicates a strongly positive correlation between variables, a τ value of -1 indicates a strongly negative correlation, and a τ

value of 0 indicates no correlation. Kendall τ tests strongly value monotonicity, and p-values from Kendall tests are useful for evaluating the significance of trends. Only Kendall p-values below 0.05 were considered significant.

6.4 Results

The properties of the completed part depend on the positions and widths of the particle distributions within the written lines. Characteristics of the final distributions, shown on pass 3b in Figure 6.8, vary between layer by layer and bath support. In both cases, particles finish closer to the inner edge of the polygon than intended. In layer-by-layer support, the final particle distribution peak position is closer to the intended position, but positions vary among the three lines of the single-layer polygon, and distributions are wide (Fig. 6.8A,C). In bath support, positions are more consistent between lines and distributions are narrower, but widths vary more among lines (Fig. 6.8B,D). Thus, for applications where particle positions are critical, such as deposition onto patterned substrates, layer-by-layer support is better. In contrast, for applications where the particle distribution must be narrow as possible, such as formation of electrical pathways,[9] or applications where particle distributions must be evenly spaced such as metamaterials, bath support is superior.

The final distribution is a culmination of several transitions in the particle distribution over the course of the print (Fig. 6.8). Line 1 is deposited with an initial distribution that is inward of the intended position (Fig. 6.8, pass 1b). Line 1 then relaxes outward and widens as it becomes the nearest neighbor to the new line, line 2 (Fig. 6.8, pass 2a). As line 2 is deposited, the nozzle shears line 1, and line 1 shifts inward and widens (Fig. 6.8, pass 2b). After the nozzle passes, line 1 relaxes again, this time shifting outward by a greater amount than the first relaxation event and widening again, as it becomes the second nearest neighbor to the new line, line 3 (Fig. 6.8, pass 3a). As line 3 is deposited and the nozzle shears line 1 and 2, line 1

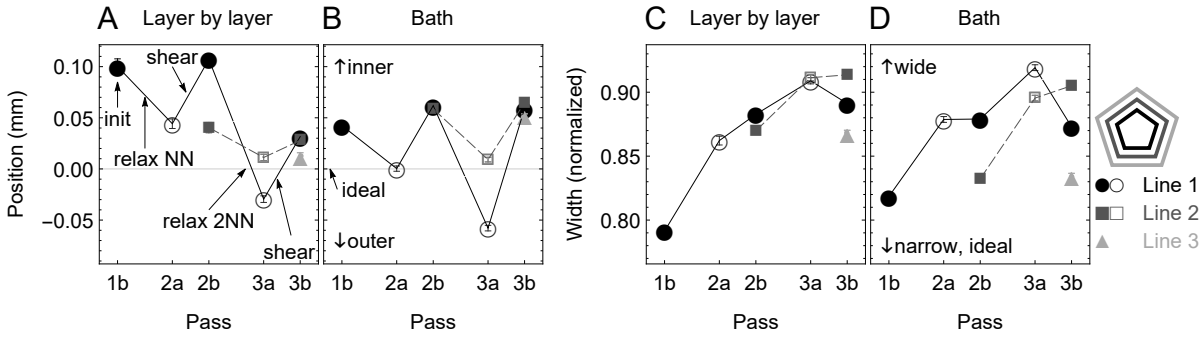

Figure 6.8: Average positions (distance between intended and actual particle peak positions) and widths of particle distributions. Distributions are measured behind (b) the nozzle (after initial deposition or after shear) and ahead (a) of the nozzle (after relaxation and before shear). The intended bounds of the line are from -0.15 mm to 0.15 mm, and positive positions are toward the inner edge of the polygon. The width is normalized by the width of a uniform distribution of particles. Error bars indicate standard error.

shifts inward and narrows (Fig. 6.8, pass 3b). Similarly, after line 2 is deposited with an initial particle distribution inward of the intended distribution, line 2 relaxes outward and widens as it becomes the nearest neighbor to the new line, line 3 (Fig. 6.8, pass 3a). Like line 1, line 2 shears inward and widens as line 3 is deposited (Fig. 6.8, pass 3b).

It is clear that in order to control the final distribution of particles, one must control the initial distribution and changes during relaxation and shear. First, consider how changes in position correlate with each other. Intuitively, the *absolute* positions of the initial, relaxed, and sheared distributions positively correlate with each other, since many changes in the distribution can remain through the course of the print (Fig. 6.S10). However, some *changes* in position do not positively correlate with each other. The farther inward the initial particle distribution is deposited, the farther outward the distribution shifts during relaxation. Likewise, the farther outward the distribution shifts during relaxation, the farther inward it shifts during deposition of neighboring lines. This is demonstrated in Figure 6.9A–C, which shows correlations between changes in particle distribution position over the course of the print. For each edge of each printed polygon, the initial position, change in position during the first relaxation

step (relax NN), and change in position during shear are each averaged across several points on the edge and across all passes. Correlations between initial positions, changes in position during relaxation for the nearest neighbor, and changes in position during shear are close to 1:1 or -1:1 relationships (Fig. 6.9A–C). The initial position negatively correlates with the change in position during relaxation for the nearest neighbor, indicating that the farther inward the initial line is deposited, the larger the outward shift in position during relaxation for that same line (Fig. 6.9A). Similarly, there is a negative correlation between the change in position during relaxation for the nearest neighbor and the change in position during shear, indicating that the farther outward the line shifts during relaxation, the farther inward the line shifts during the following shear (Fig. 6.9B). Accordingly, there is a positive correlation between the initial position and the change in position during shear, indicating that the farther inward the particles are initially deposited, the farther inward the neighboring lines shift during deposition of new lines (Fig. 6.9C).

While relaxation and shear cancel each other out with respect to the final particle distribution position, they work in concert to widen the final particle distribution. This is apparent in Figure 6.9D–F, which shows correlations between changes in width over the course of the print, collected for each edge of each printed polygon. Correlations between the initial width, change in width during relaxation for the nearest neighbor, and change in width during shear are not as strong as correlations in position. The Kendall τ parameter runs from -1 to 1 and indicates the strength of a correlation, where large magnitudes indicate strong correlations. Whereas Kendall $|\tau|$ magnitudes are between 0.2 and 0.6 for correlations between relative positions, $|\tau|$ magnitudes are between 0 and 0.4 for correlations between relative widths (Fig. 6.9). Correlations between the three combinations of the three metrics are negative, which indicates that (1) if the initial width is larger, the width increases less during relaxation, (2) if the width increases less during relaxation, the width increases *more* during shear, and (3) if the initial width is larger, the width increases *less* during shear (Fig. 6.9D,E,F). As such,

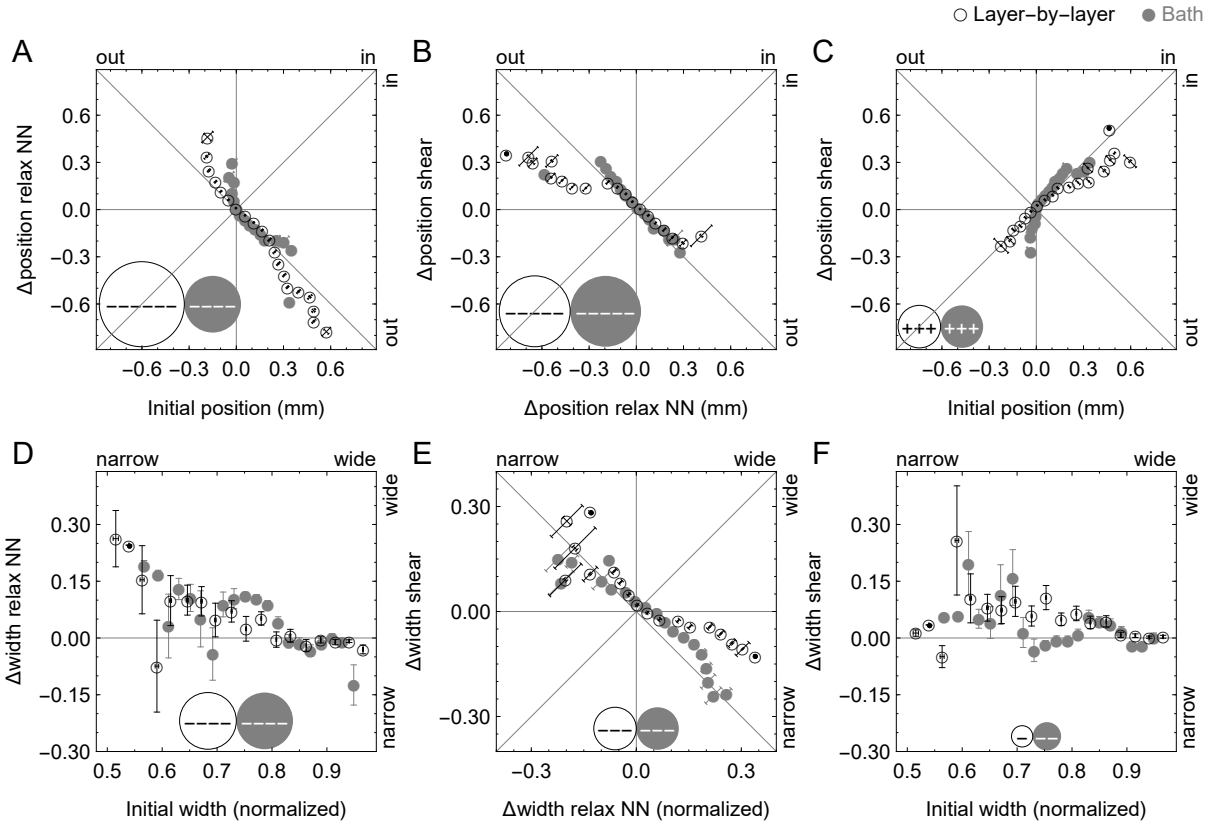

Figure 6.9: Correlations between changes in the particle distribution over the course of the print. Error bars indicate standard error with respect to $y = 0$ in D and F and the line $-x = y$ or $x = y$ in A,B,C, and E. Distribution widths are normalized by the width of a uniform particle distribution. Signs of statistically significant (p¡0.05) Kendall τ coefficients are shown. "-" indicates a negative correlation where $-0.1 < \tau < 0$, "++" indicates a stronger positive correlation where $0.1 < \tau < 0.2$, and so on, where $-1 < \tau < 1$. "NN" nearest neighbor. The nozzle inner width is 0.3 mm.

the three correlations are not intuitively linked. Based on τ values, the most likely causal relationships are (1) between the initial width and change during relaxation, and (2) between the change in width during shear and the change in width during relaxation (Fig. 6.9D,E). A narrow initial width has greater capacity to widen during relaxation. If the distribution widens more during relaxation, it is likely to narrow more during shear, so as with positions, widths demonstrate that shear mitigates the changes during relaxation. However, unlike changes in position, decreases in width during shear are not as large as corresponding increases in width during relaxation, especially for layer-by-layer support (Fig. 6.9E).

An attempt to fit the three width-width correlations to linear relationships would demonstrate that these three correlations are contradictory. In other words, if $X = -Y$ and $Y = -Z$, then $X = Z$, not $X = -Z$. Nonmonotonicity is at the root of this contradiction. The weakest correlation is between the change in width during shear and the initial width, which is non-monotonic with $0 > \tau > 0.2$ (Fig. 6.9F). One possible source of this non-monotonicity is averaging. If the initial width is small, it has a greater capacity to increase during relaxation, which is observable in Figure 6.9D, and that large increase in width during relaxation enables a large decrease in width during shear. However, if the narrow distribution manages to not widen during relaxation, possibly due to a short relaxation time or a viscous ink, the distribution will already be small and have little capacity to decrease at the moment of shear, so the distribution will widen during shear. On average, this results in close to zero change in width during shear for a small initial width.

Next, consider how the *absolute* position and width of the particle distribution correlate with each other. These correlations are useful for selecting a time to implement curing on the fly. Whether curing is implemented just after deposition, after relaxation, or after shear, there is a trade-off between the width and position of the particle distribution, where for most applications an ideal distribution would be both narrow and centered within the printed line. Figure 6.10 shows correlations between particle distribution positions and widths at several

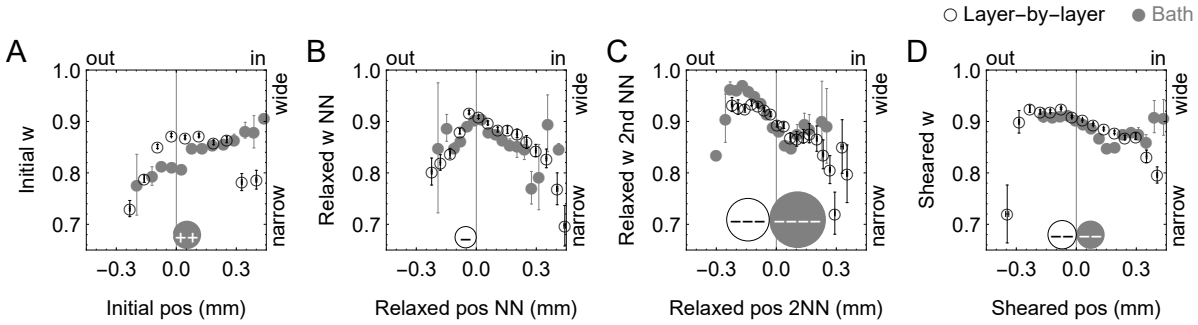

Figure 6.10: Correlations between absolute particle distribution widths (w) and positions (pos). Error bars indicate standard error. Distribution widths are normalized by the width of a uniform particle distribution. Signs of statistically significant (p¡0.05) Kendall τ coefficients are shown. "-" indicates a negative correlation where $-0.1 < \tau < 0$, "++" indicates a stronger positive correlation where $0.1 < \tau < 0.2$, and so on, where $-1 < \tau < 1$. "NN" nearest neighbor or the first relaxation step, "2NN" second nearest neighbor or the second relaxation step. The nozzle inner width is 0.3 mm.

points in the printing process. With the exception of relaxation of the second nearest neighbor, correlations between positions and widths are weak, with Kendall $|\tau| < 0.2$ (Fig. 6.10). As with width-width correlations, relationships between positions and widths are non-monotonic. For layer-by-layer support, if the initial position is at the intended position (0 mm), the initial particle distribution is at its widest (Fig. 6.10A). However, in bath support, the initial width increases monotonically as the initial position shifts inward (Fig. 6.10A).

Particle distributions after relaxation have a non-monotonic position-width relationship. The second relaxation step may be a good place to implement curing on the fly with in-situ particle distribution monitoring if both particle distribution position and width are important. For both support geometries, the distribution width sharply increases as the position shifts closer to the intended position at the center of the printed line (Fig. 6.10B), illustrating a critical trade-off between particle positioning and local particle packing density in the relaxed state. There is a distinct difference between the behavior of the relaxed nearest neighbor and second nearest neighbor. The relaxed position of the second nearest neighbor is the only distribution with a strong Kendall τ correlation. If the relaxed position is farther inward, the width is

narrower, although the behavior near the ideal position (0 mm) is inverted compared to the behavior of the nearest neighbor (Fig. 6.10C). Namely, after the particle distribution relaxes for a second time, there is a local, but not global, minimum in the particle distribution width where the particle distribution is at the ideal position in the center of the print path.

Particle distributions after shear exhibit a similar, but more muted trend to the trend in relaxation-induced changes in the particle distribution in the second nearest neighbor. The sheared width narrows as the sheared position shifts inward, with a slight local minimum in width at a position of 0.15 mm, which is the edge of the intended printed line (Fig. 6.10D). Recall from Figure 6.9 that shear undoes the effects of relaxation. As such, it makes sense that the sheared width is nearly constant as a function of sheared position. The implication of all of these trends in position and width is that there may not be a way to optimize position and width at the same time. Depending on whether the printed line is cured just after deposition, just after shear, or just after relaxation, a well-placed particle distribution may be wider than desired, and a tightly packed particle distribution may be inaccurately placed.

Depending on the desired characteristics of the particle distribution, relaxation can be useful tool or an obstacle. To understand the roots of changes in distribution during relaxation, one can measure the change in distribution as a function of time. The scaling of the change in distribution with time indicates that the observed spreading is more likely to come from capillarity than gravity. Capillary-driven contact line speeds tend to scale with time to smaller exponents, while gravity-driven contact line speeds tend to scale with time to larger exponents.[220] The change in particle distribution position during relaxation tends to scale with time to capillarity-range exponents or lower (see supplemental).

Particle image velocimetry measures ink flow velocities in the region near the nozzle. The field was split into ten interrogation regions, and the average transverse component of the flow velocity within the region was calculated. Ahead of the nozzle, fluid flows strongly inward toward existing lines (Fig. 6.11A). At the nozzle exit, fluid flows slightly inward. Just behind

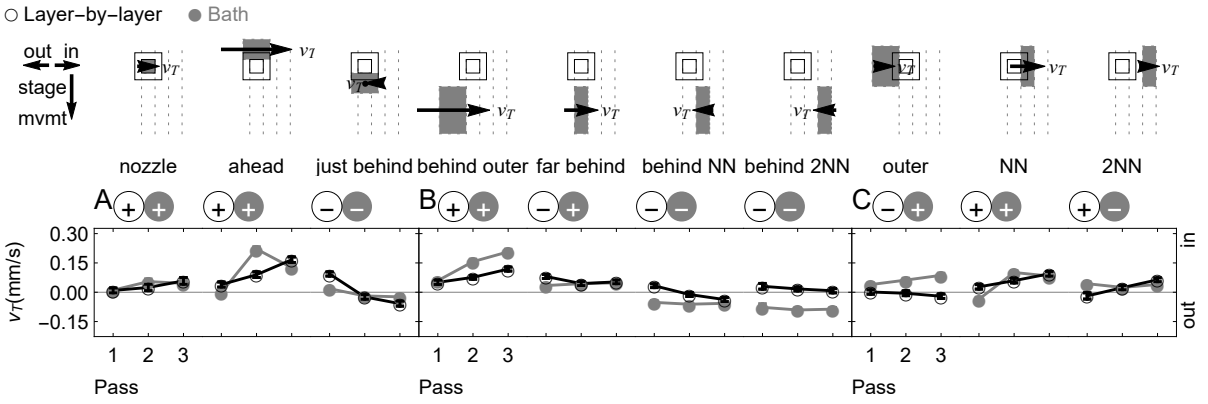

Figure 6.11: Transverse flow velocities in ten interrogation regions as a function of pass number. "NN" nearest neighbor, "2NN" second nearest neighbor. "+" and "-" signs refer to Kendall τ coefficients between pass number and transverse flow velocity.

the nozzle, the fluid flows outward. Farther behind the nozzle, fluid flows toward the print path. In the behind outer region, flows are inward, and behind in the inner regions, flows are outward, particularly in bath support (Fig. 6.11B). This flow pattern is exemplary of an inertial disturbed zone. In layer-by-layer support, transverse flow velocities behind in the nearest neighbors are close to 0. Directly to the sides of the nozzle, in bath support all flows are inward toward existing lines, but in layer-by-layer support transverse flow velocities are close to 0 on the outer side of the nozzle (Fig. 6.11C). Asymmetric flows away from or toward the print path become stronger with each pass, which is indicative of both plastic flow and inertial disturbances.

Identifying correlations between transverse flow velocities in different regions can aid in tracking the validity of the proposed theories under different conditions. In general, there are positive correlations between transverse flows in most regions (Table 6.S20). In particular, correlations between flows in neighboring regions behind the nozzle are very strong (Table 6.S20). However, there are some negative correlations, which highlight key features of the flow field. Figure 6.12 shows correlations between transverse flow velocities in several key interrogation regions, where transverse velocities in each region were averaged along the length of each edge of each printed polygon.

First, the flow field reflects the pattern predicted by the disturbed zone hypothesis, which predicts that transverse flows ahead of the nozzle oppose transverse flows just behind the nozzle, as if material ahead of the nozzle that is displaced during deposition flows back toward its previous position after deposition (Fig. 6.5). This is demonstrated by the negative correlation between flows ahead of and just behind the nozzle (Fig. 6.12A). To help to visualize this flow, consider Figure 6.7. The nozzle is static, and the stage is moving downward to the left. Ahead of the nozzle, there are two existing written lines. Just ahead of the nozzle, the existing lines are forced inward, and the flow field shows a corresponding inward flow just ahead of the nozzle (Figure 6.7A). Just behind the nozzle, the flow field curves back around the nozzle, resulting in a outward flow just behind the nozzle visible in the bottom right corner of the "just behind" region in Figure 6.7A.

In addition to inertial disturbances, the flow field could reflect plastic flow. Under plastic flow, ahead of the nozzle, the nozzle shears the surrounding support material, causing it to yield and flow away from the nozzle. Behind the nozzle, the support material reflows into the gap left by the nozzle (Fig. 6.4). Evidence of inertial disturbances is shown by the slope of the relationship between transverse flows ahead and just behind the nozzle, which differs between layer-by-layer and bath support (Fig. 6.12A). In layer-by-layer support, flows ahead of and just behind the nozzle have a close to -1:1 relationship. In contrast, for bath support, the slope of the curve indicates that the magnitude of flows just behind the nozzle is smaller than the magnitude of flows ahead of the nozzle, potentially indicating that the end of the disturbed zone wake occurs farther behind the nozzle in bath support than in layer-by-layer support.

Correlations between transverse flow velocities in the regions behind the nozzle indicate key differences between layer-by-layer and bath support. Specifically, consider correlations between the transverse flow velocity in the behind outer region and flows in the far behind and behind nearest neighbors regions, which are shown in Figure 6.12B, Figure 6.S25Y, and Figure 6.S25Z. In layer-by-layer support, the flow field behaves as if the entire region is influenced

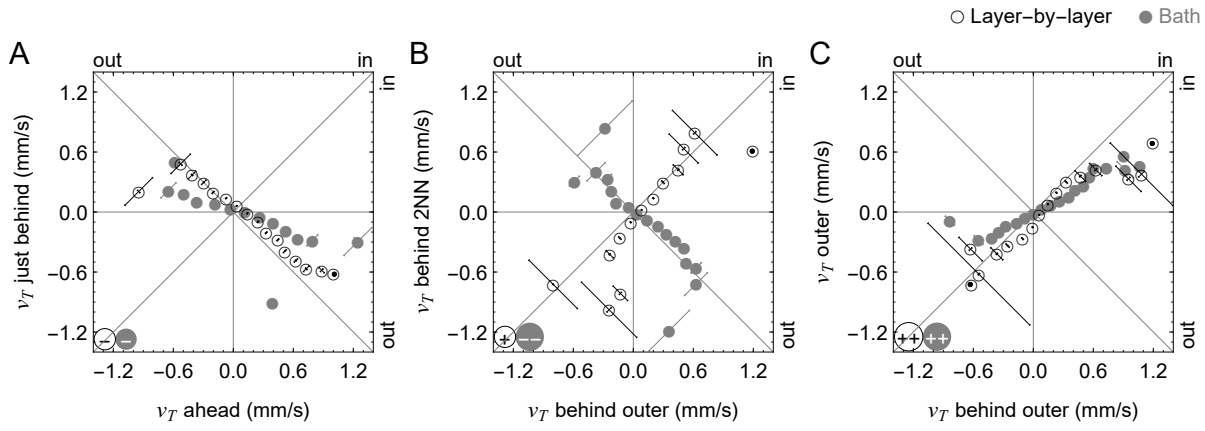

Figure 6.12: Correlations between transverse flow velocities in various regions. Error bars indicate standard error with respect to the line $-x = y$ or $x = y$. Signs of statistically significant ($p < 0.05$) Kendall τ coefficients are shown. "-" indicates a negative correlation where $-0.1 < \tau < 0$, "++" indicates a stronger positive correlation where $0.1 < \tau < 0.2$, and so on, where $-1 < \tau < 1$. "2NN" second nearest neighbor

by driving forces which all act in the same direction, for example surface tensions that pull all ink toward support material or the glass substrate, or plastic flow which pushes ink toward an unbounded outer surface. This is evidenced by positive, nearly 1:1 correlations between flow velocities in all regions behind the nozzle, whether or not the regions neighbor each other.

In contrast, in bath support the flow field is more symmetric about the deposited line, as predicted by the disturbed zone model. In bath support, correlations between neighboring regions become more negative the farther apart the regions are. Specifically, there is a positive correlation between flows in two neighboring regions: the behind outer region and far behind (in the just-deposited line). Flow velocities far behind (in the print path) have a smaller magnitude than flow velocities in the behind outer region. There is a negative correlation between flow velocities in the two regions on either side of the the deposited line: the behind outer region and behind in the nearest neighbor. Velocities behind the nozzle in the nearest neighbor have a smaller magnitude than velocities in the behind outer region. There is a negative, nearly -1:1 correlation between flow velocities in regions at the far outer and inner edges of the inspected

area: the behind outer region and behind in the second nearest neighbor (Fig. 6.12B).

The proposed spreading and disturbed zone models are not strictly necessary to understand the contrast between bath and layer-by-layer support in side-to-side symmetry about the nozzle. After all, layer-by-layer support is inherently asymmetric because for most of the print, one boundary of each deposited line is bounded, and the other is unbounded. Bath support is inherently symmetric because both sides of the deposited line are always bounded, although the boundary conditions are not exactly symmetrical because in two passes, the line is bounded by ink on one side and support on the other.

Correlations between regions to the sides of the nozzle and regions behind to the sides of the nozzle describe the wake left by the nozzle. Attenuation of inward flows in the outer region and outward flows in the inner regions indicates that the disturbed or plastic zone has ended, and all remaining flows come from longer-range effects like capillarity and gravity. Figure 6.12C shows the positive correlation between transverse flow velocities in the outer and behind outer regions. Flow velocities increase in magnitude behind the nozzle. The same holds for the second nearest neighbor (Fig. 6.S26PP). Because correlations are positive and both inward and outward flows are amplified behind the nozzle, the region behind the nozzle must either be within the upstream portion of the disturbed zone or strongly influenced by the plastic zone. The amplification of flows behind the nozzle is stronger for bath support, which could occur because more support fluid is displaced in bath support, leading to a stronger influence of the plastic zone. In the nearest neighbor, flows are attenuated behind the nozzle, indicating that the regions closer to the print path may be part of the downstream portion of the disturbed zone (Fig. 6.S25LL). This is expected, because the portions nearer to the print path are farther from the support material and would thus be more influenced by the disturbed zone than the plastic zone.

Correlations between transverse flow velocities and features of the distribution are weak but plentiful (Table 6.S19). Because it is difficult to deconvolute direct correlations between

these dependent variables and correlations via the transitive property with independent printing parameters, correlations between flow velocities and distribution metrics are not particularly useful for understanding how to manipulate changes in the filament microstructure over time. Correlations between dependent variables and independent variables could also shed light on the relative contributions of the various driving forces, but because of the previously discussed correlations between dependent variables (e.g. changes in the particle distribution during shear oppose changes during relaxation) and because of overlaps between effects (e.g. transverse flow velocities are negative under plastic flow, capillary spreading, and gravity spreading), these correlations constitute an analytical quagmire. A detailed description of these correlations can be found in the supplemental information.

6.5 Discussion

This work outlines a suite of driving forces which elucidate the effects which control the movement of fluid during direct ink writing with acoustophoresis using yield stress support material. Plastic flow, wherein yielded support material flows into the written ink lines, influences the flow field in regions near support boundaries. Inertial disturbances, wherein inertia drives ink around the nozzle, has a strong influence on the flow field and the initial and sheared particle distribution. The symmetry of the flow field about the print path in bath support indicates that plastic flow and disturbed flow likely influence the flow field more strongly in bath support. Ink lines spread onto the substrate and support material, driven largely by capillarity. The asymmetry of the flow field about the print path in layer-by-layer support indicates that spreading likely influences the flow field more strongly in layer-by-layer support. By leveraging these effects during direct ink writing of composites, the internal structure of written lines can be manipulated.

Correlations between changes in position and changes in width at various steps in the print-

ing process illustrate that plastic flow, inertial disturbances, and capillary and gravity spreading do not work in isolation. A linear superposition of these effects will not be sufficient to predict the final particle distribution in the cured line. Changes in the distribution during relaxation are proportional to shifts in the initial distribution. Only narrow initial particle distributions widen during relaxation, and particle distributions shift during relaxation in proportion to the shifts experienced during deposition, indicating that the amount of spreading is dependent on what happens to the distribution during plastic zone and inertial disturbances. Likewise, changes during shear are proportional to changes during relaxation, indicating that plastic zone and inertial disturbances impact the region differently depending on how much the line spreads during relaxation.

The symmetry of flows relative to the print path behind the nozzle highlights a prominent difference between bath support and layer-by-layer support, which could come from a combination of plastic flow, inertial disturbances, and spreading. The asymmetry of the boundary conditions in layer-by-layer support allows for asymmetric flow velocities behind the nozzle, where flow velocities behind the nozzle on the inner boundary are positively correlated with and nearly proportional to the velocities on the outer border. In contrast, the symmetry of the boundary conditions in bath support induces a negative correlation between flows on the inner and outer regions behind the nozzle. In plastic flow, inertial disturbances, and spreading, the asymmetry of the layer-by-layer support would manifest in asymmetric inward flows, while the symmetry of the bath support would promote symmetric flows about the print path. Notably, in layer-by-layer support, particle distribution positions become more centered on the third pass, when the boundary conditions become more symmetrical. In bath support, particle distribution positions become less centered on successive passes, as boundary conditions become less symmetrical.

Correlations between transverse flow velocities and particle distribution characteristics illuminate the complexity of the printing process. Because control over the particle distributions

cannot be pinpointed to flow velocities in a single region alone, and distributions instead correlate weakly with flow velocities in many regions, granular examination of the flow field is unlikely to explain how the particle distribution is established. Flows are useful for understanding the driving forces involved in the printing process, but it appears that controlling the particle distribution is more complicated than tweaking the flow field in a few key regions.

6.5.1 Plastic zone and inertial disturbances

Plastic flow and inertial disturbances should occur on short length scales, near the nozzle. Plastic flow involves flow of yielded support material into the deposited ink line. Inertial disturbances involve inertial flows of ink around the nozzle, where ink flows away from the print line ahead of and next to the nozzle, then gradually reverses and flows toward the print line behind the nozzle. Both effects should be influenced by asymmetrical boundary conditions.

The directions of fluid flow velocities and correlations between flows in different regions indicate that inertial disturbances are present in this system, and inertial disturbances are influenced by boundary conditions. Just as predicted, ink flows away from the print line next to the nozzle, and it flows toward the print line behind the nozzle. Flows ahead of the nozzle are reversed just behind the nozzle, and flow speeds just behind the nozzle are proportional to flow speeds ahead of the nozzle. As the boundary on the inner edge of the print line becomes more compliant as it is increasingly composed of ink rather than support, fluid flow velocities become faster inward near the nozzle. Correlations between flows next to and behind the nozzle indicate that plastic flow makes a greater contribution on the outer edge of the printing region, and inertial disturbances make a greater contribution on the inner edge, which makes sense because most of the outer edge is support material, and most of the inner edge is ink. Under plastic flow, the support causes transverse flow velocities in the behind outer region to increase farther inward on each pass due to less plastic zone resistance on the inner edge on

successive passes. The outward increase in flow velocity behind in the nearest neighbors on successive passes (inner boundary) indicates that the inner boundary flows behind the nozzle reverse the transverse flow velocities established next to the nozzle, which is characteristic of inertial disturbances.

Inward shifts in particle distribution position during shear likely come from inertial disturbances. Under inertial disturbances, inertia causes any ink in front of or on the inner edge of the nozzle (i.e. relaxed neighboring lines) to shear inward, and deposition of the new line prevents the sheared neighbors from immediately shifting back to their relaxed position.

6.5.2 Spreading

Spreading should occur on long time scales, far from the nozzle. Spreading can come from capillarity and gravity and can cause movement of the ink-substrate and ink-support contact lines that result in a net bulk movement of the printed line, where the direction of movement depends on the boundary conditions of the line. Outward shifts in particle distribution position during relaxation likely come from spreading. Because these shifts occur in both bath support and layer-by-layer support, the spreading is likely driven by capillarity rather than gravity, since gravity-driven spreading should be symmetrical or nonexistent in bath support. Further, because power law exponents for changes in the particle distribution during relaxation are small, spreading is more likely to come from capillarity instead of gravity, which is consistent with the long capillary lengths calculated in the Hypotheses section.[220]

In addition to longer timescale spreading, there is some evidence of capillarity on shorter time scales. Ahead of the nozzle, ink flows inward toward existing ink lines. Under plastic zone and inertial disturbances, asymmetry of the zone due to differences in compliance in the boundaries can cause this asymmetry. However, inward flows ahead of the nozzle are very strong, and it is possible that the ink's predilection toward decreasing its own surface area also

plays a role in these flows toward existing ink lines.

6.6 Conclusions

Direct ink writing with acoustophoresis can be used to print polymer matrix composite filaments containing narrow distributions of particles. The positions and widths of these particle distributions can influence the structural and functional properties of the printed line. As such, controlling the particle distribution in the final printed line is of utmost importance.

- Layer-by-layer support enables more accurate particle positioning, while bath support enables narrower particle distributions.
- The distribution changes at three points: as the filament is initially deposited on the substrate, as the filament relaxes, and as the nozzle shears the filament while writing a neighboring line.
- The farther inward the initial particle distribution is deposited, the more it shifts outward during relaxation. The farther outward a particle distribution shifts during relaxation, the more it shifts inward during shear. While the relaxation and shear process doesn't damage the final particle distribution position, it widens the particle distribution.
- There is a trade-off between the particle distribution position and width. To preserve the narrowest particle distribution, *in-situ* curing should be employed just after deposition. To preserve the most accurate particle positioning, *in-situ* curing should be employed after the first relaxation step. To balance the particle distribution width against its position, *in-situ* curing should be employed after the second relaxation step.

Critically, the final particle distribution in the written line is not identical to the particle distribution that acoustophoresis establishes inside the nozzle. Tracking the particle distribu-

tion throughout the entire printing process is useful for pinpointing times and locations in the printing process when in-situ photopolymerization should be employed. One could integrate in-situ monitoring, such that a curing lamp could be employed at the moment when the particle distribution reaches its ideal state. However, at most points in the print, there is a trade-off between the particle distribution position and width. These trends can guide in-situ monitoring for in-situ curing in order to anticipate the best achievable particle distribution.

One might notice that the particle distribution widths presented in this paper are between 50 and 100% of the maximum possible distribution width. Note that these are averaged across many printing conditions, and the results herein are meant to illustrate relative differences in distribution widths. To achieve a narrower distribution with acoustophoresis, one can use low-viscosity inks and slow extrusion speeds.[15]

Numerical models of the fluid deposition process during moderate-viscosity direct ink writing with yield stress fluid support should consider viscoplasticity, inertia, capillarity, and gravity. The effects studied in this work are not the only effects that influence moderate viscosity direct ink writing. Notably, because this work was conducted on printed polygons, it is possible that even though this work focused on the parts of the printed line that are far from the printed corners, corner effects and printing direction effects are present in these results.[18, 20] Though this work aimed to encompass the complex driving force interactions involved in direct ink writing with support material, future work on straight lines and polygons printed from the outer edge inward could help to separate the effects. Because this work focuses on transitions which happen after the ink leaves the acoustic field, it can be applied to DIW techniques beyond DIW with acoustophoresis.

6.S1 Supplemental figures and tables

6.S1.1 Hypotheses

Plastic zone flow and disturbed zone flow

Table 6.S1: Critical viscoplasticity and inertia parameters for fluids studied in this experiment. τ_y, K, and n are fitting parameters for the Herschel Bulkley model, ρ is the fluid density, Od is the Oldroyd number, Re is the Reynolds number, and speeds (3 mm/s, 12 mm/s) refer to printing speeds.

	Carbopol 1.2 w%	20 w% TEGDMA	25 w% TEGDMA	30 w% TEGDMA	35 w% TEGDMA
τ_y (kg/(m*s^2))	10	0.01	0.01	0.01	0.01
K (kg*s^{n-2}/m)	43.5	1.7	1.3	1.0	0.5
n	0.05	0.71	0.69	0.63	0.76
ρ (kg/m^3)	1109	1280	1298	1246	1326
Od 3 mm/s	2.1×10^{-1}	1.9×10^{-3}	2.5×10^{-3}	3.6×10^{-3}	5.3×10^{-3}
Od 12 mm/s	2.0×10^{-1}	6.9×10^{-4}	9.6×10^{-4}	1.5×10^{-3}	2.0×10^{-3}
Re 3 mm/s	2.1×10^{-4}	2.1×10^{-3}	2.9×10^{-3}	4.1×10^{-3}	6.7×10^{-3}
Re 12 mm/s	3.1×10^{-3}	1.3×10^{-2}	1.8×10^{-2}	2.7×10^{-2}	3.7×10^{-2}

Spreading

Figure 6.S1: Advancing, receding, and equilibrium contact angles of the inks used in this study, as a function of TEGDMA w% (20, 25, 30, 35), on glass and a thin layer of 1.2 w% Carbopol support (sup). Angles were measured using the submerged needle technique. Receding angles on support could not be collected without inducing mixing between the support and ink.

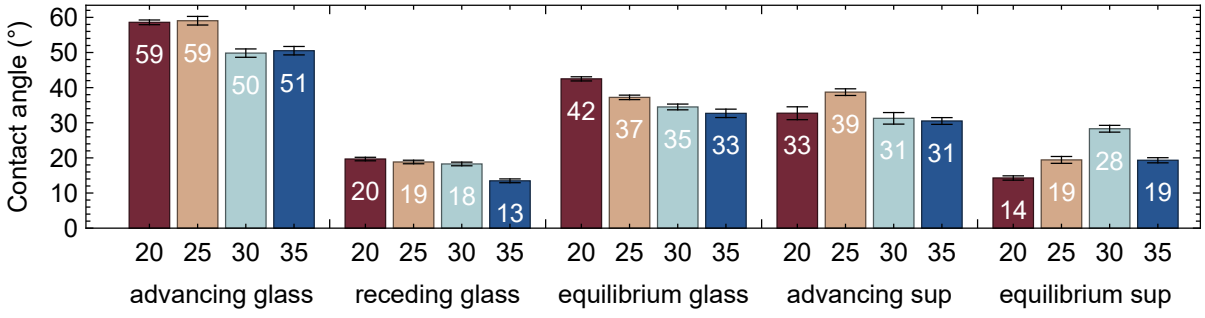

Table 6.S2: Capillary length, which is the critical length scale at which gravity has a non-negligible contribution to the shape of a droplet sitting on a substrate, and Bond number, which a dimensionless metric of the trade-off between gravity and capillarity. Surface tensions were estimated from [221] and [128].

	Carbopol 1.2 w%	20 w% TEGDMA	25 w% TEGDMA	30 w% TEGDMA	35 w% TEGDMA
Density (kg/m^3)	1109	1280	1298	1246	1326
Estimated surface tension (kg/s^2)	0.056	0.041	0.040	0.038	0.035
Capillary length (mm)	2.28	1.81	1.78	1.76	1.63
Bond number	0.017	0.027	0.028	0.029	0.034

Settling

At the end of the nozzle, the particles are focused into a square region in the center of the nozzle (Fig. 6.S2). Assuming that this microstructure is preserved as the filament is deposited on the substrate, the deposited particles will form a square distribution in the center of the printed line. In order to focus the particles into the center of the line, there must be a positive acoustic contrast between the particles and matrix. Generally, this means that the particles are denser than the polymer matrix. This is true for the silver-coated copper spheres and polyurethane-based matrix used in this study. As such, one might expect the square distribution of particles in the center of the line to settle towards the substrate, eventually spreading into a wider distribution when they encounter the substrate (Fig. 6.S2).

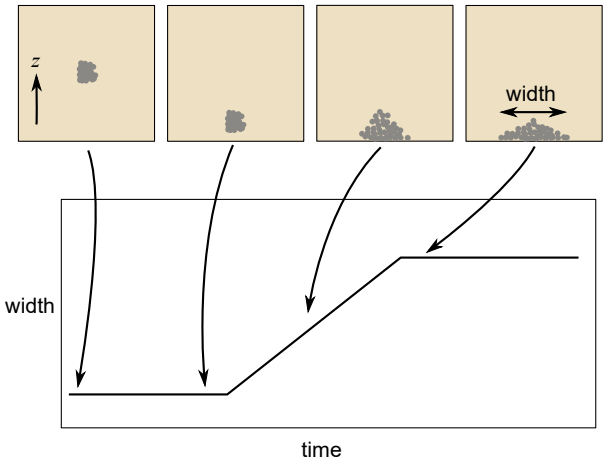

Figure 6.S2: Proposed effect of particle settling on the particle distribution width as a function of time after deposition. Schematics indicate a cross-section of the printed line with particles in gray.

The amount of time that the particles spend settling before reaching the substrate depends on Stokes' drag. Particles falling through the matrix with acceleration due to gravity g achieve a terminal velocity v as a function of the particle density ρ_p and fluid density ρ_f.[222]

$$v_g = \frac{2}{9}\frac{\rho_p - \rho_f}{\mu} g R^2 \tag{6.S1}$$

Using Equation 6.S1, the distance that particles settle during the printing of one layer can be calculated. Because particle volume fractions are low ($\approx$ 1.4 v%), Stokes settling should be sufficient, and hindered settling does not need to be considered. The largest printed polygon is an octagon with edge length 12 mm, the smallest polygon is a triangle with edge length 6 mm, and print speeds range from 3–12 mm/s. For 15 μm copper microspheres of density 8.96 g/cm^3, one can estimate the critical polygon perimeter for which particles settle to the substrate during one pass as a function of translation speed v_s, line half-width w, and settling speed v_g.

$$P_c = \frac{w v_s}{v_g} \tag{6.S2}$$

Critical perimeters are listed in Table 6.S3.

Table 6.S3: Settling of copper microspheres during a single pass around a polygon. The critical perimeter is the polygon perimeter at which particles reach the substrate during a single pass around a polygon.

	20 w% TEGDMA	25 w% TEGDMA	30 w% TEGDMA	35 w% TEGDMA
Density (kg/m^3)	1280	1298	1246	1326
Viscosity at 0.01 Hz (kg/(ms))	0.083	0.034	0.057	0.050
Settling velocity (mm/s)	0.045	0.045	0.066	0.075
Min critical perimeter P_c (mm)	9.9	10.1	6.8	6.0
Max critical perimeter P_c (mm)	39.6	40.2	27.3	23.9

As a reference point, the settling speeds in Table 6.S3 predict that particles should settle out of solution in the ink reservoir on the printer within 20–30 minutes, which is roughly twice as fast as they settle during experiments. As such, it may be reasonable to double the critical perimeters in Table 6.S3 to more realistic values of 12.0 to 80.4 mm. The polygons printed in this study have perimeters between 18 and 96 mm, so it is realistic to expect that in some tests, the particles will settle to the substrate, and in others, the particles will not reach the substrate.

From Stokes drag, higher TEGDMA loadings, which decrease the matrix viscosity, should produce larger changes in the distribution width during relaxation. Printing at faster speeds decreases the amount of time particles have to settle, leading to a smaller initial and relaxed width.

6.S1.2 Results

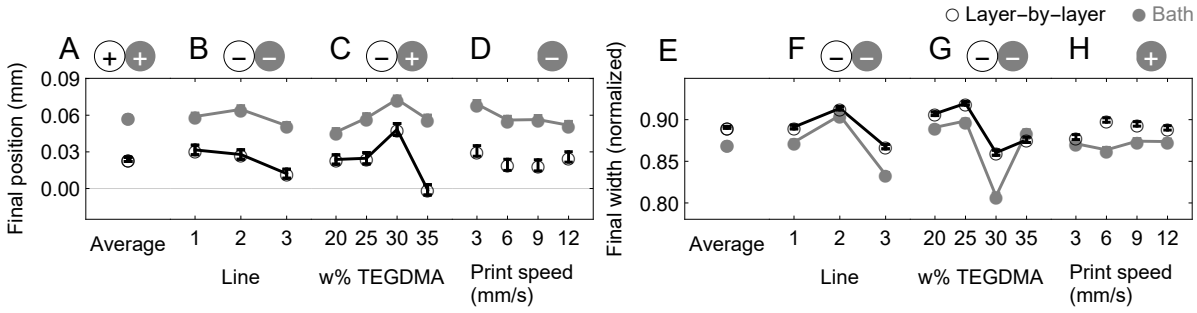

Figure 6.S3: Final particle distribution positions and widths after all lines are printed. Positive positions are inward toward existing lines and the center of the polygon. Distribution widths are normalized by the width of a uniform distribution. Error bars indicate standard error. Signs of statistically significant Kendall τ parameters are indicated.

Correlations between printing parameters and dependent variables

This section describes a new parameter τ_{all} which can be used for evaluating the accuracy of hypotheses in multivariable data sets. Altogether, while τ_{all} is a useful preliminary metric for evaluating the probability that a driving force influences a measured parameter, it struggles to distinguish between overlapping effects and assumes a linear superposition of effects, so it must be considered in the context of other results, not in isolation.

One way to extract the contributions of the hypothesized effects on the particle distribution and flow field is by comparing correlations between printing parameters and dependent variables to hypothesized correlations. In this work, polygons were printed at varying print speeds, where the flow speed is equal to the translation speed; varying TEGDMA concentrations in the ink, where increasing TEGDMA decreases the ink viscosity; and varying boundary conditions via the three passes around the polygon. For each dependent variable (for example, transverse flow velocity ahead of the nozzle), one can measure the sign of the average value and the sign of the Kendall τ correlation parameter with each independent variable (pass number, TEGDMA

concentration, and print speed). These results are shown in Fig. 6.S4 and Fig. 6.S5.

In Table 6.S4, Table 6.S5, Table 6.S6, Table 6.S7, and Table 6.S8, predictions are shown for these four signs based on trends found in the literature for each of the five driving forces: the plastic zone, disturbed zone, capillary spreading, gravity spreading, and particle settling. For example, in layer-by-layer support, the average transverse flow velocity in the nearest neighbor is predicted to be negative under plastic zone flow, capillary spreading and gravity spreading, and positive under disturbed zone flow and particle settling.

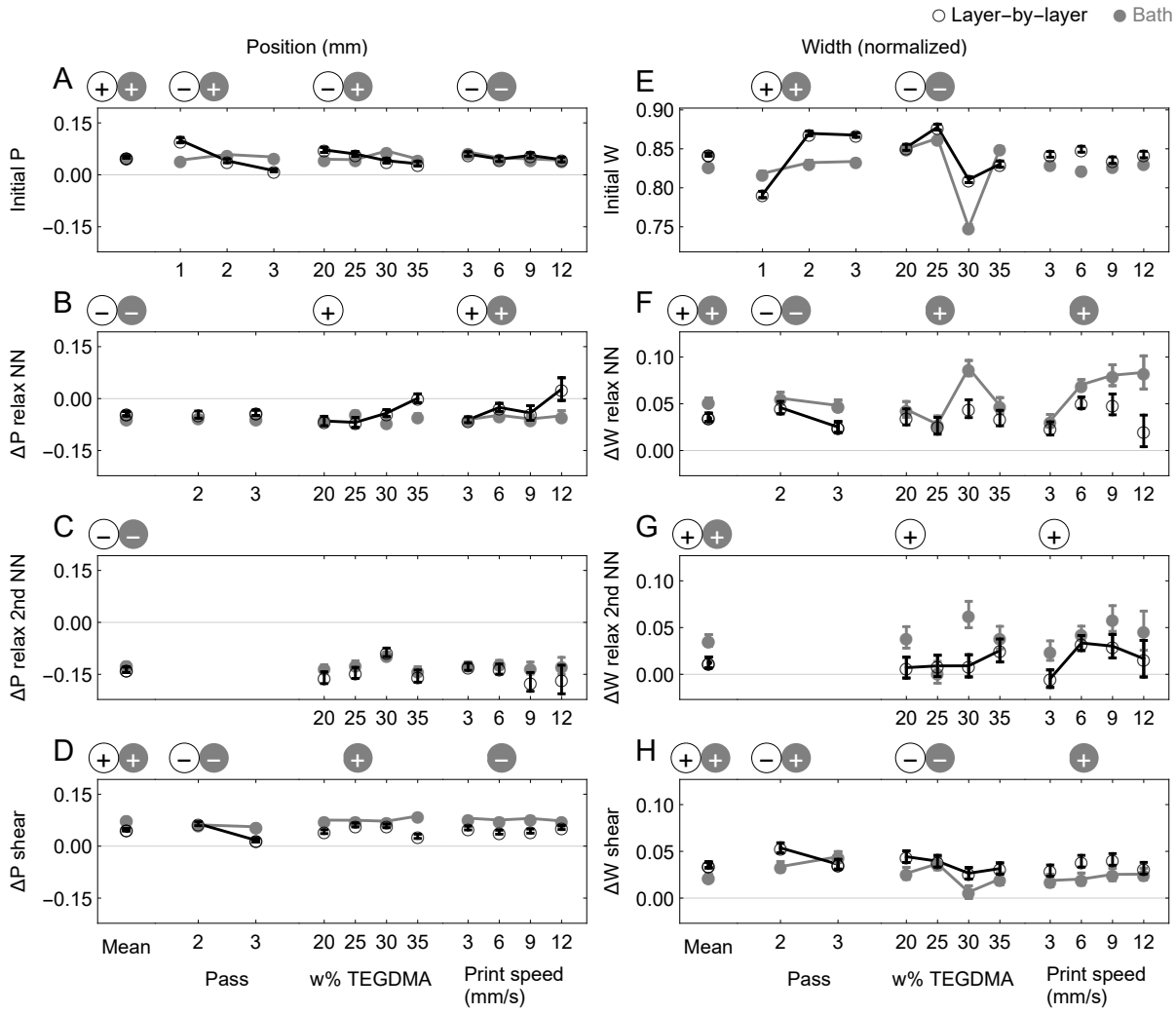

Figure 6.S4: Particle distribution positions (P) and widths (W) as a function of pass number, w% TEGDMA in the ink, and print speed (the flow speed is equal to the translation speed). Distribution widths are normalized by the width of a uniform distribution. Changes during relaxation are only collected for relaxation times above 7.5 seconds. Error bars indicate standard error. Signs of statistically significant ($p < 0.05$) Kendall τ parameters are shown.

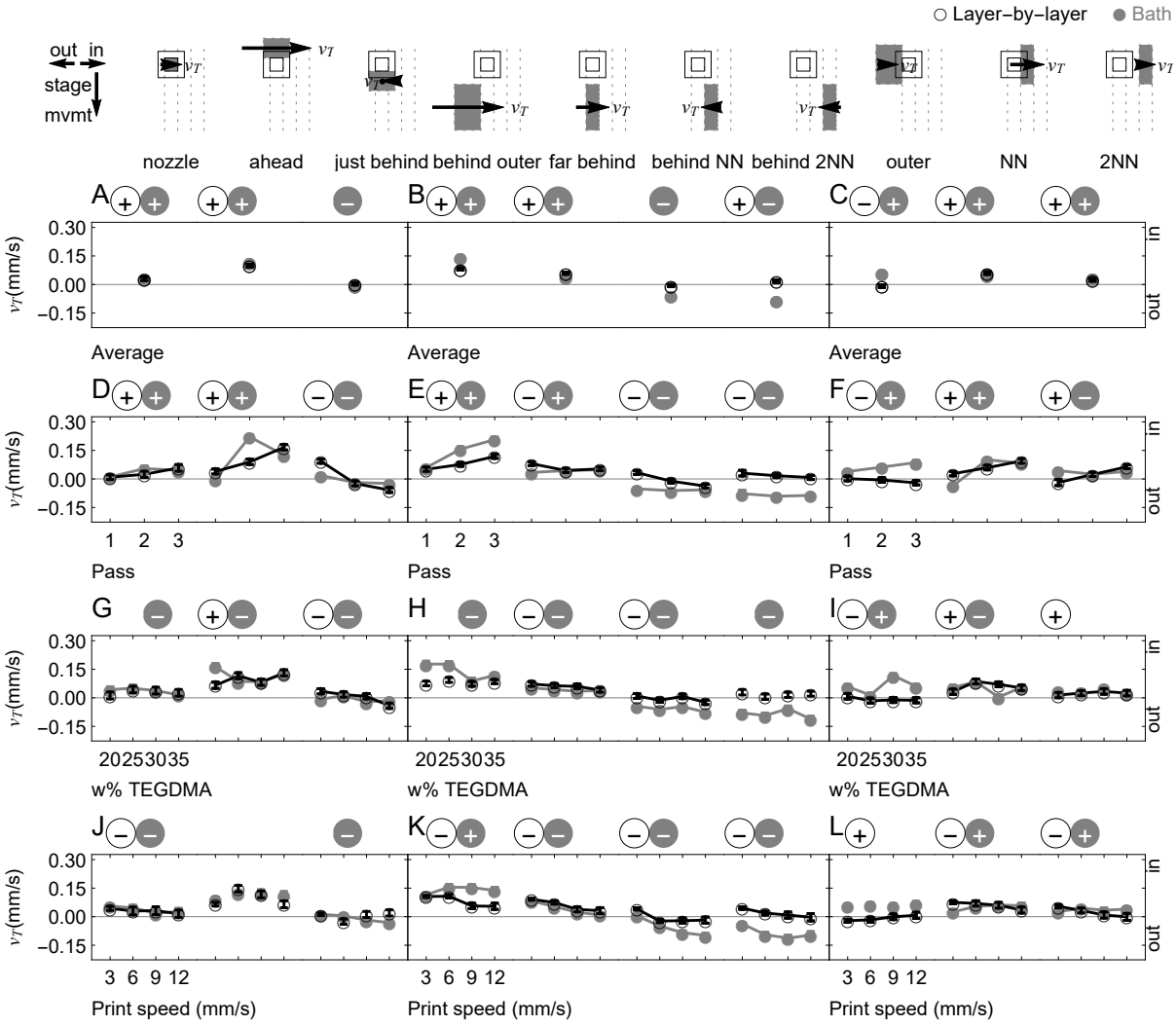

Figure 6.S5: Average transverse flow velocities within ten regions. Positive v_T signifies inward flows toward the center of the polygon and nearest neighbors. Signs of statistically significant ($p < 0.05$) Kendall τ parameters are shown. "NN" nearest neighbor, "2NN' second nearest neighbor.

Table 6.S4: Signs of predicted transverse flows and particle distribution changes due to plastic flow. Δ, pass is the change on successive passes; Δ, TEGDMA is the change with increasing TEGDMA concentration in the ink; Δ, speed is the change with increasing print speed, which is equal to the flow speed and the translation speed. "NN" nearest neighbor, "2NN" second nearest neighbor.

	nozzle	ahead	just behind	behind outer	far behind	behind NN	behind 2NN	outer	NN	2NN	Initial position	Δposition relax NN	Δposition relax 2NN	Δposition shear	Initial width	Δwidth relax NN	Δwidth relax 2NN	Δwidth shear
Layer by layer																		
Average	$-^{1}$	$-^{1}$	$-^{1}$	$+^{2}$	$-^{1}$	$-^{3}$	$-^{3}$	$+^{2}$	$-^{3}$	$-^{3}$	$-^{1}$	$-^{1}$	$-^{3}$			$-^{4}$	$-^{4}$	
Δ, pass	$+^{5}$	$+^{5}$	$+^{5}$	$+^{5}$	$+^{5}$	$+^{5}$	$+^{5}$	$+^{5}$	$+^{5}$	$+^{5}$	$+^{5}$	$+^{5}$			$-^{6}$	$+^{7}$		
Δ, TEGDMA	$-^{8}$	$-^{8}$	$-^{8}$	$+^{8}$	$-^{8}$	$-^{8}$	$-^{8}$	$+^{8}$	$-^{8}$	$-^{8}$	$-^{8}$	$-^{8}$	$-^{8}$		$-^{8}$	$-^{8}$	$-^{8}$	
Δ, speed	$-^{9}$	$-^{9}$	$-^{9}$	$+^{9}$	$-^{9}$	$-^{9}$	$-^{9}$	$+^{9}$	$-^{9}$	$-^{9}$	$-^{9}$	$-^{9}$	$-^{9}$		$-^{9}$	$-^{9}$	$-^{9}$	
Bath																		
Average	$+^{10}$	$+^{10}$	$+^{10}$	$+^{11}$	$+^{10}$	$-^{12}$	$-^{12}$	$+^{11}$	$-^{12}$	$-^{12}$	$+^{10}$	$+^{10}$	$-^{12}$			$-^{4}$	$-^{4}$	
Δ, pass	$+^{10}$	$+^{10}$	$+^{10}$	$+^{13}$	$+^{10}$	$+^{12}$	$+^{12}$	$+^{13}$	$+^{12}$	$+^{12}$	$+^{10}$	$+^{10}$			$+^{14}$	$+^{14}$		
Δ, TEGDMA	$+^{8}$	$+^{8}$	$+^{8}$	$+^{8}$	$+^{8}$	$-^{8}$	$-^{8}$	$+^{8}$	$-^{8}$	$-^{8}$	$+^{8}$	$+^{8}$	$-^{8}$		$-^{8}$	$-^{8}$	$-^{8}$	
Δ, speed	$+^{9}$	$+^{9}$	$+^{9}$	$+^{9}$	$+^{9}$	$-^{9}$	$-^{9}$	$+^{9}$	$-^{9}$	$-^{9}$	$+^{9}$	$+^{9}$	$-^{9}$		$+^{9}$	$-^{9}$	$+^{9}$	

1. On pass 1, 2, and 3, respectively, transverse flows in line with the nozzle are outward, nil, and slightly inward, leading to an average outward (negative) flow

2. On pass 1, 2, and 3, respectively, transverse flows in line with the nozzle are nil, nil, and slightly inward, leading to an average inward (positive) flow.

3. On pass 1, 2, and 3, respectively, transverse flows in line with the nozzle are outward, nil, and outward, leading to an average outward (negative) flow.
4. Flow of the yielded support material compresses the written ink line.
5. On pass 1, 2, and 3, respectively, transverse flows in line with the nozzle are outward, nil, and slightly inward, leading to an inward (positive) increase in transverse flow velocity with pass number.
6. On successive passes, with decreasing ink viscosity, and with faster speeds, the ink line compresses more because, respectively, the deposited line is more bounded, less resistant to flow, and less resistant to flow due to increased shear rate at fast speeds.
7. Flow of the yielded support material compresses the written ink line a lot less on pass 2, then a little more on pass 3
8. More TEGDMA lowers the viscosity of the ink, enabling more flow.
9. Increasing the translation speed increases the size of the plastic zone.
10. On pass 1, 2, and 3, respectively, transverse flows in line with the nozzle are nil, slightly inward, and slightly inward, leading to an average inward (positive) flow.
11. Ink flows inward on all passes.
12. Ink in the nearest neighbors shifts outward on the first pass during relaxation, then slightly shifts inward on successive passes.

13. The inner boundary becomes more compliant, and the outer boundary becomes less compliant on successive passes.

14. The ink becomes much less bounded on pass 2, then only slightly more bounded on pass 3.

Table 6.S5: Signs of predicted transverse flows and particle distribution changes due to inertial disturbed zone flow. Δ, pass is the change on successive passes; Δ, TEGDMA is the change with increasing TEGDMA concentration in the ink; Δ, speed is the change with increasing print speed, which is equal to the flow speed and the translation speed. "NN" nearest neighbor, "2NN" second nearest neighbor.

	nozzle	ahead	just behind	behind outer	far behind	behind NN	behind 2NN	outer	NN	2NN	Initial position	Δposition relax NN	Δposition relax 2NN	Δposition shear	Initial width	Δwidth relax NN	Δwidth relax 2NN	Δwidth shear
Layer by layer																		
Average	$-^{1}$	$-^{1}$	$-^{1}$	$+^{2}$	$-^{1}$	$-^{2}$	$-^{2}$	$-^{3}$	$+^{3}$	$+^{3}$	$-^{1}$	$-^{1}$	$-^{2}$	$+^{3}$		$-^{2}$	+	-
Δ, pass	$+^{4}$	$+^{4}$	$+^{4}$	$+^{4}$	$+^{4}$	$+^{4}$	$+^{4}$	$+^{4}$	$+^{4}$	$+^{4}$	$+^{4}$	$+^{4}$		$+^{4}$	$-^{5}$	$-^{4}$		$-^{4}$
Δ, TEGDMA	$+^{6}$	$+^{6}$	$-^{6}$	$-^{6}$	$-^{6}$	$+^{6}$	$+^{6}$	$+^{6}$	$-^{6}$	$-^{6}$	$+^{6}$	$-^{6}$	$+^{6}$	$-^{6}$	$-^{6}$	$-^{6}$	$-^{6}$	$+^{6}$
Δ, speed	$+^{6}$	$+^{6}$	$-^{6}$	$-^{6}$	$-^{6}$	$+^{6}$	$+^{6}$	$+^{6}$	$-^{6}$	$-^{6}$	$+^{6}$	$-^{6}$	$+^{6}$	$-^{6}$	$-^{6}$	$-^{6}$	$-^{6}$	$+^{6}$
Bath																		
Average	$+^{1}$	$+^{1}$	$+^{1}$	$+^{2}$	$+^{1}$	$-^{2}$	$-^{2}$	$-^{3}$	$+^{3}$	$+^{3}$	$+^{1}$	$+^{1}$	$-^{2}$	$+^{3}$		$-^{2}$	+	-
Δ, pass	$+^{4}$	$+^{4}$	$+^{4}$	$+^{4}$	$+^{4}$	$+^{4}$	$+^{4}$	$+^{4}$	$+^{4}$	$+^{4}$	$+^{4}$	$+^{4}$	$+^{4}$	$+^{4}$	$+^{4}$	$-^{4}$		-
Δ, TEGDMA	$-^{6}$	$-^{6}$	$+^{6}$	$-^{6}$	$+^{6}$	$+^{6}$	$+^{6}$	$+^{6}$	$-^{6}$	$-^{6}$	$-^{6}$	$+^{6}$	$+^{6}$	$-^{6}$	$-^{6}$	$-^{6}$	$-^{6}$	$+^{6}$
Δ, speed	$-^{6}$	$-^{6}$	$+^{6}$	$-^{6}$	$+^{6}$	$+^{6}$	$+^{6}$	$+^{6}$	$-^{6}$	$-^{6}$	$-^{6}$	$+^{6}$	$+^{6}$	$-^{6}$	$-^{6}$	$-^{6}$	$-^{6}$	$+^{6}$

1. The disturbed zone is larger on the inner edge than the outer edge.

2. The disturbed zone narrows behind the nozzle.

3. The disturbed zone widens at the nozzle.

4. On successive passes, the inner side of the disturbed zone grows due to a more compliant inner boundary, while the outer disturbed zone shrinks due to a less compliant outer boundary.

5. The Oldroyd number decreases on the inner edge by less than it increases on the outer edge.

6. Increasing the TEGDMA concentration in the ink and increasing the print speed elongates and narrows the disturbed zone.

Table 6.S6: Signs of predicted transverse flows and particle distribution changes due to capillary spreading. Δ, pass is the change on successive passes; Δ, TEGDMA is the change with increasing TEGDMA concentration in the ink; Δ, speed is the change with increasing print speed, which is equal to the flow speed and the translation speed. "NN" nearest neighbor, "2NN" second nearest neighbor.

	nozzle	ahead	just behind	behind outer	far behind	behind NN	behind 2NN	outer	NN	2NN	Initial position	Δposition relax NN	Δposition relax 2NN	Δposition shear	Initial width	Δwidth relax NN	Δwidth relax 2NN	Δwidth shear
Layer by layer																		
Average	$-^{1}$	$-^{1}$	$-^{1}$	$-^{1}$	$-^{1}$	$-^{2}$	$-^{2}$	$-^{1}$	$-^{2}$	$-^{2}$	$-^{1}$	$-^{1}$	$-^{2}$	$-^{1}$	$+^{3}$	$+^{3}$	$+^{4}$	$+^{3}$
Δ, pass	$+^{5}$	$+^{5}$	$+^{5}$	$+^{5}$	$+^{5}$	$+^{5}$	$+^{5}$	$+^{5}$	$+^{5}$	$+^{5}$	$+^{5}$	$+^{5}$		$+^{5}$	$+^{5}$	$+^{5}$		$+^{5}$
Δ, TEGDMA	$-^{6}$	$-^{6}$	$-^{6}$	$-^{6}$	$-^{6}$	$-^{6}$	$-^{6}$	$-^{6}$	$-^{6}$	$-^{6}$	$-^{6}$	$-^{6}$	$-^{6}$	$-^{6}$	$+^{6}$	$+^{6}$	$+^{6}$	$+^{6}$
Δ, speed	$-^{7}$	$-^{7}$	$-^{7}$	$-^{7}$	$-^{7}$	$-^{7}$	$-^{7}$	$-^{7}$	$-^{7}$	$-^{7}$	$-^{7}$	$+^{8}$	$+^{8}$	$-^{7}$	$+^{7}$	$-^{8}$	$-^{8}$	$+^{7}$
Bath																		
Average	$+^{9}$	$+^{9}$	$+^{9}$	$+^{9}$	$+^{9}$	$-^{2}$	$-^{2}$	$+^{9}$	$-^{2}$	$-^{2}$	$+^{9}$	$+^{9}$	$-^{2}$	$+^{9}$	$+^{10}$	$+^{10}$	$+^{4}$	$+^{10}$
Δ, pass	$+^{11}$	$+^{11}$	$+^{11}$	$+^{11}$	$+^{11}$	$-^{12}$	$-^{12}$	$+^{11}$	$-^{12}$	$-^{12}$	$+^{11}$	$+^{11}$		$+^{11}$	$+^{5}$	$+^{5}$		$+^{5}$
Δ, TEGDMA	$+^{6}$	$+^{6}$	$+^{6}$	$+^{6}$	$+^{6}$	$-^{6}$	$-^{6}$	$+^{6}$	$-^{6}$	$-^{6}$	$+^{6}$	$+^{6}$	$-^{6}$	$+^{6}$	$+^{6}$	$+^{6}$	$+^{6}$	$+^{6}$
Δ, speed	$+^{7}$	$+^{7}$	$+^{7}$	$+^{7}$	$+^{7}$	$-^{7}$	$-^{7}$	$+^{7}$	$-^{7}$	$-^{7}$	$+^{7}$	$-^{8}$	$+^{8}$	$+^{7}$	$+^{6}$	$-^{8}$	$-^{8}$	$+^{6}$

1. The transverse component of the contact line velocity is greater on glass than on support because the support is sloped.

2. Adding another ink line pulls existing ink lines outwards (negative).

3. The contact lines travel in opposite directions.

4. Only the outer edge of the nearest neighbor is pulled outward.
5. Ink wets ink more strongly than it wets support, so the existing lines on later passes pull the new line inward (positive) more strongly than the support did.
6. Higher TEGDMA concentrations decrease the viscosity of the ink, decreasing its resistance to flow.
7. Faster flow speeds increase the shear strain rate on the ink and decrease its viscosity, decreasing its resistance to flow.
8. Faster translation speeds decrease the relaxation time, decreasing the change during relaxation.
9. Because the support boundary conditions are symmetric, the only shift in the new line due to capillarity happens because existing ink pulls the new line inwards.
10. Only the outer edge of the nearest neighbor is pulled outward. The other contact lines stay in place.
11. On successive passes, more ink-ink contact lines are introduced, increasing the inward pull on the new line.
12. On successive passes, more ink-ink contact lines are introduced, increasing the outward pull on the existing line.

Table 6.S7: Signs of predicted transverse flows due to gravitational spreading. Δ, pass is the change on successive passes; Δ, TEGDMA is the change with increasing TEGDMA concentration in the ink; Δ, speed is the change with increasing print speed, which is equal to the flow speed and the translation speed. "NN" nearest neighbor, "2NN" second nearest neighbor.

	nozzle	ahead	just behind	behind outer	far behind	behind NN	behind 2NN	outer	NN	2NN	Initial position	Δposition relax NN	Δposition relax 2NN	Δposition shear	Initial width	Δwidth relax NN	Δwidth relax 2NN	Δwidth shear
Layer by layer																		
Average	$^{-1}_{+3}$	$^{-1}_{+3}$	$^{-1}_{+3}$	$^{-1}_{+3}$	$^{-1}_{+3}$	$^{-1}_{+3}$	$^{-1}_{+3}$	$^{-1}_{+3}$	$^{-1}_{+3}$	$^{-1}_{+3}$	$^{-1}_{+3}$	$^{-1}_{+3}$	$^{-1}$	$^{-1}_{+3}$	$^{+2}_{-4}$	$^{+2}_{-4}$	$^{+2}$	$^{+2}_{-4}$
Δ, pass	$^{+3}_{-5}$	$^{+3}_{-5}$	$^{+3}_{-5}$	$^{+3}_{-5}$	$^{+3}_{-5}$	$^{+3}_{-5}$	$^{+3}_{-5}$	$^{+3}_{-5}$	$^{+3}_{-5}$	$^{+3}_{-5}$	$^{+3}_{-5}$	$^{+3}_{-5}$	$^{+6}$	$^{+3}$	$^{+5}_{-5}$	$^{+5}_{-6}$	$^{+5}_{-6}$	$^{+5}_{-5}$
Δ, TEGDMA	$^{-5}_{-5}$	$^{-5}_{-5}$	$^{-5}_{-5}$	$^{-5}_{-5}$	$^{-5}_{-5}$	$^{-5}_{-5}$	$^{-5}_{-5}$	$^{-5}_{-5}$	$^{-5}_{-5}$	$^{-5}_{-5}$	$^{-5}_{-5}$	$^{-5}_{-5}$	$^{-5}_{-5}$	$^{-5}_{-5}$	$^{+5}_{-5}$	$^{+5}_{-6}$	$^{+5}_{-6}$	$^{+5}_{-5}$
Δ, speed																		
Bath																		
Average																		
Δ, pass																		
Δ, TEGDMA																		
Δ, speed																		

1. There is no barrier to spreading on the outer edge.
2. The center of gravity settles lower onto the substrate, widening the line.
3. On pass 1 and 2, the deposited line shifts outward, but on the last pass, the line is bordered on both sides by support, so it does not shift due to gravity.

4. On pass 1 and 2, the deposited line spreads, but on the last pass, the line is bordered on both sides by support, so it does not spread due to gravity.
5. Increasing the TEGDMA content and increasing the print speed decreases the ink viscosity, decreasing its resistance to spreading.
6. Increasing the translation speed decreases the relaxation time, decreasing changes due to relaxation.

Table 6.S8: Signs of predicted transverse flows and particle distribution changes due to particle settling. Δ, pass is the change on successive passes; Δ, TEGDMA is the change with increasing TEGDMA concentration in the ink; Δ, speed is the change with increasing print speed, which is equal to the flow speed and the translation speed. "NN" nearest neighbor, "2NN" second nearest neighbor.

	nozzle	ahead	just behind	behind outer	far behind	behind NN	behind 2NN	outer	NN	2NN	Initial position	ΔPosition relax NN	ΔPosition relax 2NN	ΔPosition shear	Initial width	ΔWidth relax NN	ΔWidth relax 2NN	ΔWidth shear
Layer by layer																		
Average	1	1	1	$-^{2}$	1	$+^{2}$	$+^{2}$	$-^{2}$	$+^{2}$	$+^{2}$						$+^{3}$	$+^{3}$	
Δ, pass				4		4	4	4	4	4								
Δ, TEGDMA				$-^{5}$		$+$	$+$	$-^{5}$	$+$	$+$					$+^{5}$	$+^{5}$	$+^{5}$	
Δ, speed				$-^{6}$		$+^{6}$	$+^{6}$	$-^{6}$	$+^{6}$	$+^{6}$					$+^{6}$	$-^{7}$	$-^{7}$	
Bath																		
Average				$-^{2}$		$+^{2}$	$+^{2}$	$-^{2}$	$+^{2}$	$+^{2}$						$+^{3}$	$+^{3}$	
Δ, pass				4		4	4	4	4	4								
Δ, TEGDMA				$-^{5}$		$+$	$+$	$-^{5}$	$+$	$+$					$+^{5}$	$+^{5}$	$+^{5}$	
Δ, speed				$-^{6}$		$+^{6}$	$+^{6}$	$-^{6}$	$+^{6}$	$+^{6}$					$+^{6}$	$-^{7}$	$-^{7}$	

1. Because settling is symmetric, flows in line with the nozzle are net nil.

2. Settling causes the particles to spread outward, resulting in inward (positive) flows inward of the nozzle in the nearest neighbors and outward (negative) flows outward of the nozzle on the left.

3. Settling increases the distribution width.

4. Settling involves movement of particles through the bulk, so boundary conditions do not specifically influence settling.

5. Increasing the TEGDMA concentration decreases the ink viscosity, increasing the terminal velocity of the settling particles.

6. Increasing the flow speed increases the shear rate on the ink, decreasing its viscosity and increasing the terminal velocity of the settling particles.

7. Increasing the translation speed decreases the relaxation time, decreasing changes due to relaxation.

Table 6.S9 shows the experimental signs of the average value of the dependent variables and the Kendall τ correlation parameters. For example, in layer-by-layer support, the average transverse flow velocity in the nearest neighbor is positive. Thus, disturbed zone flow and/or particle settling are likely influential in the nearest neighbor because they predict positive average transverse flow velocities in the nearest neighbor. To further refine whether the transverse flow velocity in the nearest neighbor is influenced more by disturbed zone flow or particle settling, one can consider the change in transverse flow velocity with print speed. The transverse flow velocity becomes more negative with increasing speed, which is predicted by plastic zone flow, disturbed zone flow, capillary spreading, and gravity spreading, but not particle settling. Thus, from these two measurements, one can postulate that disturbed zone flow is the most influential effect in the nearest neighbor. To more precisely quantify the confidence that an effect influences an independent variable (transverse flow velocity in a given region, distribution position, distribution width, change in distribution position, or change in distribution width), one can use the following metric τ_{all} which runs from -10 to 10. τ_{all} is calculated for each combination of dependent variable and driving force, for example transverse flow velocity in the nearest neighbor and disturbed zone flow. A large positive τ_{all} value indicates high confidence that the driving force influences the dependent variable. A large negative τ_{all} value indicates high confidence that the driving force does not influence the dependent variable.

Table 6.S9: Summary of signs of experimental transverse flows and particle distribution changes, from Figures 6.S4 and 6.S5. Δ, pass is the change on successive passes; Δ, TEGDMA is the change with increasing TEGDMA concentration in the ink; Δ, speed is the change with increasing print speed, which is equal to the flow speed and the translation speed. "-" indicates a negative correlation where $-0.1 < \tau < 0$, "++" indicates a stronger positive correlation where $0.1 < \tau < 0.2$, and so on, where $-1 < \tau < 1$. "NN" nearest neighbor, "2NN" second nearest neighbor.

	nozzle	ahead	just behind	behind outer	far behind	behind NN	behind 2NN	outer	NN	2NN	Initial position	Δposition relax NN	Δposition relax 2NN	Δposition shear	Initial width	Δwidth relax NN	Δwidth relax 2NN	Δwidth shear
Layer by layer																		
Average	+	+		+	+		+	-	+	+	+	-		+		+	+	+
Δ, pass	+	‡	- - -	‡	-	- -	-	-	‡	‡	-			- -	‡	-		-
Δ, TEGDMA		+	-		-	-		-	+	+	-	+	+	+	- -			-
Δ, speed	-			- -	- -	- -	-	+	-	-	-	+	+					
Bath																		
Average	+	+	-	+	+	-	-	+	+	-	+	-		+	-	-	+	+
Δ, pass	+	‡	- -	‡	+	-	-	‡	‡	-	+	-			+	+		+
Δ, TEGDMA	-	-	-	-	-	-	-	+	-		+				-	+		-
Δ, speed	-		-	+	- - -	- - -	- -	- -	-	+	-	+		-				+

$$\tau_{all} = \frac{10}{4}\Big(\mu_t \frac{\mu_e}{\mu_{max}} + \sum_{pass,TEGDMA,speed} \tau_t \times \begin{cases} \frac{\tau_e}{\tau_{max}} & p \leq 0.05 \\ 0 & p > 0.05 \end{cases}\Big) \tag{6.S3}$$

The factor of 10/4 normalizes τ_{all} to run from -10 to 10. μ_t is the predicted sign of the independent variable, -1 or 1. μ_e is the experimental average value of the independent variable. μ_{max} is the maximum absolute value of μ_e across transverse velocities in all regions, all positions and changes in position, or all changes in width, whichever set the probed independent variable belongs to. Because all widths are positive, the first term is equal to 0 when the dependent variable is initial width. The second term is summed over the independent variables pass number, TEGDMA concentration, and print speed. τ_t is the predicted Kendall τ parameter for the correlation between the independent variable and the dependent variable, -1 or 1. τ_e is the experimental τ correlation parameter between the dependent and independent variable. τ_{max} is the maximum absolute τ_e achieved in this data set for the given independent variable for all transverse velocities, positions and changes in position, or widths and changes in width, whichever set the probed independent variable belongs to. p is the p-value for the experimental Kendall τ test.

τ_{all} values are shown in Table 6.S10. For metrics with similar behaviors, the τ_{all} value is averaged. For example, "behind inner" represents two regions: behind nearest neighbor and behind second nearest neighbor, so the plastic zone/behind inner τ_{all} value is the average of the τ_{all} values for the effect of plastic zone flow on transverse flows in the two regions. A large positive τ_{all} indicates high confidence that the theory influences the given metric, while a large negative number indicates high confidence against the theory. For example, in layer-by-layer support disturbed zone flow likely is influential in the behind outer region ($\tau_{all} = 6$) but not behind inner ($\tau_{all} = -4$).

Table 6.S10: τ_{all} values indicating confidence in the effect of the five proposed effects (plastic zone, etc.) on transverse flows in various regions and changes in the particle distribution over the course of the print. "behind inner" encompasses behind nearest neighbor and behind second nearest neighbor, and "inner" encompasses the nearest neighbor and second nearest neighbor regions. For the particle distributions, both position and width are considered. τ_{all} ranges from -10 to 10, with 10 indicating high confidence in the influence of the effect on transverse flows or particle distributions and -10 indicating high confidence against the effect.

	Transverse flows								Particle distributions			
	ahead	nozzle	just behind	behind outer	far behind	behind inner	outer	inner	Initial	Δrelax NN	Δrelax 2NN	Δshear
Layer-by-layer												
Plastic zone		*-2*		1	2	1	*-1*	1		*-4*	*-1*	
Disturbed zone	*-1*			6	2	*-4*		3	*-3*	*-3*		*-2*
Capillary spreading		*-2*		2	2	1		1		1	1	*-1*
Gravity spreading		*-2*		2	2	1		1	*-2*	2	1	
Settling						*-2*			*-1*	1		
Bath												
Plastic zone		3	*-3*	3	*-2*	4	4		4	*-4*		
Disturbed zone	3	6	*-3*	7	*-2*	*-2*	2	2	4	*-2*	2	*-2*
Capillary spreading		3	*-3*	3	*-2*	4	4	*-2*	2	*-1*	2	2
Gravity spreading												
Settling						*-4*	*-3*	1	*-1*	1	1	

Table 6.S11: Expanded version of Table 6.S10.
Transverse flows

	Particle distributions																			
	ahead	nozzle	just behind	behind outer	far behind	behind NN	behind 2NN	outer	NN	2NN	Initial pos	Initial width	Δ pos relax NN	Δ pos relax 2NN	Δ width relax NN	Δ width relax 2NN	Δpos shear	Δwidth shear		
Layer-by-layer																				
Plastic zone		-2		1	2	2	1	-1		2	1		-4	2	-3	-5				
Disturbed zone	-1			6	2	-5	-3		3	3	-6		-4	2	-2	-3	-2	-2		
Capillary spreading		-2		2	2	2	1			2	1		1	2	2		-3	1		
Gravity spreading		-2		2	2	2	1			2	1	-5	1	2	3		-3	3		
Settling						-3	-1		1	-1		-2			2					
Bath																				
Plastic zone		3	-3	3	-2	5	3	4	2	-1	4	5		2	-9	-2				
Disturbed zone	3	6	-3	7	-2	-3	-1	2	4		4	5		2	-5	2	-2	-3		
Capillary spreading		3	-3	3	-2	5	4	4	-3	-1	4		-2	2		2	1	2		
Gravity spreading																				
Settling						-5	-4	-3		1		-2			2	2				

Table 6.S10 can be used to postulate what effects influence transverse flows and particle distributions in different locations and times in the printing process. In some cases, no effects predict the behavior of the system. For example, for transverse flows within the nozzle, no driving forces have positive τ_{all} confidence values.

In other cases, the behavior of the system could be explained by many driving forces. For example, in the behind outer region in layer-by-layer support, plastic zone, disturbed zone, capillary spreading, and gravity spreading all have positive τ_{all} confidence values. This could be because of overlapping predictions. The magnitude of τ_{all} is useful in this case. Disturbed zone flow is more likely than plastic zone flow to influence transverse flow in the behind outer region because it has a much larger τ_{all} value.

Far behind the nozzle, all τ_{all} parameters are equal to 2. Care must be taken when considering the meaning of this case. Similar τ_{all} values could occur where multiple driving forces predict the same trend. Consider the following example. Force A and force B both predict that the transverse flows increase with TEGDMA concentration. Only force A is influential in the system, so transverse flows increase with TEGDMA concentration. However, the resultant τ_{all} confidence values are the same for force A and force B because they predict the same trend. Alternatively, this could occur where each driving force accurately predicts different trends. Consider the following example. Force A causes transverse flows to strongly scale positively with TEGDMA and weakly scale negatively with print speed, and force B causes transverse flows to weakly scale negatively with TEGDMA and strongly scale positively with print speed. Force A and force B are both influential in the system, so the experimental transverse flow velocity increases with both TEGDMA concentration and print speed. The resultant τ_{all} confidence values for force A and force B will be similar because they each accurately predict one experimental trend.

The τ_{all} confidence analysis in Table 6.S10 indicates differences in the prominence of plastic zone flow in layer-by-layer and bath support. Confidence values for plastic zone flow are

higher in bath support than layer-by-layer support, which could be because bath support requires a larger volume of yielded support material. However, in bath support, evidence of plastic zone flow can be observed inside the nozzle, behind to the sides, and in the outer region, which are largely incongruous regions and may only match plastic zone predictions because of overlap with capillary spreading (Table 6.S10). Likewise, the evidence of plastic zone flow impacting the initial distribution might be due to overlaps with disturbed zone flow and capillary spreading (Table 6.S10).

Disturbed zone flow exhibits the highest confidence values of all of the effects, for both layer-by-layer and bath support. Disturbed zone flow is especially prominent in the behind outer region, which makes sense because that region is populated entirely by surplus ink, which would not be subjected to other effects like spreading and shear histories. Otherwise, disturbed zone flow effects can be observed in regions near the nozzle, such as ahead, within the nozzle, in the outer region, and in the inner regions. Disturbed zone flow is the effect that one can reasonably expect to be most localized to the region near the nozzle, so this agrees with expectation. Disturbed zone flow is also prominent in more regions in bath support, which could be because the larger Oldroyd numbers in bath support compact the disturbed zone into the interrogated zone, while in layer-by-layer support the disturbed zone may be larger than the interrogated zone.[100]

τ_{all} confidence values indicate low-level confidence in capillary and gravity spreading for layer-by-layer support and slightly higher confidence in capillary spreading for bath support. It is possible that both types of spreading occur in layer-by-layer support, leading to more diffuse evidence of each spreading force because contact line movement due to gravity and capillarity oppose each other at times. Because there was no predicted effect of gravity spreading in bath support, τ_{all} values must be 0 for gravity spreading in bath support. In layer-by-layer support, spreading can be more prominently observed in the particle distribution during relaxation, while in bath support, evidence of spreading can also be observed in the initial distribution and

change during shear, which could come from overlap with disturbed zone flow or interactions between effects.

Rheology

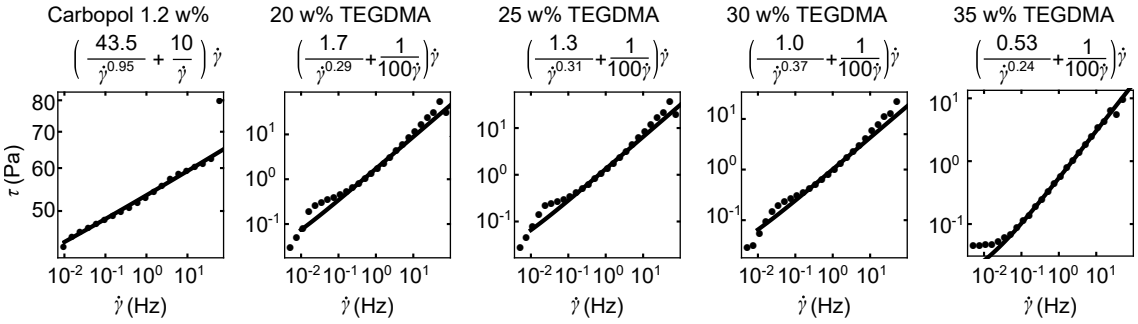

Figure 6.S6: Herschel-Bulkley fits for fluids studied in this experiment. τ is the shear stress, and $\dot{\gamma}$ is the shear strain rate.

Spreading time scales

Depending on the desired characteristics of the particle distribution, relaxation can be useful tool or an obstacle. To understand the roots of changes in distribution during relaxation, the change in distribution as a function of time can be examined. The scaling of the change in distribution with time indicates that the observed spreading is more likely to come from capillarity than gravity. Because polygons were printed with a range of perimeters and printing speeds, initial distributions and distributions after relaxation are measured at varying lengths of time apart. Based on capillarity-driven spreading, the contact line speed should scale with time raised to the 1/10 or 1/7, depending on the model used.[220] Based on gravity-driven spreading, the power law scaling should be 1/5 or 1/8.[220] Based on a combination of gravity and capillarity, scaling should be 1/4 or 1/7.[220] Assuming that the change in position during relaxation and the change in width during relaxation are proportional to the contact line velocity, the changes in position and width during relaxation as a function of time can be used to

evaluate the relative strengths of capillarity and gravity.

Measuring an exact scaling of the spreading velocity in these experiments is not straightforward. Figure 6.S7 shows the change in position and change in width during relaxation as a function of relaxation time for layer-by-layer and bath support. While long time-scale changes in position are negative, short time-scale changes are positive (Fig. 6.S7A,B). Similarly, while long time-scale changes in width are positive, short time-scale changes are negative (Fig. 6.S7C,D). Discarding the few positive changes in position, a linear regression can be fit to the log of the change in position (Δp) as a function of the log of time (t) to determine the scaling of the change in position with time (Fig. 6.S8). These fits demonstrate that the change in position scales with time following the relationship $\Delta p \propto t^{1/10}$. However, because this fit excludes some of the data set, its relevance is questionable. Instead, it may be more appropriate to assume that the change in position follows the equation $\Delta p = a + bt^c$, where a represents some constant positive shift in position that occurs at the point when the relaxed position is measured, possibly because the relaxed position is measured within the disturbed zone or plastic zone. Capping a at 0.6 mm, which is the outer width of the nozzle, the scaling exponent c is on the order of 1/100, which is smaller than any of the models in the literature (Fig. 6.S7A,B).[220] Similarly, fitting the change in width using the same model, the scaling exponent is still on the order of 1/100 (Fig. 6.S7C,D). A more accurate fit for both change in width and position can be achieved with the equation $\Delta p = a + b(t - d)^c$, assuming that for some period of time d after deposition, the printed line does not relax at all, perhaps because the line is still within the disturbed zone (Fig. 6.S9). With time parameters d near 1 second, this fit still produces scaling exponents on the order of 1/100. An experiment which probes longer relaxation times could produce a more precise scaling relationship between the change in position and relaxation time.

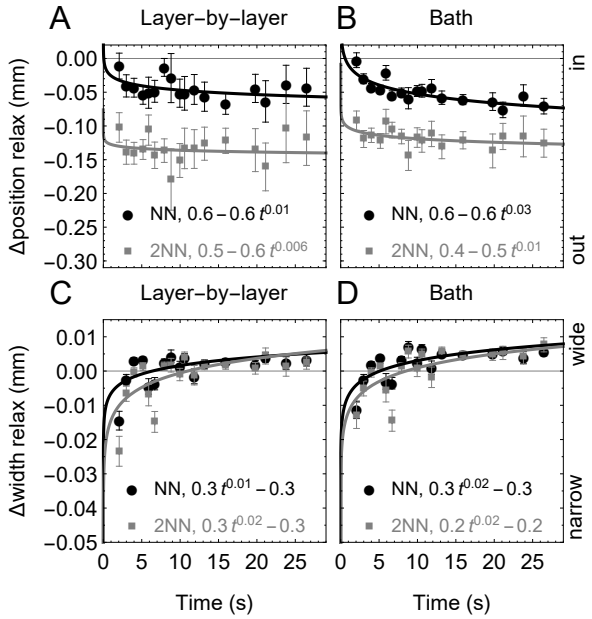

Figure 6.S7: Changes in particle distribution positions and widths during relaxation as a function of time between measurement of the initial and relaxed distributions. Error bars indicate standard error. "NN" nearest neighbor, "2NN" second nearest neighbor.

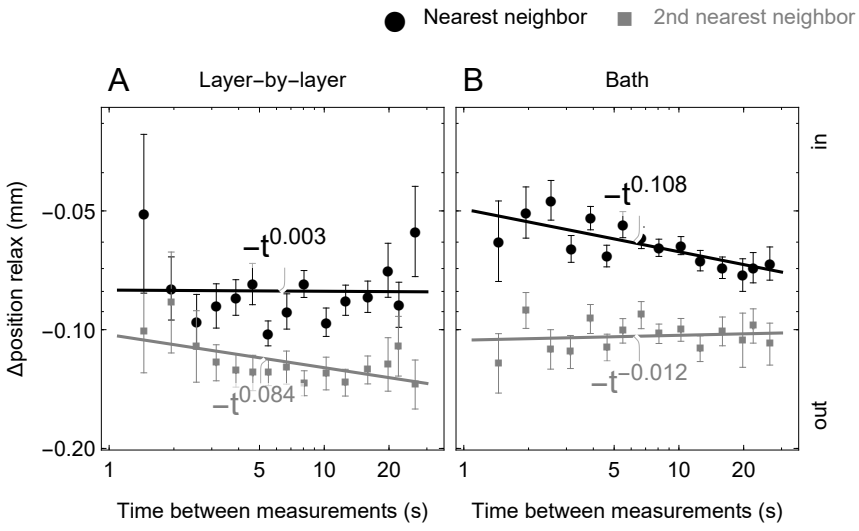

Figure 6.S8: Log-log plot of the negative change in position during relaxation as a function of relaxation time. Positive changes in position are discarded, and averages of logs are shown.

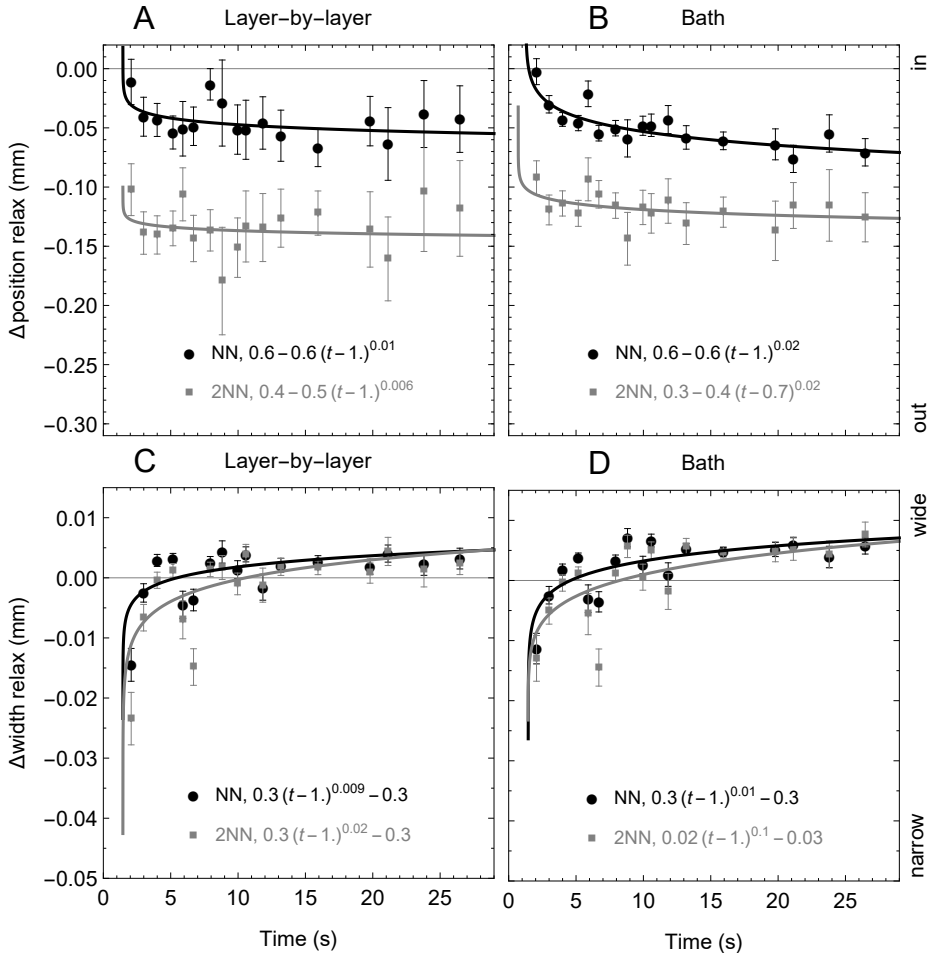

Figure 6.S9: Changes in particle distribution positions and widths during relaxation as a function of time between measurement of the initial and relaxed distributions. Error bars indicate standard error. “NN” nearest neighbor, “2NN” second nearest neighbor.

Correlations between dependent variables

Figures 6.S10–6.S26 and Tables 6.S12–6.S20 show correlations between dependent variables including transverse flow velocities in a given region, particle distribution positions and widths, and changes in particle distribution position and width over the course of the print. Kendall τ text are used to identify the significance and strength of the correlations. Correlations are considered significant where $p < 0.05$. "-" indicates a negative correlation where $-0.1 < \tau < 0$, "++" indicates a stronger positive correlation where $0.1 < \tau < 0.2$, and so on, where $-1 < \tau < 1$.

Table 6.S12: Correlations between absolute particle distribution positions.

	Relaxed position NN	Relaxed position 2NN	Sheared position
Layer-by-layer			
Initial position	+++	++	+++++++
Relaxed position NN		+++++	+++
Relaxed position 2NN			++
Bath			
Initial position	++	++	++++++
Relaxed position NN		++++++	++
Relaxed position 2NN			++

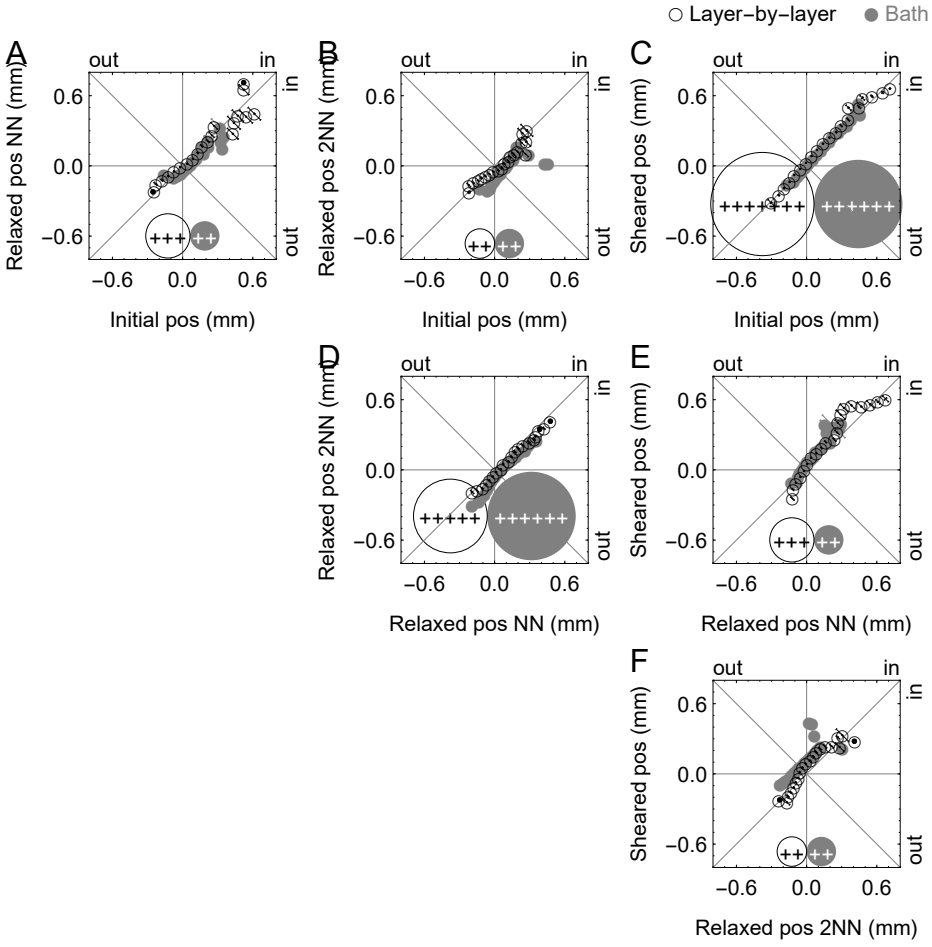

Figure 6.S10: Correlations between absolute particle distribution positions. Error bars indicate standard error with respect to the line $x = y$.

Table 6.S13: Correlations between relative particle distribution positions over the course of the print.

	Δpos relax NN	Δpos relax 2NN	Δpos shear
Layer-by-layer			
Initial pos	- - - - - -	- - - -	+++
Δpos relax NN		++++	- - - - -
Δpos relax 2NN			- - - - -
Bath			
Initial pos	- - - -	- - -	+++
Δpos relax NN		+++++	- - - - -
Δpos relax 2NN			- - - - - -

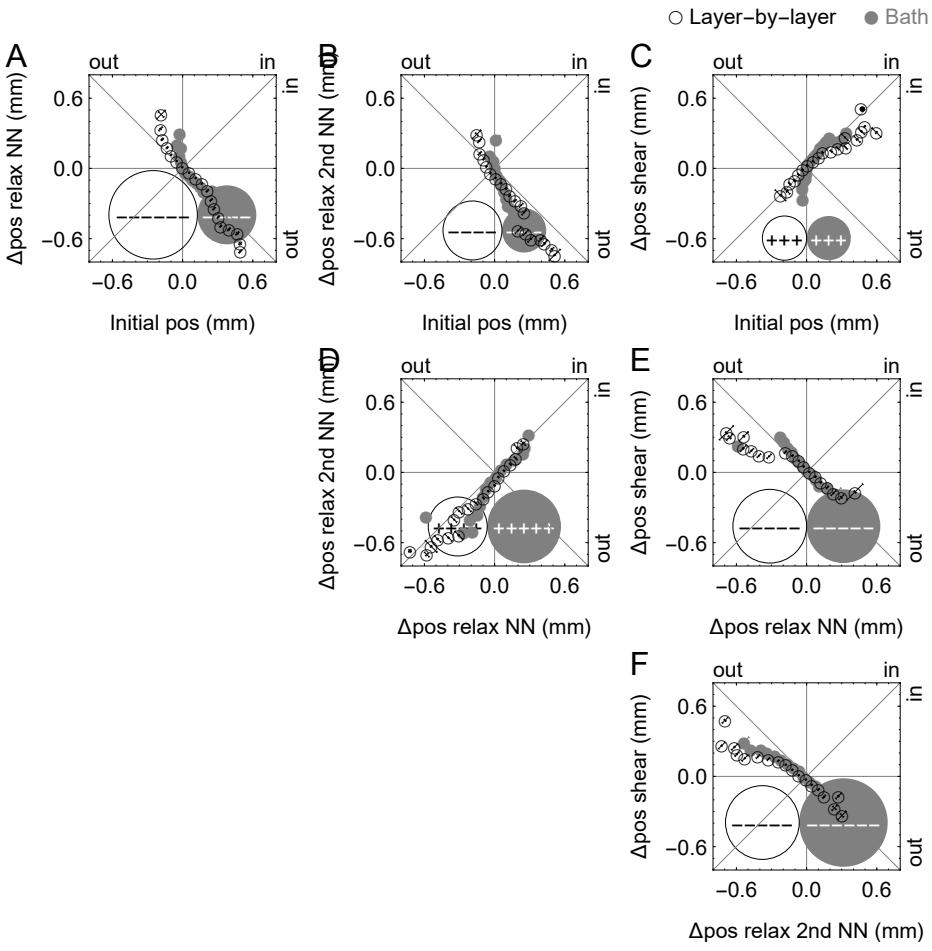

Figure 6.S11: Correlations between relative particle distribution positions over the course of the print. Error bars indicate standard error with respect to the line $x = y$.

Table 6.S14: Correlations between absolute particle distribution widths.

	Relaxed width NN	Relaxed width 2NN	Sheared width
Layer-by-layer			
Initial width	+++	++	+++
Relaxed width NN		++	+++
Relaxed width 2NN			++
Bath			
Initial width	+++	++	++
Relaxed width NN		++	++
Relaxed width 2NN			++

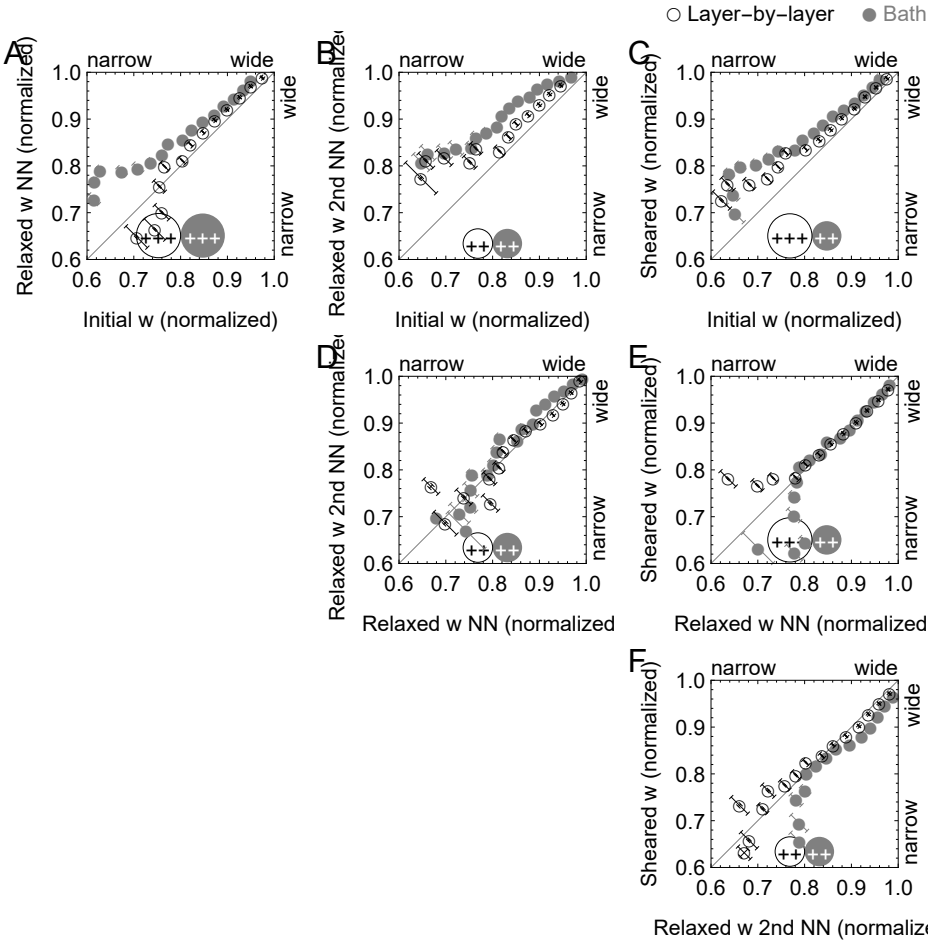

Figure 6.S12: Correlations between absolute particle distribution widths. Error bars indicate standard error with respect to the line $y = 0$ or $-x = y$ or $x = y$.

Table 6.S15: Correlations between relative particle distribution widths over the course of the print.

	Δwidth relax NN	Δwidth relax 2NN	Δwidth shear
Layer-by-layer			
Initial width	- - - -	- -	-
Δwidth relax NN		+++	- - -
Δwidth relax 2NN			- - - - -
Bath			
Initial width	- - - -		- -
Δwidth relax NN		++	- - -
Δwidth relax 2NN			- - - - - -

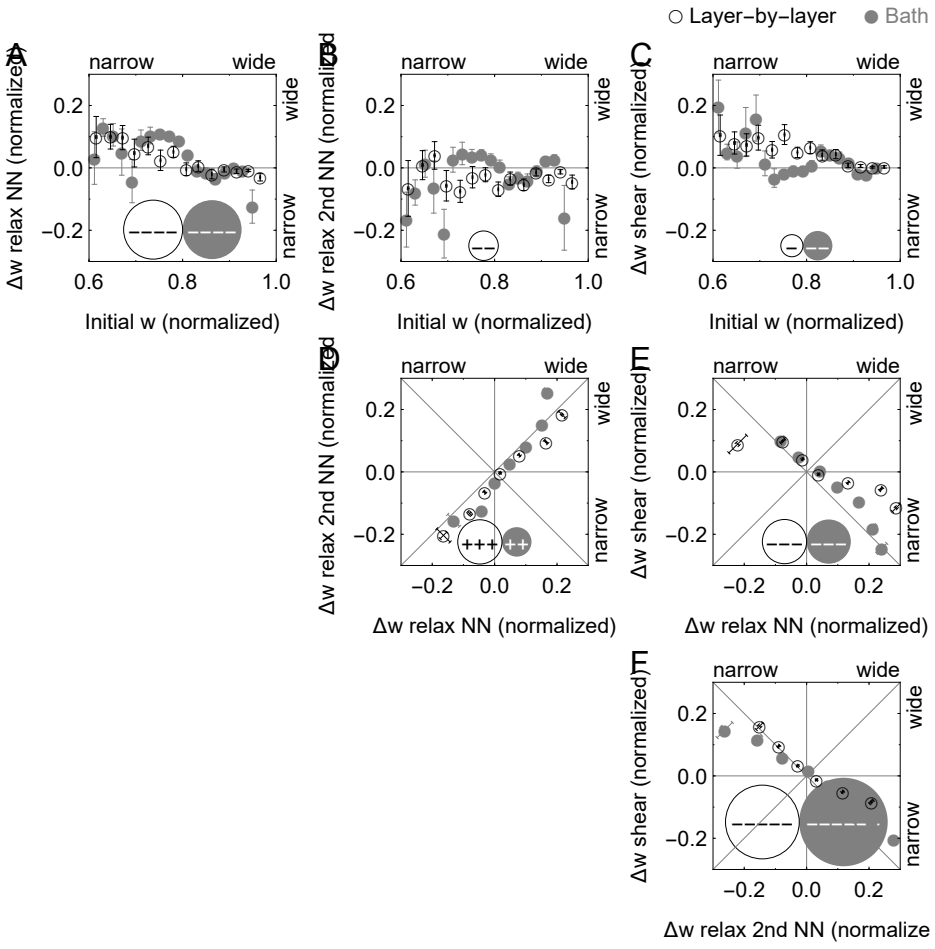

Figure 6.S13: Correlations between relative particle distribution widths over the course of the print. Error bars indicate standard error with respect to the line $y = 0$ or $-x = y$ or $x = y$.

Table 6.S16: Correlations between absolute particle distribution positions and widths.

	Initial position	Relaxed position NN	Relaxed position 2NN	Sheared position
Layer-by-layer				
Initial width			-	-
Relaxed width NN	- -	-	- - -	- -
Relaxed width 2NN	+		- - -	
Sheared width	- -		-	- -
Bath				
Initial width	++	+	-	++
Relaxed width NN			-	
Relaxed width 2NN	- -	- -	- - - -	- -
Sheared width	- -	-	-	- -

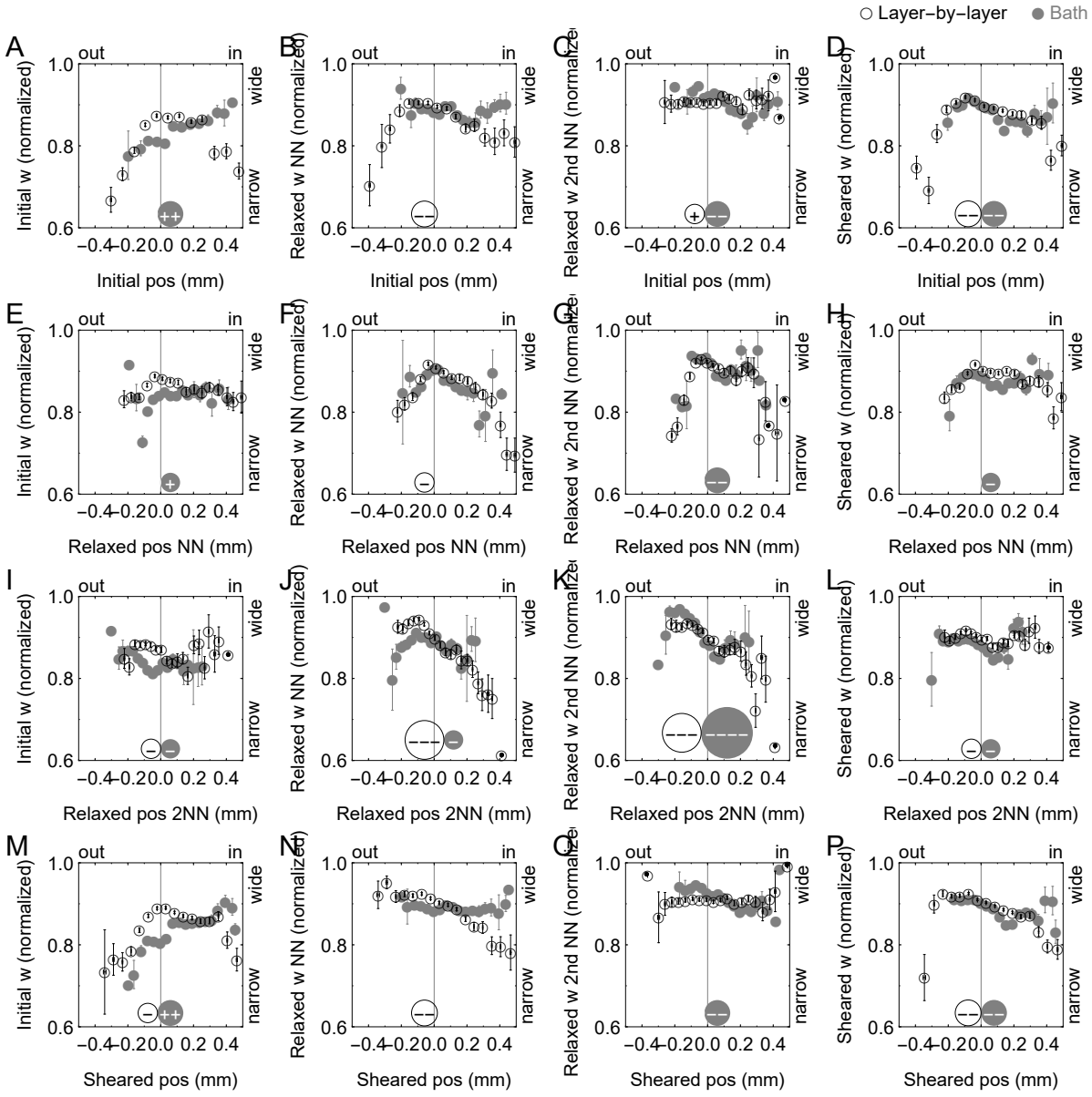

Figure 6.S14: Correlations between absolute particle distribution positions and widths. Error bars indicate standard error with respect to the line $y = 0$.

Table 6.S17: Correlations between relative particle distribution positions and widths over the course of the print.

	Initial pos	Δpos relax NN	Δpos relax 2nd NN	Δpos shear
Layer-by-layer				
Initial width	- -	++	++	-
Δwidth relax NN			- -	+
Δwidth relax 2nd NN	++	-	- - -	++
Δwidth shear	-		++	- -
Bath				
Initial width	++		- -	+
Δwidth relax NN	- -		+	
Δwidth relax 2nd NN	++	- -	- - -	++
Δwidth shear	- -	+	++	- -

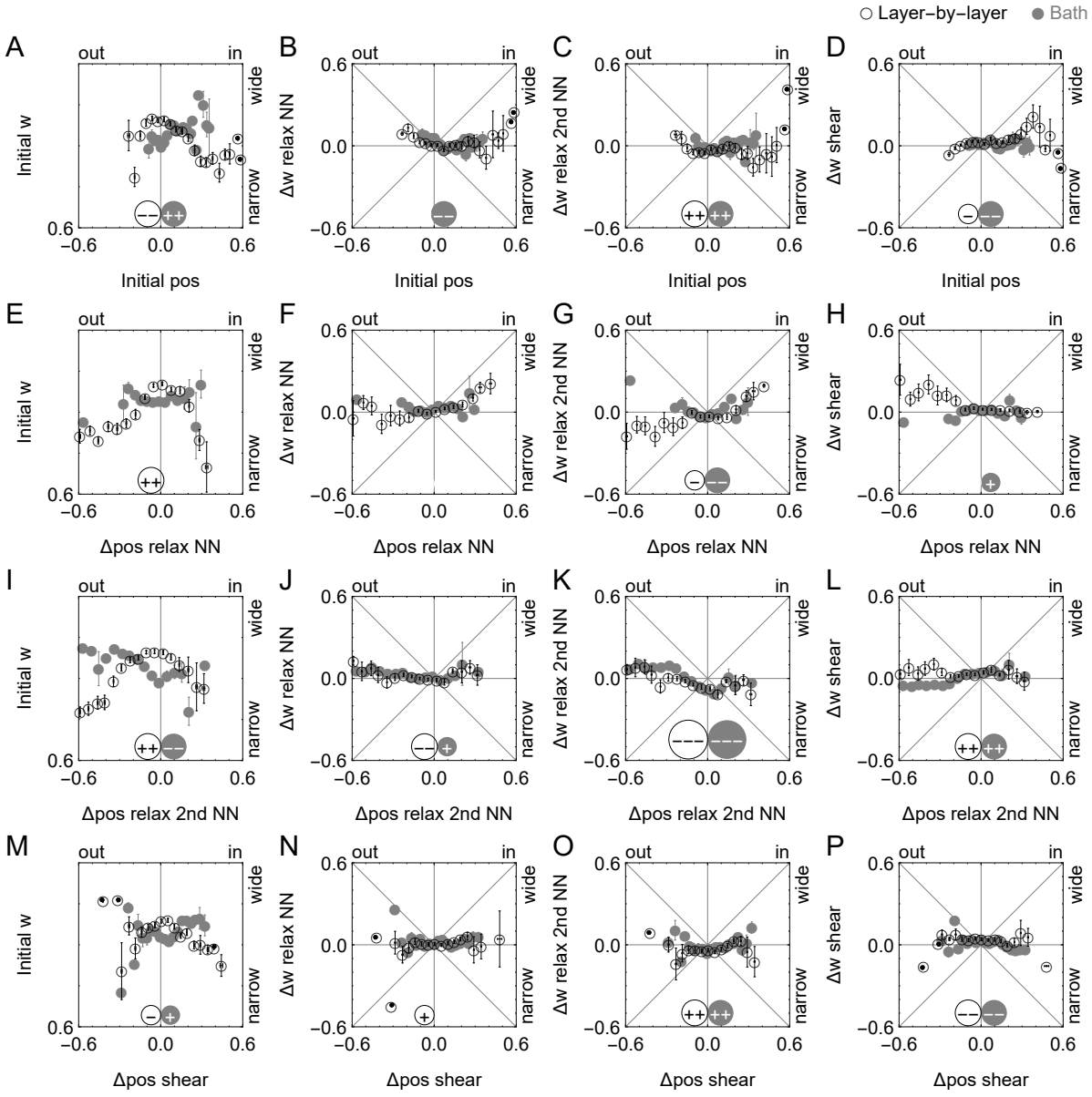

Figure 6.S15: Correlations between relative particle distribution positions and widths over the course of the print. Error bars indicate standard error with respect to the line $y = 0$.

Table 6.S18: Correlations between transverse flow velocities and absolute particle distribution positions and widths over the course of the print.

	nozzle	ahead	just behind	behind outer	far behind	behind NN	behind 2NN	outer	NN	2NN
Layer-by-layer										
Initial position	+	+		+	-	-	-	+	-	-
Relaxed position NN		+	+	+				++		
Relaxed position 2nd NN			+					++	+	
Sheared position	-			+	-	-	-	+	-	-
Initial width	-	+	-	++			+			+
Relaxed width NN			+	+	+			-		+
Relaxed width 2nd NN				+						
Sheared width				+	+	+	+	-		+
Bath										
Initial position		-		+	+	+	+	+	-	-
Relaxed position NN	-	-		+					-	+
Relaxed position 2nd NN	-	-		-		+	++			+
Sheared position		-		+		+			-	-
Initial width		+	+	+++	+	- -	- -	-	+	-
Relaxed width NN	-	+		++		-	- -	- -	+	-
Relaxed width 2nd NN		+	+	+	+		- -		++	
Sheared width		+	-			-	-	-	+	

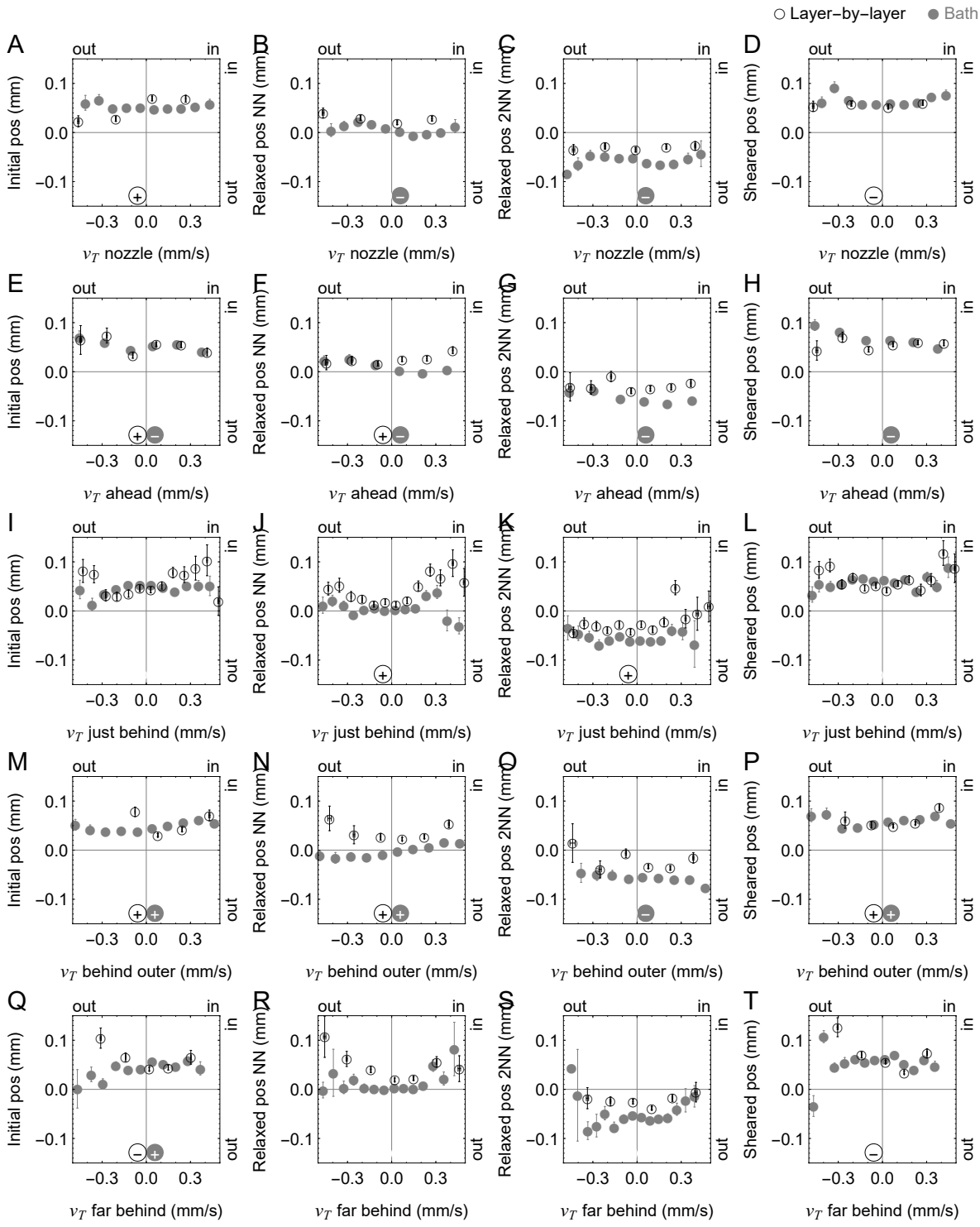

Figure 6.S16: Correlations between transverse flow velocities and absolute particle distribution positions over the course of the print. Error bars indicate standard error with respect to the line $y = 0$.

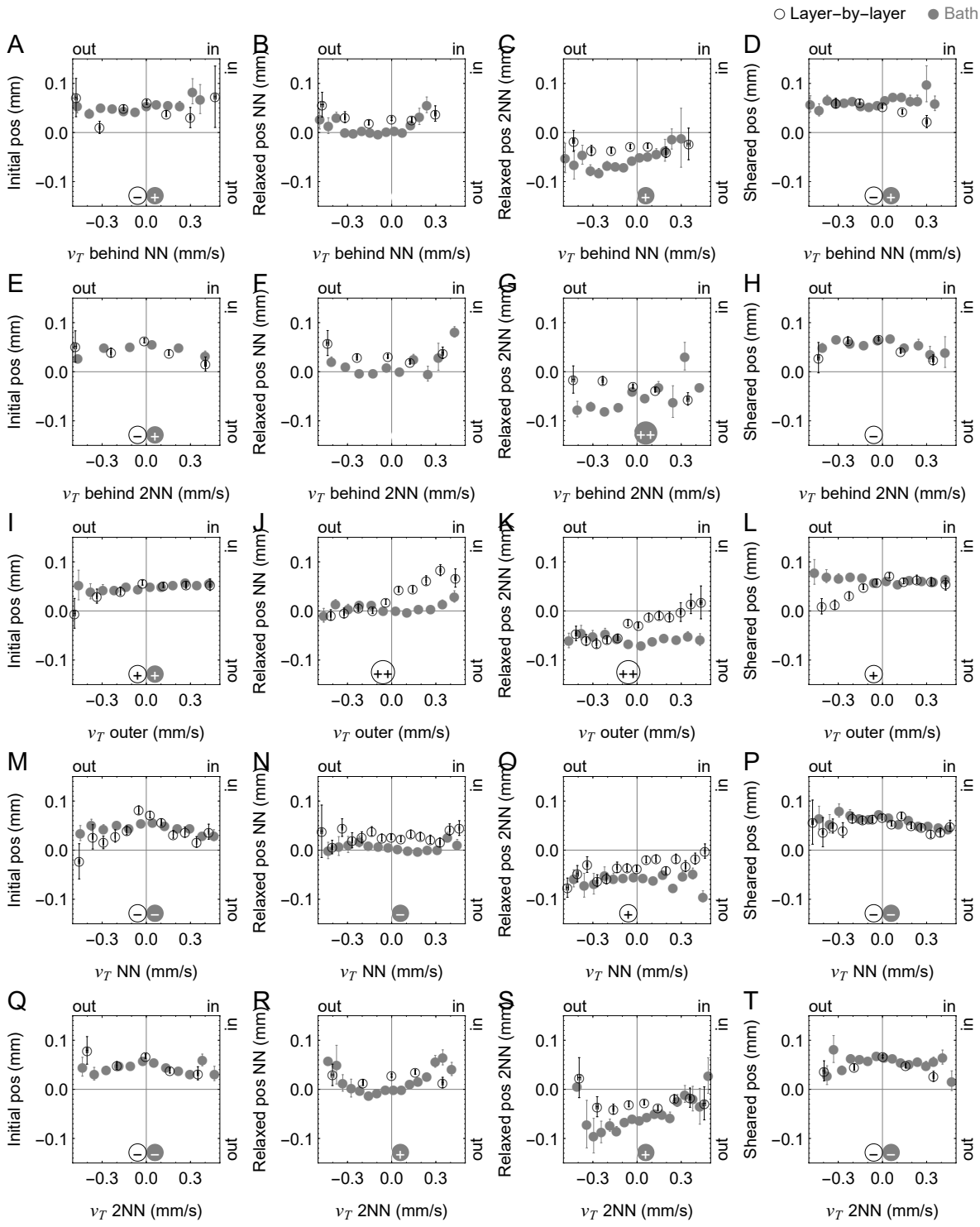

Figure 6.S17: Correlations between transverse flow velocities and absolute particle distribution positions over the course of the print. Error bars indicate standard error with respect to the line $y = 0$.

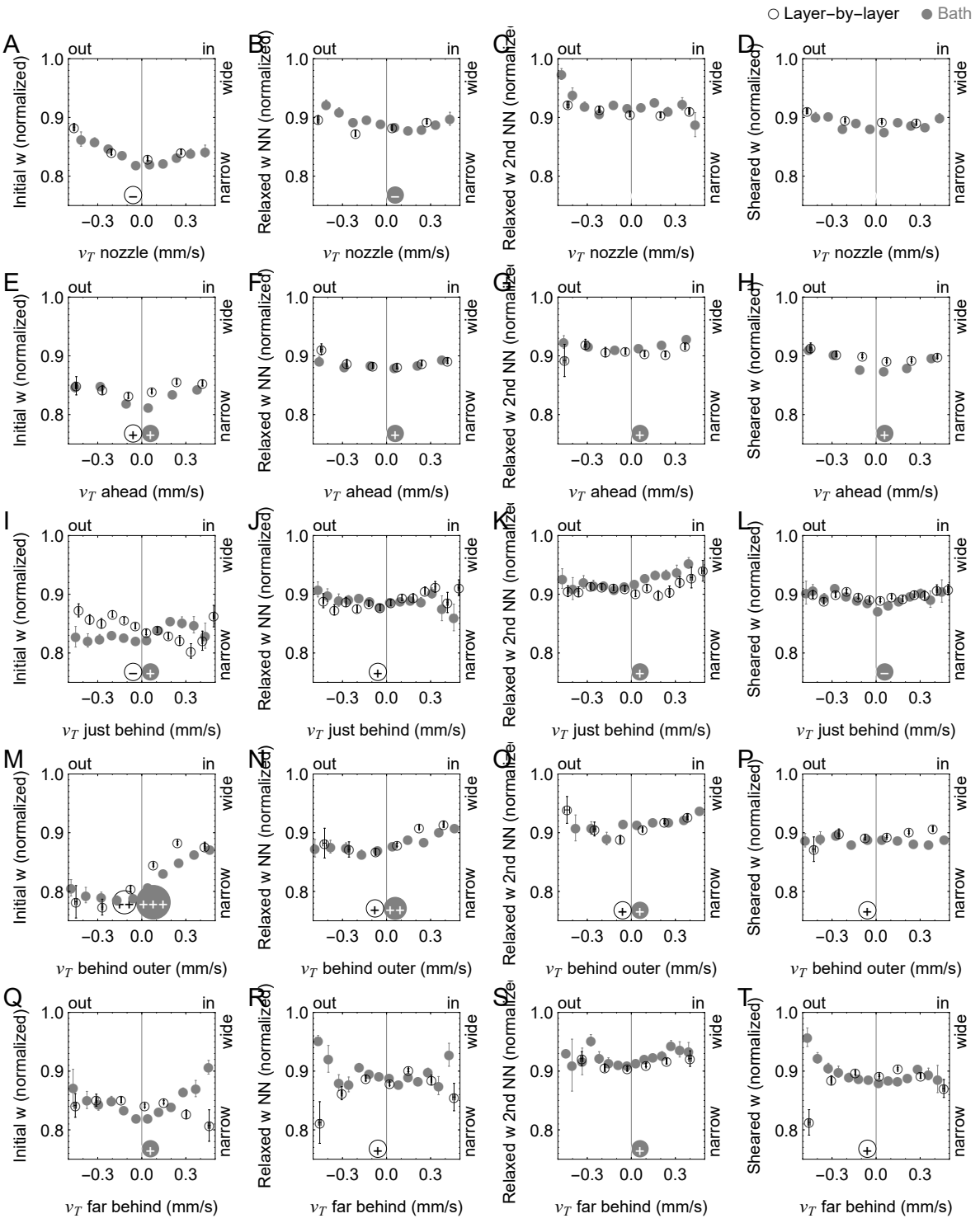

Figure 6.S18: Correlations between transverse flow velocities and absolute particle distribution widths over the course of the print. Error bars indicate standard error with respect to the line $y = 0$.

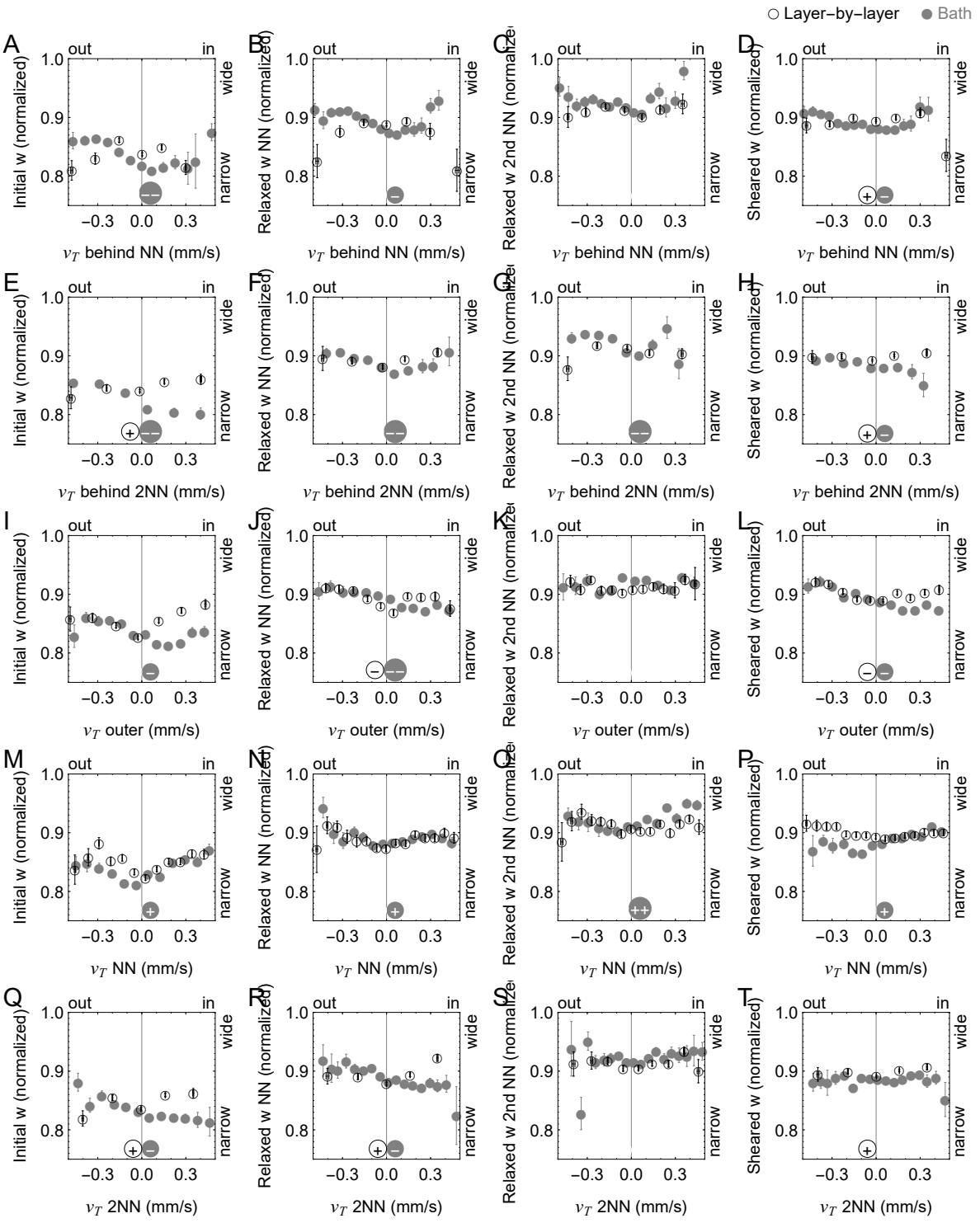

Figure 6.S19: Correlations between transverse flow velocities and absolute particle distribution widths over the course of the print. Error bars indicate standard error with respect to the line $y = 0$.

Table 6.S19: Correlations between transverse flow velocities and relative particle distribution positions and widths over the course of the print.

	nozzle	ahead	just behind	behind outer	far behind	behind NN	behind 2NN	outer	NN	2NN
Layer-by-layer										
Initial pos	+	++	-		-	-	-	++		
Δpos relax NN	-		+	+	+	+	+			
Δpos relax 2nd NN		-	+	+	+	++	+	+	+	
Δpos shear			-		-	-	-	-	-	-
Initial width	-	+		+++	+	+	+	+		
Δwidth relax NN	+			- -	+			-		
Δwidth relax 2nd NN		+				-	-	+		
Δwidth shear		-		-		+		-		+
Bath										
Initial pos		-		+	+	+	+	+	- -	-
Δpos relax NN	-				-	-		-	+	++
Δpos relax 2nd NN	-			- -		+	+	+		++
Δpos shear	+									- -
Initial width		+	+	+++	+	- -	- -	-	++	-
Δwidth relax NN	-	-	-	- -	-				- -	
Δwidth relax 2nd NN			+	++		-	-	+		-
Δwidth shear	+		-	- -		++	++		+	++

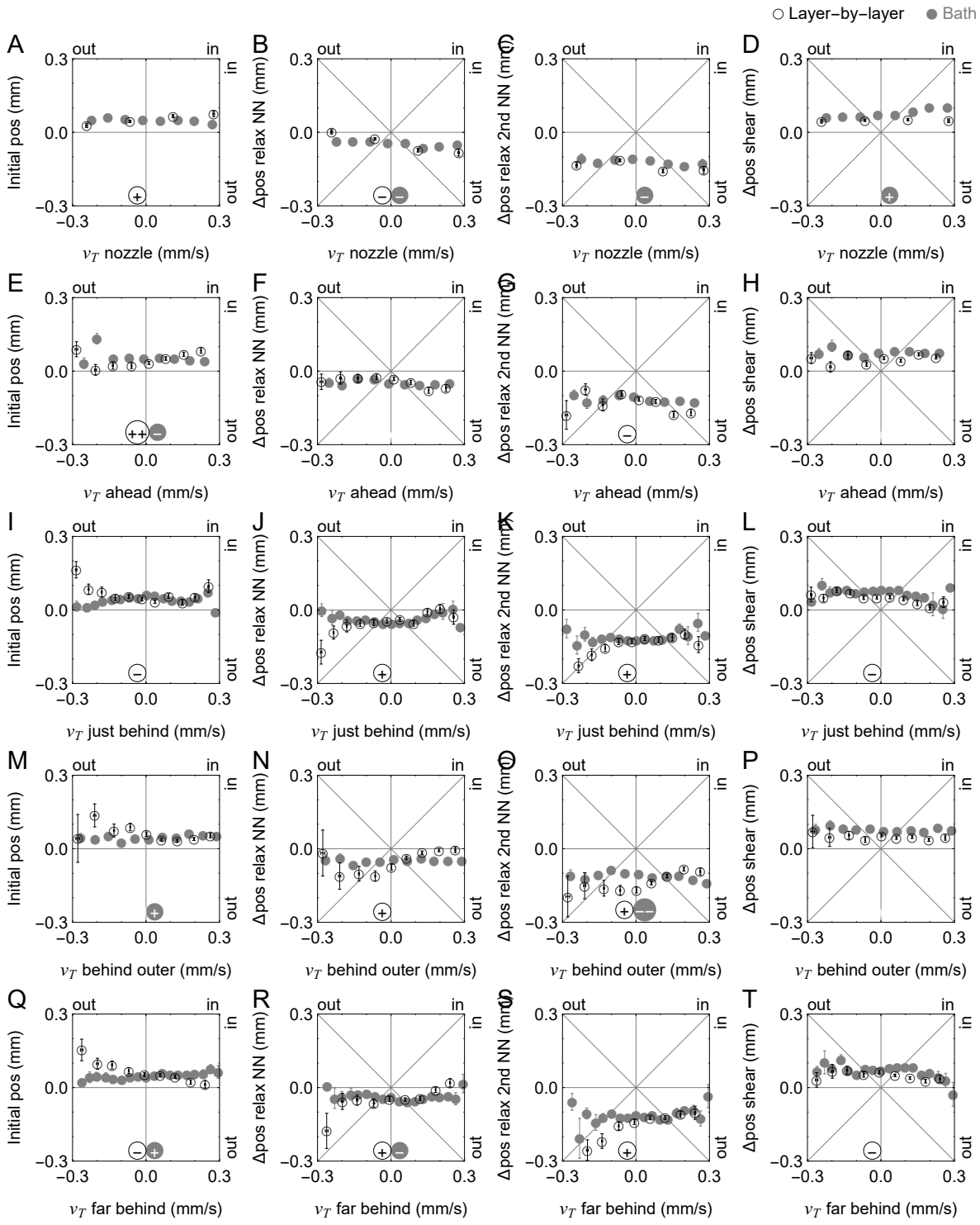

Figure 6.S20: Correlations between transverse flow velocities and relative particle distribution positions over the course of the print. Error bars indicate standard error with respect to the line $y = 0$.

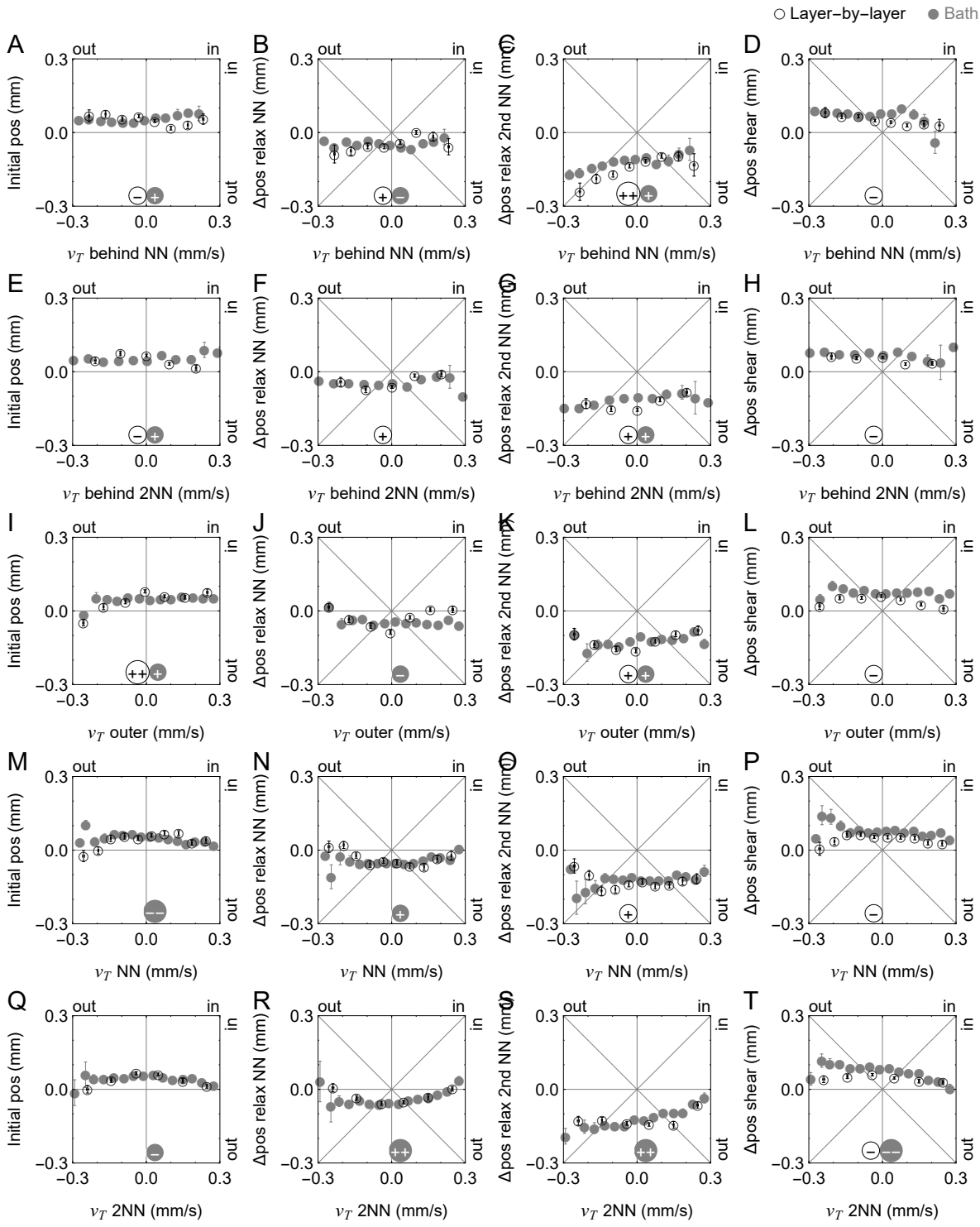

Figure 6.S21: Correlations between transverse flow velocities and relative particle distribution positions over the course of the print. Error bars indicate standard error with respect to the line $y = 0$.

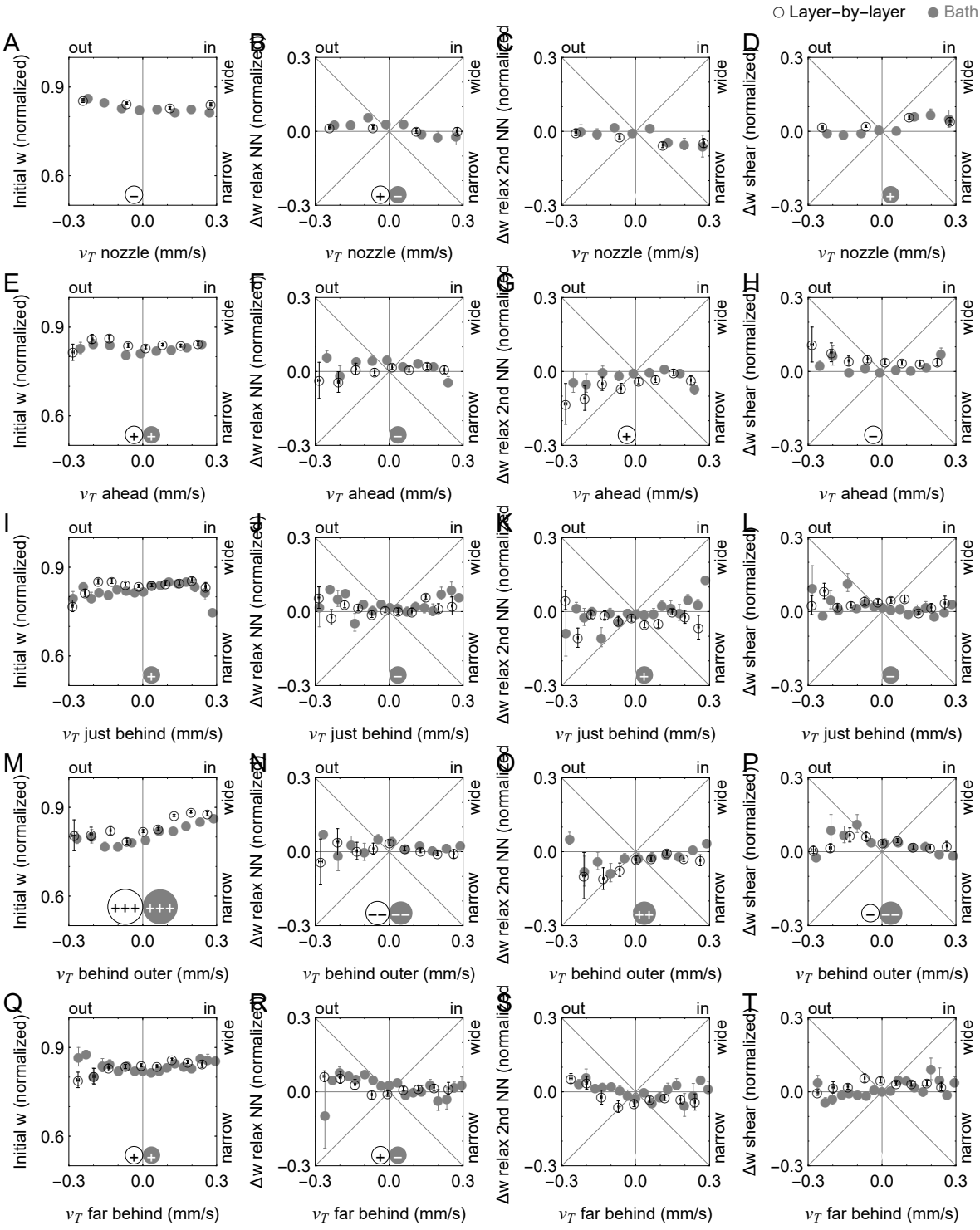

Figure 6.S22: Correlations between transverse flow velocities and relative particle distribution widths over the course of the print. Error bars indicate standard error with respect to the line $y = 0$.

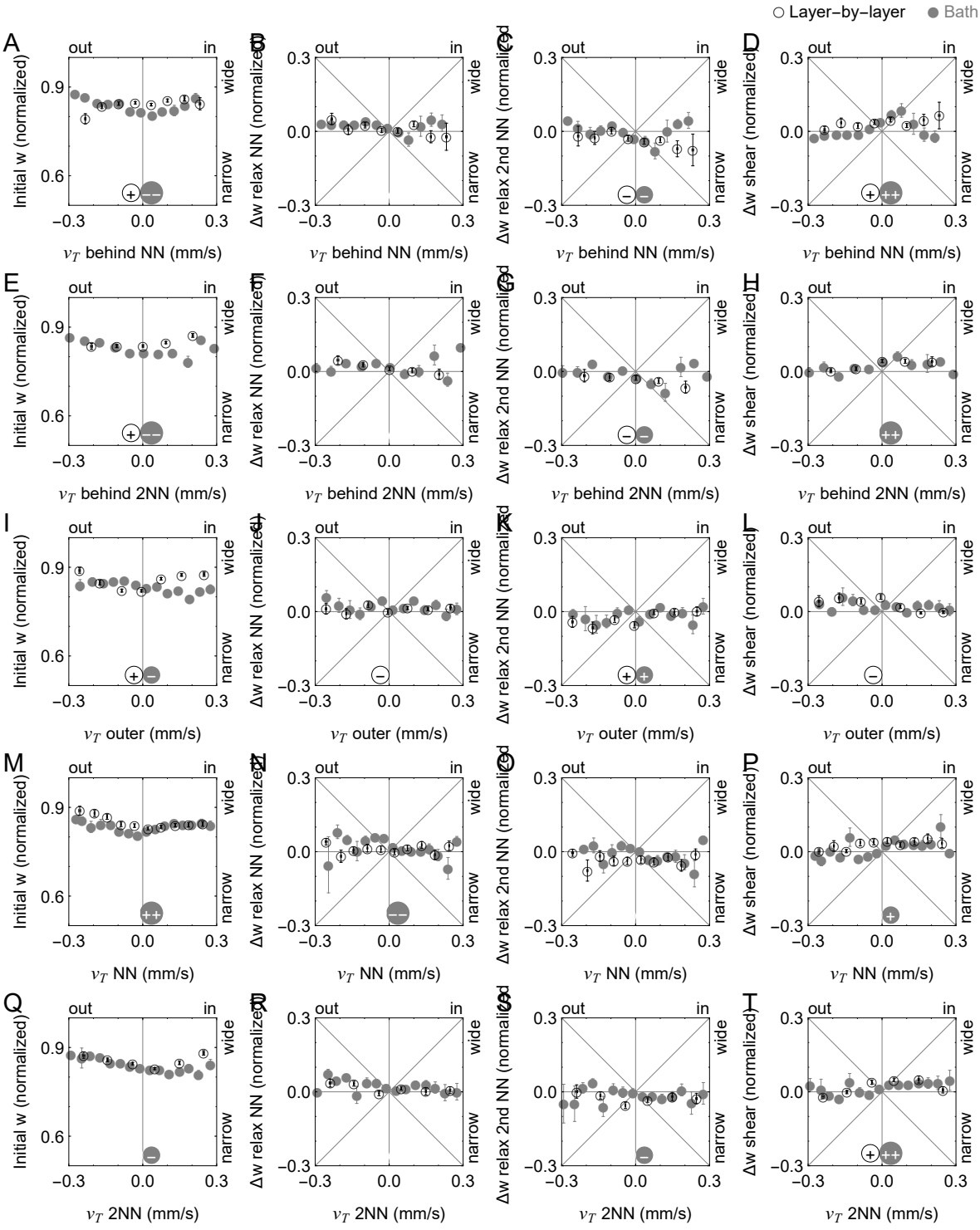

Figure 6.S23: Correlations between transverse flow velocities and relative particle distribution widths over the course of the print. Error bars indicate standard error with respect to the line $y = 0$.

Table 6.S20: Correlations between transverse flow velocities in different regions.

	nozzle	ahead	just behind	behind outer	far behind	behind NN	behind 2NN	outer	NN	2NN
Layer-by-layer										
nozzle		++	-				+	+	+	+
ahead			-	+		-	-	++	++	+
just behind				+	++++	+++	++	++	++	
behind outer					++	+	+	++	+	++
far behind						+++	++	+	++	+
behind NN							+++	+	+	+
behind 2NN								+	+	++
outer									+	+
NN										+++
2NN										
Bath										
nozzle		+	+	+	+	+		+	++	+
ahead			-	+	+	-	-	++	+++	
just behind				++	+++	++	+	+	++	++
behind outer					+	- -	- -	++	+	-
far behind						++++	++	++	++	++
behind NN							++++	+	+	++
behind 2NN								+		++
outer									+	+
NN										++
2NN										

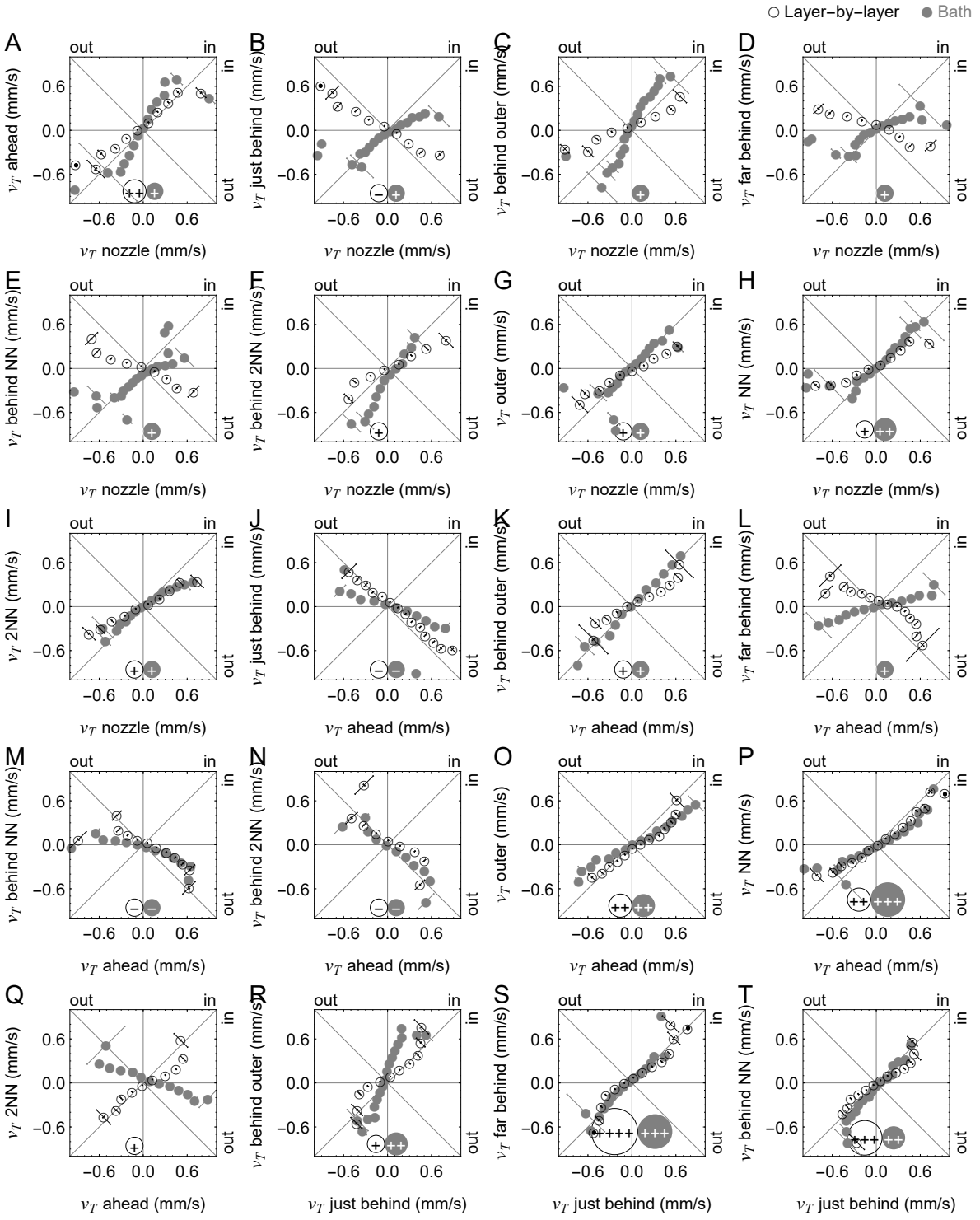

Figure 6.S24: Correlations between transverse flow velocities in different regions. Error bars indicate standard error with respect to the line $-x = y$ or $x = y$.

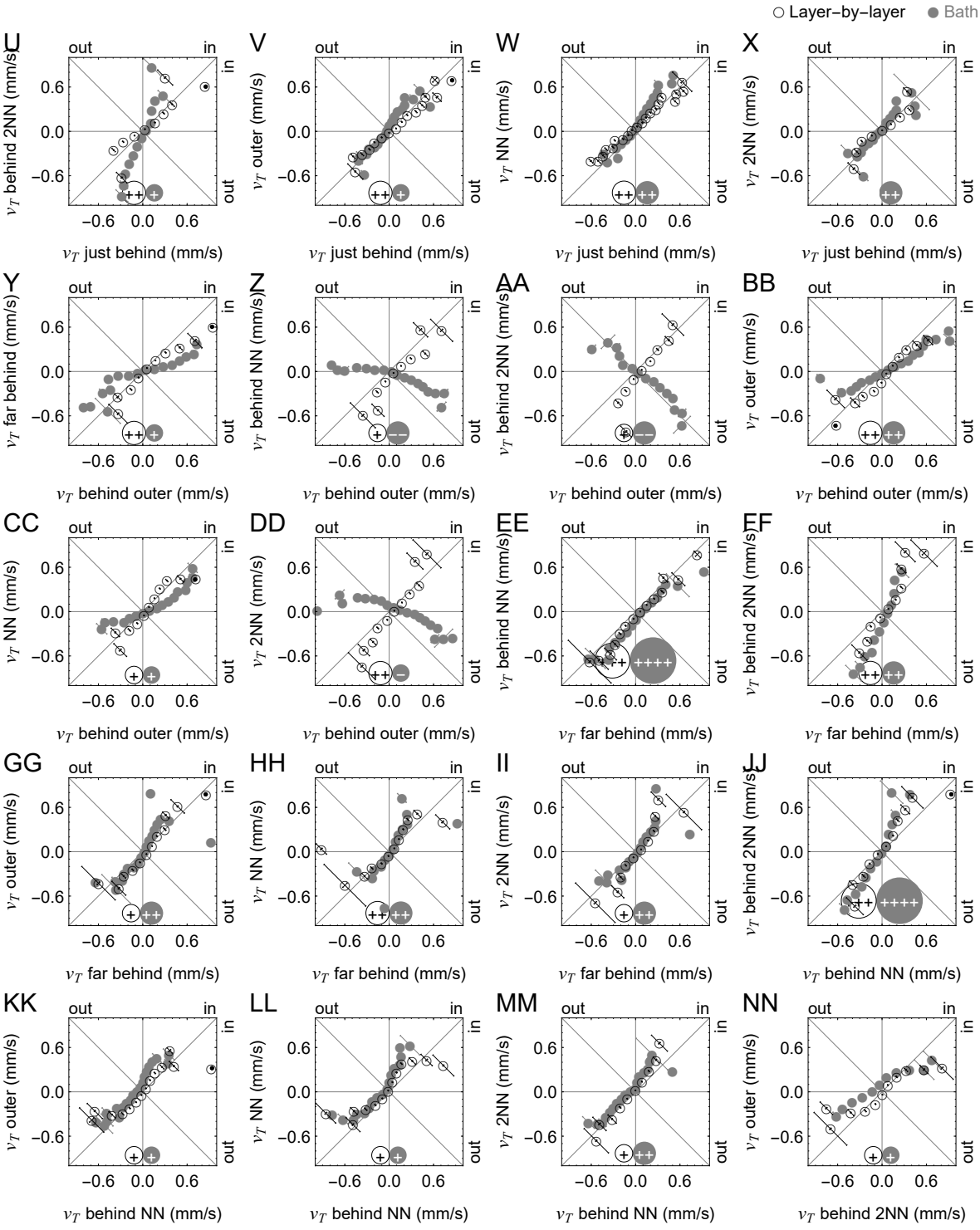

Figure 6.S25: Correlations between transverse flow velocities in different regions. Error bars indicate standard error with respect to the line $-x = y$ or $x = y$.

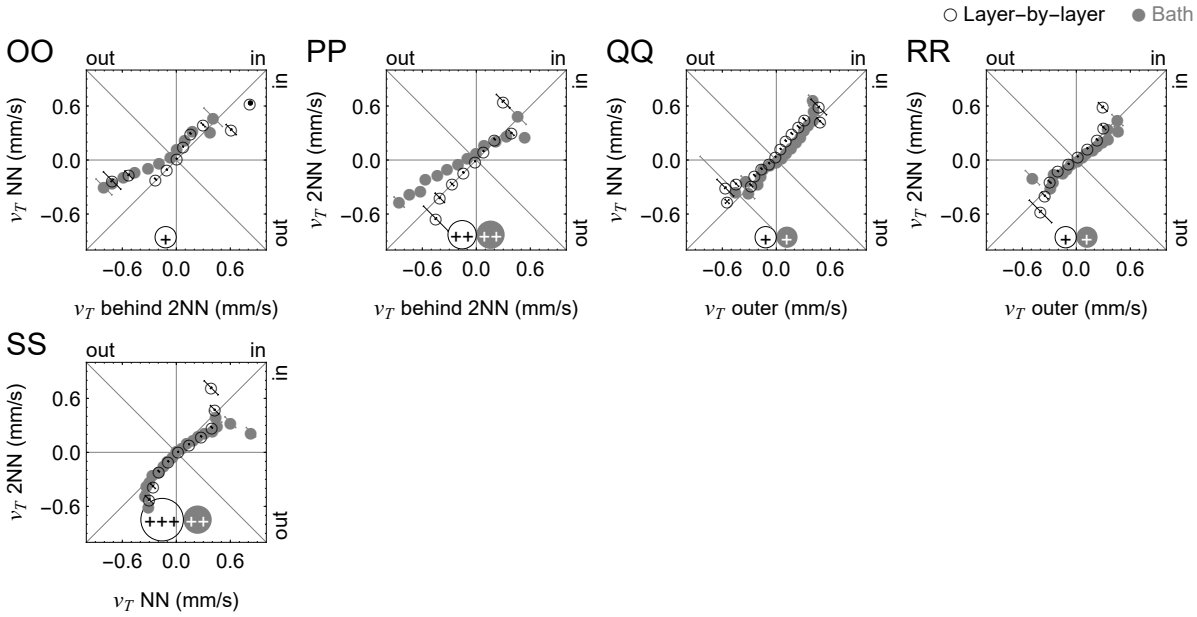

Figure 6.S26: Correlations between transverse flow velocities in different regions. Error bars indicate standard error with respect to the line $-x = y$ or $x = y$.

Chapter 7

Printed polygons: Printing direction dependent microstructures

7.1 Introduction

Direct ink writing (DIW) is an additive manufacturing technique that can produce complex geometries across a broad range of compositions and microstructures, including ceramics,[62, 223] hydrogel cell scaffolds,[120, 114, 224] conductive alloys,[106, 113] and polymer-ceramic composites.[61, 225] Especially for two-phase or composite materials, spatial gradients in structural and functional properties can be integrated with geometric features via techniques which control microstructures "on-the-fly" during printing such as acoustophoresis,[9, 13, 15, 17, 21] magnetic fields,[38] and multimaterial mixing.[80, 82, 83] Advancing microstructural control capabilities requires a fundamental understanding of processing-structure relationships in DIW of multi-phase materials. One of the most critical processing-structure relationships is between printing direction and the resultant filament microstructure.

One of the central challenges of controlling microstructure during DIW is the presence of complex flow fields that connect the particle distribution in the nozzle to the distribution in

the deposited line. Here, acoustic focusing is used to establish a narrow, anisotropic particle distribution in the nozzle (Fig. 7.1C). Critically, flows transverse to the printing direction on the substrate may disrupt this "target" microstructure and influence the final distribution of particles in the printed filament. These flows can cause narrow particle distributions established inside the nozzle to shift within the print path or widen as the filament exits the nozzle (Fig. 7.1A,B). In this work, transverse flow velocities are measured on the substrate experimentally, using inks with suspended particles and *in-situ* optical imaging to track fluid movement.

Several effects lead to print direction dependent microstructures. In this study, square nozzles are used because they enable effective acoustic control over microstructures in the nozzle.[9, 13, 15] While conceptually such anisotropic nozzles can be rotated to preserve alignment with the print path, doing so is a complicated controls problem. By investigating the mechanisms through which this misalignment influences filament microstructure, this work highlights more elegant strategies for achieving microstructural control in DIW. A yield stress support material, implemented in a layer-by-layer or bath geometry, introduces a second source of direction dependent microstructures (Fig. 7.1D). Additionally, calibration of the stage introduces direction dependence. Understanding all of these sources is critical for controlling the microstructure of printed parts.

To diagnose sources of print direction dependent flows and particle distributions, this work postulates several physical mechanisms and propose corresponding idealized analytical models of the flow patterns as a function of printing direction. To illustrate how to use the models and identify strategies for controlling the mechanisms, these models are fit to experimental observations. This identifies dominant mechanisms within this printing system and more general guidelines for selecting printing parameters which mitigate or accentuate direction dependence. Briefly, the mechanisms considered here are: (1) misalignment of the acoustic focusing direction and print direction, which alters the orientation of particle packing, (2) flows in a zone around the nozzle that disturb flows parallel to the printing direction (i.e. the disturbed zone),

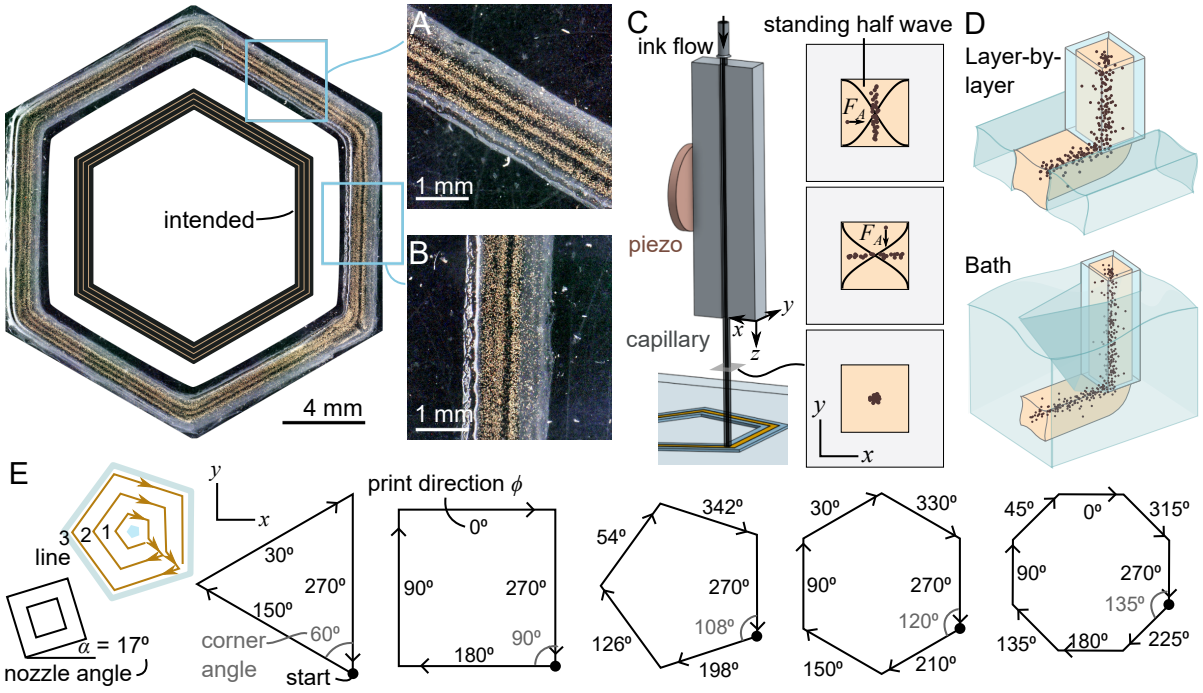

Figure 7.1: A-B) A single-layer, 3 line hexagon composed of silver-coated copper microspheres embedded in a polyurethane-based matrix. Acoustophoresis establishes a narrow distribution of copper spheres in each line, but the particle distributions are wider and less evenly spaced in (B) than (A) due to the printing direction. C) Ink is extruded onto a glass slide through a glass capillary seated in a stainless steel block glued to a piezoelectric actuator. Two standing acoustic half waves in the x and y directions drive particles with acoustic force F_A toward the center of the channel. D) In layer-by-layer support, a nozzle writes into a gap left by a written support pattern. In bath support, a nozzle is submerged into a continuous volume of support. E) Single-layer polygons consisting of various printing directions are printed from inside to outside.

(3) reshaping of the fluid column exiting the nozzle as it is driven to lie flat on the substrate with a symmetrical fluid surface, (4) overlaps between the written line and existing features, and (5) motor errors which misalign designed and written paths. The models which describe these effects assume idealized flows and assume that changes in particle distributions result directly from transverse flows within the filament.

A	Area of interrogation region
c_x, c_y	Scaling factor that represents actual speed of x, y motor
D	Disturbed zone coefficient
dx, dy	Length of origin miscalibration in x, y
f	Dimensionless basis function
F	Focusing anisotropy coefficient
F_A	Primary acoustic radiation force that moves particles toward nodes
L	Experimental particle distribution position
L_d, L_m, L_o, L_r, L_s	Particle distribution position due to disturbed zone, motor error, origin miscalibration, fluid reshaping, solid rotation
L_i	Direction-independent particle distribution position
M	Motor error coefficient
O_x, O_y	Origin miscalibration in x, y coefficients
P	Dimension parallel to the print direction
r	Thickness of disturbed zone
R	Fluid reshaping coefficient
S	Solid rotation coefficient
T	Dimension transverse to the print direction
v	Intended stage translation speed
v_{ave}	Average transverse flow velocity for all points
v_d	Flow velocity along nozzle surface within disturbed zone
v_e	Flow velocity of excess fluid being reshaped during fluid reshaping
v_T	Experimental transverse flow velocity
v_{Td}, v_{Tm}, v_{To}, v_{Tr}, v_{Ts}	Average transverse flow velocity due to disturbed zone, motor error, origin miscalibration, fluid reshaping, solid rotation
v_{Ti}	Direction independent transverse flow velocity
v_{Tj}	Pre-center adjustment direction independent transverse flow velocity
w	Inner half-width of nozzle
w_{Fa}	Particle distribution width due to acoustic focusing anisotropy
w_{Fp}	Experimental width of printed particle distribution
w_{Fx}	Dimensionless value representing aspect ratio of particle distribution in nozzle (0–1)
w_i	Direction-independent distribution width
w_p	Scaling factor representing width of particle distribution in the nozzle
w_u	Width of uniform particle distribution
x, y, z	Global G-code coordinates

Table 7.1: Variables used in this work

α	Nozzle angle relative to the printer x axis
Kendall τ	Parameter which indicates strength of correlation
τ_d, τ_m, τ_o, τ_r, τ_s	Time it takes the distribution to shift under disturbed zone, motor error, origin miscalibration, fluid reshaping, solid rotation
ϕ	Printing direction angle relative to the printer x axis

Table 7.2: Variables used in this work, continued

7.2 Hypotheses

This section describes six effects which contribute to printing direction dependent microstructures (Table 7.3). For each effect, a dependence of either particle distribution position and transverse flow velocity or particle distribution width on the printing direction ϕ is formulated. A linear superposition of these models is used to fit experimental data and thus diagnose sources of print direction dependent microstructures and flows. Microstructure anisotropy involves a rotationally asymmetric distribution of particles in the center of the nozzle, which can be created using acoustic focusing. The disturbed zone is a region wherein fluid flows around the nozzle instead of flowing along the direction of the stage movement. Fluid reshaping and solid rotation are two ways that a particle distribution can shift as a rectangular filament is deposited onto a substrate. Origin miscalibration and motor error come from finite tolerances in 3D printer calibration.

Some printing direction-dependent effects are present in any square nozzle, some are present when using layer-by-layer support, some are present only when defining anisotropic particle distributions in the nozzle, and some are present whenever using a 3-axis gantry (Table 7.3). Because these concepts are constructed from idealized flow patterns based on volume conservation, each mechanism is proposed to only influence certain characteristics of the printed filament. Focusing anisotropy influences the initial particle distribution width. Disturbed zone, fluid reshaping, solid rotation, origin miscalibration, and motor error influence transverse flows and the initial particle distribution position. Analytical expressions for transverse flow velocity

	Conditions				Affected metrics		
Effect	Asym distributions	Asymmetric nozzle	Global positioning	3-axis gantry	Transverse flows	Distribution position	Distribution width
Focusing anisotropy	x						x
Disturbed zone		x			x	x	
Fluid reshaping		x			x	x	
Solid rotation		x			x	x	
Origin miscalibration			x		x	x	
Motor error				x	x	x	

Table 7.3: Conditions under which the studied effects are present and metrics which quantify the effect. "Asym distributions" are rotationally asymmetric distributions inside of the nozzle. A rotationally "asymmetric nozzle" could be a square, rectangle, oval, or any other non-circular shape. "Global positioning" refers to conditions which impact the position of the line in global coordinates, including calibration of the two nozzle positions and tilt of the bottom of the nozzle.

and initial distribution width as a function of the six effects are listed in Equations 7.1–7.9. The initial distribution position can be determined by multiplying the transverse flow velocity expression by a time parameter τ. Detailed derivations are included in the supplemental information. A linear superposition of effects combines Equations 7.1–7.9 into a unified model in Equations 7.10–7.15.

Several models predict that transverse flows and particle distribution characteristics vary depending on the print direction ϕ and the nozzle orientation α (Fig. 7.1E). Angles are measured relative to the positive x axis of the printer as dictated by the G-code. For this study, five polygons were printed at fixed orientations, such that a fixed set of print directions was studied (Fig. 7.1E). The nozzle angle α is fixed at 17°. α is not 0 because of accumulated rotations at various joints in the fixture that connects the nozzle to the printer, but it is constant for all data collected in this study. The difference in angle between the print direction and nozzle orientation $\phi - \alpha$ is important for the focusing anisotropy, disturbed zone, fluid reshaping, and

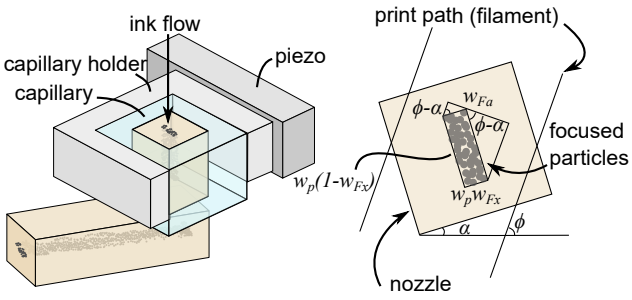

Figure 7.2: The focusing zone in the nozzle has dimensions $w_p(1 - w_{Fx})$ and $w_p w_{Fx}$. This results in a projected focusing zone w_{Fa} that depends on line orientation ϕ.

solid rotation models, which are the models that come from the rotational asymmetry of the nozzle. The origin miscalibration and motor error models only depend on the print direction ϕ.

7.2.1 Focusing anisotropy

In the acoustophoresis apparatus used in this study, a glass capillary rests inside a stainless steel capillary holder, and a piezoelectric transducer is fixed to the side of the capillary holder (Fig. 7.1C, Fig. 7.2). The primary acoustic radiation force that pushes particles toward the center of the nozzle is stronger in the direction of the capillary that is supported by two stainless steel walls, instead of the direction that is supported by only one wall. As such, the distribution of particles is rectangular within a cross-section of the nozzle. Rotationally asymmetric particle distributions are also inherent to rectangular nozzles[9, 13, 15] and can be achieved in multi-material mixing nozzles.[80, 82, 83]

The dimensionless particle distribution width due to focusing anisotropy w_{Fa}/w_p is described by Equation 7.1, where w_p is a scaling factor representing the size of the rectangular particle distribution, and w_{Fx} is a dimensionless value between 0 and 1 representing the aspect ratio of the rectangular particle distribution (Fig. 7.2). This width is the projection of the focused rectangular particle distribution onto the surface transverse to the extruded filament. Based on this experimental setup, it is reasonable to expect $w_{Fx} < 0.5$, which means that the

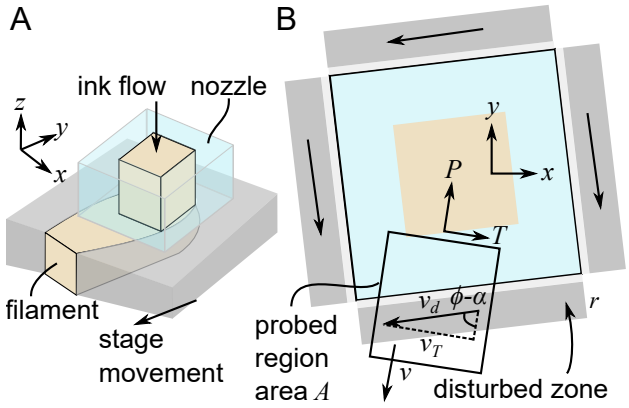

Figure 7.3: Variables used in derivation of disturbed zone transverse flows. A) Three-dimensional model of disturbed zone. B) Fluid flows parallel to the nozzle surface within a disturbed zone of size r.

particle distribution is narrowest in the direction that is supported by two stainless steel walls.

$$\frac{w_{Fa}}{w_p} = w_{Fx}|\sin(\phi-\alpha)| + (1-w_{Fx})|\cos(\phi-\alpha)| \tag{7.1}$$

7.2.2 Disturbed zone

Within some distance r of the nozzle, assume that any fluid present flows along the surface of the nozzle with velocity v_d (Fig. 7.3). This region is the disturbed zone. In this work, flow velocities are analyzed within several interrogation regions relative to the nozzle, so these flows can be split along the nozzle surface into flows within the print path and to the sides of the print path.

Transverse flows v_{Td} aligned with the center of the nozzle are summarized in Equation 7.2, which is based on a projection of the flow velocity parallel to the nozzle surface onto the line transverse to the extruded filament. w is the inner half-width of the nozzle, and A is the

inspected region of interest area.

$$\frac{v_{Td}A}{v_d wr} = \begin{cases} 1 & 0 < \phi - \alpha < \pi/8 \\ 2\sqrt{2}\sin(\phi - \alpha - \pi/2) & \pi/8 < \phi - \alpha < 3\pi/8 \\ -1 & 3\pi/8 < \phi - \alpha < \pi/2 \end{cases} \tag{7.2}$$

To the sides of the print path, the transverse flows on the sides v_{Td} are summarized in Equation 7.3.

$$\frac{v_{Td}A}{v_d wr} = \begin{cases} 2\sqrt{2}\sin(\pi/4 - \phi + \alpha) - 1 & 0 < \phi - \alpha < \pi/8 \\ 0 & \pi/8 < \phi - \alpha < 3\pi/8 \\ 2\sqrt{2}\sin(\pi/4 - \phi + \alpha) + 1 & 3\pi/8 < \phi - \alpha < \pi/2 \end{cases} \tag{7.3}$$

7.2.3 Fluid reshaping and solid rotation

When the nozzle is set at an angle relative to the filament, i.e. $(\phi - \alpha) \pmod{\pi/2} > 0$, the ink column must change its shape or rotate during deposition so that the ink rests flat on the substrate. There is a continuum of ways to produce this change. Here two extremes are presented. Fluid reshaping occurs in low-viscosity fluid-like inks, where the square column reshapes to a curved surface once it contacts the substrate (Fig. 7.4). Solid rotation occurs in high-viscosity solid-like inks, where the entire filament undergoes an affine rotation on its leading corner to lie flat on the substrate (Fig. 7.5).

Under fluid reshaping, assume that any fluid area that falls outside of the print path is pushed into the print path at velocity v_e, and any fluid ahead of the nozzle that is not centered is pushed toward the center with velocity v_e. To the sides of the print path, the measured transverse flow due to fluid reshaping v_{Tr} is shown in Equation 7.4 as a function of the inspected

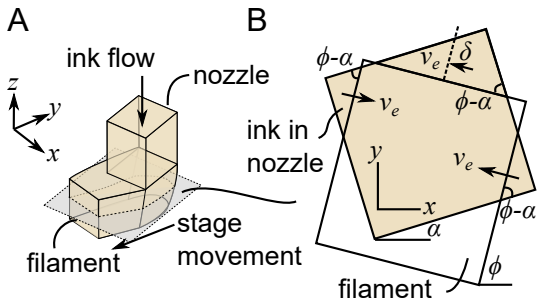

Figure 7.4: A) A square filament reshapes to have curved surfaces on the substrate. B) At some print directions, part of the square nozzle falls outside of the intended filament area.

region of interest area A and the nozzle inner half-width w.

$$\frac{|v_{Tr}|A}{v_e w^2} = \frac{\left|\csc(\alpha-\phi)\sec(\phi-\alpha)(1-\cos(\phi-\alpha)+\sin(\alpha-\phi))^2\right|}{2(\sqrt{2}-1)^2} \tag{7.4}$$

In this data set, $\alpha = 17^\circ$ due to accumulated rotations at various joints in the print head fixture. Ahead of the nozzle, evaluated for $\alpha = 17^\circ$, the transverse flow due to fluid reshaping v_{Tr} is shown in Equation 7.5.

$$\begin{aligned}\frac{v_{Tr}A}{v_e w^2} =& \frac{-43\,\mathrm{sign}(\sin(\phi-62^\circ))}{48}\times \\ & \left|\frac{-5\cos(\phi-17^\circ)+4\cos(2\phi-34^\circ)-\cos(39^\circ+3\phi)+\sin(39^\circ+3\phi)-5\sin(17^\circ-\phi)}{\sin(17^\circ-\phi)\cos(\phi-17^\circ)}\right| \\ & \times\left|\frac{(1-\cos(\phi-17^\circ)+\sin(17^\circ-\phi))^2}{\sin(17^\circ-\phi)\cos(\phi-17^\circ)}\right|\end{aligned} \tag{7.5}$$

Under solid rotation, assume that the solid filament hits the substrate, bends over on its leading corner, then twists to rest on the substrate (Fig. 7.5). The measured transverse flow is the projection of this rotation onto the plane of the substrate. In other words, the center of the filament displaces laterally across the print path by some distance over some length of time. The measured transverse flow v_{Ts} as a function of the time τ_s that it takes the filament to rotate

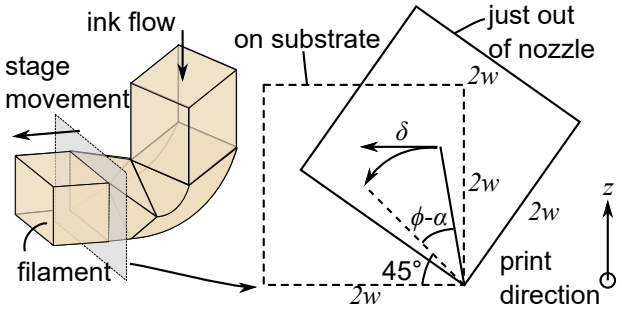

Figure 7.5: A solid filament rotates when it hits the substrate so that it rests flat on the substrate.

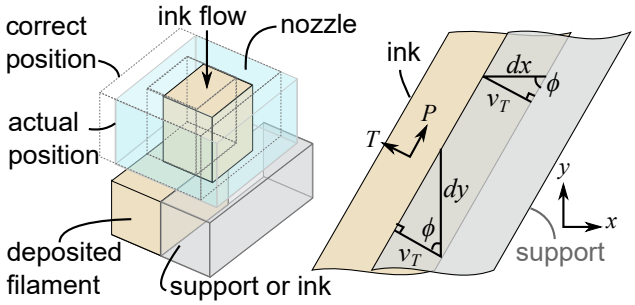

Figure 7.6: The nozzle origin is calibrated too far to the right within this image, resulting in collisions between ink and existing support or ink. Collisions induce a transverse flow v_T.

onto the substrate and nozzle inner half-width w is shown in Equation 7.6.

$$\frac{v_{Ts}\tau_s}{w} = \begin{cases} 1 - \sqrt{2}\cos(\pi/4 + \phi - \alpha) & 0 < \phi - \alpha < \pi/4 \\ 0 & \phi - \alpha = \pi/4 \\ -1 - \sqrt{2}\cos(\pi/4 + \phi - \alpha) & \pi/4 < \phi - \alpha < \pi/2 \end{cases} \tag{7.6}$$

7.2.4 Origin miscalibration

In this work, support material is incorporated in two ways. One is layer-by-layer support, wherein an inner support polygon and an outer support polygon are printed using a dedicated support nozzle before the ink nozzle prints the main polygon. If the support and ink nozzle origins are miscalibrated, the deposited ink will collide with existing material, leading to a lateral shift in its position and a corresponding transverse flow.

If the ink nozzle origin x_0 is off by dx, the magnitude of the transverse flow v_{To} due to origin miscalibration is defined by Equation 7.7, where τ_o is the time it takes for the filament to displace.

$$\frac{v_{To}\tau_o}{|dx|} = \sin\phi \frac{-\operatorname{sign}(\sin\phi) - \operatorname{sign}(dx) + 1/3(\operatorname{sign}(\sin\phi) - \operatorname{sign}(dx))}{2} \tag{7.7}$$

If the ink nozzle origin y_0 is off by dy, the magnitude of the shift is

$$\frac{v_{To}\tau_o}{|dy|} = -\cos\phi \frac{\operatorname{sign}(\cos\phi) - \operatorname{sign}(dy) - 1/3(\operatorname{sign}(\cos\phi) + \operatorname{sign}(dy))}{2} \tag{7.8}$$

The 1/3 terms in Equation 7.7 and 7.8 come from the frequency of collisions between ink and layer-by-layer support in three-line polygons. On one side of the polygon, only one out of the three lines of the ink polygon collides with support (Fig. 7.S9). Whereas the other five components of the unified model can be converted from normalized velocities to a normalized positions simply by replacing the transverse velocity v_T with a position over time term L/τ, origin miscalibration requires an extra modification. For fitting distribution positions, distributions are fit separately in the three lines, so the factor of 1/3 in Equation 7.7 and 7.8 is replaced with a factor of 1, removing the assumption about which lines shift and instead directly identifying which lines shift due to origin miscalibration. Ultimately, this turns out to be all three lines.

7.2.5 Motor error

During *in-situ* monitoring of the print path, the position of the print path within the image frame can be determined from the G-code, knowing how the camera frame relates to the gantry frame. However, if the motors on the printer are calibrated such that the x motor speed is scaled by a factor c_x and the y motor speed is scaled by a factor c_y, the orientation of the print path

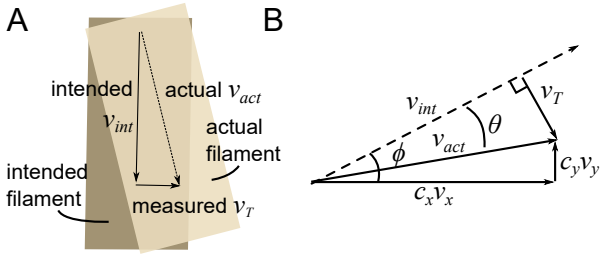

Figure 7.7: A) If the printer motors are miscalibrated, the print path will be rotated relative to the intended print path, resulting in a measured transverse flow. B) The x and y motor velocities are scaled by a factor of c_x and c_y, resulting in a detected transverse flow v_T.

will be rotated relative to the intended orientation of the print path, and a transverse flow across the filament will be erroneously detected. Furthermore, the written structure will be distorted and have inaccurate dimensions. Any printer can only be calibrated to a finite tolerance, so while this problem can be mitigated, it cannot be eliminated. The magnitude of the detected transverse flow relative to the intended translation speed v is shown in Equation 7.9.

$$\frac{v_{Tm}}{v(c_y - c_x)} = \cos\phi \sin\phi \tag{7.9}$$

7.2.6 Fitting models to experimental profiles

A model is proposed for direction dependent microstructures based on a linear combination of Equations 7.1–7.9 used in a superposition approach that describes the total velocity as a sum of contributions from each mechanism. Each of these equations serves as a basis function. Equations 7.1–7.9 express the distribution width and transverse flows as dimensionless functions that range from 0 to 1 (for the distribution width) and -1 to 1 (for transverse flows) as a function of printing direction ϕ. Using a linear superposition of scaled basis functions, one can fit a unified model to the experimental data. Specifically, transverse flow velocities and particle distribution positions and widths are measured as a function of ϕ and can be fit in terms of scaling coefficients and basis functions which depend on ϕ. These scaling coefficients are

indicators of how influential a given mechanism is within a set of experiments. Note that these models are built on $\cos\phi$, $\sin\phi$, and $\cos\phi\sin\phi$. As such, merely plotting experimental data as a function of ϕ will not be useful, as one would be pressed to express the data as a sum of several similar sinusoids with the same period. Instead, it is useful to plot the experimental and theoretical data as a function of $\cos\phi$, $\sin\phi$, and $\cos\phi\sin\phi$. Shown in Figure 7.8, each model exhibits a unique dependence on $\cos\phi$, $\sin\phi$, or $\cos\phi\sin\phi$ within the set of directions tested. For example, motor miscalibration is the only mechanism which leads to a non-zero slope in $\cos\phi\sin\phi$ for octagons and hexagons, so any slope in $\cos\phi\sin\phi$ in the experimental hexagons and octagons can be attributed to motor error. By extracting these unique characteristics from experimental data, one can diagnose sources of direction dependence and compare coefficients between printing parameters to identify strategies for controlling direction dependence.

To fit the experimental distribution width, assume that the distribution width is a linear combination of an initial width w_i and the variation due to the printing direction w_{Fa}/w_p. Then, the width of the printed distribution w_{Fp} normalized by the width of a uniform distribution w_u can be described by Equation 7.10.

$$\frac{w_{Fp}}{w_u} = \frac{w_i}{w_u} + F\frac{w_{Fa}}{w_p} \tag{7.10}$$

The normalized initial width w_i/w_u represents a combination of some minimum distribution width that can be achieved in the nozzle due to scaling factors such as the size and volume fraction of particles, viscosity of the matrix, and flow speed.[15, 16] The initial width w_i/w_u accounts for widening of the distribution as it exits the nozzle due to inertial flows and interfacial effects.[19] The parameter F scales the amplitude of the theoretical profile, representing the contribution of focusing anisotropy to the experimental distribution width. In Equation 7.10, only the second term varies as a function of the print direction ϕ.

To fit transverse flows, a more involved procedure is required. Assume that the experimen-

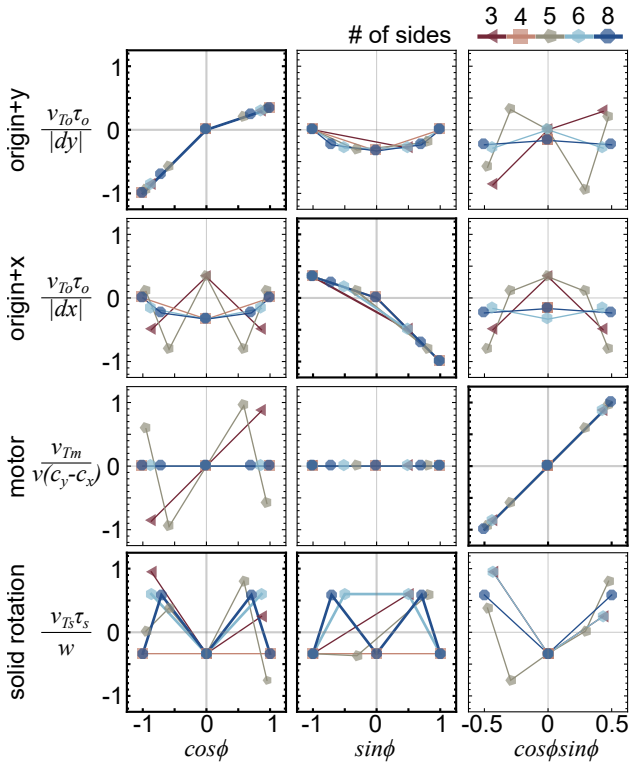

Figure 7.8: A representative set of basis functions for extracting direction dependence coefficients for transverse flow velocities as described by Equation 7.11. Plots used for fitting coefficients are in bold. Lines are only visualization aides; the continuous and non-averaged expressions are plotted as a function of ϕ, $\cos\phi$, $\sin\phi$, and $\cos\phi\sin\phi$ in the supplemental information.

tal transverse flows are a result of a linear superposition of an orientation-**i**ndependent flow speed, **d**isturbed zone, fluid **r**eshaping, **s**olid rotation, **o**rigin miscalibration in x and y, and **m**otor error.

$$v_T = v_{Ti} + D\frac{v_{Td}A}{v_d wr} + R\frac{|v_{Tr}|A}{v_e w^2} + S\frac{v_{Ts}\tau_s}{w} + O_x\frac{v_{To}\tau_o}{|dx|} + O_y\frac{v_{To}\tau_o}{|dy|} + M\frac{v_{Tm}}{v(c_y - c_x)} \quad (7.11)$$

The orientation-independent transverse flow velocity v_{Ti} and the scaling coefficients D, R, S, O_x, O_y, and M have units of mm/s because the experimental average transverse flow velocity v_T has units of mm/s, and they are multiplied by dimensionless expressions. Note that each dimensionless term is expressed in terms of a theoretical transverse velocity divided by some factor with units of mm/s. For example, the dimensionless disturbed zone factor $v_{Td}A/(v_d wr)$ is a transverse flow from the disturbed zone v_{Td} which has units mm/s, divided by a velocity and area adjustment $v_d wr/A$ which has units of mm/s $\times$ mm^2/mm^2. The coefficient D encompasses both a dimensionless scaling constant that describes the importance of the disturbed zone and the scale of $v_d wr/A$ in mm/s.

Fitting transverse flows and fitting the particle distribution position follow a similar workflow. The following methods are tailored to the transverse flow, but distribution positions can be fitted using the same method, assuming that all effects happen over a period of time τ. Specifically, instead of transverse flow velocity v_T, a position L in mm is fit. Instead of an initial velocity v_{Ti}, an initial position L_i in mm is determined. For fitting positions, the constants D, R, S, O_x, O_y, and M are in mm. For many components of the linear superposition, this requires replacing the transverse flow component $v_{T\xi}$ with a position over time component

L_ξ/τ_ξ.

$$L = L_i + D\frac{L_d A}{\tau_d v_d w r} + R\frac{|L_r|A}{\tau_e v_e w^2} + S\frac{L_s}{w} + O_x\frac{L_o}{|dx|} + O_y\frac{L_o}{|dy|} + M\frac{L_m}{\tau_m v(c_y - c_x)} \quad (7.12)$$

For both transverse flows and distribution positions, the coefficients D, R, S, O_x, O_y, and M can be extracted using critical differences in how the basis functions depend on $\cos\phi$, $\sin\phi$, and $\cos\phi\sin\phi$ (Fig. 7.8).

For printed squares, hexagons, and octagons, a non-zero slope in $\cos\phi$ only appears for origin miscalibration in y (Fig. 7.8). The coefficient O_y can be extracted using this slope. Because the basis function for origin miscalibration in $+dy$ is not just the negative of the basis function for origin miscalibration in $-dy$, one must first detect whether origin miscalibration is positive or negative using the slope of the transverse flow as a function of $\cos\phi$. If the slope is positive, one should use the $+dy$ basis function. If it is negative, one should use the $-dy$ basis function.

Next, when fitting transverse flows the experimental data must be rescaled so all of the data can be used for slope extraction, limiting measurement error. When fitting distribution positions, this rescaling step can be skipped because each of the three lines of the polygon is fit individually. When using the $+dy$ basis function, all experimental flows for $\cos\phi > 0$ must be rescaled to $v_{ave} + 3(v - v_{ave})$, where v_{ave} is the average transverse flow velocity for all data points. When using the $-dy$ basis function, all flows for $\cos\phi < 0$ must be rescaled. If the basis function was rescaled in the same way, the resultant slope would be 1. As such, the slope of the rescaled experimental data is the constant O_y, which represents the contribution to transverse flows of the origin miscalibration in y.

By averaging collected points as a function of $\cos\phi$, $\sin\phi$, and $\cos\phi\sin\phi$, the symmetry of printed polygons relative to the printer x and y axes can be leveraged. Asymmetrical polygons

can be used to evaluate the final fit. For printed squares, hexagons, and octagons, which have symmetry in x and y, a non-zero slope in $\sin\phi$ only appears for origin miscalibration in x. The same procedure as origin miscalibration in y can be used, with a minor change. If the initial slope is negative, the origin miscalibration $+dx$ should be used. If the initial slope is positive, the origin miscalibration $-dx$ should be used. Accordingly, if using the $+dx$ basis function, flows for $\sin\phi < 0$ should be rescaled, and if using the $-dx$ basis function, flows for $\sin\phi > 0$ should be rescaled. The slope of the rescaled data is the constant O_x, which represents the contribution to transverse flows of the origin miscalibration in x.

For printed octagons, a non-zero slope in $\cos\phi\sin\phi$ is only present for motor error. The slope of the basis function as a function of $\cos\phi\sin\phi$ is 2. Thus, the constant M is the slope of the experimental data as a function of $\cos\phi\sin\phi$ divided by 2.

Once the constants O_x, O_y, and M have been extracted, the next step is to subtract the scaling constants multiplied by their bases from the experimental velocity v_T, leaving only D, R, and S to be determined. Unfortunately, the remaining effects, which all depend on some trigonometric evaluation of the difference between the printing angle and nozzle angle $\phi - \alpha$, have similar basis functions and no single feature can be extracted to separate the effects. To evaluate which effect is most likely the cause of any ϕ dependence which remains after correction for origin miscalibration and motor error, it is practical to assume that only one effect out of disturbed zone, fluid reshaping, and solid rotation influences the transverse flow and determine the resultant fitting error. As such, one can separately find the constants D, R, and S, and then use root mean square error to evaluate which basis function best fits the data.

For disturbed zone, fluid reshaping, and solid rotation, transverse flow basis functions for printed hexagons and octagons have an amplitude in $\cos\phi$ and $\sin\phi$ (Fig. 7.8). The amplitudes

of the basis functions listed in Table 7.S2 are used to determine D, R, and S via Equation 7.13,

$$K = \left(\frac{a_{h\sin}}{a_{hb}} + \frac{a_{h\cos}}{a_{hb}} + \frac{a_{o\sin}}{a_{ob}} + \frac{a_{o\cos}}{a_{ob}}\right)/4 \tag{7.13}$$

where K is the coefficient D, R, or S. The amplitude of the hexagons is $a_{h\_}$ and the amplitude of octagons is $a_{o\_}$. The experimental amplitude in $\sin$ is $a_{\_\sin}$ and the amplitude in $\cos$ is $a_{\_\cos}$. The basis function amplitude is $a_{\_b}$, which is the same for the $\sin$ and $\cos$ profiles. To follow the anticipated flow directions predicted by the theory, D, R, and S should be positive.

Because the aim of this step is to remove the amplitude in ϕ that is present in the experimental data, an additional factor is necessary to shift the theoretical contribution of K so that it is centered on $v_T = 0$. The D, R, or S contribution to the theoretical profile is thus

$$v_{TK} = Kf - K(c_h + c_o)/2 \tag{7.14}$$

where f is the dimensionless basis function, and c_h and c_o are the centers of the hexagon and octagon basis functions, which are the same for the $\sin$ and $\cos$ basis functions. This contribution v_{TK} is subtracted from the corrected experimental velocity (which had already been corrected for origin miscalibration and motor error). The average transverse velocity of the remaining profile is the pre-adjustment orientation-independent velocity v_{Tj}. One can use v_{Tj} to construct a fitted profile for v_T with the collected coefficients D, R, or S, O_x, O_y, and M with Equation 7.11. For example, to construct a fitted profile for the disturbed zone model, Equation 7.15 is used.

$$v_T = v_{Tj} - D\frac{(c_h + c_o)}{2} + D\frac{v_{Td}A}{v_d wr} + O_x\frac{v_{To}\tau_o}{|dx|} + O_y\frac{v_{To}\tau_o}{|dy|} + M\frac{v_{Tm}}{v(c_y - c_x)} \tag{7.15}$$

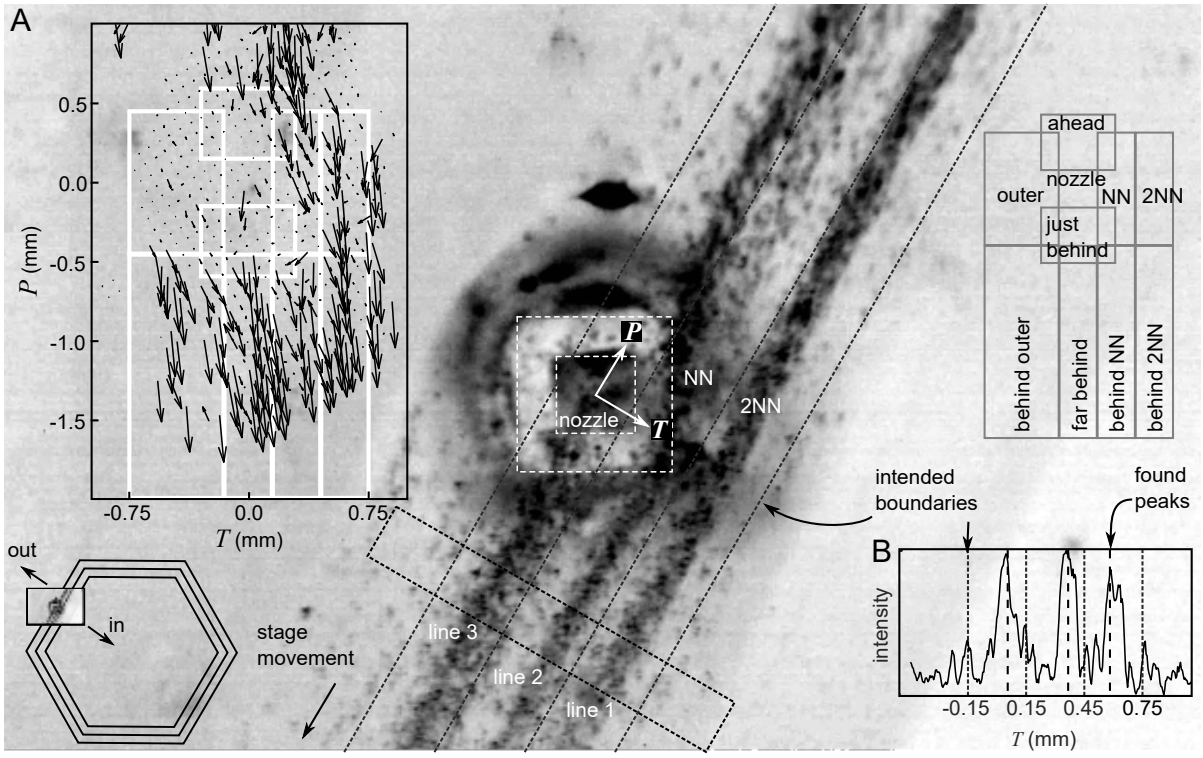

Figure 7.9: Example of analyzed frame, for layer-by-layer support. Image is inverted. A) Fluid displacement field is measured using PIV and rotated into the Parallel-Transverse coordinate system. Probed regions are outlined in white. B) Intensities are summed along the parallel direction ahead of and behind the nozzle. Distribution positions and widths are found as a function of transverse position.

The term $v_{Ti} = v_{Tj} - D(c_h + c_o)/2$ can be used to determine the adjusted orientation-independent velocity. The root mean square error difference between the experimental data and the fitted profile can be used to indicate whether disturbed zone, fluid reshaping, or solid rotation best describes the data.

7.3 Experimental approach

This paper draws from the same data set that is used in Refs. [19, 20], but this work focuses specifically on direction-dependent behaviors. Data and code can be found at Ref. [218].

Inks consisted of diurethane dimethacrylate (UDMA) (Sigma Aldrich, mixture of isomers with topanol inhibitor), triethylene glycol dimethacrylate (TEGDMA) (Sigma Aldrich, with MEHQ inhibitor), fumed silica (Evonik Aerosil R106), camphorquinone (CQ) (Sigma Aldrich), and 2-(Dimethylaminoethylmethacrylate) (DMAEMA) (Sigma Aldrich, with monomethyl ether hydroquinone inhibitor). Bases were mixed in a 92:8 UDMA:fumed silica weight ratio and mixed in a planetary mixer (Thinky ARE-310) at 2000 rpm for 3 minutes. Inks were then mixed in 80:20, 75:25, 70:30, and 65:35 base:TEGDMA weight ratios with 0.2 w% CQ and 0.8 w% DMAEMA, plus 10 w% ($\approx$1.4 v%) silver-coated copper microspheres (Potters Beads Conduct-O-Fil, SC15S15, diameter 15 μm), which were acoustically focused and acted as PIV markers. Carbopol support gels were mixed by adding 1.2 w% Carbomer 940 to deionized water (pH 3-4) and mixing with an overhead stirrer for 5 minutes at 1500 rpm or until dissolved. Gels were then neutralized using 50% NaOH (Sigma Aldrich) and mixed in a planetary mixer (Thinky ARE-310) at 2000 rpm for 3 minutes to remove bubbles.

Single-layer, three-line equilaterial triangles, squares, pentagons, hexagons, and octagons with 6, 8, 10, and 12 mm edge lengths were printed onto a glass slide mounted on a 3-axis stage (Fig. 7.1C,E). For layer-by-layer support, first, the three-line inner support polygon was printed from inside to outside, then the three-line outer support polygon from inside to outside, then the three-line ink polygon from inside to outside. For bath support, a 1 mm-thick layer of support was spread onto the substrate using a spatula with the 3D-printed slide holder lip as a template, and then the three-line ink polygon was printed from inside to outside into the bath.

Inks and support gels were extruded through square borosilicate capillaries (Vitrocom, 0.3 mm ID, 0.6 mm OD, 50 mm length) onto glass slides. The ink capillary was seated in a stainless steel block containing a 0.7 mm square groove lined with ultrasonic coupling gel. A piezoelectric actuator (15 mm diameter x 1 mm thick Navy I material, American Piezo) was adhered to the steel block using epoxy (Devcon HP250). The piezo was driven using a signal generator (HP 33120A) and amplifier (Mini-Circuits LZY-22+), and signals were measured

using an oscilloscope (Agilent DSO-X 2024A). Sinusoidal signals were generated at 2.249 MHz and a peak-to-peak voltage of 50 V_{pp}. The piezo was thermally coupled to a copper cooling stage using thermal couplant (Wakefield type 120). Steel ferrules were bonded to capillaries using epoxy (Devcon HP250). Ink and support were extruded using a mass flow controller (Fluigent MFCS-EZ) at pressures calibrated by measuring masses extruded at fixed pressures and times. For ink, flow speeds were matched to translation speeds and ranged from 3 to 12 mm/s. Layer-by-layer supports were printed at a stage speed of 10 mm/s and an estimated flow speed of 15 mm/s. The point where the nozzle touches the substrate was defined as $z = 0$. Parts were printed at a stand-off distance and line spacing of 0.3 mm, which is the inner width of the capillary.

The flow field was illuminated using light transmitted through a red filter cube, to prevent curing. Videos were collected from underneath the nozzle through the glass substrate using a Point Grey Grasshopper GS3-U3-2356C-C camera with an Infinity Infinitube FM-200 objective and $\times$0.66 lens, at 86 fps.

Fluid flows were measured in Matlab R2018b using a modified version of OpenPIV (Fig. 7.9).[177] The full frame was normalized from 0 to 1, and only interrogation regions with an average intensity above 0.1 and a maximum intensity above 0.5 were inspected. Collected vectors were filtered to remove outliers, but holes were not filled. Distributions were collected using Matlab R2018b. Backgrounds were removed using a 15 px disk structuring element. The P–T origin is defined at the nozzle center, and the inner half-width is w. Particle distributions were detected behind the nozzle between $T = -3w$ and $T = 7w$. The collected region was summed along the P dimension to produce intensity profiles like the one shown in Figure 7.9B. Peaks were identified using the Matlab function *findpeaks* with a minimum peak-to-peak distance of w. Frames in which the corner of the polygon is visible were removed. The width is the standard deviation of the distribution within w of the peak, normalized by the width of a uniform distribution of width $2w$.

Kendall τ tests were used to evaluate correlations between printing parameters and fitted coefficients.[219] Kendall τ tests strongly value monotonicity, and p-values from Kendall tests are useful for evaluating the significance of trends. Only Kendall p-values below 0.05 were considered significant.

7.4 Results

7.4.1 Particle distribution width

Digital image analysis of *in-situ* videos of the printed line just behind the nozzle indicates that the width of the distribution of particles in the printed line varies as a function of the print direction. Focusing anisotropy predicts that the distribution width should vary as a function of print direction because the distribution of particles in the nozzle is rectangular, and the width of the distribution in the line will be the projection of the rectangle onto the cross-section of the print direction (Fig. 7.2). The experimental results can be compared to the theory by plotting the distribution width as a function of the print direction ϕ (Fig. 7.10).

Consider the theoretical focusing width profiles in Figure 7.10A,B. Recall Equation 7.1. Focusing anisotropy produces a profile w_{Fa}/w_p with some amplitude that depends on w_{Fx}, which represents the aspect ratio of the rectangular particle distribution in the nozzle. $w_{Fx} = 0$ indicates that the focused particle distribution is an elongated rectangle where acoustophoresis is only effective in one direction, while $w_{Fx} = 1/2$ represents a square particle distribution distribution, where acoustophoresis is equally effective in both directions within the cross-section of the nozzle.

Next, recall Equation 7.10. The experimental profile should be some constant term, plus a scaling factor F multiplied by a theoretical profile somewhere in between Figure 7.10A and B. The experimental profile in Figure 7.10C resembles the theoretical profile for an elongated

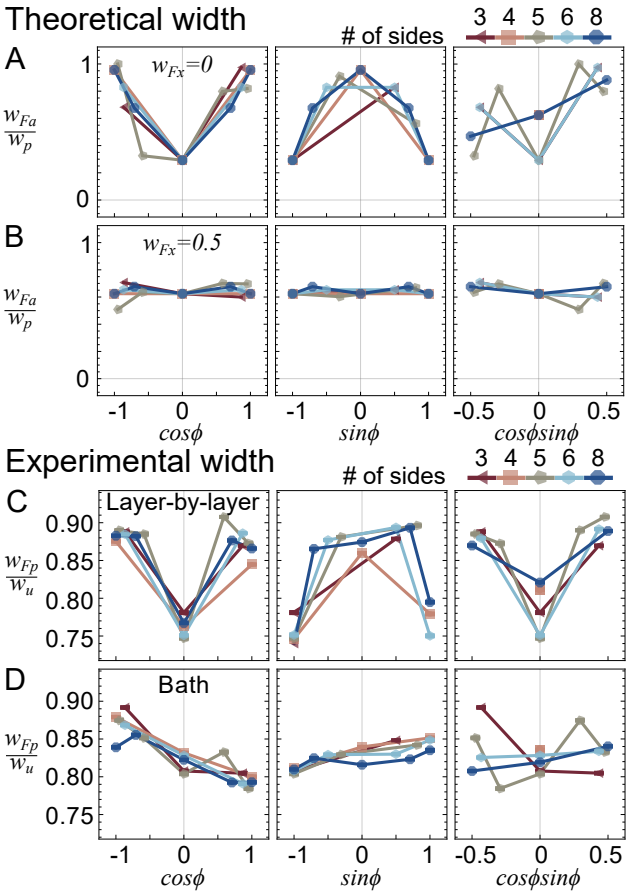

Figure 7.10: (A,B) Theoretical focusing widths for varying focused zone aspect ratios w_{Fx}, as a function of printing direction ϕ. (C,D) Experimental width of particle distribution in the just-deposited line, normalized by the width of a uniform distribution of particles.

rectangular distribution in Figure 7.10A. Notably, the layer-by-layer profile in Figure 7.10C has larger variations as a function of ϕ than the bath profile in Figure 7.10D. These increased variations could come from two sources. First, the aspect ratio metric w_{Fx} could be smaller in layer-by-layer support leading to a basis function that looks more like Figure 7.10A for layer-by-layer support and Figure 7.10B for bath support. Second, the basis function could be the same for the two support geometries, and the scaling factor F, which represents the contribution of focusing error to the particle distribution width, could be larger for layer-by-layer support. Because w_{Fx} describes the distribution inside the nozzle and should not depend on the type of support used, the discrepancy in the amplitudes between the types of support likely comes from the second explanation, and the anisotropy of the particle distribution in the nozzle is suppressed during extrusion in bath support, potentially due to fluid reshaping or solid rotation.

7.4.2 Transverse flows

Particle image velocimetry of the flow fields near the nozzle indicates that flow fields vary as a function of the printing direction ϕ. The procedure in section 7.2.6 was used to fit the experimental flow fields to the linear model. An example of a fitted profile is shown in Figure 7.11. The model accurately predicts many of the printing direction dependencies observed in the experimental profile, such that corrected profiles that subtract the fitted model from the experimental profile have little dependence on the printing direction ϕ. Where print speeds in this experiment varied between 3 and 12 mm/s and transverse flow velocities are on the order of 0.1 mm/s, the model fits the orientation dependence of flows to within an error of 0.02 mm/s (Fig. 7.S17). In this and the following section, recall that these polygons are printed clockwise from inside to outside, from the point of view of the nozzle. “Inward” refers to the center of the polygon and existing lines, while “outward” refers to the outer edge of the polygon and new

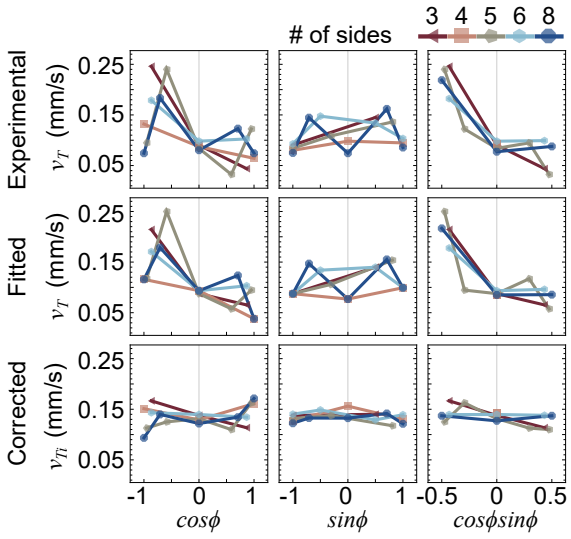

Figure 7.11: An example of an experimental transverse flow velocity profile for layer-by-layer support, inspecting the region ahead of the nozzle. The fitted profile uses coefficient values R, O_x, O_y, and M extracted from the experimental profile to construct a profile using Equation 7.15. Note that a purely theoretical profile would use theory to derive values for the coefficients D, R, S, O_x, O_y, and M, but the fitted profile uses coefficients extracted from the experimental profile, so the fitted profile should not be considered raw theory. The corrected profile is the experimental profile subtracted by the fitted profile. An ideal corrected profile would have no variation in v_{Ti} with ϕ.

lines.

Because disturbed zone, solid rotation, and fluid reshaping produce similar ϕ dependencies, for each experimental profile three fitted profiles, one using the disturbed zone basis function, one using solid rotation, and one using fluid reshaping. The quality of each fit was evaluated by calculating the error between the fitted profile and the experimental profile. The three models produced profiles with similar error sizes (Fig. 7.S17). Fluid reshaping often produces larger fitting errors, especially to the sides of the nozzle, likely because the amplitudes of the basis functions for the sides of the nozzle are small, necessitating a larger coefficient which amplifies errant trends. Solid rotation provided the best fit for most of the data sets. The remainder of this section will only report solid rotation coefficients, keeping in mind that these coefficients are meant to represent some combination of disturbed zone, solid rotation, and fluid reshaping effects.

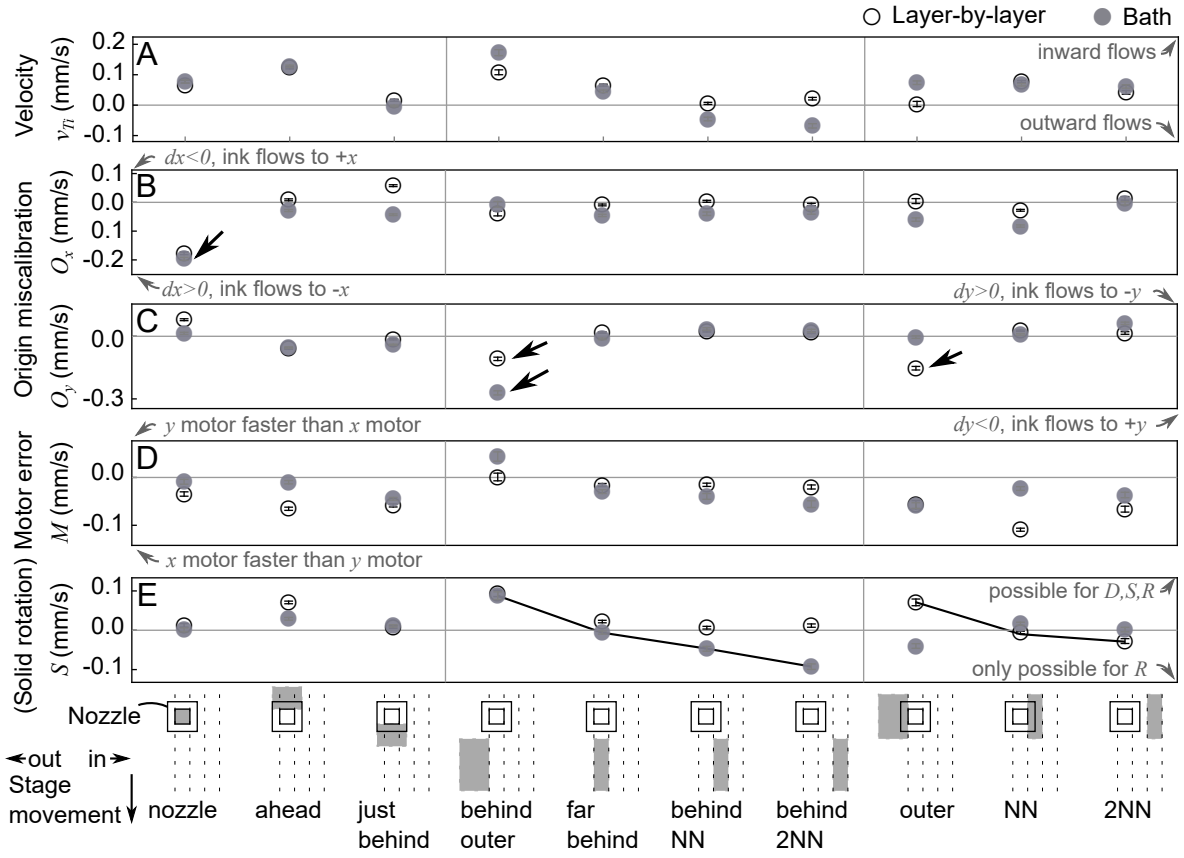

Figure 7.12: A) The velocity v_{Ti} is the direction-independent velocity collected after removing O_x, O_y, M, and S. B–E) Fitting coefficients as described by Equation 7.11 for B,C) origin, D) motor, and E) solid rotation models fit to average transverse flows in ten regions of interest, for layer-by-layer and bath support. Error bars represent fitting error and are smaller than markers. The solid rotation constant S represents a superposition of solid rotation, disturbed zone, and fluid reshaping. Black arrows and lines point to features of interest.

Extracted direction-independent transverse flow velocities v_{Ti} paint a picture of fluid flowing around the nozzle, with an overall preference toward the inner edge of the printed polygon (Fig. 7.12A). Within and ahead of the nozzle, fluid flows inward toward the existing ink and support. In layer-by-layer support, ink in the inner regions flows inward, and ink in the outer region has negligible transverse flows. In bath support, ink to the sides of the nozzle flows inward. For both supports, behind the nozzle, ink flows toward the freshly written line, and ink within the freshly written line flows inward toward the existing written lines.

For flow fields in most regions, origin miscalibration in x coefficients O_x are negative, especially within the nozzle and to a lesser extent regions touching the nozzle, indicating that fluid is being pushed toward negative x, in global (G-code) coordinates (Fig. 7.12B). Origin x coefficients are more negative for bath support, indicating that fluid is pushed a farther distance in bath support. Origin miscalibration in y coefficients O_y are negative in the outer and behind outer regions, indicating fluid is being pushed toward positive y in global coordinates (Fig. 7.12). Origin y coefficients are close to zero elsewhere, indicating that most regions are insensitive to miscalibration in y under the printing conditions used in this experiment. Motor coefficients M are negative, indicating that $c_x > c_y$. In other words, the y motor is too slow, or the x motor is too fast (Fig. 7.12). Motor coefficients are largest directly to the sides of the nozzle, indicating that printed shape distortions in x and y manifest most clearly in the flow field nearest the nozzle. In regions touching the nozzle, layer-by-layer motor coefficients are more negative than bath motor coefficients. Behind the nozzle, bath motor coefficients are more negative than layer-by-layer motor coefficients.

Recall that in Figure 7.12, solid rotation coefficients S are meant to encompass disturbed zone, solid rotation, and fluid reshaping effects. Disturbed zone and solid rotation should have positive coefficients. A negative S representing disturbed zone effects would imply that near the nozzle, fluid flows backwards against the direction of flow of the rest of the field. A negative S representing solid rotation would imply that the filament rotates the opposite direction around

its leading corner than would be expected based on the location of its center of gravity. Fluid reshaping should have positive S coefficients on the outer regions and center of the print path and negative S coefficients on the inner regions, such that ink that falls outside of the print path flows toward the center of the print path. As such, negative S coefficients are an indicator that fluid reshaping is dominant over solid rotation and disturbed zone effects. In both supports, S coefficients are positive in the outer regions and negative in the inner regions (Fig. 7.12). In bath support, this transition happens behind the nozzle, so it is reasonable to expect that fluid reshaping is important for bath support behind the nozzle. In layer-by-layer support, this transition happens strongly next to the nozzle and weakly behind the nozzle, so it is reasonable to expect that fluid reshaping is important for layer-by-layer support close to the nozzle.

One might notice that behind the nozzle, motor error coefficients M, solid rotation coefficients S, and direction-independent velocities v_{Ti} all become more negative in regions progressing from outward to inward (Fig. 7.12). It is possible that faster direction-independent transverse flows could accentuate the effects of motor error and solid rotation, disturbed zone, and fluid reshaping. However, this trend does not occur directly to the sides of the nozzle, indicating that these similar trends may not be directly correlated.

Although the support geometry influences direction dependent effects, the ink composition, print speed, and polygon edge length have limited effects on the fitting coefficients within the probed range. While these trends are not statistically significant in all regions, increasing the TEGDMA concentration (decreasing the ink viscosity), decreasing the print speed, and increasing the edge length decrease the magnitude of O_y (Fig. 7.S18, 7.S19, 7.S20). Decreasing the ink viscosity decreases the magnitude of the motor coefficient (Fig. 7.S18), and increasing the polygon edge length increases the magnitude of the motor coefficient (Fig. 7.S20). Because distortions in the printed shape should come only from the gantry motors, it is unclear why these printing parameters influence the motor error coefficient. Decreasing the viscosity decreases the magnitude of the solid rotation coefficient, which as discussed before heavily

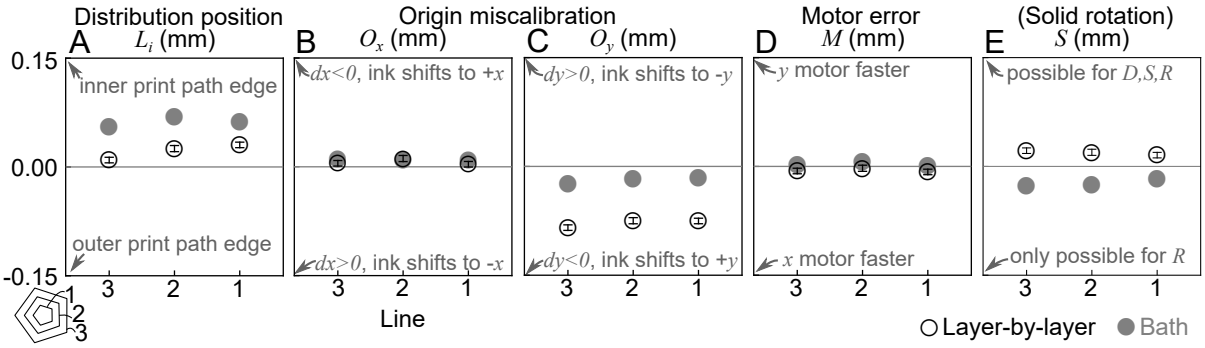

Figure 7.13: A) The position L_i is the direction-independent particle distribution position collected after removing O_x, O_y, M, and S. B–E) Fitting coefficients as described by Equation 7.12 for B,C) origin, D) motor, and E) solid rotation models fit to average particle distribution positions in the three lines, measured in the third pass. The solid rotation constant S represents a combination of the solid rotation, disturbed zone, and fluid reshaping models. The print path is 0.3 mm wide.

reflects fluid reshaping effects (Fig. 7.S18). This could come from increased reshaping at the surface of the filament and less deformation at the center due to decreased viscosity.

7.4.3 Distribution positions

Final distribution positions were determined by detecting local maxima in the light intensity profiles across the region just behind the nozzle in the third pass. Orientation-independent particle distribution positions are inward from the intended position at $L_i = 0$, shifting toward the inner edge of the printed polygon and the existing lines (Fig. 7.13A). Lines shift farther inward in bath support than in layer-by-layer support.

Origin miscalibration coefficients O_x and O_y for distribution positions describe systemic shifts in the particle distributions in global coordinates. Origin miscalibration in y coefficients are negative and large compared to the final positions (Fig. 7.13C). Ink systemically shifts toward $+y$, indicating that the flows toward $+y$ in the outer region determined during coefficient fitting for transverse flows may have an impact on the final distribution. Particle distribution position shifts in y are greater for layer-by-layer support than for bath support. Recall that the

magnitude of O_y was bigger in layer-by-layer support than bath support for the outer region and bigger in bath support than layer-by-layer support for the behind outer region, so it is possible that flows in the outer region influence the particle distribution more strongly than flows in the behind outer region. Alternatively, distributions may be more vulnerable to systemic shifts in global coordinates in layer-by-layer support, and those shifts may not be traceable to flows in a single interrogation region.

Solid rotation coefficients S describe the contributions of disturbed zone, solid rotation, and fluid rotation to the distribution position. The particle distribution position should result from some combination of flows in the inner and outer sides and center of the print path. Because of the set of printing directions used in this study, solid rotation and disturbed zone models predict a net inward shift toward existing lines. Fluid reshaping models predict a net inward shift from flows in the center and outer regions, but a net outward shift from flows in the inner regions. Thus, as with transverse flow velocities, negative S coefficients indicate that fluid reshaping dominates solid rotation and disturbed zone effects. Solid rotation constants for particle distributions are positive (inward shift) for layer-by-layer support and negative (outward shift) for bath support. This result agrees with the transverse flow fitting, because solid rotation coefficients are more negative in bath support than layer-by-layer support for both transverse flows and particle distributions.

Origin miscalibration coefficients in x are close to 0, indicating that the flows toward $-x$ under the nozzle determined during coefficient fitting for transverse flows do not have an effect on the final distribution of particles (Fig. 7.13B). The motor error model predicts that miscalibration of the motor speeds rotates the printed line out of the expected print path used for video analysis, shifting the average particle distribution position off-center relative to the expected print path. Motor coefficients for distribution positions are close to 0, indicating that the negative motor coefficients found during flow analysis do not manifest in large changes in the particle distribution position (Fig. 7.13D).

Printing parameters do not have a strong impact on particle distribution position fitting coefficients (Fig. 7.S22). Kendall τ tests indicate that the viscosity of the ink, the print speed, and the size of the printed polygon have few statistically significant impacts on the fitting coefficients for distribution positions. Most significantly, increasing the TEGDMA concentration in the ink and thus decreasing its viscosity shifts the motor error from positive to negative for both types of support. The motor error should be constant as a function of TEGDMA, since it should come from the gantry itself. This trend indicates that another mechanism not considered here may have a dependence on printing direction that is similar to motor error.

7.5 Discussion

The experimental particle distribution width in layer-by-layer support has a stronger dependence on the printing direction ϕ than the distribution in bath support. Comparing the experimental distribution width to the theoretical width, the shape of the printing direction-width profile indicates that the distribution of particles in the nozzle is rectangular rather than square, with a large aspect ratio. Bath support has a smaller dependence on printing direction than layer-by-layer support likely because bath support distorts the filament as it exits the nozzle, canceling out one source of direction dependence with another source of direction dependence. The focusing anisotropy theory assumes that the distribution of particles in the line stays perfectly preserved as it exits the nozzle, and only the polymer matrix around it distorts to fill space, e.g. via fluid reshaping. However, bath support provides a hydrostatic stress that pushes on the filament as it exits the nozzle that likely distorts the entirety of the filament, not just the surface. The nature of this bulk distortion may depend on the printing direction, just as fluid reshaping and solid rotation depend on the printing direction, so the effect of this hydrostatic stress may compensate for the orientation effects of focusing anisotropy. In contrast, in layer-by-layer support, the ink is printed into an empty space occupied only by air, so the forces

exerted on the deposited filament are imposed mostly on the surface, not the bulk, allowing the distribution of particles to remain uninfluenced during extrusion.

Direction-independent transverse flows indicate that ink flows around the nozzle and converges toward the freshly printed line. Overall, fluid flows toward existing ink and the inner edge of the polygon. Ink flowing around the nozzle roughly matches the patterns predicted by the disturbed zone model. Ink flowing toward existing ink lines may come from capillarity or from relaxation of stressed support material. A more detailed treatment of the sources of the direction-independent flow field is presented in a separate paper.[19]

The disturbed zone, solid rotation, and fluid reshaping models all describe behaviors that depend on the difference in angle between the printing direction and the square nozzle orientation $\phi - \alpha$. While the disturbed zone model describes fluid flowing around the nozzle, the solid rotation and fluid reshaping models describe a square filament changing shape or orientation so the filament lies flat on the substrate. All three of these effects could be mitigated by a rotating stage which maintains a constant $\phi - \alpha$. The overlap in behaviors among the disturbed zone, solid rotation, and fluid reshaping models has trade-offs. The overlap is disadvantageous because the disturbed zone model is phenomenologically different from the solid rotation and fluid reshaping models, since the disturbed zone model is mostly concerned with how the nozzle influences fluid that is already on the substrate while the other two models are concerned with geometric transformations of the ink being deposited. Correction of these two types of errors during printing likely requires different types of approaches. For example, narrowing the disturbed zone may require increasing the Reynolds number [213, 214, 215, 216], while limiting fluid reshaping may require decreasing the surface tension of the ink. The overlap is advantageous because direct ink writing encompasses inks with a wide range of rheological properties, ranging from low-viscosity inks such as aqueous alginate solutions to high-viscosity viscoelastic inks such as epoxy-based composites.[91, 120] Most inks used in DIW will follow behaviors somewhere in between the solid rotation and fluid reshaping models, so the similar-

ity of the models is useful because either model can be used to fit behaviors of most DIW inks. In these experiments, negative solid rotation S transverse flow coefficients in the inner regions of the nozzle indicate that fluid reshaping is prominent for these polyurethane-based shear thinning composite inks, which fits expectations because the inks follow fluid-like rheology with a storage modulus that is less than the loss modulus at all shear stress values (Fig. 7.S23).

Fluid reshaping is prominent near the nozzle in layer-by-layer support and far from the nozzle in bath support. This difference in length scale may occur because of the hydrostatic stress in the space between the nozzle and support. Fluid reshaping necessitates a change in the shape of the ink surface. In bath support, the extruded ink is in contact with support material on all sides and the nozzle above. In layer-by-layer support, the front edge and for most lines the outer side of the ink surface is exposed to air, and the fluid is in contact with the nozzle above (Fig. 7.1D). Thus, because the layer-by-layer case is less bounded, the fluid surface can deform faster in layer-by-layer support than in bath support.

Origin miscalibration constants represent systemic shifts in global (G-code) coordinates that could result from a systemic misalignment of the support and ink nozzle origins in layer-by-layer support. Recall that O_x and O_y encompass the strength of the effect in the given region, as well as the size of the miscalibration error $|dx|$ or $|dy|$ divided by the time scale τ that the ink spends being pushed out of the way. The majority of the ink displacement process should happen under the nozzle, since the ink will collide with existing lines as soon as it leaves the nozzle. As such, the origin miscalibration constants O_x and O_y for transverse flows should be larger close to the nozzle. The large O_x coefficient for transverse flows within the nozzle matches this expectation.

The O_y coefficient for transverse flows is largest in the outer region and behind outer region. Additionally, the origin miscalibration O_y coefficients for particle distribution positions indicate that all three lines shift to positive y. O_x coefficients are larger than O_y coefficients, indicating that in this set of experiments miscalibration error in x tends to be larger than in y.

Further, origin miscalibration constants are non-zero for both layer-by-layer and bath support, and shifts in position are larger for layer-by-layer support than for bath support, which fits expectation because bath support constrains the printed line more. If collisions with the support alone caused these shifts, there would only be shifts in line 3, the entire flow field would have similar origin miscalibration coefficients, and coefficients for bath support would be equal to zero. Capillarity may cause this deviation from the theory. The origin miscalibration models are scaled assuming that if the line is deposited too far away from an existing line, nothing will happen, and that the line will only shift if it collides with an existing line. However, if the line is deposited only slightly too far away from an existing line, capillarity may draw the new line toward the existing line. This would increase the average transverse inward flow beyond the expected transverse flow and produce a large origin miscalibration coefficient O. The sizes of the coefficients further support the possibility of capillarity. Miscalibration error in y may be small enough that capillarity causes systemic shifts in y, but the error in x is too large to enable capillarity to have an effect. A second possible source of the deviation from the theory is a tilted nozzle. The position of bath support cannot be calibrated relative to the ink because the support bath is volumetrically continuous, so collisions and capillarity would not causes these systemic shifts. Instead, systemic shifts in one direction for both types of support may come from a tilted nozzle or an uneven nozzle bottom edge, such that the bottom of the nozzle is not perfectly level in the $x - y$ plane. Because coefficients are larger in layer-by-layer support, global shifts in layer-by-layer support likely come from collisions, capillarity, and nozzle tilt, while global shifts in bath support only come from nozzle tilt.

The results of this study indicate that for the 3-axis printer used in these experiments, the x motor is too fast, or the y motor is too slow. Though the motor coefficients M are small for transverse flows and negligible for distribution positions, indicating that these speed errors are small, motor errors can have two adverse impacts under less favorable printing conditions. First, the geometric fidelity of the printed structure will be slightly inaccurate, where the struc-

ture will be too small or too large in the dimension of the inaccurate motor. Second, *in-situ* monitoring of the print path will yield inaccurate measurements because the print path will not be where the monitoring software expects it to be. Both of these problems can be corrected by using the methods described herein to detect motor errors, then fixing them via hardware (e.g. recalibrating or replacing the motor) or software (e.g. altering the G-code to take these errors into account). Additionally, several trends indicate that another mechanism may produce similar direction dependent effects to motor error. Although motor error should only depend on the printer stage, the support type and ink composition influence measured motor error coefficients, indicating that this other mechanism likely depends on rheology.

7.6 Conclusions

This work proposed an analytical model that describes printing direction-dependent effects on the flow field near the nozzle and the microstructure of the printed line. Using acoustophoresis, a narrow distribution of particles was established in the nozzle. The distribution changes upon exiting the nozzle. By tracking fluid flows transverse to the printing direction and measuring the width and peak position of the particle distribution in the printed line, it was determined that the proposed model predicts many of the direction dependencies that occur during direct ink writing. By comparing the model's fitting parameters between layer-by-layer and bath support geometries, strategies to mitigate the various direction-dependent effects were determined.

When attempting to amplify or extinguish printing direction dependence in direct ink writing, one should consider six sources (Table 7.4). *In-situ* monitoring of the flow field and particle distributions can be used to detect and correct these errors during printer calibration. Additional parameter studies may illuminate more ways to manipulate the severity of these effects. Installing a rotary stage onto the gantry such that the printing direction will always be constant relative to the nozzle orientation may extinguish all of these effects simultaneously but would

Source	Consequence	Remedy
Rotational asymmetry of the filament microstructure inside the nozzle	Direction-dependent microstructures	Use bath support
Misalignment of the ink and support nozzles, capillarity, and a tilted nozzle	Systemic movement of the filament in global coordinates	Calibrate nozzle positions and orientations precisely, use bath support
Motor calibration errors	Distortion of the printed structure	Calibrate motor speeds precisely, alter G-code to compensate for errors
Disturbed zone around nozzle	Asymmetric flows around the nozzle	Use layer-by-layer support*
Low-viscosity inks: fluid reshaping	Direction-dependent microstructures	Use layer-by-layer support*
High-viscosity inks: solid rotation	Direction-dependent microstructures	Use layer-by-layer support*

Table 7.4: Sources of direction dependence in direct ink writing. Remedies may be augmented by further studies. *These three sources overlap, so the remedy may not extinguish all 3 sources.

require more complex G-code.

While the proposed model was developed for a square nozzle using acoustophoresis to establish a particle distribution and using a yield stress fluid support material, it can be adapted to various printing modalities. Rotationally asymmetric microstructures could be established inside the nozzle using magnetic or electric fields. The derivations shown in the supplemental information can be reformulated for rectangular, oval, or other shapes of nozzles. Direction dependencies that result from these nozzle asymmetries may be corrected by using a rotary stage that maintains consistency between the translation direction and the nozzle orientation.

Additionally, long-range effects can be mitigated by incorporating curing just outside of the nozzle or partial curing inside of the nozzle, which would trap particles in place within the ink filament. While the origin miscalibration model was derived with misalignment of the ink and support nozzles in mind, it can be broadly applied to any effect which causes systemic flows in one global direction. Motor error is broadly applicable to any system that uses a 3-axis gantry to deposit filaments including DIW and fused deposition modeling. Further, while these models center around the distribution of particles inside of the printed line, they can also be used to understand the movement of the filament as a whole and can be applied to homogeneous inks.

7.S1 Supplemental figures and tables

7.S1.1 Hypotheses

Focusing anisotropy

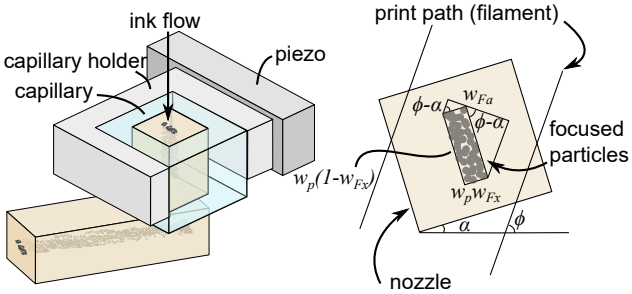

Figure 7.S1: The focusing zone in the nozzle has dimensions $w_p(1 - w_{Fx})$ and $w_p w_{Fx}$. This results in a projected focusing zone w_{Fa} that depends on line orientation ϕ.

In this work, acoustophoresis produces a narrow rectangular distribution of particles at the center of a square glass capillary which acts as a nozzle. A piezoelectric actuator establishes two standing bulk acoustic waves in the two dimensions transverse to fluid flow (Fig. 7.S1). Particles are drawn toward the nodes of the acoustic waves with primary acoustic radiation force F_A. Combined, this ideally would push the particles to a point at the center of the square

nozzle. However, two factors cause the particles to focus to a rectangle instead of a point: drag and anisotropic resonance.

Inside the nozzle within the focusing zone, particles experience a drag force that opposes the primary acoustic radiation force that moves particles toward the center of the nozzle. Chapter 4 showed that balancing these forces produces an expression for terminal velocity that can be used to determine the width of the focused particle distribution w_{Fi} along the dimension i,

$$w_{Fi} = W - \frac{\pi a^2 \beta_f p_o^2 \phi L}{9W\mu v} \tag{7.S1}$$

where ϕ is the acoustic contrast factor

$$\phi = \frac{5\rho_p - 2\rho_f}{2\rho_p + \rho_f} - \frac{\beta_p}{\beta_f} \tag{7.S2}$$

and W is the channel width, a is the particle radius, β_p and β_f are the compressibilities of the particle and fluid, ρ_p and ρ_f are the densities of the particle and fluid, p_o is the acoustic wave amplitude, L is the focusing zone length (roughly the nozzle length), μ is the fluid viscosity, and v is the flow speed in the nozzle.[15] Thus, because of drag, the distribution has a finite width instead of narrowing to a point.

Acoustophoresis in square channels produces rectangular distributions of particles, not circular distributions, because acoustophoresis employs primary acoustic radiation forces which are perpendicular to the channel walls. As such, the distribution will have dimensions $w_p w_{Fx}$ and $w_p(1 - w_{Fx})$ where w_{Fx} is between 0 and 1 (Fig. 7.S1). The design of the stainless steel capillary holder promotes a focusing width $w_{Fx} < 1/2$, because both capillary walls are in contact with the steel holder in the x direction, while only one wall is in contact in the perpendicular direction (Fig. 7.S1). The other perpendicular wall is in loose contact with a compliant light barrier that is not acoustically coupled to the piezo, resulting in a lower primary acoustic radiation force F_A in the perpendicular direction. In terms of Equation 7.S1, this can be viewed

as a larger acoustic wave amplitude p_o in x.

Assume that the distribution of particles in the printed line, when viewed from above, will be a projection of the rectangular particle distribution along the printing direction. Thus, the width of the distribution within the printed line w_{Fa} can be expressed using Equation 7.S3, where w_p is a scaling factor representing the size of the rectangular particle distribution, while w_{Fx} remains a descriptor of the distribution aspect ratio.

$$\frac{w_{Fa}}{w_p} = w_{Fx}|\sin(\phi - \alpha)| + (1 - w_{Fx})|\cos(\phi - \alpha)| \tag{7.S3}$$

Plotting Equation 7.S3 as a function of the printing angle ϕ, the focusing width is an absolute sine with π periodicity as a function of printing orientation ϕ (Fig. 7.S2). If $w_{Fx} = 1$, the focusing width reaches a minimum at $\phi = \alpha$, where the print direction is aligned with the nozzle tilt. If $w_{Fx} = 0$, the focusing width reaches a minimum at $\phi = \alpha + \pi/2$, where the print direction is orthogonal to the nozzle tilt. If $w_{Fx} = 0.5$, the focusing width reaches minima whenever the filament is parallel to or normal to the nozzle tilt, at $\phi = \alpha$ and $\phi = \alpha + \pi/2$.

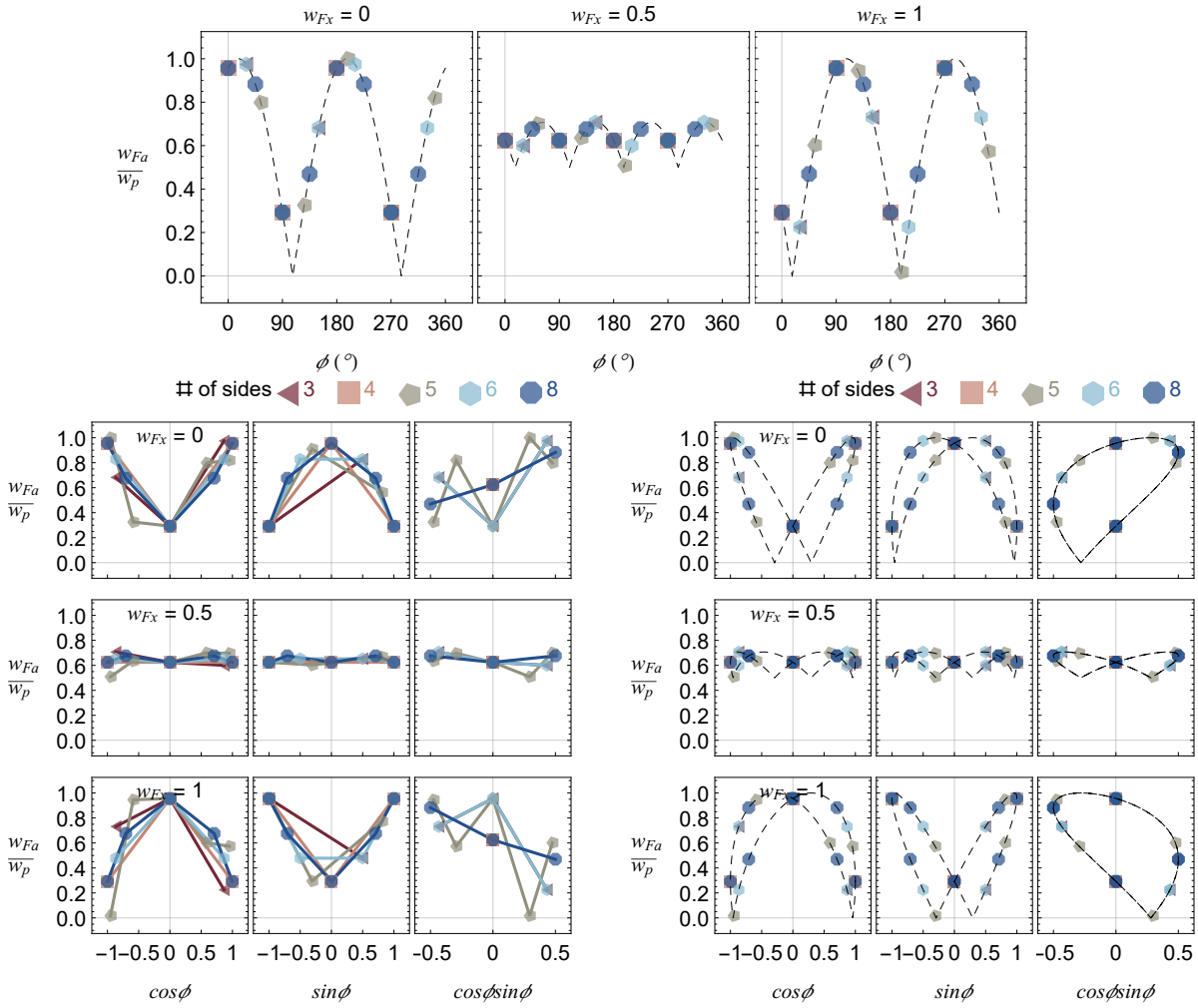

Figure 7.S2: ϕ dependence and basis functions for focusing anisotropy. Dotted lines (top, bottom right) indicate the theoretical expression. Points indicate the printing directions used in this study, split by polygon. Solid lines are visualization aides which connect points which are averaged in the horizontal axis (bottom left).

Disturbed zone

In both layer-by-layer support and a support bath, when the nozzle is traveling near an existing ink filament, a disturbed zone will exist within the existing and newly deposited filaments (Fig. 7.S3A,C). Within this disturbed zone, transverse flows will be present.[213, 214, 215, 216] For a nozzle with $\alpha = 0$, where the flat edge of the nozzle is perpendicular to the

print direction, these transverse flows will be outward ahead of the nozzle and inward behind the nozzle (Fig. 7.S3C).[216]

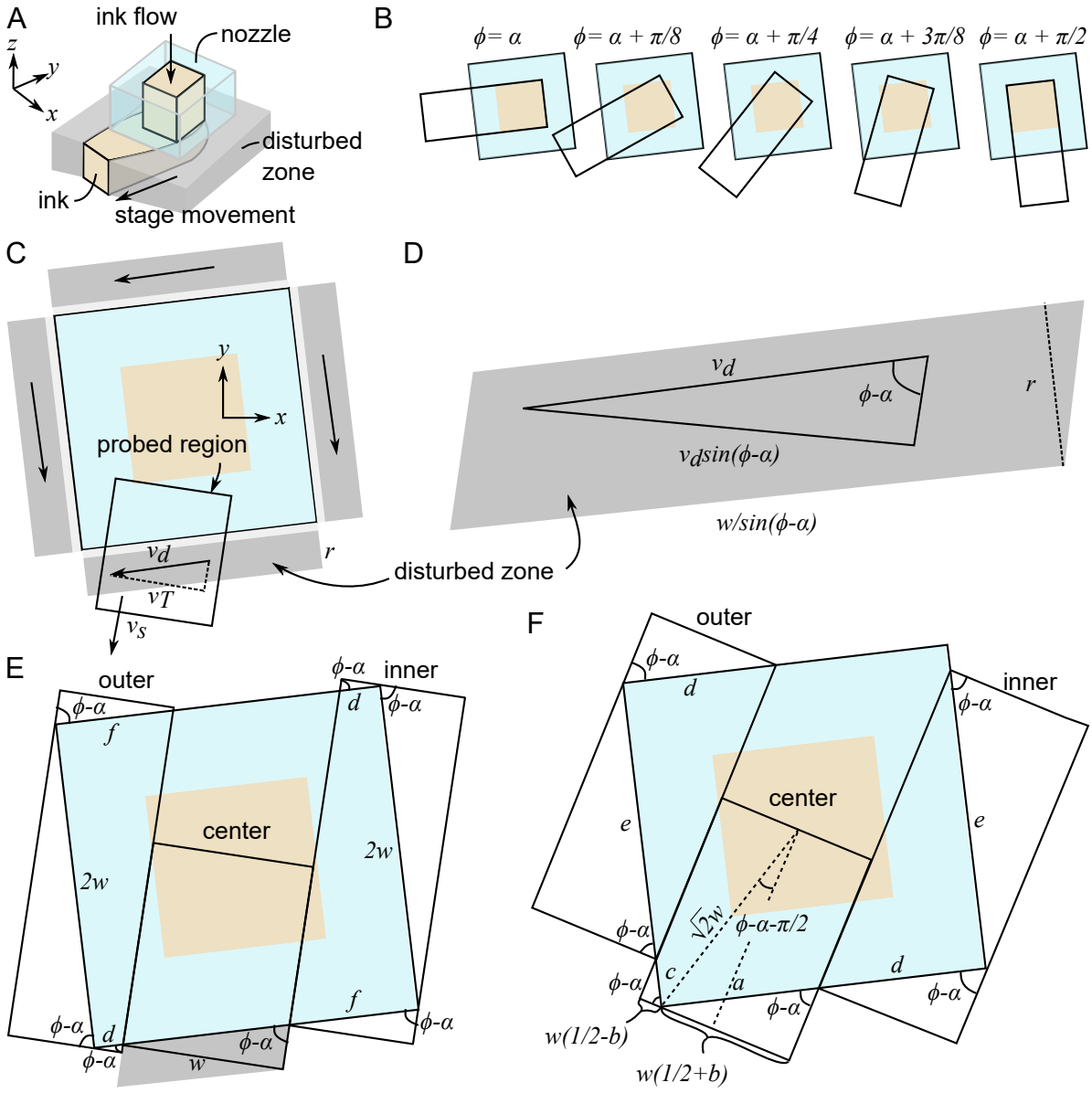

Figure 7.S3: Variables used in derivation of disturbed zone transverse flows. A) Three-dimensional model of disturbed zone. B) Breaks in the piecewise function occur where the filament intersects with the nozzle corner. C) Fluid flows parallel to the nozzle surface within a disturbed zone of size r. D) Transverse flows in the disturbed zone are a projection of flows parallel to the nozzle surface onto the transverse direction. E,F) Angles of intersections between the outer, center, and inner interrogation regions and the nozzle, E) when the filament does not intersect the nozzle corner and F) when the filament intersects the nozzle corner.

To determine orientation dependence, assume that any ink present near the nozzle flows parallel to the surface of the nozzle at a velocity v_d within a disturbed zone of thickness r (Fig. 7.S3C). Outside of the disturbed zone, flow is uniform along the direction of stage movement with speed v_s (Fig. 7.S3C). The transverse flow within the disturbed zone depends on the print direction.

Probing a region of width w, ahead of the nozzle and directly behind the nozzle, the measured transverse flow within the probed zone can be determined by multiplying the transverse flow within the disturbed zone by the area of the probed disturbed zone divided by the total area of the interrogation region A.

For example, consider the center region in Figure 7.S3E, where $3\pi/8 < \phi - \alpha < \pi/2$. The transverse flow velocity is $-v_d \sin(\phi - \alpha)$ and the area of the trapezoidal probed zone is $rw/\sin(\phi - \alpha)$ (Fig. 7.S3D). Taking the product of the transverse flow velocity and the probed disturbed zone area, the measured transverse flow is

$$v_{Td}A = -v_d wr \tag{7.S4}$$

The outer region in Figure 7.S3E intersects with three sides of the nozzle, so the transverse flow is a sum of flows in three trapezoids:

$$v_{Td}A = v_d r(2w)\cos(\phi - \alpha) - v_d rd\sin(\phi - \alpha) - v_d rf\sin(\phi - \alpha) \tag{7.S5}$$

From Figure 7.S3E,

$$d + f = (2w - w/\sin(\phi - \alpha)) \tag{7.S6}$$

Thus, Equation 7.S5 can be simplified:

$$v_{Td}A = v_d r w(2\cos(\phi - \alpha) - 2\sin(\phi - \alpha) + 1) \tag{7.S7}$$

A similar analysis can be used to determine flows in the inner region, and for $0 < \phi - \alpha < \pi/8$.

When $\pi/8 < \phi - \alpha < 3\pi/8$, each region intersects two sides of the nozzle (Fig. 7.S3F). In the center, the two regions have lengths a and c, where

$$a\sin(\phi - \alpha) = w(1/2 + b) \tag{7.S8}$$

and

$$c\cos(\phi - \alpha) = w(1/2 - b) \tag{7.S9}$$

and

$$b = \sqrt{2}\sin(\phi - \alpha - \pi/2) \tag{7.S10}$$

via trigonometry. The total flow is

$$v_{Td}A = v_d r c\cos(\phi - \alpha) - v_d r a\sin(\phi - \alpha) \tag{7.S11}$$

Simplifying Equation 7.S11,

$$v_{Td}A = 2\sqrt{2}v_d w r\sin(\phi - \alpha - \pi/2) \tag{7.S12}$$

To the outer side of the nozzle, the transverse flow is

$$v_{Td}A = v_d \cos(\phi - \alpha) er - v_d \sin(\phi - \alpha) dr \tag{7.S13}$$

where $e = 2w - c$ and $d = 2w - a$. Evaluating,

$$v_{Td}A = v_d r(2w(\cos(\phi - \alpha) - \sin(\phi - \alpha)) - 2\sqrt{2}\sin(\phi - \alpha - \pi/2)) \tag{7.S14}$$

Knowing that $\cos x - \sin x = \sqrt{2}\sin(\pi/4 - x)$, Equation 7.S14 simplifies to $v_T A = 0$.

Transverse flows in central regions are summarized in Equation 7.S15

$$\frac{v_{Td}A}{v_d wr} = \begin{cases} 1 & 0 < \phi - \alpha < \pi/8 \\ 2\sqrt{2}\sin(\phi - \alpha - \pi/2) & \pi/8 < \phi - \alpha < 3\pi/8 \\ -1 & 3\pi/8 < \phi - \alpha < \pi/2 \end{cases} \tag{7.S15}$$

The transverse flows in the regions on the sides of the print path are summarized in Equation 7.S16.

$$\frac{v_{Td}A}{v_d wr} = \begin{cases} 2\sqrt{2}\sin(\pi/4 - \phi + \alpha) - 1 & 0 < \phi - \alpha < \pi/8 \\ 0 & \pi/8 < \phi - \alpha < 3\pi/8 \\ 2\sqrt{2}\sin(\pi/4 - \phi + \alpha) + 1 & 3\pi/8 < \phi - \alpha < \pi/2 \end{cases} \tag{7.S16}$$

Both in line with and to the sides of the filament, the resultant transverse flows have minor discontinuities at $\alpha + \pi/8$ and $\alpha + 3\pi/8$ ($\alpha + \pi/8$ and $\alpha + 3\pi/8$) and are periodic in $\pi/2$ (Fig. 7.S4).

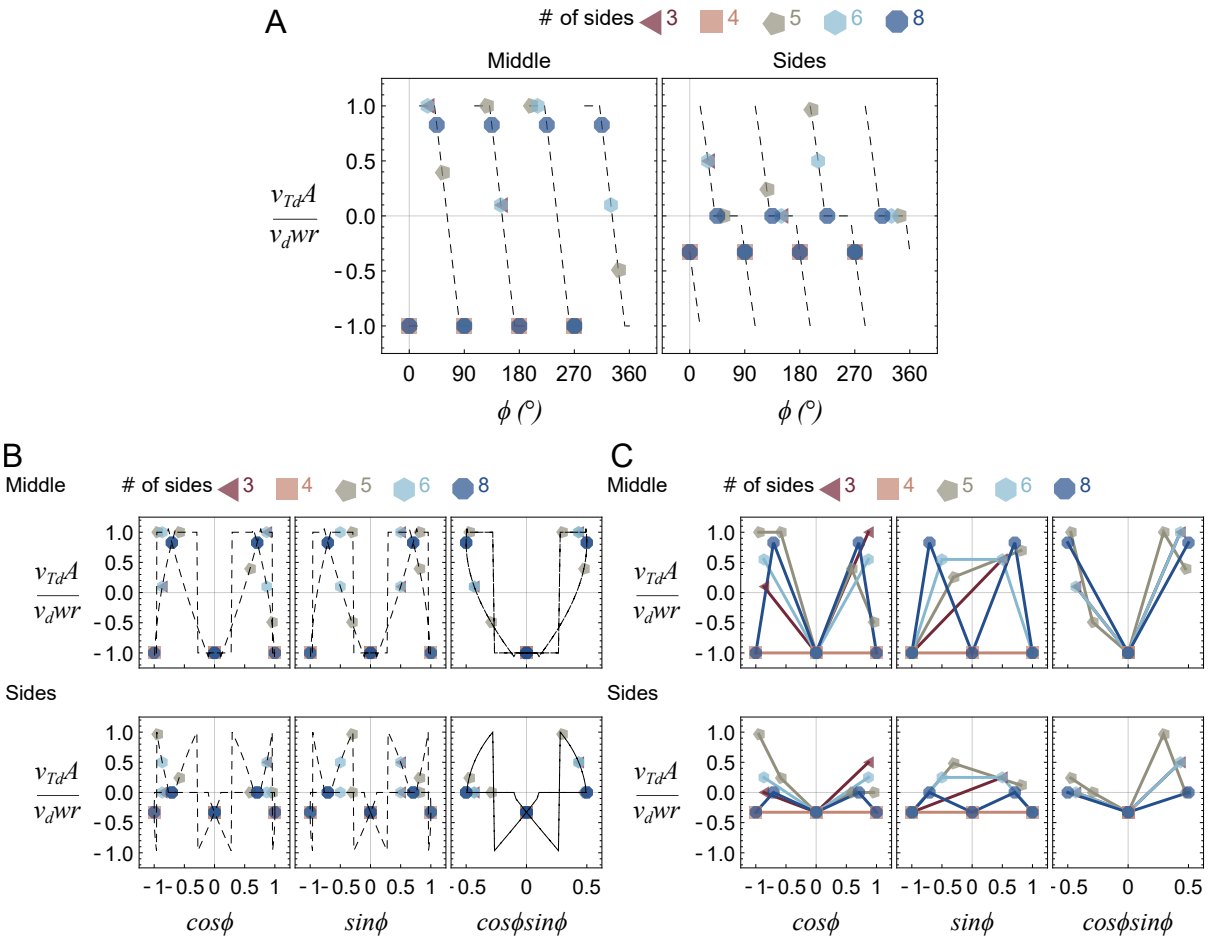

Figure 7.S4: Theoretical transverse flows as a function of print direction ϕ and basis functions for the disturbed zone model. Dotted lines (A,B) indicate the theoretical expression. Points indicate the printing directions used in this study, split by polygon. Solid lines are visualization aides which connect points which are averaged in the horizontal axis (C).

Fluid reshaping

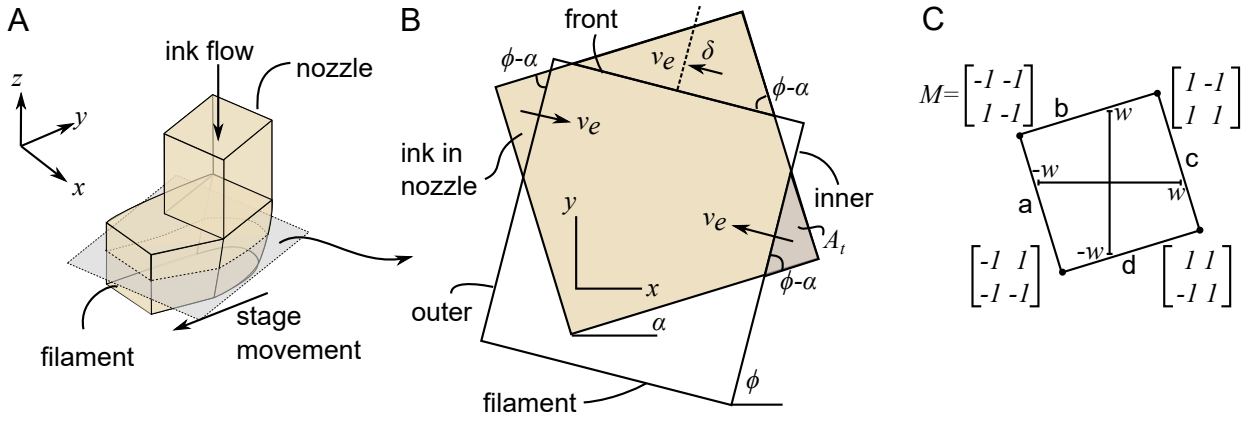

Figure 7.S5: A-B) At some print directions, part of the square nozzle falls outside of the intended filament area. C) Coordinates of nozzle corners.

Because this work uses a square nozzle, at certain orientations the outer corners of the nozzle fall outside of the programmed print path (Fig. 7.S5B). To the sides of the print path, if there is already support or ink in those regions, assume that all of the area of that triangle is pushed toward the center of the print path (Fig. 7.S5B). Assume that the flow within the interrogation region of size A inward or outward from the nozzle is the product of the area of the triangle A_t and the average flow velocity within the triangle v_e.

$$v_{Tr}A = A_t v_e \tag{7.S17}$$

Inward from the nozzle, $v_e < 0$. Outward from the nozzle, $v_e > 0$, where positive velocities point inward toward the center of the polygon. The area of the triangle can be determined using the intersections of the nozzle edges with the filament edges. The corners of the nozzle are

$$\begin{pmatrix} x \\ y \end{pmatrix} = w\boldsymbol{M} \begin{pmatrix} \cos\alpha \\ \sin\alpha \end{pmatrix} \tag{7.S18}$$

where the nozzle half-width is w. The corners of the filament are

$$\begin{pmatrix} x \\ y \end{pmatrix} = w\boldsymbol{M} \begin{pmatrix} \cos\phi \\ \sin\phi \end{pmatrix} \tag{7.S19}$$

Values for $\boldsymbol{M}$ are shown in Figure 7.S5C. The nozzle edges are defined as linear equations:

$$\begin{aligned} y_a &= -x\cot\alpha - \sin\alpha - \cos\alpha\cot\alpha \\ y_b &= x\tan\alpha + \cos\alpha + \sin\alpha\tan\alpha \\ y_c &= -x\cot\alpha + \sin\alpha + \cos\alpha\cot\alpha \\ y_d &= x\tan\alpha - \cos\alpha - \sin\alpha\tan\alpha \end{aligned} \tag{7.S20}$$

The filament edges are defined as linear equations:

$$\begin{aligned} y_{outer} &= x\tan\phi + \cos\phi + \sin\phi\tan\phi \\ y_{front} &= -x\cot\phi + \sin\phi + \cos\phi\cot\phi \\ y_{inner} &= x\tan\phi - \cos\phi - \sin\phi\tan\phi \end{aligned} \tag{7.S21}$$

	outer	front	inner
$0 < \phi - \alpha < \pi/2$	a,b	b,c	c,d
$\pi/2 < \phi - \alpha < \pi$	d,a	a,b	b,c
$\pi < \phi - \alpha < 3\pi/2$	c,d	d,a	a,b
$3\pi/2 < \phi - \alpha < 2\pi$	b,c	c,d	d,a

Table 7.S1: Nozzle edges which intersect with the given filament edge.

The area of the triangle can be determined from the intersections between the filament edge of interest (outer, front, inner) and two nozzle edges of interest (a,b,c,d) and the intersections between the nozzle edges of interest. For example, to determine the area of the inner triangle

and $\phi - \alpha = \pi/4$, the intersections between y_c and y_{inner}, between y_d and y_{inner}, and the corner between y_c and y_d should be used. The three intersections have coordinates (x_1, y_1), (x_2, y_2), and (x_3, y_3). The area of the triangle is

$$A_t = \left| \frac{x_1(y_2 - y_3) + x_2(y_3 - y_1) + x_3(y_1 - y_2)}{2} \right| \tag{7.S22}$$

Simplified, the transverse flow in the inner and outer edges of the print path is shown in Equation 7.S23.

$$\frac{|v_{Tr}|A}{v_e w^2} = \frac{\left| \csc(\alpha - \phi) \sec(\phi - \alpha)(1 - \cos(\phi - \alpha) + \sin(\alpha - \phi))^2 \right|}{2(\sqrt{2} - 1)^2} \tag{7.S23}$$

Outward from the nozzle, v_T is positive. Inward from the nozzle, v_T is negative. This transverse flow is continuous and periodic on $\pi/2$ as a function of ϕ (Fig. 7.S6).

The transverse flow in the corner in the front of the nozzle can be modeled by multiplying the area of that triangle by the distance δ between the center of the flow path (a line defined by points (x_1, y_1) and (x_2, y_2)) and the triangle centroid (x_0, y_0) (Fig. 7.S5B).

$$v_{Tr}A = A_t v_e \delta / w \tag{7.S24}$$

The distance that the triangle centroid shifts can be determined using the distance from a point (x_0, y_0) to a line $((x_1, y_1), (x_2, y_2))$.

$$\delta = \frac{(y_2 - y_1)x_0 - (x_2 - x_1)y_0 + x_2 y_1 - y_2 x_1}{\sqrt{(y_2 - y_1)^2 + (x_2 - x_1)^2}} \tag{7.S25}$$

In this data set, $\alpha = 17^\circ$ due to accumulated rotations at various joints in the print head

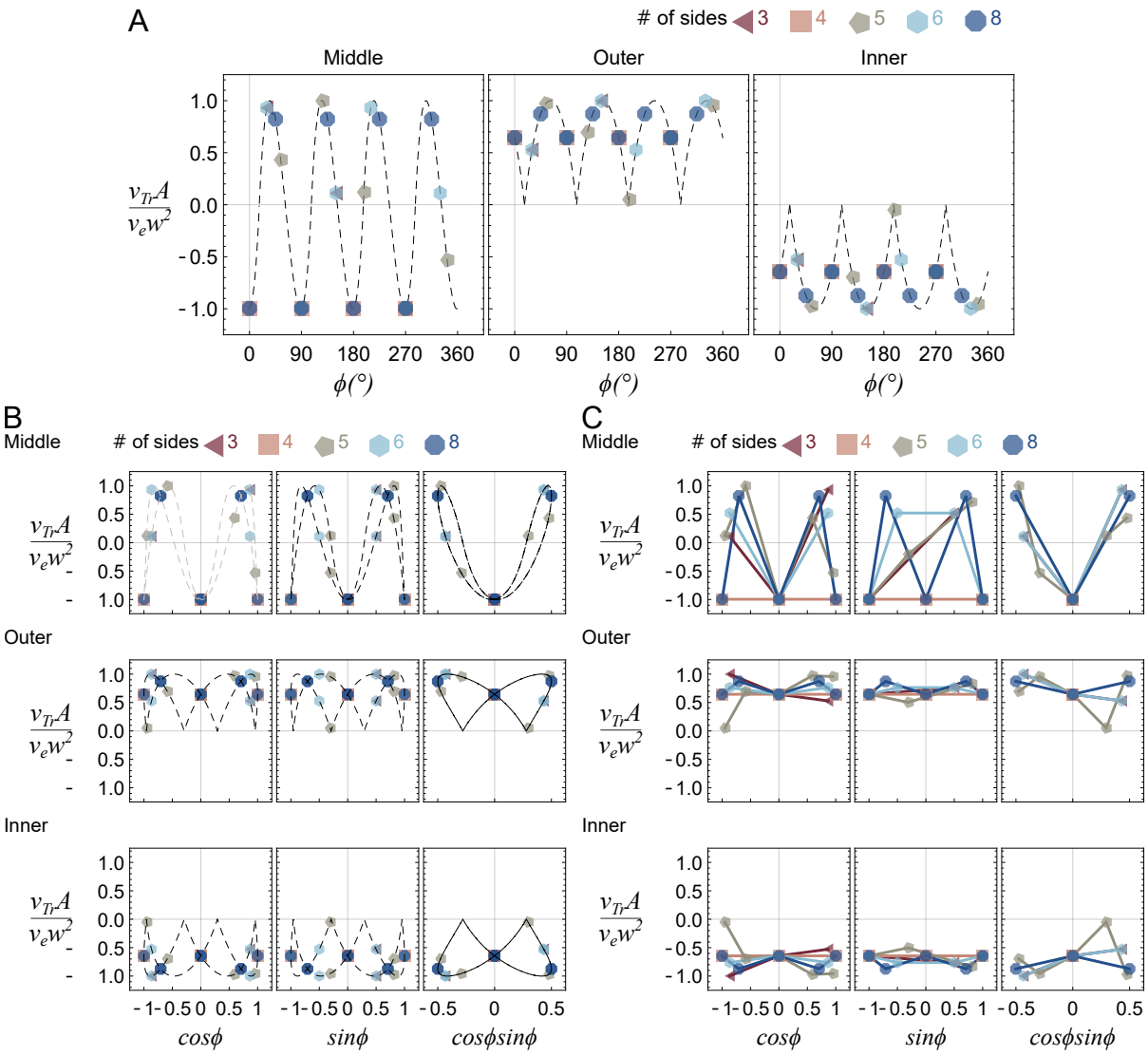

Figure 7.S6: Theoretical dimensionless transverse flows as a function of ϕ and basis functions for fluid reshaping. Dotted lines (A,B) indicate the theoretical expression. Points indicate the printing directions used in this study, split by polygon. Solid lines are visualization aides which connect points which are averaged in the horizontal axis (C).

fixture. Evaluated, the transverse flow ahead of the nozzle is shown in Equation 7.S26.

$$\begin{aligned}\frac{v_{Tr}A}{v_e w^2} =& \frac{-43\,\mathrm{sign}(\sin(\phi - 62°))}{48} \times \\ & \left|\frac{-5\cos(\phi - 17°) + 4\cos(2\phi - 34°) - \cos(39° + 3\phi) + \sin(39° + 3\phi) - 5\sin(17° - \phi)}{\sin(17° - \phi)\cos(\phi - 17°)}\right| \\ & \times \left|\frac{(1 - \cos(\phi - 17°) + \sin(17° - \phi))^2}{\sin(17° - \phi)\cos(\phi - 17°)}\right|\end{aligned} \tag{7.S26}$$

The resultant transverse flows are continuous and periodic on $\pi/2$ as a function of ϕ.

Solid rotation

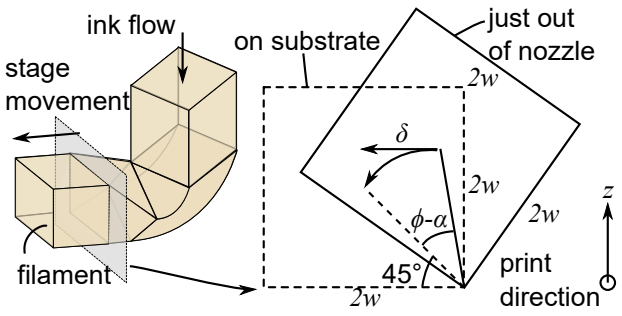

Figure 7.S7: A solid filament rotates when it hits the substrate so that it rests flat on the substrate.

Assume that the filament is a solid with a square cross-section. Depending on the print direction, the filament will be deposited on one of its corners (Fig. 7.S7). Contact with the substrate will cause the filament to rotate with the leading corner of the filament as the fulcrum.

This rotation will cause the center of the filament to shift by a distance δ.

$$\frac{\delta}{w} = \begin{cases} \frac{\sqrt{2}}{2} - \cos(\pi/4 + \phi - \alpha) & 0 < \phi - \alpha < \pi/4 \\ 0 & \phi - \alpha = \pi/4 \\ -\frac{\sqrt{2}}{2} - \cos(\pi/4 + \phi - \alpha) & \pi/4 < \phi - \alpha < \pi/2 \end{cases} \tag{7.S27}$$

The shift will occur over a time τ_s which leads to a transverse flow velocity $v_T = \delta/\tau_s$.

$$v_T = \delta/\tau_s \tag{7.S28}$$

The resultant transverse flow can be expressed in terms of the rotation time t and the nozzle width w.

$$\frac{v_{Ts}\tau_s}{w} = \begin{cases} \frac{\sqrt{2}}{2} - \cos(\pi/4 + \phi - \alpha) & 0 < \phi - \alpha < \pi/4 \\ 0 & \phi - \alpha = \pi/4 \\ -\frac{\sqrt{2}}{2} - \cos(\pi/4 + \phi - \alpha) & \pi/4 < \phi - \alpha < \pi/2 \end{cases} \tag{7.S29}$$

The resultant theoretical transverse flow is discontinuous at $\alpha + \pi/4$ and periodic on $\pi/2$ (Fig. 7.S8).

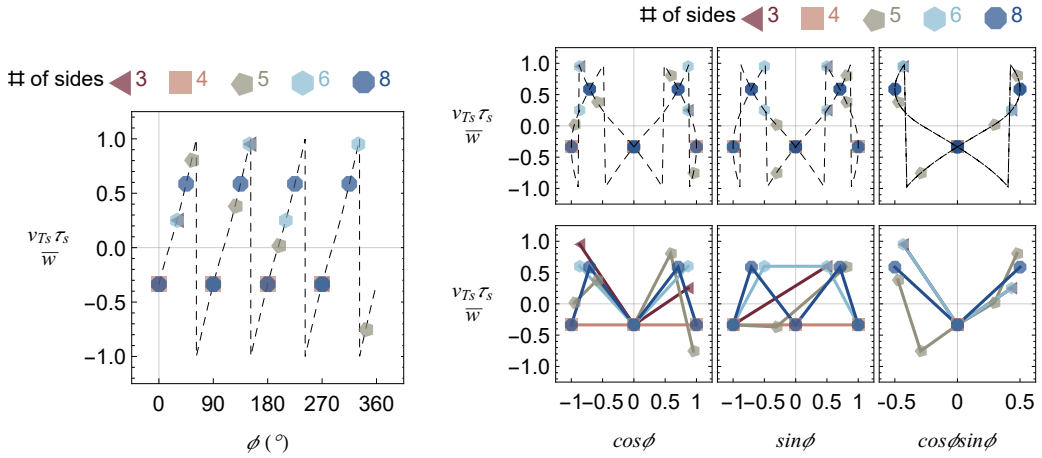

Figure 7.S8: Theoretical transverse flows as a function of print direction ϕ and basis functions for solid rotation. Dotted lines (left, top right) indicate the theoretical expression. Points indicate the printing directions used in this study, split by polygon. Solid lines are visualization aides which connect points which are averaged in the horizontal axis (bottom right).

Miscalibration of nozzle origins

For layer-by-layer support, if the ink and support nozzle origins are miscalibrated, ink will collide with existing lines of support or ink during the deposition process (Fig. 7.S9).

Assume that the support is immovable, such that the collision will cause the ink line to shift normal to the print direction ϕ. Collisions will only occur in certain print directions, in certain orientations (Fig. 7.S9A).

If the ink nozzle origin x_0 is off by dx, the magnitude of the shift is defined by Equation 7.S30, where τ_o is the time it takes for the filament to displace.

$$\frac{v_{To}\tau_o}{|dx|} = \sin\phi \frac{-\operatorname{sign}(\sin\phi) - \operatorname{sign}(dx) + 1/3(\operatorname{sign}(\sin\phi) - \operatorname{sign}(dx))}{2} \tag{7.S30}$$

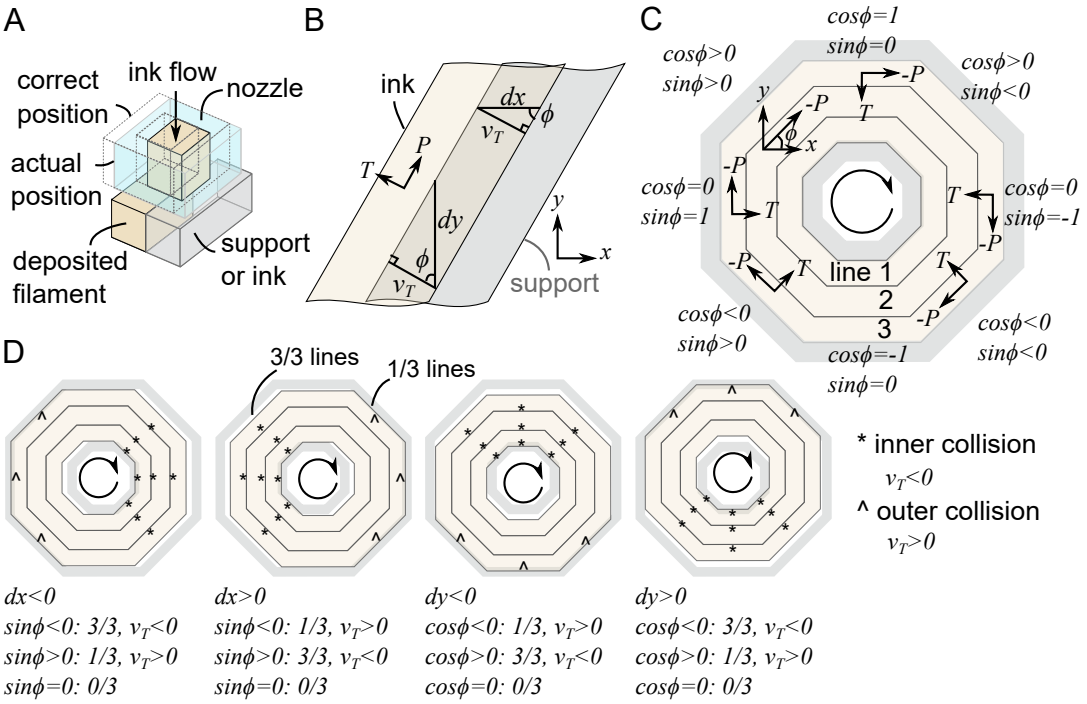

Figure 7.S9: A) The nozzle origin is calibrated too far to the right, resulting in collisions between ink and existing support or ink. B) Collisions induce a transverse flow v_T. C, D) The number of passes around the polygon which feature collisions with existing features depends on the printing direction ϕ.

If the ink nozzle origin y_0 is off by dy, the magnitude of the shift is

$$\frac{v_{To}\tau_o}{|dy|} = -\cos\phi\frac{\text{sign}(\cos\phi) - \text{sign}(dy) - 1/3(\text{sign}(\cos\phi) + \text{sign}(dy))}{2} \tag{7.S31}$$

The 1/3 terms in Equation 7.S30 and 7.S31 come from the frequency of collisions between ink and layer-by-layer support in three-line polygons (Fig. 7.S9C,D). On one side of the polygon, only one out of the three lines of the ink polygon collides with support. For fitting distribution positions, the three lines are separately fit, so the factor of 1/3 is replaced with a factor of 1, removing the assumption about which lines shift and instead directly identifying which lines shift due to origin miscalibration.

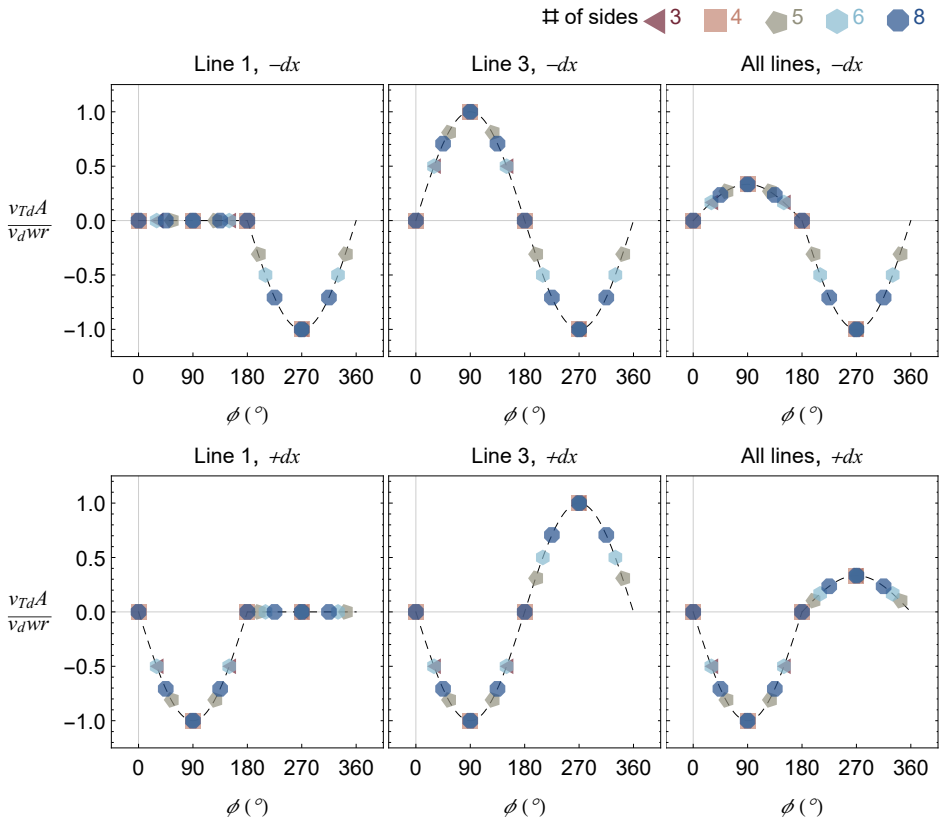

Figure 7.S10: Theoretical transverse flows as a function of ϕ for origin miscalibration in x. Dotted lines indicate the theoretical expression. Points indicate the printing directions used in this study, split by polygon.

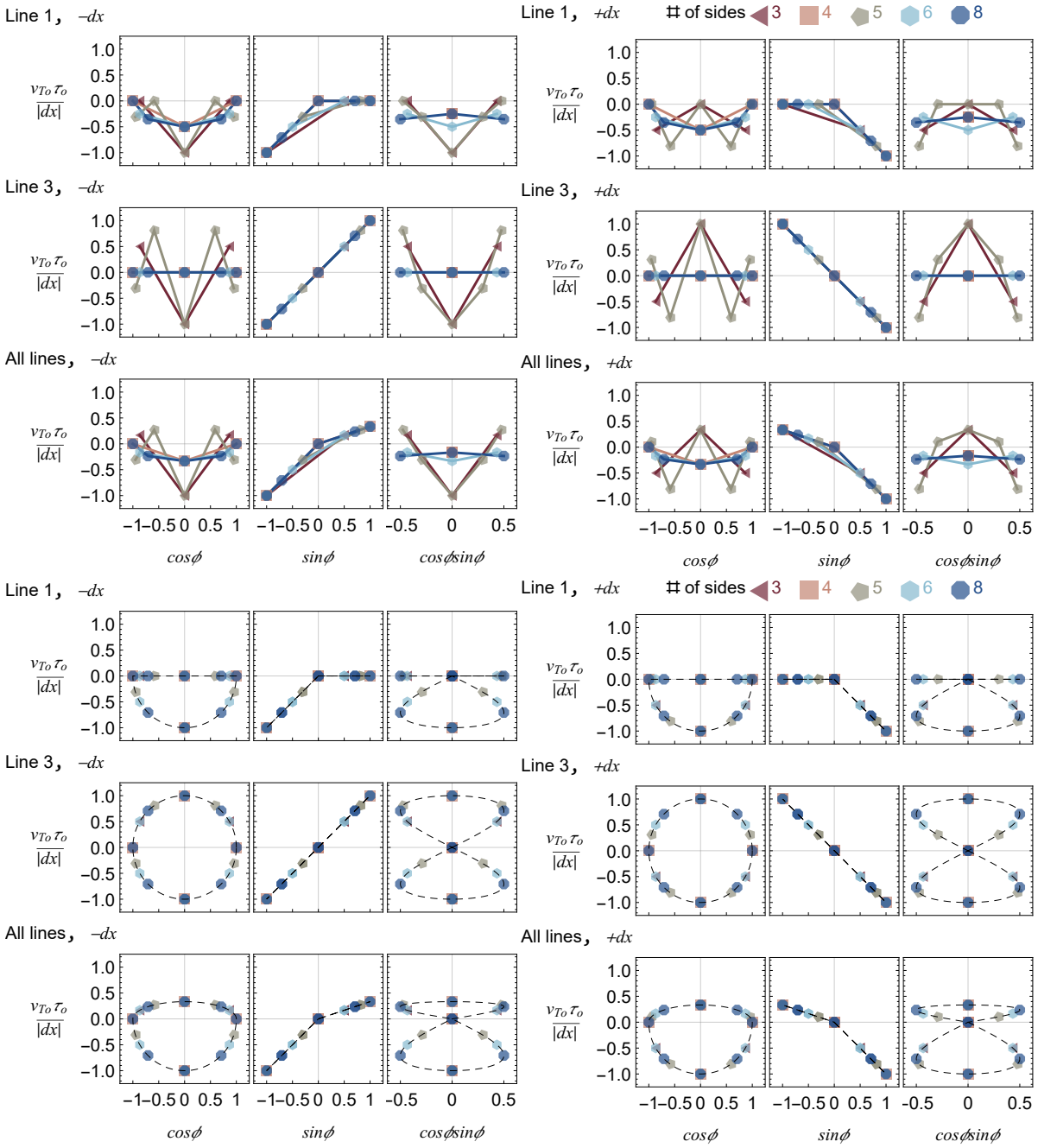

Figure 7.S11: Theoretical transverse flow basis functions for origin miscalibration in x. Dotted lines (bottom) indicate the theoretical expression. Points indicate the printing directions used in this study, split by polygon. Solid lines are visualization aides which connect points which are averaged in the horizontal axis (top).

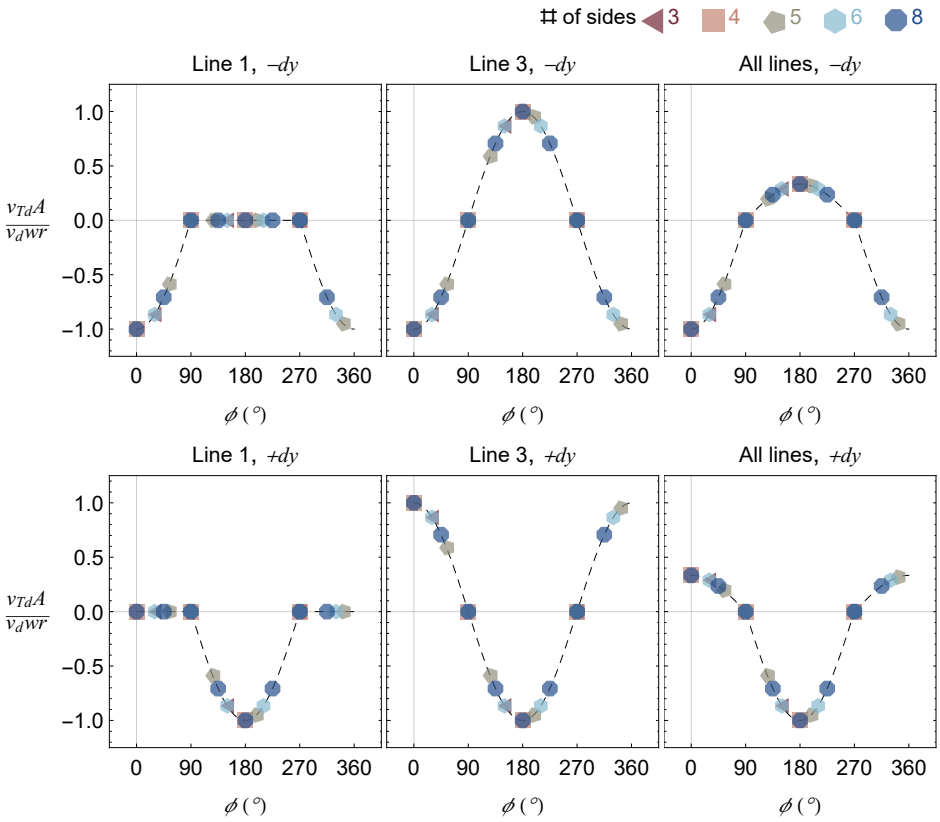

Figure 7.S12: Theoretical transverse flows as a function of ϕ for origin miscalibration in y. Dotted lines indicate the theoretical expression. Points indicate the printing directions used in this study, split by polygon.

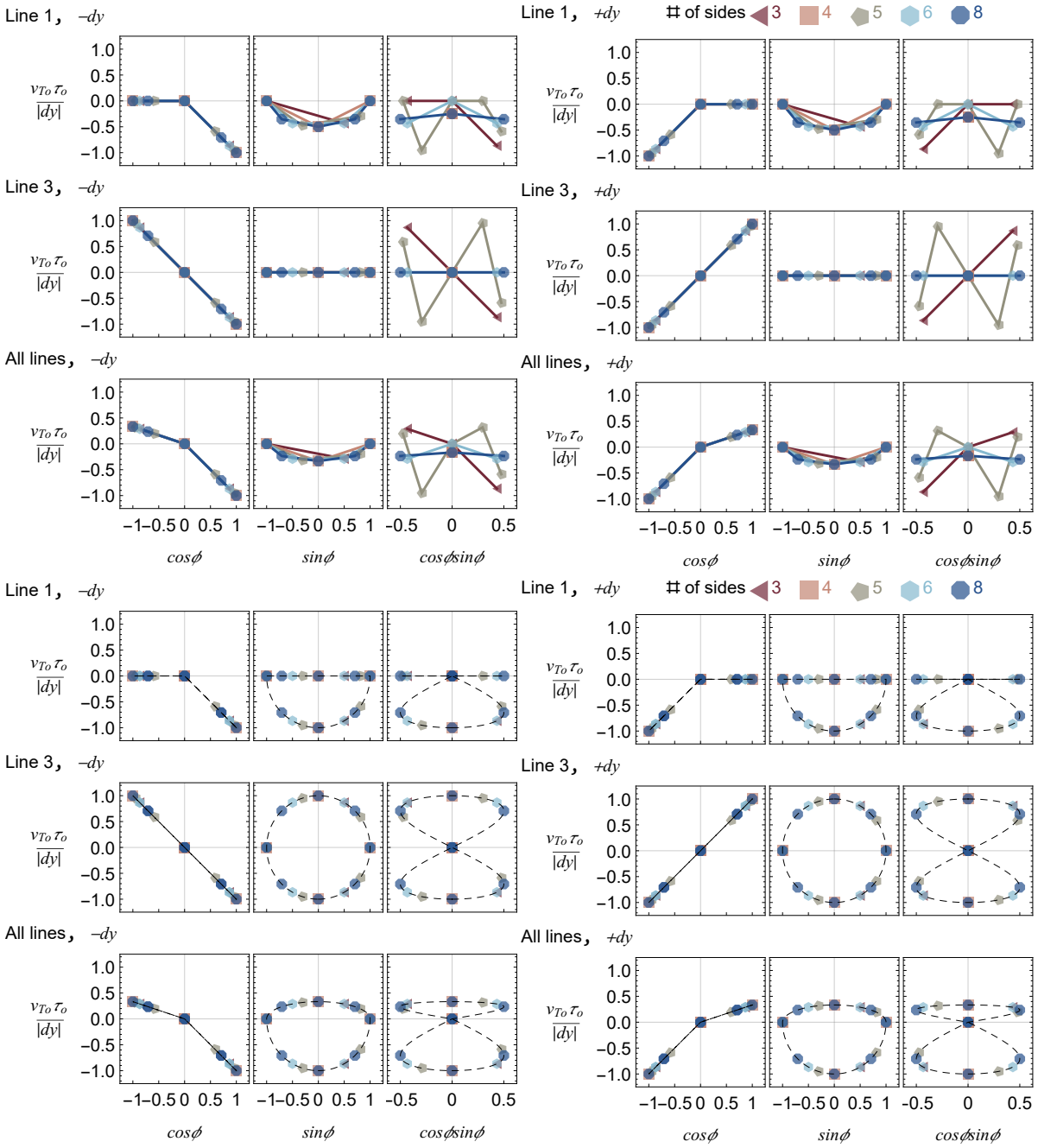

Figure 7.S13: Theoretical transverse flow basis functions for origin miscalibration in y. Dotted lines (bottom) indicate the theoretical expression. Points indicate the printing directions used in this study, split by polygon. Solid lines are visualization aides which connect points which are averaged in the horizontal axis (top).

Motor error

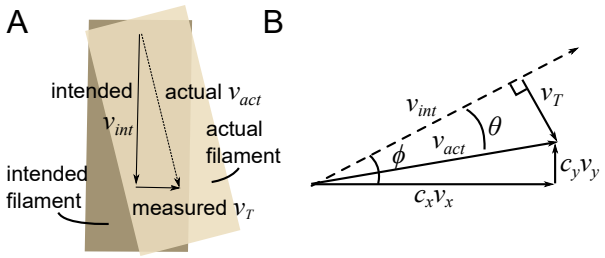

Figure 7.S14: A) If the printer motors are miscalibrated, the print path will be rotated relative to the intended print path, resulting in a measured transverse flow. B) The x and y motor velocities are scaled by a factor of c_x and c_y, resulting in a detected transverse flow v_T.

If the motor is too slow or too fast, the actual print path will be deflected from the intended print path. Because the analysis method used in these experiments measures flows relative to the intended path, real flows parallel to the print path will be misread as transverse flows across the filament if the motor speeds are miscalibrated. Where v is the intended translation speed, the intended velocity is defined:

$$\vec{v}_{int} = \begin{pmatrix} v \sin\phi \\ v \cos\phi \end{pmatrix} \tag{7.S32}$$

The magnitude of the detected transverse velocity can be determined using the sin of the angle between the intended and actual vectors θ.

$$v_{Tm} = v_{act} \sin\theta \tag{7.S33}$$

The angle can be determined using the cross product of the two vectors

$$\sin\theta = \frac{|v_{int} \times v_{act}|}{|v_{int}||v_{act}|} \tag{7.S34}$$

As such, the transverse velocity due to motor contributions v_{Tm} can be simplified to

$$v_{Tm} = \frac{|v_{int} \times v_{act}|}{|v_{int}|} \tag{7.S35}$$

If the x motor is scaled by a factor c_x and the y motor is scaled by a factor c_y, the actual velocity is

$$\vec{v}_{act} = \begin{pmatrix} v c_x \cos\phi \\ v c_y \sin\phi \end{pmatrix} \tag{7.S36}$$

The magnitude of the detected transverse flow is thus

$$\frac{v_{Tm}}{v(c_y - c_x)} = \cos\phi \sin\phi \tag{7.S37}$$

The transverse velocity for a scaled change in motor speed is continuous and sinusoidal with π periodicity (Fig. 7.S14).

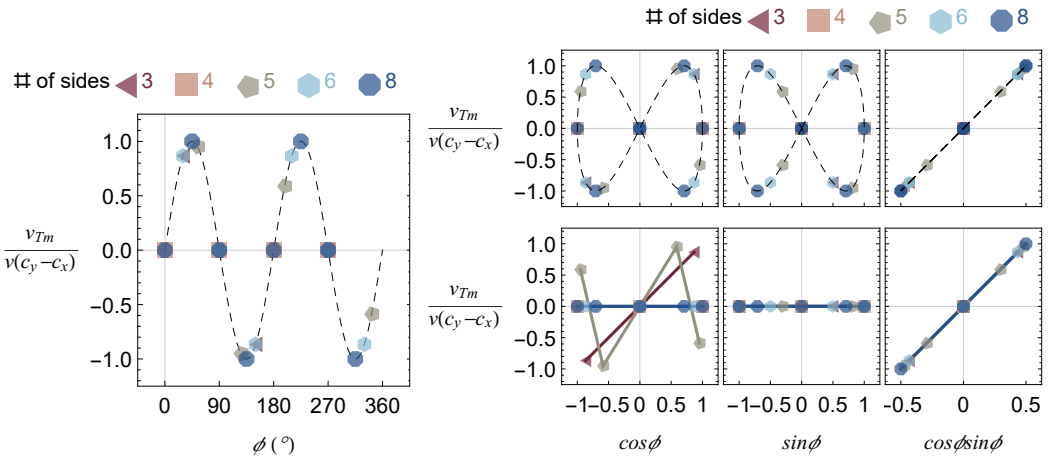

Figure 7.S15: Theoretical transverse flows as a function of print direction ϕ and basis functions for motor miscalibration. Dotted lines (left, top right) indicate the theoretical expression. Points indicate the printing directions used in this study, split by polygon. Solid lines are visualization aides which connect points which are averaged in the horizontal axis (bottom right).

Fitting models to experimental profiles

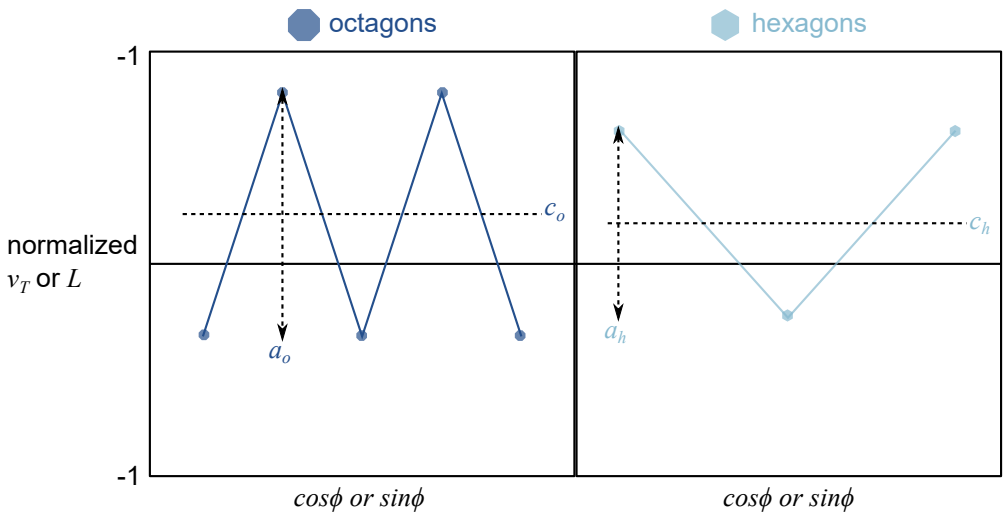

Figure 7.S16: Schematic of amplitudes and centers of basis functions.

	Hexagon amplitude a_{hb}	Octagon amplitude a_{ob}	Hexagon midpoint c_{hb}	Octagon midpoint c_{ob}
Disturbed zone center (D)	1.55	1.83	-0.23	-0.09
Disturbed zone sides (D)	0.58	0.33	-0.04	-0.16
Solid rotation (S)	0.94	0.92	0.13	0.13
Fluid reshaping outer (R)	0.12	0.23	0.70	0.76
Fluid reshaping center (R)	1.52	1.82	-0.24	-0.09
Fluid reshaping inner (R)	-0.12	-0.23	-0.70	-0.76

Table 7.S2: Dimensionless amplitudes and midpoints of hexagon and octagon profiles for D, R, and S basis functions for stated regions relative to the print path.

7.S1.2 Results

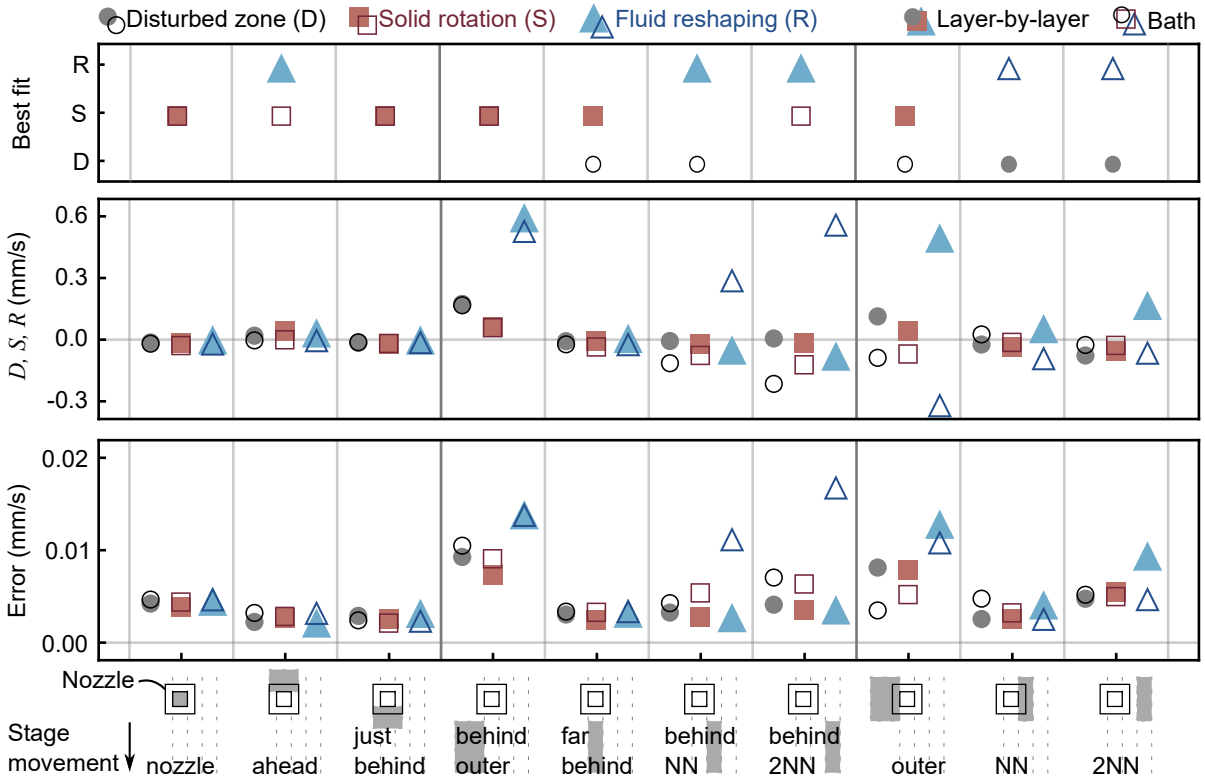

Figure 7.S17: Fit disturbed zone, solid rotation, and fluid rotation coefficients D, S, and R across different interrogation regions near the nozzle for transverse flows in layer-by-layer and bath support. "Best fit" indicates the model which produces the smallest error for the region and type of support. "Error" indicates the difference between the theoretical reconstruction and the experimental data. Differences in fitting quality between the three fitting models are small, but fluid reshaping usually produces the worst fit. "NN" is the nearest neighbor inward from the print path relative to the center of the polygon, and "2NN" is the second nearest neighbor.

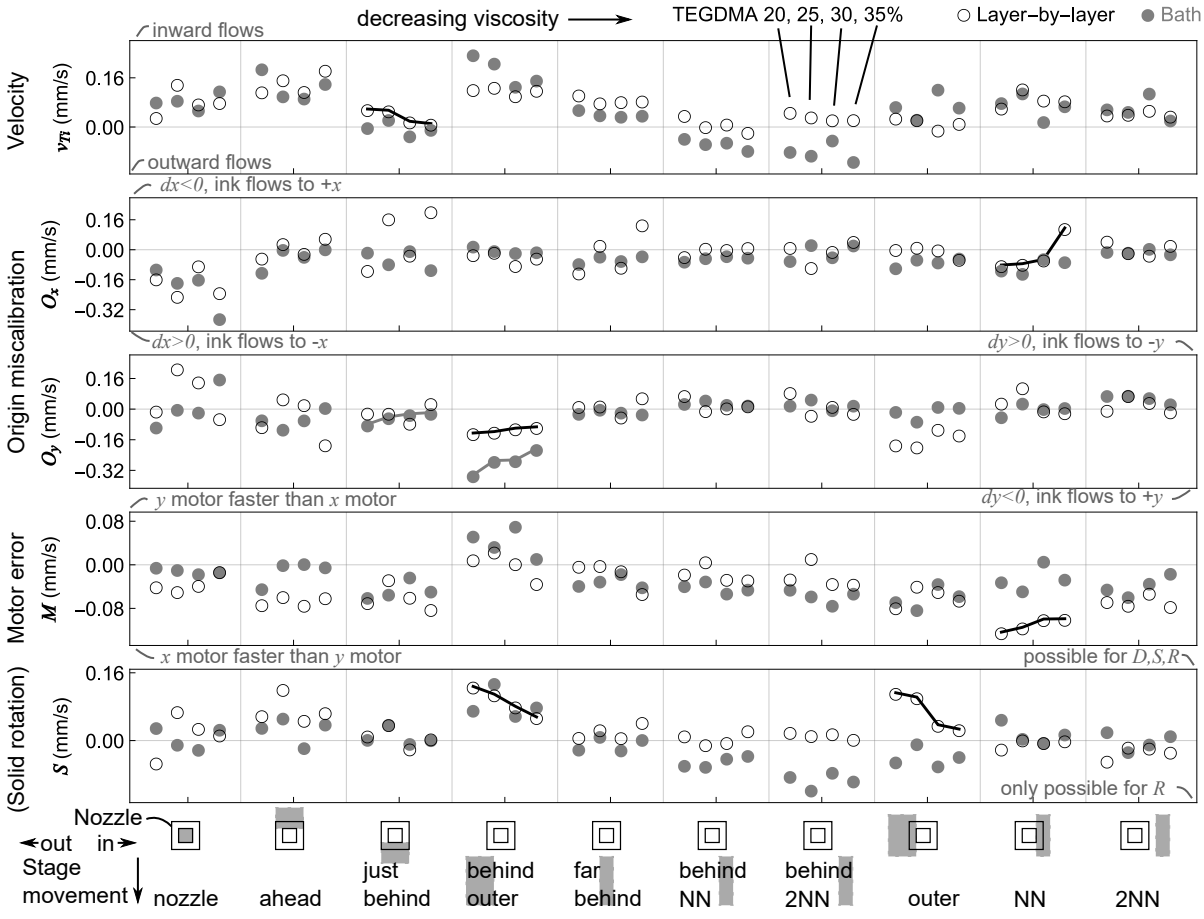

Figure 7.S18: Fit direction-independent velocities v_{Ti}, origin miscalibration coefficients O_x and O_y, motor error coefficients M, and solid rotation coefficients S across different interrogation regions near the nozzle for particle distribution positions in layer-by-layer and bath support with varying TEGDMA concentration in the ink. Lines indicate trends with statistically significant ($p < 0.05$) Kendall tau parameters.

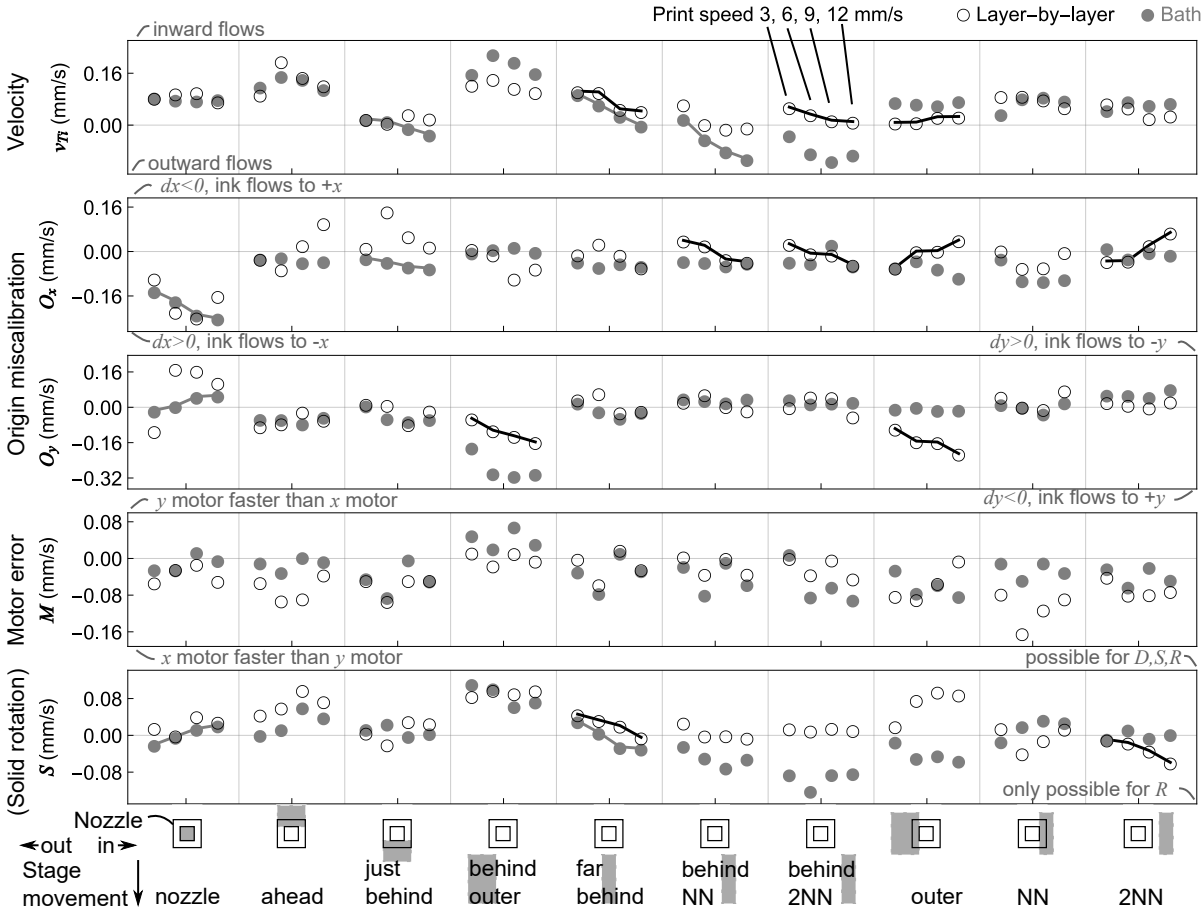

Figure 7.S19: Fit direction-independent velocities v_{Ti}, origin miscalibration coefficients O_x and O_y, motor error coefficients M, and solid rotation coefficients S across different interrogation regions near the nozzle for particle distribution positions in layer-by-layer and bath support with varying print speed, where the translation speed is the same as the fluid extrusion speed inside the nozzle. Lines indicate trends with statistically significant ($p < 0.05$) Kendall tau parameters.

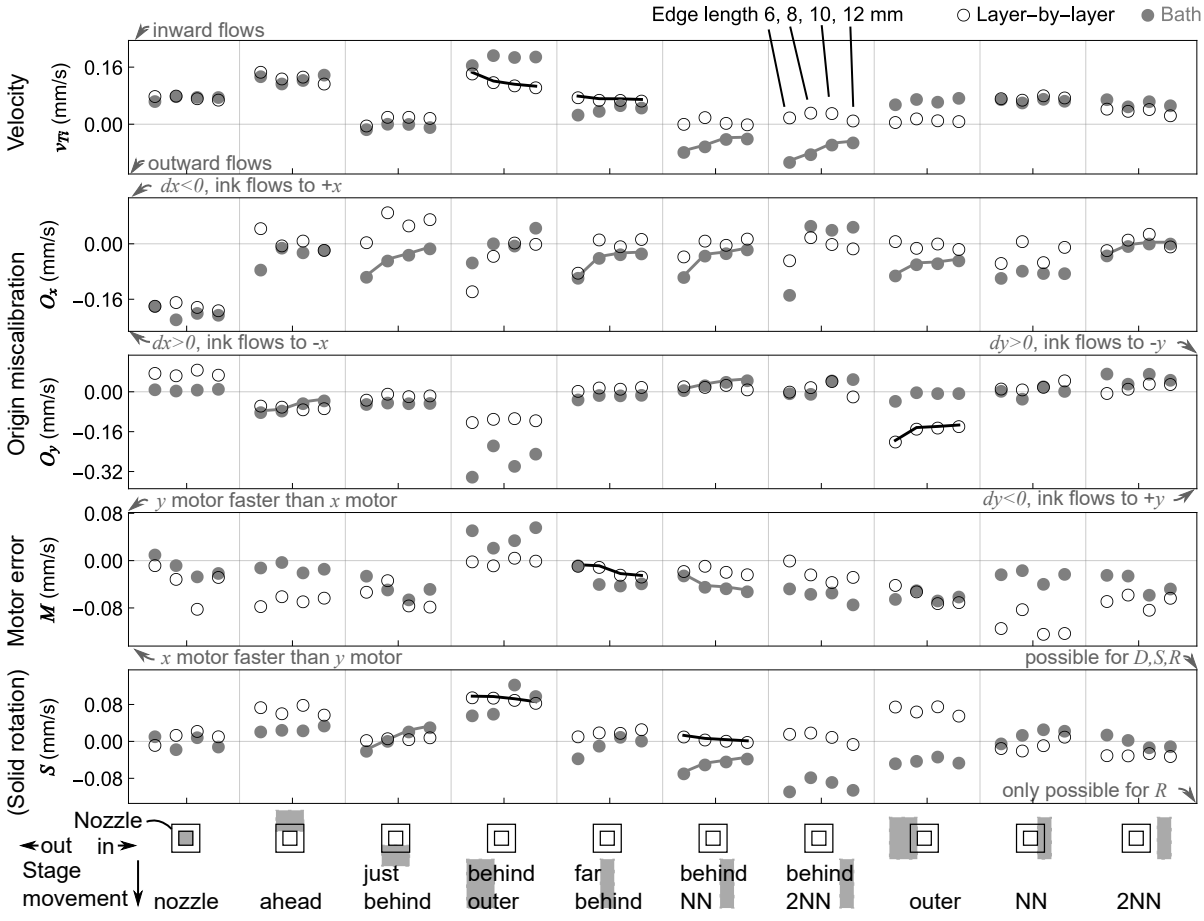

Figure 7.S20: Fit direction-independent velocities v_{Ti}, origin miscalibration coefficients O_x and O_y, motor error coefficients M, and solid rotation coefficients S across different interrogation regions near the nozzle for particle distribution positions in layer-by-layer and bath support with varying polygon edge length. Lines indicate trends with statistically significant ($p < 0.05$) Kendall tau parameters.

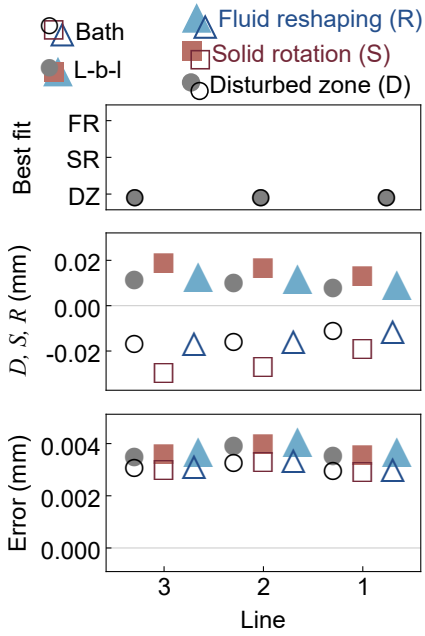

Figure 7.S21: Fit disturbed zone, solid rotation, and fluid rotation coefficients D, S, and R across different interrogation regions near the nozzle for particle distribution positions in layer-by-layer and bath support. "Best fit" indicates the coefficient which produces the smallest error for the region and type of support. "Error" indicates the difference between the theoretical reconstruction and the experimental data. Differences in fitting quality between the three fitting models are negligible. Single-layer polygons are printed in three lines from inside to outside.

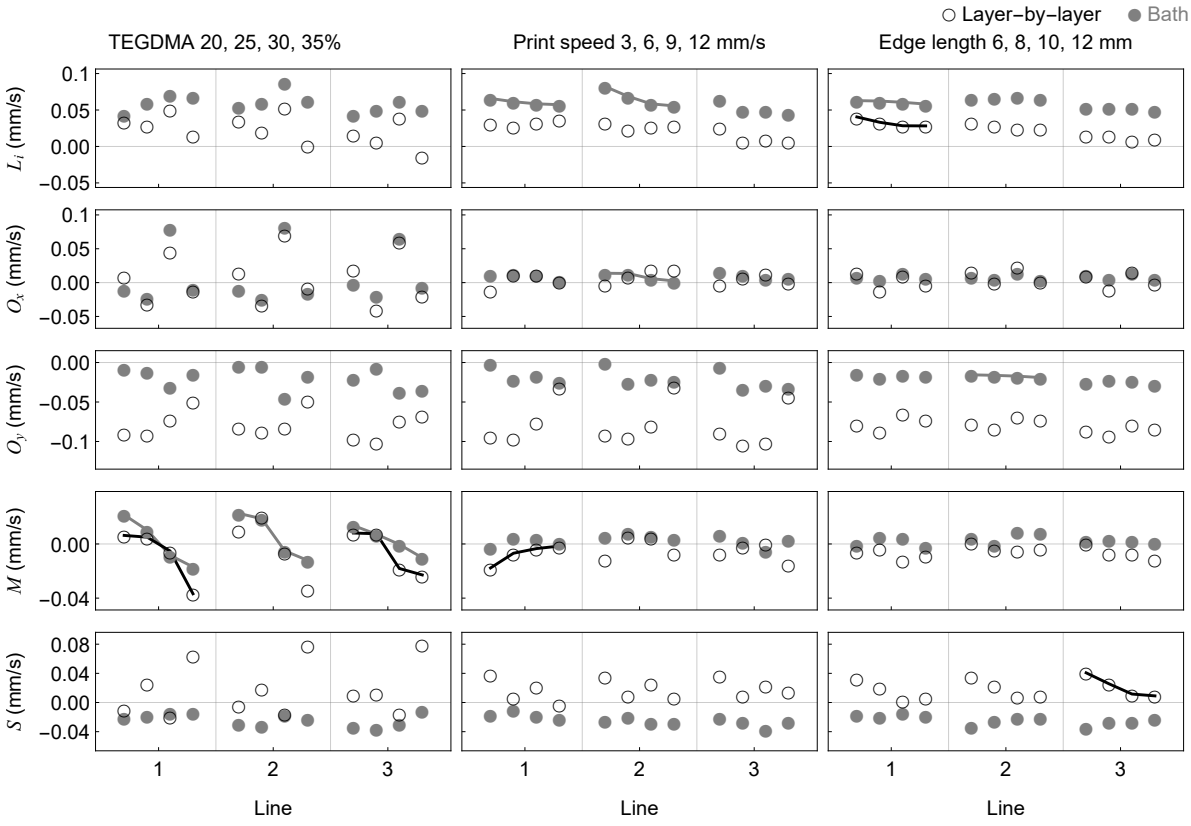

Figure 7.S22: Fit direction-independent particle distribution positions L_i, origin miscalibration coefficients O_x and O_y, motor error coefficients M, and solid rotation coefficients S across different passes near the nozzle for particle distribution positions in layer-by-layer and bath support with varying TEGDMA concentration in the ink, print speed, and polygon edge length. Lines indicate trends with statistically significant ($p < 0.05$) Kendall tau parameters. Single-layer polygons are printed in three lines from inside to outside.

7.S1.3 Rheology

Viscosities were measured using a TA Instrument Company ARES-LS1 rheometer with 25 mm diameter flat plates and a 2 mm gap at room temperature. Dynamic frequency sweeps were conducted at 10% strain with increasing frequency. Dynamic strain sweeps were conducted at 10 Hz with increasing strain. To avoid curing and settling effects, inks did not contain photoinitiators or particles.

The Carbopol support gel is commonly referred to as a liquid-like solid or a yield stress material because it behaves like an elastic solid at low stresses and a viscous gel at high stresses. The support material yields between 10 Pa and 100 Pa, depending on whether one is using the nonlinearity or crossover definition of yield stress (Fig. 7.S23B). After yielding, Carbopol behaves like a power law fluid, where the viscosity is proportional to the shear strain rate$^{-0.9}$ (Fig. 7.S23A).

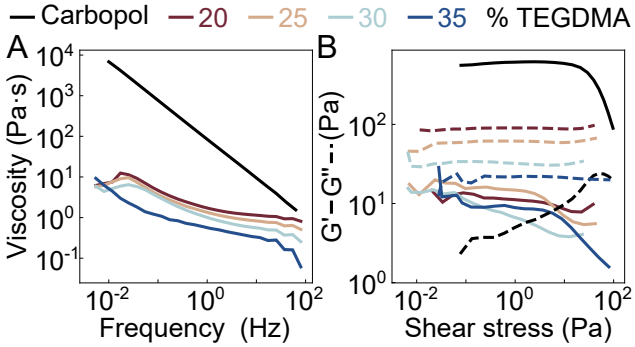

Figure 7.S23: A) Viscosity as a function of frequency and B) Storage modulus (solid) and loss modulus (dashed) as a function of shear stress for Carbopol support and inks with varying w% TEGDMA. Carbopol stresses in (A) range from 40-60 Pa, indicating that the Carbopol has yielded during the test.

The inks used in this study are liquid-like at all stresses, whereby the loss modulus is always greater than the storage modulus (Fig. 7.S23B). These inks are shear thinning but have a weaker rate dependence than the support material. In these inks, TEGDMA acts as a diluent, so increasing the TEGDMA concentration decreases the loss modulus and viscosity (Fig. 7.S23).

Chapter 8

Printed polygons: Distortion at corners

8.1 Introduction

Extrusion-based additive manufacturing techniques enable fabrication of structures from a wide range of material systems. Fused deposition modeling can be used to print viscous thermoplastics, while direct ink writing (DIW) can be used to print a diverse array of materials from low-viscosity inviscid biocompatible hydrogels[120] to viscous nanoclay-epoxy composites[61] to colloidal ceramic gels[103]. However, extrusion-based techniques inherently face challenges at corners of printed geometries. The shape and microstructure of the printed line change wherever the moving nozzle or moving stage changes direction. These changes at corners could degrade the functionality of printed composite structures. For example, when printing self-insulated electrically conductive filaments,[9] defects in the printed microstructure at corners could create shorts in the conductive pathways. Alternatively, when printing filaments with aligned and positioned cells,[14, 22] distortion at corners could hinder cell adhesion and tissue formation.

Changes in microstructure at corners can be broken into three effects: smoothing, swelling, and ringing. Smoothing occurs when the printed line bends inward at the corner (Fig. 8.1),

either because the printer has been programmed to traverse a blunt path to avoid swelling and ringing[226] or because the deposited fluid changes shape at the corner after deposition.[227] Swelling occurs (Fig. 8.1) when excess fluid is generated at the corner because the nozzle must retrace its path at the corner, a pattern known as double deposition. Swelling can also occur when the translation speed is decreased at corners to avoid smoothing and ringing.[226, 228, 229] Ringing occurs because rapid changes in print direction can induce vibrations in the positioning gantry which manifest in ripples on the surface of the printed structure.[230, 231] Slower translation speeds limit the impacts of smoothing, swelling and ringing but also limit the throughput of extrusion-based techniques, so alternate strategies for limiting these effects are needed.

Previously, strategies for mitigating the adverse effects of smoothing, swelling, and ringing have been studied for fused deposition modeling, where inks are viscous enough that capillarity can be ignored.[226, 230, 229, 231] Strategies for mitigating the adverse effects of smoothing have been studied for direct liquid writing, where ink viscosities are low enough that viscous dissipation can be ignored.[227] However, DIW encompasses inks with a wide range of rheological properties, and a model is needed to describe the corner behavior of inks within a viscosity range where viscous dissipation and interfacial energies are both significant. Here, a three-part model is proposed that describes changes in the printed line at corners as a result of interfacial energy-driven smoothing, double deposition-driven swelling, and ringing due to rapid acceleration.

To characterize the corner behavior of moderate-viscosity direct-write inks, DIW with acoustophoresis is used to write dental resin-based composite lines containing a narrow distribution of metallic microparticles at the center. In DIW with acoustophoresis, a piezoelectric transducer attached to the print nozzle establishes a standing bulk acoustic wave inside of the nozzle. Given a sufficient acoustic contrast factor (which depends on the densities and compressibilities of the particles and fluid matrix), the particles align and move toward the nodes

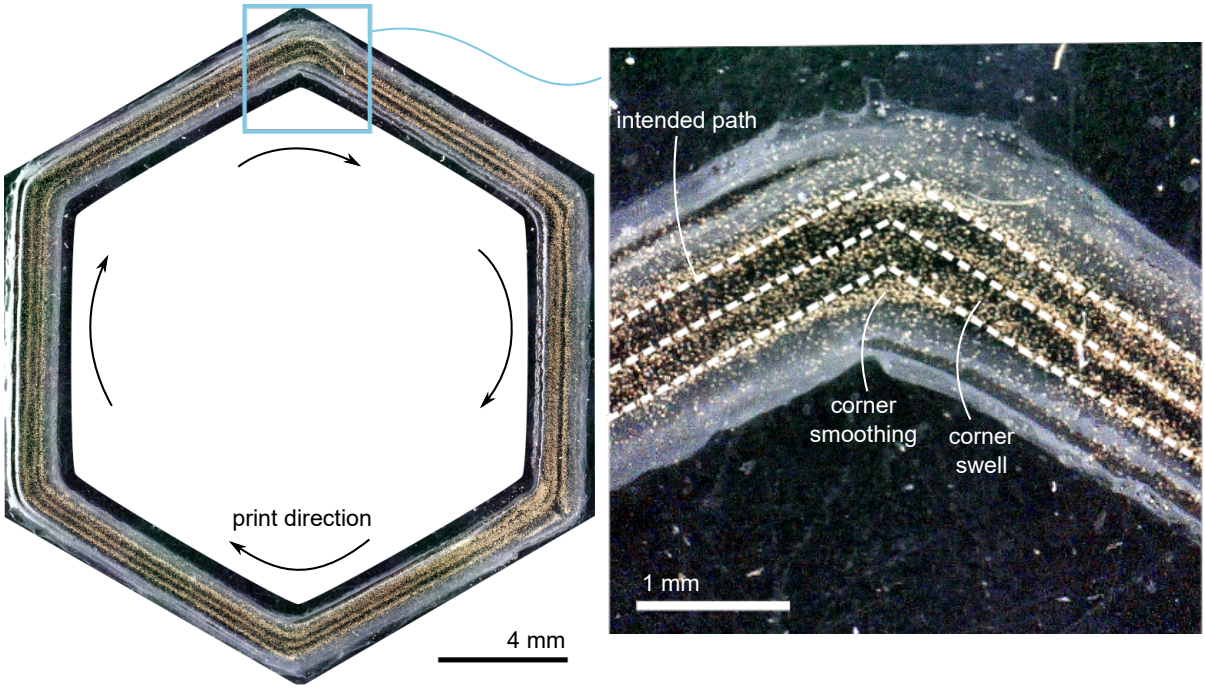

Figure 8.1: A single layer hexagon printed with DIW with acoustophoresis experiences inaccurate particle positioning at corners due to corner smoothing.

or antinodes of the standing wave.[8, 13, 16, 125] Acoustophoresis has been used to align and position particles ranging from cells to carbon fibers to metallic microspheres.[9, 13, 22] Here, a square glass capillary is used as a print nozzle and dense metallic microparticles in a polyurethane-based matrix, so standing waves are generated in both directions transverse to the direction of flow, and particles move to a point in the center of the nozzle (Fig. 8.2C). The capillary is seated in a stainless steel channel holder glued to a piezoelectric transducer (Fig. 8.2B). The piezo is thermally coupled to a liquid-cooled stage which keeps the system at room temperature.[15] The nozzle extrudes continuous lines of ink onto a glass slide mounted on a stage which moves in three dimensions (Fig. 8.2A). In doing so, composite lines can be written which contain a narrow distribution of microparticles at the center. The position and width of this particle distribution are used as metrics to track the shape of the line at the corner and corresponding changes in the microstructure of the line at the corner.

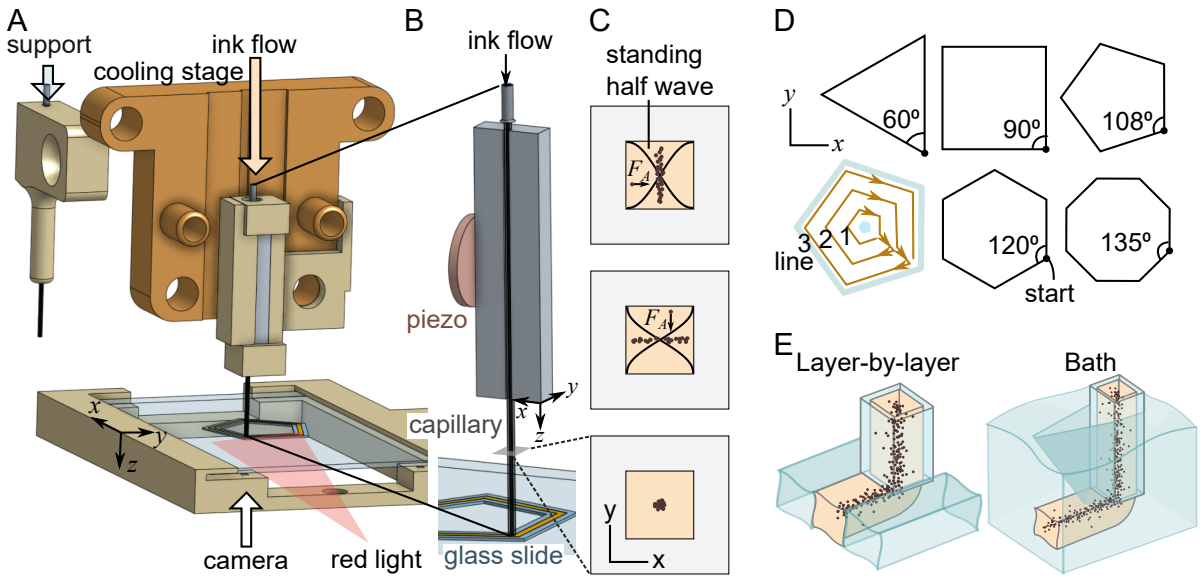

Figure 8.2: A) Using layer-by-layer support, the stage travels between support and ink nozzles while videos are collected from underneath the nozzle. x, y, and z refer to G-code coordinates. B) Ink is extruded onto a glass slide through a glass capillary seated in a stainless steel block glued to a piezo. C) Two standing half-waves in the x and y directions drive particles with acoustic force F_A toward the center of the channel. D) Printed polygons probe five corner angles. E) Layer-by-layer support is deposited in a specific pattern, while bath support fills the entire print envelope.

The moderate-viscosity inks used in this study are shear thinning, but they do not exhibit solid-like behaviors at low shear stresses, which are critical for printing self-supporting structures.[91, 103] To support the printed structures, this work uses a water-based Carbopol support gel which has been used as a support bath for similar low-viscosity inks including hydrogels, silicone elastomers, and liquid metal.[99, 117, 118, 122, 212] Carbopol gels act as Bingham plastics, so they exhibit elastic solid-like behaviors at low shear stresses and shear thinning liquid-like behaviors above a yield stress. The gels can be used as a support bath, where a submerged nozzle plastically deforms the bath locally, and the solid-like bath holds the printed line in place (Fig. 8.2E).[99, 117, 118, 122, 212] The gels can also be extruded layer-by-layer from a separate support nozzle to write designed shapes before ink deposition (Fig. 8.2E). Because the support geometry imposes different stresses on the printed ink, the two geometries produce different corner behaviors. This work tests both support geometries and finds that bath support limits changes in particle distribution at the corner, improving microstructural uniformity across the print.

To test the influence of the sharpness of the corner on corner behaviors, single-layer, three-pass equilateral triangles, squares, pentagons, hexagons, and octagons are printed (Fig. 8.2D). This work focuses on how the particle distributions at the corners in the first pass change over the course of the print. The difference in particle distribution position and width between the center of the polygon edge and the corner is measured just after deposition, after the structure has had time to relax, and after the nozzle returns to write the second line and shears the first line. This work finds that corner swelling and ringing strongly influence the microstructure of the just-deposited line, and interfacial energy-driven corner smoothing changes the microstructure of the line during relaxation. Further, shear from the nozzle during deposition of subsequent lines can help to mitigate the effects of swelling, ringing, and smoothing in existing lines.

8.2 Theory

This work probes the impact of corner angle θ, print speed v_s, and ink composition on corner defects. In these experiments, the print speed represents both the flow rate in the nozzle and the translation speed of the stage, which are matched, although only the translation speed matters for these derivations. Herein, models are developed to predict two metrics: the differences in particle distribution peak position and width between the corner and center of the polygon edge:

$$\Delta Position(\theta, v_s, ink) = Position(corner) - Position(center) \tag{8.1}$$

$$\Delta Width(\theta, v_s, ink) = Width(corner) - Width(center) \tag{8.2}$$

Both metrics are corner defects. $\Delta Position$ represents a path shift at the corner, while $\Delta Width$ represents spreading at the corner. With the following theories, $\Delta Position(\theta, v_s, ink)$ and $\Delta Width(\theta, v_s, ink)$ are predicted due to smoothing, swelling, and ringing. Experimentally, $\Delta Position(\theta, v_s, ink)$ and $\Delta Width(\theta, v_s, ink)$ are measured and compared to the predicted values to determine the contributions of smoothing, swelling, and ringing.

8.2.1 Interfacial energy-driven smoothing

In low-viscosity liquid elbows, capillarity drives fluid to flow toward the inner edge of the elbow due to a Laplace pressure differential between the inner and outer edge of the elbow that depends on the radii of curvature of the inner (r_1) and outer (r_2) surfaces of the elbow and the surface tension of the ink γ (Fig. 8.3A). The change in Laplace pressure from points A to C is

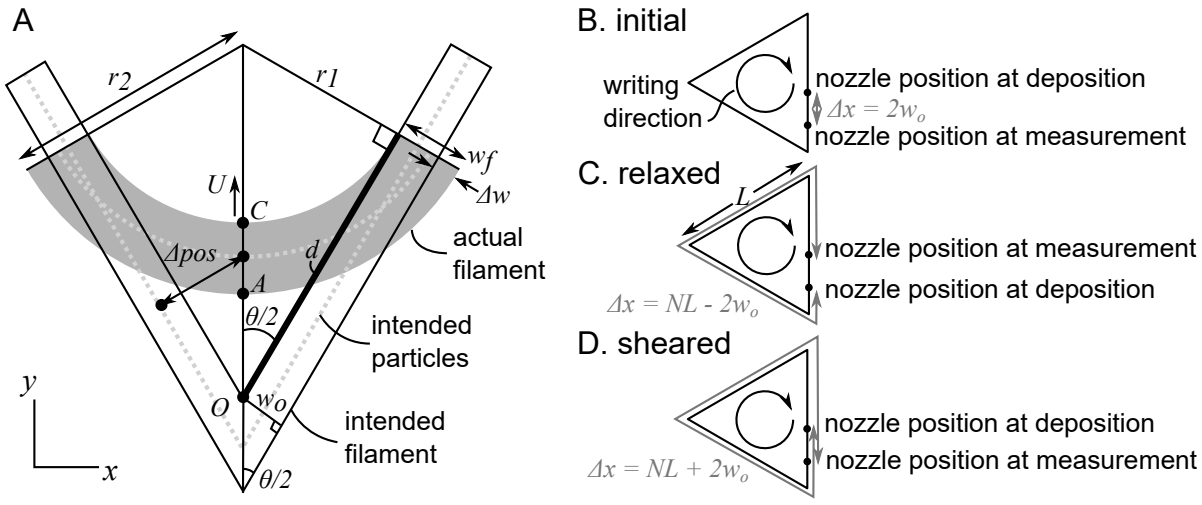

Figure 8.3: Laplace pressure-driven smoothing. A) Schematic of variables used in derivation. The intended sharp corner (black outline) is replaced by a smooth arc (gray shaded area), shifting and widening the particle distribution. d is the length of the bold line. B-D) Lengths traveled by the nozzle Δx at the measurement of the initial, relaxed, and sheared distributions.

given by

$$\Delta P_{AC} = \gamma\left(\frac{1}{r_1} + \frac{1}{r_2}\right) \tag{8.3}$$

One previously proposed model finds that an inviscid liquid elbow can achieve capillary equilibrium by forming a spherical sector-shaped bulge at the corner.[227] For the inks used in this study, this bulge-based model predicts that a surface energy-driven energy barrier will suppress bulge formation (supplemental). Although the bulge-based model may contribute to some print speed-dependent effects to be discussed later, the printed geometries of the moderate viscosity inks used in this paper exhibit arcs at corners rather than bulges (Fig. 8.1). Thus, this work proposes an additional model for the position and width of the line based on the Laplace pressure differential, which drives movement of fluid from the outer edge of the corner toward the inner edge. The model uses viscous dissipation to determine the shape of the corner after a finite time. This model is derived for an ink corner with no support material. The model can be

extended in future work by incorporating support material. With support material, a resisting force would be imposed on the inner edge of the corner, and the surface tension would be different on the inner and outer edges of the corner.

Assume that a designed infinitely sharp corner with corner angle θ is replaced by an arc of equal area to the intended filament (Fig. 8.3A). The intended filament width is w_o. The arc has thickness w_f. The distance between the inner corner of the intended filament and the intersection between the inner edge of the arc and the inner edge of the intended filament is the displaced length d. To determine $\Delta Width$ and $\Delta Position$ given the corner angle θ and the initial line width w_o, the displaced length d and the arc thickness w_f must be determined. The arc thickness w_f and the displaced length d relate in such a way that d and w_f must be determined numerically using the equations listed in this section.

From geometry,

$$r_1 = d \tan \frac{\theta}{2} \tag{8.4}$$

and

$$r_2 = r_1 + w_f \tag{8.5}$$

Equation 8.4 and 8.5 can be incorporated into Equation 8.3 to determine the Laplace pressure differential as a function of the displaced length d and the arc thickness w_f.

$$\Delta P(d, w_f) = \gamma\Big(\frac{1}{d \tan(\theta/2)} + \frac{1}{d \tan(\theta/2) + w_f}\Big) \tag{8.6}$$

Assume that point C on the inner ink-substrate contact line advances toward the center of the arc with velocity U (Fig. 8.3A). Note that as point C moves, the center of the arc also moves. The velocity is proportional to the Laplace pressure differential between the inner and

outer surfaces of the corner. U can be expressed as a function of the displaced length d:

$$U(d, w_f) = \frac{\Delta P(d, w_f)\lambda}{\eta} \tag{8.7}$$

η is the viscosity of the ink, and λ is a length scale along which the contact line is driven. λ encompasses several thermodynamic parameters and molecular length scales.[232] In this work, λ is empirically set equal to 1 μm, which brings the predicted values to the same order of magnitude of the experimental values. Increasing λ generally increases the predicted values of $\Delta Position$ and $\Delta Width$ uniformly across printing parameters (supplemental).

The distance between point C and the inner point of the intended print path corner O can be expressed in terms of d, as follows (Fig. 8.3A):

$$\overline{CO} = d\sec(\theta/2) - d\tan(\theta/2) = d\Big(\frac{1-\sin(\theta/2)}{\cos(\theta/2)}\Big) \tag{8.8}$$

Even though the contact line velocity depends on the displaced length d, assume that the contact line velocity over the entire smoothing process is constant and equal to the velocity at the final displaced length d. The distance that the contact line travels $\overline{CO}$ can thus be determined as a function of the contact line velocity.

$$\overline{CO} = U(d, w_f)\frac{\Delta x}{v_s} = \frac{\Delta x \Delta P(d, w_f)\lambda}{\eta v_s} \tag{8.9}$$

where Δx is the length that the stage travels between deposition and measurement, and v_s is the stage translation speed. By setting Equation 8.8 equal to Equation 8.9, the displaced length d can be determined for the traveled lengths Δx of interest.

The initial distribution is measured $\Delta x \approx 2w_o$ behind the nozzle just after deposition (Fig.

8.3B), so the displaced length d for the initial distribution is

$$d_{init} = \frac{2w_o \Delta P(d, w_f)\lambda}{\eta v_s} \frac{\cos(\theta/2)}{1 - \sin(\theta/2)} \tag{8.10}$$

The relaxed particle distribution is measured after traveling a length $\Delta x \approx NL - 2w_o$ around the polygon where N is the number of sides on the polygon (3, 4, 5, 6, or 8 in these experiments), and L is the polygon edge length (10 mm in these experiments) (Fig. 8.3C). The displaced length d for the relaxed distribution is

$$d_{relax} = \frac{(NL - 2w_o)\Delta P(d, w_f)\lambda}{\eta v_s} \frac{\cos(\theta/2)}{1 - \sin(\theta/2)} \tag{8.11}$$

The sheared particle distribution is measured after traveling $\Delta x \approx NL + 2w_o$ (Fig. 8.3C), so the displaced length d for the sheared distribution is

$$d_{shear} = \frac{(NL + 2w_o)\Delta P(d, w_f)\lambda}{\eta v_s} \frac{\cos(\theta/2)}{1 - \sin(\theta/2)} \tag{8.12}$$

Note that the displaced lengths in Equations 8.10–8.12 depend on the arc thickness w_f. w_f can be determined by setting the area of the arc equal to the area of the print path it is reforming.

$$\frac{\pi - \theta}{2}(r_2^2 - r_1^2) = 2w_o d + w_o^2 \cot\frac{\theta}{2} \tag{8.13}$$

Substituting Equation 8.4 and 8.5 into Equation 8.13:

$$0 = \frac{\pi - \theta}{2} w_f^2 + (\pi - \theta) d \tan\frac{\theta}{2} w_f - \left(2w_o d + w_o^2 \cot\frac{\theta}{2}\right) \tag{8.14}$$

The arc thickness w_f can be determined as a function of d using the quadratic formula.

$$w_f(d) = \frac{-(\pi-\theta)d\tan(\theta/2) + \sqrt{(\pi-\theta)^2 d^2 \tan^2(\theta/2) - 2(\pi-\theta)(-2w_o d - w_o^2\cot(\theta/2))}}{\pi-\theta} \tag{8.15}$$

By combining Equation 8.15 with Equations 8.10–8.12 and Equation 8.6, the value of the displaced length d and the arc thickness w_f can be numerically determined in the initial measurement, after relaxation, and after shear. To evaluate these equations, this work uses the ink viscosity at a shear strain rate of 0.01 Hz, which is the lowest strain rate at which viscosities were measured (supplemental). Surface tensions are estimated by using the surface tensions measured in Ref. [128], which use similar ink compositions, but with 16:84 wt silica:wt UDMA instead of 8:92 wt silica:wt UDMA. Because the surface tensions of the 16 wt% silica inks are within 1 mJ/m^2 of the surface tensions of inks without silica,[128, 170] it is unlikely that the 8 wt% difference in silica content will produce an appreciable difference in the estimated $\Delta Width$ and $\Delta Position$.

Knowing d and w_f, one can estimate $\Delta Width$ and $\Delta Position$. Because w_f indicates the entire width of the printed filament, one can estimate the width of the particle distribution inside the printed filament by assuming that the particle distribution width is some fraction of the filament width. In this paper, the particle distribution width $\Delta Width$ is arbitrarily assumed to be one tenth of the printed filament width. A different assumption would scale all $\Delta Width$ values uniformly, but trends as a function of printing parameters would remain the same.

$$\Delta Width_{smooth}(\theta, v_s, ink) = \frac{w_f - w_o}{10} \tag{8.16}$$

From geometry, the change in the position of the center of the line (the particle distribution

position) between the corner and center of the edge is

$$\Delta Position_{smooth}(\theta, v_s, ink) = d\tan(\theta/2) + w_o/2 - (d\tan(\theta/2) + w_f/2)\sin(\theta/2) \quad (8.17)$$

Thus, from a corner angle θ, ink composition, and translation speed v_s, the change in particle distribution position and width at the corner can be predicted. These changes can be compared to measured experimental changes in particle distribution position and width at the corner.

8.2.2 Double deposition-driven swelling

Geometric constraints imply that excess ink is deposited at corners during extrusion. Excess ink can come from two sources: double deposition and acceleration. Double deposition, where the nozzle must retrace some area on which it has already written, occurs in any scheme involving extrusion of filaments, including direct ink writing and fused deposition modeling.[229] Acceleration influences the corner shape at fast printing speeds. In these experiments, translation speeds are between 3 and 12 mm/s, which is slow enough that the 3-axis gantry used in this experiment accelerates over a trivial distance at corners. Specifically, the Shopbot ramp speed used here (the jerk speed, in extrusion-based 3D printing parlance) is greater than 12 mm/s, so linear speeds along the path center are not reduced before reaching the corner. A model that includes acceleration is described in the supplemental information. Here, a simplified analytical model is used to estimate how double deposition causes a change in distribution width and position at the corner.

Double deposition occurs because every time the print path changes direction, the nozzle retraces some area that it already covered. Conventionally, the double deposition area is calculated assuming that the nozzle is circular with radius $w_o/2$ (Fig. 8.4A). If the nozzle stops

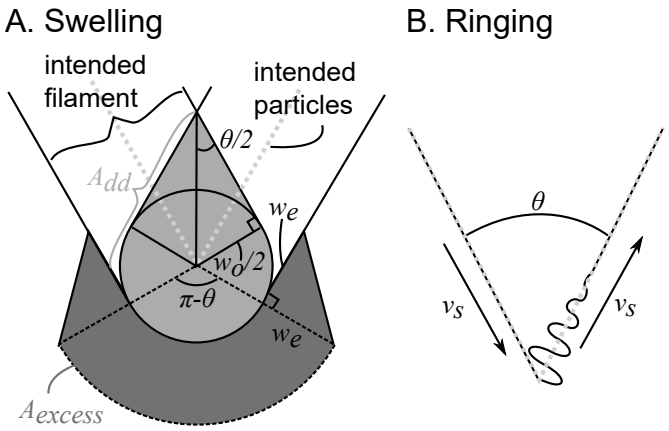

Figure 8.4: A) Double deposition-driven swelling. B) Ringing due to fast turns. In this schematic, v_s can be conceptualized as the nozzle translation speed.

moving at the corner, the resultant traced path will have an outer radius of $w_o/2$. In the experiments in this paper, the nozzle has a square cross-section, so the corner should match the square cross-section of the nozzle. However, the orientation of that square would vary based on the orientation of the corner. On average, it is assumed that the nozzle is circular with radius $w_o/2$. Also, it is assumed that the entire printed corner is of height h, so displaced volumes of ink are analogous to displaced areas of ink.

The the area of excess deposited ink is equal to the double deposition area A_{dd}, which can be expressed in terms of the corner angle θ and the corner width w_o.[229]

$$A_{excess} = A_{dd} = \frac{w_o^2}{4}\Big(\cot\Big(\frac{\theta}{2}\Big) + \frac{\pi+\theta}{2}\Big) \tag{8.18}$$

Ideally, the excess fluid would be deposited on the outer edge, in a sharp tip that falls within the intended print path.[229] However, this sharp tip disagrees with numerical models and experimental results that indicate that the printed corner exhibits a rounded tip.[226, 228, 233] Numerical models indicate that some of this excess volume will fall inside of the intended print path, and some will fall outside.[226] For a 90° corner, the volume of excess fluid deposited outside the print path corner is 2–3 times the volume deposited inside the corner.[226] This

ratio expands to 10 times for 30° corners.[226] There is no accurate analytical model which predicts the ratio of excess volume deposited inside the corner to outside the corner. For simplicity, it is assumed that all of the excess fluid is deposited outside of the corner in an arc of thickness w_e, flanked by two triangles of height and width w_e (Fig. 8.4A). The material in these triangles helps to produce a smooth transition between the excess volume arc and the rest of the print path. Although the shape of this excess area contains unrealistically sharp edges, it approximates the shape of experimentally printed and numerically simulated corners.[226] Using geometry, the excess area depends on the arc width w_e:

$$A_{excess} = \frac{\pi - \theta}{2}\left(\left(w_e + \frac{w_o}{2}\right)^2 - \left(\frac{w_o}{2}\right)^2\right) + w_e^2 \tag{8.19}$$

With this, the arc width w_e can be expressed in terms of the intended line width w_o, corner angle θ, and excess corner area A_{excess}:

$$w_e = \frac{-(\pi - \theta)w_o/2 + \sqrt{((\pi - \theta)w_o/2)^2 + 4((\pi - \theta)/2 + 1)A_{excess}}}{\pi - \theta + 2} \tag{8.20}$$

Equation 8.20 can be evaluated as a function of the intended line width w_o and the corner angle θ by substituting Equation 8.18 into Equation 8.20.

The difference in line width between the corner and the intended line width is w_e. In this paper, the particle distribution width is assumed to be one tenth of the line width. Again, assuming a different particle distribution width ratio would not change the scaling of the change in width with corner angle, print speed, or ink viscosity. As such, the difference in particle distribution between the corner and center of the edge is:

$$\Delta Width_{swell}(\theta) = w_e/10 \tag{8.21}$$

Because the middle of the line and thus the particle distribution peak position shifts outward

toward negative positions at the corner, the difference in the particle distribution peak position between the corner and center of the edge is

$$\Delta Position_{swell}(\theta) = -w_e/2 \tag{8.22}$$

As the corner angle increases, the excess volume from double deposition decreases, so the magnitude of the change in position and width at the corner decreases.

Thus, the change in particle distribution position and width at the corner due to double deposition-driven corner swelling can be predicted and compared to measured experimental changes in the particle distribution position and width at the corner.

8.2.3 Ringing

If the translation speed is not reduced to zero at a corner, the rapid change in direction and speed that occurs at the corner induces vibrations in the 3-axis gantry.[226, 230] These vibrations produce oscillatory deviations in the print path which effectively widen the printed line at the corner (Fig. 8.4B). Because the oscillations are centered within the print path, the oscillations should not change the position of the line at the corner.

$$\Delta Position_{ring} = 0 \tag{8.23}$$

Ringing should only impact the printed line coming out of the corner, not going into it (Fig. 8.4B). Faster, sharper turns result in more ringing because they impose larger changes in speed over a small distance.[230] Assume that ringing is extinguished at the center of the polygon edge. Assume that the amplitude of the oscillations and thus the width of the particle distribution at the corner scales with the change in velocity between the incoming and outgoing

print paths:

$$\Delta Width_{ring}(\theta, v_s) = C(2v_s \cos(\theta/2)) \tag{8.24}$$

where C is a damping factor that is empirically set to $C = 1/300$ seconds. Choosing a different value for C does not impact the scaling of the change in width as a function of printing parameters and part design.

8.3 Experimental approach

This paper draws from the same data set that is used in Refs. [18, 19], but this work only uses the first deposited line of the three-pass polygon, only uses 10 mm edge lengths, and focuses specifically on corners. Data and code can be found at Ref. [218].

8.3.1 Materials

Inks consisted of diurethane dimethacrylate (UDMA) (Sigma Aldrich, mixture of isomers with topanol inhibitor), triethylene glycol dimethacrylate (TEGDMA) (Sigma Aldrich, with MEHQ inhibitor), fumed silica (Evonik Aerosil R106), camphorquinone (CQ) (Sigma Aldrich), and 2-(Dimethylaminoethylmethacrylate) (DMAEMA) (Sigma Aldrich, with monomethyl ether hydroquinone inhibitor). Bases were mixed in a 92:8 UDMA:fumed silica weight ratio and mixed in a planetary mixer (Thinky ARE-310) at 2000 rpm for 3 minutes. Inks were then mixed in 80:20, 75:25, 70:30, and 65:35 base:TEGDMA weight ratios with 0.2 w% CQ and 0.8 w% DMAEMA, plus 10 w% (≈1.4 v%) silver-coated copper microspheres (Potters Beads Conduct-O-Fil, SC15S15, diameter 15 μm), which were acoustically focused in the nozzle. Carbopol support gels were mixed by adding 1.2 w% Carbomer 940 to deionized water (pH 3-4) and mixing with an overhead stirrer for 5 minutes at 1500 rpm or until dissolved. Gels were

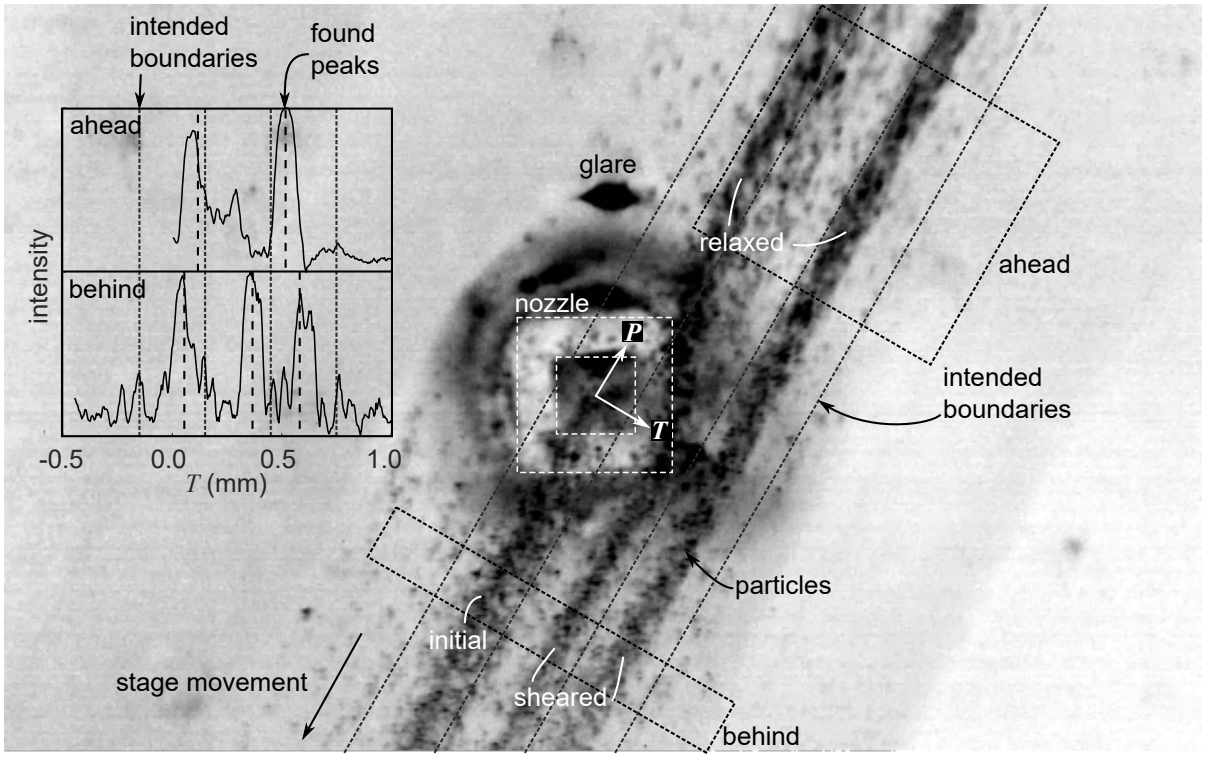

Figure 8.5: Example of analyzed frame, for layer-by-layer support. Image is inverted. Inset: Intensities are summed along the parallel direction ahead of and behind the nozzle. Distribution positions and widths are found as a function of transverse position.

then neutralized using 50% NaOH (Sigma Aldrich) and mixed in a planetary mixer (Thinky ARE-310) at 2000 rpm for 3 minutes to remove bubbles.

8.3.2 Nozzle configuration and video collection

Inks and support gels were extruded through square borosilicate capillary nozzles (Vitrocom, 0.3 mm ID, 0.6 mm OD, 50 mm length) onto glass slides. The ink capillary was seated in a stainless steel block containing a 0.7 mm square groove lined with ultrasonic coupling gel. A piezoelectric actuator (15 mm diameter x 1 mm thick Navy I material, American Piezo) was adhered to the steel block using epoxy (Devcon HP250). The piezo was driven using a signal generator (HP 33120A) and amplifier (Mini-Circuits LZY-22+), and signals were measured using an oscilloscope (Agilent DSO-X 2024A). Sinusoidal signals were generated at 2.249 MHz and a peak-to-peak voltage of 50 V_{pp}. The piezo was thermally coupled to a copper cooling stage using thermal couplant (Wakefield type 120). Steel ferrules were bonded to capillaries using epoxy (Devcon HP250). Ink and support were extruded using a mass flow controller (Fluigent MFCS-EZ) at pressures calibrated by measuring masses extruded at fixed pressures and times. For ink, average flow speeds inside the nozzle were set equal to stage translation speeds.

The ink nozzle and substrate were illuminated using light transmitted through a red filter cube, to prevent curing. Videos were collected from underneath the nozzle through the glass substrate using a Point Grey Grasshopper GS3-U3-2356C-C camera with an Infinity Infinitube FM-200 objective and $\times$0.66 lens, at 86 fps.

For layer-by-layer support, the support gel was extruded through a square borosilicate capillary at a stage speed of 10 mm/s and an estimated flow speed of 15 mm/s. For bath support, a 1 mm-thick layer of support was spread onto the substrate. The point where the nozzle touches the substrate was defined as $z = 0$. Parts were printed at a stand-off distance and line spacing

of 0.3 mm, which is the inner width of the capillary. First, the three-line inner support polygon was printed from inside to outside, then the three-line outer support polygon from inside to outside, then the three-line ink polygon from inside to outside. Future experiments could print polygons from outside to inside to further examine the role of boundary conditions on corner defects. Equilateral triangles, squares, pentagons, hexagons, and octagons were printed with 10 mm edge lengths (Fig. 8.2).

Distributions were collected using Matlab R2018b. Backgrounds were removed using a 15 px disk structuring element. Where the origin is at the nozzle center and the inner nozzle width is w, the largest fully imaged region upstream of the nozzle from $T = 0$ to $T = 3.5w$ and downstream of the nozzle from $T = -1.5w$ to $T = 3.5w$ were each summed along the print direction. Peaks were identified using the Matlab function *findpeaks* with a minimum peak-to-peak distance of $w/2$. Frames in which the corner of the polygon is visible were removed. The width is the standard deviation of the distribution within $w/2$ on either side of the peak. Width and position measurements at the corners were taken from the starting and ending 2.5 mm of the 10 mm edge, and measurements at the center of the edge were taken from the middle 2 mm of the 10 mm edge (Fig. 8.6). The change in position and width at the corner are measured as the value at the corner, subtracted by the value at the center (Eq. 8.1, 8.2).

8.4 Results

Videos of the region near the nozzle during printing indicate that the behavior of the particle distribution at corners changes during the course of the print, and the nature of those changes depends on the geometry of the support material. In this section, an edge is a straight segment that connects a starting corner to an ending corner. Distances are measured from the starting corner (Fig. 8.6). Positive particle distribution positions are toward the inner edge of the polygon, while negative positions are toward the outer edge. Ideally, the change in the particle

distribution position and width at the corner would be zero, ensuring consistency in microstructure throughout the print. In other words, the final location of the particle distribution is in the center of the designed print path, and the particle distribution is just as narrow at the corner as it is in the middle of a straight segment. Particle distributions are measured at three points in the printing process. (1) Corner defects can come from the deposition process and manifest in the initial distribution. (2) Defects can evolve over time during relaxation, so relaxed distributions are measured just before the next neighboring line is printed. (3) Finally, defects can appear when the nozzle returns to write a neighboring filament and shears the existing filament, so sheared distributions are measured just after the next neighboring line is printed. Initial and sheared distributions behave similarly, and relaxed distributions exhibit distinct trends.

In this section, experimental changes in particle distribution at the corner $\Delta Position$ and $\Delta Width$ are measured. Trends in these values as a function of distance from the corner, corner angle, and print speed are compared to the theoretical contributions of swelling, smoothing, and ringing. Because all three theories were constructed with arbitrary scaling factors, only trends are compared between observations and predictions.

The variation in the particle distribution as a function of distance from the corner can be used to diagnose sources of corner defects. The change in particle distribution position $\Delta Position$ along the length of the edge varies based on support geometry. Figure 8.6A shows the particle distribution position and width as a function of distance from the starting corner. Figure 8.6B shows an exaggerated illustration of the particle distribution position and width on a printed hexagon to aid visualization. Smoothing causes inward shifts in position at corners, while swelling causes outward shifts at corners. In layer-by-layer support, the initial distribution shifts outward at corners, as predicted by swelling. In bath support, the initial distribution shifts slightly inward at corners, as predicted by smoothing. During relaxation, prior to the nozzle returning to write a neighboring line, the distribution changes. In layer-by-layer support, the relaxed distribution still bows inward at the center of the edge, but it sharply shifts

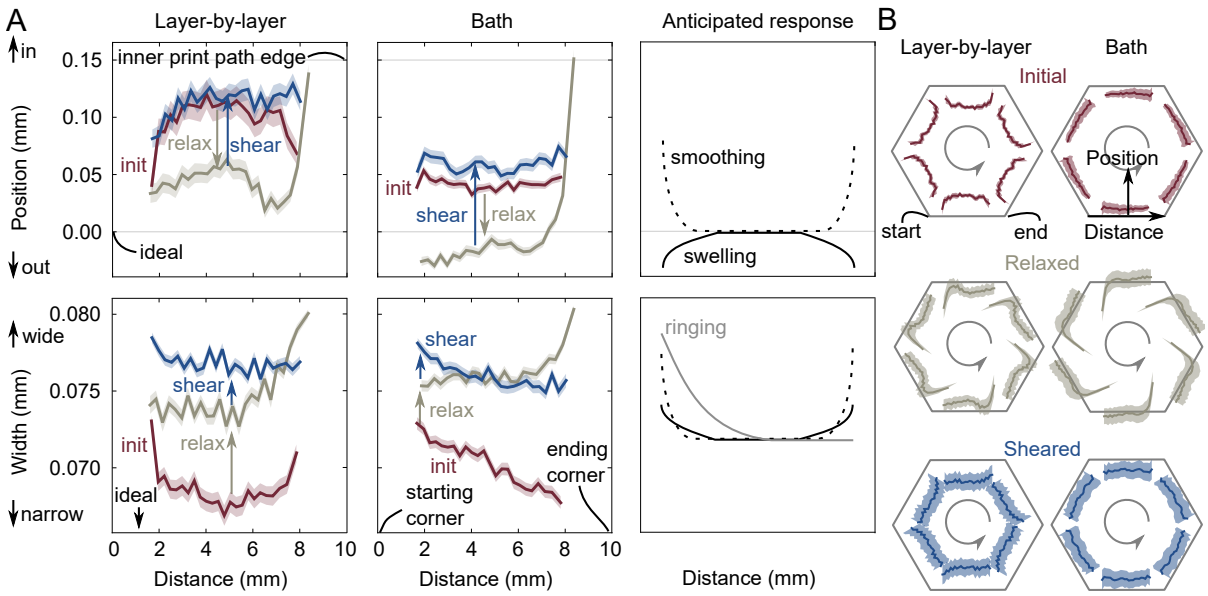

Figure 8.6: Shifts in particle distribution center and width over the polygon edge. A) Particle distribution position and width as a function of distance from the corner, for line 1 averaged over all edges, corner angles, print speeds, and ink compositions. Width is the standard deviation of the particle distribution. Shaded areas indicate standard error over many printing parameters. Anticipated response is arbitrarily scaled. B) Exaggerated illustrations of the initial, relaxed, and sheared particle distributions in printed hexagons. Dark lines represent the position, while light areas represent the distribution width. Because the scale has been amplified for visual comprehension, the jumps between the end of one edge and the start of the next in the relaxed state are not as jagged in reality.

inward at the ending corner, exhibiting traits of both swelling (at the center) and smoothing (at the corner). In bath support, although the distribution initially had an outward bow at the center of the edge, the distribution adopts a slight inward bow at the center during relaxation. Like layer-by-layer support, in bath support the relaxed distribution position sharply shifts inward at the ending corner, exhibiting traits of both swelling (at the center) and smoothing (at the corner). After the nozzle passes to write a new line, shearing the existing line, distributions once again resemble their initial positions. In layer-by-layer support, the sheared distribution shifts outward at corners, exhibiting traits of swelling. In bath support, the sheared distribution shifts inward at corners, exhibiting traits of smoothing.

Like the change in distribution position, the change in distribution width along the length of the edge also depends on support geometry (see results in Fig. 8.6). Smoothing and swelling cause the distribution to widen at both corners, while ringing only causes the particle distribution to widen at the starting corner. In layer-by-layer support, the initial distribution widens sharply at the starting and ending corners as predicted by the swelling and smoothing models, but in bath support, the initial distribution narrows gradually from the starting corner to the ending corner as predicted by the ringing model. After the line has had time to relax, in both support geometries the relaxed distribution widens sharply at the ending corner, amplifying an existing trend in layer-by-layer support but creating a new effect in bath support. After the nozzle returns to write a new line and shears the existing line, the sheared distribution width follows similar behaviors to the initial distribution. In layer-by-layer support, the sheared distribution only slightly widens at the starting corner but becomes roughly uniform along the edge length. Similarly, in bath support the sheared distribution narrows along the length of the edge as it did initially, but the sheared variation over the edge is less severe than the initial variation over the edge.

The difference in particle distribution position and width between the corner and middle of the polygon edge can further elucidate the sources of corner defects. Figure 8.7 shows

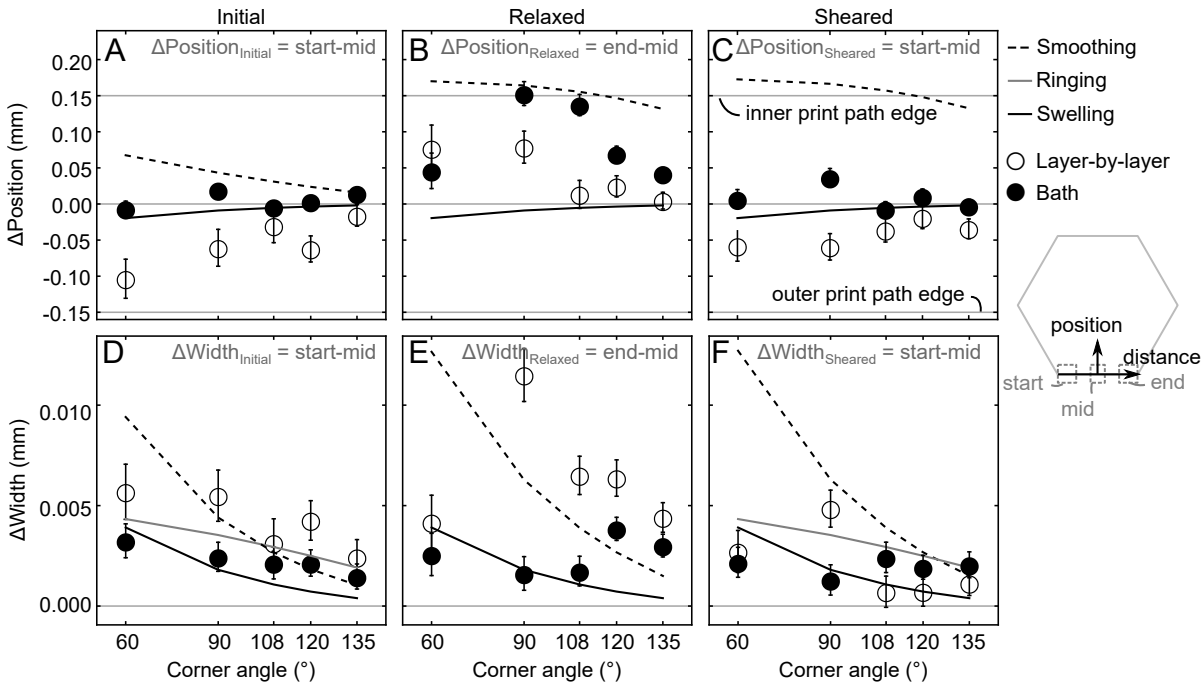

Figure 8.7: Corner defect path shifts (A–C) and particle distribution spreading (D–F) at the corner as a function of polygon corner angle. Theoretical contributions of the smoothing, swelling, and ringing models are shown with continuous lines. Error bars indicate standard error.

these differences as a function of the corner angle, and Figure 8.8 shows these differences as a function of print speed, which is equal to both the flow speed in the nozzle and the translation speed of the stage. Comparing experimental changes to the changes predicted in Equations 8.16, 8.17, 8.21, 8.22, 8.23, and 8.24 as shown by the continuous lines in Figure 8.7 and 8.8 indicates which of the three mechanisms is the most likely source of corner defects. Note that there is no predicted relaxed change in width due to ringing because the relaxed change in width is measured between the ending corner and center of the edge, and ringing only impacts the starting corner. Because the initial and sheared distributions are measured behind the nozzle, differences are measured between the middle of the edge and the starting corner. Because the relaxed distribution is measured ahead of the nozzle, differences are measured between the middle of the edge and the ending corner.

The smoothing, swelling, and ringing models predict that the changes in the particle distribution at the corner vary with corner angle, ink composition, and print speed. Within the probed range, experimental effects of ink composition on changes at the corner are weak and may be found in the supplemental information. Trends as a function of corner angle and print speed are more conclusive.

The dependence of changes in the particle distribution at the corner on corner angle can be used to diagnose sources of microstructural defects at the corner. The initial and sheared changes in position $\Delta Position$ for layer-by-layer support are negative and decrease in magnitude with increasing corner angle, matching the swelling model (Fig. 8.7A,C). In bath support, initial and sheared changes in position $\Delta Position$ are close to 0 for all corner angles, which could come from a combination of the two opposing mechanisms or from a suppression of both smoothing and swelling. For both supports, the relaxed change in position is positive and decreases in magnitude with increasing corner angle, matching the smoothing model (Fig. 8.7B).

The smoothing and swelling models both predict that the change in width at the corner $\Delta Width$ decreases with increasing corner angle. For both support geometries, the initial change in width decreases with increasing corner angle, matching both models (Fig. 8.7D). In contrast, the relaxed change in width for bath support and sheared changes in width for both supports decrease, then increase with increasing corner angle, indicating that another effect may cause the particle distribution at the corner to widen at large corner angles during relaxation and possibly during shear (Fig. 8.7E).

The relaxed change in width $\Delta Width$ in layer-by-layer support (Fig. 8.7E) and change in position $\Delta Position$ in both types of support (Fig. 8.7B) decrease sharply from a corner angle of 90° to 135°, but the changes are incongruously small at a corner angle of 60° for the position in bath support and width in layer-by-layer support. This may come from the design of the print path. The length of the polygon edge (10 mm) is established at the outer edge of

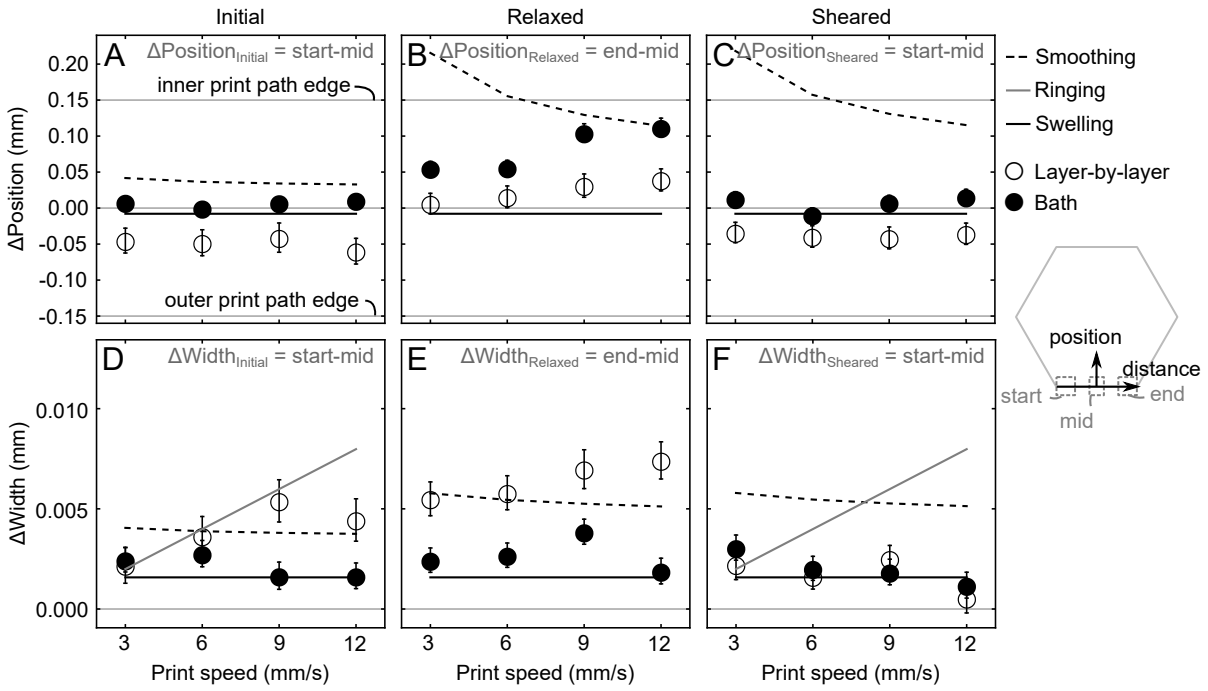

Figure 8.8: Corner defect path shifts (A–C) and particle distribution spreading (D–F) at the corner as a function of print speed, which represents both the translation and flow speeds. Theoretical contributions of the smoothing, swelling, and ringing models are shown with continuous lines. Error bars indicate standard error.

the polygon, so the length of the inner edge of the polygon decreases at sharper corner angles, leading to smaller differences between the center and corner at 60°. Alternatively, at a large spreading length scaling factor λ, the change in position due to corner smoothing decreases at 60°, but not by as much as the experimental results (Fig. 8.S3).

The dependence of changes in the particle distribution at the corner on the print speed can be used to diagnose sources of microstructural defects at the corner. The smoothing model predicts that as the print speed increases, the change in position at the corner $\Delta Position$ should decrease (Fig. 8.8A–C). The swelling model predicts no print speed dependence because the model only considers double deposition, not acceleration at the corner. Experimental data indicate that for both supports, the initial and sheared changes in position do not change by more than one standard error across the tested print speeds, indicating that either the swelling

model or no model dominates the initial and sheared change in position at the corner (Fig. 8.8A,C). The relaxed changes in position are positive and increase with print speed (Fig. 8.8B). Although the smoothing model predicts positive changes in position at the corner, it predicts that those changes should decrease with increasing print speed. As such, neither smoothing nor swelling describes the relaxed change in position as a function of print speed.

The smoothing model predicts that the change in width $\Delta Width$ should slightly decrease with increasing print speed, the swelling model predicts no dependence on print speed, and the ringing model predicts that the change in width should increase with print speed (Fig. 8.8D–F). The initial and relaxed change in width are mostly invariant with print speed for bath support (Fig. 8.8D,E). The initial change in width increases with print speed for layer-by-layer support, as predicted by the ringing model (Fig. 8.8D). The relaxed change in width also increases with print speed in layer-by-layer support (Fig. 8.8E). This trend is not a residual effect from ringing in the initial change in width, because ringing occurs at the starting corner, and the relaxed change in width is measured at the ending corner. As such, none of the discussed theories explain the increase in relaxed change in width with print speed. Sheared changes in width at the corner decrease with increasing print speed for both supports, qualitatively matching the smoothing model but exhibiting a more severe dependence on print speed than predicted by the smoothing model (Fig. 8.8F).

8.5 Discussion

A summary of the instances where the experiments qualitatively match the proposed theories is shown in Table 8.1. Because smoothing due to capillarity is hindered by viscous dissipation, smoothing should be influential on long time scales, after relaxation. Swelling should act on short time scales and be visible in the initial distribution because it is not hindered by viscous dissipation, and excess fluid must be deposited somewhere immediately. Similarly,

	Layer-by-layer			Bath		
	Distance	Corner angle	Print speed	Distance	Corner angle	Print speed
Initial position	**sw**	**sw**	**sw**	sm	**sw**+sm or none	**sw** or none
Initial width	sm or **sw**	any	ri	ri	any	**sw** or none
Relaxed position	sm+**sw**	sm	?	sm+**sw**	sm	?
Relaxed width	sm or **sw**	?	?	sm or **sw**	?	**sw** or none
Sheared position	**sw**	**sw**	**sw**	sm	**sw**+sm or none	**sw** or none
Sheared width	none	?	sm	ri	?	sm

Table 8.1: Summary of cases where theory fits the experiments, in terms of the position or width as a function of distance or the trend in Δposition or Δwidth as a function of corner angle or print speed. Experiments match the smoothing (sm), ringing (ri), and/or swelling (**sw**) theory, exhibit trends that could come from a combination of theories or from the absence of all effects (none), or exhibit trends that occur in none of the theories (?).

ringing should act immediately and be visible in the initial distribution because it is directly changes the path along which the stage travels. In Table 8.1, no single theory explains every behavior of the initial, relaxed, or sheared distribution in layer-by-layer or bath support. Rather, various theories match the various experimental behaviors, suggesting that several mechanisms influence the particle distribution at each point in the printing process. Further, because some behaviors are not explained by any of the considered mechanisms, it is possible that the process is also influenced by other driving forces.

The initial change in the distribution at the corner is dominated by swelling and ringing, especially in layer-by-layer support. The prominence of swelling and ringing in the initial distribution supports the hypothesis that swelling and ringing should act on short timescales. In bath support, changes at the corner in the initial distribution are mild. One explanation for these small changes is that smoothing and swelling are both present and cancel each other out. A more likely explanation is that both swelling and smoothing are suppressed in the initial distribution in bath support. The suppression of swelling and smoothing in bath support may come from hydrostatic stress. In layer-by-layer support, the inner edge of the corner is supported by support material, and the outer edge is exposed to air (Fig. 8.2). As such, the

support material prevents deposition of excess volume on the inner edge, so all excess fluid should be deposited on the outer edge. Moreover, because there is only air on the outer edge of the corner, the excess fluid is capable of concentrating into more of a bulge as predicted by the model proposed by Huang, et. al.[227] In contrast, in bath support, the corner is supported on the inner and outer edges by support material, so there is less of a preference for excess fluid to be deposited on the outer edge than in layer-by-layer support. Furthermore, because the corner is supported on its outer edge by support material, the hydrostatic stress from the support material may spread the excess ink out onto a long arc of the corner (i.e. longer triangles in the swelling model in Figure 8.4A) rather than allowing the ink to concentrate into a capillarity-driven bulge.

Smoothing occurs during relaxation for both support types, which supports the hypothesis that smoothing acts on longer time-scales because of viscous dissipation (Table 8.1). After relaxation, particle distribution positions are still shifted inward at the center of the edge, exhibiting residual effects from swelling. Very close to the corner the particle distribution sharply shifts inward, matching smoothing (Fig. 8.6). This suggests that smoothing influences the position within a smaller distance from the corner than swelling but is capable of creating larger shifts in position than swelling. Layer-by-layer support produces smaller relaxed changes in position at the corner and larger changes in width at the corner than bath support. The difference in the change in position between the relaxed and initial states is roughly the same for layer-by-layer and bath support. As such, the difference in relaxed change in position between bath and layer-by-layer support is likely a residual difference from the initial distribution, where the change in position in bath support was already more positive than the change in layer-by-layer support. Because both support geometries support the inner edge of the corner, both types of support experience the same hydrostatic resistance to Laplace pressure-driven smoothing. Although the surface energy at the outer edge of the layer-by-layer supported corner is different from the surface energy at the outer edge of the bath supported corner, this

difference in surface energy does not appear to produce a large difference in smoothing between the support types.

The sheared change in position and width at the corner largely follow the swelling model, like the initial change in position and width. This match in trends is misleading: swelling should occur instantly at the point of deposition and should not occur again in an already-deposited line. It is more useful to consider the forces imposed by the nozzle that has returned to print a new line. For the initial and relaxed distribution, changes at the corner occur largely because the corners shift more than the center. In contrast, in the sheared distribution the center shifts more than the corners. Consider Figure 8.5. The nozzle is moving toward the top right corner of the image, and the two relaxed lines are shifting toward the center of the polygon, in the bottom right corner of the image. During relaxation, the entire line shifts outward toward negative positions (Fig. 8.6). During shear, the nozzle shifts the existing line inward toward positive positions and away from the nozzle. The corners shift inward by less than the center because the corners are farther away from the nozzle due to capillarity-driven smoothing during relaxation. As such, although the sheared change in position at the corner exhibits some characteristics of both smoothing and swelling, it is reasonable to expect that neither smoothing or swelling is directly in control of the change in distribution between the sheared and relaxed states. This framework of viewing the nozzle as a shearing force can be used to understand why the sheared change in width at the corner does not strongly decrease as a function of corner angle, despite the predictions of all three models. The framework also helps to explain why the change in width at the corner decreases more steeply as a function of print speed than predicted by smoothing. As the nozzle deposits a new line on the outer perimeter of the existing line, the new line swells and rings at the corners, driving that new excess volume into the existing line and narrowing the existing line at the corner. Effectively, ringing and swelling in a neighboring line attenuate the effects of ringing and swelling in the original line.

This result is useful because it implies that the final particle distribution at the end of printing should not vary greatly between corners of different angles, ensuring consistent properties throughout the print. Moreover, the sheared distribution is the best indicator of the final distribution of particles in the printed structure. Ideally, the change in position and change in width at the corner would be zero, ensuring a consistent distribution of particles throughout the entire print. Bath support achieves the smallest sheared change in position, and the sheared change in width is roughly the same between the two support geometries. As such, bath support should produce more consistent particle distributions than layer-by-layer support in structures printed with DIW with acoustophoresis.

The changes in relaxed position and width at the corner exhibit unexpected trends in print speed. Whereas the smoothing model predicts a small change and the swelling model predicts no change at higher print speeds, experimental data show large changes for both at faster print speeds. It is unlikely that ringing directly explains this effect because ringing is caused by vibrations which occur just after the printer changes direction, so oscillations in the print path should only occur at the starting corner. The relaxed distribution is measured at the ending corner. Instead, faster print speeds may enhance the effects of capillarity. Specifically, increasing the flow speed and the translation speed increases the shear strain rate on the ink, lowering its viscosity and accelerating Laplace pressure-driven corner smoothing. Alternatively, the higher shear strain rate and larger vibrations in the moving stage at fast translation speeds may provide sufficient energy to overcome the energy barrier that suppresses capillarity-driven bulge formation as predicted by the model proposed by Huang, et. al. (see supplemental).[227] The formation of a bulge in the inner edge of the corner would widen the distribution and shift it inward, matching the trend shown in the relaxed distribution (Fig. 8.8). However, the arc-shaped geometry exhibited by the corners printed in this study does not match the geometry predicted by the bulge-based model, so a model that combines the Huang, et. al. model with the model proposed in this paper may match these experiments more comprehensively.

The data do not convey a conclusive argument as to which support geometry is more vulnerable to ringing. Two trends convey opposing narratives. First, in bath support the initial and sheared particle distribution gradually narrows over the length of the edge as predicted by ringing, while in layer-by-layer support the particle distribution widens sharply at the starting and ending corners as predicted by smoothing and swelling, suggesting that bath support is more vulnerable to ringing. Second, ringing causes the initial change in width at the corner to increase with increasing print speeds, which is prominent for layer-by-layer support but not present in bath support, suggesting that layer-by-layer support is more vulnerable to ringing. One could argue that bath support should be more impacted by ringing because it more precisely preserves the line as written, whereas layer-by-layer support allows the line to blur more, allowing the other effects to overpower ringing. Alternatively, one could argue that bath support provides extra damping that prevents vibrations from impacting the printed line because the nozzle is fully submerged in bath support, so the stage is more closely coupled to the nozzle in bath support than in layer-by-layer support. Because of these two opposing trends and because there are some gaps in explanation in Table 8.1, it is possible that these experimental trends have been mischaracterized here as ringing, and the trends may come from another source not considered here.

8.6 Conclusions

During deposition of lines containing a narrow distribution of particles via direct ink writing with acoustophoresis, three effects cause changes in the particle distribution at printed corners. First, capillarity causes the corner to widen and travel inward, via corner smoothing. Corner smoothing occurs on long timescales and manifests after the printed corner has had time to relax. Second, the change in direction at the corner causes the nozzle to retrace a double deposition area. The excess volume from this double deposition is largely diverted to the outer

edge of the corner, via corner swelling. Corner swelling occurs quickly during deposition and manifests in the initially deposited line. Third, when a 3-axis gantry changes direction without decelerating into the corner, the printer vibrates and traces an oscillatory path as it exits the corner, effectively widening the distribution of particles, via ringing. Ringing occurs quickly during deposition and manifests in the initially deposited line. In other moderate-viscosity direct ink writing applications without acoustophoresis or support material, it is reasonable to expect all three of these effects to still influence the shape and position of printed corners.

There is much evidence of corner swelling in the initial and sheared particle distribution, particularly in layer-by-layer support. There is also evidence of smoothing in both types of support in the relaxed distribution, but some trends in the relaxed distribution remain unexplained. It is possible that another mechanism that strongly increases with print speed also induces corner defects during relaxation. Alternatively, the formulation of the smoothing model without support material could lead to an inaccurate scaling. Faster print speeds could increase the shear strain rate on the viscoelastic support material, yielding a larger volume of support and enabling smoothing to progress over a longer timescale. Finally, although there is strong evidence of swelling in the sheared particle distribution position, there is less evidence of swelling in the sheared distribution width. This is likely because corner defects in sheared distributions are controlled by the behavior of neighboring lines. The sheared corner doesn't swell again; the new corner swells and causes the existing corner to shift along with it, as demonstrated in the straight segments of polygons.[19] In straight segments, sheared distribution widths do not correlate with initial distribution widths, which may explain why only sheared positions match the swelling model, not sheared widths.

To ensure consistent properties throughout the print, it is necessary to limit changes in the particle distribution at corners and to limit differences in the particle distribution among corners of different angles. Some of these effects may be remediated using *in-situ* curing. The inks used in this work are photopolymers, so a curing lamp in the direct-write printer could preserve

printed microstructures at chosen points in the printing process.

- To suppress particle positioning defects at corners, use a support bath, and design toolpaths with obtuse corners.
- To limit the effects of swelling and ringing, cure the deposited structure only after relaxation, because relaxation offsets their effects.
- To limit the effects of smoothing, cure the deposited structure just after deposition or just after the whole layer is complete.

8.S1 Supplemental figures and tables

8.S1.1 Theory

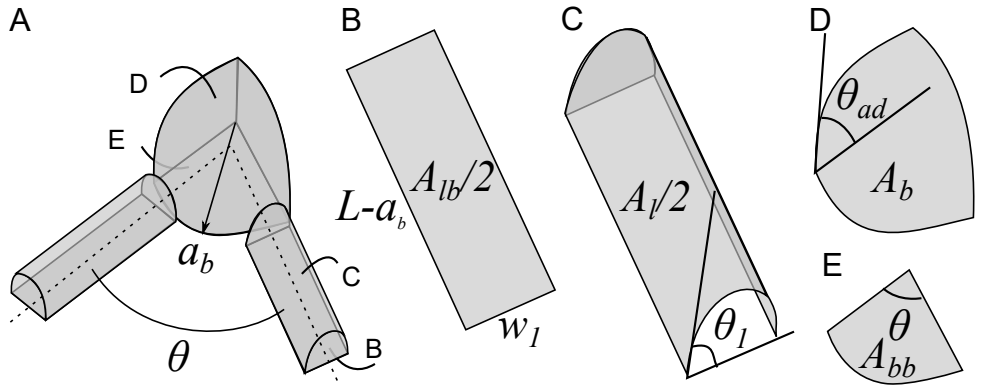

Figure 8.S1: Geometry of bulge-based corner smoothing model.

The bulge-based corner smoothing model described here is adapted from Ref. [227]. The model assumes that at a liquid elbow between two lines with circular segment cross-sections will split into three shapes: two shorter lines with circular segment cross-sections and one

bulge shaped as a spherical sector. The total energy of the system E_{tot} can be determined from the interfacial energies γ and interfacial areas A:

$$E_{tot} = \gamma_{LG}(A_b + A_l) + (\gamma_{SL} - \gamma_{SG})(A_{bb} + A_{lb}) \tag{8.S1}$$

where LG is ink-gas, SL is substrate-ink, and SG is a substrate-gas interface. The equilibrium contact angle θ_{eq} provides a relationship between the surface energies:

$$\gamma_{LG}\cos\theta_{eq} + \gamma_{SL} = \gamma_{SG} \tag{8.S2}$$

Substituting Equation 8.S2 into Equation 8.S1, the total energy normalized by the ink surface energy γ_{LG} is:

$$\frac{E_{tot}}{\gamma_{LG}} = A_b + A_l - \cos\theta_{eq}(A_{bb} + A_{lb}) \tag{8.S3}$$

The areas A_b, A_l, A_{bb}, and A_{lb} can be determined from geometry.

The width of the lines is w_1. Because this nozzle inner width is 0.3 mm, this value is set here to 0.3 mm.

$$w_1 = 0.3 \quad \text{mm} \tag{8.S4}$$

The total volume of the system is the area of the nozzle (w_1^2) multiplied by the length of the elbow, which is set here to half the length of a polygon edge.

$$V_{tot} = 2Lw_1^2 \tag{8.S5}$$

$$L = 5 \quad \text{mm} \tag{8.S6}$$

Given a bulge radius a_b, the area of the surface of the bulge A_b depends on the advancing

contact angle θ_{ad}.

$$A_b = \frac{\theta}{2\pi}\pi a_b^2\Big(1+\tan^2\Big(\frac{\theta_{ad}}{2}\Big)\Big) \tag{8.S7}$$

The area of the base of the bulge A_{bb} is

$$A_{bb} = \frac{\theta}{2\pi}\pi a_b^2 \tag{8.S8}$$

The volume of the bulge V_b is

$$V_b = \left(\frac{\theta}{2\pi}\right)^{3/2}\left(\frac{\pi\tan(\theta_{ad}/2)(3+\tan^2(\theta_{ad}/2))}{6}\right)a_b^3 \tag{8.S9}$$

The volume of the lines V_l is

$$V_l = V_{tot} - V_b \tag{8.S10}$$

From the volume of the lines, the contact angle of the lines can be determined. This equation can be solved using the Mathematica function FindRoot.

$$\frac{\theta_1 - \sin\theta_1\cos\theta_1}{\sin^2\theta_1} == \frac{V_1}{2L(w_1/2)^2} \tag{8.S11}$$

The area of the base of the lines is

$$A_{lb} = 2w_1(L-a_b) \tag{8.S12}$$

and the area of the surface of the lines is

$$A_l = \frac{V_l}{w_1/2}\Big(\frac{2\theta_1\sin\theta_1}{\theta_1-\sin\theta_1\cos\theta_1}\Big) \tag{8.S13}$$

Given a corner angle θ, a polygon edge length $2L$, an advancing contact angle θ_{ad}, and an

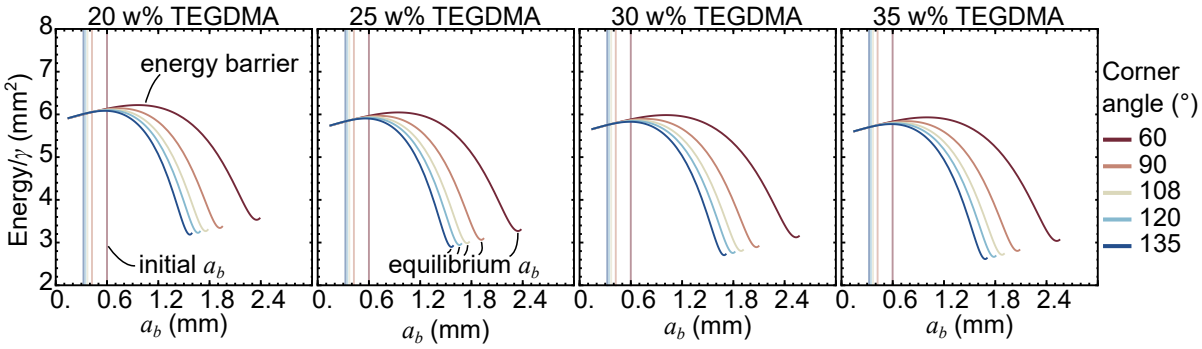

Figure 8.S2: Energy per surface tension E_{tot}/γ_{LG} as a function of bulge radius a_b, for corner angles and inks used in this study.

equilibrium contact angle θ_{eq}, the equilibrium radius of the bulge is the radius a_b that minimizes the energy determined in Equation 8.S3. This value is determined here numerically for each combination of ink and corner angle using the contact angles in Table 8.S1, which were measured using sessile droplets and the submerged needle technique.

w% TEGDMA	θ_{ad} (°)	θ_{eq} (°)
20	58.59 (0.67)	42.50 (0.59)
25	59.05 (1.23)	37.23 (0.64)
30	49.83 (1.19)	34.50 (0.82)
35	50.52 (1.20)	32.68 (1.20)

Table 8.S1: Advancing and static contact angles for inks with varying TEGDMA loadings. Parentheticals indicate standard error.

The equilibrium measured radius of the bulge should be a_b for initial, relaxed, and sheared distributions. However, for the inks used in this study, the energy curve from Equation 8.S3 has an energy barrier (Fig. 8.S2). The initial radius $a_b = w_1/\sin(\theta/2)$ is less than the radius at the energy barrier. Because the inks are supported on their inner edge by a viscous Bingham plastic support material, it is unlikely that enough energy will be supplied to the system to overcome the energy barrier, so bulges will not form. As such, a different model is proposed here to predict the effect of capillarity, described in the main body of the chapter.

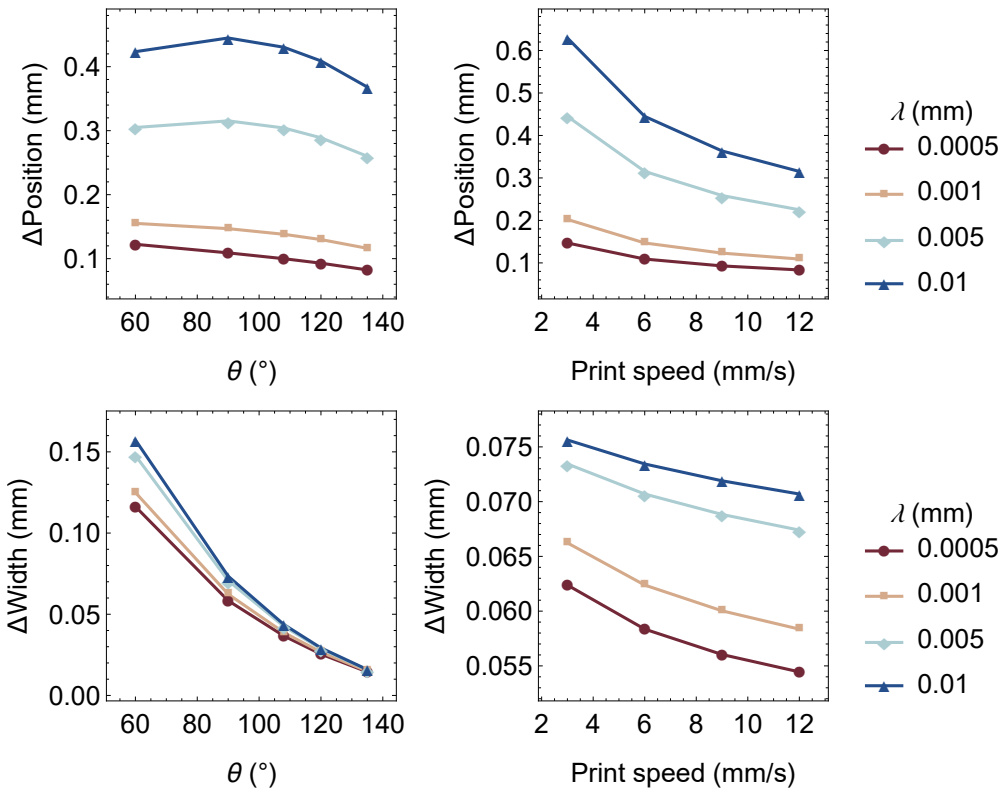

Figure 8.S3: Scaling of change in particle distribution position and width at the corner after shear for varying spreading length scales λ.

8.S1.2 Corner swelling with acceleration

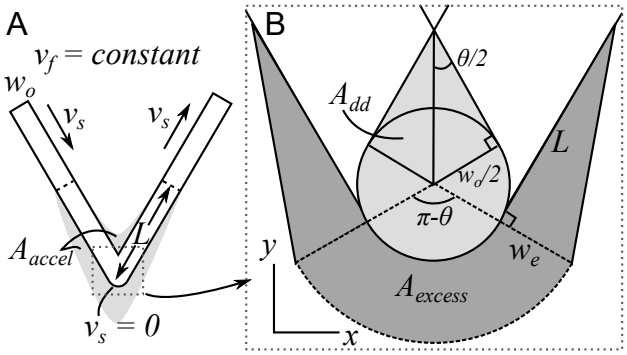

Figure 8.S4: Schematic of corner swell due to A) acceleration and B) double deposition.

There are two ways to structure the print path at a corner. First, the motor can cheat corners, sweeping an arc instead of a point. This is known as the *blended-move* scheme, which results in corner smoothing.[226, 229] Second, the motor can slow to a speed v_c (the jerk speed or ramp speed) at the corner, then accelerate. The jerk speed v_c depends on hardware capabilities and software settings, since the 3-axis gantry can only achieve a certain instantaneous acceleration, and jerk speeds which are too high will cause ringing. The Shopbot Desktop 3-axis stage used in these experiments uses this second method, known as *stop-at-turn*, which results in corner swelling.[226, 229] *Stop-at-turn* produces accurate nozzle positioning, but because the nozzle continues to extrude fluid at the same rate while the translation speed decreases, extra fluid is extruded at the corner (Fig. 8.S4A). The model used in the main body of the text assumes that the jerk speed is the same as the print speed, which is true for the experiments covered in this paper but will often not be true in other printing scenarios. Here, an analytical model which includes acceleration at the corner is described.

The amount of time that the nozzle spends decelerating to a translation speed of v_c and

accelerating at the corner t is

$$t_{accel} = \frac{2(v_s - v_c)}{a} \tag{8.S14}$$

Within that deceleration/acceleration zone, the average translation speed is $(v_s - v_c)/2$. As such, the length of the deceleration zone, which is equal to the length of the acceleration zone L, is

$$L = \frac{v_s - v_c}{2}\frac{t_{accel}}{2} = \frac{(v_s - v_c)^2}{2a} \tag{8.S15}$$

Under ideal conditions where the nozzle can instantaneously change speed, the amount of time spent in the zone of the same length

$$t_{ideal} = \frac{2L}{v_s} = \frac{(v_s - v_c)^2}{v_s a} \tag{8.S16}$$

As such, the added time spent in the acceleration/deceleration zone is

$$\Delta t_{excess} = t_{accel} - t_{ideal} = \frac{v_s^2 + v_c^2}{v_s a} \tag{8.S17}$$

During that added time, the nozzle extrudes an excess volume V_{accel} of ink

$$V_{accel} = v_f A_{nozzle} \Delta t_{excess} \tag{8.S18}$$

The experiments in this work use a flow speed equal to the translation speed, $v_f = v_s$ and a square nozzle of inner width w_o. As such,

$$V_{accel} = \frac{(v_s^2 - v_c^2)w_o^2}{a} \tag{8.S19}$$

In addition to acceleration, double deposition produces excess fluid (Fig. 8.S4B). Double

deposition occurs because every time the print path changes direction, the nozzle retraces some area that it already covered. Conventionally, the double deposition area is calculated assuming that the nozzle is circular with radius $w_o/2$ (Fig. 8.S4B). If the nozzle stops moving at the corner, the resultant traced path will have an outer radius of $w_o/2$. In the experiments in this paper, the nozzle has a square cross-section, so the corner should match the square cross-section of the nozzle. However, the orientation of that square would vary based on the orientation of the corner. On average, this work assumes that the shape of the corner is a circle with radius $w_o/2$.

The double deposition area A_{dd} can be expressed in terms of the corner angle θ and the corner width w_o.[229]

$$A_{dd} = 2(1/2)(w_o/2)(w_o/2\cot(\theta/2)) + (\pi+\theta)\pi(w_o/2)^2 \tag{8.S20}$$

Assuming that the height of the deposited line is the stand-off distance h, the excess volume from double deposition V_{dd} is thus

$$V_{dd} = \frac{w_o^2 h}{4}\Big(\cot\left(\frac{\theta}{2}\right) + \frac{\pi}{2} + \frac{\theta}{2}\Big) \tag{8.S21}$$

The total excess volume of fluid is

$$V_{excess} = V_{dd} + V_{accel} \tag{8.S22}$$

Ideally, the excess fluid would be deposited on the outer edge, in a sharp tip that falls within the intended print path.[229] However, this sharp tip disagrees with numerical models and experimental results that indicate that the printed corner exhibits a rounded tip.[226, 228, 233] Numerical models indicate that some of this excess volume will fall inside of the intended print path, and some will fall outside.[226] For a 90° corner, the volume of excess fluid deposited

outside the print path corner is 2–3 times the volume deposited inside the corner.[226] This ratio expands to 10 times for 30° corners.[226] There is no accurate analytical model which predicts the ratio of excess volume deposited inside the corner to outside the corner. For simplicity, this work assumes that all of the fluid is deposited outside of the corner in an arc of thickness w_e that borders the circular shape of the corner, flanked by two triangles of height L and width w_e, where L is the length of the deceleration/acceleration zone. This entire area has height h, which is the stand-off distance between the nozzle and the substrate. Using Equation 8.S22,

$$\frac{V_{excess}}{h} = \frac{\pi - \theta}{2\pi}\pi\left(\left(w_e + \frac{w_o}{2}\right)^2 - \left(\frac{w_o}{2}\right)^2\right) + w_e L \tag{8.S23}$$

Solving for the arc width w_e,

$$w_e = \frac{-((\pi - \theta)w_o/2 + L) + \sqrt{((\pi - \theta)w_o/2 + L)^2 + 2(\pi - \theta)V_{excess}/h}}{\pi - \theta} \tag{8.S24}$$

The difference in line width between the corner and the center of the edge is w_e. The difference in the position of the center of the line between the corner and center is $-w_e/2$, because the center of the line shifts outward toward negative positions.

As the corner angle increases, the excess volume from double deposition decreases. However, the arc length $\pi - \theta$ decreases while L remains the same, so more volume must be fit into a smaller length along the outside of the corner. As a result, w_e increases with corner angle. Note that this is the opposite of the trend predicted by double deposition alone and does not describe the experimental data collected in this paper.

8.S1.3 Rheology

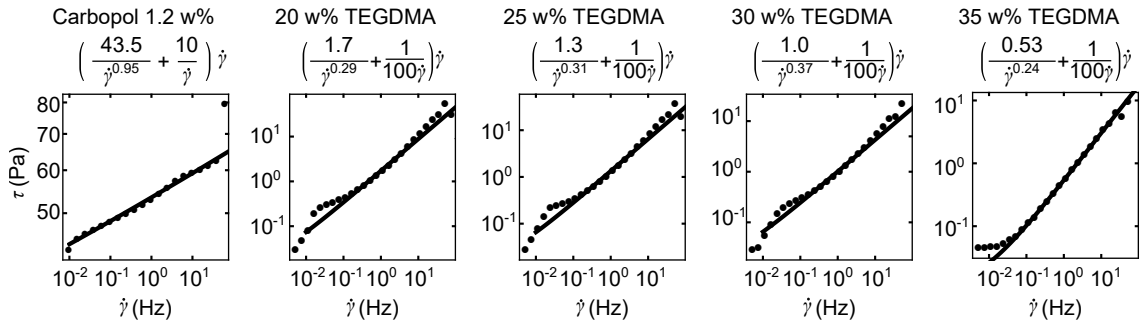

Figure 8.S5: Viscosity as a function of frequency for Carbopol support and inks with varying w% TEGDMA, fitted to the Herschel Bulkley model.

Viscosities were measured using a TA Instrument Company ARES-LS1 rheometer with 25 mm diameter flat plates and a 2 mm gap at room temperature. Dynamic frequency sweeps were conducted at 10% strain with increasing frequency. Dynamic strain sweeps were conducted at 10 Hz with increasing strain. To avoid curing and settling effects, inks did not contain photoinitiators or particles.

The inks used in this study are liquid-like at all stresses, whereby the loss modulus is always greater than the storage modulus (Fig. 8.S5B). These inks are shear thinning but have a weaker rate dependence than the support material. In these inks, TEGDMA acts as a diluent, so increasing the TEGDMA concentration decreases the loss modulus and viscosity (Fig. 8.S5).

8.S1.4 Ink composition effects on changes at the corner

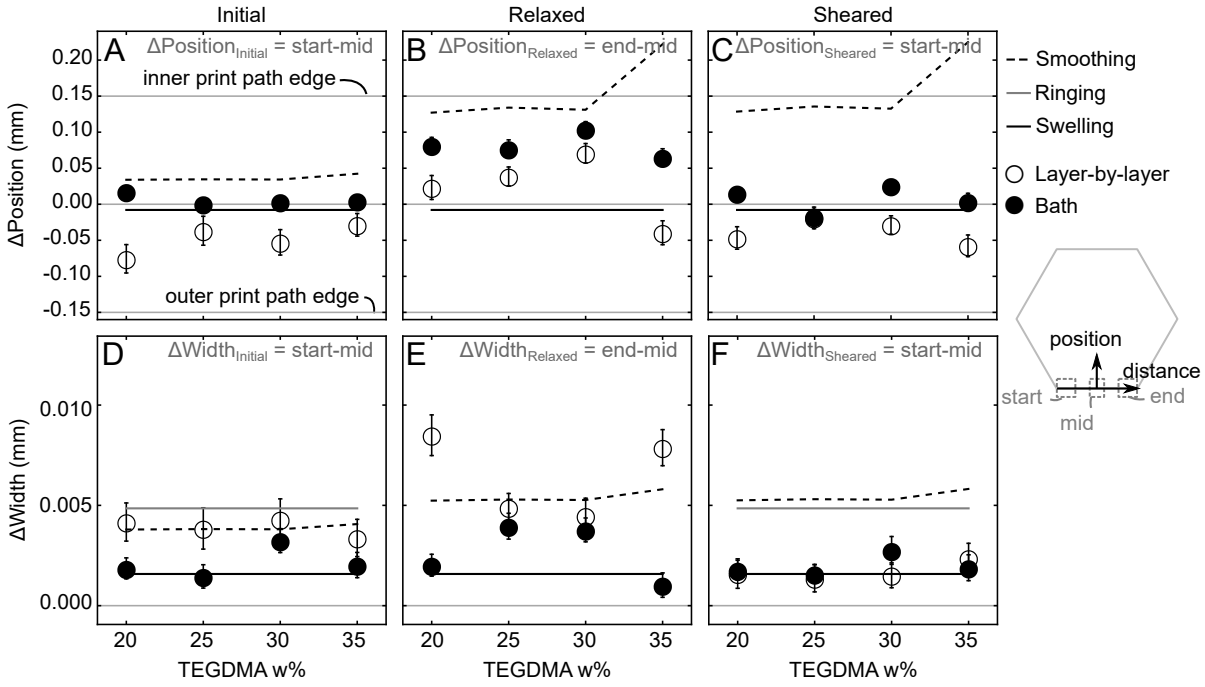

Figure 8.S6: Change in position and width of the particle distribution at the corner as a function of ink composition. Theoretical contributions of the smoothing, swelling, and ringing models are shown. Error bars indicate standard error.

The smoothing model only predicts a subtle dependency of change in width and position at the corner as a function of ink composition. At the highest TEGDMA loading and thus lowest viscosity, the smoothing model predicts an inward, positive shift in change in position and an increase in change in width. Experimental data indicate no strong dependence of change in position and change in width on TEGDMA content.

Chapter 9

Conclusions and future work

The work described in this dissertation describes a set of fundamental processing-structure relationships in direct ink writing with acoustic focusing (DIWA). These relationships are governed by acoustic forces, gravity, inertia, interfacial energy, viscoplasticity, viscous dissipation, and part design. We mapped a range of material properties, printing parameters, and part designs and examined the internal and external structure of printed filaments.

The tools that engineers and designers can use to manipulate the internal and external structures of printed filaments during DIWA are summarized here.

Increasing the viscosity of the matrix:

- Narrows the particle distribution in the nozzle and printed line[15]
- Increases filament spreading onto the substrate[15]
- Decreases filament stability for a given flow speed-translation speed combination[128]

In the models used in this work, viscosities have largely been modeled as Newtonian, even though the inks used in these studies are non-Newtonian. There are opportunities to reformulate Equations 4.6 and 5.2 for non-Newtonian fluids, where viscosities are spatially varying due to local gradients in shear stress. Numerical models may allow for greater accuracy than

analytical models in this regard. There is also space to expand these studies to a wider range of ink viscosities. Though the viscosities in these studies were chosen to enable both form holding and acoustophoresis, DIW inks for other applications may lie outside of the chosen viscosity ranges.

Using layer-by-layer support instead of bath support:

- Improves deposited particle distribution positioning accuracy[19]
- Widens deposited particle distributions[19]
- Limits direction dependent particle distribution positions due to flows around the nozzle and rotation of the deposited filament[18]
- Exacerbates direction dependent particle distribution widths due to asymmetry of the particle distribution in the nozzle[18]
- Exacerbates geometric inaccuracies at printed corners[20]

Chapter 4 and 5 demonstrate that there are clear advantages to using low viscosity matrices in DIWA. Chapter 6-8 demonstrate that support material enables printing of those low viscosity matrices without sacrificing form holding. Future work should implement support material and low viscosity matrices to print functional composites with designed microstructures via DIWA. For example, layer-by-layer support could be combined with Ref. [9] to produce three-dimensional flexible circuits with variable electrical conductivity filaments from a single ink reservoir. Alternatively, bath support could be combined with Ref. [22] and [212] to produce three-dimensional alginate bio-implants laden with tightly concentrated bundles of aligned cells. The UDMA-based ink formulations used in Chapters 5–8 were borrowed from a dental resin application.[170] Layer-by-layer support could be used to print dental crowns with aligned ceramic rods which mimic the hierarchical alignment of rods found in biogenic enamel.

A simpler biomimetic structure would be the layered precessing fiber orientation pattern known as the Bouligand structure found in the dactyl club of the mantis shrimp.[234] On this application in particular, DIWA has an advantage over stereolithography with acoustophoresis because DIW is capable of writing a continuum of fiber orientations, whereas stereolithography without a rotary stage is limited to a quantized set of orientations.

Increasing the surface energy of the nozzle (i.e. no fluorinated coating):

- Increases nozzle wetting[128]

Further work could probe whether nozzle functionalization can limit interactions between the nozzle and existing filaments, reducing changes during shear.

Increasing the acoustic wave amplitude:

- Narrows the particle distribution in the nozzle and printed line[15]

While the benefits of a large acoustic wave amplitude are clear, there are literal energy costs associated with driving the piezo at high voltages. Further studies could compare the energy used by the various field-assisted additive manufacturing techniques listed in the introduction in order to inform environmentally sustainable approaches to composite additive manufacturing.

Increasing the flow speed:

- Widens the particle distribution in the nozzle and printed line[15]
- Increases filament stability for a given translation speed[128]

Increasing the stand-off distance:

- Decreases filament stability for a given flow speed-translation speed combination[128]
- Increases nozzle wetting[128]
- Increases transverse flows[128]

While many works set the flow speed equal to the translation speed and the stand-off distance equal to the nozzle inner width, Chapter 5 demonstrates that these printing conditions are well within the region of stable print beads, and printing closer to the instability zone could improve preservation of filament microstructures during deposition and limit nozzle wetting. Chapter 5 poses a viscocapillary model for predicting print bead stability which can be used to select flow speeds, translation speeds, and stand-off distances. In order to improve the accuracy and adaptability of the model, further works could reformulate the model for other nozzle geometries and could build on the two-dimensional model to include three-dimensional effects.

In-situ curing should be employed:

- Partially inside the nozzle to preserve the narrowest particle distribution[15]
- Just after deposition to preserve the narrow particle distributions[19]
- After some relaxation time to preserve the most accurate particle positioning[19]

While *in-situ* curing has been proposed as a tool to preserve designed filament microstructures, further work is necessary to implement and evaluate *in-situ* curing. Particularly for partial curing inside the nozzle, ink compositions, curing parameters, and printing speeds will need to be calibrated in order to prevent nozzle clogging. Though Chapters 6–8 explicitly probed interactions between newly deposited filaments and existing filaments, further studies will be necessary to determine how a cured filament influences deposition of a new filament.

Bibliography

[1] G. Gao, B. S. Kim, J. Jang, and D.-w. Cho, *Recent strategies in extrusion-based three-dimensional cell printing toward organ biofabrication*, *ACS Biomaterials Science and Engineering* **5** (2019), no. 3 1150–1169.

[2] C. Zhu, A. J. Pascall, N. Dudukovic, M. A. Worsley, J. D. Kuntz, E. B. Duoss, and C. M. Spadaccini, *Colloidal Materials for 3D Printing*, *Annual Review of Chemical and Biomolecular Engineering* **10** (2019) 17–42.

[3] I. T. Ozbolat and M. Hospodiuk, *Current advances and future perspectives in extrusion-based bioprinting*, *Biomaterials* **76** (2016) 321–343.

[4] D. M. Kirchmajer, R. Gorkin, and M. in het Panhuis, *An overview of the suitability of hydrogel-forming polymers for extrusion-based 3D-printing*, *Journal of Materials Chemistry B* **3** (2015), no. 20 4105–4117.

[5] X. Wang, S. Xu, S. Zhou, W. Xu, M. Leary, P. Choong, M. Qian, M. Brandt, and Y. M. Xie, *Topological design and additive manufacturing of porous metals for bone scaffolds and orthopaedic implants: A review*, *Biomaterials* **83** (2016) 127–141.

[6] X. Wang, M. Jiang, Z. Zhou, J. Gou, and D. Hui, *3D printing of polymer matrix composites: A review and prospective*, *Composites Part B: Engineering* **110** (2017) 442–458.

[7] B. P. Conner, G. P. Manogharan, A. N. Martof, L. M. Rodomsky, C. M. Rodomsky, D. C. Jordan, and J. W. Limperos, *Making sense of 3-D printing: Creating a map of additive manufacturing products and services*, *Additive Manufacturing* **1** (2014) 64–76.

[8] R. R. Collino, T. R. Ray, R. C. Fleming, C. H. Sasaki, H. Haj-Hariri, and M. R. Begley, *Acoustic field controlled patterning and assembly of anisotropic particles*, *Extreme Mechanics Letters* **5** (2015) 37–46.

[9] D. S. Melchert, R. R. Collino, T. R. Ray, N. Dolinski, L. Friedrich, M. R. Begley, and D. S. Gianola, *Flexible conductive composites with programmed electrical anisotropy using acoustophoresis*, *Advanced Materials Technologies* **4** (2019), no. 12 1900586.

[10] Y. Y. Sriphutkiat, S. Kasetsirikul, D. Ketpun, Y. Zhou, and X. Wang, *Cells alignment and accumulation using acoustic nozzle for 3D printing*, *Proc. Of the 3rd Intl. Conf. on Progress in Additive Manufacturing* (2018), no. 2424-8967 383–388.

[11] J. P. Armstrong and M. M. Stevens, *Using remote fields for complex tissue engineering*, *Trends in Biotechnology* **In Press** (2019) 1–10.

[12] M. Akella and J. J. Juárez, *High-throughput acoustofluidic self-assembly of colloidal crystals*, *ACS Omega* **3** (2018), no. 2 1425–1436.

[13] R. R. Collino, T. R. Ray, R. C. Fleming, J. D. Cornell, B. G. Compton, and M. R. Begley, *Deposition of ordered two-phase materials using microfluidic print nozzles with acoustic focusing*, *Extreme Mechanics Letters* **8** (2016) 96–106.

[14] Y. Sriphutkiat, S. Kasetsirikul, D. Ketpun, and Y. Zhou, *Cell alignment and accumulation using acoustic nozzle for bioprinting*, *Scientific Reports* **9** (2019) 17774.

[15] L. Friedrich, R. Collino, T. Ray, and M. Begley, *Acoustic control of microstructures during direct ink writing of two-phase materials*, *Sensors and Actuators A: Physical* **268** (2017) 213–221.

[16] R. R. Collino, T. R. Ray, L. M. Friedrich, J. D. Cornell, C. D. Meinhart, and M. R. Begley, *Scaling relationships for acoustic control of two-phase microstructures during direct-write printing*, *Materials Research Letters* **6** (2018), no. 3 191–198.

[17] E. R. Dauson, K. B. Gregory, R. A. Heard, I. J. Oppenheim, S. W. Wong, and C. C. Zhou, *Ultrasonic microparticle alignment and direct ink writing using glass capillaries*, in *Proc. SPIE 10968, Behavior and Mechanics of Multifunctional Materials XIII*, p. 109680N, 2019.

[18] L. Friedrich and M. Begley, *Printing direction dependent microstructures in direct ink writing*, *Submitted for publication* (2020).

[19] L. Friedrich and M. Begley, *Changes in filament microstructures during direct ink writing with yield stress fluid support*, *Submitted for publication* (2020).

[20] L. Friedrich and M. Begley, *Corner accuracy in direct ink writing with support material*, *Submitted for publication* (2020).

[21] M. A. Whittaker, E. R. Dauson, J. A. Parra-Raad, R. A. Heard, and I. J. Oppenheim, *Ultrasonic alignment of microparticles in nozzle-like geometries*, in *Behavior and Mechanics of Multifunctional Materials and Composites XII*, p. 105960X, 2018.

[22] J. P. K. Armstrong, J. L. Puetzer, A. Serio, A. G. Guex, M. Kapnisi, A. Breant, Y. Zong, V. Assal, S. C. Skaalure, O. King, T. Murty, C. Meinert, A. C. Franklin, P. G. Bassindale, M. K. Nichols, C. M. Terracciano, D. W. Hutmacher, B. W. Drinkwater,

T. J. Klein, A. W. Perriman, and M. M. Stevens, *Engineering anisotropic muscle tissue using acoustic cell patterning*, *Advanced Materials* **30** (2018), no. 43 1802649.

[23] P. Chansoria and R. Shirwaiker, *Characterizing the process physics of ultrasound-assisted bioprinting*, *Scientific Reports* **9** (2019) 13889.

[24] F. Gesellchen, A. L. Bernassau, T. Déjardin, D. R. Cumming, and M. O. Riehle, *Cell patterning with a heptagon acoustic tweezer-application in neurite guidance*, *Lab on a Chip* **14** (2014), no. 13 2266–2275.

[25] S. M. Naseer, A. Manbachi, M. Samandari, P. Walch, Y. Gao, Y. S. Zhang, F. Davoudi, W. Wang, K. Abrinia, J. M. Cooper, A. Khademhosseini, and S. R. Shin, *Surface acoustic waves induced micropatterning of cells in gelatin methacryloyl (GelMA) hydrogels.*, *Biofabrication* **9** (2017), no. 1 015020.

[26] M.-S. Scholz, B. Drinkwater, and R. Trask, *Ultrasonic assembly of anisotropic short fibre reinforced composites*, *Ultrasonics* **54** (2014), no. 4 1015–1019.

[27] J. Greenhall and B. Raeymaekers, *3D printing macroscale engineered materials using ultrasound directed self-assembly and stereolithography*, *Advanced Materials Technologies* **2** (2017), no. 9 1–7.

[28] D. E. Yunus, S. Sohrabi, R. He, W. Shi, and Y. Liu, *Acoustic patterning for 3D embedded electrically conductive wire in stereolithography*, *Journal of Micromechanics and Microengineering* **27** (2017), no. 4 045016.

[29] L. Lu, Z. Zhang, J. Xu, and Y. Pan, *3D-printed polymer composites with acoustically assembled multidimensional filler networks for accelerated heat dissipation*, *Composites Part B: Engineering* **174** (2019) 106991.

[30] L. Lu, X. Tang, S. Hu, and Y. Pan, *Acoustic field-assisted particle patterning for smart polymer composite fabrication in stereolithography*, *3D Printing and Additive Manufacturing* **5** (2018), no. 2 151–159.

[31] M. Prisbrey, J. Greenhall, F. Guevara Vasquez, and B. Raeymaekers, *Ultrasound directed self-assembly of three-dimensional user-specified patterns of particles in a fluid medium*, *Journal of Applied Physics* **121** (2017), no. 1 014302.

[32] M. Saito and Y. Imanishi, *Host-guest composites containing ultrasonically arranged particles*, *Journal of materials science* **35** (2000), no. 10 2373–2377.

[33] K. Melde, E. Choi, Z. Wu, S. Palagi, T. Qiu, and P. Fischer, *Acoustic fabrication via the assembly and fusion of particles*, *Advanced Materials* **30** (2017), no. 3 1704507.

[34] T. Stichel, T. Laumer, T. Baumüller, P. Amend, and S. Roth, *Powder layer preparation using vibration-controlled capillary steel nozzles for additive manufacturing*, *Physics Procedia* **56** (2014) 157–166.

[35] F. Ning and W. Cong, *Microstructures and mechanical properties of Fe-Cr stainless steel parts fabricated by ultrasonic vibration-assisted laser engineered net shaping process*, *Materials Letters* **179** (2016) 61–64.

[36] F. Ning, Y. Hu, Z. Liu, W. Cong, Y. Li, and X. Wang, *Ultrasonic vibration-assisted laser engineered net shaping of Inconel 718 parts: A feasibility study*, *Procedia Manufacturing* **10** (2017) 771–778.

[37] D. Foresti, K. T. Kroll, R. Amissah, F. Sillani, K. A. Homan, D. Poulikakos, and J. A. Lewis, *Acoustophoretic printing*, *Science Advances* **4** (2018), no. 8 1–10.

[38] J. J. Martin, A. Caunter, A. Dendulk, S. Goodrich, R. Pembroke, D. Shores, and R. M. Erb, *Direct-write 3D printing of composite materials with magnetically aligned discontinuous reinforcement*, in *Micro- and Nanotechnology Sensors, Systems, and Applications IX*, p. 101941I, 2017.

[39] J. J. Martin, M. S. Riederer, M. D. Krebs, and R. M. Erb, *Understanding and overcoming shear alignment of fibers during extrusion*, *Soft Matter* **11** (2015), no. 2 400–405.

[40] D. Kokkinis, M. Schaffner, and A. R. Studart, *Multimaterial magnetically assisted 3D printing of composite materials*, *Nature Communications* **6** (2015) 8643.

[41] A. R. A. Fattah, E. Meleca, S. Mishriki, A. Lelic, F. Geng, R. P. Sahu, S. Ghosh, and I. K. Puri, *In situ 3D label-free contactless bioprinting of cells through diamagnetophoresis*, *ACS Biomaterials Science and Engineering* **2** (2016), no. 12 2133–2138.

[42] S. Ghosh, M. Tehrani, M. Al-Haik, and I. Puri, *Patterning the stiffness of elastomeric nanocomposites by magnetophoretic control of cross-linking impeder distribution*, *Materials* **8** (2015), no. 2 474–485.

[43] F. L. Bargardi, H. Le Ferrand, R. Libanori, and A. R. Studart, *Bio-inspired self-shaping ceramics*, *Nature Communications* **7** (2016) 13912.

[44] T. Ahn, H. J. Kim, J. Lee, D. G. Choi, J. Y. Jung, J. H. Choi, S. Jeon, J. D. Kim, and J. H. Jeong, *A facile patterning of silver nanowires using a magnetic printing method*, *Nanotechnology* **26** (2015), no. 34.

[45] L. Lu, P. Guo, and Y. Pan, *Magnetic-field-assisted projection stereolithography for three-dimensional printing of smart structures*, *Journal of Manufacturing Science and Engineering* **139** (2017), no. 7 071008.

[46] L. Lu, E. Baynojir Joyee, and Y. Pan, *Correlation between microscale magnetic particle distribution and magnetic-field-responsive performance of three-dimensional printed composites*, *Journal of Micro and Nano-Manufacturing* **6** (2017), no. 1 010904.

[47] L. Ren, B. Li, Z. Song, Q. Liu, L. Ren, and X. Zhou, *Bioinspired fiber-regulated composite with tunable permanent shape and shape memory properties via 3d magnetic printing*, *Composites Part B: Engineering* **164** (2019) 458–466.

[48] L. Ren, B. Li, Z. Song, Q. Liu, L. Ren, and X. Zhou, *3D printing of structural gradient soft actuators by variation of bioinspired architectures*, *Journal of Materials Science* **54** (2019), no. 8 6542–6551.

[49] J. J. Martin, B. E. Fiore, and R. M. Erb, *Designing bioinspired composite reinforcement architectures via 3D magnetic printing*, *Nature Communications* **6** (2015) 8641.

[50] T. Nakamoto and S. Kojima, *Layered thin film micro parts reinforced with aligned short fibers in laser stereolithography by applying magnetic field*, *Journal of Advanced Mechanical Design, Systems and Manufacturing* **6** (2012), no. 6 849–858.

[51] H. Song, J. Spencer, A. Jander, J. Nielsen, J. Stasiak, V. Kasperchik, and P. Dhagat, *Inkjet printing of magnetic materials with aligned anisotropy*, *Journal of Applied Physics* **115** (2014), no. 17 17E308.

[52] L. Wang, F. Li, M. Kuang, M. Gao, J. Wang, Y. Huang, L. Jiang, and Y. Song, *Interface manipulation for printing three-dimensional microstructures under magnetic guiding*, *Small* **11** (2015), no. 16 1900–1904.

[53] B. Nagarajan, A. F. Eufracio Aguilera, M. Wiechmann, A. J. Qureshi, and P. Mertiny, *Characterization of magnetic particle alignment in photosensitive polymer resin: A preliminary study for additive manufacturing processes*, *Additive Manufacturing* **22** (2018) 528–536.

[54] C. Lee and J. A. Tarbutton, *Electric poling-assisted additive manufacturing process for PVDF polymer-based piezoelectric device applications*, *Smart Materials and Structures* **23** (2014), no. 9 095044.

[55] C. Lee and J. A. Tarbutton, *Electric poling-assisted additive manufacturing process for lead-free piezoelectric device fabrication*, *Procedia Manufacturing* **1** (2015) 320–326.

[56] H. Kim, F. Torres, D. Villagran, C. Stewart, Y. Lin, and T. L. B. Tseng, *3D printing of BaTiO3/PVDF composites with electric in situ poling for pressure sensor applications*, *Macromolecular Materials and Engineering* **302** (2017), no. 11 1700229.

[57] H. Lee, B. Seong, J. Kim, Y. Jang, and D. Byun, *Direct alignment and patterning of silver nanowires by electrohydrodynamic jet printing*, *Small* **10** (2014), no. 19 3918–3922.

[58] Y. Yang, Z. Chen, X. Song, Z. Zhang, J. Zhang, K. K. Shung, Q. Zhou, and Y. Chen, *Biomimetic anisotropic reinforcement architectures by electrically assisted nanocomposite 3D printing*, *Advanced Materials* **29** (2017), no. 11 1605750.

[59] L. R. J. Holmes and J. C. Riddick, *Research summary of an additive manufacturing technology for the fabrication of 3D composites with tailored internal structure*, *Journal of Materials* **66** (2014), no. 2 270–274.

[60] P. Calvert, T. L. Lin, and H. Martin, *Extrusion freeform fabrication of chopped-fibre reinforced composites*, *High Performance Polymers* **9** (1997), no. 4 449–456.

[61] B. G. Compton and J. A. Lewis, *3D-printing of lightweight cellular composites*, *Advanced Materials* **26** (2014), no. 34 5930–5935.

[62] G. Franchin, L. Wahl, and P. Colombo, *Direct ink writing of ceramic matrix composite structures*, *Journal of the American Ceramic Society* **100** (2017), no. 10 4397–4401.

[63] G. Franchin, H. Maden, L. Wahl, A. Baliello, M. Pasetto, and P. Colombo, *Optimization and characterization of preceramic inks for direct ink writing of ceramic matrix composite structures*, *Materials* **11** (2018), no. 4 515.

[64] A. Sydney Gladman, E. A. Matsumoto, R. G. Nuzzo, L. Mahadevan, and J. A. Lewis, *Biomimetic 4D printing*, *Nature Materials* **15** (2016), no. 4 413–418.

[65] M. K. Hausmann, P. A. Rühs, G. Siqueira, J. Läuger, R. Libanori, T. Zimmermann, and A. R. Studart, *Dynamics of Cellulose Nanocrystal Alignment During 3D Printing*, *ACS Nano* **12** (2018), no. 7 6926–6937.

[66] N. S. Hmeidat, J. W. Kemp, and B. G. Compton, *High-strength epoxy nanocomposites for 3D printing*, *Composites Science and Technology* **160** (2018) 9–20.

[67] C. Mahajan and D. Cormier, *3D printing of carbon fiber composites with preferentially aligned fibers*, *Proceedings of the 2015 Industrial and Systems Engineering Reserach Conference* (2015) 2953–2963.

[68] J. Peng, T. L. Lin, and P. Calvert, *Orientation effects in freeformed short-fiber composites*, *Composites Part A: Applied Science and Manufacturing* **30** (1999), no. 2 133–138.

[69] R. A. Bubeck, M. Most, and T. Zhang, *3D printing and evaluation of novel nanographene-containing abs thermoplastics*, in *Polymer-Based Additive Manufacturing: Recent Developments*, pp. 53–68. American Chemical Society, 2019.

[70] D. Correa, A. Papadopoulou, C. Guberan, N. Jhaveri, S. Reichert, A. Menges, and S. Tibbits, *3D-printed wood: Programming hygroscopic material transformations*, *3D Printing and Additive Manufacturing* **2** (2015), no. 3 106–116.

[71] J. Liu, W. Li, Y. Guo, H. Zhang, and Z. Zhang, *Improved thermal conductivity of thermoplastic polyurethane via aligned boron nitride platelets assisted by 3D printing*, *Composites Part A: Applied Science and Manufacturing* **120** (2019) 140–146.

[72] M. L. Shofner, K. Lozano, F. J. Rodríguez-Macías, and E. V. Barrera, *Nanofiber-reinforced polymers prepared by fused deposition modeling*, *Journal of applied polymer science* **89** (2003), no. 11 3081–3090.

[73] M. Shofner, F. Rodrguez-Macas, R. Vaidyanathan, and E. Barrera, *Single wall nanotube and vapor grown carbon fiber reinforced polymers processed by extrusion freeform fabrication*, *Composites Part A: Applied Science and Manufacturing* **34** (2003), no. 12 1207–1217.

[74] H. L. Tekinalp, V. Kunc, G. M. Velez-Garcia, C. E. Duty, L. J. Love, A. K. Naskar, C. A. Blue, and S. Ozcan, *Highly oriented carbon fiber-polymer composites via additive manufacturing*, *Composites Science and Technology* **105** (2014) 144–150.

[75] S. Yu, Y. H. Hwang, J. Y. Hwang, and S. H. Hong, *Analytical study on the 3D-printed structure and mechanical properties of basalt fiber-reinforced PLA composites using X-ray microscopy*, *Composites Science and Technology* **175** (2019) 18–27.

[76] G. B. Jeffery, *The motion of ellipsoidal particles immersed in a viscous fluid*, *Proceedings of the Royal Society A: Mathematical, Physical and Engineering Sciences* **102** (1922), no. 715 161.

[77] J. R. Raney, B. G. Compton, J. Mueller, T. J. Ober, K. Shea, and J. A. Lewis, *Rotational 3D printing of damage-tolerant composites with programmable mechanics*, *Proceedings of the National Academy of Sciences* **115** (2018), no. 6 1198–1203.

[78] Y. D. Erdem, S. Wentao, S. Salman, and L. Yaling, *Shear induced alignment of short nanofibers in 3D printed polymer composites*, *Nanotechnology* **27** (2016) 495302.

[79] A. Blaeser, D. F. Duarte Campos, U. Puster, W. Richtering, M. M. Stevens, and H. Fischer, *Controlling shear stress in 3D bioprinting is a key factor to balance printing resolution and stem cell integrity*, *Advanced Healthcare Materials* **5** (2016), no. 3 326–333.

[80] J. O. Hardin, T. J. Ober, A. D. Valentine, and J. A. Lewis, *Microfluidic printheads for multimaterial 3D printing of viscoelastic inks*, *Advanced Materials* **27** (2015), no. 21 3279–3284.

[81] D. Kokkinis, F. Bouville, and A. R. Studart, *3D printing of materials with tunable failure via bioinspired mechanical gradients*, *Advanced Materials* **30** (2018) 1705808.

[82] J. M. Ortega, M. Golobic, J. D. Sain, J. M. Lenhardt, A. S. Wu, S. E. Fisher, L. X. Perez Perez, A. W. Jaycox, J. E. Smay, E. B. Duoss, and T. S. Wilson, *Active mixing of disparate inks for multimaterial 3D printing*, *Advanced Materials Technologies* **4** (2019), no. 7 1800717.

[83] L. Ren, Z. Song, H. Liu, Q. Han, C. Zhao, B. Derby, Q. Liu, and L. Ren, *3D printing of materials with spatially non-linearly varying properties*, *Materials and Design* **156** (2018) 470–479.

[84] W. Liu, Y. S. Zhang, M. A. Heinrich, F. De Ferrari, H. L. Jang, S. M. Bakht, M. M. Alvarez, J. Yang, Y. C. Li, G. Trujillo-de Santiago, A. K. Miri, K. Zhu, P. Khoshakhlagh, G. Prakash, H. Cheng, X. Guan, Z. Zhong, J. Ju, G. H. Zhu, X. Jin, S. R. Shin, M. R. Dokmeci, and A. Khademhosseini, *Rapid continuous multimaterial extrusion bioprinting*, *Advanced Materials* **29** (2017), no. 3 1604630.

[85] N. Oxman, E. Tsai, and M. Firstenberg, *Digital anisotropy: A variable elasticity rapid prototyping platform*, *Virtual and Physical Prototyping* **7** (2012), no. 4 261–274.

[86] R. L. Truby and J. A. Lewis, *Printing soft matter in three dimensions*, *Nature* **540** (2016), no. 7633 371–378.

[87] J. Wang and L. L. Shaw, *Fabrication of functionally graded materials via Inkjet color printing*, *Journal of the American Ceramic Society* **89** (2006), no. 10 3285–3289.

[88] A. F. Demirörs, D. Courty, R. Libanori, and A. R. Studart, *Periodically microstructured composite films made by electric- and magnetic-directed colloidal assembly*, *Proceedings of the National Academy of Sciences* **113** (2016), no. 17 4623–4628.

[89] S. Z. Guo, M. C. Heuzey, and D. Therriault, *Properties of polylactide inks for solvent-cast printing of three-dimensional freeform microstructures*, *Langmuir* **30** (2014), no. 4 1142–1150.

[90] J. E. Fromm, *Numerical calculation of the fluid dynamics of drop-on-demand jets*, *IBM Journal of Research and Development* **28** (1984), no. 3 322–333.

[91] C. Duty, C. Ajinjeru, V. Kishore, B. Compton, N. Hmeidat, X. Chen, P. Liu, A. Hassen, J. Lindahl, and V. Kunc, *What makes a material printable? A viscoelastic model for extrusion-based 3d printing of polymers*, *Journal of Manufacturing Processes* **35** (2018) 526–537.

[92] T. Jiang, J. G. Munguia-Lopez, S. Flores-Torres, J. Kort-Mascort, and J. M. Kinsella, *Extrusion bioprinting of soft materials: An emerging technique for biological model fabrication*, *Applied Physics Reviews* **6** (2019), no. 1 011310.

[93] W. Sun and Y.-X. Yuan, *Solving Nonlinear Least-Squares Problems*, in *Optimization Theory and Methods*, vol. 1, pp. 353–383. Springer, 2006.

[94] G. M. Gratson and J. A. Lewis, *Phase behavior and rheological properties of polyelectrolyte inks for direct-write assembly*, *Langmuir* **21** (2005), no. 1 457–464.

[95] J. A. Lewis, J. E. Smay, J. Stuecker, and J. Cesarano, *Direct ink writing of three-dimensional ceramic structures*, *Journal of the American Ceramic Society* **89** (2006), no. 12 3599–3609.

[96] J. E. Smay, J. Cesarano, and J. A. Lewis, *Colloidal inks for directed assembly of 3-D periodic structures*, *Langmuir* **18** (2002), no. 14 5429–5437.

[97] C. S. O'Bryan, T. Bhattacharjee, S. R. Niemi, S. Balachandar, N. Baldwin, S. T. Ellison, C. R. Taylor, W. G. Sawyer, and T. E. Angelini, *Three-dimensional printing with sacrificial materials for soft matter manufacturing*, *MRS Bulletin* **42** (2017), no. 8 571–577.

[98] R. D. Farahani, M. Dubé, and D. Therriault, *Three-dimensional printing of multifunctional nanocomposites: Manufacturing techniques and applications*, *Advanced Materials* **28** (2016), no. 28 5764–5821.

[99] T. Bhattacharjee, S. M. Zehnder, K. G. Rowe, S. Jain, R. M. Nixon, W. G. Sawyer, and T. E. Angelini, *Writing in the granular gel medium*, *Science Advances* **1** (2015), no. 8 e1500655.

[100] A. Grosskopf, R. Truby, H. Kim, A. Perazzo, J. A. Lewis, and H. A. Stone, *Viscoplastic matrix materials for embedded 3D printing*, *ACS Applied Materials & Interfaces* **10** (2018), no. 27 23353–23361.

[101] H. Chen, X. Wang, F. Xue, Y. Huang, K. Zhou, and D. Zhang, *3D printing of SiC ceramic: Direct ink writing with a solution of preceramic polymers*, *Journal of the European Ceramic Society* (2018).

[102] F. Liravi, R. Darleux, and E. Toyserkani, *Additive manufacturing of 3D structures with non-Newtonian highly viscous fluids: Finite element modeling and experimental validation*, *Additive Manufacturing* **13** (2017) 113–123.

[103] J. Lewis, *Direct ink writing of 3D functional materials*, *Advanced Functional Materials* **16** (2006), no. 17 2193–2204.

[104] R. B. Rao, K. L. Krafcik, A. M. Morales, and J. A. Lewis, *Microfabricated deposition nozzles for direct-write assembly of three-dimensional periodic structures*, *Advanced Materials* **17** (2005), no. 3 289–293.

[105] T. A. Baer, R. A. Cairncross, P. R. Schunk, R. R. Rao, and P. A. Sackinger, *A finite element method for free surface flows of incompressible fluids in three dimensions. Part II. Dynamic wetting lines*, *International Journal for Numerical Methods in Fluids* **33** (2000), no. 3 405–427.

[106] A. Shen, D. Caldwell, A. W. Ma, and S. Dardona, *Direct write fabrication of high-density parallel silver interconnects*, *Additive Manufacturing* **22** (2018) 343–350.

[107] S. Ubal, B. Xu, B. Derby, and P. Grassia, *Continuous deposition of a liquid thread onto a moving substrate. numerical analysis and comparison with experiments*, *Journal of Fluids Engineering* **134** (2012), no. 2 021301.

[108] A. Gleadall, I. Ashcroft, and J. Segal, *VOLCO: A predictive model for 3D printed microarchitecture*, *Additive Manufacturing* **21** (2018) 605–618.

[109] M. E. A. Papon, A. Haque, and M. A. R. Sharif, *Effect of nozzle geometry on melt flow simulation and structural property of thermoplastic nanocomposites in fused deposition modeling*, in *American Society of Composites 32nd Technical Conference*, (West Lafayette, Indiana), 2017.

[110] H. Yuk and X. Zhao, *A new 3D printing strategy by harnessing deformation, instability, and fracture of viscoelastic inks*, *Advanced Materials* **30** (2018) 1704028.

[111] M. Athanasiadis, A. Pak, D. Afanasenkau, and I. R. Minev, *Direct writing of elastic fibers with optical, electrical, and microfluidic functionality*, *Advanced Materials Technologies* **4** (2019) 1800659.

[112] B. M. Rauzan, A. Z. Nelson, S. E. Lehman, R. H. Ewoldt, and R. G. Nuzzo, *Particle-free emulsions for 4D printing elastomers*, *Advanced Functional Materials* **28** (2018) 1707032.

[113] J. W. Boley, E. L. White, G. T. Chiu, and R. K. Kramer, *Direct writing of gallium-indium alloy for stretchable electronics*, *Advanced Functional Materials* **24** (2014), no. 23 3501–3507.

[114] T. J. Hinton, Q. Jallerat, R. N. Palchesko, J. H. Park, M. S. Grodzicki, H.-J. Shue, M. H. Ramadan, A. R. Hudson, and A. W. Feinberg, *Three-dimensional printing of complex biological structures by freeform reversible embedding of suspended hydrogels*, *Science Advances* **1** (2015), no. 9 e1500758.

[115] G. Luo, Y. Yu, Y. Yuan, X. Chen, Z. Liu, and T. Kong, *Freeform, reconfigurable embedded printing of all-aqueous 3D architectures*, *Advanced Materials* **31** (2019), no. 49 1904631.

[116] J. J. Senior, M. E. Cooke, L. M. Grover, and A. M. Smith, *Fabrication of complex hydrogel structures using suspended layer additive manufacturing (SLAM)*, *Advanced Functional Materials* **29** (2019), no. 49 1904845.

[117] K. J. Leblanc, S. R. Niemi, A. I. Bennett, K. L. Harris, K. D. Schulze, W. G. Sawyer, C. Taylor, and T. E. Angelini, *Stability of high speed 3D printing in liquid-like solids*, *ACS Biomaterials Science and Engineering* **2** (2016), no. 10 1796–1799.

[118] T. J. Hinton, A. Hudson, K. Pusch, A. Lee, and A. W. Feinberg, *3D printing PDMS elastomer in a hydrophilic support bath via freeform reversible embedding*, *ACS Biomaterials Science and Engineering* **2** (2016), no. 10 1781–1786.

[119] D. L. Tokpavi, A. Magnin, and P. Jay, *Very slow flow of Bingham viscoplastic fluid around a circular cylinder*, *Journal of Non-Newtonian Fluid Mechanics* **154** (2008), no. 1 65–76.

[120] Y. Jin, A. Compaan, W. Chai, and Y. Huang, *Functional nanoclay suspension for printing-then-solidification of liquid materials*, *ACS Applied Materials and Interfaces* **9** (2017), no. 23 20057–20066.

[121] Y. Jin, K. Song, N. Gellermann, and Y. Huang, *Printing of hydrophobic materials in fumed silica nanoparticle suspension*, *ACS Applied Materials & Interfaces* **11** (2019) 29207–29217.

[122] C. S. O'Bryan, T. Bhattacharjee, S. L. Marshall, W. G. Sawyer, and T. E. Angelini, *Commercially available microgels for 3D bioprinting*, *Bioprinting* **11** (2018) e00037.

[123] J. T. Muth, P. G. Dixon, L. Woish, L. J. Gibson, and J. A. Lewis, *Architected cellular ceramics with tailored stiffness via direct foam writing*, *Proceedings of the National Academy of Sciences* **114** (2017), no. 8 1832–1837.

[124] A. Lenshof, C. Magnusson, and T. Laurell, *Acoustofluidics 8: Applications of acoustophoresis in continuous flow microsystems*, *Lab on a Chip* **12** (2012), no. 7 1210–1223.

[125] T. Laurell, F. Petersson, and A. Nilsson, *Chip integrated strategies for acoustic separation and manipulation of cells and particles*, *Chemical Society Reviews* **36** (2007), no. 3 492–506.

[126] A. Lenshof, M. Evander, T. Laurell, and J. Nilsson, *Acoustofluidics 5: Building microfluidic acoustic resonators*, *Lab on a Chip* **12** (2012), no. 4 684–695.

[127] H. Bruus, *Acoustofluidics 7: The acoustic radiation force on small particles*, *Lab on a Chip* **12** (2012), no. 6 1014–1021.

[128] L. Friedrich and M. Begley, *In situ characterization of low-viscosity direct ink writing: stability, wetting, and rotational flows*, *Journal of Colloid and Interface Science* **529** (2018) 599–609.

[129] Mathworks, "lsqnonlin."

[130] X. Ding, J. Liu, and T. A. L. Harris, *A review of the operating limits in slot die coating processes*, *AIChE Journal* **62** (2016), no. 7 2508–2524.

[131] B. G. Higgins and L. E. Scriven, *Capillary pressure and viscous pressure drop set bounds on coating bead operability*, *Chemical Engineering Science* **35** (1980), no. 3 673–682.

[132] C. I. Wolfram Research, Inc., *Mathematica, version 11.1*, 2017.

[133] L. G. Shapiro and G. C. Stockman, *Computer Vision*. Prentice-Hall, Inc., Upper Saddle River, New Jersey, 1 ed., 2001.

[134] T. Hassner and C. Liu, *Dense image correspondences for computer vision*. Springer, 2015.

[135] D. Fleet and Y. Weiss, *Motion Analysis, Optical Flow & Tracking*, in *Handbook of Mathematical Models in Computer Vision* (N. Paragios, Y. Chen, and O. Faugeras, eds.), ch. Optical Fl, pp. 237–257. Springer, Boston, MA, 2006.

[136] D. A. Forsyth and J. Ponce, *Computer vision: a modern approach*. Prentice Hall, Upper Saddle River, New Jersey, 1 ed., 2003.

[137] C. J. Hansen, R. Saksena, D. B. Kolesky, J. J. Vericella, S. J. Kranz, G. P. Muldowney, K. T. Christensen, and J. A. Lewis, *High-throughput printing via microvascular multinozzle arrays*, *Advanced Materials* **25** (2013), no. 1 96–102.

[138] J. Bruneaux, D. Therriault, and M. C. Heuzey, *Micro-extrusion of organic inks for direct-write assembly*, *Journal of Micromechanics and Microengineering* **18** (2008) 115020.

[139] M. T. Roberts, A. Mohraz, K. T. Christensen, and J. A. Lewis, *Direct flow visualization of colloidal gels in microfluidic channels*, *Langmuir* **23** (2007), no. 17 8726–8731.

[140] A. A. Armstrong, J. Norato, A. G. Alleyne, and A. J. Wagoner Johnson, *Direct process feedback in extrusion-based 3D bioprinting*, *Biofabrication* **12** (2019), no. 1 015017.

[141] A. Nibali, Z. He, S. Morgan, and L. Prendergast, *Numerical Coordinate Regression with Convolutional Neural Networks*, *arXiv* (2018) 1–10, [1801.0737].

[142] A. Nguyen, J. Yosinski, and J. Clune, *Deep Neural Networks are Easily Fooled : High Confidence Predictions for Unrecognizable Images*, in *The IEEE Conference on Computer Vision and Pattern Recognition (CVPR)*, pp. 427–436, 2015.

[143] P. Mukhopadhyay and B. B. Chaudhuri, *A survey of Hough Transform*, *Pattern Recognition* **48** (2015), no. 3 993–1010.

[144] M. Raffel, C. E. Willert, S. T. Wereley, and J. Kompenhans, *Particle Image Velocimetry: A Practical Guide*. Springer Berlin Heidelberg, Berlin, Heidelberg, 2 ed., 2007.

[145] S. T. Wereley and C. D. Meinhart, *Recent Advances in Micro-Particle Image Velocimetry*, *Annual Review of Fluid Mechanics* **42** (2010), no. 1 557–576.

[146] D. K. Owens and R. C. Wendt, *Estimation of the surface free energy of polymers*, *Journal of Applied Polymer Science* **13** (1969), no. 8 1741–1747.

[147] C. M. S. Vicente, P. S. Andre, and R. A. S. Ferreira, *Simple measurement of surface free energy using a web cam*, *Revista Brasileira de Ensino de Fisica* **34** (2012), no. 3 3312.

[148] A. Bateni, S. S. Susnar, A. Amirfazli, and A. W. Neumann, *A high-accuracy polynomial fitting approach to determine contact angles*, *Colloids and Surfaces A: Physicochemical and Engineering Aspects* **219** (2003), no. 1-3 215–231.

[149] P. Cheng, D. Li, L. Boruvka, Y. Rotenberg, and A. W. Neumann, *Automation of axisymmetric drop shape analysis for measurements of interfacial tensions and contact angles*, *Colloids and Surfaces* **43** (1990), no. 2 151–167.

[150] G. Bracco and B. Holst, *Surface science techniques*, vol. 51. Springer, 2013.

[151] E. W. Weisstein, "Levenberg-Marquardt Method."

[152] T. S. Ahearn, R. T. Staff, T. W. Redpath, and S. I. K. Semple, *The use of the LevenbergMarquardt curve-fitting algorithm in pharmacokinetic modelling of DCE-MRI data*, *Physics in Medicine and Biology* **50** (2005), no. 9 N85–N92.

[153] A. Benjeddou, E. Jankovich, and T. Hadhri, *Determination of the parameters of the Ogden law using biaxial data and Levenberg-Marquardt-Fletcher algorithm*, *Journal of Elastomers and Plastics* **25** (1993) 224–248.

[154] J. D. Berry, M. J. Neeson, R. R. Dagastine, D. Y. C. Chan, and R. F. Tabor, *Measurement of surface and interfacial tension using pendant drop tensiometry*, *Journal of Colloid and Interface Science* **454** (2015) 226–237.

[155] L. S. H. Ngia and J. Sjoberg, *Efficient training of neural nets for nonlinear adaptive filtering using a recursive Levenberg-Marquardt algorithm*, *IEEE Transactions on Signal Processing* **48** (2000), no. 7 1915–1927.

[156] X. Wang, J. Xiong, L. Geng, J. Zheng, and S. Zhu, *Parameter identification of doubly-fed induction generator by the Levenberg-Marquardt-Fletcher method*, in *IEEE Power and Energy Society General Meeting*, pp. 1–5, 2013.

[157] R. Fletcher, *A modified Marquardt subroutine for non-linear least squares*, tech. rep., United Kingdom Atomic Energy Authority Research Group, 1971.

[158] D. W. Marquardt, *An algorithm for least-squares estimation of nonlinear parameters*, *Journal of the Society for Industrial and Applied Mathematics* **11** (1963), no. 2 431–441.

[159] A. Conn, N. Gould, and P. L. Toint, *Trust Region Methods*. SIAM, 2000.

[160] J. Nocedal and S. J. Wright, *Numerical Optimization*. Springer, 2006.

[161] Y. Bard, *Nonlinear Parameter Estimation*. Academic Press, 1974.

[162] K. Amini and F. Rostami, *Three-steps modified Levenberg-Marquardt method with a new line search for systems of nonlinear equations*, *Journal of Computational and Applied Mathematics* **300** (2016) 30–42.

[163] W. Zhou, *On the convergence of the modified Levenberg-Marquardt method with a nonmonotone second order Armijo type line search*, *Journal of Computational and Applied Mathematics* **239** (2013), no. 1 152–161.

[164] N. Yamashita and M. Fukushima, *On the rate of convergence of the Levenberg-Marquardt method*, *Computing* **15** (2001) 239–249.

[165] J. Y. Fan and Y. X. Yuan, *On the quadratic convergence of the Levenberg-Marquardt method without nonsingularity assumption*, *Computing* **74** (2005), no. 1 23–39.

[166] J. Fan and J. Pan, *Convergence properties of a self-adaptive Levenberg-Marquardt algorithm under local error bound condition*, *Computational Optimization and Applications* **34** (2006), no. 1 47–62.

[167] C. Ma and L. Jiang, *Some research on Levenberg-Marquardt method for the nonlinear equations*, *Applied Mathematics and Computation* **184** (2007), no. 2 1032–1040.

[168] J. Fan and J. Pan, *A note on the Levenberg-Marquardt parameter*, *Applied Mathematics and Computation* **207** (2009), no. 2 351–359.

[169] J.-Y. Fan, *A modified Levenberg-Marquardt algorithm for singular system of nonlinear equations*, *Journal of Computational Mathematics* **21** (2003), no. 5 625–636.

[170] S. Asmusen, G. Arenas, W. D. Cook, and C. Vallo, *Photobleaching of camphorquinone during polymerization of dimethacrylate-based resins*, *Dental Materials* **25** (2009), no. 12 1603–1611.

[171] L. Friedrich and M. Begley, *In situ digital image analysis in direct ink writing*, in *Polymer-Based Additive Manufacturing: Recent Developments*, pp. 131–149. American Chemical Society, 2019.

[172] J. Buolamwini and T. Gebru, *Gender shades: Intersectional accuracy disparities in commercial gender classification*, *Proceedings of Machine Learning Research* **81** (2018) 1–15.

[173] J. Zhao, T. Wang, M. Yatskar, V. Ordonez, and K.-W. Chang, *Men Also Like Shopping: Reducing Gender Bias Amplification using Corpus-level Constraints*, *arXiv* (2017) [arXiv:1707.0945].

[174] M. Bennamoun and G. Mamic, *Recognition by parts and part segmentation techniques*, in *Object recognition: fundamentals and case studies*, pp. 230–233. Springer, 2002.

[175] L. Friedrich, *In situ characterization of low-viscosity direct ink writing: stability, wetting, and rotational flows*, *Mendeley Data* **v1** (2018).

[176] M. Bennamoun and B. Boashash, *A structural-description-based vision system for automatic object recognition*, *IEEE Transactions on Systems, Man, and Cybernetics, Part B: Cybernetics* **27** (1997), no. 6 893–906.

[177] Z. J. Taylor, R. Gurka, G. A. Kopp, and A. Liberzon, *Long-duration time-resolved PIV to study unsteady aerodynamics*, *IEEE Transactions on Instrumentation and Measurement* **59** (2010), no. 12 3262–3269.

[178] A. Schroeder and C. E. Willert, *Particle image velocimetry : new developments and recent applications*. Springer, 2008.

[179] W. Zhong, F. Li, Z. Zhang, L. Song, and Z. Li, *Short fiber reinforced composites for fused deposition modeling*, *Materials Science and Engineering: A* **301** (2001), no. 2 125–130.

[180] X. Tian, T. Liu, C. Yang, Q. Wang, and D. Li, *Interface and performance of 3D printed continuous carbon fiber reinforced PLA composites*, *Composites Part A: Applied Science and Manufacturing* **88** (2016) 198–205.

[181] T. Serra, J. Planell, and M. Navarro, *High-resolution PLA-based composite scaffolds via 3-D printing technology*, *Acta Biomaterialia* **9** (2013), no. 3 5521–5530.

[182] Y. Luo, C. Wu, A. Lode, and M. Gelinsky, *Hierarchical mesoporous bioactive glass/alginate composite scaffolds fabricated by three-dimensional plotting for bone tissue engineering*, *Biofabrication* **5** (2013), no. 1 015005.

[183] T. Sun, Q. Huang, Q. Shi, H. Wang, X. Liu, M. Seki, M. Nakajima, and T. Fukuda, *Magnetic assembly of microfluidic spun alginate microfibers for fabricating three-dimensional cell-laden hydrogel constructs*, *Microfluidics and Nanofluidics* **19** (2015), no. 5 1169–1180.

[184] P. van der Asdonk, S. Kragt, and P. H. J. Kouwer, *Directing soft matter in water using electric fields*, *ACS Applied Materials & Interfaces* **8** (2016), no. 25 16303–16309.

[185] A. J. Pascall, F. Qian, G. Wang, M. A. Worsley, Y. Li, and J. D. Kuntz, *Light-directed electrophoretic deposition: A new additive manufacturing technique for arbitrarily patterned 3D composites*, *Advanced Materials* **26** (2014), no. 14 2252–2256.

[186] T. M. Llewellyn-Jones, B. W. Drinkwater, and R. S. Trask, *3D printed components with ultrasonically arranged microscale structure*, *Smart Materials and Structures* **25** (2016), no. 2 02LT01.

[187] J. de Ruiter, J. M. Oh, D. van den Ende, and F. Mugele, *Dynamics of Collapse of Air Films in Drop Impact*, *Physical Review Letters* **108** (2012), no. 7 074505.

[188] Y. Son, *Determination of shear viscosity and shear rate from pressure drop and flow rate relationship in a rectangular channel*, *Polymer* **48** (2007), no. 2 632–637.

[189] D. C. Montgomery, *Design and Analysis of Experiments*. John Wiley & Sons, Inc., 8 ed., 2013.

[190] A. Shauly, A. Averbakh, A. Nir, and R. Semiat, *Slow viscous flows of highly concentrated suspensionsPart II: Particle migration, velocity and concentration profiles in rectangular ducts*, *International Journal of Multiphase Flow* **23** (1997), no. 4 613–629.

[191] D. Leighton and A. Acrivos, *The shear-induced migration of particles in concentrated suspensions*, *Journal of Fluid Mechanics* **181** (1987), no. 1987 415–439.

[192] J. Lighthill, *Acoustic streaming*, *Journal of sound and vibration* **61** (1978), no. 3 391–418.

[193] M. D. Haslam and B. Raeymaekers, *Aligning carbon nanotubes using bulk acoustic waves to reinforce polymer composites*, *Composites Part B: Engineering* **60** (2014) 91–97.

[194] F. G. Mitri, F. H. Garzon, and D. N. Sinha, *Characterization of acoustically engineered polymer nanocomposite metamaterials using x-ray microcomputed tomography*, *Review of Scientific Instruments* **82** (2011), no. 3 034903.

[195] Z. Rozynek, M. Han, F. Dutka, P. Garstecki, A. Józefczak, and E. Luijten, *Formation of printable granular and colloidal chains through capillary effects and dielectrophoresis*, *Nature Communications* **8** (2017) 15255.

[196] J. P. Lewicki, J. N. Rodriguez, C. Zhu, M. A. Worsley, A. S. Wu, Y. Kanarska, J. D. Horn, E. B. Duoss, J. M. Ortega, W. Elmer, R. Hensleigh, R. A. Fellini, and M. J. King, *3D-printing of meso-structurally ordered carbon fiber/polymer composites with unprecedented orthotropic physical properties*, *Scientific Reports* **7** (2017) 43401.

[197] G. Siqueira, D. Kokkinis, R. Libanori, M. K. Hausmann, A. S. Gladman, A. Neels, P. Tingaut, T. Zimmermann, J. A. Lewis, and A. R. Studart, *Cellulose nanocrystal inks for 3D printing of textured cellular architectures*, *Advanced Functional Materials* **27** (2017) 1604619.

[198] A. Cameron, *Basic Lubrication Theory*. Ellis Horwood Limited, West Sussex, England, 3 ed., 1981.

[199] P. Ekworapoj, R. Magaraphani, and D. C. Martin, *Heat effect on viscosity and curing of light-cured dental resin and mechanical strength of conventional dental composites.*, *Journal of Metals, Materials and Minerals* **12** (2002), no. 1 39–50.

[200] U. Srinivasan, M. R. Houston, R. T. Howe, and R. Maboudian, *Alkyltrichlorosilane-based self-assembled monolayer films for stiction reduction in silicon micromachines*, *Journal of Microelectromechanical Systems* **7** (1998), no. 2 252–259.

[201] E. Asmussen and A. Peutzfeldt, *Surface energy characteristics of adhesive monomers*, *Dental Materials* **14** (1998) 21–28.

[202] M. S. Carvalho and H. S. Kheshgi, *Low-flow limit in slot coating: Theory and experiments*, *AIChE Journal* **46** (2000), no. 10 1907–1917.

[203] Y. Shikhmurzaev, *Capillary Flows with Forming Interfaces*. Chapman & Hall/CRC, 2007.

[204] O. E. Yildirim and O. A. Basaran, *Deformation and breakup of stretching bridges of Newtonian and shear-thinning liquids: Comparison of one- and two-dimensional models*, *Chemical Engineering Science* **56** (2001), no. 1 211–233.

[205] M. Yao and G. H. McKinley, *Numerical simulation of extensional deformations of viscoelastic liquid bridges in filament stretching devices*, *Journal of Non-Newtonian Fluid Mechanics* **74** (1998), no. 1 47–88.

[206] S. Middleman, *Stability of a viscoelastic jet*, *Chemical Engineering Science* **20** (1965) 1037–1040.

[207] J. P. Lenczyk and K. M. Kiser, *Stability of vertical jets of non-Newtonian fluids*, *AIChE Journal* **17** (1971), no. 4 826–831.

[208] C.-F. Lin, B.-K. Wang, C. Tiu, and T.-J. Liu, *On the pinning of downstream meniscus for slot die coating*, *Advances in Polymer Technology* **32** (2013), no. S1 E250–E257.

[209] J. Nam and M. S. Carvalho, *Flow in tensioned-web-over-slot die coating: Effect of die lip design*, *Chemical Engineering Science* **65** (2010), no. 13 3957–3971.

[210] Y. Kim, H. Yuk, R. Zhao, S. A. Chester, and X. Zhao, *Printing ferromagnetic domains for untethered fast-transforming soft materials*, *Nature* **558** (2018) 274–279.

[211] Z. Ma, A. W. Holle, K. Melde, T. Qiu, K. Poeppel, V. M. Kadiri, and P. Fischer, *Acoustic holographic cell patterning in a biocompatible hydrogel*, *Advanced Materials* (2019) 1904181.

[212] Y. Jin, A. Compaan, T. Bhattacharjee, and Y. Huang, *Granular gel support-enabled extrusion of three-dimensional alginate and cellular structures*, *Biofabrication* **8** (2016), no. 2 025016.

[213] A. K. Dhiman, R. P. Chhabra, and V. Eswaran, *Steady flow of power-law fluids across a square cylinder*, *Chemical Engineering Research and Design* **84** (2006), no. A4 300–310.

[214] A. K. Dhiman, R. P. Chhabra, and V. Eswaran, *Steady flow across a confined square cylinder: Effects of power-law index and blockage ratio*, *Journal of Non-Newtonian Fluid Mechanics* **148** (2008), no. 1-3 141–150.

[215] P. Dey and A. K. R. Das, *A numerical study on effect of corner radius and Reynolds number on fluid flow over a square cylinder*, *Sādhanā* **42** (2017), no. 7 1155–1165.

[216] P. K. Rao, A. K. Sahu, and R. P. Chhabra, *Momentum and heat transfer from a square cylinder in power-law fluids*, *International Journal of Heat and Mass Transfer* **54** (2011), no. 1-3 390–403.

[217] C. W. Extrand and S. I. Moon, *When sessile drops are no longer small: Transitions from spherical to fully flattened*, *Langmuir* **26** (2010), no. 14 11815–11822.

[218] L. Friedrich, *PIV and digital image analysis of direct ink writing with acoustophoresis and yield stress fluid support*, *Mendeley Data* **V1** (2020).

[219] M. G. Kendall, *A new measure of rank correlation*, *Biometrika* **30** (1938), no. 1-2 81–93.

[220] D. Bonn, J. Eggers, J. Indekeu, J. Meunier, and E. Rolley, *Wetting and spreading*, *Reviews of Modern Physics* **81** (2009), no. 2 739–805.

[221] L. Jørgensen, M. Le Merrer, H. Delanoë-Ayari, and C. Barentin, *Yield stress and elasticity influence on surface tension measurements*, *Soft Matter* **11** (2015) 5111–5121.

[222] G. G. Stokes, *On the effect of internal friction of fluids on the motion of pendulums*, *Transactions of the Cambridge Philosophical Society* **9** (1851), no. ii 8–106.

[223] E. Duoss, M. Twardowski, and J. Lewis, *Sol-gel inks for direct-write assembly of functional oxides*, *Advanced Materials* **19** (2007), no. 21 3485–3489.

[224] R. A. Barry, R. F. Shepherd, J. N. Hanson, R. G. Nuzzo, P. Wiltzius, and J. A. Lewis, *Direct-write assembly of 3D hydrogel scaffolds for guided cell growth*, *Advanced Materials* **21** (2009), no. 23 2407–2410.

[225] J. Taboas, R. Maddox, P. Krebsbach, and S. Hollister, *Indirect solid free form fabrication of local and global porous, biomimetic and composite 3D polymer-ceramic scaffolds*, *Biomaterials* **24** (2003), no. 1 181–194.

[226] R. Comminal, M. P. Serdeczny, D. B. Pedersen, and J. Spangenberg, *Motion planning and numerical simulation of material deposition at corners in extrusion additive manufacturing*, *Additive Manufacturing* **29** (2019) 100753.

[227] K.-M. Huang, T.-Y. Tsou, C.-W. Chang, and Y.-C. Liao, *Stability analysis of printed liquid elbows*, *Langmuir* **33** (2017), no. 2 645–651.

[228] P. Kulkarni and D. Dutta, *Deposition strategies and resulting part stiffnesses in fused deposition modeling*, *Journal of Manufacturing Science and Engineering* **121** (1999), no. 1 93–103.

[229] W. Han, M. A. Jafari, S. C. Danforth, and A. Safari, *Tool path-based deposition planning in fused deposition processes*, *Journal of Manufacturing Science and Engineering* **124** (2002), no. 2 462.

[230] C. Okwudire, S. Huggi, S. Supe, C. Huang, and B. Zeng, *Low-level control of 3D printers from the cloud: A step toward 3d printer control as a service*, *Inventions* **3** (2018), no. 3 56.

[231] M. Galati, P. Minetola, G. Marchiandi, E. Atzeni, F. Calignano, A. Salmi, and L. Iuliano, *A methodology for evaluating the aesthetic quality of 3D printed parts*, *Procedia CIRP* **79** (2019) 95–100.

[232] T. D. Blake, *The physics of moving wetting lines*, *Journal of Colloid and Interface Science* **299** (2006) 1–13.

[233] J.-H. Kao and F. B. Prinz, *Optimal motion planning for deposition in layered manufacturing*, in *1998 ASME Design Engineering Technical Conferences*, pp. 1–10, 1998.

[234] L. K. Grunenfelder, S. Herrera, and D. Kisailus, *Crustacean-derived biomimetic components and nanostructured composites*, *Small* **10** (2014), no. 16 3207–3232.